NEUROTRANSMITTER TRANSPORTERS: FROM THE BIOPHYSICS OF THE TRANSPORT PROCESS TO ITS IMPLICATIONS FOR SYNAPSE AND CIRCUIT FUNCTION

EDITED BY: Annalisa Scimemi, Renae Ryan and Susan L. Ingram

PUBLISHED IN: Frontiers in Cellular Neuroscience

frontiers Research Topics

ISSN 1664-8714
ISBN 978-2-88976-516-4
DOI 10.3389/978-2-88976-516-4

About Frontiers

Frontiers is more than just an open-access publisher of scholarly articles: it is a pioneering approach to the world of academia, radically improving the way scholarly research is managed. The grand vision of Frontiers is a world where all people have an equal opportunity to seek, share and generate knowledge. Frontiers provides immediate and permanent online open access to all its publications, but this alone is not enough to realize our grand goals.

Frontiers Journal Series

The Frontiers Journal Series is a multi-tier and interdisciplinary set of open-access, online journals, promising a paradigm shift from the current review, selection and dissemination processes in academic publishing. All Frontiers journals are driven by researchers for researchers; therefore, they constitute a service to the scholarly community. At the same time, the Frontiers Journal Series operates on a revolutionary invention, the tiered publishing system, initially addressing specific communities of scholars, and gradually climbing up to broader public understanding, thus serving the interests of the lay society, too.

Dedication to Quality

Each Frontiers article is a landmark of the highest quality, thanks to genuinely collaborative interactions between authors and review editors, who include some of the world's best academicians. Research must be certified by peers before entering a stream of knowledge that may eventually reach the public - and shape society; therefore, Frontiers only applies the most rigorous and unbiased reviews.
Frontiers revolutionizes research publishing by freely delivering the most outstanding research, evaluated with no bias from both the academic and social point of view. By applying the most advanced information technologies, Frontiers is catapulting scholarly publishing into a new generation.

What are Frontiers Research Topics?

Frontiers Research Topics are very popular trademarks of the Frontiers Journals Series: they are collections of at least ten articles, all centered on a particular subject. With their unique mix of varied contributions from Original Research to Review Articles, Frontiers Research Topics unify the most influential researchers, the latest key findings and historical advances in a hot research area! Find out more on how to host your own Frontiers Research Topic or contribute to one as an author by contacting the Frontiers Editorial Office: frontiersin.org/about/contact

NEUROTRANSMITTER TRANSPORTERS: FROM THE BIOPHYSICS OF THE TRANSPORT PROCESS TO ITS IMPLICATIONS FOR SYNAPSE AND CIRCUIT FUNCTION

Topic Editors:
Annalisa Scimemi, University at Albany, United States
Renae Ryan, The University of Sydney, Australia
Susan L. Ingram, Oregon Health and Science University, United States

Citation: Scimemi, A., Ryan, R., Ingram, S. L., eds. (2022). Neurotransmitter Transporters: From the Biophysics of the Transport Process to its Implications for Synapse and Circuit Function. Lausanne: Frontiers Media SA.
doi: 10.3389/978-2-88976-516-4

Table of Contents

frontiers in Cellular Neuroscience

MINI REVIEW
published: 02 February 2021
doi: 10.3389/fncel.2021.637784

Disruption of Glutamate Transport and Homeostasis by Acute Metabolic Stress

Stefan Passlick[1]*, *Christine R. Rose*[2], *Gabor C. Petzold*[3,4] and *Christian Henneberger*[1,3,5]*

[1]Institute of Cellular Neurosciences, Medical Faculty, University of Bonn, Bonn, Germany, [2]Institute of Neurobiology, Faculty of Mathematics and Natural Sciences, Heinrich Heine University Duesseldorf, Duesseldorf, Germany, [3]German Center for Neurodegenerative Diseases (DZNE), Bonn, Germany, [4]Division of Vascular Neurology, University Hospital Bonn, Bonn, Germany, [5]Institute of Neurology, University College London, London, United Kingdom

High-affinity, Na^+-dependent glutamate transporters are the primary means by which synaptically released glutamate is removed from the extracellular space. They restrict the spread of glutamate from the synaptic cleft into the perisynaptic space and reduce its spillover to neighboring synapses. Thereby, glutamate uptake increases the spatial precision of synaptic communication. Its dysfunction and the entailing rise of the extracellular glutamate concentration accompanied by an increased spread of glutamate result in a loss of precision and in enhanced excitation, which can eventually lead to neuronal death *via* excitotoxicity. Efficient glutamate uptake depends on a negative resting membrane potential as well as on the transmembrane gradients of the co-transported ions (Na^+, K^+, and H^+) and thus on the proper functioning of the Na^+/K^+-ATPase. Consequently, numerous studies have documented the impact of an energy shortage, as occurring for instance during an ischemic stroke, on glutamate clearance and homeostasis. The observations range from rapid changes in the transport activity to altered expression of glutamate transporters. Notably, while astrocytes account for the majority of glutamate uptake under physiological conditions, they may also become a source of extracellular glutamate elevation during metabolic stress. However, the mechanisms of the latter phenomenon are still under debate. Here, we review the recent literature addressing changes of glutamate uptake and homeostasis triggered by acute metabolic stress, i.e., on a timescale of seconds to minutes.

Keywords: glutamate transport, EAAT, astrocyte, metabolic stress, ischemia, stroke, excitotoxicity

OPEN ACCESS

Edited by:
Annalisa Scimemi, University at Albany, United States

Reviewed by:
Christof Grewer, Binghamton University, United States
Brian Billups, Australian National University, Australia

***Correspondence:**
Stefan Passlick
stefan.passlick@uni-bonn.de
Christian Henneberger
christian.henneberger@uni-bonn.de

Specialty section:
This article was submitted to Cellular Neurophysiology, a section of the journal Frontiers in Cellular Neuroscience

Received: *04 December 2020*
Accepted: *11 January 2021*
Published: *02 February 2021*

Citation:
Passlick S, Rose CR, Petzold GC and Henneberger C (2021) Disruption of Glutamate Transport and Homeostasis by Acute Metabolic Stress. Front. Cell. Neurosci. 15:637784. doi: 10.3389/fncel.2021.637784

INTRODUCTION

Excitatory synaptic transmission in the brain is mediated by the precisely timed and highly localized release of the neurotransmitter glutamate from presynaptic release sites into the synaptic cleft and the subsequent activation of postsynaptic receptors. After the initial dilution of glutamate in the synaptic cleft (Zheng et al., 2008; Scimemi and Beato, 2009), the fast clearance of glutamate from the extracellular space (ECS) restricts its spread. Thereby, it limits the activation of extrasynaptic receptors and the amount of glutamate "spilling over" onto nearby neurons. High-affinity glutamate transporters located on the fine perisynaptic processes of astrocytes (PAPs) are believed to mediate most of the glutamate clearance in the brain under physiological conditions (Danbolt, 2001; Rose et al., 2017). Multiple studies have demonstrated the role of glutamate uptake

for synaptic transmission and plasticity (for review see Tzingounis and Wadiche, 2007; Valtcheva and Venance, 2019). However, its relevance becomes particularly apparent when it is impaired (Rose et al., 2017; Pajarillo et al., 2019). The uptake of glutamate against its steep concentration gradient is mainly powered by the transmembrane driving force for Na^+ at a negative membrane potential, both of which are maintained by the Na^+/K^+-ATPase. During conditions of metabolic stress such as ischemic stroke, the lack of ATP leads to a breakdown of ionic gradients and cellular depolarization, reducing the driving force for glutamate uptake. The resulting increased lifetime of glutamate in the ECS leads to increased activation of synaptic and extrasynaptic glutamate receptors and receptors on nearby neurons, which provokes further excitation and intracellular Ca^{2+} elevations, driving a vicious circle eventually culminating in irreversible excitotoxic cell death (Dirnagl et al., 1999; Grewer et al., 2008).

In an ischemic stroke, two characteristic zones can be distinguished (Rossi et al., 2007). The ischemic core is in the direct vicinity of the clogged blood vessel, where energy supply is almost completely lost and irreversible cell death occurs within minutes. The tissue surrounding the core, called the penumbra, suffers from reduced perfusion and thus lower energy levels but recovery is still possible. However, peri-infarct depolarizations (PIDs), which are waves of spreading depression that originate in the core and propagate through the penumbra into the healthy tissue, impose an additional metabolic burden on the tissue (Dirnagl et al., 1999; Rossi et al., 2007; Dreier, 2011).

Disentangling the sequence of events and identifying the relevant cellular mechanisms during this acute form of metabolic stress is vital for developing novel treatments. Indeed, multiple studies have shown that glutamate homeostasis is perturbed and, in many ways, responsible for ischemic cell death. However, some findings are still controversial (Rossi et al., 2007; Rose et al., 2017; Zhang et al., 2019; Belov Kirdajova et al., 2020) and there are multiple reasons for that. These include the complexity of the pathological condition itself, the large number of potentially relevant cellular mechanisms, and the variety of experimental conditions across different studies. In this mini-review, we discuss the impact of metabolic stress on glutamate homeostasis in the cortex, focusing on mechanisms that are activated during transient (seconds to minutes) episodes of metabolic stress, as is for instance the case in the penumbra after a stroke or during transient ischemic attacks.

TRANSPORTER AVAILABILITY AND LOCATION

Expression of Glutamate Transporters

Mammalian cells express five different subtypes of excitatory amino acid transporters (EAAT1–5; Danbolt, 2001). In the hippocampus and neocortex, EAAT1 (= glutamate/aspartate transporter, GLAST) and EAAT2 (= glutamate transporter-1, GLT-1) are the predominantly expressed subtypes. However, the relative expression and functional significance for the uptake of synaptically released glutamate can vary significantly even within subregions of the neocortex (Romanos et al., 2019). EAAT1 and EAAT2 are considered to be mainly astrocytic while EAAT3 (= excitatory amino acid carrier 1, EAAC1) and EAAT4 are predominantly found in neurons (Danbolt, 2001; Massie et al., 2008; Holmseth et al., 2012; Rose et al., 2017). In the adult hippocampus, for instance, it was shown that ∼10% of EAAT2 is expressed by neurons where it localizes mainly to axon terminals (Danbolt, 2001; Furness et al., 2008) while neuronal EAAT3 on the other hand is located on the postsynaptic membrane (Holmseth et al., 2012). While the density of glutamate transporters is significantly higher on astrocytes compared to neurons (for the hippocampus see for instance Holmseth et al., 2012), all subtypes are strategically located close to the synaptic glutamate release site.

Changes in glutamate transporter expression can occur on multiple levels, including transcriptional control, epigenetic DNA modifications, and regulation of translation. Furthermore, post-translational modifications such as phosphorylation, nitrosylation, and ubiquitination determine the availability of functional glutamate transporters (Pajarillo et al., 2019). For instance, EAAT2 is subject to nitrosylation, which was shown to influence uptake efficiency (Raju et al., 2015). In the case of ischemia, the extent of expression changes depends on the stage and/or severity of metabolic stress although results in the literature are heterogeneous (Zhang et al., 2019). While some studies indicate that expression of EAAT1 and/or EAAT2 is increased in the early stages of an ischemic event and decreased in later stages (Arranz et al., 2010; Liu et al., 2012; Girbovan and Plamondon, 2015), others demonstrated the opposite (Torp et al., 1995; Rao et al., 2001a; Fang et al., 2014). Intriguingly, it was also shown more recently that EAAT1 and EAAT2 mRNAs are found in astrocyte processes along with the machinery for local translation and that the distribution of mRNAs was altered after fear conditioning (Sakers et al., 2017; Mazaré et al., 2020). It is therefore tempting to speculate that changes in the translation of glutamate transporters might also occur locally in response to acute metabolic stress. However, such changes of transporter expression are likely to play a role over longer time scales than the seconds to minutes of interest here.

Localization of Glutamate Transporters

The availability of functional glutamate transporters depends, apart from transcription and translation, on the regulation of glutamate transporter insertion and internalization as well as lateral diffusion in the cell membrane. Insertion and internalization were shown to change in response to glutamate application (Duan et al., 1999) and are likely to be regulated by Ca^{2+} dynamics (Rose et al., 2017). Substances promoting retention of glutamate transporters in the membrane were demonstrated to have neuroprotective effects, similar to increasing expression (Martínez-Villarreal et al., 2012; Li et al., 2015). Single-molecule tracking experiments revealed that, once inside the membrane, glutamate transporters are quite mobile, their diffusion is modulated by neuronal activity and they become more stable near synapses (Murphy-Royal et al., 2015). Likewise, glutamate application was shown to affect the formation and stability of EAAT2 clusters inside

the astrocyte membrane (Al Awabdh et al., 2016) while blocking synaptic activity reduced the density and perisynaptic localization of EAAT2 clusters in developing astrocytes (Benediktsson et al., 2012). Since inhibiting transporter mobility directly affected synaptic transmission (Murphy-Royal et al., 2015), there is a dynamic and plastic interplay between synaptic glutamate release and local transporter availability. Furthermore, elevated glutamate levels increased ubiquitination of EAAT2 leading to its internalization in HEK293 cells (Ibáñez et al., 2016). For these reasons, it is plausible that PIDs, associated with large extracellular glutamate and intracellular Ca^{2+} transients (Rakers and Petzold, 2017), may affect transporter membrane diffusion, insertion, and internalization. However, little is known on how metabolic stress precisely affects glutamate transporter trafficking. It, therefore, remains to be established if such processes play a role in, for instance, the initial stages of an ischemic stroke or during PIDs.

In addition to the density of glutamate transporters in the membrane, the physical distance between the glutamate release site and the transporters directly influences the lifetime and spread of glutamate in the ECS. Neuronal membranes facing the synaptic cleft itself contain few transporters (Furness et al., 2008). However, after escaping the synaptic cleft, the radius of action of glutamate is determined by diffusion and the hindrance thereof either by physical barriers or by binding and uptake by transporters (Zheng et al., 2008; Scimemi and Beato, 2009). Hence, glutamate transporters located close to the synaptic cleft limit the diffusion of glutamate to extrasynaptic sites, where high-affinity *N*-methyl-D-aspartate receptors (NMDARs) and metabotropic glutamate receptors (mGluRs) are localized, and prevent the spillover to neighboring neurons (Scimemi et al., 2004; Zheng et al., 2008; Henneberger et al., 2020; Herde et al., 2020).

Under physiological conditions, glutamate uptake is predominantly mediated by astrocytic glutamate transporters (Danbolt, 2001; Rose et al., 2017). For this reason, the perisynaptic geometry and abundance of PAPs and their role in glutamate uptake has been intensely studied. A reduction of astroglial coverage of synapses during lactation in the supraoptic nucleus, for example, was shown to increase glutamate spread leading to changes in presynaptic transmitter release (Oliet et al., 2001). In contrast, invasion of the synaptic cleft by astrocytic processes in Connexin 30 knockout mice increased the control of synaptic transmission by glutamate uptake (Pannasch et al., 2014). Along these lines, we recently demonstrated that spine size negatively correlates with the local efficacy of glutamate uptake in the hippocampus (Herde et al., 2020). Another study suggested that rearrangements of the astrocytic cytoskeleton induced changes in glutamate uptake which were linked to altered activity of the Na^+/K^+-ATPase (Sheean et al., 2013). Together, these results highlight that even small changes in the submicron structure of astrocytic processes can have significant consequences for the time course of extracellular glutamate transients and thus on the activation of extrasynaptic glutamate receptors and neighboring neurons. Since changes in cellular morphology as a consequence of ischemia and metabolic stress have been described for different cell types including astrocytes (Risher et al., 2009; Anderova et al., 2011), it is safe to assume that these will directly affect extracellular glutamate dynamics after the onset of metabolic stress.

Notably, we and others have also shown that astrocytic processes are mobile (Haber et al., 2006; Bernardinelli et al., 2014) and withdraw from synapses after induction of long-term potentiation (LTP) of synaptic transmission, which increases glutamate spread and spillover enhancing NMDAR activation (Henneberger et al., 2020). Interestingly, brief episodes of metabolic stress were shown to induce LTP too, a phenomenon known as ischemic LTP (Lenz et al., 2015) that also depends on NMDARs (Maggio et al., 2015). This raises the question if metabolic stress induces a similar withdrawal of astrocytic processes or whether swelling of astrocytic processes (Risher et al., 2009) is more prominent, and how either displacement of glutamate transporters changes extracellular glutamate dynamics in the perisynaptic space.

IMPAIRMENT OF TRANSPORTER FUNCTION

Reduced Uptake and Reversal-Ion Homeostasis and the Direction of Glutamate Transport

When compared to the sub-micromolar extracellular glutamate concentration (Herman and Jahr, 2007), the intracellular glutamate concentration in neurons and astrocytes is much higher with estimates ranging from high micromolar to low millimolar (Nedergaard et al., 2002; Rossi et al., 2007). Glutamate uptake against this steep concentration gradient is achieved by the co-transport of three Na^+ and one H^+ and the export of one K^+ and is accompanied by an uncoupled anion flux (Danbolt, 2001; Fahlke and Nilius, 2016). Therefore, glutamate transport is very sensitive to changes of the Na^+ gradient.

The Na^+ gradient across the membrane is largely maintained by the Na^+/K^+-ATPase and therefore highly dependent on energy in the form of ATP. During metabolic stress, reduced levels of ATP lead to malfunction of the Na^+/K^+-ATPase and cellular depolarization, a degradation of ionic gradients, and also extracellular glutamate accumulation (Rossi et al., 2007). Cellular depolarization and the degradation of ion gradients both directly reduce the driving force for Na^+ and, thereby, glutamate transport. Also, due to the high K^+ membrane conductance of astrocytes, extracellular rises in K^+ during metabolic stress strongly depolarize these cells, which further reduces the driving force for glutamate uptake. Furthermore, extracellular accumulation of glutamate likely accelerates the decay of ionic gradients in cells with a large contribution to glutamate uptake such as astrocytes, because of the ion transport associated with it. During extreme energy failure, e.g., in the core region of an ischemic stroke, this may lead to a reversal of glutamate uptake, i.e., to the export of glutamate from the cytosol to the ECS (Rossi et al., 2000; Grewer et al., 2008). Whether or not such a reversal occurs depends on how strongly the

ionic gradients and membrane potential are degraded. Modeling studies of glutamate transport predict that determining this tipping point requires quantitative information about the intra- and extracellular concentrations of glutamate, Na^+, K^+, and H^+ in the course of metabolic stress (Bergles et al., 2002; Rossi et al., 2007; Grewer et al., 2008), which is currently not available.

Importantly, an impairment of glutamate uptake is likely sufficient to facilitate the failure of extracellular glutamate homeostasis. Indeed, even moderate depolarization of the astrocytic membrane potential (Stephan et al., 2012) and/or increases of the Na^+ concentration (Kelly et al., 2009) were shown to reduce the uptake capacity significantly (Felix et al., 2020). We recently demonstrated that even transient episodes of metabolic stress during chemical ischemia in acute brain slices as well as during PIDs *in vivo* induce significant increases in the neuronal as well as astrocytic Na^+ concentration (Gerkau et al., 2018). Thus, acute and/or transient metabolic stress can impair glutamate uptake substantially. This will promote local glutamate accumulation and glutamate spread into the tissue (**Figure 1**) because inhibition of glutamate uptake increases the lifetime of glutamate in the ECS and its spread (Henneberger et al., 2020; Herde et al., 2020). However, glutamate uptake is not the only mechanism that determines extracellular glutamate concentrations and their diffusion. It is for instance well-known that ischemia and metabolic stress can induce cell swelling and a decrease of the ECS (Syková and Nicholson, 2008; Risher et al., 2009; Anderova et al., 2011). The same amount of glutamate released into a smaller ECS would intuitively lead to higher extracellular glutamate concentrations. At the same time, the tortuosity of the ECS can be increased by ischemia (Syková and Nicholson, 2008), which would on its own reduce the diffusion of glutamate in the ECS. Therefore, it will be interesting to test what the net effect of metabolic stress on glutamate spread in the ECS is.

Interestingly, regional variations in glutamate uptake mechanisms could lead to differential susceptibility to metabolic stress across brain regions. For instance, the differentially expressed glutamate transporters EAAT1 and EAAT2 were shown to differ in their uptake kinetics with EAAT2 being more effective (Arriza et al., 1994). Furthermore, it was shown that glutamate uptake in the cortex was slowed by increased presynaptic activity (Armbruster et al., 2016) while no such adaption was found in the hippocampus (Diamond and Jahr, 2000; Diamond, 2005). Similarly, employing the glutamate sensor iGluSnFR, other studies have found that glutamate clearance is faster in the hippocampus compared to the cortex (Pinky et al., 2018) and that its activity-dependence differs between somatosensory and frontal cortex (Romanos et al., 2019). Although the mechanisms underlying this activity-dependence are not fully established, it seems likely that they are engaged by the widespread glutamate increases accompanying PIDs (Fabricius et al., 1993; Rakers and Petzold, 2017) and, in fact, also contribute to the latter.

Once taken up by astrocytes, the enzyme glutamine synthetase (GS) converts glutamate to glutamine. The non-toxic glutamine is then shuttled back to neurons where it is converted to glutamate or GABA (Schousboe et al., 2014). The ATP-dependent conversion by GS is also inhibited during metabolic stress likely inducing glutamate accumulation in astrocytes further reducing the driving force for glutamate uptake. Consequently, it was shown that inhibiting GS increased NMDAR currents in cortical neurons indicating that accumulation of glutamate in astrocytes reduced the uptake capacity promoting glutamate spread (Trabelsi et al., 2017). Similarly, a modeling study found a direct relationship between intracellular glutamate concentration and glutamate uptake capacity (Flanagan et al., 2018).

In summary, although many links are still missing, present data indicate that acute metabolic stress affects a wide range of cellular processes that directly interfere with glutamate clearance *via* transporters, which in turn can affect the accumulation and spread of glutamate in the ECS (**Figure 1**).

Neuronal vs. Glial Glutamate Transporters

The precise differential contribution of astrocytic and neuronal glutamate transporters to glutamate clearance during physiological but also pathophysiological conditions remains a matter of debate. The commonly accepted notion is that astrocytes take up >90% of the synaptically released glutamate (Danbolt, 2001; Diamond, 2005; Rose et al., 2017). This is supported by genetic ablation studies which found that an astrocyte-specific knockout of EAAT2 showed by far the most severe phenotype of all transporter knockouts including strong seizure activity leading to neonatal death (Petr et al., 2015). However, constitutive as well as neuron-specific knockout experiments indicated that neuronal EAAT2 is particularly important for glutamate uptake into synaptosomes (Furness et al., 2008; Petr et al., 2015). It should also be noted that the knockout approach depicts the most drastic model to study protein function and compensatory effects need to be considered. Also, the relative impact of neuronal glutamate uptake might increase during acute metabolic stress when astrocytic glutamate uptake is compromised though not entirely lost.

Still, most studies identified glial glutamate transporters as the main source of glutamate *via* reverse transport during severe ischemia whereas increased glutamate release from neurons is mainly *via* vesicular release (Jabaudon et al., 2000; Andrade and Rossi, 2010). Other reports, however, suggested that the reversal of neuronal glutamate transporters is responsible for glutamate release during early phases of ischemia (Rossi et al., 2000; Hamann et al., 2002). This was supported by the observation that myelin damage in the corpus callosum during ischemic conditions is almost exclusively caused by axonal glutamate release while reverse transport by astrocytes did not contribute significantly (Doyle et al., 2018). On the other hand, selective knockdown of the mainly astrocytic glutamate transporter EAAT2 increased infarct volume in an *in vivo* model of stroke while knockdown of the primarily neuronal EAAT3 had no such effect (Rao et al., 2001b). Furthermore, it was recently demonstrated that brain slices from mice with astrocyte-specific EAAT2 deletion were more susceptible to spreading depression compared to EAAT1 or EAAT3 knockout mice indicating a stronger influence of glial compared to neuronal glutamate transporters (Aizawa et al., 2020).

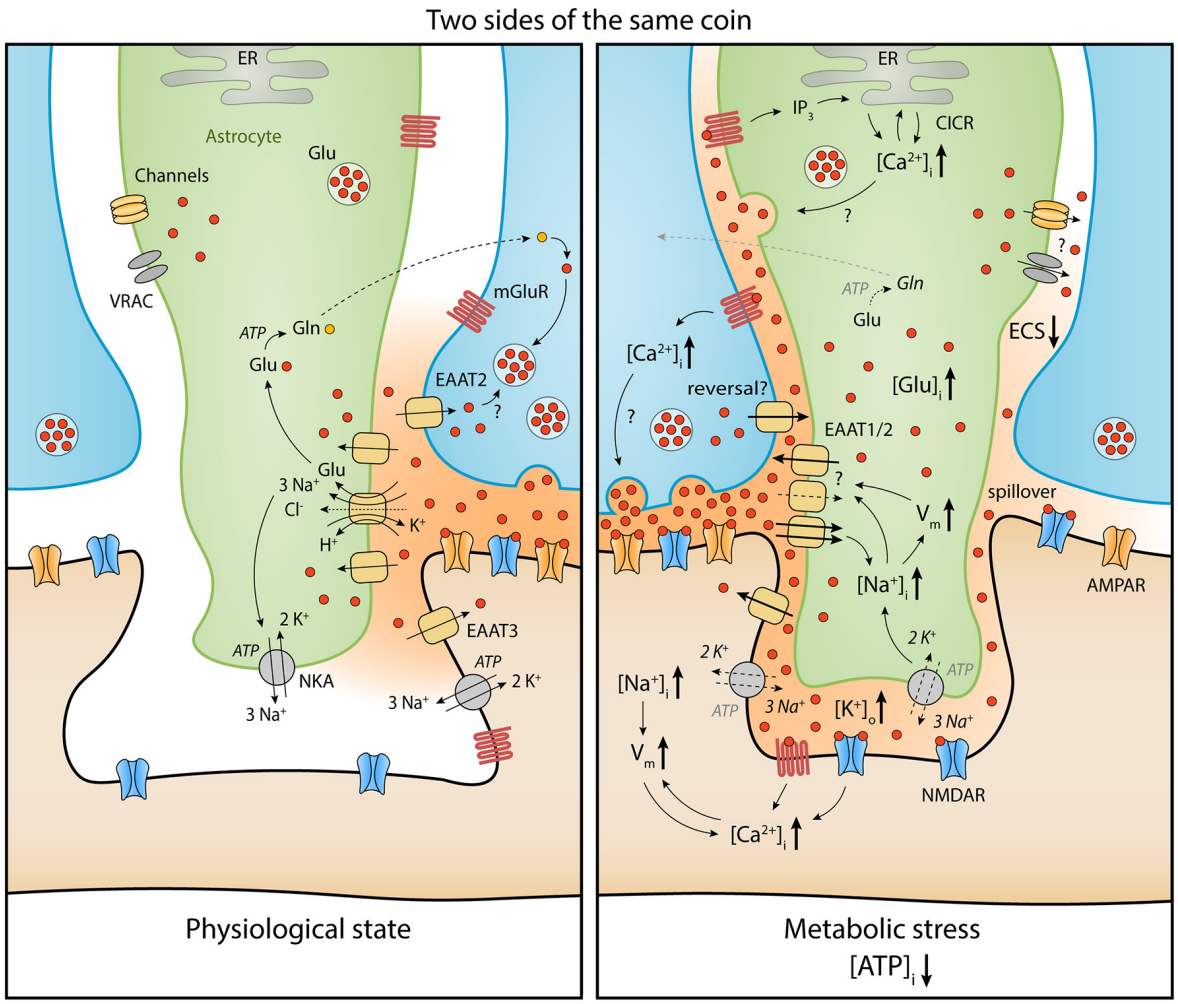

FIGURE 1 | Comparison of extracellular glutamate (red) homeostasis under physiological conditions (left) and during metabolic stress (right) at a synapse (presynaptic bouton in blue, postsynaptic dendritic spine in brown, perisynaptic astrocyte process in green). A moderate reduction of ATP in astrocytes and neurons leads to depolarization of the membrane potential (V_m) and intracellular increases of Na^+ and Ca^{2+} as well as extracellular increases of K^+. As a consequence, the driving force for glutamate uptake is diminished and cell swelling reduces the extracellular space (ECS) fraction, which increases extracellular glutamate levels (see text). This leads to stronger activation of glutamate receptors on neurons (e.g., *N*-methyl-D-aspartate receptors, NMDARs) and astrocytes (e.g., metabotropic glutamate receptors, mGluRs) and a further increase in intracellular Ca^{2+} and Na^+ concentrations and depolarization. In astrocytes, glutamate release through volume-regulated anion channels (VRACs), as well as Ca^{2+}-dependent mechanisms, can amplify extracellular glutamate increases during acute metabolic stress. Open questions (?) regarding glutamate homeostasis are related to the quantitative role of glutamate transporter dysfunction, the relationship between acute metabolic stress and changes of presynaptic release, the role of active astrocytic signaling, and the geometrical rearrangement of astrocytes and neurons during metabolic stress and its impact on extracellular glutamate spread. Abbreviations: AMPAR, α-amino-3-hydroxy-5-methyl-4-isoxazolepropionic acid receptor; CICR, Ca^{2+}-induced Ca^{2+} release; EAAT, excitatory amino acid transporter; ECS, extracellular space; ER, endoplasmatic reticulum; Gln, Glutamine; Glu, Glutamate; IP_3, inositol triphosphate; mGluR, metabotropic glutamate receptor; NKA, Na^+/K^+-ATPase; NMDAR, N-methyl-D-aspartate receptor; VRAC, volume-regulated anion channel. Note: schematic distribution of glutamate molecules not directly representative of their concentration.

Although the exact contributions of neuronal vs. glial glutamate transporters during metabolic stress are still under debate, it is quite likely that both are dysregulated at some stage and thus both do contribute to the failure of extracellular glutamate homeostasis. The degree to which either cell type plays a role will not only depend on its physiological contribution to glutamate uptake but also on how metabolic stress impairs concentration gradients and the membrane potential in a given cell type (Rossi et al., 2007).

Astrocytic Glutamate Release Beyond Reverse Transport

While the vesicular and non-vesicular routes of glutamate release from neurons are established (see above for glutamate transporters), mechanisms of astrocytic glutamate release are still debated. In addition to reverse transport, several studies indicate that astrocytes are capable of regulated, and in many cases Ca^{2+}-dependent, vesicular as well as channel-mediated glutamate release (Bohmbach et al., 2018; Mahmoud et al.,

2019). We recently showed that intracellular Na^+ increases during acute metabolic stress induce Ca^{2+} elevations *via* reversal of the Na^+/Ca^{2+}-exchanger in neurons and astrocytes (Gerkau et al., 2018). Furthermore, we demonstrated that preventing inositol triphosphate receptor type 2-mediated release of Ca^{2+} from intracellular stores reduced the PID-induced Ca^{2+} increases in astrocytes and, at the same time, the duration of extracellular glutamate transients *in vivo*, leading to a secondary neuroprotective decrease of Ca^{2+} elevations in neurons (Rakers and Petzold, 2017). This suggests that astrocytic Ca^{2+} signals during PIDs could trigger astrocytic glutamate release, although the exact chain of events remains to be uncovered. Another relevant mechanism is astrocytic release *via* volume-regulated anion channels (VRACs), which are Ca^{2+}-independent (Mahmoud et al., 2019; Yang et al., 2019). Importantly, VRACs were implicated in glutamate release in the penumbra while reversal of transport was suggested to be more important in the core (Feustel et al., 2004). Also, the VRAC Swell1 was recently shown to mediate ischemia-induced glutamate release from astrocytes with Swell1 knockout mice exhibiting significantly smaller infarct volumes (Yang et al., 2019). Together, these studies indicate that astrocytes can drive glutamate elevations during metabolic stress, ischemia, and stroke by mechanisms independent from high-affinity glutamate transporters.

CONCLUSION

Accumulating data indicate that metabolic stress acutely impairs glutamate uptake promoting glutamate accumulation and spread further aggravating excitotoxicity. Glutamate transporter dysfunction scales with the severity of metabolic stress ranging from subtle changes of uptake efficiency to a reversal of uptake. A variety of factors can potentially contribute, including lateral diffusion, localization, and abundance of glutamate transporters, their biophysical properties, and their driving forces. Given this complexity, it is no surprise that disentangling the sequence of events triggered by acute metabolic stress has remained challenging. Novel tools such as optical glutamate sensors (Marvin et al., 2013; Helassa et al., 2018) have more recently allowed researchers to gain new insights into extracellular glutamate dynamics and the role of glutamate transporters (Armbruster et al., 2016, 2020; Romanos et al., 2019; Henneberger et al., 2020; Herde et al., 2020). They also promise to provide new insights into unresolved questions regarding altered glutamate transport in metabolic stress (Rakers and Petzold, 2017). Regarding glutamate excitotoxicity, it will also be important to reveal if metabolic stress also perturbs NMDAR co-agonist supply and transport (see Henneberger et al., 2013), which could amplify the damage caused by impaired glutamate homeostasis.

AUTHOR CONTRIBUTIONS

All authors contributed to the conception and writing of this review and approved the submitted and final published version.

FUNDING

Research in CH's laboratory was supported by DFG grants SFB1089 B03, SPP1757 HE6949/1, FOR2795, HE6949/3 and HE6949/5. SP was supported by a DFG start-up funding grant within the FOR2795. CRR received support by DFG grants SPP 1757 RO2327/8-2, FOR 2795 RO2327/13-1 and 14-1. GCP was supported by DFG grant FOR 2795 PE1193/6-1 and the DZNE.

REFERENCES

Aizawa, H., Sun, W., Sugiyama, K., Itou, Y., Aida, T., Cui, W., et al. (2020). Glial glutamate transporter GLT-1 determines susceptibility to spreading depression in the mouse cerebral cortex. *Glia* 68, 2631–2642. doi: 10.1002/glia.23874

Al Awabdh, S., Gupta-Agarwal, S., Sheehan, D. F., Muir, J., Norkett, R., Twelvetrees, A. E., et al. (2016). Neuronal activity mediated regulation of glutamate transporter GLT-1 surface diffusion in rat astrocytes in dissociated and slice cultures. *Glia* 64, 1252–1264. doi: 10.1002/glia.22997

Anderova, M., Vorisek, I., Pivonkova, H., Benesova, J., Vargova, L., Cicanic, M., et al. (2011). Cell death/proliferation and alterations in glial morphology contribute to changes in diffusivity in the rat hippocampus after hypoxia-ischemia. *J. Cereb. Blood Flow Metab.* 31, 894–907. doi: 10.1038/jcbfm.2010.168

Andrade, A. L., and Rossi, D. J. (2010). Simulated ischaemia induces Ca^{2+}-independent glutamatergic vesicle release through actin filament depolymerization in area CA1 of the hippocampus. *J. Physiol.* 588, 1499–1514. doi: 10.1113/jphysiol.2010.187609

Armbruster, M., Dulla, C. G., and Diamond, J. S. (2020). Effects of fluorescent glutamate indicators on neurotransmitter diffusion and uptake. *eLife* 9:e54441. doi: 10.7554/eLife.54441

Armbruster, M., Hanson, E., and Dulla, C. G. (2016). Glutamate clearance is locally modulated by presynaptic neuronal activity in the cerebral cortex. *J. Neurosci.* 36, 10404–10415. doi: 10.1523/JNEUROSCI.2066-16.2016

Arranz, A. M., Gottlieb, M., Pérez-Cerdá, F., and Matute, C. (2010). Increased expression of glutamate transporters in subcortical white matter after transient focal cerebral ischemia. *Neurobiol. Dis.* 37, 156–165. doi: 10.1016/j.nbd.2009.09.019

Arriza, J. L., Fairman, W. A., Wadiche, J. I., Murdoch, G. H., Kavanaugh, M. P., and Amara, S. G. (1994). Functional comparisons of three glutamate transporter subtypes cloned from human motor cortex. *J. Neurosci.* 14, 5559–5569. doi: 10.1523/JNEUROSCI.14-09-05559.1994

Belov Kirdajova, D., Kriska, J., Tureckova, J., and Anderova, M. (2020). Ischemia-triggered glutamate excitotoxicity from the perspective of glial cells. *Front. Cell. Neurosci.* 14:51. doi: 10.3389/fncel.2020.00051

Benediktsson, A. M., Marrs, G. S., Tu, J. C., Worley, P. F., Rothstein, J. D., Bergles, D. E., et al. (2012). Neuronal activity regulates glutamate transporter dynamics in developing astrocytes. *Glia* 60, 175–188. doi: 10.1002/glia.21249

Bergles, D. E., Tzingounis, A. V., and Jahr, C. E. (2002). Comparison of coupled and uncoupled currents during glutamate uptake by GLT-1 transporters. *J. Neurosci.* 22, 10153–10162. doi: 10.1523/JNEUROSCI.22-23-10153.2002

Bernardinelli, Y., Randall, J., Janett, E., Nikonenko, I., König, S., Jones, E. V., et al. (2014). Activity-dependent structural plasticity of perisynaptic astrocytic domains promotes excitatory synapse stability. *Curr. Biol.* 24, 1679–1688. doi: 10.1016/j.cub.2014.06.025

Bohmbach, K., Schwarz, M. K., Schoch, S., and Henneberger, C. (2018). The structural and functional evidence for vesicular release from astrocytes *in situ*. *Brain Res. Bull.* 136, 65–75. doi: 10.1016/j.brainresbull.2017.01.015

Danbolt, N. C. (2001). Glutamate uptake. *Prog. Neurobiol.* 65, 1–105. doi: 10.1016/s0301-0082(00)00067-8

Diamond, J. S. (2005). Deriving the glutamate clearance time course from transporter currents in CA1 hippocampal astrocytes: transmitter uptake gets faster during development. *J. Neurosci.* 25, 2906–2916. doi: 10.1523/JNEUROSCI.5125-04.2005

Diamond, J. S., and Jahr, C. E. (2000). Synaptically released glutamate does not overwhelm transporters on hippocampal astrocytes during high-frequency stimulation. *J. Neurophysiol.* 83, 2835–2843. doi: 10.1152/jn.2000.83.5.2835

Dirnagl, U., Iadecola, C., and Moskowitz, M. A. (1999). Pathobiology of ischaemic stroke: an integrated view. *Trends Neurosci.* 22, 391–397. doi: 10.1016/s0166-2236(99)01401-0

Doyle, S., Hansen, D. B., Vella, J., Bond, P., Harper, G., Zammit, C., et al. (2018). Vesicular glutamate release from central axons contributes to myelin damage. *Nat. Commun.* 9:1032. doi: 10.1038/s41467-018-03427-1

Dreier, J. P. (2011). The role of spreading depression, spreading depolarization and spreading ischemia in neurological disease. *Nat. Med.* 17, 439–447. doi: 10.1038/nm.2333

Duan, S., Anderson, C. M., Stein, B. A., and Swanson, R. A. (1999). Glutamate induces rapid upregulation of astrocyte glutamate transport and cell-surface expression of GLAST. *J. Neurosci.* 19, 10193–10200. doi: 10.1523/JNEUROSCI.19-23-10193.1999

Fabricius, M., Jensen, L. H., and Lauritzen, M. (1993). Microdialysis of interstitial amino acids during spreading depression and anoxic depolarization in rat neocortex. *Brain Res.* 612, 61–69. doi: 10.1016/0006-8993(93)91644-8

Fahlke, C., and Nilius, B. (2016). Molecular physiology of anion channels: dual function proteins and new structural motifs–a special issue. *Pflugers Arch.* 468, 369–370. doi: 10.1007/s00424-016-1791-z

Fang, Q., Hu, W.-W., Wang, X.-F., Yang, Y., Lou, G.-D., Jin, M.-M., et al. (2014). Histamine up-regulates astrocytic glutamate transporter 1 and protects neurons against ischemic injury. *Neuropharmacology* 77, 156–166. doi: 10.1016/j.neuropharm.2013.06.012

Felix, L., Delekate, A., Petzold, G. C., and Rose, C. R. (2020). Sodium fluctuations in astroglia and their potential impact on astrocyte function. *Front. Physiol.* 11:871. doi: 10.3389/fphys.2020.00871

Feustel, P. J., Jin, Y., and Kimelberg, H. K. (2004). Volume-regulated anion channels are the predominant contributors to release of excitatory amino acids in the ischemic cortical penumbra. *Stroke* 35, 1164–1168. doi: 10.1161/01.STR.0000124127.57946.a1

Flanagan, B., McDaid, L., Wade, J., Wong-Lin, K., and Harkin, J. (2018). A computational study of astrocytic glutamate influence on post-synaptic neuronal excitability. *PLoS Comput. Biol.* 14:e1006040. doi: 10.1371/journal.pcbi.1006040

Furness, D. N., Dehnes, Y., Akhtar, A. Q., Rossi, D. J., Hamann, M., Grutle, N. J., et al. (2008). A quantitative assessment of glutamate uptake into hippocampal synaptic terminals and astrocytes: new insights into a neuronal role for excitatory amino acid transporter 2 (EAAT2). *Neuroscience* 157, 80–94. doi: 10.1016/j.neuroscience.2008.08.043

Gerkau, N. J., Rakers, C., Durry, S., Petzold, G. C., and Rose, C. R. (2018). Reverse NCX attenuates cellular sodium loading in metabolically compromised cortex. *Cereb. Cortex* 28, 4264–4280. doi: 10.1093/cercor/bhx280

Girbovan, C., and Plamondon, H. (2015). Resveratrol downregulates type-1 glutamate transporter expression and microglia activation in the hippocampus following cerebral ischemia reperfusion in rats. *Brain Res.* 1608, 203–214. doi: 10.1016/j.brainres.2015.02.038

Grewer, C., Gameiro, A., Zhang, Z., Tao, Z., Braams, S., and Rauen, T. (2008). Glutamate forward and reverse transport: from molecular mechanism to transporter-mediated release after ischemia. *IUBMB Life* 60, 609–619. doi: 10.1002/iub.98

Haber, M., Zhou, L., and Murai, K. K. (2006). Cooperative astrocyte and dendritic spine dynamics at hippocampal excitatory synapses. *J. Neurosci.* 26, 8881–8891. doi: 10.1523/JNEUROSCI.1302-06.2006

Hamann, M., Rossi, D. J., Marie, H., and Attwell, D. (2002). Knocking out the glial glutamate transporter GLT-1 reduces glutamate uptake but does not affect hippocampal glutamate dynamics in early simulated ischaemia. *Eur. J. Neurosci.* 15, 308–314. doi: 10.1046/j.0953-816x.2001.01861.x

Helassa, N., Dürst, C. D., Coates, C., Kerruth, S., Arif, U., Schulze, C., et al. (2018). Ultrafast glutamate sensors resolve high-frequency release at Schaffer collateral synapses. *Proc. Natl. Acad. Sci. U S A* 115, 5594–5599. doi: 10.1073/pnas.1720648115

Henneberger, C., Bard, L., King, C., Jennings, A., and Rusakov, D. A. (2013). NMDA receptor activation: two targets for two co-agonists. *Neurochem. Res.* 38, 1156–1162. doi: 10.1007/s11064-013-0987-2

Henneberger, C., Bard, L., Panatier, A., Reynolds, J. P., Kopach, O., Medvedev, N. I., et al. (2020). LTP induction boosts glutamate spillover by driving withdrawal of perisynaptic astroglia. *Neuron* 108, 919.e11–936.e11. doi: 10.1016/j.neuron.2020.08.030

Herde, M. K., Bohmbach, K., Domingos, C., Vana, N., Komorowska-Müller, J. A., Passlick, S., et al. (2020). Local efficacy of glutamate uptake decreases with synapse size. *Cell Rep.* 32:108182. doi: 10.1016/j.celrep.2020.108182

Herman, M. A., and Jahr, C. E. (2007). Extracellular glutamate concentration in hippocampal slice. *J. Neurosci.* 27, 9736–9741. doi: 10.1523/JNEUROSCI.3009-07.2007

Holmseth, S., Dehnes, Y., Huang, Y. H., Follin-Arbelet, V. V., Grutle, N. J., Mylonakou, M. N., et al. (2012). The density of EAAC1 (EAAT3) glutamate transporters expressed by neurons in the mammalian CNS. *J. Neurosci.* 32, 6000–6013. doi: 10.1523/JNEUROSCI.5347-11.2012

Ibáñez, I., Díez-Guerra, F. J., Giménez, C., and Zafra, F. (2016). Activity dependent internalization of the glutamate transporter GLT-1 mediated by β-arrestin 1 and ubiquitination. *Neuropharmacology* 107, 376–386. doi: 10.1016/j.neuropharm.2016.03.042

Jabaudon, D., Scanziani, M., Gähwiler, B. H., and Gerber, U. (2000). Acute decrease in net glutamate uptake during energy deprivation. *Proc. Natl. Acad. Sci. U S A* 97, 5610–5615. doi: 10.1073/pnas.97.10.5610

Kelly, T., Kafitz, K. W., Roderigo, C., and Rose, C. R. (2009). Ammonium-evoked alterations in intracellular sodium and pH reduce glial glutamate transport activity. *Glia* 57, 921–934. doi: 10.1002/glia.20817

Lenz, M., Vlachos, A., and Maggio, N. (2015). Ischemic long-term-potentiation (iLTP): perspectives to set the threshold of neural plasticity toward therapy. *Neural Regen Res* 10, 1537–1539. doi: 10.4103/1673-5374.165215

Li, D., Hérault, K., Zylbersztejn, K., Lauterbach, M. A., Guillon, M., Oheim, M., et al. (2015). Astrocyte VAMP3 vesicles undergo Ca^{2+} -independent cycling and modulate glutamate transporter trafficking. *J. Physiol.* 593, 2807–2832. doi: 10.1113/JP270362

Liu, Y.-X., Zhang, M., Liu, L.-Z., Cui, X., Hu, Y.-Y., and Li, W.-B. (2012). The role of glutamate transporter-1a in the induction of brain ischemic tolerance in rats. *Glia* 60, 112–124. doi: 10.1002/glia.21252

Maggio, N., Shavit Stein, E., and Segal, M. (2015). Ischemic LTP: NMDA-dependency and dorso/ventral distribution within the hippocampus. *Hippocampus* 25, 1465–1471. doi: 10.1002/hipo.22467

Mahmoud, S., Gharagozloo, M., Simard, C., and Gris, D. (2019). Astrocytes maintain glutamate homeostasis in the CNS by controlling the balance between glutamate uptake and release. *Cells* 8:184. doi: 10.3390/cells8020184

Martínez-Villarreal, J., García Tardón, N., Ibáñez, I., Giménez, C., and Zafra, F. (2012). Cell surface turnover of the glutamate transporter GLT-1 is mediated by ubiquitination/deubiquitination. *Glia* 60, 1356–1365. doi: 10.1002/glia.22354

Marvin, J. S., Borghuis, B. G., Tian, L., Cichon, J., Harnett, M. T., Akerboom, J., et al. (2013). An optimized fluorescent probe for visualizing glutamate neurotransmission. *Nat. Methods* 10, 162–170. doi: 10.1038/nmeth.2333

Massie, A., Cnops, L., Smolders, I., McCullumsmith, R., Kooijman, R., Kwak, S., et al. (2008). High-affinity Na+/K+-dependent glutamate transporter EAAT4 is expressed throughout the rat fore- and midbrain. *J. Comp. Neurol.* 511, 155–172. doi: 10.1002/cne.21823

Mazaré, N., Oudart, M., Moulard, J., Cheung, G., Tortuyaux, R., Mailly, P., et al. (2020). Local translation in perisynaptic astrocytic processes is specific and changes after fear conditioning. *Cell Rep.* 32:108076. doi: 10.1016/j.celrep.2020.108076

Murphy-Royal, C., Dupuis, J. P., Varela, J. A., Panatier, A., Pinson, B., Baufreton, J., et al. (2015). Surface diffusion of astrocytic glutamate transporters shapes synaptic transmission. *Nat. Neurosci.* 18, 219–226. doi: 10.1038/nn.3901

Nedergaard, M., Takano, T., and Hansen, A. J. (2002). Beyond the role of glutamate as a neurotransmitter. *Nat. Rev. Neurosci.* 3, 748–755. doi: 10.1038/nrn916

Oliet, S. H., Piet, R., and Poulain, D. A. (2001). Control of glutamate clearance and synaptic efficacy by glial coverage of neurons. *Science* 292, 923–926. doi: 10.1126/science.1059162

Pajarillo, E., Rizor, A., Lee, J., Aschner, M., and Lee, E. (2019). The role of astrocytic glutamate transporters GLT-1 and GLAST in neurological disorders: potential targets for neurotherapeutics. *Neuropharmacology* 161:107559. doi: 10.1016/j.neuropharm.2019.03.002

Pannasch, U., Freche, D., Dallérac, G., Ghézali, G., Escartin, C., Ezan, P., et al. (2014). Connexin 30 sets synaptic strength by controlling astroglial synapse invasion. *Nat. Neurosci.* 17, 549–558. doi: 10.1038/nn.3662

Petr, G. T., Sun, Y., Frederick, N. M., Zhou, Y., Dhamne, S. C., Hameed, M. Q., et al. (2015). Conditional deletion of the glutamate transporter GLT-1 reveals that astrocytic GLT-1 protects against fatal epilepsy while neuronal GLT-1 contributes significantly to glutamate uptake into synaptosomes. *J. Neurosci.* 35, 5187–5201. doi: 10.1523/JNEUROSCI.4255-14.2015

Pinky, N. F., Wilkie, C. M., Barnes, J. R., and Parsons, M. P. (2018). Region- and activity-dependent regulation of extracellular glutamate. *J. Neurosci.* 38, 5351–5366. doi: 10.1523/JNEUROSCI.3213-17.2018

Raju, K., Doulias, P.-T., Evans, P., Krizman, E. N., Jackson, J. G., Horyn, O., et al. (2015). Regulation of brain glutamate metabolism by nitric oxide and S-nitrosylation. *Sci. Signal.* 8:ra68. doi: 10.1126/scisignal.aaa4312

Rakers, C., and Petzold, G. C. (2017). Astrocytic calcium release mediates peri-infarct depolarizations in a rodent stroke model. *J. Clin. Invest.* 127, 511–516. doi: 10.1172/JCI89354

Rao, V. L., Bowen, K. K., and Dempsey, R. J. (2001a). Transient focal cerebral ischemia down-regulates glutamate transporters GLT-1 and EAAC1 expression in rat brain. *Neurochem. Res.* 26, 497–502. doi: 10.1023/a:1010956711295

Rao, V. L., Dogan, A., Todd, K. G., Bowen, K. K., Kim, B. T., Rothstein, J. D., et al. (2001b). Antisense knockdown of the glial glutamate transporter GLT-1, but not the neuronal glutamate transporter EAAC1, exacerbates transient focal cerebral ischemia-induced neuronal damage in rat brain. *J. Neurosci.* 21, 1876–1883. doi: 10.1523/JNEUROSCI.21-06-01876.2001

Risher, W. C., Andrew, R. D., and Kirov, S. A. (2009). Real-time passive volume responses of astrocytes to acute osmotic and ischemic stress in cortical slices and *in vivo* revealed by two-photon microscopy. *Glia* 57, 207–221. doi: 10.1002/glia.20747

Romanos, J., Benke, D., Saab, A. S., Zeilhofer, H. U., and Santello, M. (2019). Differences in glutamate uptake between cortical regions impact neuronal NMDA receptor activation. *Commun. Biol.* 2:127. doi: 10.1038/s42003-019-0367-9

Rose, C. R., Felix, L., Zeug, A., Dietrich, D., Reiner, A., and Henneberger, C. (2017). Astroglial glutamate signaling and uptake in the hippocampus. *Front. Mol. Neurosci.* 10:451. doi: 10.3389/fnmol.2017.00451

Rossi, D. J., Brady, J. D., and Mohr, C. (2007). Astrocyte metabolism and signaling during brain ischemia. *Nat. Neurosci.* 10, 1377–1386. doi: 10.1038/nn2004

Rossi, D. J., Oshima, T., and Attwell, D. (2000). Glutamate release in severe brain ischaemia is mainly by reversed uptake. *Nature* 403, 316–321. doi: 10.1038/35002090

Sakers, K., Lake, A. M., Khazanchi, R., Ouwenga, R., Vasek, M. J., Dani, A., et al. (2017). Astrocytes locally translate transcripts in their peripheral processes. *Proc. Natl. Acad. Sci. U S A* 114, E3830–E3838. doi: 10.1073/pnas.1617782114

Schousboe, A., Scafidi, S., Bak, L. K., Waagepetersen, H. S., and McKenna, M. C. (2014). Glutamate metabolism in the brain focusing on astrocytes. *Adv. Neurobiol.* 11, 13–30. doi: 10.1007/978-3-319-08894-5_2

Scimemi, A., and Beato, M. (2009). Determining the neurotransmitter concentration profile at active synapses. *Mol. Neurobiol.* 40, 289–306. doi: 10.1007/s12035-009-8087-7

Scimemi, A., Fine, A., Kullmann, D. M., and Rusakov, D. A. (2004). NR2B-containing receptors mediate cross talk among hippocampal synapses. *J. Neurosci.* 24, 4767–4777. doi: 10.1523/JNEUROSCI.0364-04.2004

Sheean, R. K., Lau, C. L., Shin, Y. S., O'Shea, R. D., and Beart, P. M. (2013). Links between L-glutamate transporters, Na+/K+-ATPase and cytoskeleton in astrocytes: evidence following inhibition with rottlerin. *Neuroscience* 254, 335–346. doi: 10.1016/j.neuroscience.2013.09.043

Stephan, J., Haack, N., Kafitz, K. W., Durry, S., Koch, D., Hochstrate, P., et al. (2012). Kir4.1 channels mediate a depolarization of hippocampal astrocytes under hyperammonemic conditions *in situ*. *Glia* 60, 965–978. doi: 10.1002/glia.22328

Syková, E., and Nicholson, C. (2008). Diffusion in brain extracellular space. *Physiol. Rev.* 88, 1277–1340. doi: 10.1152/physrev.00027.2007

Torp, R., Lekieffre, D., Levy, L. M., Haug, F. M., Danbolt, N. C., Meldrum, B. S., et al. (1995). Reduced postischemic expression of a glial glutamate transporter, GLT1, in the rat hippocampus. *Exp. Brain Res.* 103, 51–58. doi: 10.1007/BF00241964

Trabelsi, Y., Amri, M., Becq, H., Molinari, F., and Aniksztejn, L. (2017). The conversion of glutamate by glutamine synthase in neocortical astrocytes from juvenile rat is important to limit glutamate spillover and peri/extrasynaptic activation of NMDA receptors. *Glia* 65, 401–415. doi: 10.1002/glia.23099

Tzingounis, A. V., and Wadiche, J. I. (2007). Glutamate transporters: confining runaway excitation by shaping synaptic transmission. *Nat. Rev. Neurosci.* 8, 935–947. doi: 10.1038/nrn2274

Valtcheva, S., and Venance, L. (2019). Control of long-term plasticity by glutamate transporters. *Front. Synaptic Neurosci.* 11:10. doi: 10.3389/fnsyn.2019.00010

Yang, J., Del Carmen, M., Chen, J., Osei-Owusu, J., Chu, J., and Qiu, Z. (2019). Glutamate-releasing SWELL1 channel in astrocytes modulates synaptic transmission and promotes brain damage in stroke. *Neuron* 102, 813.e6–827.e6. doi: 10.1016/j.neuron.2019.03.029

Zhang, L.-N., Hao, L., Guo, Y.-S., Wang, H.-Y., Li, L.-L., Liu, L.-Z., et al. (2019). Are glutamate transporters neuroprotective or neurodegenerative during cerebral ischemia? *J. Mol. Med.* 97, 281–289. doi: 10.1038/aps.2014.1

Zheng, K., Scimemi, A., and Rusakov, D. A. (2008). Receptor actions of synaptically released glutamate: the role of transporters on the scale from nanometers to microns. *Biophys. J.* 95, 4584–4596. doi: 10.1529/biophysj.108.129874

Conflict of Interest: The authors declare that the research was conducted in the absence of any commercial or financial relationships that could be construed as a potential conflict of interest.

frontiers in Cellular Neuroscience

ORIGINAL RESEARCH
published: 26 March 2021
doi: 10.3389/fncel.2021.661412

The Effect of GLT-1 Upregulation on Extracellular Glutamate Dynamics

*Crystal M. Wilkie, Jessica C. Barron, Kyle J. Brymer, Jocelyn R. Barnes, Firoozeh Nafar and Matthew P. Parsons**

Division of Biomedical Sciences, Faculty of Medicine, Memorial University, St. John's, NL, Canada

Pharmacological upregulation of glutamate transporter-1 (GLT-1), commonly achieved using the beta-lactam antibiotic ceftriaxone, represents a promising therapeutic strategy to accelerate glutamate uptake and prevent excitotoxic damage in neurological conditions. While excitotoxicity is indeed implicated in numerous brain diseases, it is typically restricted to select vulnerable brain regions, particularly in early disease stages. In healthy brain tissue, the speed of glutamate uptake is not constant and rather varies in both an activity- and region-dependent manner. Despite the widespread use of ceftriaxone in disease models, very little is known about how such treatments impact functional measures of glutamate uptake in healthy tissue, and whether GLT-1 upregulation can mask the naturally occurring activity-dependent and regional heterogeneities in uptake. Here, we used two different compounds, ceftriaxone and LDN/OSU-0212320 (LDN), to upregulate GLT-1 in healthy wild-type mice. We then used real-time imaging of the glutamate biosensor iGluSnFR to investigate functional consequences of GLT-1 upregulation on activity- and regional-dependent variations in glutamate uptake capacity. We found that while both ceftriaxone and LDN increased GLT-1 expression in multiple brain regions, they did not prevent activity-dependent slowing of glutamate clearance nor did they speed basal clearance rates, even in areas characterized by slow uptake (e.g., striatum). Unexpectedly, ceftriaxone but not LDN decreased glutamate release in the cortex, suggesting that ceftriaxone may alter release properties independent of its effects on GLT-1 expression. In sum, our data demonstrate the complexities of glutamate uptake by showing that GLT-1 expression does not necessarily translate to accelerated uptake. Furthermore, these data suggest that the mechanisms underlying activity- and regional-dependent differences in glutamate dynamics are independent of GLT-1 expression levels.

Keywords: glutamate transporter, uptake, ceftriaxone, iGluSnFR, neurotransmission

OPEN ACCESS

Edited by:
Annalisa Scimemi, University at Albany, United States

Reviewed by:
Moritz Armbruster, Tufts University School of Medicine, United States
Paluri Sai Shantanu Rao, University of Findlay, United States

***Correspondence:**
Matthew P. Parsons
matthew.parsons@med.mun.ca

Specialty section:
This article was submitted to Cellular Neurophysiology, a section of the journal Frontiers in Cellular Neuroscience

Received: *30 January 2021*
Accepted: *05 March 2021*
Published: *26 March 2021*

Citation:
Wilkie CM, Barron JC, Brymer KJ, Barnes JR, Nafar F and Parsons MP (2021) The Effect of GLT-1 Upregulation on Extracellular Glutamate Dynamics. Front. Cell. Neurosci. 15:661412. doi: 10.3389/fncel.2021.661412

INTRODUCTION

Ceftriaxone is a cephalosporin antibiotic that is commonly used to enhance glutamate transporter expression in cell and animal models of central nervous system (CNS) disease. As excess glutamate can have detrimental effects on brain tissue (Hardingham and Bading, 2010; Parsons and Raymond, 2014), various excitatory amino acid transporters (EAATs) are required to set both spatial and temporal limits on glutamate's excitatory actions. In 2005, a screen of over 1,000 compounds

demonstrated that ceftriaxone effectively upregulated glutamate transporter-1 (GLT-1) (Rothstein et al., 2005), the brain's most abundant glutamate transporter. GLT-1 accounts for over 1% of the total tissue protein in the hippocampus (Lehre and Danbolt, 1998). Found primarily on astrocytes—but also present on axon terminals (Chen et al., 2004; Furness et al., 2008)—GLT-1 is an essential glutamate transporter that plays a key role in clearing glutamate following its release into the extracellular space. Knocking out GLT-1 globally (Tanaka et al., 1997) or selectively in astrocytes (Petr et al., 2015) results in lethal seizures. Furthermore, impaired GLT-1 expression and/or function is implicated in a wide variety of CNS conditions. Since ceftriaxone was first demonstrated as a potent stimulator of GLT-1 expression in 2005, it has been used extensively in the literature to provide neuroprotection in disease models. With few exceptions, ceftriaxone shows neuroprotective effects in rodent models of amyotrophic lateral sclerosis, Alzheimer disease, Huntington disease, Parkinson disease, epilepsy and ischemia, to name a few (for recent reviews, see Smaga et al., 2020; Yimer et al., 2019).

The beneficial effects of ceftriaxone in these preclinical studies appear to be straight-forward; ceftriaxone provides neuroprotection by increasing GLT-1 expression and accelerating glutamate uptake, thereby minimizing glutamate toxicity. However, surprisingly few studies have quantified the effect of GLT-1 upregulation on the dynamics of extracellular glutamate following synaptic release. When glutamate uptake is assessed by exposing ceftriaxone-treated cells or tissues to exogenous radiolabeled glutamate over a timescale of minutes, increased absorption of the exogenous glutamate is typically enhanced as a result of the increased GLT-1 protein expression (Rothstein et al., 2005). When provided with 5–10 minutes or more to absorb exogenous glutamate, preparations with more transporters will typically absorb more glutamate. In contrast, synaptically released glutamate transients are extremely fast and can cause a localized increase in the extracellular glutamate concentration to 1 mM for 1–2 milliseconds before returning to basal nanomolar levels (Bergles et al., 1999; Clements et al., 1992). Thus, *in situ* glutamate dynamics are extremely complex and depend on many factors in addition to overall transporter expression levels. For example, glutamate clearance rates depend on the proximity of perisynaptic astrocytic processes to the synapse (Henneberger et al., 2020), synapse size (Herde et al., 2020), astrocyte resting membrane potential (Djukic et al., 2007), transporter surface mobility (Murphy-Royal et al., 2015) as well as the architecture and tortuosity of the extracellular space (Hrabětová, 2005). Posttranslational modifications of glutamate transporters, including phosphorylation and palmitoylation, can also influence transporter-mediated uptake (Casado et al., 1993; Huang et al., 2010; Pita-Almenar et al., 2006). In addition, glutamate clearance is influenced by the duration and frequency of synaptic activity, and can vary in a region-dependent manner (Armbruster et al., 2016; Pinky et al., 2018; Romanos et al., 2019). Despite the widespread use of ceftriaxone to enhance glutamate uptake capacity, it is largely unknown whether pharmacological upregulation of GLT-1 has any influence over the complexities of synaptically released glutamate dynamics in intact tissue.

Here, we used two different compounds—ceftriaxone and LDN/OSU-0212320 (LDN) (Kong et al., 2014)—to increase GLT-1 expression in healthy mice and quantified clearance rates of synaptically released glutamate in real-time using the fluorescence glutamate sensor iGluSnFR (Marvin et al., 2013). We explored the effect of GLT-1 upregulation on glutamate dynamics in multiple brain regions and in response to varying durations of neural activity. We found that despite elevated expression of GLT-1, ceftriaxone and LDN did not speed basal glutamate clearance, had minimal effect on activity-dependent slowing of glutamate clearance, and did not speed glutamate clearance in brain regions characterized by slow glutamate dynamics (e.g. striatum). Furthermore, ceftriaxone decreased glutamate release in the cortex through a GLT-1-independent mechanism. Our results demonstrate the complexities of glutamate uptake and show that increasing GLT-1 expression does not necessarily translate to accelerated uptake.

MATERIALS AND METHODS

Animals

Wild-type (WT) male FVB/N mice were ordered from Charles River at 3–4 weeks of age. They were housed in ventilated cage racks in groups of 3–4 and kept on a 12:12 light:dark cycle with *ad libitum* food and water. All procedures were approved by Memorial University's Animal Care Committee and were in accordance with the guidelines set by the Canadian Council on Animal Care. After arriving at our housing facility, all mice were allowed a minimum acclimation period of three days before stereotaxic surgery.

Stereotaxic Surgery

Male FVB/N mice (4–6 weeks of age) were anesthetized by isoflurane inhalation (3%) and maintained with 1.5–2% isoflurane for the duration of the surgical procedure. Mice were secured within the ear bars of a standard stereotaxic apparatus and subcutaneously (s.c.) injected with 0.5 ml of 0.9% sterile saline containing 2 mg/kg meloxicam. A 0.2 ml bolus of 0.2% lidocaine was injected below the scalp and a small incision was then made in the scalp and the underlying skull was exposed. For each region, a total volume of 1 µl of PENN.AAV.GFAP.iGluSnFr.WPRE.SV40 (which was a gift from Loren Looger; Addgene plasmid # 98930; http://n2t.net/addgene:98930; RRID:Addgene_98930) was injected into the cortex, hippocampus or striatum at an injection rate of 5 nl/s. The Hamilton syringe was left in place for an additional 5 minutes following the injection. The following co-ordinates were used with respect to bregma: cortex – 0.7 mm anterior, 2.0 mm lateral, 0.6 mm ventral; hippocampus – 2.6 mm posterior, 2.4 mm lateral, 1.2 to 1.4 mm ventral to brain surface; striatum – 0.7 mm anterior, 2.0 mm lateral, 2.6 mm ventral to brain surface. After the 5 minutes, the syringe was slowly withdrawn, the incision was sutured, and mice were injected with 0.5 ml 0.9% saline (s.c.) before being placed on a heating pad for approximately 30 minutes to accelerate recovery.

Ceftriaxone and LDN/OSU-212320 Treatments

Following the surgical procedure, mice were injected with either ceftriaxone or LDN. For the ceftriaxone experiments, mice (now 5–7 weeks of age) received intraperitoneal (i.p.) injections of 200 mg/kg/day ceftriaxone for 5–7 days (Rothstein et al., 2005). Ceftriaxone was dissolved in 0.9% saline; thus, control mice received daily i.p. injections of 0.9% saline a day for 5–7 days. Ceftriaxone (or saline) injections began 1–2 weeks after the stereotaxic injection of iGluSnFR. Glutamate imaging experiments and tissue extraction for western blot both occurred the day after the last ceftriaxone injection. For the LDN experiments, mice (now 5–7 weeks of age) received a single i.p. injection of 40 mg/kg (Kong et al., 2014). LDN was dissolved in the vehicle described by Kong et al. (2014); thus, control mice for this group received a single injection of vehicle. The single LDN (or vehicle) injection was administered 2–3 weeks after the stereotaxic injection of iGluSnFR.

Slice Preparation

The day after the last injection of saline/ceftriaxone, or the day after the single injection of vehicle/LDN, mice were anesthetized with isoflurane, decapitated and the brain was quickly removed and placed in ice-cold oxygenated (95% O^2/5% CO^2) slicing solution. Slicing solution consisted of of 125 mM NaCl, 2.5 mM KCl, 25 mM $NaHCO_3$, 1.25 mM NaH_2PO_4, 2.5 mM $MgCl_2$, 0.5 mM $CaCl_2$, 10 mM D-(+)-Glucose. Coronal sections (350 μm) of each brain region were cut using a Leica VT1000 S vibratome. Slices were then recovered at room temperature in oxygenated artificial cerebral spinal fluid (ACSF) composed of 125 mM NaCl, 2.5 mM KCl, 25 mM $NaHCO_3$, 1.25 mM NaH_2PO_4, 1.0 mM $MgCl_2$, 2.0 mM $CaCl_2$, 10 mM D-(+)-Glucose. Slices were left to recover in ACSF for at least 45 minutes before experimentation.

Imaging and Image Analysis

Slices were transferred to a recording chamber and imaged with an Olympus BX-61 microscope. A peristaltic pump (MP-II, Harvard Apparatus) was used to perfuse oxygenated ACSF at a flow rate of 2 ml/min through the recording chamber throughout the experiments. An in-line heater and temperature controller (TC-344C, Harvard Apparatus) was used to maintain the recording ACSF at a temperature of 32°C. Glass stimulating electrodes (1–2 MΩ resistance) were pulled to a tip resistance of 1–2 MΩ using a Narishige PB-7 pipette puller. Glass stimulating electrodes were filled with ACSF and placed in either the deep layers of the cortex overlying the striatum, the Schaffer collateral pathway of the hippocampus, or in the dorsal striatum. The stimulating electrode was placed at a depth of at least 50 μm below the slice surface. Clampex software (Molecular Devices) was used to coordinate LED illumination (Prior, Lumen 300), electrical stimulation from an Iso-flex stimulus isolator (AMPI), and image acquisition with a high-speed EM-CCD camera (Andor, iXon Ultra 897). iGluSnFR excitation and emission wavelengths were filtered using a standard GFP filter cube and were delivered and collected through a 4×/0.28 NA objective (Olympus). iGluSnFR responses were evoked with 2, 5, 10, 20, 30, 40, or 50 pulses at 100 Hz, delivered at a stimulus intensity of 75 μA. The resulting iGluSnFR transients were recorded using Andor Solis software, with 4 × 4 pixel binning and an exposure time just under 5 ms to achieve an acquisition rate of 205 frames per second. Evoked iGluSnFR responses for 2, 5, 10, 20, 30, 40, and 50 pulses were each averaged over stimulus 5 trials, with non-stimulus trials used to control for mild bleaching. Stimulus and non-stimulus trials were interleaved at an interval of 10 seconds; thus successive stimulation trials were separated by 20 seconds. The average of the non-stimulus trial images were subtracted from the average of the stimulus trials using the IOS and VSD signal processor plugin for ImageJ. Fluorescent intensity changes were quantified in a 10 × 10 pixel (160 × 160 μm) region of interest (ROI) adjacent to the stimulating electrode. These ROIs were drawn 50–100 μm away from the stimulating electrode to avoid areas of tissue damage associated with the electrode placement. Changes in iGluSnFR intensity within the ROI were expressed as %ΔF/F. For each stimulation paradigm (e.g., 2 pulses and 5 pulses), the %ΔF/F values of the iGluSnFR transient were used to calculate a peak response, decay tau and area under the curve (AUC). Decay tau and AUC values were calculated in GraphPad Prism (version 9). Decay tau was calculated by fitting a single-exponential non-linear curve that started at the end of the electrical stimulation. For example, for 50 pulses (100 Hz) starting at time = 0 ms, the curve fit would be applied to time = 500 ms onward. The "fire" heat map in ImageJ was applied to maximal projection stacks to visualize the iGluSnFR response. The "volume viewer" 3D plugin in ImageJ was also used to help visualize the response along the z-(time) axis.

Western Blotting

Only one hemisphere (right) was injected for iGluSnFR imaging experiments; thus, the non-injected left hemisphere was used to collect tissue for western blot analysis. The cortex, hippocampus, and striatum were each dissected and homogenized, and western blots were performed exactly as described previously (Pinky et al., 2018).

Drugs

Ceftriaxone was ordered from Sigma-Aldrich (C5793) and dissolved in 0.9% saline solution and administered in a dose of 200 mg/kg. LDN was ordered from Tocris (Cat. No. 5082) and dissolved in a vehicle solution consisting of 500 μl of 1% DMSO/1% polyethylene glycol 400/0.2% Tween 80/10% hydroxypropyl-β-cyclodextrin/saline.

Statistics

The statistical test used for each analysis is clearly indicated in results text. p-values of <0.05 were considered significant. For imaging experiments n-values refer to the number of slices from the following animal numbers: Saline $n = 7$ mice; ceftriaxone $n = 7$ mice; vehicle $n = 9$ mice; LDN $n = 9$ mice.

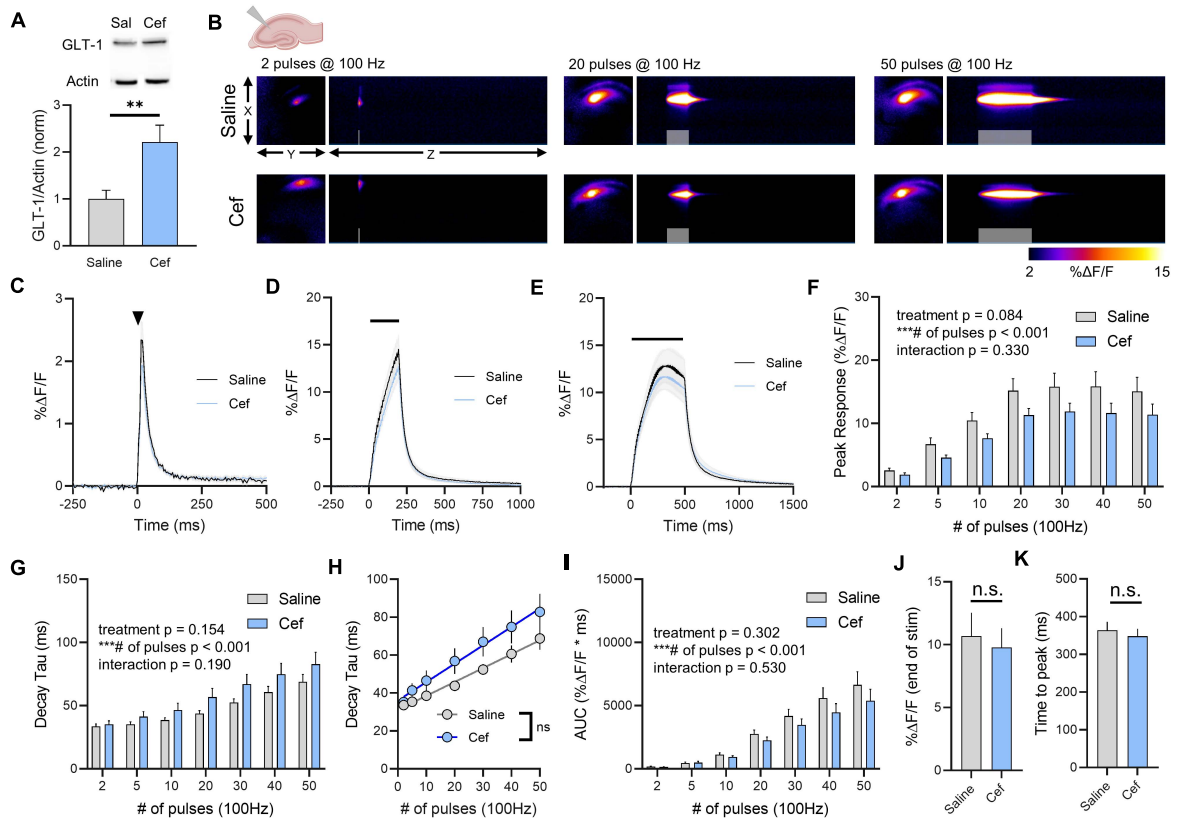

FIGURE 1 | The effect of ceftriaxone on glutamate dynamics in the hippocampus. **(A)** GLT-1 expression in hippocampal tissue from saline and ceftriaxone (Cef)-treated mice. **(B)** Representative images depicting the iGluSnFR response evoked by 2 (left), 20 (middle), and 50 (right) pulses of electrical stimulation at 100 Hz in saline- (top) and Cef-treated (bottom) mice. X–Y images (2048 × 2048 μm) depict the maximal projection image of the iGluSnFR response, while the X–Z image (2048 μm vertically x 1945 ms horizontally) depicts the iGluSnFR response over time (z-axis). Gray shading indicates the onset and duration of electrical stimulation at 100 Hz. **(C–E)** Mean (± S.E.M in gray) iGluSnFR responses to 2 **(C)**, 20 **(D)**, and 50 **(E)** pulses at 100 Hz in saline- and Cef-treated mice. Electrical stimulation is denoted by the arrowhead in **(C)** and the horizontal lines in **(D)** and **(E)**. **(F)** Mean (± S.E.M) iGluSnFR response peaks. **(G)** Mean (± S.E.M) iGluSnFR decay tau values. **(H)** Linear regression to assess the magnitude of the activity-dependent increase in iGluSnFR decay tau. **(I)** Mean (± S.E.M) iGluSnFR area under the curve (AUC). **(J)** Mean (± S.E.M) of the iGluSnFR response size (%ΔF/F) at the termination of the 50-pulse stimulation paradigm (50 pulses at 100 Hz). **(K)** Mean (± S.E.M) of the time required for the iGluSnFR response to reach a peak during the 50-pulse stimulation paradigm. $^{**}p < 0.01$, $^{***}p < 0.001$. n.s. not significant. Brain slice schematic in **(B)** was created using Biorender.com.

RESULTS

Ceftriaxone Effects on GLT-1 Expression and Glutamate Dynamics in the Hippocampus

To explore the effects of GLT-1 upregulation on real-time measures of extracellular glutamate dynamics, healthy male FVB/N mice were treated with ceftriaxone for 5–7 days (200 mg/kg/day, i.p.). Ceftriaxone treatment resulted in a significant increase in total GLT-1 expression in the hippocampus as detected by western blot (**Figure 1A**, saline $n = 7$, ceftriaxone $n = 7$, t-test, $p = 0.008$). This result is in agreement with numerous previous studies on the effects of ceftriaxone on GLT-1 expression in the hippocampus (for review, see Smaga et al., 2020). To determine whether this increased GLT-1 expression had any impact on either basal glutamate clearance or activity-dependent slowing (Armbruster et al., 2016; Pinky et al., 2018) of glutamate clearance in the hippocampus, we visualized extracellular glutamate transients by imaging iGluSnFR at 205 frames per second. Neural activity was evoked by stimulating the Schaffer collateral pathway with a range of stimulations. A heat-map depicting representative iGluSnFR responses to 2, 20, and 50 pulses is shown in **Figure 1B**, and average iGluSnFR responses to 2, 20, and 50 pulses are shown in **Figures 1C–E**, respectively. Response peaks, indicative of the relative amount of glutamate released (Koch et al., 2018), were not significantly different in saline compared to ceftriaxone-treated mice, although a strong non-significant trend toward a reduction in iGluSnFR peaks was observed in the ceftriaxone group. As expected, there was a significant effect of the number of pulses, with longer 100 Hz stimulations generating larger iGluSnFR peaks (**Figure 1F**, saline $n = 14$, ceftriaxone $n = 16$, two-way RM ANOVA, treatment $p = 0.084$, # of pulses $p < 0.001$, interaction $p = 0.330$). Regardless of treatment (i.e., saline or ceftriaxone), the average iGluSnFR response size increased from 2 up to 20 pulses before reaching a plateau.

As ceftriaxone significantly increased hippocampal GLT-1 expression, we asked whether this was reflected by faster iGluSnFR decay tau values, as iGluSnFR decay kinetics have previously been shown to serve as a sensitive measure of relative changes in glutamate clearance rates (Armbruster et al., 2016; Barnes et al., 2020; Dvorzhak et al., 2019; Parsons et al., 2016; Pinky et al., 2018; Romanos et al., 2019). As we and others have shown before (Armbruster et al., 2016; Pinky et al., 2018), increasing the duration of 100 Hz stimulation resulted in activity-dependent slowing of glutamate clearance rates as quantified by the decay tau of the iGluSnFR transient. Unexpectedly, neither basal glutamate clearance nor the activity-dependent slowing of glutamate clearance were affected by ceftriaxone-induced GLT-1 upregulation (**Figure 1G**, saline $n = 14$, ceftriaxone $n = 16$, two-way RM ANOVA, treatment $p = 0.154$, # of pulses $p < 0.001$, interaction $p = 0.190$). As an additional quantification method to focus exclusively on activity-dependent slowing of glutamate clearance, we used linear regression to determine the relationship between the number of pulses (and therefore, the duration of the 100 Hz stimulation) and the decay tau. We found a significant positive correlation between number of pulses and iGluSnFR decay tau for both saline- (**Figure 1H**, linear regression, $r = 0.710$, $p < 0.001$) and ceftriaxone-treated mice (**Figure 1H**, linear regression, $r = 0.528$, $p < 0.001$), further confirming that glutamate clearance is slowed in an activity-dependent manner. However, there was no significant difference between the linear regression slopes for saline- and ceftriaxone-treated mice ($p = 0.173$), suggesting that the activity-dependent slowing of glutamate clearance occurred at similar rates in both groups. In addition, we quantified iGluSnFR AUC as a relative measure of the total amount of extracellular glutamate accumulation during each stimulation. Not surprisingly, iGluSnFR AUC significantly increased with an increasing number of pulses. However, ceftriaxone treatment had no effect on iGluSnFR AUC (**Figure 1I**, saline $n = 14$, ceftriaxone $n = 16$, two-way RM ANOVA, treatment $p = 0.302$, # of pulses $p < 0.001$, interaction $p = 0.530$). As iGluSnFR responses often peaked prior to the end of the stimulation for the longer stimulus trains, we also quantified the response size at the end of the 50-pulse stimulation, which was not significantly different between saline and ceftriaxone groups (**Figure 1J**, unpaired t-test, $p = 0.702$). Similarly, the time to reach a peak during the 50-pulse stimulation was not affected by ceftriaxone treatment (**Figure 1K**, unpaired t-test, $p = 0.594$). Together, these data demonstrate that while ceftriaxone successfully increased hippocampal GLT-1 expression in the healthy mouse brain, it was without effect on real-time measurements on the extracellular dynamics of synaptically released glutamate. Moreover, GLT-1 overexpression was unable to overcome activity-dependent slowing of glutamate clearance.

Ceftriaxone Effects on GLT-1 Expression and Glutamate Dynamics in the Cortex

As glutamate clearance rates differ depending on the brain region under investigation (Pinky et al., 2018), we repeated the above experiments in cortical tissue, specifically the deep layers of the cortex near the border of primary somatosensory and motor cortex. Ceftriaxone treatment resulted in a significant increase in total GLT-1 expression in the cortex as detected by western blot (**Figure 2A**, saline $n = 7$, ceftriaxone $n = 7$, t-test, $p = 0.045$). Neural activity was evoked by stimulating approximately 100–200 μm dorsal to the corpus callosum overlying the striatum. A heat-map depicting representative iGluSnFR responses to 2, 20, and 50 pulses is shown in **Figure 2B**, and average iGluSnFR responses to 2, 20 and 50 pulses are shown in **Figures 2C–E**, respectively. Similar to the trend observed in the hippocampus where iGluSnFR peaks tended to be smaller following ceftriaxone treatment, we observed the same decrease here, although the result in the cortex was statistically significant. That is, iGluSnFR response size was reduced in the cortex of ceftriaxone-treated mice compared to saline controls. Response size consistently increased with increased durations of 100 Hz stimulation for both groups, and the response was reduced by ceftriaxone (**Figure 2F**, saline $n = 15$, ceftriaxone $n = 16$, two-way RM ANOVA, treatment $p = 0.011$, # of pulses $p < 0.001$, interaction $p = 0.004$, with *post hoc* differences observed for 20, 30, and 40 pulses, Sidak's multiple comparisons test). This result suggests that ceftriaxone has an unexpected effect of decreasing glutamate release in the cortex.

Increasing the duration of 100 Hz stimulation resulted in activity-dependent slowing of glutamate clearance rates as quantified by the decay tau of the cortical iGluSnFR transient. As we saw in the hippocampus, neither basal glutamate clearance nor the activity-dependent slowing of glutamate clearance were affected by ceftriaxone-induced GLT-1 upregulation in the cortex (**Figure 2G**, saline $n = 15$, ceftriaxone $n = 16$, two-way RM ANOVA, treatment $p = 0.083$, # of pulses $p < 0.001$, interaction $p = 0.194$). In fact, the non-significant trend we observed for a treatment effect ($p = 0.083$) reflected a slight tendency for mean clearance rates to be slower, not faster, following ceftriaxone treatment. Nonetheless, this did not reach statistical significance and therefore we conclude that ceftriaxone was without effect on iGluSnFR decay kinetics in the cortex. There was a significant positive correlation between number of pulses and iGluSnFR decay tau for both saline- (**Figure 2H**, linear regression, $r = 0.807$, $p < 0.001$) and ceftriaxone-treated mice (**Figure 2H**, linear regression, $r = 0.635$, $p < 0.001$), confirming that glutamate clearance is slowed in an activity-dependent manner in the cortex. However, there was no significant difference between the linear regression slopes for saline- and ceftriaxone-treated mice ($p = 0.376$), suggesting that the activity-dependent slowing of glutamate clearance occurred at similar rates in both groups. iGluSnFR AUC significantly increased with an increasing number of pulses, and ceftriaxone treatment significantly reduced iGluSnFR AUC (**Figure 2I**, saline $n = 15$, ceftriaxone $n = 16$, Two-way RM ANOVA, treatment $p = 0.038$, # of pulses $p < 0.001$, interaction p = 0.004, with *post hoc* differences observed for 40 and 50 pulses, Sidak's multiple comparisons test). iGluSnFR response size at the end of the 50-pulse stimulation was not significantly different between saline and ceftriaxone groups (**Figure 2J**, unpaired t-test, $p = 0.092$). The time to reach a peak during the 50-pulse stimulation was also not affected by ceftriaxone treatment (**Figure 2K**, unpaired t-test, $p = 0.375$).

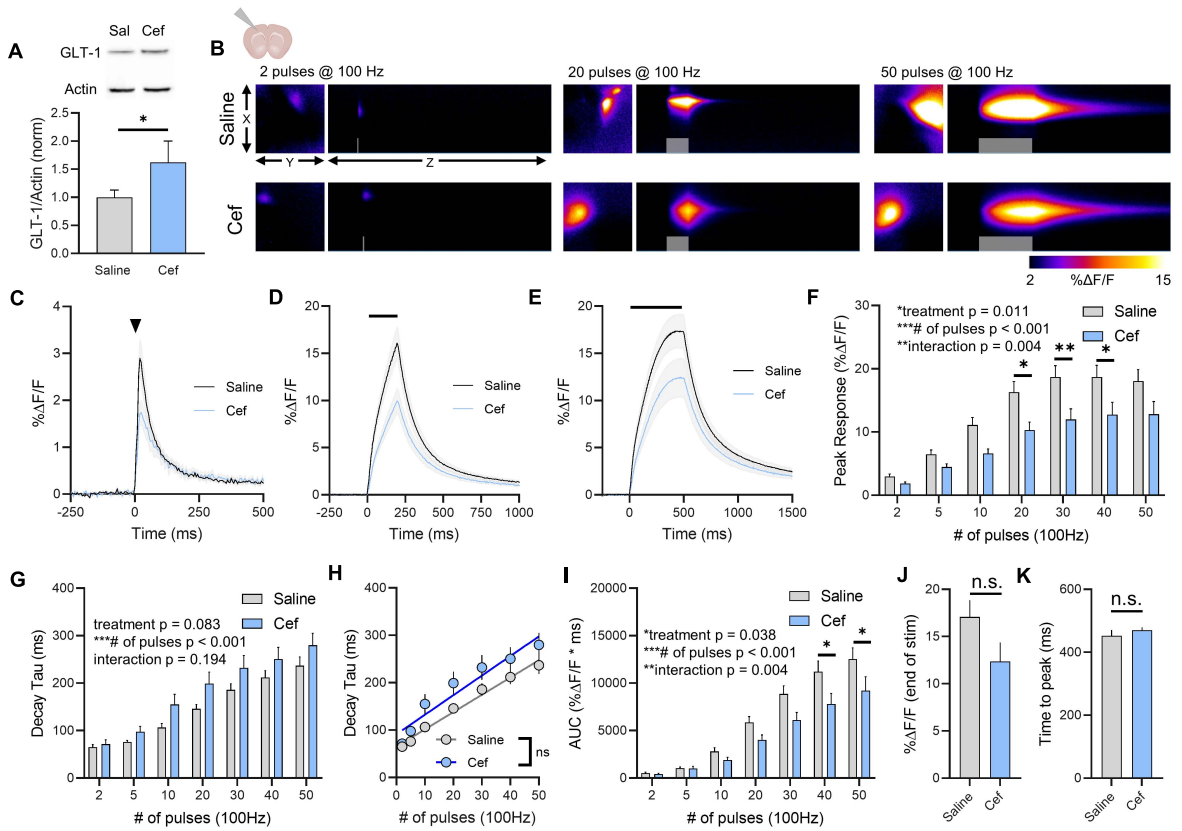

FIGURE 2 | The effect of ceftriaxone on glutamate dynamics in the cortex. **(A)** GLT-1 expression in cortical tissue from saline and ceftriaxone (Cef)-treated mice. **(B)** Representative images depicting the iGluSnFR response evoked by 2 (left), 20 (middle), and 50 (right) pulses of electrical stimulation at 100 Hz in saline- (top) and Cef-treated (bottom) mice. X–Y images (2048 × 2048 μm) depict the maximal projection image of the iGluSnFR response, while the X–Z image (2048 μm vertically x 1945 ms horizontally) depicts the iGluSnFR response over time (z-axis). Gray shading indicates the onset and duration of electrical stimulation at 100 Hz. **(C–E)** Mean (± S.E.M in gray) iGluSnFR responses to 2 **(C)**, 20 **(D)**, and 50 **(E)** pulses at 100 Hz in saline- and Cef-treated mice. Electrical stimulation is denoted by the arrowhead in **(C)** and the horizontal lines in **(D)** and **(E)**. **(F)** Mean (± S.E.M) iGluSnFR response peaks. **(G)** Mean (± S.E.M) iGluSnFR decay tau values. **(H)** Linear regression to assess the magnitude of the activity-dependent increase in iGluSnFR decay tau. **(I)** Mean (± S.E.M) iGluSnFR area under the curve (AUC). **(J)** Mean (± S.E.M) of the iGluSnFR response size (%ΔF/F) at the termination of the 50-pulse stimulation paradigm (50 pulses at 100 Hz). **(K)** Mean (± S.E.M) of the time required for the iGluSnFR response to reach a peak during the 50-pulse stimulation paradigm. Sidak's multiple comparisons *post hoc* test was used in **(F)** and **(I)**. $^{*}p < 0.05$, $^{**}p < 0.01$, $^{***}p < 0.001$. n.s. not significant. Brain slice schematic in **(B)** was created using Biorender.com.

Together, these results demonstrate that ceftriaxone does not accelerate cortical glutamate clearance but can negatively regulate glutamate release during neural activity in the cortex. As we observed in the hippocampus, GLT-1 overexpression was unable to overcome activity-dependent slowing of glutamate clearance in the cortex.

Ceftriaxone Effects on GLT-1 Expression and Glutamate Dynamics in the Striatum

We repeated the above experiments in the dorsal striatum, as a previous study from our lab demonstrated that glutamate clearance rates in the striatum are particularly slow compared to the hippocampus (Pinky et al., 2018); thus we hypothesized that GLT-1 overexpression may accelerate the slow glutamate clearance characteristic of this area. Ceftriaxone treatment resulted in a significant increase in total GLT-1 expression in the striatum as detected by western blot (**Figure 3A**, saline $n = 7$, ceftriaxone $n = 7$, t-test, $p = 0.049$). Neural activity was evoked by stimulating the dorsal striatum, approximately 100–200 μm ventral to the corpus callosum. A heat-map depicting representative iGluSnFR responses to 2, 20, and 50 pulses is shown in **Figure 3B**, and average iGluSnFR responses to 2, 20, and 50 pulses are shown in **Figures 3C–E**, respectively. Unlike the non-significant trend and the significant reduction of iGluSnFR peaks observed in the hippocampus and cortex, ceftriaxone had no effect whatsoever on iGluSnFR peaks in the striatum (**Figure 3F**, saline $n = 17$, ceftriaxone $n = 20$, two-way RM ANOVA, treatment $p = 0.982$, # of pulses $p < 0.001$, interaction $p = 0.999$). Increasing the duration of 100 Hz stimulation resulted in activity-dependent slowing of glutamate clearance, but there was no effect of ceftriaxone on iGluSnFR decay tau values (**Figure 3G**, saline $n = 17$, ceftriaxone $n = 20$, two-way RM ANOVA, treatment $p = 0.145$, # of pulses $p < 0.001$, interaction $p = 0.986$).

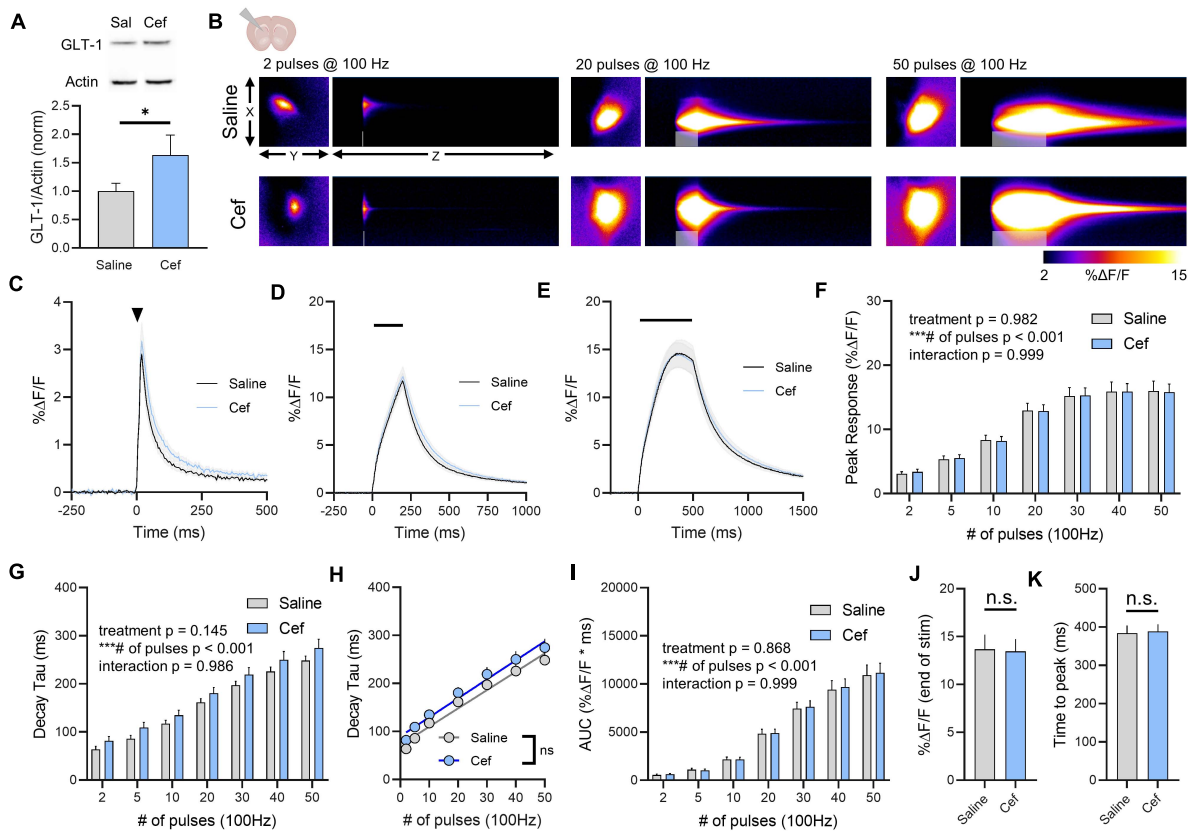

FIGURE 3 | The effect of ceftriaxone on glutamate dynamics in the striatum. **(A)** GLT-1 expression in striatal tissue from saline and ceftriaxone (Cef)-treated mice. **(B)** Representative images depicting the iGluSnFR response evoked by 2 (left), 20 (middle) and 50 (right) pulses of electrical stimulation at 100 Hz in saline- (top) and Cef-treated (bottom) mice. X–Y images (2048 × 2048 μm) depict the maximal projection image of the iGluSnFR response while the X–Z image (2048 μm vertically x 1945 ms horizontally) depicts the iGluSnFR response over time (z-axis). Gray shading indicates the onset and duration of electrical stimulation at 100 Hz. **(C–E)** Mean (± S.E.M in gray) iGluSnFR responses to 2 **(C)**, 20 **(D)**, and 50 **(E)** pulses at 100 Hz in saline- and Cef-treated mice. Electrical stimulation is denoted by the arrowhead in **(C)** and the horizontal lines in **(D)** and **(E)**. **(F)** Mean (± S.E.M) iGluSnFR response peaks. **(G)** Mean (± S.E.M) iGluSnFR decay tau values. **(H)** Linear regression to assess the magnitude of the activity-dependent increase in iGluSnFR decay tau. **(I)** Mean (± S.E.M) iGluSnFR area under the curve (AUC). **(J)** Mean (± S.E.M) of the iGluSnFR response size (%$\Delta F/F$) at the termination of the 50-pulse stimulation paradigm (50 pulses at 100 Hz). **(K)** Mean (± S.E.M) of the time required for the iGluSnFR response to reach a peak during the 50-pulse stimulation paradigm. *$p < 0.05$, ***$p < 0.001$. n.s. not significant. Brain slice schematic in **(B)** was created using Biorender.com.

There was a significant positive correlation between number of pulses and iGluSnFR decay tau for both saline- (**Figure 3H**, linear regression, $r = 0.891$, $p < 0.001$) and ceftriaxone-treated mice (**Figure 3H**, linear regression, $r = 0.748$, $p < 0.001$), but there was no significant difference between the linear regression slopes for saline- and ceftriaxone-treated mice ($p = 0.702$), suggesting that the activity-dependent slowing of glutamate clearance occurred at similar rates in both groups. iGluSnFR AUC significantly increased with an increasing number of pulses, but ceftriaxone was without effect on iGluSnFR AUC (**Figure 3I**, saline $n = 17$, ceftriaxone $n = 20$, two-way RM ANOVA, treatment $p = 0.868$, # of pulses $p < 0.001$, interaction p = 0.999). iGluSnFR response size at the end of the 50-pulse stimulation was not significantly different between saline and ceftriaxone groups (**Figure 3J**, unpaired t-test, $p = 0.918$). The time to reach a peak during the 50-pulse stimulation was also not affected by ceftriaxone treatment (**Figure 3K**, unpaired t-test, $p = 0.876$). In all, evoked iGluSnFR transients were nearly identical between saline- and ceftriaxone-treated mice despite the ceftriaxone-induced increase in GLT-1 expression.

In all, ceftriaxone exhibited no ability to accelerate glutamate clearance rates in either the hippocampus, cortex or striatum. As we demonstrated before, these brain regions exhibit differences in the rate at which they clear evoked glutamate release, with the hippocampus clearing glutamate significantly faster than the cortex and striatum (Pinky et al., 2018). Similar regional differences were observed here (**Figure 4A**, hippocampus $n = 14$, cortex $n = 15$, striatum $n = 17$, Two-way RM ANOVA, region $p < 0.001$, # of pulses $p < 0.001$, interaction $p < 0.001$), and ceftriaxone did not impact the observed regional differences in clearance rates. That is, regional differences in iGluSnFR decay tau were still readily observed in ceftriaxone-treated mice (**Figure 4B**, hippocampus $n = 16$, cortex $n = 16$, striatum $n = 20$, two-way RM ANOVA, region $p < 0.001$, # of pulses $p < 0.001$, interaction $p < 0.001$). Together, these data demonstrate that ceftriaxone does not accelerate glutamate clearance in any region

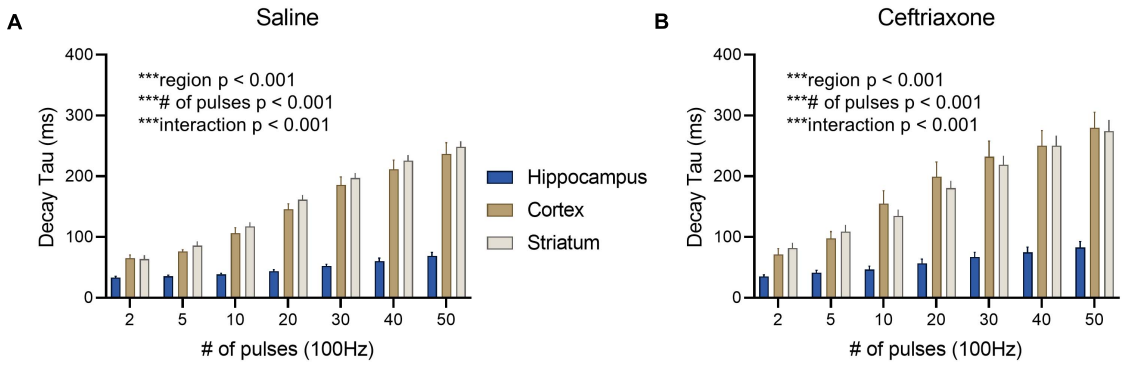

FIGURE 4 | The effect of ceftriaxone on regional differences in glutamate clearance. **(A)** Mean (± S.E.M) iGluSnFR decay tau values to compare regional differences in glutamate clearance in saline-treated mice. **(B)** Mean (± S.E.M) iGluSnFR decay tau values to compare regional differences in glutamate clearance in ceftriaxone-treated mice. ***$p < 0.001$.

tested, and that it can negatively regulate glutamate release in a region-dependent manner.

LDN/OSU 212320 Effects on GLT-1 Expression and Glutamate Dynamics in the Hippocampus

More recently, a small molecule called LDN was shown to significantly increase GLT-1 expression (Kong et al., 2014). As LDN likely relies on a different mechanism of GLT-1 upregulation compared to ceftriaxone, we decided to repeat the ceftriaxone experiments, but now comparing LDN treatment to vehicle-treated mice. We reasoned that there may be differences in the subcellular localization and/or functional properties of the GLT-1 produced by LDN treatment compared to ceftriaxone, as we saw no evidence of ceftriaxone to accelerate glutamate clearance rates. LDN treatment resulted in a significant increase in total GLT-1 expression in the hippocampus (**Figure 5A**, vehicle $n = 9$, LDN $n = 9$, t-test, $p = 0.040$). Next, neural activity was evoked by stimulating the Schaffer collateral pathway in the hippocampus. A heat-map depicting representative iGluSnFR responses to 2, 20, and 50 pulses is shown in **Figure 5B**, and average iGluSnFR responses to 2, 20, and 50 pulses are shown in **Figures 5C–E**, respectively. LDN did not have any effect on iGluSnFR peaks (**Figure 5F**, vehicle $n = 13$, LDN $n = 12$, Two-way RM ANOVA, treatment $p = 0.333$, # of pulses $p < 0.001$, interaction $p = 0.225$) or iGluSnFR decay (**Figure 5G**, vehicle $n = 13$, LDN $n = 12$, two-way RM ANOVA, treatment $p = 0.732$, # of pulses $p < 0.001$, interaction $p = 0.145$).

There was a significant positive correlation between number of pulses and iGluSnFR decay tau for both saline- (**Figure 5H**, linear regression, $r = 0.667$, $p < 0.001$) and LDN-treated mice (**Figure 5H**, $r = 0.594$, linear regression, $p < 0.001$), demonstrating that activity-dependent slowing of glutamate clearance was observed in both groups. However, the slopes of the linear regression lines were significantly different, with LDN-treated mice exhibiting a reduced slope ($p = 0.021$). This result suggests that LDN exerts a mild effect on activity-dependent slowing of glutamate clearance; clearance rates are still slower with increasing durations of activity following LDN treatment, but they do not slow to the same extent as observed in vehicle-treated mice. Total glutamate accumulation was unaffected by LDN treatment, as no significant differences were observed for iGluSnFR AUC (**Figure 5I**, vehicle $n = 13$, LDN $n = 12$, two-way RM ANOVA, treatment $p = 0.702$, # of pulses $p < 0.001$, interaction $p = 0.795$). iGluSnFR response size at the end of the 50-pulse stimulation was not significantly different between vehicle and LDN groups (**Figure 5J**, unpaired t-test, $p = 0.722$). The time to reach a peak during the 50-pulse stimulation was also not affected by LDN treatment (**Figure 5K**, unpaired t-test, $p = 0.585$).

LDN/OSU 212320 Effects on GLT-1 Expression and Glutamate Dynamics in the Cortex

In the cortex, LDN significantly increased GLT-1 expression compared to vehicle treatment (**Figure 6A**, vehicle $n = 9$, LDN $n = 9$, t-test, $p = 0.048$). A heat-map depicting representative iGluSnFR responses to 2, 20, and 50 pulses is shown in **Figure 6B**, and average iGluSnFR responses to 2, 20, and 50 pulses are shown in **Figures 6C–E**, respectively. In the cortex, LDN was without effect on iGluSnFR peak (**Figure 6F**, vehicle $n = 10$, LDN $n = 12$, two-way RM ANOVA, treatment $p = 0.656$, # of pulses $p < 0.001$, interaction $p = 0.762$) and was also without effect on iGluSnFR decay (**Figure 6G**, vehicle $n = 10$, LDN $n = 12$, two-way RM ANOVA, treatment $p = 0.346$, # of pulses $p < 0.001$, interaction $p = 0.841$). Both vehicle- and LDN-treated mice exhibited activity-dependent slowing of glutamate clearance (**Figure 6H**, linear regression, vehicle $r = 0.815$, $p < 0.001$, LDN $r = 0.803$, $p < 0.001$) and the slowing occurred at a similar magnitude (difference between slopes $p = 0.446$). LDN also had no effect on iGluSnFR AUC values in the cortex (**Figure 6I**, vehicle $n = 10$, LDN $n = 12$, two-way RM ANOVA, treatment $p = 0.536$, # of pulses $p < 0.001$, interaction $p = 0.855$). iGluSnFR response size at the end of the 50-pulse stimulation was not significantly different between vehicle and LDN groups (**Figure 6J**, unpaired t-test, $p = 0.625$). The time to reach a peak during the 50-pulse

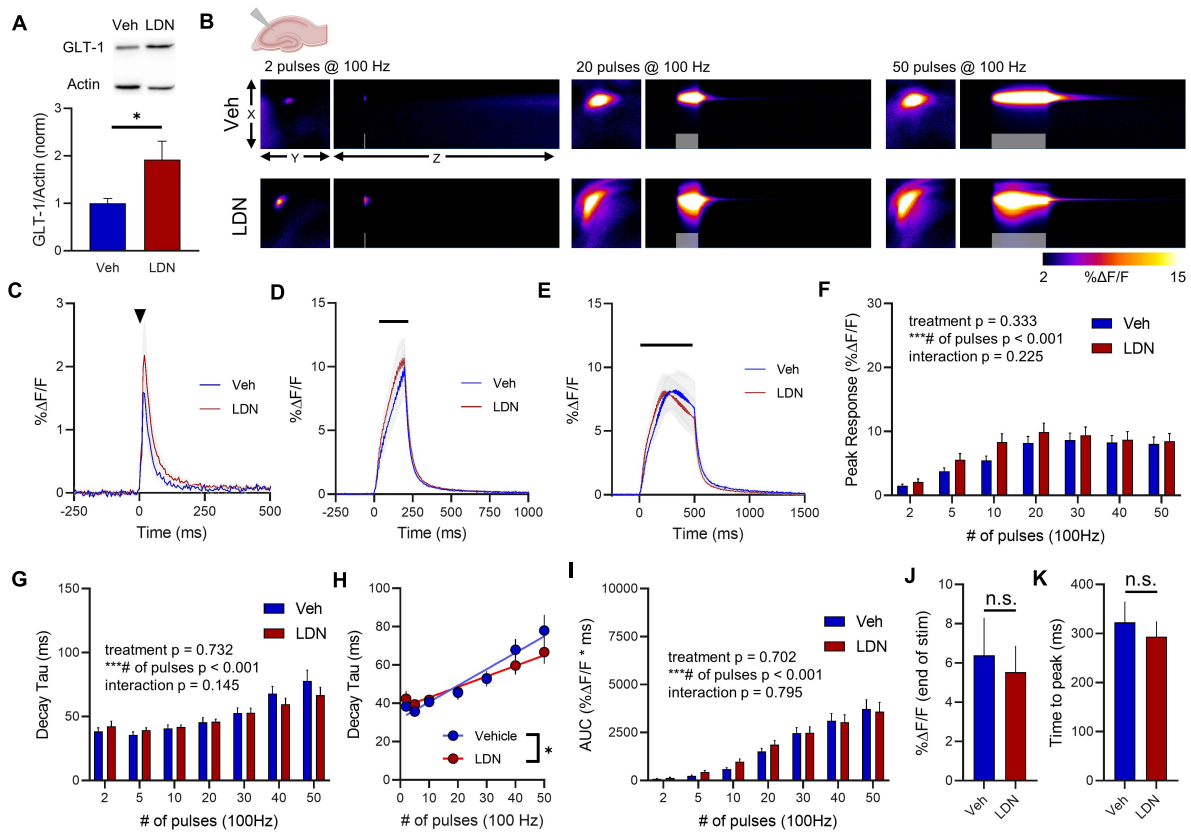

FIGURE 5 | The effect of LDN on glutamate dynamics in the hippocampus. **(A)** GLT-1 expression in hippocampal tissue from vehicle (Veh)- and LDN-treated mice. **(B)** Representative images depicting the iGluSnFR response evoked by 2 (left), 20 (middle), and 50 (right) pulses of electrical stimulation at 100 Hz in Veh- (top) and LDN-treated (bottom) mice. X–Y images (2048 × 2048 μm) depict the maximal projection image of the iGluSnFR response, while the X–Z image (2048 μm vertically x 1945 ms horizontally) depicts the iGluSnFR response over time (z-axis). Gray shading indicates the onset and duration of electrical stimulation at 100 Hz. **(C–E)** Mean (± S.E.M in gray) iGluSnFR responses to 2 **(C)**, 20 **(D)**, and 50 **(E)** pulses at 100 Hz in Veh- and LDN-treated mice. Electrical stimulation is denoted by the arrowhead in **(C)** and the horizontal lines in **(D)** and **(E)**. **(F)** Mean (± S.E.M) iGluSnFR response peaks. **(G)** Mean (± S.E.M) iGluSnFR decay tau values. **(H)** Linear regression to assess the magnitude of the activity-dependent increase in iGluSnFR decay tau. **(I)** Mean (± S.E.M) iGluSnFR area under the curve (AUC). **(J)** Mean (± S.E.M) of the iGluSnFR response size (%ΔF/F) at the termination of the 50-pulse stimulation paradigm (50 pulses at 100 Hz). **(K)** Mean (± S.E.M) of the time required for the iGluSnFR response to reach a peak during the 50-pulse stimulation paradigm. *$p < 0.05$, ***$p < 0.001$. n.s. not significant. Brain slice schematic in **(B)** was created using Biorender.com.

stimulation was also not affected by LDN treatment (**Figure 6K**, unpaired *t*-test, $p = 0.334$).

LDN/OSU 212320 Effects on GLT-1 Expression and Glutamate Dynamics in the Striatum

In the striatum, LDN significantly increased GLT-1 expression compared to vehicle treatment (**Figure 7A**, vehicle $n = 9$, LDN/OSU $n = 9$, *t*-test, $p = 0.023$). A heat-map depicting representative iGluSnFR responses to 2, 20, and 50 pulses is shown in **Figure 7B**, and average iGluSnFR responses to 2, 20 and 50 pulses are shown in **Figures 7C–E**, respectively. In the striatum, LDN was without effect on iGluSnFR peak (**Figure 7F**, vehicle $n = 16$, LDN $n = 14$, two-way RM ANOVA, treatment $p = 0.812$, # of pulses $p < 0.001$, interaction $p = 0.998$) and was also without effect on iGluSnFR decay (**Figure 7G**, vehicle $n = 16$, LDN $n = 14$, two-way RM ANOVA, treatment $p = 0.384$, # of pulses $p < 0.001$, interaction $p = 0.962$). Both vehicle- and LDN-treated mice exhibited activity-dependent slowing of glutamate clearance (**Figure 7H**, linear regression, vehicle $r = 0.829$, $p < 0.001$, LDN $r = 0.777$, $p < 0.001$) and the slowing occurred at a similar magnitude (difference between slopes p = 0.586). LDN also had no effect on iGluSnFR AUC values in the striatum (**Figure 7I**, vehicle $n = 16$, LDN $n = 14$, two-way RM ANOVA, treatment $p = 0.949$, # of pulses $p < 0.001$, interaction $p = 0.999$). iGluSnFR response size at the end of the 50-pulse stimulation was not significantly different between vehicle and LDN groups (**Figure 7J**, unpaired *t*-test, $p = 0.940$). The time to reach a peak during the 50-pulse stimulation was also not affected by LDN treatment (**Figure 7K**, unpaired *t*-test, $p = 0.709$).

Vehicle-treated mice displayed clear regional differences in glutamate clearance rates (**Figure 8A**, hippocampus $n = 13$, cortex $n = 10$, striatum $n = 16$, two-way RM ANOVA, region $p < 0.001$, # of pulses $p < 0.001$, interaction $p < 0.001$). Like ceftriaxone, LDN did not accelerate glutamate clearance in the slower regions,

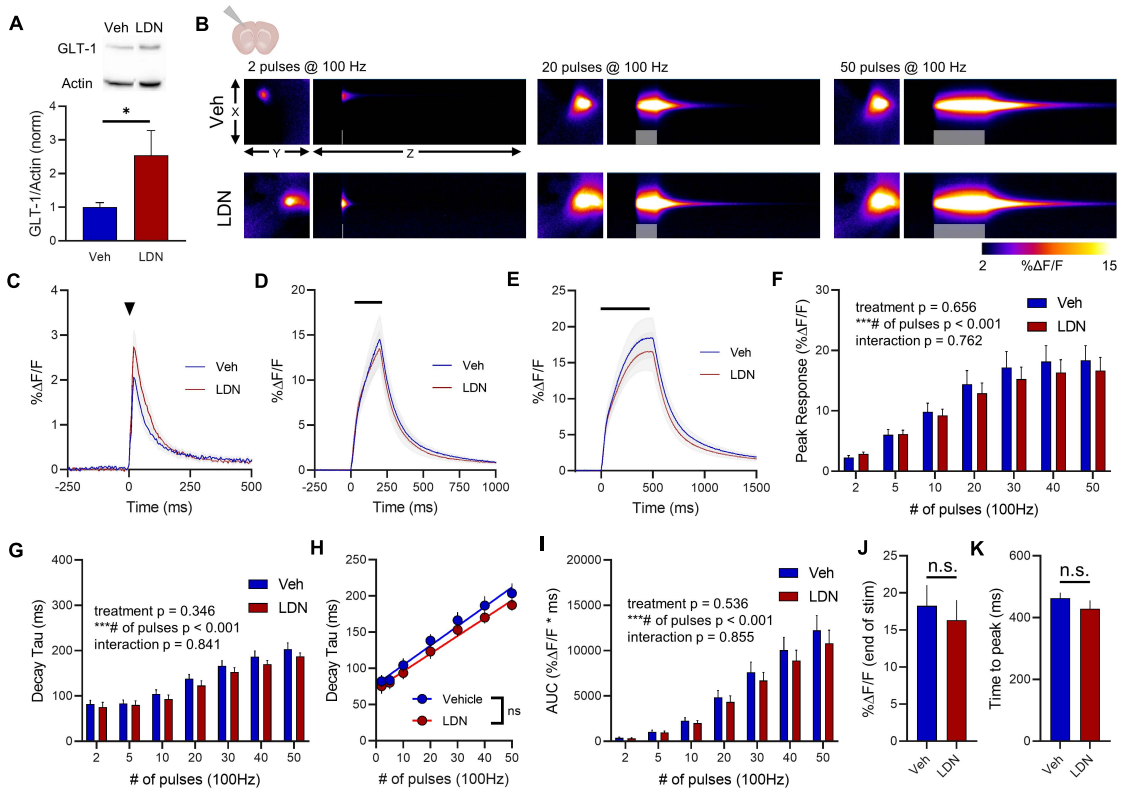

FIGURE 6 | The effect of LDN on glutamate dynamics in the cortex. **(A)** GLT-1 expression in cortical tissue from vehicle (Veh)- and LDN-treated mice. **(B)** Representative images depicting the iGluSnFR response evoked by 2 (left), 20 (middle), and 50 (right) pulses of electrical stimulation at 100 Hz in Veh- (top) and LDN-treated (bottom) mice. X–Y images (2048 × 2048 μm) depict the maximal projection image of the iGluSnFR response while the X–Z image (2048 μm vertically x 1945 ms horizontally) depicts the iGluSnFR response over time (z-axis). Gray shading indicates the onset and duration of electrical stimulation at 100 Hz. **(C–E)** Mean (± S.E.M in gray) iGluSnFR responses to 2 **(C)**, 20 **(D)**, and 50 **(E)** pulses at 100 Hz in Veh- and LDN-treated mice. Electrical stimulation is denoted by the arrowhead in **(C)** and the horizontal lines in **(D)** and **(E)**. **(F)** Mean (± S.E.M) iGluSnFR response peaks. **(G)** Mean (± S.E.M) iGluSnFR decay tau values. **(H)** Linear regression to assess the magnitude of the activity-dependent increase in iGluSnFR decay tau. **(I)** Mean (± S.E.M) iGluSnFR area under the curve (AUC). **(J)** Mean (± S.E.M) of the iGluSnFR response size (%$\Delta F/F$) at the termination of the 50-pulse stimulation paradigm (50 pulses at 100 Hz). **(K)** Mean (± S.E.M) of the time required for the iGluSnFR response to reach a peak during the 50-pulse stimulation paradigm. *$p < 0.05$, ***$p < 0.001$. n.s. not significant. Brain slice schematic in **(B)** was created using Biorender.com.

and clear regional differences were still observed following LDN treatment despite the increase in GLT-1 expression (**Figure 8B**, hippocampus $n = 12$, cortex $n = 12$, striatum $n = 14$, two-way RM ANOVA, region $p < 0.001$, # of pulses $p < 0.001$, interaction $p < 0.001$).

DISCUSSION

In the present study, we demonstrate that pharmacological upregulation of GLT-1 has a minimal impact on real-time measurements of extracellular glutamate dynamics. While our experiments were performed on healthy mice where GLT-1 expression is already expressed at a very high density (Lehre and Danbolt, 1998), we were surprised to find that enhanced GLT-1 expression was generally unable to counter any activity-dependent slowing of glutamate clearance nor was it able to speed glutamate clearance in an area like the striatum, where glutamate clearance is considerably slower than in the hippocampus (Pinky et al., 2018). Using both ceftriaxone and LDN as pharmacological means to increase GLT-1 expression, we found that only LDN was able to exert a small but significant brake on the activity-dependent slowing of glutamate clearance, and this effect was limited to the hippocampus. Both compounds significantly increased total GLT-1 protein expression in the hippocampus, cortex and striatum; yet, aside from the aforementioned LDN effect in the hippocampus, they did not alter basal or activity-dependent changes in glutamate clearance rates. Overall, our data caution the common interpretation that more GLT-1 protein translates to accelerated glutamate uptake. Glutamate uptake is a complex process that relies on much more than just the expression levels of the transporters themselves.

Comparison With Previous Studies on GLT-1 Upregulation in Healthy Tissue

A recent review paper provides an excellent and thorough review on the effects of ceftriaxone on GLT-1 expression, both in healthy

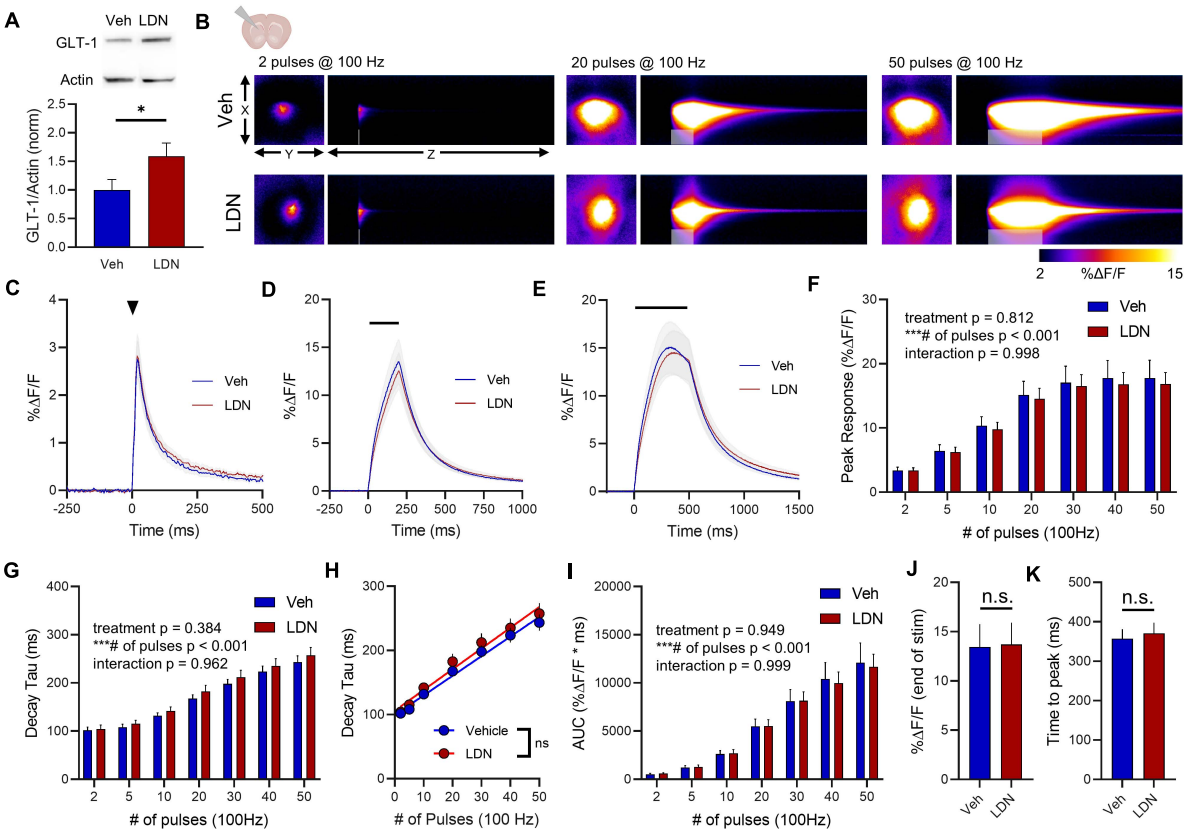

FIGURE 7 | The effect of LDN on glutamate dynamics in the striatum. **(A)** GLT-1 expression in striatal tissue from vehicle (Veh)- and LDN-treated mice. **(B)** Representative images depicting the iGluSnFR response evoked by 2 (left), 20 (middle), and 50 (right) pulses of electrical stimulation at 100 Hz in Veh- (top) and LDN-treated (bottom) mice. X–Y images (2048 × 2048 μm) depict the maximal projection image of the iGluSnFR response, while the X–Z image (2048 μm vertically x 1945 ms horizontally) depicts the iGluSnFR response over time (z-axis). Gray shading indicates the onset and duration of electrical stimulation at 100 Hz. **(C–E)** Mean (± S.E.M in gray) iGluSnFR responses to 2 **(C)**, 20 **(D)**, and 50 **(E)** pulses at 100 Hz in Veh- and LDN-treated mice. Electrical stimulation is denoted by the arrowhead in **(C)** and the horizontal lines in **(D)** and **(E)**. **(F)** Mean (± S.E.M) iGluSnFR response peaks. **(G)** Mean (± S.E.M) iGluSnFR decay tau values. **(H)** Linear regression to assess the magnitude of the activity-dependent increase in iGluSnFR decay tau. **(I)** Mean (± S.E.M) iGluSnFR area under the curve (AUC). **(J)** Mean (± S.E.M) of the iGluSnFR response size (%ΔF/F) at the termination of the 50-pulse stimulation paradigm (50 pulses at 100 Hz). **(K)** Mean (± S.E.M) of the time required for the iGluSnFR response to reach a peak during the 50-pulse stimulation paradigm. $^{*}p < 0.05$, $^{***}p < 0.001$. n.s. not significant. Brain slice schematic in **(B)** was created using Biorender.com.

brain tissue and in neurological disease models (Smaga et al., 2020). The authors noted that ceftriaxone consistently increases GLT-1 in the hippocampus, but that ceftriaxone-induced changes in GLT-1 expression were less consistent in other brain regions. In the present study, both ceftriaxone and LDN resulted in a significant increase in GLT-1 expression in the hippocampus, cortex and striatum. Nonetheless, this increased expression was without any clear effect on glutamate uptake rates as measured by evoked iGluSnFR transients in acute brain slices. To complement the summary tables in this recent review paper (Smaga et al., 2020), we have created another table here that summarizes the effects of ceftriaxone on glutamate uptake measurements in healthy (control) cells or tissues (**Table 1**). In many of these studies, glutamate uptake was quantified by exposing cell cultures, acute slices or synaptosome preparations to exogenous radiolabeled glutamate for approximately 5–10 minutes and measuring how much of the exogenous glutamate was absorbed by the preparation over that time. While serving as an effective means to determine the overall uptake capacity of a given preparation, this technique tells us little about the speed at which glutamate is cleared from the extracellular space following its release from presynaptic terminals. By nature, iGluSnFR decay tau values are significantly slower than the actual uptake rate of glutamate, which is estimated to increase to 1 mM for 1–2 milliseconds following synaptic release (Bergles et al., 1999; Clements et al., 1992); nonetheless, iGluSnFR represents a sensitive means to detect relative changes in clearance rates under different experimental conditions, and can do so on a millisecond timescale. As summarized in **Table 1**, the bulk of studies that report enhanced glutamate uptake following ceftriaxone treatment quantified the uptake of exogenous radiolabeled glutamate over multiple minutes (Beller et al., 2011; Chotibut et al., 2014; Hu et al., 2015; Lee et al., 2008; Liu et al., 2013; Rothstein et al., 2005; Thöne-Reineke et al., 2008; Verma et al., 2010; Yang et al., 2011). In contrast, the studies that quantified glutamate uptake using iGluSnFR or

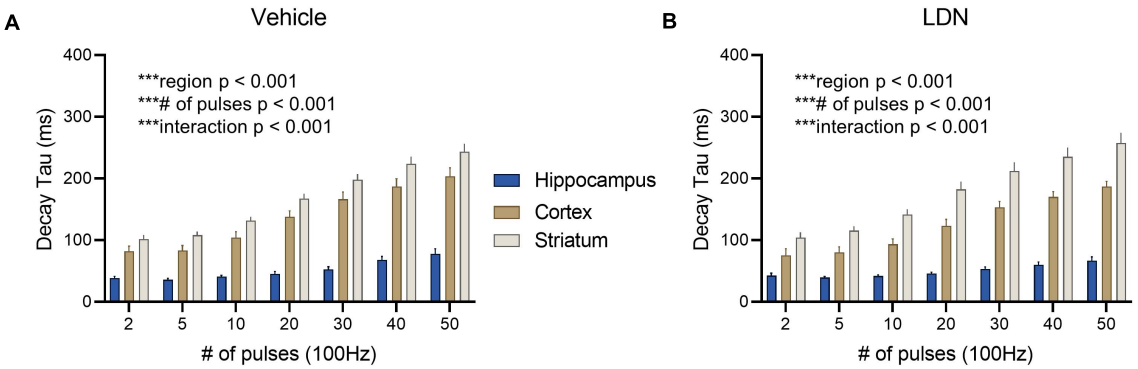

FIGURE 8 | The effect of LDN on regional differences in glutamate clearance. **(A)** Mean (± S.E.M) iGluSnFR decay tau values to compare regional differences in glutamate clearance in vehicle-treated mice. **(B)** Mean (± S.E.M) iGluSnFR decay tau values to compare regional differences in glutamate clearance in LDN-treated mice. ***$p < 0.001$.

TABLE 1 | Effects of ceftriaxone on glutamate uptake in healthy cells, tissues, and animals.

References	Preparation	Ceftriaxone treatment	Uptake quantification	Effect on uptake
Rothstein et al., 2005	Mouse cortex homogenates	200 mg/kg/day for 7 days (i.p.)	L-[^{3}H]-glutamate for 10 min	∼150% increase
Rothstein et al., 2005	Mouse Spinal cord cultures	10–100 μM, applied for 7 days	L-[^{3}H]-glutamate for 10 min	∼200% increase (100 μM)
Lee et al., 2008	Primary human fetal astrocytes	10 μM, applied for 2 days	L-[^{3}H]-glutamate for 10 min	∼115% increase
Miller et al., 2008	Mouse striatum *in vivo* microdialysis	200 mg/kg/day for 7 days (i.p.)	No-net-flux microdialysis	∼25% increase
Thöne-Reineke et al., 2008	Rat cortical astrocyte cultures	10 μM, applied for 5 days	L-[^{3}H]-glutamate for 10 min	∼20% increase
Verma et al., 2010	Rat glial enriched fraction	100 mg/kg/day for 5 days (i.v.)	L-[^{3}H]-glutamate for 30 min	∼85% increase
Beller et al., 2011	Rat cortical cultures (mixed neuron/glia)	100 μM and 1 mM, applied for 5 days	L-[^{3}H]-glutamate for 10 min	∼30% increase (100 μM); ∼250% increase (1 mM)
Yang et al., 2011	Mouse lumbar spinal cord synaptosomes	200 mg/kg/day for 7 days (i.p.)	L-[^{3}H]-glutamate for 10 min	∼125% increase
Liu et al., 2013	Rat primary neuronal cultures	1 μM, applied for 2 days	L-[^{3}H]-glutamate for 10 min	∼20% increase
Chotibut et al., 2014	Rat striatal synaptosomes	200 mg/kg/day for 7 days (i.p.)	14C(U)-L-glutamate for 1.5 min	∼50% increase
Hu et al., 2015	Rat hippocampal cell suspension	200 mg/kg/day for 7 days (i.p.)	L-[^{3}H]-glutamate for 15 min	∼125% increase
Carbone et al., 2012	Mouse striatal astrocyte cultures	10 μM, 100 μM or 1 mM, applied for 3 days	L-[^{3}H]-glutamate for 5 min	No significant effect at 10 μM, 100 μM; ∼15% decrease at 1 mM
Rothstein et al., 2005	Acute hippocampal slices	200 mg/kg/day for 7 days (i.p.)	Transporter currents measured from individual astrocytes	No significant effect
Melzer et al., 2008	Rat mixed glial cultures	10–500 μM, applied for 5 days	L-[^{3}H]-glutamate for 5 min	No significant effect
Trantham-Davidson et al., 2012	Rat acute nucleus accumbens core slices	200 mg/kg/day for 5 days (i.p.)	L-[^{3}H]-glutamate for 15 min	No significant effect
Zhang et al., 2015	Rat cortical astrocyte cultures	100 μM, applied for 2 days	D-[^{3}H]-aspartate for 10 min	No significant effect
Hefendehl et al., 2016	*In vivo* two-photon imaging	200 mg/kg/day for 5 days (i.p.)	Decay of sensory-evoked iGluSnFR transients	No significant effect
Higashimori et al., 2016	Mouse cortical synaptosomes	200 mg/kg/day for 21 days (i.p.)	L-[^{3}H]-glutamate for 6 minutes	No significant effect
Agostini et al., 2020	Zebrafish isolated brain tissue	100 μM, 5 × 1 h applications over 3 days	L-[^{3}H]-glutamate for 7 min	No significant effect
Wilkie et al., 2020	Mouse acute hippocampal slices	200 mg/kg/day for 7 days (i.p.)	Decay of synaptically evoked iGluSnFR transients	No significant effect

electrophysiological recordings of transporter currents from astrocytes demonstrate no significant effect of ceftriaxone on glutamate uptake rates in healthy brain tissue (Hefendehl et al., 2016; Rothstein et al., 2005; Wilkie et al., 2020). In the present study, we extend on this observation by showing that GLT-1 upregulation by either ceftriaxone or LDN has very little impact whatsoever on the speed at which synaptically released glutamate is cleared from the extracellular space. Similarly, ceftriaxone treatment in healthy mice does not affect the decay kinetics of NMDAR-mediated excitatory postsynaptic currents (Shen et al., 2014; Valtcheva and Venance, 2016). In addition to cautioning the common interpretation that GLT-1 expression

correlates with uptake rates, our data demonstrate that activity-dependent slowing of glutamate clearance is not overcome by GLT-1 upregulation and that the slow clearance (relative to the hippocampus) in the cortex and the striatum is not due to low GLT-1 expression.

Ceftriaxone but Not LDN Reduced Glutamate Release in the Cortex

One unexpected observation was that following ceftriaxone treatment, iGluSnFR peaks were significantly reduced in the cortex. This effect in unlikely to be explained by increased GLT-1 expression, as LDN treatment also increased GLT-1 expression but was without effect on iGluSnFR response size. Ceftriaxone has been shown to also increase the activity of the cystine/glutamate antiporter system x_c^- (Lewerenz et al., 2009). System x_c^- exchanges extracellular cystine for intracellular glutamate, thereby moving glutamate into the extracellular space. The extracellular glutamate derived from the antiporter can increase the endogenous glutamate tone acting on presynaptic group II/III metabotropic glutamate receptors that inhibit canonical synaptic glutamate release (Baker et al., 2002; Baskys and Malenka, 1991; Bridges et al., 2012; Moran et al., 2005). The group II/III metabotropic glutamate receptor agonist LY379268 has previously been shown to reduce evoked iGluSnFR peaks (Koch et al., 2018). While this provides a putative explanation for ceftriaxone's effect on iGluSnFR peak, it is not clear why such an effect would only be observed in the cortex. Indeed, system x_c^- is known to make a considerable contribution to extracellular glutamate levels elsewhere, particularly in the striatum (Baker et al., 2002), and ceftriaxone had no effect whatsoever on iGluSnFR peaks in the striatum in the current study. Alternatively, it is possible that ceftriaxone treatment reduces cortical neuron excitability. Ceftriaxone was previously shown to reduce neuronal excitability in the spinal cord following cervical nerve root injury (Nicholson et al., 2014). If a similar ceftriaxone-induced reduction in excitability occurs in the cortex of healthy mice, it is conceivable that the stimulus trains in the present study resulted in lower cortical neuron excitation and therefore less glutamate release in ceftriaxone-treated animals. At present, the mechanism underlying the observed ceftriaxone-induced reduction in cortical glutamate release is unknown.

Ceftriaxone and LDN in Neurological Conditions

Despite the general lack of effect of ceftriaxone and LDN on iGluSnFR measurements of glutamate dynamics in the present study, it is undeniable that both compounds can exert a neuroprotective effect in numerous animal models of brain disease. For example, ceftriaxone has been shown to exert a beneficial effect in animal models of Alzheimer disease (Zumkehr et al., 2015), Parkinson disease (Kumar et al., 2016), Huntington disease (Miller et al., 2008), amyotrophic lateral sclerosis (Rothstein et al., 2005), multiple sclerosis (Melzer et al., 2008), traumatic brain injury (Cui et al., 2014) and ischemia (Hu et al., 2015), among others (for recent reviews see Smaga et al., 2020; Yimer et al., 2019). Ceftriaxone's aforementioned effect on the cystine/glutamate antiporter system x_c^- may partially explain some of its protective effects that are independent of GLT-1 expression. Low intracellular cystine can cause glutathione deficiencies and oxidative stress; thus, by increasing intracellular cystine through cystine/glutamate antiporters, ceftriaxone can provide neuroprotection by boosting antioxidant defense. Indeed, it was shown that ceftriaxone increases nuclear levels of the transcription factor Nrf2, which increases the expression of the xCT subunit of the cystine/glutamate antiporter. The ceftriaxone-induced xCT increase correlated with intracellular levels of the antioxidant glutathione, an effect that offered neuroprotection *in vitro* that was independent of glutamate transporter expression (Lewerenz et al., 2009).

LDN also exhibits protective effects in many similar disease models (Kong et al., 2014; Takahashi et al., 2015). The present study was limited to healthy brain tissue, in an effort to understand how GLT-1 upregulation affects glutamate uptake's natural heterogeneities from one brain region to the next and following different durations of neural activity. In diseases that are characterized by reduced GLT-1 expression and slow uptake, it is likely that a significant proportion of ceftriaxone's and LDN's protective effects indeed result from their ability to normalize GLT-1 expression and uptake rates. Indeed, this was nicely demonstrated in an *in vivo* two-photon iGluSnFR imaging study in the APPPS1 mouse model of Alzheimer disease. In brain areas immediately adjacent to amyloid plaques, the authors noted a slower decay of sensory-evoked iGluSnFR transients. After ceftriaxone treatment and restoration of GLT-1 expression adjacent to amyloid plaques, iGluSnFR decay values were indistinguishable from control mice. Interestingly, and in agreement with the results shown here, ceftriaxone treatment in control mice did not accelerate the decay of sensory-evoked iGluSnFR responses (Hefendehl et al., 2016).

CONCLUSION

In sum, our data demonstrate that assumptions on the clearance rate of synaptically released glutamate cannot be made based on GLT-1 expression alone. Both ceftriaxone and LDN significantly increased total GLT-1 levels in the hippocampus, cortex and striatum yet had minimal impact on the clearance rate of extracellular glutamate following evoked synaptic release. Transporter-mediated uptake is complex and relies on numerous factors in addition to the total protein level of GLT-1 in a given region. For example, one critical factor is where the ceftriaxone- and LDN-induced GLT-1 is expressed at the subcellular level. Interestingly, it was shown that LDN/OSU-0215111—a derivative of the LDN compound used in the present study—increased GLT-1 expression in subcellular fractions enriched in perisynaptic astrocytic processes, but not in fractions containing cell bodies or synaptosomes (Foster et al., 2018). The results of this paper suggest that LDN/OSU-0215111 initiates local GLT-1 protein synthesis at perisynaptic astrocytic processes. In contrast, an immunogold electron microscopy study demonstrated that ceftriaxone increased GLT-1 in axon terminals but not in

perisynaptic astrocytic processes (Capuani et al., 2016). Together with the results of the present paper, it is suggested that increased GLT-1 protein cannot be interpreted to mean accelerated uptake. Future efforts will focus on real-time measures of glutamate clearance in disease states and the effects of pharmacological normalization of glutamate transporters.

DATA AVAILABILITY STATEMENT

The original contributions presented in the study are included in the article/supplementary material, further inquiries can be directed to the corresponding author/s.

ETHICS STATEMENT

The animal study was reviewed and approved by the Memorial University Institutional Animal Care Committee.

AUTHOR CONTRIBUTIONS

CW performed the experiments. CW, MP, and JRB analyzed the data. MP, CW, JCB, and KB wrote the manuscript. MP designed the experiments. MP and FN supervised the project. All authors contributed to the article and approved the submitted version.

FUNDING

Funding for this project was obtained from research grants from the Natural Sciences and Engineering Research Council of Canada and from Epilepsy Newfoundland.

ACKNOWLEDGMENTS

We thank the animal care staff at Memorial University for assistance with animal housing.

REFERENCES

Agostini, J. F., Costa, N. L. F., Bernardo, H. T., Baldin, S. L., Mendes, N. V., de Pieri Pickler, K., et al. (2020). Ceftriaxone attenuated anxiety-like behavior and enhanced brain glutamate transport in zebrafish subjected to alcohol withdrawal. *Neurochem. Res.* 45, 1526–1535. doi: 10.1007/s11064-020-03008-z

Armbruster, M., Hanson, E., and Dulla, C. G. (2016). Glutamate clearance is locally modulated by presynaptic neuronal activity in the cerebral cortex. *J. Neurosci.* 36, 10404–10415. doi: 10.1523/JNEUROSCI.2066-16.2016

Baker, D. A., Xi, Z. X., Shen, H., Swanson, C. J., and Kalivas, P. W. (2002). The origin and neuronal function of in vivo nonsynaptic glutamate. *J. Neurosci.* 22, 9134–9141. doi: 10.1523/jneurosci.22-20-09134.2002

Barnes, J. R., Mukherjee, B., Rogers, B. C., Nafar, F., Gosse, M., and Parsons, M. P. (2020). The relationship between glutamate dynamics and activity-dependent synaptic plasticity. *J. Neurosci.* 40, 2793–2807. doi: 10.1523/JNEUROSCI.1655-19.2020

Baskys, A., and Malenka, R. C. (1991). Agonists at metabotropic glutamate receptors presynaptically inhibit EPSCs in neonatal rat hippocampus. *J. Physiol.* 444, 687–701. doi: 10.1113/jphysiol.1991.sp018901

Beller, J. A., Gurkoff, G. G., Berman, R. F., and Lyeth, B. G. (2011). Pharmacological enhancement of glutamate transport reduces excitotoxicity in vitro. *Restor. Neurol. Neurosci.* 29, 331–346. doi: 10.3233/RNN-2011-603

Bergles, D. E., Diamond, J. S., and Jahr, C. E. (1999). Clearance of glutamate inside the synapse and beyond. *Curr. Opin. Neurobiol.* 9, 293–298. doi: 10.1016/S0959-4388(99)80043-9

Bridges, R., Lutgen, V., Lobner, D., and Baker, D. A. (2012). Thinking outside the cleft to understand synaptic activity: contribution of the cystine-glutamate antiporter (System Xc-) to normal and pathological glutamatergic signaling. *Pharmacol. Rev.* 64, 780–802. doi: 10.1124/pr.110.003889

Capuani, C., Melone, M., Tottene, A., Bragina, L., Crivellaro, G., Santello, M., et al. (2016). Defective glutamate and K + clearance by cortical astrocytes in familial hemiplegic migraine type 2. *EMBO Mol. Med.* 8, 967–986. doi: 10.15252/emmm.201505944

Carbone, M., Duty, S., and Rattray, M. (2012). Riluzole elevates GLT-1 activity and levels in striatal astrocytes. *Neurochem. Int.* 60, 31–38. doi: 10.1016/j.neuint.2011.10.017

Casado, M., Bendahan, A., Zafra, F., Danbolt, N. C., Aragon, C., Gimenez, C., et al. (1993). Phosphorylation and modulation of brain glutamate transporters by protein kinase C. *J. Biol. Chem.* 268, 27313–27317. doi: 10.1016/S0021-9258(19)74251-3

Chen, W., Mahadomrongkul, V., Berger, U. V., Bassan, M., DeSilva, T., Tanaka, K., et al. (2004). The glutamate transporter GLT1a is expressed in excitatory axon terminals of mature hippocampal neurons. *J. Neurosci.* 24, 1136–1148. doi: 10.1523/JNEUROSCI.1586-03.2004

Chotibut, T., Davis, R. W., Arnold, J. C., Frenchek, Z., Gurwara, S., Bondada, V., et al. (2014). Ceftriaxone increases glutamate uptake and reduces striatal tyrosine hydroxylase loss in 6-OHDA Parkinson's model. *Mol. Neurobiol.* 49, 1282–1292. doi: 10.1007/s12035-013-8598-0

Clements, J. D., Lester, R. A., Tong, G., Jahr, C. E., and Westbrook, G. L. (1992). The time course of glutamate in the synaptic cleft. *Science* 258, 1498–1501. doi: 10.1126/science.1359647

Cui, C., Cui, Y., Gao, J., Sun, L., Wang, Y., Wang, K., et al. (2014). Neuroprotective effect of ceftriaxone in a rat model of traumatic brain injury. *Neurol. Sci.* 35, 695–700. doi: 10.1007/s10072-013-1585-4

Djukic, B., Casper, K. B., Philpot, B. D., Chin, L.-S., and McCarthy, K. D. (2007). Conditional knock-out of Kir4.1 leads to glial membrane depolarization, inhibition of potassium and glutamate uptake, and enhanced short-term synaptic potentiation. *J. Neurosci.* 27, 11354–11365. doi: 10.1523/JNEUROSCI.0723-07.2007

Dvorzhak, A., Helassa, N., Török, K., Schmitz, D., and Grantyn, R. (2019). Single synapse indicators of impaired glutamate clearance derived from fast iGlu u imaging of cortical afferents in the striatum of normal and huntington (Q175) mice. *J. Neurosci.* 39, 3970–3982. doi: 10.1523/jneurosci.2865-18.2019

Foster, J. B., Zhao, F., Wang, X., Xu, Z., Lin, K., Askwith, C. C., et al. (2018). Pyridazine-derivatives enhance structural and functional plasticity of tripartite synapse via activation of local translation in astrocytic processes. *Neuroscience* 388, 224–238. doi: 10.1016/j.neuroscience.2018.07.028

Furness, D. N., Dehnes, Y., Akhtar, A. Q., Rossi, D. J., Hamann, M., Grutle, N. J., et al. (2008). A quantitative assessment of glutamate uptake into hippocampal synaptic terminals and astrocytes: new insights into a neuronal role for excitatory amino acid transporter 2 (EAAT2). *Neuroscience* 157, 80–94. doi: 10.1016/j.neuroscience.2008.08.043

Hardingham, G. E., and Bading, H. (2010). Synaptic versus extrasynaptic NMDA receptor signalling: implications for neurodegenerative disorders. *Nat. Rev. Neurosci.* 11, 682–696. doi: 10.1038/nrn2911

Hefendehl, J. K., LeDue, J., Ko, R. W. Y., Mahler, J., Murphy, T. H., and MacVicar, B. A. (2016). Mapping synaptic glutamate transporter dysfunction in vivo to regions surrounding Aβ plaques by iGluSnFR two-photon imaging. *Nat. Commun.* 7:13441. doi: 10.1038/ncomms13441

Henneberger, C., Bard, L., Panatier, A., Reynolds, J. P., Kopach, O., Medvedev, N. I., et al. (2020). LTP induction boosts glutamate spillover by driving withdrawal of perisynaptic astroglia. *Neuron* 108, 919.e11–936.e11. doi: 10.1016/j.neuron.2020.08.030

Herde, M. K., Bohmbach, K., Domingos, C., Vana, N., Komorowska-Müller, J. A., Passlick, S., et al. (2020). Local efficacy of glutamate uptake decreases with synapse size. *Cell Rep.* 32:108182. doi: 10.1016/j.celrep.2020.108182

Higashimori, H., Schin, C. S., Chiang, M. S. R., Morel, L., Shoneye, T. A., Nelson, D. L., et al. (2016). Selective deletion of astroglial FMRP dysregulates glutamate transporter GLT1 and contributes to fragile X syndrome phenotypes in vivo. *J. Neurosci.* 36, 7079–7094. doi: 10.1523/JNEUROSCI.1069-16.2016

Hrabětová, S. (2005). Extracellular diffusion is fast and isotropic in the stratum radiatum of hippocampal CA1 region in rat brain slices. *Hippocampus* 15, 441–450. doi: 10.1002/hipo.20068

Hu, Y. Y., Xu, J., Zhang, M., Wang, D., Li, L., Li, W., et al. (2015). Ceftriaxone modulates uptake activity of glial glutamate transporter-1 against global brain ischemia in rats. *J. Neurochem.* 132, 194–205. doi: 10.1111/jnc.12958

Huang, K., Kang, M. H., Askew, C., Kang, R., Sanders, S. S., Wan, J., et al. (2010). Palmitoylation and function of glial glutamate transporter-1 is reduced in the YAC128 mouse model of Huntington disease. *Neurobiol. Dis.* 40, 207–215. doi: 10.1016/j.nbd.2010.05.027

Koch, E. T., Woodard, C. L., and Raymond, L. A. (2018). Direct assessment of presynaptic modulation of cortico-striatal glutamate release in a huntington's disease mouse model. *J. Neurophysiol.* 120, 3077–3084. doi: 10.1152/jn.00638.2018

Kong, Q., Chang, L. C., Takahashi, K., Liu, Q., Schulte, D. A., Lai, L., et al. (2014). Small-molecule activator of glutamate transporter EAAT2 translation provides neuroprotection. *J. Clin. Invest.* 124, 1255–1267. doi: 10.1172/JCI66163

Kumar, A., Paeger, L., Kosmas, K., Kloppenburg, P., Noegel, A. A., and Peche, V. S. (2016). Neuronal actin dynamics, spine density and neuronal dendritic complexity are regulated by CAP2. *Front. Cell. Neurosci.* 10:180. doi: 10.3389/fncel.2016.00180

Lee, S. G., Su, Z. Z., Emdad, L., Gupta, P., Sarkar, D., Borjabad, A., et al. (2008). Mechanism of ceftriaxone induction of excitatory amino acid transporter-2 expression and glutamate uptake in primary human astrocytes. *J. Biol. Chem.* 283, 13116–13123. doi: 10.1074/jbc.M707697200

Lehre, K. P., and Danbolt, N. C. (1998). The number of glutamate transporter subtype molecules at glutamatergic synapses: chemical and stereological quantification in young adult rat brain. *J. Neurosci.* 18, 8751–8757.

Lewerenz, J., Albrecht, P., Tien, M. L. T., Henke, N., Karumbayaram, S., Kornblum, H. I., et al. (2009). Induction of Nrf2 and xCT are involved in the action of the neuroprotective antibiotic ceftriaxone in vitro. *J. Neurochem.* 111, 332–343. doi: 10.1111/j.1471-4159.2009.06347.x

Liu, C. H., Jiao, H., Guo, Z. H., Peng, Y., and Wang, W. Z. (2013). Up-regulated GLT-1 resists glutamate toxicity and attenuates glutamate-induced calcium loading in cultured neurocytes. *Basic Clin. Pharmacol. Toxicol.* 112, 19–24. doi: 10.1111/bcpt.12011

Marvin, J. S., Borghuis, B. G., Tian, L., Cichon, J., Harnett, M. T., Akerboom, J., et al. (2013). An optimized fluorescent probe for visualizing glutamate neurotransmission. *Nat. Methods* 10, 162–170. doi: 10.1038/nmeth.2333

Melzer, N., Meuth, S. G., Torres-Salazar, D., Bittner, S., Zozulya, A. L., Weidenfeller, C., et al. (2008). A β-lactam antibiotic dampens excitotoxic inflammatory CNS damage in a mouse model of multiple sclerosis. *PLoS One* 3:e0003149. doi: 10.1371/journal.pone.0003149

Miller, B. R., Dorner, J. L., Shou, M., Sari, Y., Barton, S. J., Sengelaub, D. R., et al. (2008). Up-regulation of GLT1 expression increases glutamate uptake and attenuates the Huntington's disease phenotype in the R6/2 mouse. *Neuroscience* 153, 329–337. doi: 10.1016/j.neuroscience.2008.02.004

Moran, M. M., McFarland, K., Melendez, R. I., Kalivas, P. W., and Seamans, J. K. (2005). Cystine/glutamate exchange regulates metabotropic glutamate receptor presynaptic inhibition of excitatory transmission and vulnerability to cocaine seeking. *J. Neurosci.* 25, 6389–6393. doi: 10.1523/JNEUROSCI.1007-05.2005

Murphy-Royal, C., Dupuis, J. P., Varela, J. A., Panatier, A., Pinson, B., Baufreton, J., et al. (2015). Surface diffusion of astrocytic glutamate transporters shapes synaptic transmission. *Nat. Neurosci.* 18, 219–226. doi: 10.1038/nn.3901

Nicholson, K. J., Gilliland, T. M., and Winkelstein, B. A. (2014). Upregulation of GLT-1 by treatment with ceftriaxone alleviates radicular pain by reducing spinal astrocyte activation and neuronal hyperexcitability. *J. Neurosci. Res.* 92, 116–129. doi: 10.1002/jnr.23295

Parsons, M. P., and Raymond, L. A. (2014). Extrasynaptic NMDA receptor involvement in central nervous system disorders. *Neuron* 82, 279–293. doi: 10.1016/j.neuron.2014.03.030

Parsons, M. P., Vanni, M. P., Woodard, C. L., Kang, R., Murphy, T. H., and Raymond, L. A. (2016). Real-time imaging of glutamate clearance reveals normal striatal uptake in Huntington disease mouse models. *Nat. Commun.* 7:11251. doi: 10.1038/ncomms11251

Petr, G. T., Sun, Y., Frederick, N. M., Zhou, Y., Dhamne, S. C., Hameed, M. Q., et al. (2015). Conditional deletion of the glutamate transporter GLT-1 reveals that astrocytic GLT-1 protects against fatal epilepsy while neuronal GLT-1 contributes significantly to glutamate uptake into synaptosomes. *J. Neurosci.* 35, 5187–5201. doi: 10.1523/JNEUROSCI.4255-14.2015

Pinky, N. F., Wilkie, C. M., Barnes, J. R., and Parsons, M. P. (2018). Region- and activity-dependent regulation of extracellular glutamate. *J. Neurosci.* 38, 5351–5366. doi: 10.1523/JNEUROSCI.3213-17.2018

Pita-Almenar, J. D., Collado, M. S., Colbert, C. M., and Eskin, A. (2006). Different mechanisms exist for the plasticity of glutamate reuptake during early long-term potentiation (LTP) and late LTP. *J. Neurosci.* 26, 10461–10471. doi: 10.1523/JNEUROSCI.2579-06.2006

Romanos, J., Benke, D., Saab, A. S., Zeilhofer, H. U., and Santello, M. (2019). Differences in glutamate uptake between cortical regions impact neuronal NMDA receptor activation. *Commun. Biol.* 2:127. doi: 10.1038/s42003-019-0367-9

Rothstein, J. D., Patel, S., Regan, M. R., Haenggeli, C., Huang, Y. H., Bergles, D. E., et al. (2005). β-Lactam antibiotics offer neuroprotection by increasing glutamate transporter expression. *Nature* 433, 73–77. doi: 10.1038/nature03180

Shen, H., Scofield, M. D., Boger, H., Hensley, M., and Kalivas, P. W. (2014). Synaptic glutamate spillover due to impaired glutamate uptake mediates heroin relapse. *J. Neurosci.* 34, 5649–5657. doi: 10.1523/JNEUROSCI.4564-13.2014

Smaga, I., Fierro, D., Mesa, J., Filip, M., and Knackstedt, L. A. (2020). Molecular changes evoked by the beta-lactam antibiotic ceftriaxone across rodent models of substance use disorder and neurological disease. *Neurosci. Biobehav. Rev.* 115, 116–130. doi: 10.1016/j.neubiorev.2020.05.016

Takahashi, K., Kong, Q., Lin, Y., Stouffer, N., Schulte, D. A., Lai, L., et al. (2015). Restored glial glutamate transporter EAAT2 function as a potential therapeutic approach for Alzheimer's disease. *J. Exp. Med.* 212, 319–332. doi: 10.1084/jem.20140413

Tanaka, K., Tanaka, K., Watase, K., Manabe, T., and Yamada, K. (1997). Epilepsy and exacerbation of brain injury in mice lacking the glutamate transporter GLT-1 epilepsy and exacerbation of brain injury in mice lacking the glutamate transporter GLT-1. *Science* 1699, 1699–1703. doi: 10.1126/science.276.5319.1699

Thöne-Reineke, C., Neumann, C., Namsolleck, P., Schmerbach, K., Krikov, M., Schefe, J. H., et al. (2008). The β-lactam antibiotic, ceftriaxone, dramatically improves survival, increases glutamate uptake and induces neurotrophins in stroke. *J. Hypertens.* 26, 2426–2435. doi: 10.1097/HJH.0b013e328313e403

Trantham-Davidson, H., Lalumiere, R. T., Reissner, K. J., Kalivas, P. W., and Knackstedt, L. A. (2012). Ceftriaxone normalizes nucleus accumbens synaptic transmission, glutamate transport, and export following cocaine self-administration and extinction training. *J. Neurosci.* 32, 12406–12410. doi: 10.1523/JNEUROSCI.1976-12.2012

Valtcheva, S., and Venance, L. (2016). Astrocytes gate Hebbian synaptic plasticity in the striatum. *Nat. Commun.* 7:13845. doi: 10.1038/ncomms13845

Verma, R., Mishra, V., Sasmal, D., and Raghubir, R. (2010). Pharmacological evaluation of glutamate transporter 1 (GLT-1) mediated neuroprotection following cerebral ischemia/reperfusion injury. *Eur. J. Pharmacol.* 638, 65–71. doi: 10.1016/j.ejphar.2010.04.021

Wilkie, C. M., Barnes, J. R., Benson, C. L. M., Brymer, K. J., Nafar, F., and Parsons, M. P. (2020). Hippocampal synaptic dysfunction in a mouse model of huntington disease is not alleviated by ceftriaxone treatment. *eNeuro* 7:ENEURO.0440-19.2020. doi: 10.1523/ENEURO.0440-19.2020

Yang, M., Roman, K., Chen, D. F., Wang, Z. G., Lin, Y., and Stephens, R. L. (2011). GLT-1 overexpression attenuates bladder nociception and local/cross-organ sensitization of bladder nociception. *Am. J. Physiol. Ren. Physiol.* 300, 1353–1359. doi: 10.1152/ajprenal.00009.2011

Yimer, E. M., Hishe, H. Z., and Tuem, K. B. (2019). Repurposing of the β-lactam antibiotic, ceftriaxone for neurological disorders: a review. *Front. Neurosci.* 13:236. doi: 10.3389/fnins.2019.00236

Zhang, Y., Zhang, X., and Qu, S. (2015). Ceftriaxone protects astrocytes from MPP+ via suppression of NF-κB/JNK/c-Jun signaling. *Mol. Neurobiol.* 52, 78–92. doi: 10.1007/s12035-014-8845-z

Zumkehr, J., Rodriguez-Ortiz, C. J., Cheng, D., Kieu, Z., Wai, T., Hawkins, C., et al. (2015). Ceftriaxone ameliorates tau pathology and cognitive decline via restoration of glial glutamate transporter in a mouse model of Alzheimer's disease. *Neurobiol. Aging* 36, 2260–2271. doi: 10.1016/j.neurobiolaging.2015.04.005

Conflict of Interest: The authors declare that the research was conducted in the absence of any commercial or financial relationships that could be construed as a potential conflict of interest.

frontiers in Cellular Neuroscience

ORIGINAL RESEARCH
published: 09 April 2021
doi: 10.3389/fncel.2021.662216

Acetylcholine Receptor Stimulation Activates Protein Kinase C Mediated Internalization of the Dopamine Transporter

*Suzanne M. Underhill * and Susan G. Amara*

National Institute of Mental Health, National Institutes of Health (NIH), Bethesda, MD, United States

The dopamine transporter (DAT) clears neurotransmitters from the extracellular space and serves as an important regulator of signal amplitude and duration at sites of dopamine release. Several different intracellular signaling pathways have been observed to modulate DAT activity through the regulation of the trafficking of the carriers to and from the cell surface. Acute activation of protein kinase C (PKC) by phorbol esters facilitates clathrin-dependent internalization of the DAT in a variety of model systems; however, the physiological stimuli and cell-surface receptor systems that activate PKC and regulate the DAT in dopamine neurons remain elusive. We report here that stimulation of M_1/M_5 muscarinic receptors in midbrain cultures decreases the ability of dopamine neurons to transport dopamine through DAT. Application of the cholinomimetic drug carbachol leads to a decrease in DAT activity in primary cultures while the M_1/M_5-specific antagonist, pirenzepine, blocks these effects. The M_3 antagonist, DAU 5884, does not affect, but a positive modulator of M_5, VU 0238429, enhances the loss of DAT function in response to carbachol and acetylcholine. These data implicate M_1/M_5 receptors on dopamine neurons in the modulation of DAT function. Bisindolylmaleimide, a PKC inhibitor, blocks the effects of carbachol stimulation on dopamine uptake, supporting a role for PKC in muscarinic receptor-mediated DAT internalization. Furthermore, as shown previously for PKC-induced internalization, downregulation of the DAT is dependent on both clathrin and dynamin. A G_q-specific inhibitor peptide also blocks the effects of carbachol on DAT in primary cultures, confirming G_q as the G-protein that couples M_1/M_5 receptors to PKC activation in these cells. In acute midbrain slices, biotinylation of cell-surface proteins revealed the loss of dopamine transport mediated by muscarinic receptor stimulation was, indeed, due to loss of membrane expression of the DAT in endogenous tissue. These data indicate that stimulation of cholinergic pathways can lead to modulation of dopamine through internalization of the DAT.

Keywords: dopamine transporter, muscarinic receptor, trafficking, protein kinase C, internalization

OPEN ACCESS

Edited by:
Annalisa Scimemi, University at Albany, United States

Reviewed by:
James Foster, University of North Dakota, United States
Bjoern Falkenburger, Technische Universität Dresden, Germany

****Correspondence:***
Suzanne M. Underhill
suzanne.underhill@nih.gov

Specialty section:
This article was submitted to Cellular Neurophysiology, a section of the journal Frontiers in Cellular Neuroscience

Received: *31 January 2021*
Accepted: *11 March 2021*
Published: *09 April 2021*

Citation:
Underhill SM and Amara SG (2021) Acetylcholine Receptor Stimulation Activates Protein Kinase C Mediated Internalization of the Dopamine Transporter. Front. Cell. Neurosci. 15:662216. doi: 10.3389/fncel.2021.662216

INTRODUCTION

The dopamine transporter (DAT) clears neurotransmitters from the extracellular space and serves as an important regulator of signal amplitude and duration at sites of dopamine release. In both dopamine (DA) neurons and transfected cell lines, the activation of several different intracellular signaling pathways has been observed to modulate DAT activity by regulating the trafficking of carriers to and from the cell surface (Mortensen and Amara, 2003). Protein kinase C (PKC) signaling has been extensively studied as a mechanism for regulating transporter cell surface density, and it has been well-established that acute activation of PKC by phorbol esters facilitates internalization of the transporter in a variety of model systems. However, the physiological stimuli and cell systems that activate PKC and potentially regulate the DAT in dopamine neurons within the mammalian brain remain elusive.

There are several G-protein coupled receptors (GPCRs) that may be coupled to cascades that lead to PKC-activation that are present on dopamine neurons, several of which belong to the muscarinic acetylcholine receptor family. Acetylcholine receptors fall into two broad categories, nicotinic and muscarinic receptors. Nicotinic receptors are ligand-gated ion channels while muscarinic receptors are GPCRs. Of the five isoforms of muscarinic receptors, M_1, M_3, and M_5 are $G_{Q/11}$-coupled while M_2 and M_4 are G_i-coupled. $G_{Q/11}$-coupled GPCRs may lead to PKC activation and suggest a mechanism by which DAT may be modulated through PKC in dopamine neurons through stimulation of M_1, M_3, and/or M_5 receptors.

In this study, we explored this question and further characterized the intracellular mechanism of DAT internalization in response to acetylcholine receptor stimulation in dopamine neurons. DAT internalization has been well described in response to both amphetamine (Kahlig et al., 2006; Hong and Amara, 2013; Wheeler et al., 2015) and phorbol esters, such as PMA (Vaughan et al., 1997; Zhu et al., 1997; Daniels and Amara, 1999; Melikian and Buckley, 1999). However, internalization of the DAT transporter by amphetamine or PMA occurs through distinct cellular pathways, the former being mediated by a clathrin-independent and RhoA-dependent process while the latter is explicitly clathrin-dependent (Daniels and Amara, 1999; Hong and Amara, 2013; Wu et al., 2015). This report addresses the mechanism of DAT internalization in response to muscarinic receptor stimulation in dopamine neurons.

MATERIALS AND METHODS

Primary MidBrain Cultures

All procedures using animals were conducted in compliance with protocols approved by the ACUC at the National Institutes of Health (NIH). Primary cultures were obtained as described previously (Wheeler et al., 2015) from midbrains of E15 Swiss-Webster mice following isofluorane anesthesia and cervical dislocation of the pregnant dam. The tissue was gently triturated, plated at a density of 0.16 midbrains per 12-mm poly-D-lysine coated coverslips or 0.33 per 25-mm coverslip. Cells were grown in Modified Eagle Medium (MEM) supplemented with 5% horse serum and 5% fetal calf serum for 2–5 weeks to facilitate the formation of synapses and expression of DAT, vMAT, and M_1/M_5 (**Figures 1**, **3**). Neuromag was used to transfect primary neurons according to the manufacturer's directions (OZ Biosciences, NM50200).

^{3}H-Dopamine Transport Assays

Cells were exposed to vehicle or drug treatments for 30 min at 37° in MEM, without serum. Cells were then washed and dopamine transport was determined by a 7-min incubation with 50 nM ^{3}H-dopamine and 20 μM cold dopamine in phosphate-buffered saline (PBS) supplemented with 1 mM calcium chloride and 100 μM magnesium chloride. Cells were washed with PBS, lysed with scintillation fluid, and the cpm obtained on a Beckman scintillation counter. Control samples treated with the DAT-specific antagonist GBR-12909 (10 nM, Tocris, 0421) were used to determine non-specific background radiation in primary cultures. Data are presented with the background-subtracted and normalized to vehicle-treated controls. Assays were performed on at least three different occasions from three different culture-dates. Vehicle control values were at least 2-fold above the background determined by inhibition of DAT-specific uptake with GBR-12909.

Biotinylation of Acute Brain Slices

Cell-surface proteins in acute brain slices was performed as described previously (Underhill et al., 2014). Briefly, 12–24 week-old Swiss-Webster mice were anesthetized with isofluorane, euthanized by cervical dislocation, and decapitated. Brains were isolated and 1-mm mid-brain sections were cut with a brain slicer matrix in ice-cold Hank's Buffered Saline Solution. Slices were transferred to 1 ml of artificial cerebrospinal fluid (aCSF, in mM: 126 NaCl, 2.5 KCl, 2.4 $CaCl_2$, 1.2 $MgCl_2$, 1.2 NaH_2PO_4, 21.4 $NaHCO_3$, 11.1 D-Dextrose, pH 7.4) with 50 μM kynurenic acid (Sigma, K3375) to prevent excitotoxic cell damage and allowed to rest for 30–60 min at room temperature. Treatments of slices were performed in 1 ml of aCSF bubbled with 95% oxygen and 5% carbon dioxide at 37°C in a water bath for 30 min, chilled to 4°C on ice for 10 min, and incubated in NHS-SS-biotin (Thermo Fisher, 21331) in biotinylation buffer (in mM: 2 $CaCl_2$, 150 NaCl, and 10 triethanolamine, pH 7.5) for 20 min at 4°C on ice. The biotin reagent was quenched with 50 mM glycine for 10 min and then washed off with PBS. Tissue was lysed in 1 ml 1% triton buffer and dounce homogenized. Nuclear fractions were removed by centrifugation for 20 min at 15,000 rpm at 4°C. Biotinylated proteins were isolated by incubation overnight at 4°C with Ultralink immobilized Pierce NeutrAvidin beads (Thermo Fisher, 29200) and analyzed by western blot.

Western Blots

Protein samples were loaded in Tris-Glycine gels (4–12%, Thermo Fisher, SV04125) in Laemmi's buffer supplemented with 200 mM DTT. Gels were transferred to PVDF membrane, blocked with 5% milk, and probed with primary antibodies (1:1,000) overnight. Membranes were washed with PBS-Tween and secondary antibodies (HRP-conjugated donkey anti-rabbit,

1:10,000) were applied for 1 h in 5% milk and washed with PBS-tween. Probes were imaged with chemiluminescence and quantified only in non-saturating images by ImageJ. Data were adjusted for total input from lysate samples taken before NeutrAvidin isolation of biotinylated proteins. Total inputs did not vary across these assays consistent with equal protein concentrations and sample loading across preparations.

Immunocytochemistry

Cultured cells were fixed with 4% paraformaldehyde at 4°C for 20 min and washed with PBS. Cells were permeablized with a 5-min treatment with 0.25% Triton X-100 and then blocked with 5% normal goat serum (NGS) for 1 h at room temperature. Primary antibodies were diluted in 5% NGS were incubated on the cells overnight at 4°C. Secondary antibodies were applied for 1 h at room temperature in 5% NGS at room temperature. Cultures were then washed with PBS and mounted in AntiFade reagent. Images were acquired with a Nikon Axiovert confocal microscope.

Reagents

Primary antibodies included rabbit anti-M_1 (Abcam, ab111100), rabbit anti-M_5 (Abcam, ab41171), chicken anti-tyrosine hydroxylase (Aves, TYH), rat anti-DAT (Thermo Fisher, mAb16), and rabbit anti-vMAT (Millipore, AB1598P). HRP, Dylight-488, or Alexa 568 conjugated secondary antibodies were from Jackson Immunoresearch. Dynole 34-2 and Pitstop 2 and the negative control were both from Abcam. Custom-designed TAT-peptides were ordered from LifeTein.

Quantitation and Statistics

All cell culture assays were performed on cultures from at least three separate preparations. For ^{3}H_DA uptake assays, one coverslip was used as an n of 1. M_1/M_5 immunolabeling was manually counted over 11 60× fields of view from three different culture dates. One-hundred and fifty-five and 112 TH(+) cells were assessed for M_1 or M_5 co-expression, respectively. Clathrin and DAT colocalization was quantified by ImageJ using sub-threshold images. All statistics were performed with GraphPad Prism software. $^*P \leq 0.05$, $^{**}P \leq 0.01$, $^{***}P \leq 0.001$ and $^{****}P \leq 0.0001$ throughout the manuscript for one-way ANOVA, two-way ANOVA or t-test evaluations.

RESULTS

Dopamine transport in neurons is modified by stimulation of muscarinic acetylcholine (Ach) receptors. Dopamine neurons were cultivated from E15 mouse mid-brains. Dopamine neurons in these cultures expressed DAT, tyrosine hydroxylase (TH), and the vesicular monoamine transporter 2 (vMAT2; **Figure 1A**), as expected for well-differentiated DA neurons in culture. DAT transport activity was assessed in these cultures with ^{3}H-dopamine and defined as that which was sensitive to the DAT-specific inhibitor GBR12909. We found that a 30-min pre-treatment of these cultures with phorbol 12-myristate 13-acetate (PMA, 10 μM) decreased subsequent GBR12909-sensitive, DAT-mediated transport of ^{3}H-dopamine in these cultures (**Figure 1B**). This effect was blocked by co-application of the PKC inhibitor bisindolylmaleimide (BIM, 1 μM) 5 min before and concurrent with PMA pretreatment, indicating that the loss of DAT transport activity depends on PKC activation. Similarly, we found that pre-treatment with the muscarinic receptor agonist carbachol (30 μM) could also decrease dopamine transport. The effects of carbachol pre-treatment on DAT transport were also inhibited by BIM. These data indicate that muscarinic Ach receptors can stimulate PKC to affect DAT function in DA neurons. Amphetamine and methamphetamine pretreatments also decreased DAT transport capacity in these midbrain neurons, however, these effects were not altered by PKC inhibition by BIM.

M_1/M_5 muscarinic receptors alter DAT function. Carbachol is known to stimulate all five of the muscarinic GPCRs. Isoforms 1, 3, and 5 are $G_q/11$ coupled, suggesting a mechanism by which carbachol could stimulate PKC, while isoforms 2 and 4 are G_i-coupled. We tested antagonists to isoforms M_1/M_5 and M_3 in combination with carbachol. The M_1/M_5 antagonist pirenzepine blocked the effects of carbachol on dopamine transport (**Figure 2A**). The M_3 antagonist DAU5884 did not affect while the M_5 positive allosteric modulator VU 0238429 potentiated the effect of carbachol and acetylcholine on DAT activity (**Figures 2A,C,D**). The insets indicate the EC50 values for carbachol (**Figure 2C**) or acetylcholine (**Figure 2D**) with and without VU 0238429 to perform the statistical evaluation. Further, the M_1/M_5 receptor agonist McN-A-343 mimicked the effects of carbachol in decreasing DAT transport capacity, supporting the role of M_1/M_5 receptor stimulation in DAT modulation (**Figure 2B**).

Consistent with the pharmacological profile indicating that the DA neurons in primary culture can be modulated by M_1 and M_5 receptors, we found expression of both of these receptors in DA neurons (**Figure 3**). However, only ∼40% of the dopamine neurons expressed these receptors, indicating a population of DA neurons would not be affected by muscarinic receptor agonists. With the antibodies currently available, we were not able to further characterize M_1/M_5 expression in the same cells.

Mechanism of DAT Regulation by M_1/M_5 Receptors PMA/PKC stimulated internalization of DAT is a dynamin (Gabriel et al., 2013) and clathrin-dependent (Daniels and Amara, 1999) process whereas AMPH-mediated DAT internalization is also dynamin-dependent (Saunders et al., 2000) but is clathrin-independent (Wheeler et al., 2015). In primary midbrain cultures, both carbachol and amphetamine produced a loss of DAT activity that was blocked by the dynamin inhibitor dynole 34-2 (**Figure 4A**), confirming that the effects of both drugs depend on dynamin. Inhibition of the formation of clathrin-coated pits by Pitstop 2 also blocked the downregulation of the DAT by carbachol (**Figure 4B**) demonstrating that the process depends on clathrin. The negative control compound for Pitstop 2 did not have any effect on carbachol-mediated DAT internalization.

M_1 and M_5 receptors are G_Q-coupled. The G_Q μ-subunit of G-proteins signals by increasing inositol triphosphate (IP3) and diacylglycerol (DAG), which acts as a second messenger to mobilize intracellular calcium stores and activate PKC. We

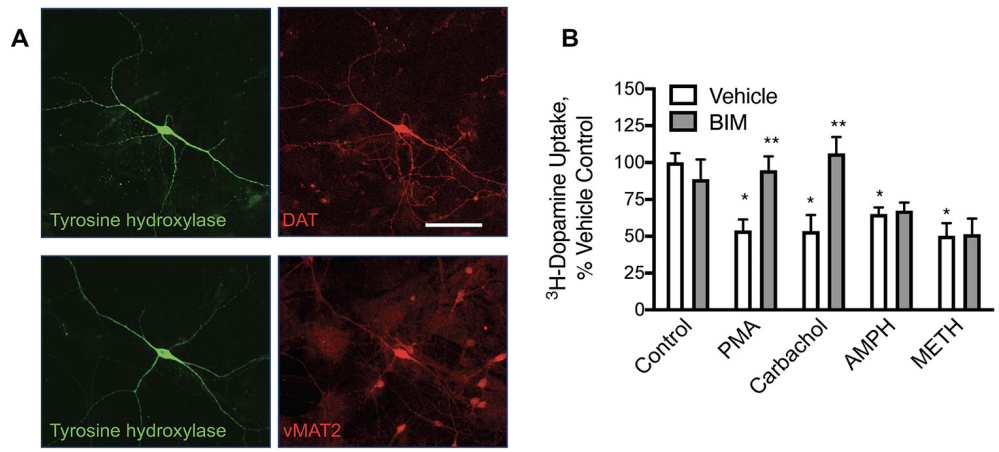

FIGURE 1 | In primary midbrain cultures, phorbol 12-myristate 13-acetate (PMA) and carbachol-mediated loss of dopamine transporter (DAT) function are protein kinase C (PKC) mediated while amphetamine (AMPH) and methamphetamine (METH)-mediated redistribution are not. **(A)** Primary midbrain cultures have dopamine (DA) neurons that express tyrosine hydroxylase (TH), DAT, and the vesicular monoamine transporter 2 (vMAT2; scale bar is 50 μm). **(B)** Pre-treatment of these cultures with PMA (10 μM), carbachol (30 μM), amphetamine (10 μM, AMPH), and methamphetamine (10 μM METH) all decreased transport capacity of DAT (defined as GBR-12909 sensitive ^{3}H-dopamine uptake). Bisindolylmaleimide I (BIM, 1 μM) inhibited the effects of PMA and carbachol, substantiating a PKC-mediated effect on DAT by these agonists. BIM did not alter the loss of DAT activity mediated by pretreatment with AMPH or METH indicating independent mechanisms of DAT internalization [$n = 3$; $^*P < 0.01$ from Vehicle control (first bar white bar) while $^{**}P < 0.01$ from own vehicle by two-way ANOVA].

designed short peptides based on the C-terminus of various GPCR α-subunits that we have shown interfere selectively with their respective signaling pathways (Underhill et al., 2019). These peptides were made cell-permeable with the addition of a short TAT domain (YGRKKRRQRRR), as described previously (Underhill et al., 2019). Interfering with G_S or G_{11} subunits did not affect the carbachol-mediated loss of DAT uptake; however, the G_Q interfering peptide could completely abolish the effect (**Figure 4C**).

To further investigate the role of clathrin in M_1/M_5 stimulated internalization of DAT, we coexpressed GFP-tagged clathrin light chain and mCherry-tagged DAT in primary cultured neurons. These cells were then treated with vehicle control, carbachol, or amphetamine, and we measured the colocalization of the DAT with clathrin in response to these stimuli (**Figure 5**). Carbachol treatment enhanced the colocalization of the transporter with the coat protein, clathrin.

Carbachol treatment causes clathrin-mediated DAT internalization. To further investigate the role of clathrin in M_1/M_5 stimulated internalization of DAT, we coexpressed GFP-tagged clathrin light chain and mCherry-tagged DAT in primary cultured neurons. These cells were then treated with vehicle control, carbachol, or amphetamine, and we measured the colocalization of the DAT with clathrin in response to these stimuli (**Figure 5**). Carbachol treatment enhanced the colocalization of the transporter with the vesicle coat protein, clathrin.

Modulation of DAT transport function may result from several actions on the DAT; however, we hypothesized that muscarinic receptor stimulation causes loss of DAT function through the trafficking of the carrier away from the plasma membrane through a mechanism similar to that observed with PKC activation by PMA. We treated mid-brain acute slices from adult mice with vehicle, amphetamine, or carbachol. Subsequently, all surface proteins were labeled with a cell-impermeable biotin reagent. The tissue was lysed, biotinylated proteins isolated, and analyzed by western blot. Membrane localized, biotin accessible DAT was significantly decreased in tissues treated with amphetamine or carbachol (**Figure 6**). These results were observed in both male and female female-derived tissues and we did not detect any difference across the groups.

DISCUSSION

The regulated internalization of the dopamine transporter contributes to increases in extracellular dopamine. Efforts have focused on two major endocytic mechanisms for the DAT: amphetamine-mediated internalization which depends on dynamin and the activation of another GTPase, RhoA (Wheeler et al., 2015), and PKC-mediated internalization which depends on dynamin and the formation of clathrin-coated pits (Daniels and Amara, 1999). Although several GPCRs linked to PKC activation could potentially regulate the DAT, muscarinic M_5 receptors are strong candidates for several reasons. M_5 GPCRs are expressed by midbrain DA neurons, are coupled to PKC activation, and have been shown to produce prolonged facilitation of dopamine release *in vivo* (Forster et al., 2002; Foster et al., 2014). In the current study, we show here that stimulation of the M_1/M_5 muscarinic acetylcholine receptors on DA neurons leads to activation of PKC and endocytosis of DAT, a series of events that could contribute to the elevations in extracellular DA concentrations observed *in vivo*.

Mechanism of M_1/M_5-mediated internalization. Previous studies have used the phorbol ester PMA to stimulate PKC and observe the internalization of DAT (Doolen and Zahniser, 2002).

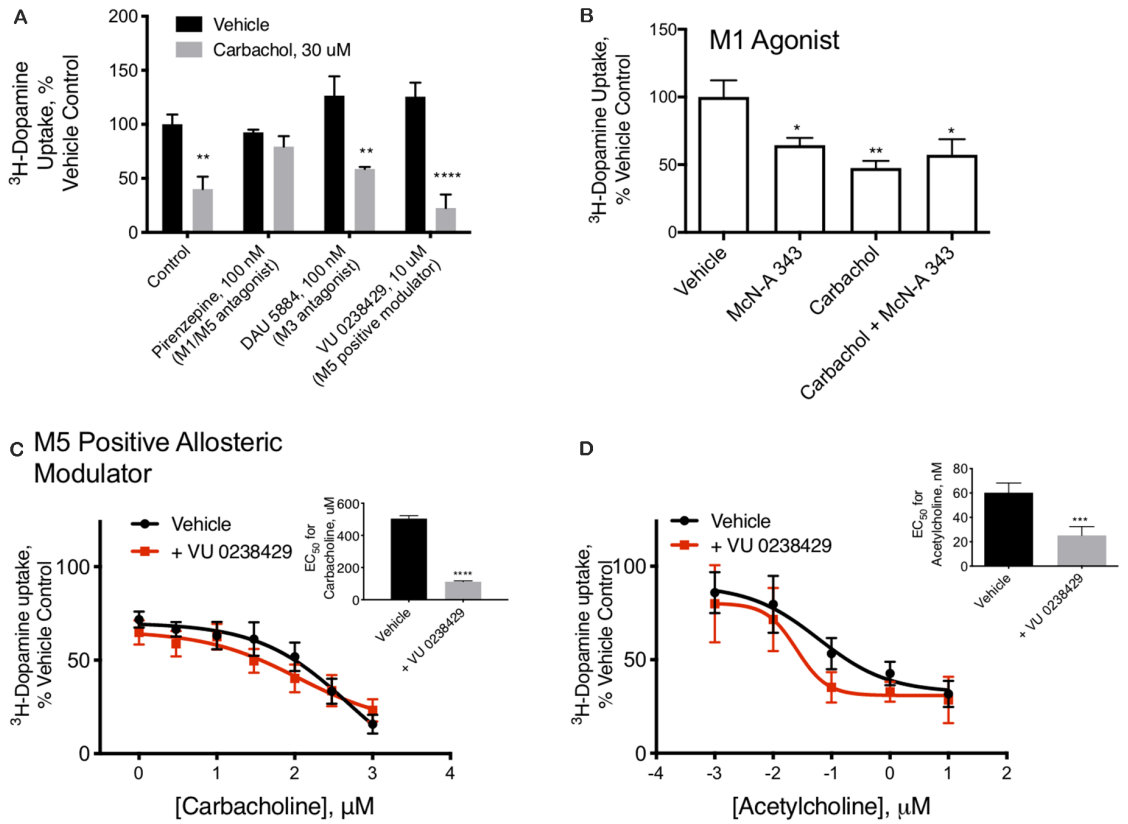

FIGURE 2 | M_1/M_5 receptors mediate DAT redistribution. **(A)** In primary midbrain cultures, the effect of carbachol pretreatment on DAT-mediated dopamine transport were was blocked by the M_1/M_5 antagonist pirenzepine (100 µM). The M_3 antagonist, DAU 5884 (1 µM), had no effect ondid not affect the activity of the DAT. The positive M_5 modulator VU 0238429 (10 µM) potentiated the effects of carbachol (n = 6, 6, 4, 3, 5, 4, 6, 4, $^{**}P \leq 0.01$ and $^{****}P \leq 0.0001$ by two-way ANOVA). **(B)** Pretreatment of primary midbrain cultures with the M_1/M_5 agonist, McN-A-343 (10 µM), decreased DAT-mediated dopamine transport. McN-A-343 did not demonstrate an additive effect with carbachol, suggesting they are both affecting DAT localization through muscarinic receptor activation (n = 4, $^{*}P \leq 0.05$ and $^{**}P \leq 0.01$ by one-way ANOVA). **(C)** Co-application of the M_5-positive modulator VU 0238429 potentiates the effects of carbachol in primary midbrain cultures (n = 7, $^{***}P \leq 0.001$ by t-test). **(D)** Acetylcholine-mediated internalization of DAT in primary cultures is also enhanced by co-application of VU 0238429 (n = 4, $^{***}P \leq 0.001$ by t-test).

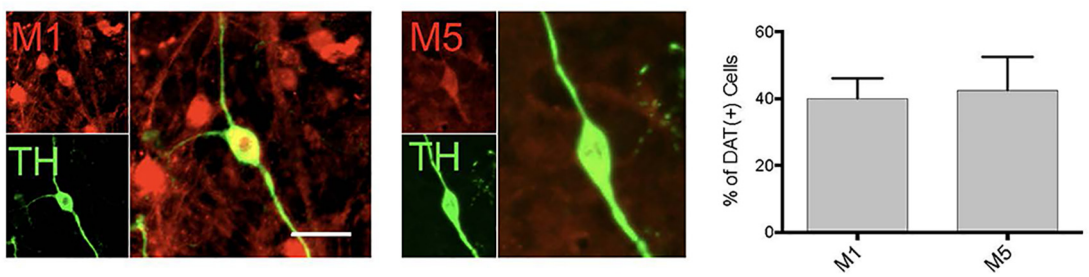

FIGURE 3 | DA neurons in primary midbrain culture also express muscarinic acetylcholine receptors. Cultured TH(+) (green) neurons were found to also express M_1 and M_5 receptors (red). Quantitation of the number of TH(+) neurons that also expressed M_1 or M_5 indicated that 40% of TH neurons expression expressed M_1 and 42.5% express M_5 [n = 11 fields of view, 155 and 112 TH(+) cells assessed for M_1 or M_5 co-expression, respectively; scale bar 25 µm].

M_1/M_5 muscarinic acetylcholine receptors are G_Q coupled, resulting in phospholipase C activation, DAG release, Ca^{2+}-release, and activation of PKC. We report here that M_1/M_5-receptor receptor-stimulated PKC activation is sufficient to internalize DAT in dopamine neurons. The mechanism of PKC-mediated internalization of DAT is dependent on dynamin and clathrin (Daniels and Amara, 1999), similar to what we report here for the action of carbachol.

PKC activation by PMA leads to ubiquitination of the transporter (Miranda et al., 2005). DAT is then internalized

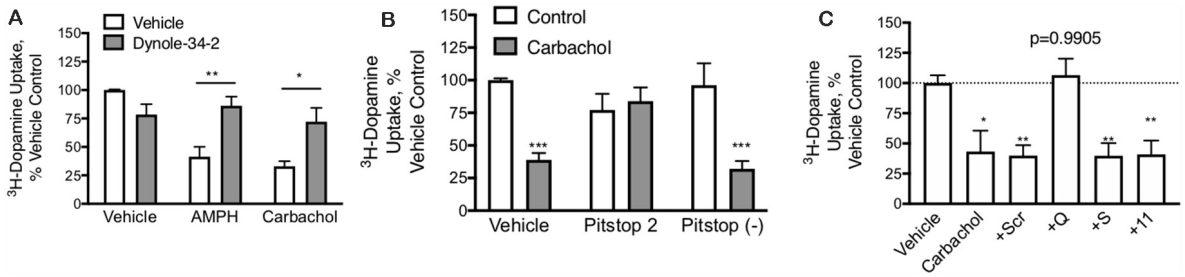

FIGURE 4 | DAT-mediated internalization by carbachol is dependent on both dynamin and clathrin. **(A)** In primary midbrain cultures, dynole (50 μM), an inhibitor of dynamin, prevented DAT internalization in response to both AMPH (10 μM) and carbachol (30 μM). These data further support the internalization of the transporter as the mechanism of loss of DAT function (n = 3, $^*P \leq 0.05$ and $^{**}P \leq 0.01$ by two-way ANOVA). **(B)** Pitstop II (30 μM), a clathrin inhibitor, prevents DAT internalization in response to carbachol. There was no affect effect of this clathrin inhibition on AMPH-mediated DAT internalization, consistent with prior studies demonstrating this as a clathrin-independent process (n = 3, $^{***}P \leq 0.001$ by two-way ANOVA). **(C)** TAT-fused peptides that were designed to interfere with GPCRs coupled to G_Q, G_S, or G_{11} alpha subunits were applied to dopamine neurons in primary culture (70 μM). Subsequent treatment of these cultures with carbachol led to the loss of DAT-mediated DA transport under all conditions, except the TAT-G_Q pre-treated cultures (n = 5, $^*P \leq 0.05$ and $^{**}P \leq 0.01$ by one-way ANOVA).

and sent towards a degradation pathway within 2 h of PKC activation (Daniels and Amara, 1999; Mortensen et al., 2008; Hong and Amara, 2013). It is unclear whether M_1/M_5-stimulated DAT internalization follows the same fate. Other studies have implicated the Ras-like GTPase Rin (Navaroli et al., 2011) and CDC42-activated, nonreceptor tyrosine kinase, Ack1 (Wu et al., 2015) to be involved in PKC-mediated DAT trafficking. How the various pathways and regulatory molecules are distributed across different subcellular compartments and anatomical regions will determine the potential impact of M_1/M_5-mediated internalization of the DAT on dopamine signaling. Understanding the precise localization of PKC-coupled GPCRs relative to the DAT is critical for establishing the physiological impact of PKC-regulated DAT trafficking. We found M_1/M_5 receptor stimulation of DAT(+) neurons in culture and acute brain slices was sufficient to modulate DAT membrane localization indicating the M_1/M_5 receptors are near DAT in DA neurons—whether, in axons, dendrites or discrete subcellular membrane domains remains to be further investigated.

In the absence of a physiological ligand that signals through PKC, the relevance of DAT internalization associated with the direct activation of PKC by PMA has remained unresolved. Moreover, PMA effects have not been observed consistently in cultured midbrain DA neurons. For example, one study that used a fluorescently cocaine-analog to probe trafficking of endogenous DAT in cultured midbrain neurons showed no evidence of PMA-induced internalization (Eriksen et al., 2009). The absence of an effect could have several explanations including off-target effects of PMA, which activates a broad range of PKC isoforms or an altered conformation of the ligand-bound carrier that precludes PMA-induced endocytosis. In support of this latter possibility, the Vaughan lab has reported that the DAT inhibitor GBR12909 blocked PMA-mediated phosphorylation of DAT indicating some that the conformational state of DAT can alter PKC-mediated effects on the carrier (Gorentla and Vaughan, 2005). To avoid the potential confounds associated with using PMA in brain preparations we have used a more physiologically-relevant endogenous receptor to activate PKC, Our results show that in primary DA neuron cultures and acute brain slices, M_1/M_5 receptor stimulation produces a robust downregulation of the DAT through a G_q-coupled pathway, indicating that the endogenous DAT is responsive to GPCR-mediated PKC activation.

Interestingly, the membrane trafficking of several other neurotransmitter transporters is also affected by PKC activation. The norepinephrine transporter, NET, is internalized in response to methacholine in SKNSH cells (Apparsundaram et al., 1998a), and PMA in HEK-293, LLC-PK1, and COS-7 cells (Apparsundaram et al., 1998b). Expression of M_1/M_5 receptors in norepinephrine neurons or other G_Q-coupled GPCRs suggest a physiological stimulus that may modulate norepinephrine signaling. The GABA transporter, GAT1, is also redistributed in response to PKC, mediated by acetylcholine, glutamate, and serotonin receptors (Beckman et al., 1999). We have found that PMA triggers internalization of the glutamate transporters EAAT1, EAAT2a (Susarla and Robinson, 2008), and EAAT2b (data not shown). Interestingly, PKC activation through PMA or platelet-derived growth factor (PDGF) stimulation leads to an increase in EAAT3 membrane localization several models (Gonzalez et al., 2003; Fournier et al., 2004). M_1/M_5 stimulation could contribute to EAAT3 trafficking that might be particularly important in GABA-ergic neurons where EAAT3 provides glutamate to these cells as a precursor to GABA synthesis. One report suggests that PMA can increase EAAT4 chloride currents that may be in response to PKC-induced regulation of that transporter (Fang et al., 2006). However, there was no measurable change in glutamate uptake, suggesting that the change in EAAT4 function may not be due to the altered trafficking of the carrier. Modulation of plasma membrane neurotransmitter transporters through G_Q-coupled receptors, such as M_1/M_5 may play critical roles in neurotransmitter tone throughout the brain.

Circuits affected by M_1/M_5-mediated trafficking of DAT. M_1/M_5 receptors have been implicated in the mental decline in Alzheimer's and Parkinson's diseases as well as schizophrenia, all of which have been linked to various degrees of dysregulation in dopamine neurons (Conn et al., 2009). There is a large

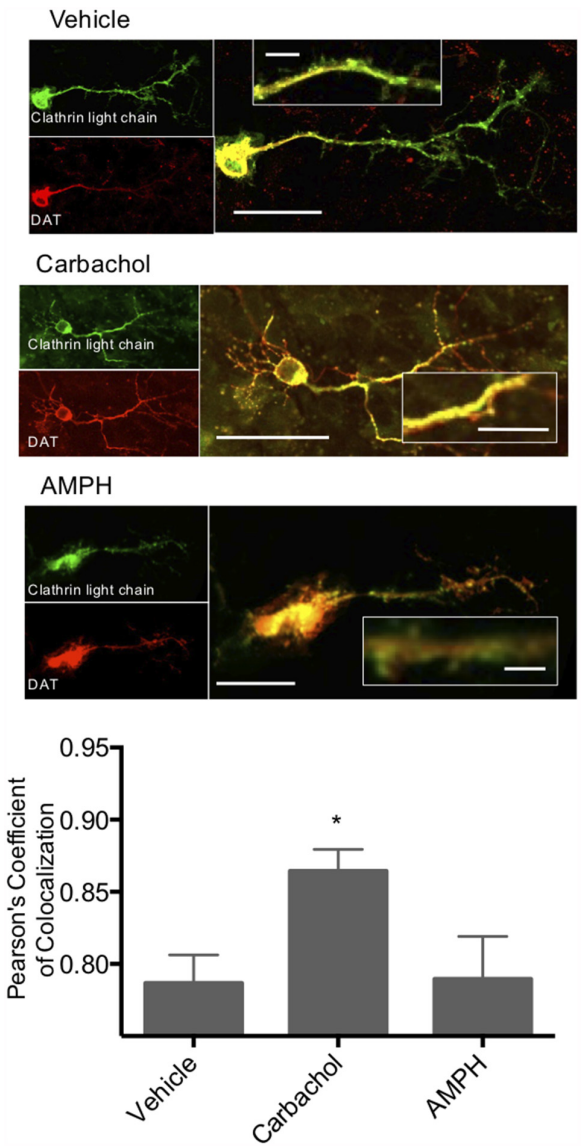

FIGURE 5 | Clathrin and DAT colocalize in response to carbachol. Primary midbrain neurons were transfected with a GFP-tagged clathrin light chain and an mCherry-tagged DAT. Colocalization of these two proteins was significantly increased in response to carbachol treatment (30 μM). Treatment of the cultures with amphetamine did not alter co-localization. *Indicates $p < 0.05$ by one-way ANOVA. $n = 19$, 15, and 12, respectively. Scale *bars* = 50 μm for merged images, 10 μm for the insets.

body of evidence that cholinergic inputs to the midbrain and basal ganglia circuitry modulate the activity and release properties of dopamine neurons (Forster et al., 2002; Threlfell et al., 2010, 2012; Foster et al., 2014). The phenomena that we describe here of M_1/M_5 receptor stimulation internalizing DAT indicates a precise mechanism by which acetylcholine can modulate dopamine neurons and extracellular dopamine concentrations directly. Targeting this particular pathway with the further development and exploration of drugs targeted to the M_1/M_5 receptor may lead to the development of better therapeutics.

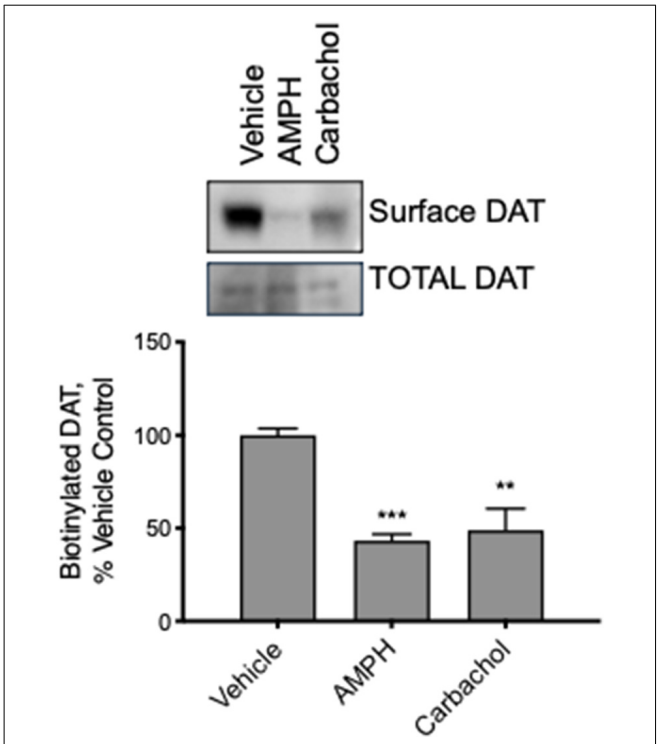

FIGURE 6 | DAT internalizes in response to AMPH and carbachol in acute brain slices from adult mice. We exposed slices from mature mouse brain to vehicle, AMPH or carbachol for 30 min and then biotinylated all the surface proteins, isolated the biotinylated proteins, and assessed DAT localization by Western blot. Carbachol (30 μM) as well as AMPH (10 μM), as well as AMPH (10 M), decreased the amount of biotinylated, membrane membrane-localized DAT ($n = 3$, $^{**}P \leq 0.01$ and $^{***}P \leq 0.001$ by one-way ANOVA).

DATA AVAILABILITY STATEMENT

The original contributions presented in the study are included in the article, further inquiries can be directed to the corresponding author.

ETHICS STATEMENT

The animal study was reviewed and approved by NIMH Animal Care Committee approved under protocol #LMCN-1.

AUTHOR CONTRIBUTIONS

SU contributed to the conception and design of the study, performed the experiments, analyzed the data, and wrote the first draft and revisions of the manuscript. SA contributed to the conception and design of the study, manuscript revisions and approved the submitted version. All authors contributed to the article and approved the submitted version.

FUNDING

This work was funded by the Intramural Research Program (ZIAMH002946).

REFERENCES

Apparsundaram, S., Galli, A., DeFelice, L. J., Hartzell, H. C., and Blakely, R. D. (1998a). Acute regulation of norepinephrine transport: I. protein kinase C-linked muscarinic receptors influence transport capacity and transporter density in SK-N-SH cells. *J. Pharmacol. Exp. Ther.* 287, 733–743.

Apparsundaram, S., Schroeter, S., Giovanetti, E., and Blakely, R. D. (1998b). Acute regulation of norepinephrine transport: II. PKC-modulated surface expression of human norepinephrine transporter proteins. *J. Pharmacol. Exp. Ther.* 287, 744–751.

Beckman, M. L., Bernstein, E. M., and Quick, M. W. (1999). Multiple G protein-coupled receptors initiate protein kinase C redistribution of GABA transporters in hippocampal neurons. *J. Neurosci.* 19:RC9. doi: 10.1523/JNEUROSCI.19-11-j0006.1999

Conn, P. J., Jones, C. K., and Lindsley, C. W. (2009). Subtype-selective allosteric modulators of muscarinic receptors for the treatment of CNS disorders. *Trends Pharmacol. Sci.* 30, 148–155. doi: 10.1016/j.tips.2008.12.002

Daniels, G. M., and Amara, S. G. (1999). Regulated trafficking of the human dopamine transporter. Clathrin-mediated internalization and lysosomal degradation in response to phorbol esters. *J. Biol. Chem.* 274, 35794–35801. doi: 10.1074/jbc.274.50.35794

Doolen, S., and Zahniser, N. R. (2002). Conventional protein kinase C isoforms regulate human dopamine transporter activity in *Xenopus oocytes*. *FEBS Lett.* 516, 187–190. doi: 10.1016/s0014-5793(02)02554-1

Eriksen, J., Rasmussen, S. G., Rasmussen, T. N., Vaegter, C. B., Cha, J. H., Zou, M. F., et al. (2009). Visualization of dopamine transporter trafficking in live neurons by use of fluorescent cocaine analogs. *J. Neurosci.* 29, 6794–6808. doi: 10.1523/JNEUROSCI.4177-08.2009

Fang, H., Huang, Y., and Zuo, Z. (2006). Enhancement of substrate-gated Cl-currents *via* rat glutamate transporter EAAT4 by PMA. *Am. J. Physiol. Cell. Physiol.* 290, C1334–C1340. doi: 10.1152/ajpcell.00443.2005

Forster, G. L., Yeomans, J. S., Takeuchi, J., and Blaha, C. D. (2002). M_5 muscarinic receptors are required for prolonged accumbal dopamine release after electrical stimulation of the pons in mice. *J. Neurosci.* 22:RC190. doi: 10.1523/JNEUROSCI.22-01-j0001.2002

Foster, D. J., Gentry, P. R., Lizardi-Ortiz, J. E., Bridges, T. M., Wood, M. R., Niswender, C. M., et al. (2014). M_5 receptor activation produces opposing physiological outcomes in dopamine neurons depending on the receptor's location. *J. Neurosci.* 34, 3253–3262. doi: 10.1523/JNEUROSCI.4896-13.2014

Fournier, K. M., Gonzalez, M. I., and Robinson, M. B. (2004). Rapid trafficking of the neuronal glutamate transporter, EAAC1: evidence for distinct trafficking pathways differentially regulated by protein kinase C and platelet-derived growth factor. *J. Biol. Chem.* 279, 34505–34513. doi: 10.1074/jbc.M404032200

Gabriel, L. R., Wu, S., Kearney, P., Bellve, K. D., Standley, C., Fogarty, K. E., et al. (2013). Dopamine transporter endocytic trafficking in striatal dopaminergic neurons: differential dependence on dynamin and the actin cytoskeleton. *J. Neurosci.* 33, 17836–17846. doi: 10.1523/JNEUROSCI.3284-13.2013

Gonzalez, M. I., Bannerman, P. G., and Robinson, M. B. (2003). Phorbol myristate acetate-dependent interaction of protein kinase Cα and the neuronal glutamate transporter EAAC1. *J. Neurosci.* 23, 5589–5593. doi: 10.1523/JNEUROSCI.23-13-05589.2003

Gorentla, B. K., and Vaughan, R. A. (2005). Differential effects of dopamine and psychoactive drugs on dopamine transporter phosphorylation and regulation. *Neuropharmacology* 49, 759–768. doi: 10.1016/j.neuropharm.2005.08.011

Hong, W. C., and Amara, S. G. (2013). Differential targeting of the dopamine transporter to recycling or degradative pathways during amphetamine- or PKC-regulated endocytosis in dopamine neurons. *FASEB J.* 27, 2995–3007. doi: 10.1096/fj.12-218727

Kahlig, K. M., Lute, B. J., Wei, Y., Loland, C. J., Gether, U., Javitch, J. A., et al. (2006). Regulation of dopamine transporter trafficking by intracellular amphetamine. *Mol. Pharmacol.* 70, 542–548. doi: 10.1124/mol.106.023952

Melikian, H. E., and Buckley, K. M. (1999). Membrane trafficking regulates the activity of the human dopamine transporter. *J. Neurosci.* 19, 7699–7710. doi: 10.1523/JNEUROSCI.19-18-07699.1999

Miranda, M., Wu, C. C., Sorkina, T., Korstjens, D. R., and Sorkin, A. (2005). Enhanced ubiquitylation and accelerated degradation of the dopamine transporter mediated by protein kinase C. *J. Biol. Chem.* 280, 35617–35624. doi: 10.1074/jbc.M506618200

Mortensen, O. V., and Amara, S. G. (2003). Dynamic regulation of the dopamine transporter. *Eur. J. Pharmacol.* 479, 159–170. doi: 10.1016/j.ejphar.2003.08.066

Mortensen, O. V., Larsen, M. B., Prasad, B. M., and Amara, S. G. (2008). Genetic complementation screen identifies a mitogen-activated protein kinase phosphatase, MKP3, as a regulator of dopamine transporter trafficking. *Mol. Biol. Cell* 19, 2818–2829. doi: 10.1091/mbc.e07-09-0980

Navaroli, D. M., Stevens, Z. H., Uzelac, Z., Gabriel, L., King, M. J., Lifshitz, L. M., et al. (2011). The plasma membrane-associated GTPase Rin interacts with the dopamine transporter and is required for protein kinase C-regulated dopamine transporter trafficking. *J. Neurosci.* 31, 13758–13770. doi: 10.1523/JNEUROSCI.2649-11.2011

Saunders, C., Ferrer, J. V., Shi, L., Chen, J., Merrill, G., Lamb, M. E., et al. (2000). Amphetamine-induced loss of human dopamine transporter activity: an internalization-dependent and cocaine-sensitive mechanism. *Proc. Natl. Acad. Sci. U S A* 97, 6850–6855. doi: 10.1073/pnas.110035297

Susarla, B. T., and Robinson, M. B. (2008). Internalization and degradation of the glutamate transporter GLT-1 in response to phorbol ester. *Neurochem. Int.* 52, 709–722. doi: 10.1016/j.neuint.2007.08.020

Threlfell, S., Clements, M. A., Khodai, T., Pienaar, I. S., Exley, R., Wess, J., et al. (2010). Striatal muscarinic receptors promote activity dependence of dopamine transmission *via* distinct receptor subtypes on cholinergic interneurons in ventral versus dorsal striatum. *J. Neurosci.* 30, 3398–3408. doi: 10.1523/JNEUROSCI.5620-09.2010

Threlfell, S., Lalic, T., Platt, N. J., Jennings, K. A., Deisseroth, K., and Cragg, S. J. (2012). Striatal dopamine release is triggered by synchronized activity in cholinergic interneurons. *Neuron* 75, 58–64. doi: 10.1016/j.neuron.2012.04.038

Underhill, S. M., Hullihen, P. D., Chen, J., Fenollar-Ferrer, C., Rizzo, M. A., Ingram, S. L., et al. (2019). Amphetamines signal through intracellular TAAR1 receptors coupled to Gα13 and GαS in discrete subcellular domains. *Mol. Psychiatry* doi: 10.1038/s41380-019-0469-2. [Online ahead of print].

Underhill, S. M., Wheeler, D. S., Li, M., Watts, S. D., Ingram, S. L., and Amara, S. G. (2014). Amphetamine modulates excitatory neurotransmission through endocytosis of the glutamate transporter EAAT3 in dopamine neurons. *Neuron* 83, 404–416. doi: 10.1016/j.neuron.2014.05.043

Vaughan, R. A., Huff, R. A., Uhl, G. R., and Kuhar, M. J. (1997). Protein kinase C-mediated phosphorylation and functional regulation of dopamine transporters in striatal synaptosomes. *J. Biol. Chem.* 272, 15541–15546. doi: 10.1074/jbc.272.24.15541

Wheeler, D. S., Underhill, S. M., Stolz, D. B., Murdoch, G. H., Thiels, E., Romero, G., et al. (2015). Amphetamine activates Rho GTPase signaling to mediate dopamine transporter internalization and acute behavioral effects of amphetamine. *Proc. Natl. Acad. Sci. U S A* 112, E7138–E7147. doi: 10.1073/pnas.1511670112

Wu, S., Bellve, K. D., Fogarty, K. E., and Melikian, H. E. (2015). Ack1 is a dopamine transporter endocytic brake that rescues a trafficking-dysregulated ADHD coding variant. *Proc. Natl. Acad. Sci. U S A* 112, 15480–15485. doi: 10.1073/pnas.1512957112

Zhu, S. J., Kavanaugh, M. P., Sonders, M. S., Amara, S. G., and Zahniser, N. R. (1997). Activation of protein kinase C inhibits uptake, currents and binding associated with the human dopamine transporter expressed in *Xenopus oocytes*. *J. Pharmacol. Exp. Ther.* 282, 1358–1365.

Conflict of Interest: The authors declare that the research was conducted in the absence of any commercial or financial relationships that could be construed as a potential conflict of interest.

frontiers in Cellular Neuroscience

REVIEW
published: 13 April 2021
doi: 10.3389/fncel.2021.670346

Regulation of Glutamate, GABA and Dopamine Transporter Uptake, Surface Mobility and Expression

*Renae M. Ryan[1], Susan L. Ingram[2] and Annalisa Scimemi[3]**

[1] School of Medical Sciences, Faculty of Medicine and Health, University of Sydney, Sydney, NSW, Australia, [2] Department of Neurological Surgery, Oregon Health & Science University, Portland, OR, United States, [3] Department of Biology, SUNY Albany, Albany, NY, United States

Neurotransmitter transporters limit spillover between synapses and maintain the extracellular neurotransmitter concentration at low yet physiologically meaningful levels. They also exert a key role in providing precursors for neurotransmitter biosynthesis. In many cases, neurons and astrocytes contain a large intracellular pool of transporters that can be redistributed and stabilized in the plasma membrane following activation of different signaling pathways. This means that the uptake capacity of the brain neuropil for different neurotransmitters can be dynamically regulated over the course of minutes, as an indirect consequence of changes in neuronal activity, blood flow, cell-to-cell interactions, etc. Here we discuss recent advances in the mechanisms that control the cell membrane trafficking and biophysical properties of transporters for the excitatory, inhibitory and modulatory neurotransmitters glutamate, GABA, and dopamine.

Keywords: glutamate, GABA, dopamine, transporter, uptake, surface mobility

OPEN ACCESS

Edited by:
Fiorenzo Conti,
Marche Polytechnic University, Italy

Reviewed by:
Janosch P. Heller,
Dublin City University, Ireland
Michael B. Robinson,
Children's Hospital of Philadelphia Research Institute, United States

***Correspondence:**
Annalisa Scimemi
scimemia@gmail.com;
ascimemi@albany.edu

Specialty section:
This article was submitted to Cellular Neurophysiology, a section of the journal Frontiers in Cellular Neuroscience

Received: *21 February 2021*
Accepted: *15 March 2021*
Published: *13 April 2021*

Citation:
Ryan RM, Ingram SL and Scimemi A (2021) Regulation of Glutamate, GABA and Dopamine Transporter Uptake, Surface Mobility and Expression. Front. Cell. Neurosci. 15:670346. doi: 10.3389/fncel.2021.670346

GLUTAMATE TRANSPORTERS

In addition to being one of the most abundant amino acids and the main excitatory neurotransmitter in the brain, glutamate controls synapse formation, and maturation, acts as an energy substrate for oxidative metabolism, contributes to the antioxidant properties of glutathione, and can be used as a building block for non-ribosomal peptide synthesis and as the precursor for the biosynthesis of the inhibitory neurotransmitter GABA (Sieber and Marahiel, 2005; Brosnan and Brosnan, 2013; Martinez-Lozada et al., 2016; Walker and van der Donk, 2016). In addition, in the developing brain, glutamate guides cell proliferation, migration, differentiation, and survival of neural progenitor cells (Jansson et al., 2013). Because of the plethora of effects that glutamate can exert, its lifetime in the extracellular space needs to be finely controlled through the activity of a family of Na^+- and K^+-dependent secondary active transporters. Geneticists, structural biologists, physiologists and clinicians all have their preferred nomenclature to refer to the five known glutamate transporters subtypes, summarized as follows: (i) Slc1a1/SLC1A1/EAAC1/EAAT3; (ii) Slc1a2/SLC1A2/GLT1/EAAT2; (iii) Slc1a3/SLC1A3/GLAST/EAAT1; (iv) Slc1a6/SLC1A6/EAAT4; (v) Slc1a7/SLC1A7/EAAT5. The use of each terminology is physiologically meaningful, as it refers to the genes encoding each transporter in rodents (Slc1a1, Slc1a2, Slc1a3, Slc1a6, Slc1a7) and in humans (SLC1A1, SLC1A2, SLC1A3, SLC1A6, SLC1A7), or the protein product in rodents (EAAC1, GLT1, GLAST, EAAT4-5) and humans (EAAT1-5). For simplicity, in this review, we refer to them as EAAT1-5. Different subtypes of glutamate transporters are differentially expressed in neuronal and glial cells (Danbolt, 2001). Accordingly, the glutamate transporters EAAT1-2 are

mostly expressed in astrocytes, whereas EAAT3-5 are mostly expressed in neurons. Two of the neuronal transporters are predominantly expressed in the cerebellum (EAAT4) or retina (EAAT5), with a low yet experimentally measurable concentration in the forebrain (Dehnes et al., 1998; Danbolt, 2001). The others (i.e., EAAT1, EAAT2, and EAAT3) are expressed broadly throughout the brain, at varying levels.

Structural information of the glutamate transporters comes from prokaryote homologs such as Glt_{Ph} and Glt_{Tk} which share ∼35 amino acid identity with human EAAT2 (Yernool et al., 2004; Boudker et al., 2007; Reyes et al., 2009; Verdon and Boudker, 2012; Guskov et al., 2016; Scopelliti et al., 2018) and more recent crystal and cryo-EM structures of human transporters including EAAT1, EAAT3, and ASCT2 (Canul-Tec et al., 2017; Garaeva et al., 2018; Garaeva et al., 2019; Yu et al., 2019; Wang and Boudker, 2020) (**Figure 1**). All members of this family appear to assemble as trimers, with each monomer capable of transporting substrate and coupled ions, generating stoichiometric and non-stoichiometric currents, independently of the two other monomers (Grewer et al., 2005; Koch et al., 2007; Leary et al., 2007). The transporters are composed of a "transport domain" which binds and transports substrate and coupled ions, and a "scaffold domain" that forms inter-protomer contacts and interacts with the lipid membrane (Boudker et al., 2007; Reyes et al., 2009). Glt_{Ph} transports aspartate together with three Na^+ ions into the cytoplasm using a twisting elevator mechanism (Reyes et al., 2009; Ryan and Vandenberg, 2016) and generates a stoichiometrically uncoupled Cl^- conductance (Boudker et al., 2007; Ryan and Mindell, 2007; Reyes et al., 2009).

In contrast to prokaryotes, for all eukaryotic transporters, glutamate uptake is driven by the electrochemical gradient for Na^+ and H^+ ions, and the rate limiting step is the counter-transport of one K^+ ion across the membrane (Zerangue and Kavanaugh, 1996). The stoichiometry of the transport process is the inward movement of 1 glutamate (which carries a negative charge): 3 Na^+: 1 H^+, followed by the counter-transport of 1 K^+, leading to the net influx of two positive charges per transport cycle (Zerangue and Kavanaugh, 1996; Levy et al., 1998). In addition, these transporters mediate a glutamate-dependent anion flux, which under physiological conditions is carried by Cl^- ions (Picaud et al., 1995; Wadiche et al., 1995b; Eliasof and Jahr, 1996). The chloride channel forms at the interface of the transport and scaffold domains during the transport cycle (Ryan et al., 2004; Cater et al., 2014, 2016; Cheng et al., 2017; Kolen et al., 2020; Chen et al., 2021) and the direction of this flux is determined by the driving force for chloride (i.e., the difference between membrane potential and reversal potential for chloride). The function of the chloride current remains incompletely understood but it has been suggested that it might serve to counterbalance the influx of positive charges due to glutamate transport and prevent cell depolarization (Grewer and Rauen, 2005). This hypothesis would only hold true in the presence of a positive driving force for chloride, causing an inward movement of chloride into the cell. This occurs when the reversal potential for chloride is more hyperpolarized than the membrane potential. This condition, however, is not fulfilled in developing neurons. Here, the reversal potential for chloride is more depolarized than in mature neurons, due to a delayed expression of the potassium chloride co-transporter KCC2, and a consequently higher intracellular chloride concentration in developing compared to mature neurons (Rivera et al., 1999). Other physiological roles for the chloride conductance have been demonstrated with EAAT5 in the retina, where it regulates cell activity and neurotransmitter release (Picaud et al., 1995; Veruki et al., 2006) and in cerebellar astrocytes, where the chloride currents of EAAT1/2 affects the resting intracellular chloride concentration (Sonders and Amara, 1996; Untiet et al., 2017).

Similarities and Distinctive Biophysical Features of Different Glutamate Transporter Subtypes

The general mechanisms of substrate transport, identified through studies of uptake of radiolabeled substrates or voltage-clamp recordings of transporter currents under steady-state conditions, are roughly similar among different glutamate transporter types. For all of them, the transport efficiency is in the order of ∼50%, which means that − perhaps surprisingly − these molecules translocate into the cell cytoplasm only 50% of all glutamate molecules they bind (Tzingounis and Wadiche, 2007). The remaining 50% of glutamate molecules that unbind from the transporters are released back in the extracellular space, and ultimately bind to nearby glutamate receptors, neuronal or glial transporters. This low transport efficiency can lead to an apparently paradoxical prolongation of glutamate lifetime in the extracellular space (Scimemi et al., 2009). Since the rates of glutamate binding to receptors and transporters are relatively similar, the likelihood that a glutamate molecule unbound from a transporter will eventually bind to a receptor or another transporter depends on the relative abundance of receptors compared to that of transporters. Typically, the surface density of expression of transporters in glial membranes is four orders of magnitude higher than that of glutamate receptors in extra-synaptic neuronal membrane (Lehre and Danbolt, 1998). For this reason, the most likely ultimate fate of glutamate molecules unbound from transporters is to be bound again by other transporter molecules (Leary et al., 2011).

Non-rate-limiting partial reaction steps, obtained by perturbing the steady-state and by subsequently following the kinetics of the relaxation to a new steady-state (i.e., the pre-steady-state kinetics), are similar for EAAT1-3 (Grewer and Rauen, 2005). However, the pre-steady-state kinetics and steady-state turnover rats are significantly slower for EAAT4 (Mim et al., 2005). There are also notable differences in the steady state affinity of different transporter types (k_m EAAT1: 48 ± 10 μM; EAAT2: 97 ± 4 μM; EAAT3: 62 ± 8 μM; EAAT4: 0.6 μM; Wadiche and Kavanaugh, 1998; Grewer et al., 2000; Bergles et al., 2002), and in the ratio of substrate transport versus anion permeation (Arriza et al., 1994; Seal and Amara, 1999; Mim et al., 2005; Torres-Salazar and Fahlke, 2007). Interestingly, and in contrast to EAAT1-3, the apparent affinity for glutamate is voltage dependent for EAAT4 and increases with negative voltages, suggesting higher glutamate buffering capacity for EAAT4 than other glutamate transporters (Mim et al., 2005).

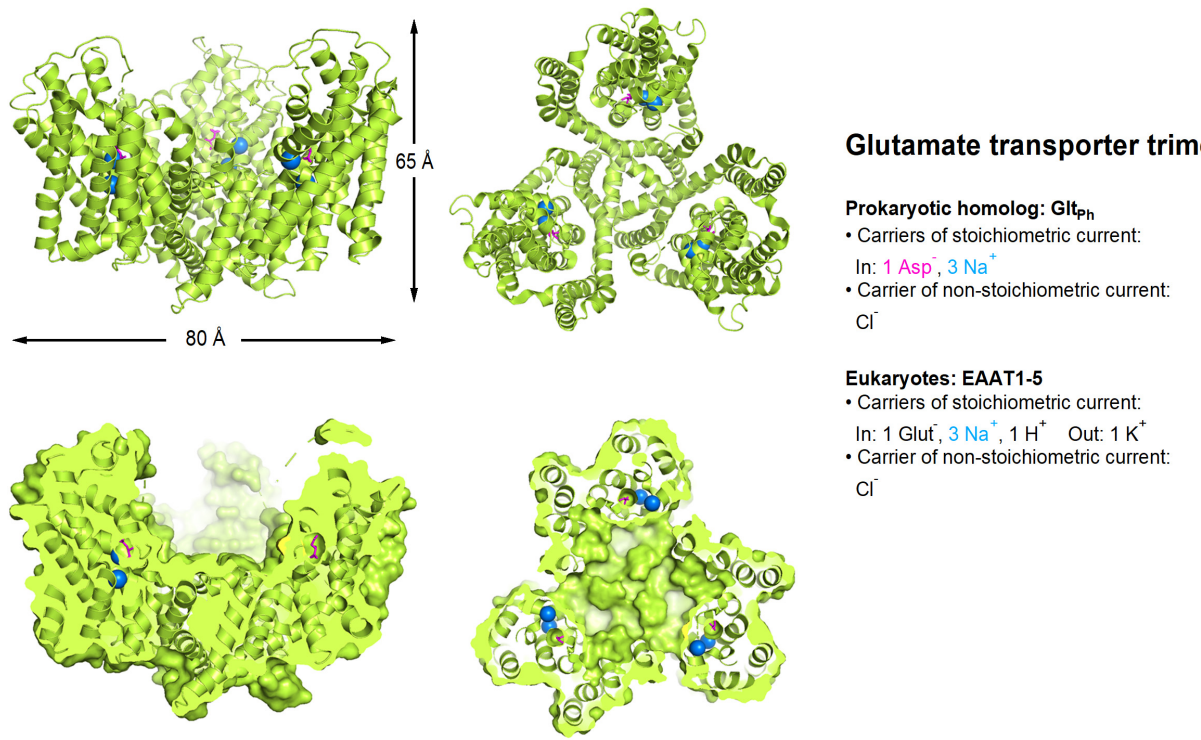

FIGURE 1 | Crystal structure of Glt$_{Ph}$, a bacterial homolog of glutamate transporters (PDB: 2NWX). **(A)** Side view of the glutamate transporter trimer parallel to the membrane, using a ribbon (*top*) and a surface representation sliced through the center of the transporter basin (*bottom*). **(B)** As in A, viewed from the extracellular side of the membrane. Aspartate (*magenta*) and sodium ions (*blue*) are represented as spheres. **(C)** Summary of the main feature of the stoichiometric and non-stoichiometric current mediated by glutamate transporters in prokaryotes and eukaryotes, respectively. Image generated using The PyMOL Molecular Graphics System (Version 2.3.2; Schrödinger, 2010).

The fact that EAAT4 has a 10-fold higher affinity for glutamate but a 10-fold slower translocation rate than other transporters has led to hypothesize that the main functional role of EAAT4 is accounted for by its ability to generate a stoichiometrically uncoupled anion current (Fairman et al., 1995; Lin et al., 1998). Others have suggested that these biophysical properties would allow EAAT4 to clear glutamate away from synapses, where its concentration is lower than at the outer boundary of the synaptic cleft (Mim et al., 2005). Consistent with this hypothesis, one of the most prominent roles of EAAT4 is to limit metabotropic glutamate receptor activation in cerebellar Purkinje cells, in sub-cellular domains where the density of expression of these receptors and EAAT4 are both high (Wadiche and Jahr, 2005).

Glutamate transport via EAAT4 has a unique voltage-dependence. Its maximum transport activity is detected at $-20\ mV < V_m < 0\ mV$ and the transporter inactivates at more negative membrane potentials (Mim et al., 2005). Membrane hyperpolarization promotes glutamate transport via other glutamate transporters, which have reversal potentials of 9.3 ± 0.7 mV (EAAT1), >80 mV (EAAT2) and 38.0 ± 2.7 mV (EAAT3) (Arriza et al., 1994). At hyperpolarized potentials, not only transport, but also the anion conductance of EAAT4 is inhibited (Mim et al., 2005). This means that at membrane potentials close to the resting potential of neurons, glutamate is bound strongly to all transporters, but its transport via EAAT4 is inhibited (Mim et al., 2005).

There are differences in the sodium requirement for activation of the anion conductance between neuronal and glial glutamate transporters (Wadiche et al., 1995a; Grewer et al., 2000, 2001; Otis and Kavanaugh, 2000). For EAAT3, the anion conductance can be activated by glutamate and Na^+ ions from both sides of the membrane (Watzke and Grewer, 2001). The activation of the anion conductance by sodium alone has only been demonstrated for EAAT3-4, while EAAT1-2 mediate glutamate- and sodium-independent anion conducting states (Divito et al., 2017). For EAAT4-5, the anion conductance is particularly large compared to their glutamate transport capacity (Sonders and Amara, 1996; Seal et al., 2001). Consequently, transport currents generated by EAAT1-3 are easily measured experimentally using heterologous expression systems, whereas those mediated by EAAT4-5 are relatively small (Wadiche et al., 1995a; Grewer et al., 2001; Mitrovic et al., 2001; Watzke et al., 2001).

The existence of functional differences in the properties of glutamate transporter subtypes indicates that the function of these molecules is much more complex than previously thought, and that an evaluation of the physiological implications

of glutamate transporters cannot bypass an understanding of the biophysical properties of these molecules in their native environments.

The Surface Mobility and Cellular Distribution of EAAT2

Out of all glutamate transporter types, EAAT2 has the highest density of expression in the adult brain, and is responsible for the largest proportion of glutamate transport (Minelli et al., 2001). In astrocytes, 70–75% of all EAAT2 is expressed on the plasma membrane (Michaluk et al., 2020). In the hippocampus, cerebellum and neocortex, EAAT2 is expressed mostly in astrocytic processes, in the vicinity and at a distance from the synaptic cleft (Danbolt et al., 1992; Levy et al., 1993; Rothstein et al., 1994; Torp et al., 1994; Chaudhry et al., 1995; Lehre et al., 1995). EAAT2 exists in at least three splice variants which differ only in their C-terminal domain. EAAT2a is the predominant variant, and represents ∼90%, whereas EAAT2b and EAAT2c represent ∼6% and ∼1% of total EAAT2 protein, respectively (Chen et al., 2002; Rauen et al., 2004; Holmseth et al., 2009). These variants have similar regional distribution and although they are all primarily expressed in astrocytes, they have also been detected in neurons (Schmitt et al., 2002; Chen et al., 2004; Maragakis et al., 2004; Bassan et al., 2008; Gonzalez-Gonzalez et al., 2008a; Holmseth et al., 2009). EAAT2a is more abundantly expressed than EAAT2b, and is a presynaptic glutamate transporter (Berger et al., 2005; Rimmele and Rosenberg, 2016). Within the hippocampus, 14–29% of axon terminals express EAAT2a (Chen et al., 2004). Though EAAT2a and EAAT2b share similar functional properties, they differ for the sequence of their extreme intracellular C-terminus (Chen et al., 2002; Sullivan et al., 2004). Unlike EAAT2a, EAAT2b has a PDZ binding domain that makes it capable of binding to proteins like PICK1, PSD95, and DLG1 (Bassan et al., 2008; Gonzalez-Gonzalez et al., 2008a; Underhill et al., 2015). These, in turn, can alter the currents mediated by the EAAT2b transporter (Sogaard et al., 2013). EAAT2a forms heteromers with EAAT2b, which have been proposed to stabilize EAAT2a around synapses (Haugeto et al., 1996; Peacey et al., 2009).

EAAT2 is highly mobile on the plasma membrane of astrocytes (D^* = 0.15–0.23 $\mu m^2/s$) (though a lower value of D^* = 0.039 $\mu m^2/s$ has been measured using quantum dots; Al Awabdh et al., 2016), and the rate with which it diffuses along the plasma membrane can be increased by glutamate binding to EAAT2 or to AMPA, NMDA and metabotropic glutamate receptors, and can be reduced by blocking glutamate binding to EAAT2 (Benediktsson et al., 2012; Murphy-Royal et al., 2015; Michaluk et al., 2020). The surface diffusion of the EAAT2 variants EAAT2a and EAAT2b is more confined at astrocytic processes proximal to synapses, especially for EAAT2b (Al Awabdh et al., 2016). Consistent with previous work, glutamate increases the surface mobility of both EAAT2 variants, whereas blocking synaptic activity reduces it (Al Awabdh et al., 2016). The more confined diffusion of EAAT2b may be attributed to the presence of the PDZ domain, which allows EAAT2b to interact with scaffolding proteins and anchor it to macromolecular complexes that astrocytes form in subcellular domains opposite to neuronal presynaptic terminals (Al Awabdh et al., 2016). There is also evidence that membrane raft association regulates the targeting and function of glutamate transporters, especially for EAAT2 (Butchbach et al., 2004).

Glutamate transporters have been suggested to become incorporated into the plasma membrane through exocytosis (Cheng et al., 2002; Chowdhury et al., 2002; Robinson, 2002; Fournier et al., 2004; Karylowski et al., 2004; Zeigerer et al., 2004), and several components of this molecular machinery have been identified in astrocytes (Parpura et al., 1995; Hepp et al., 1999; Zhang et al., 2004). Consistent with these findings, calcium-dependent exocytosis of EAAT2 has been detected using FM dyes in cultured astrocytes (Stenovec et al., 2008). The same experiments showed that EAAT2 has a punctate distribution along the astrocytic plasma membrane, suggesting that the glutamate uptake capacity of these cells varies depending on the local density of expression of glutamate transporters (Stenovec et al., 2008). Interestingly, recent work indicate that the lifetime of EAAT2 on the astrocyte plasma membrane is ∼22 s (Michaluk et al., 2020). Whereas lateral diffusion could serve as a mechanism for transporter turnover away from synapses, where the diffusivity of these molecules is higher, endo/exocytosis from/to the plasma membrane to intracellular organelles could contribute to transporter turnover in astrocytic processes nearby synapses, where the diffusivity of these molecules is lower (Michaluk et al., 2020).

Although 80–90% of EAAT2 is localized in astrocytes, there is a small proportion (5–10%) in neuronal axon terminals (Rauen and Kanner, 1994; Torp et al., 1994; Schmitt et al., 1996; Torp et al., 1997; Chen et al., 2004; Furness et al., 2008; Melone et al., 2009, 2011, 2019). In neurons, EAAT2 co-localizes with the α_1 and α_3 isoforms of the Na^+/K^+-ATPase, but this co-localization is looser than that with the α_2 isoform in astrocytes, suggesting a less efficient interaction between EAAT2 and the Na^+/K^+-ATPase in neurons (Melone et al., 2019). Neuronal EAAT2 appears to be required to provide glutamate to synaptic mitochondria, and is therefore linked to energy metabolism (Petr et al., 2015; Fischer et al., 2018; McNair et al., 2019, 2020; Sharma et al., 2019). By contrast, astrocytic EAAT2 is crucial to ensure survival, resistance to epilepsy, and prevent cognitive decline. Loss of neuronal and astrocytic EAAT2 have both implications on long-term memory and spatial reference learning, but the time scale over which they exert these effects is different (Sharma et al., 2019). Loss of astrocytic EAAT2 leads to early deficits, whereas loss of neuronal EAAT2 leads to late-onset deficits in long-term memory and spatial reference learning (Sharma et al., 2019). These findings are important because they identify neuronal and astrocytic EAAT2 as contributing to different aspects of cognitive function and, potentially, as different therapeutic targets in cognitive decline (Petr et al., 2015; Fischer et al., 2018; McNair et al., 2019, 2020; Sharma et al., 2019).

Multiple studies have shown that there are interesting relationships between astrocytic coverage, glutamate transporter expression and synaptic size (Ventura and Harris, 1999; Genoud et al., 2006; Witcher et al., 2007; Lushnikova et al., 2009; Witcher et al., 2010; Patrushev et al., 2013; Medvedev et al., 2014;

Gavrilov et al., 2018; Herde et al., 2020). For example, in the rodent hippocampus, only 40–60% of synapses have astrocytic processes, and these cover only 53% of their perimeter (Ventura and Harris, 1999; Witcher et al., 2007, 2010). The size of a spine correlates with its release probability (Schikorski and Stevens, 1997). Astrocytes are closer to smaller spines (Medvedev et al., 2014), but the overall astrocytic coverage does not change with spine size (Gavrilov et al., 2018). Although there is less EAAT2 at smaller spines, its density is higher (Herde et al., 2020). These findings have important implications for understanding how glutamate transporters control spillover at synapses with different size (Scimemi et al., 2004), and the implications of this phenomenon on synaptic and astrocyte plasticity (Wenzel et al., 1991; Matsusaki et al., 2001; Bernardinelli et al., 2014; Perez-Alvarez et al., 2014).

Transcriptional, Translational, and Post-translational Regulation of Glutamate Transporters

Despite current agreements on the presence of EAAT2 in neurons, in the 1990s, some groups failed to find EAAT2 proteins in subsets of cortical neurons (Rothstein et al., 1994; Chaudhry et al., 1995; Lehre et al., 1995), in contrast to others (Torp et al., 1994; Schmitt et al., 1996; Torp et al., 1997). The discrepancy between these findings was attributed to the existence of a post-transcriptional and post-translational control of EAAT2 expression (Gegelashvili and Schousboe, 1997; Anderson and Swanson, 2000; Plachez et al., 2000). In fact, like most membrane proteins, glutamate transporters can be regulated at the gene expression, protein targeting and trafficking, and post-translational level.

The gene structure and organization of most glutamate transporters identified in the late 1990s showed that the promoter regions are highly conserved between mouse and human (Hagiwara et al., 1996; Stoffel et al., 1996). These regions do not contain a TATA box but a GC box and, in humans, an E box (Martinez-Lozada et al., 2016). The genes encoding different glutamate transporters contain different excision/splicing sites for different exons, which can generate variant mRNA species and proteins. Accordingly, multiple studies have reported the existence of several mRNA size classes encoding EAAT1 and EAAT3 (Pines et al., 1992; Tanaka, 1993; Mukainaka et al., 1995; Nakayama et al., 1996; Palos et al., 1996; Gegelashvili and Schousboe, 1997). This might be due to differences in polyadenylation and the existence of mRNAs with different coding capacity (Gegelashvili and Schousboe, 1997).

When glutamate transporters and their human homologs were first cloned, knowledge on the elements regulating their transcription largely relied on information collected from ASCT1, a neutral amino acid transporter of the same family of high affinity transporters as glutamate transporters (Hofmann et al., 1994). ASCT1 has 39–44% amino acid sequence identity, similar hydropathy profiles, *trans*-membrane organization and conservation of crucial function-related motifs compared to EAAT2 (Gegelashvili and Schousboe, 1997). According to these initial reports, the promoter region of EAAT2 was thought to contain at least five consensus sequences for the *Sp1* transcription factor (*krox24, krox20, Egr3, NGFI-C)*, involved in cell differentiation (Hofmann et al., 1994; Gegelashvili and Schousboe, 1997). By the early 2000's, cloning and bioinformatics works established that the promoter region for EAAT1-2 is highly conserved: not only does it not have a TATA box, but lacks well-defined *cis*-elements and contains five consensus sequences for *Sp1* and GC-rich repeats, also found in humans (Su et al., 2003). The search for regulatory transcription factors has led to the identification of the Nuclear Factor of Activated T cells (NFAT), the *N*-myc proto-oncogene protein (*N*-myc), and the Nuclear Factor κB (NF-κB), and a consensus NF-κB binding sequence in the 5′-UTR region of the *Slc1a2* gene in humans (Meyer et al., 1996; Su et al., 2003). The Tumor Necrosis Factor α (TNFα), a cytokine involved in the acute phase of inflammatory reactions, decreases EAAT2 mRNA expression by increasing NF-κB activation (Su et al., 2003), perhaps by promoting NF-kB interactions with other transcription factors (Sitcheran et al., 2005). The ability of transcription factors to regulate gene expression can change the sensitivity of glutamate transporter expression to other regulatory proteins. For example, TNFα regulates the activity of the Yin Yang 1 (YY1) transcription factor which, when bound to the EAAT2 promoter, changes the effect of NF-κB from activation to suppression (Karki et al., 2014). In turn, NF-κB regulates YY1 expression. These findings suggest the existence of complex interplays between NF-κB and YY1 for the transcriptional regulation of EAAT2 expression.

Over the last two decades, other groups have identified factors, cis-regulatory elements and epigenetic mechanisms regulating EAAT1-2 transcription, but many unknowns remain about the molecular mechanisms regulating EAAT3-5 expression. In **Table 1**, we provide a summary of current studies on modulation of glutamate transporters listed in PubMed. One can easily note that in many cases, the results are conflicting. One may argue that inconsistencies are inevitable when studying a given transporter in different cell types and animal species. However, in some cases these considerations do not allow to resolve conflicting results from different laboratories. For this reason, in this review, we limit our discussion to forms of modulation of glutamate transporters for which some consensus exists.

There is a general agreement on the fact that in cultured neurons, PACAP, cAMP, and PKA-dependent pathways increase EAAT1 expression (Martinez-Lozada et al., 2016) and uptake (Hertz et al., 1978; Gegelashvili et al., 1996). Presumably this effect is mediated by activation of the transcription factor cAMP-response element binding protein (CREB), but the transcription factors or the *cis* elements of the promoter responsible for this effect have not been identified (Martinez-Lozada et al., 2016). This form of transcriptional regulation may provide a pathway through which activation of G-protein membrane receptors coupled to cAMP and PKA-dependent signaling pathways indirectly affect glutamate uptake, as it has been shown in other contexts for D_2 dopamine receptors or α_1 and β-adrenergic receptors (Kerkerian et al., 1987).

Stable epigenetic alterations of glutamate transporter gene expression are heritable in the short term, but do not involve DNA mutations. These include methylation and histone

TABLE 1 | Regulating factors of glutamate transporter uptake and expression.

Agent	Assay	N/A	EAAT1	EAAT2	EAAT3	EAAT4
Glutamate						
Glutamate	Uptake		(Bernabe et al., 2003) ms cereb astro			
Glutamate	Uptake		(Bernabe et al., 2003) ms cort astro			
cAMP and analogues						
cAMP	Uptake		(Gegelashvili et al., 1996) ms cort astro			
cAMP	Expression		(Gegelashvili et al., 1996) ms cort astro			
PKA activators						
Forskolin	Uptake			(Adolph et al., 2007) rat cort astro		
Forskolin	Uptake	(Yang et al., 2004) ms cort nrn				
Forskolin	Uptake				(Dowd and Robinson, 1996) C6 glioma	
Forskolin	Uptake				(Trotti et al., 2001) Xenopus ooc	
PKA inhibitors						
H89	Uptake		(Guillet et al., 2005) rat cort nrn	(Guillet et al., 2005) rat cort nrn	(Guillet et al., 2005) rat cort nrn	
H89	Uptake	(Yang et al., 2004) ms cort nrn				
H89	Uptake		(Adolph et al., 2007) rat cort astro			
H89	Expression		(Guillet et al., 2005) rat cort nrn	(Guillet et al., 2005) rat cort nrn	(Guillet et al., 2005) rat cort nrn	
PKB (Akt)						
Akt	Uptake			(Li et al., 2006) rat cort astro		
Akt	Uptake					(Bohmer et al., 2004) Xenopus ooc
Akt	Expression		(Li et al., 2006) rat cort astro	(Li et al., 2006) rat cort astro		
PKC activators						
DOG	Uptake				(Trotti et al., 2001) Xenopus ooc	
PDBu	Uptake				(Trotti et al., 2001) Xenopus ooc	
PMA	Uptake		(Conradt and Stoffel, 1997) Xenopus ooc			
PMA	Uptake		(Conradt and Stoffel, 1997) HEK293			
PMA	Uptake		(Wang Z. et al., 2003) rat Muller cells			
PMA	Uptake			(Sogaard et al., 2013) Xenopus ooc		
PMA	Uptake			(Sogaard et al., 2013) Xenopus ooc		
PMA	Uptake			(Sheldon et al., 2008) C6 glioma		
PMA	Uptake			(Kalandadze et al., 2002) C6 glioma		

(Continued)

TABLE 1 | Continued

Agent	Assay	N/A	EAAT1	EAAT2	EAAT3	EAAT4
PMA	Uptake			(Gonzalez-Gonzalez et al., 2008b) COS7		
PMA	Uptake			(Gonzalez-Gonzalez et al., 2008b) MDCK		
PMA	Uptake			(Ganel and Crosson, 1998) Y-79 retblast		
PMA	Uptake			(Adolph et al., 2007) rat cort astro		
PMA	Uptake			(Zhou and Sutherland, 2004) rat cort astro		
PMA	Uptake			(Kalandadze et al., 2002) rat nrn astro		
PMA	Uptake				(Trotti et al., 2001) Xenopus ooc	
PMA	Uptake				(Padovano et al., 2009) MDCK	
PMA	Uptake	(Yang et al., 2004) ms cort nrn				
PMA	Uptake		(Guillet et al., 2005) rat cort nrn	(Guillet et al., 2005) rat cort nrn	(Guillet et al., 2005) rat cort nrn	
PMA	Uptake			(Bassan et al., 2008) rat cort nrn		
PMA	Uptake			(Tan et al., 1999) LM-GLT1-8		
PMA	Uptake			(Tan et al., 1999) MCB-GLT1-6		
PMA	Uptake					(Fang et al., 2006) Xenopus ooc
PMA	Uptake	(Karatas-Wulf et al., 2009) ms cereb gra				
PMA	Uptake		(Susarla et al., 2004) rat cort astro			
PMA	Uptake			(Casado et al., 1993) C6 glioma		
PMA	Uptake				(Dowd and Robinson, 1996) C6 glioma	
PMA	Uptake				(Gonzalez et al., 2002) C6 glioma	
PMA	Uptake				(Sims et al., 2000) C6 glioma	
PMA	Uptake				(Davis et al., 1998) C6 glioma	
PMA	Uptake					(Park et al., 2008) Xenopus ooc
TPA	Uptake		(Gonzalez et al., 1999) ck cereb astro			
TPA	Uptake		(Bernabe et al., 2003) ms cereb astro			
TPA	Uptake		(Bernabe et al., 2003) ms cort astro			
PMA	Expression		(Susarla et al., 2004) rat cort astro			

(Continued)

TABLE 1 | Continued

Agent	Assay	N/A	EAAT1	EAAT2	EAAT3	EAAT4
PMA	Expression		(Guillet et al., 2005) rat cort nrn	(Guillet et al., 2005) rat cort nrn	(Guillet et al., 2005) rat cort nrn	
PMA	Expression			(Garcia-Tardon et al., 2012) Xenopus ooc		
PMA	Expression			(Susarla and Robinson, 2008) C6 glioma		
PMA	Expression			(Gonzalez-Gonzalez et al., 2008b) COS7		
PMA	Expression			(Gonzalez-Gonzalez et al., 2008b) MDCK		
PMA	Expression			(Zhou and Sutherland, 2004) rat cort astro		
PMA	Expression			(Karatas-Wulf et al., 2009) ms cereb gran (EAAT2a)		
PMA	Expression				(Padovano et al., 2009) MDCK	
PMA	Expression		(Bull and Barnett, 2002) rat ret			
PMA	Expression			(Bassan et al., 2008) rat cort nrn		
PMA	Expression			(Karatas-Wulf et al., 2009) ms cereb gran (EAAT2b)	(Karatas-Wulf et al., 2009) ms cereb gran	
PMA	Expression				(Fournier et al., 2004) C6 glioma	
PMA	Expression				(Gonzalez et al., 2002) C6 glioma	
PMA	Expression				(Davis et al., 1998) C6 glioma	
PMA	Expression				(Fournier et al., 2004) rat cort nrn	
PMA	Expression				(Gonzalez et al., 2002) rat cort nrn	
TPA	Expression		(Espinoza-Rojo et al., 2000) ck cereb astro			
TPA	Expression		(Conradt and Stoffel, 1997) Xenopus ooc			
TPA	Expression		(Conradt and Stoffel, 1997) HEK293			
TPA	Expression		(Espinoza-Rojo et al., 2000) ck cereb astro			
PKC inhibitors						
BIM-1	Uptake		(Susarla and Robinson, 2003) ms cort astro			
BIM-2	Uptake	(Yang et al., 2004) ms cort nrn				
BIM-2	Uptake		(Gonzalez et al., 2002) C6 glioma			
BIM-2	Uptake		(Susarla and Robinson, 2003) ms cort astro			
BIM-2	Uptake		(Wang Z. et al., 2003) rat ret astro			

(Continued)

TABLE 1 | Continued

Agent	Assay	N/A	EAAT1	EAAT2	EAAT3	EAAT4
Chelerythrine	Uptake		(Adolph et al., 2007) rat cort astro (Bull and Barnett, 2002) rat retina			
Chelerythrine	Uptake					(Yoo et al., 2008) Xenopus ooc
Chelerythrine	Uptake					(Park et al., 2008) Xenopus ooc
Gö6976	Uptake		(Susarla and Robinson, 2003) ms cort astro (Gonzalez et al., 2002) C6 glioma			
Rottlerin	Uptake		(Susarla and Robinson, 2003) ms cort astro (Bull and Barnett, 2002) rat retina			
Staurosporine	Uptake					(Yoo et al., 2008) Xenopus ooc
Staurosporine	Uptake		(Guillet et al., 2005) rat cort nrn (Susarla and Robinson, 2003) ms cort astro	(Guillet et al., 2005) rat cort nrn	(Guillet et al., 2005) rat cort nrn	
Staurosporine	Uptake					(Park et al., 2008) Xenopus ooc
Chelerythrine	Expression		(Bull and Barnett, 2002) rat ret (Bull and Barnett, 2002) rat ret			
Gö6976	Expression				(Gonzalez et al., 2002) C6 glioma (Gonzalez et al., 2002) rat cort nrn	
Rottlerin	Expression		(Susarla and Robinson, 2003) ms cort astro (Wang Z. et al., 2003) rat ret astro (Bull and Barnett, 2002) rat ret			
Staurosporine	Expression			(Karatas-Wulf et al., 2009) ms cereb gran (EAAT2b) (Karatas-Wulf et al., 2009) ms cereb gran (EAAT2a)	(Karatas-Wulf et al., 2009) ms cereb gran	
PI3K inhibitors						
Wortmannin	Uptake		(Guillet et al., 2005) rat cort nrn	(Guillet et al., 2005) rat cort nrn	(Guillet et al., 2005) rat cort nrn (Davis et al., 1998) C6 glioma	
Wortmannin	Uptake					(Yoo et al., 2008) Xenopus ooc
Wortmannin	Uptake					(Park et al., 2008) Xenopus ooc
Wortmannin	Expression		(Guillet et al., 2005) rat cort nrn	(Guillet et al., 2005) rat cort nrn	(Guillet et al., 2005) rat cort nrn (Davis et al., 1998) C6 glioma	
LY294002	Expression			(Wu et al., 2010) rat cort astro		

(Continued)

TABLE 1 | Continued

Agent	Assay	N/A	EAAT1	EAAT2	EAAT3	EAAT4
N-glycosylation						
N-glycosilation	Expression		(Conradt et al., 1995) Xenopus ooc		(Ferrer-Martinez et al., 1995) NBL-1	
Arachidonic acid						
AA	Uptake	(Volterra et al., 1992) rat synapt				
AA	Uptake	(Volterra et al., 1992) rat cort astro				
AA	Uptake		(Zerangue et al., 1995) Xenopus ooc	(Zerangue et al., 1995) Xenopus ooc	(Zerangue et al., 1995) Xenopus ooc	
Calcium channels						
Cd^{2+}	Uptake				(Yang et al., 2004) ms cort nrn	
w-CTX	Uptake				(Yang et al., 2004) ms cort nrn	
Nifedipine	Uptake				(Yang et al., 2004) ms cort nrn	
Cd^{2+}	Expression				(Yang et al., 2004) ms cort nrn	
w-CTX	Expression				(Yang et al., 2004) ms cort nrn	
Nifedipine	Expression				(Yang et al., 2004) ms cort nrn	
Calcium stores						
SKF96365	Uptake				(Yang et al., 2004) ms cort nrn	
Caffeine	Expression				(Yang et al., 2004) ms cort nrn	
Thapsigargin	Expression				(Yang et al., 2004) ms cort nrn	
SKF96365	Expression				(Yang et al., 2004) ms cort nrn	
Histamine						
Histamine	Uptake			(Fang et al., 2014) rat hipp slice		
Histamine	Expression			(Fang et al., 2014) rat hipp slice		
Growth factors						
EGF	Uptake				(Sims et al., 2000) C6 glioma	
IGF-1	Uptake		(Gamboa and Ortega, 2002) chick cereb astro			
NGF	Uptake				(Sims et al., 2000) C6 glioma	
PDGF	Uptake				(Sims et al., 2000) C6 glioma	
BDNF	Expression		(Figiel et al., 2003) rat cort astro	(Figiel et al., 2003) rat cort astro		
EGF	Expression		(Figiel et al., 2003) rat cort astro	(Figiel et al., 2003) rat cort astro		
FGF-2	Expression		(Figiel et al., 2003) rat cort astro	(Figiel et al., 2003) rat cort astro		
GDNF	Expression		(Figiel et al., 2003) rat cort astro	(Figiel et al., 2003) rat cort astro		
IGF-1	Expression		(Gamboa and Ortega, 2002) ck cereb glia			
PACAP	Expression		(Figiel et al., 2003) rat cort astro	(Figiel et al., 2003) rat cort astro		

(Continued)

TABLE 1 | Continued

Agent	Assay	N/A	EAAT1	EAAT2	EAAT3	EAAT4
PDGF	Expression		(Figiel et al., 2003) rat cort astro	(Figiel et al., 2003) rat cort astro		
PDGF	Expression				(Fournier et al., 2004) C6 glioma	
PDGF	Expression				(Sims et al., 2000) C6 glioma	
TGFa	Expression		(Figiel et al., 2003) rat cort astro	(Figiel et al., 2003) rat cort astro		
Polyunsaturated fatty acids						
DHA	Uptake		(Berry et al., 2005) HEK293	(Berry et al., 2005) HEK293	(Berry et al., 2005) HEK293	
Reactive oxygen species						
ROS	Uptake	(Volterra et al., 1994a) rat cort astro				
Other						
A23187	Uptake			(Tan et al., 1999) LM		
A23187	Uptake			(Tan et al., 1999) MCB		
Allopregnanolone	Uptake				(Perego et al., 2012) rat Schwann	
Bradykinin	Uptake				(Lim et al., 2008) hum ARPE	(Lim et al., 2008) hum ARPE
Carbamazepine	Uptake				(Lee et al., 2005) C6 glioma	
Carbamazepine	Uptake					(Lee et al., 2005) COS7
Corticosterone	Uptake				(Kang et al., 2010) Xenopus ooc	
Desflurane	Uptake				(Park et al., 2015) Xenopus ooc	
DHEA	Uptake			(Chen et al., 2017) rat hipp astro		
Endothelin-1	Uptake		(Leonova et al., 2001) rat cort astro			
Ethanol	Uptake					(Yoo et al., 2008) Xenopus ooc
Ethanol	Uptake					(Park et al., 2008) Xenopus ooc
HCMV	Uptake	(Zhang et al., 2014) hum astro	(Zhang et al., 2014) hum astro	(Zhang et al., 2014) hum astro		
Histamine	Uptake			(Fang et al., 2014) rat cort astro		
IL-1b	Uptake		(Yan et al., 2014) rat spinal cord	(Yan et al., 2014) rat spinal cord		
Insulin	Uptake				(Sims et al., 2000) C6 glioma	
Nedd4-2	Uptake					(Bohmer et al., 2004) Xenopus ooc
NO	Uptake	(Pogun et al., 1994; Pogun and Kuhar, 1994) rat synapt				
NO	Uptake	(Piani et al., 1993) ms cort astro				
Okadaic acid	Uptake			(Tan et al., 1999) LM		

(Continued)

TABLE 1 | Continued

Agent	Assay	N/A	EAAT1	EAAT2	EAAT3	EAAT4
Okadaic acid	Uptake			(Tan et al., 1999) MCB		
PICK1	Uptake			(Sogaard et al., 2013) Xenopus ooc		
PS1−/− ms	Uptake	(Yang et al., 2004) ms cort nrn		(Yang et al., 2004) ms cort nrn		
Rheb1−/− ms	Uptake					(Jiang et al., 2016) ms cereb
Riluzole	Uptake				(Dall'Igna et al., 2013) C6 glioma	
SGK1	Uptake					(Bohmer et al., 2004) Xenopus ooc
SGK2	Uptake					(Bohmer et al., 2004) Xenopus ooc
SGK3	Uptake					(Bohmer et al., 2004) Xenopus ooc
Allopregnanolone	Expression				(Perego et al., 2012) rat Schwann	
Bradykinin	Expression				(Lim et al., 2008) hum ARPE	(Lim et al., 2008) hum ARPE
DHEA	Expression			(Chen et al., 2017) rat hipp astro		
GW7647	Expression			(Huang et al., 2017) rat cort astro		
Histamine	Expression			(Fang et al., 2014) rat cort astro		
Insulin	Expression			(Ji et al., 2011) rat cort astro		
Morphine	Expression		(Tai et al., 2007) rat spin cord	(Tai et al., 2007) rat spin cord	(Tai et al., 2007) rat spin cord	
Nedd4-2	Expression			(Garcia-Tardon et al., 2012) Xenopus ooc		
Nedd4-2	Expression					(Bohmer et al., 2004) Xenopus ooc
Palmitic acid	Expression			(Huang et al., 2017) rat cort astro		
PRE084	Expression			(Chen et al., 2017) rat hippo astro		
PS1-/- ms	Expression				(Yang et al., 2004) ms cort nrn	
Rapamycin	Expression			(Ji et al., 2013) rat cort astro		
Rapamycin	Expression			(Wu et al., 2010) rat cort astro		
Rheb1-/- ms	Expression					(Jiang et al., 2016) ms cereb
Riluzole	Expression				(Dall'Igna et al., 2013) C6 glioma	
SGK1	Expression					(Bohmer et al., 2004) Xenopus ooc
SmoA1	Expression			(Wang et al., 2017) rat cort astro		
Sonic hedgehog	Expression			(Wang et al., 2017) rat cort astro		
WY14,643	Expression			(Huang et al., 2017) rat cort astro		

The table provides a summary of the results obtained in the literature regarding the mechanisms controlling the rate of glutamate uptake and the expression of glutamate transporters in a variety of animal models and expression systems. The cells in the first column of the table are color-coded to highlight studies focusing on glutamate uptake (light blue) or glutamate transporter expression (dark blue). The third column, labeled N/A, refers to studies that did not distinguish among different glutamate transporter subtypes. The cells in the last four columns are color-coded to highlight increases (green), decreases (orange), or no change (gray) in glutamate transporter uptake or expression. Abbreviations: mouse (ms), human (hum), cortex (cort), cerebellum (cereb), hippocampus (hipp), spinal cord (spin cord), astrocyte (astro), neuron (nrn), granule cell (gran), Schwann cells (Schwann), oocyte (ooc), retina (ret), retinoblastoma (retblast), synaptosome (synapt), arachidonic acid (AA), Bisindolylmaleimide (BIM), ω-conotoxin (ω-CTX), dehydroepiandrosterone (DHEA), phorbol 12-myristate 13-acetate (PMA), and 12-0-tetradecanoylphorbol-13-acetate (TPA).

modifications, and there are multiple CpG regions in the promoter for EAAT2 where methylation can occur (Zschocke et al., 2005). One of the consequences of methylation is that it alters the ability of glucocorticoids to change EAAT2 expression. Accordingly, in the cerebellum, where the EAAT2 promoter is hyper-methylated, glucocorticoids are unable to change EAAT2 expression (Zschocke et al., 2005). By contrast, in the forebrain, where the EAAT2 promoter is hypo-methylated, glucocorticoid up-regulate EAAT2 expression (Zschocke et al., 2005).

Phosphorylation and glycosylation are two documented forms of post-translational modifications for glutamate transporters (Gegelashvili and Schousboe, 1997). Accordingly, increasing protein kinase C (PKC) activation by phorbol esters leads to increased phosphorylation of EAAT2 at the residue Ser113 and increased glutamate uptake (Roginski et al., 1993). *N*-glycosylation promotes EAAT3 expression, but has no effect on EAAT1 (Conradt et al., 1995; Ferrer-Martinez et al., 1995).

Arachidonic acid, produced via activation of NMDA receptors in neurons and metabotropic glutamate receptors in astrocytes, can directly interact with different types of glutamate transporters, with different effects. For example, it reduces glutamate uptake via EAAT1, enhances glutamate uptake via EAAT2 and leads to a moderate increase of glutamate uptake via EAAT3 (Chan et al., 1983; Volterra et al., 1992; Trotti et al., 1995). Arachidonic acid can lead to the activation of PKC, promoting glutamate uptake via EAAT2. Metabolites of arachidonic acid can be a source of reactive oxygen species (ROS), which inhibit glutamate uptake but increase the transporters' steady state affinity for glutamate (Volterra et al., 1994b).

There is a growing awareness that these forms of regulation are complex not only because they likely differ among species, cell types and brain regions, but also because they interact with one another in ways that can be difficult to reproduce in reduced preparations but that affect the function of these transporters *in vivo*. These currently unknowns are likely going to be addressed by using experimental approaches that allow manipulation of different regulation factor *in situ*, and in a cell-specific manner.

Activity-Dependent Modulation of Glutamate Transporter Trafficking

The first observation that glutamate itself can modulate its uptake came from data showing that glutamate uptake is increased in astrocyte cultures supplemented with conditioned media from neuronal cultures (Drejer et al., 1983; Voisin et al., 1993). Pure astrocytic cultures only express EAAT1, but co-culture of neurons and astrocytes increases EAAT1 expression and induces EAAT2 expression (Gegelashvili and Schousboe, 1997; Swanson et al., 1997). This effect depends on p42/44 MAP kinases activation via the tyrphostin-sensitive Receptor Tyrosine Kinase (RTK) signaling pathway, and is abolished by inhibitors of PI3K, tyrosine kinase and NF-kB (Swanson et al., 1997; Zelenaia et al., 2000). Similarly, decreased glutamate uptake via EAAT1-2 (not EAAT3) occurs in response to axotomy of glutamatergic neurons of cortical lesions (McGeer et al., 1977; Shifman, 1991; Ginsberg et al., 1995; Levy et al., 1995). Together, these forms of activity-dependent regulation of EAAT2 expression allow this transporter to be more abundant and less mobile in astrocytic processes close to active glutamatergic synapses, an effect that can provide an effective strategy to limit glutamate spillover away from the synaptic cleft.

Similarly, to glutamate, glutamate transporter substrates like D-Aspartate and ligands like L-*trans*-PDC and TBOA can also produce a redistribution of EAAT1 on the cell membrane (Shin et al., 2009). Consistent with these findings, treating astrocyte cultures with kainate, dbcAMP or AMPA receptor agonists increases D-aspartate uptake and EAAT1 protein expression (Gegelashvili et al., 1996). It is unclear whether these effects are due to binding to AMPA receptors or are due to release of diffusible molecules (e.g., arachidonic acid, diacylglycerol, nitric oxide) through more complex intracellular signaling cascades (Gegelashvili and Schousboe, 1997).

Physiological Roles of Glutamate Transporters

The role of glutamate transporters in regulation of phasic and tonic extracellular glutamate levels is critical for neuronal signaling and controlling excitotoxicity (Rothstein et al., 1996). Spillover of glutamate and inter-synaptic cross-talk have been associated with multiple neuropsychiatric disorders, including schizophrenia, epilepsy, addiction, depression and obsessive compulsive disorder (O'Donovan et al., 2017; Bellini et al., 2018; Malik and Willnow, 2019). Knock-out mouse models of different subtypes of glutamate transporters have revealed major motor deficits with decreased levels of glial transporters EAAT1-2 (Rothstein et al., 1996), with more subtle behavioral deficits with loss of the neuronal transporter EAAT3 (Peghini et al., 1997; Bellini et al., 2018).

In humans, decreased expression and reduced function of EAAT2 are associated with amyotrophic lateral sclerosis (ALS) (Rothstein et al., 1995; Bruijn et al., 1997; Rosenblum and Trotti, 2017). In transgenic mice expressing an N-terminal fragment of mutant huntingtin (R6/2), there is an age-dependent downregulation of EAAT2, which leads to a progressive increase in the extracellular glutamate (Behrens et al., 2002). Other glutamate transporters, however, remain unchanged, suggesting that EAAT2-mediated excitotoxicity might contribute to Huntington's disease (Behrens et al., 2002). In the few identified polymorphisms of the gene encoding EAAT3, dicarboxylic aminoaciduria, a deficit in kidney function was prominent, as well as family linkage to schizophrenia and obsessive–compulsive disorders (OCD) (Bailey et al., 2011; Porton et al., 2013). In mice, loss or increased EAAT3 are associated with increased anxiety and OCD-like behaviors, suggesting that preserving an optimal expression of this transporter is key for the function of neuronal circuits affected by this disease (Zike et al., 2017; Bellini et al., 2018; Delgado-Acevedo et al., 2019). Significant lower levels of EAAT2 have also been reported *in vitro* (Scimemi et al., 2013) and *in vivo*, in animal models of Alzheimer's disease (Wilson et al., 2003; Dabir et al., 2006; Mookherjee et al., 2011; Schallier et al., 2011;

Hefendehl et al., 2016), as well as in humans affected by this disease (Li et al., 1997; Jacob et al., 2007; Scott et al., 2011; Leng et al., 2021), whereas promoting EAAT2 expression improves cognitive function (Fan et al., 2018). Several mutations in the gene that encodes EAAT1 have also been linked to the neurological disease Episodic Ataxia Type 6 (Choi et al., 2017; Chivukula et al., 2020). The most well-studied mutation (P290R) results in reduced glutamate transport activity and a large increase in the uncoupled anion conductance, the latter property being suggested to be responsible for the phenotype in studies using a *Drosophila melanogaster* model (Winter et al., 2012; Parinejad et al., 2016). Further understanding of how these transporters are regulated in specific circuits and synapses may allow for design of therapeutics that correct for specific deficits in transporter function.

GABA TRANSPORTERS

In mammals, GABA transporters are classified into four subtypes, based on amino acid sequence homology and pharmacological properties. These include GAT1-3 and the betaine GABA transporter BGT1. Out of these, GAT1 and GAT3 account for the largest proportion of GABA uptake in the CNS, and for this reason, they will be the focus of our attention in this review. Structural information of the GABA transporters comes from prokaryote homologs such as LeuT$_{Aa}$ (**Figure 2**; Yamashita et al., 2005). In the neocortex, GAT1 is expressed robustly in GABAergic axon terminals, astrocytic processes, oligodendrocytes and microglial cells (Fattorini et al., 2020). The expression of GAT1 is pronounced in the axon terminal of chandelier GABAergic neurons (known as "cartridges"), which provide inhibitory inputs to the axon initial segment of pyramidal cells (Woo et al., 1998). In young mice (P9), GAT1 is also transiently expressed somatically, but this somatic expression is lost in juvenile mice (P29) (Yan et al., 1997; Yan and Ribak, 1998). Presynaptic boutons in the cerebellum and hippocampus express 800–1,300 μm^{-2} GAT1 molecules, with a preferential perisynaptic localization (Chiu et al., 2002; Melone et al., 2015). These density values drop to 640 μm^{-2} GAT1 molecules along the length of the axon (Chiu et al., 2002), whereas the surface density of GAT1 in astrocytic membranes is 3.5 times higher than in axon terminals (Melone et al., 2015). GAT3 is mainly localized in peri-synaptic astrocytic processes, but has also been detected in brainstem and cortical neurons (Clark et al., 1992; Melone et al., 2003, 2005, 2015). These findings are important

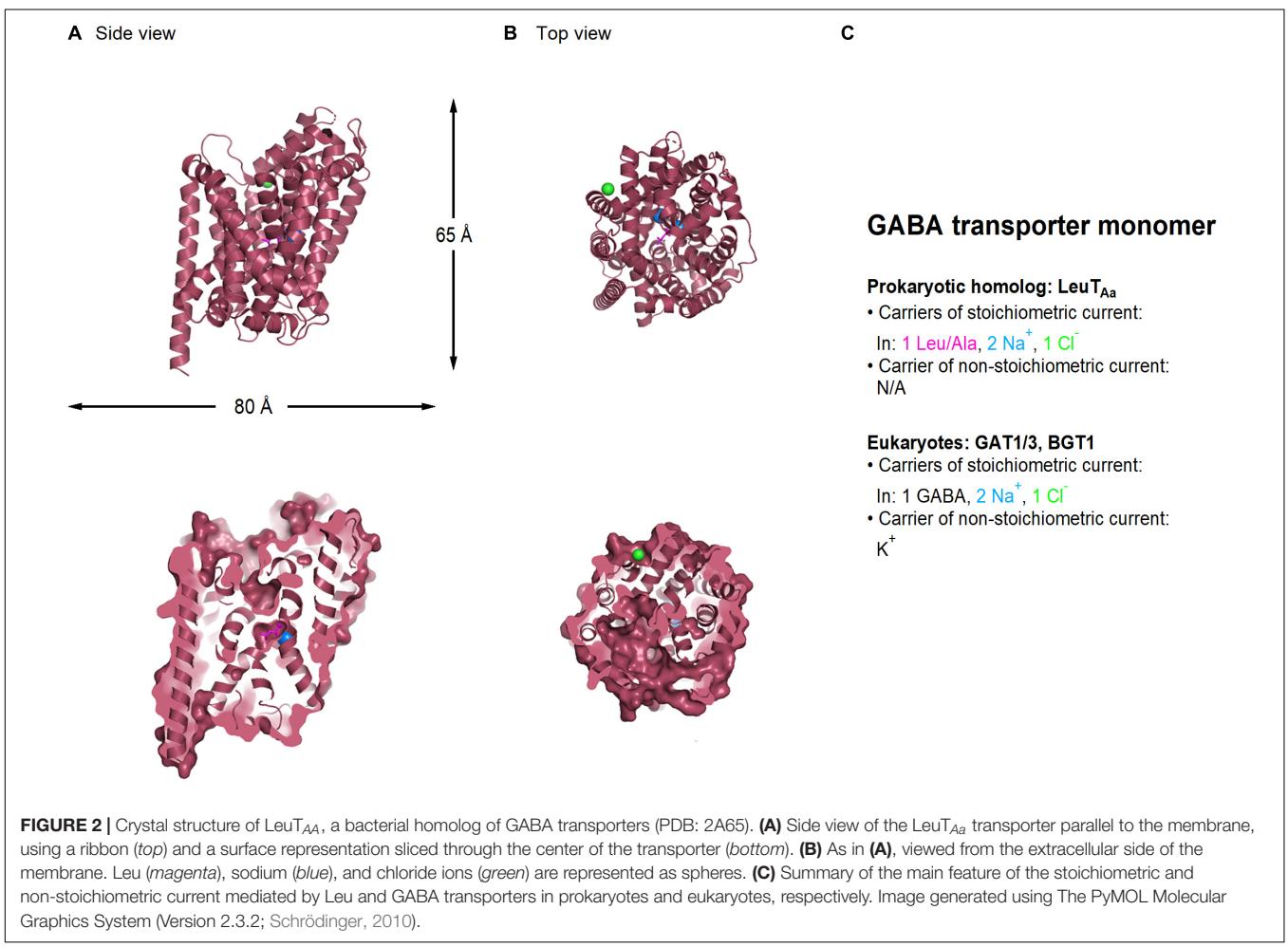

FIGURE 2 | Crystal structure of LeuT$_{AA}$, a bacterial homolog of GABA transporters (PDB: 2A65). **(A)** Side view of the LeuT$_{Aa}$ transporter parallel to the membrane, using a ribbon (*top*) and a surface representation sliced through the center of the transporter (*bottom*). **(B)** As in **(A)**, viewed from the extracellular side of the membrane. Leu (*magenta*), sodium (*blue*), and chloride ions (*green*) are represented as spheres. **(C)** Summary of the main feature of the stoichiometric and non-stoichiometric current mediated by Leu and GABA transporters in prokaryotes and eukaryotes, respectively. Image generated using The PyMOL Molecular Graphics System (Version 2.3.2; Schrödinger, 2010).

because they provide anatomical evidence to the fact that no GABA transporter can be described as being purely neuronal or glial, although they may have a preferential distribution in a given cell type depending on the age and brain region of different animal models.

Both GAT1 and GAT3 transporters translocate the zwitterion GABA across the membrane by coupling its movement to the co-transport of two Na^+ and one Cl^- ion, leading to the net influx of one positive charge per transport cycle (1 GABA: 2 Na^+: 1 Cl^-) (Radian and Kanner, 1983; Keynan and Kanner, 1988). In addition to this stoichiometric current, GABA transporters mediate an agonist-independent leak current carried by alkali ions, which can be detected in mammalian expression systems but not in *Xenopus laevis* oocytes (Cammack and Schwartz, 1996; Eckstein-Ludwig et al., 1999; Lu and Hilgemann, 1999; MacAulay et al., 2002; Matthews et al., 2009). This current can generate a local change in membrane voltage and/or membrane resistance, which can be more or less pronounced depending on the magnitude and direction of the driving force for the permeant ions and the local density of the transporters. Changes in membrane resistance are important because they act as a local shunt capable of hampering action potential propagation and cell excitability.

As in the case of glutamate transporters, we provide a summary of current studies on modulation of GABA transporters listed in PubMed (**Table 2**).

The Surface Mobility and Cellular Distribution of GAT1

The GABA transporter GAT1 has a membrane pool of 61–63% (Chiu et al., 2002). Fluorescence Recovery After Photobleaching (FRAP) experiments in neuroblastoma 2a cells show that 50% of membrane GAT1 is immobile, likely due to the existence of tight interactions between GAT1 and the actin cytoskeleton, mediated by the adaptor protein ezrin (Imoukhuede et al., 2009). Accordingly, depolymerizing actin or interrupting the GAT1 PDZ-interacting domain increases the transporter mobility, whereas depolymerizing microtubules does not (Imoukhuede et al., 2009). Numerous mechanisms contribute to cycle this pool of transporter to and from the plasma membrane. Specifically, there are two regions in the C-terminal domain of GAT1 that are responsible for supporting GAT1 export from the endoplasmic reticulum and for putting GAT1 under the control of the exocyst (Farhan et al., 2004; Moss et al., 2009). In addition to these, the MAGUK protein Pals1 is co-expressed with GAT1 in COS7 cells and contributes to stabilize GAT1 on the cell membrane (McHugh et al., 2004).

Regulation of GABA Uptake

The control of GABA uptake can be expressed through changes in the rate with which GABA transporters are trafficked and redistributed in the plasma membrane, with consequences on the number of transporter molecules available for binding extracellular GABA, or by modulating the biophysical properties of GABA transporters (e.g., V_{max}, k_m, etc.). Neurons regulate the surface expression of GAT1 in parallel with that of extracellular neurotransmitter levels. GABA transporters interact with the SNARE proteins syntaxin 1A and Munc-18 through molecular interactions modulated by PKC (Beckman et al., 1998; Deken et al., 2000; Geerlings et al., 2001; Horton and Quick, 2001). These transporters are associated with presynaptic vesicles similar to synaptic vesicles, capable of undergoing clathrin-mediated internalization and endosomal sorting (Barbaresi et al., 2001). Despite being morphologically similar to synaptic vesicles, and despite the fact that they can be released at similar rates in a calcium dependent manner, they lack synaptophysin and vesicular GABA transporters (Deken et al., 2003). It has been suggested that these GABA transporter-containing vesicles might represent a population of endocytic or exocytic vesicles acting as cargos for the assembly of synaptic domains distinct from the active zone (Deken et al., 2003).

PKC modulation is important to change the number of functional GABA transporters expressed on the plasma membrane (Corey et al., 1994; Quick et al., 1997). In *Xenopus laevis* oocytes, PKC activation with PMA promotes GAT1 translocation to the cell membrane at low basal GAT1 expression levels, but this effect is not detected at high levels of expression of GAT1. The rate of GABA uptake can also be altered by PKC (Corey et al., 1994; Quick et al., 1997). Accordingly, inhibiting PKC reduces GABA uptake through a reduction of V_{max} (not k_m), whereas inhibiting protein phosphatase 2B increases it. These forms of PKC-dependent modulation differ in cultured neurons and isolated nerve terminals, where surface expression of GAT1 is decreased by PKC dependent phosphorylation (Beckman et al., 1999; Wang and Quick, 2005; Cristovao-Ferreira et al., 2009).

Another protein kinase, PKA, stimulates GABA transport via GAT1 and activates a GAT1-mediated cationic current during opioid withdrawal (Bagley et al., 2005). This enhanced PKA signaling contributes to increase neuronal action potential firing rates in opioid-sensitive PAG neurons during opioid withdrawal (Bagley et al., 2005).

In the area CA1 of the rat hippocampus, chronic stimulation of cannabinoid receptors CB1/2 reduces GAT1 gene expression (Higuera-Matas et al., 2012). Conversely, an endogenous agonist of endocannabinoid receptors, 2-arachidonoylglycerol (2-AG), increases GABA uptake (Romero et al., 1998; Venderova et al., 2005). CB1 receptors have been suggested to interact or co-localize with β_2 adrenergic receptors (Hudson et al., 2010), the activation of which also increases GAT1 expression and GABA uptake (Martins et al., 2018). The ability of β_2 adrenergic receptors to promote GABA uptake (and that of β_1 adrenergic receptors to inhibit it) are mediated by a PKA pathway controlled by cannabinoid receptors, because the modulation of GABA update by adrenergic receptors is inhibited by the cannabinoid receptor agonist WIN55,212-2 (Martins et al., 2018).

In astrocytes, GABA uptake via GAT1, not GAT3, is modulated by neurotrophic factors like BDNF (Vaz et al., 2011). This is due to the ability of BDNF to inhibit dynamin/clathrin-dependent constitutive internalization of GAT1, effectively increasing the lifetime of GAT1 on the cell membrane. The effect of BDNF is mediated by activation of a truncated form of the

TABLE 2 | Regulating factors of GABA transporter Uptake and expression.

Agent	Assay	N/A	GAT1	GAT2	GAT3
GABA					
GABA	Uptake		(Bernstein and Quick, 1999) rat hipp nrn		
GABA	Uptake	(Bahena-Trujillo and Arias-Montano, 1999) rat SNr synapt			
GABA	Expression		(Bernstein and Quick, 1999) rat hipp nrn		
GABA (brief)	Expression		(Hu and Quick, 2008) rat cort nrn		
GABA (long)	Expression		(Hu and Quick, 2008) rat cort nrn		
GABA transporter inhibitors					
Nipecotic acid	Uptake	(Voutsinos et al., 1998) rat cereb punch			
Nipecotic acid	Uptake		(Bernstein and Quick, 1999) rat hipp nrn		
Nipecotic acid	Uptake	(Bahena-Trujillo and Arias-Montano, 1999) rat SNr synapt			
NO-711	Uptake		(Fan et al., 2006) rat hipp nrn		
SKF89976A	Uptake		(Bernstein and Quick, 1999) rat hipp nrn		
SKF89976A	Uptake	(Bahena-Trujillo and Arias-Montano, 1999) rat SNr synapt			
SKF89976A	Uptake	(Law et al., 2000) rat hipp nrn			
SKF89976A	Uptake	(Deken et al., 2000) rat hipp nrn			
SKF89976A	Uptake		(Wang D. et al., 2003) rat hipp nrn		
SKF89976A	Uptake		(Hu and Quick, 2008) rat cort nrn		
Nipecotic acid	Expression		(Hu and Quick, 2008) rat cort nrn		
SKF89976A	Expression		(Bernstein and Quick, 1999) rat hipp nrn		
cAMP and analogs					
8-Br-cAMP	Uptake	(Tian et al., 1994) rat striatum synapt			
8-Br-cAMP	Uptake	(Bahena-Trujillo and Arias-Montano, 1999) rat SNr synapt			
PKA activators					
Forskolin	Uptake	(Tian et al., 1994) rat striatum synapt			
Forskolin	Uptake	(Bahena-Trujillo and Arias-Montano, 1999) rat SNr synapt			
Forskolin	Uptake		(Corey et al., 1994) rat hipp synapt		
Forskolin	Uptake		(Cristovao-Ferreira et al., 2013) rat cort astro		(Cristovao-Ferreira et al., 2013) rat cort astro

(Continued)

TABLE 2 | Continued

Agent	Assay	N/A	GAT1	GAT2	GAT3
PKA inhibitors					
H89	Uptake		(Corey et al., 1994) rat hipp synapt		
PKC activator					
K252A	Uptake	(Law et al., 2000) rat hipp nrn			
Indolactam V	Uptake		(Corey et al., 1994) Xenopus ooc		
OAG	Uptake		(Corey et al., 1994) Xenopus ooc		
PMA	Uptake		(Corey et al., 1994) Xenopus ooc		
PMA	Uptake		(Quick et al., 1997) Xenopus ooc		
PMA	Uptake	(Law et al., 2000) rat hipp nrn			
PMA	Uptake	(Schitine et al., 2015) chick Müller glia			
SC-10	Uptake		(Corey et al., 1994) Xenopus ooc		
TPA	Uptake	(Bahena-Trujillo and Arias-Montano, 1999) rat SNr synapt			
TPA	Expression		(Schitine et al., 2015) chick Müller glia		(Schitine et al., 2015) chick Müller glia
PKC inhibitor					
BIM-1	Uptake		(Corey et al., 1994) Xenopus ooc		
BIM-1	Uptake		(Quick et al., 1997) Xenopus ooc		
BIM-1	Uptake		(Corey et al., 1994) rat hipp synapt		
BIM-1	Expression		(Corey et al., 1994) Xenopus ooc		
PTK inhibitor					
Genistein	Uptake	(Law et al., 2000) rat hipp nrn			
Genistein	Expression		(Law et al., 2000) rat hipp nrn		
Protein phosphatase inhibitor					
Calyculin A	Uptake	(Goncalves et al., 1999) sheep cort synapt			
Cyclosporin A	Uptake	(Goncalves et al., 1999) sheep cort synapt			
Cyclosporine A	Uptake		(Corey et al., 1994) Xenopus ooc		
Okadaic acid	Uptake		(Corey et al., 1994) Xenopus ooc		
Okadaic acid	Uptake	(Tian et al., 1994) rat striatum synapt			
Okadaic acid	Uptake	(Goncalves et al., 1999) sheep cort synapt			
Pervanadate	Uptake	(Law et al., 2000) rat hipp nrn			
Growth factors					
BDNF	Uptake	(Law et al., 2000) rat hipp nrn			

(Continued)

TABLE 2 | Continued

Agent	Assay	N/A	GAT1	GAT2	GAT3
Adenosine and adenosine receptors					
Adenosine deaminase	Uptake		(Corey et al., 1994) rat hipp synapt		
Adenosine deaminase	Uptake		(Cristovao-Ferreira et al., 2013) rat cort astro		(Cristovao-Ferreira et al., 2013) rat cort astro
CGS21680	Uptake		(Corey et al., 1994) rat hipp synapt		
CGS21680	Uptake		(Cristovao-Ferreira et al., 2013) rat cort astro		(Cristovao-Ferreira et al., 2013) rat cort astro
DPCPX	Uptake		(Corey et al., 1994) rat hipp synapt		
DPCPX	Uptake		(Cristovao-Ferreira et al., 2013) rat cort astro		(Cristovao-Ferreira et al., 2013) rat cort astro
SCH58261	Uptake		(Corey et al., 1994) rat hipp synapt		
SCH58261	Uptake		(Cristovao-Ferreira et al., 2013) rat cort astro		(Cristovao-Ferreira et al., 2013) rat cort astro
CGS21680	Expression		(Corey et al., 1994) rat hipp synapt		
SNARE complex					
Botulinum toxins	Uptake		(Quick et al., 1997) Xenopus ooc		
Botulinum toxin B	Uptake	(Deken et al., 2000) rat hipp nrn			
Botulinum toxin B	Uptake		(Wang D. et al., 2003) rat hipp nrn		
Botulinum toxin C	Uptake	(Deken et al., 2000) rat hipp nrn			
Botulinum toxin C	Uptake		(Wang D. et al., 2003) rat hipp nrn		
Botulinum toxin C	Uptake		(Wang D. et al., 2003) Xenopus ooc		
SNAP25	Uptake		(Fan et al., 2006) PC12		
SNAP25 siRNA	Uptake		(Fan et al., 2006) rat hipp rnr		
SNAP25 siRNA	Uptake		(Fan et al., 2006) PC12		
Syntaxin 1A	Uptake		(Beckman et al., 1998) rat hipp nrn		
Syntaxin 1A	Uptake		(Deken et al., 2000) 1F9		
Syntaxin 1A	Uptake		(Wang D. et al., 2003) rat hipp nrn		
Syntaxin 1A	Uptake		(Fan et al., 2006) PC12		
Syntaxin 1A	Uptake		(Fan et al., 2006) HEK293	(Fan et al., 2006) HEK293	(Fan et al., 2006) HEK293
Syntaxin 1A siRNA	Uptake		(Fan et al., 2006) rat hipp rnr		
Syntaxin 1A siRNA	Uptake		(Fan et al., 2006) PC12		
VAMP2 siRNA	Uptake		(Fan et al., 2006) rat hipp rnr		
Botulinum toxins	Expression		(Quick et al., 1997) Xenopus ooc		

(Continued)

TABLE 2 | Continued

Agent	Assay	N/A	GAT1	GAT2	GAT3
Botulinum toxin C	Expression		(Deken et al., 2000) rat hipp nrn		
Syntaxin 1A	Expression		(Deken et al., 2000) rat hipp nrn		
Syntaxin 1A	Expression		(Fan et al., 2006) PC12		
GABA receptors					
Bicuculline	Expression		(Hu and Quick, 2008) rat cort nrn		
Glutamate and glutamate receptors					
Glutamate	Uptake	(Schitine et al., 2015) chick Müller glia			
Kainate	Uptake	(Schitine et al., 2015) chick Müller glia			
Kynurenic acid	Uptake	(Harsing et al., 2001) rat striatum slices			
NMDA	Uptake	(Harsing et al., 2001) rat striatum slices			
NMDA	Uptake	(Schitine et al., 2015) chick Müller glia			
Glutamate	Expression		(Schitine et al., 2015) chick Müller glia		(Schitine et al., 2015) chick Müller glia
Divalent cations					
Ca^{2+}	Uptake	(Goncalves et al., 1997) sheep cort synapt			
Ca^{2+}	Uptake	(Goncalves et al., 1999) sheep cort synapt			
Ca^{2+}	Uptake	(Cordeiro et al., 2000) sheep cort synapt			
Mn^{2+}	Uptake	(Anderson et al., 2007) rat striatum synapt			
Mn^{2+}	Expression		(Anderson et al., 2008) rat striatum		
Mn^{2+}	Expression		(Anderson et al., 2008) rat globus pallidus		
Mn^{2+}	Expression		(Anderson et al., 2008) rat hipp		
Mn^{2+}	Expression		(Anderson et al., 2008) rat SN		
Mn^{2+}	Expression		(Anderson et al., 2008) rat cereb		
Other					
ACHC	Uptake		(Bernstein and Quick, 1999) rat hipp nrn		
ATP	Uptake	(Schitine et al., 2015) Chick Muller glia			
b-Alanine	Uptake	(Voutsinos et al., 1998) rat cereb punch			
b-Alanine	Uptake	(Bahena-Trujillo and Arias-Montano, 1999) rat SNr synapt			
Cholera toxin	Uptake		(Cristovao-Ferreira et al., 2013) rat cort astro		(Cristovao-Ferreira et al., 2013) rat cort astro
CPA	Uptake		(Corey et al., 1994) rat hipp synapt		
CPA	Uptake		(Cristovao-Ferreira et al., 2013) rat cort astro		(Cristovao-Ferreira et al., 2013) rat cort astro

(Continued)

TABLE 2 | Continued

Agent	Assay	N/A	GAT1	GAT2	GAT3
Daidzein	Uptake	(Law et al., 2000) rat hipp nrn			
5,7-DHT	Uptake	(Voutsinos et al., 1998) rat cereb punch			
Gabapentin	Uptake		(Whitworth and Quick, 2001) rat hipp nrn		
Glycine	Uptake	(Harsing et al., 2001) rat striatum slices			
Inosine	Uptake		(Corey et al., 1994) rat hipp synapt		
KCl	Uptake	(Schitine et al., 2015) chick Müller glia			
NaIO4	Uptake		(Hu et al., 2011) HEK293		
NOC-18	Uptake		(Fan et al., 2006) rat hipp nrn		
PACAP6-38	Uptake	(Schitine et al., 2015) chick Müller glia			
Pals1	Uptake		(McHugh et al., 2004) COS		
PDD	Uptake		(Corey et al., 1994) rat hipp synapt		
Pertussis toxin	Uptake		(Cristovao-Ferreira et al., 2013) rat cort astro		(Cristovao-Ferreira et al., 2013) rat cort astro
Pregabalin	Uptake		(Whitworth and Quick, 2001) rat hipp nrn		
Sialidase	Uptake		(Hu et al., 2011) CHO, HEK293		
Sucrose	Uptake		(Deken et al., 2003) rat hipp nrn		
U73122	Uptake		(Corey et al., 1994) rat hipp synapt		
5,7-DHT	Expression		(Voutsinos et al., 1998) rat cereb punch	(Voutsinos et al., 1998) rat cereb punch	(Voutsinos et al., 1998) rat cereb punch
KCl	Expression		(Hu and Quick, 2008) rat cort nrn		
Gabapentin	Expression		(Whitworth and Quick, 2001) rat hipp nrn		
NOC-18	Expression		(Fan et al., 2006) rat hipp nrn		
Pals1	Expression		(McHugh et al., 2004) COS		
Pregabalin	Expression		(Whitworth and Quick, 2001) rat hipp nrn		
Sucrose	Expression		(Deken et al., 2003) rat hipp nrn		
TTX	Expression		(Hu and Quick, 2008) rat cort nrn		

The table provides a summary of the results obtained in the literature regarding mechanisms controlling the rate of GABA Uptake and its expression in a variety of animal models and expression systems. The color coding of each cell and abbreviations are as described for ***Table 1****. SNr, substantia nigra pars reticulata; ACHC, cis-1,3-aminocyclohexane carboxylic acid; CPA, α-cyclopiazonic acid; 5,7-DHT, 5,7-dihydroxytryptamine; OAG, oleyl-acetyl glycerol; PDD, 4 alpha-phorbol-12,13-didecanoate.*

TrkB receptor, is coupled to a PLC-γ/PKC-δ and ERK/MAPK pathway, and requires activation of adenosine A2A receptors (Vaz et al., 2011). The cross talk between A2A receptors and BDNF is likely due to the fact that activation of A2A receptors activates TrkB and induces its translocation to lipid rafts (Tebano et al., 2008; Assaife-Lopes et al., 2010). This type of modulation differs in neurons, where BDNF can still inhibit GABA uptake via GAT1 in conjunction with A2A receptors, but here the BDNF

modulation persists in the presence of A2A receptor antagonists or upon removal of extracellular adenosine (Vaz et al., 2008).

Physiological Roles of GABA Transporters

Genetic variants in the solute carrier family 6 member 1 (SLC6A1) gene, encoding GAT1, are associated with various neurodevelopmental disorders, including epilepsy with myoclonic atonic seizures, autism spectrum disorder and intellectual disability (Bhat et al., 2020; Goodspeed et al., 2020). Knockout mouse models of GAT1, as well as GAT1 inhibitors, have shown a range of physiological effects that indicate that GAT1, through its exquisite regulation of GABA in the brain, may be an interesting target for therapies for neuropsychiatric diseases (Salat and Kulig, 2011; Egawa and Fukuda, 2013; Bhat et al., 2020). GAT1 inhibitors, such as tiagabine, NO-711 and DDPM-2571, have anti-seizure, antinociceptive, antiallodynic and anxiolytic properties (Laughlin et al., 2002; Todorov et al., 2005; Pakulska, 2007; Xu et al., 2008; Salat et al., 2017). Loss of GAT1 in the *nucleus accumbens* has also been observed in mice treated with chronic social defeat stress paralleling observations in patients with major depressive disorder (MDD) (Heshmati et al., 2020).

During epileptic seizures, the ionic gradient that typically supports GABA uptake from the extracellular space can be dissipated or even inverted, promoting GABA release through the reversed activity of GABA transporters like GAT3 (Raiteri et al., 2002; Wu et al., 2003; Richerson and Wu, 2004; Kinney, 2005). Under these conditions, the reversal of GABA uptake could provide a useful mechanism to curtail seizure propagation. With some exceptions (Xie et al., 2017), single nucleotide polymorphisms in SLC6A11, the gene encoding human GAT3, have been detected in patients with antiepileptic drug resistance (Kim et al., 2011). It is possible that a dysfunction of GAT3 could alter both phasic and tonic GABAergic transmission in the epileptic brain.

GATs regulate neurotransmission in other complex ways. As mentioned above, substrate transport through GAT elicits an inward current that can directly excite neurons (Bagley et al., 2005, 2011). GAT1 also generates a sodium-dependent capacitive current that can also contribute to shunting (Mager et al., 1993). Efflux of GABA into the extracellular space contributes to tonic currents mediated by $GABA_A$ receptors in hippocampal neurons (Wu et al., 2007) and glia (Barakat and Bordey, 2002). Tonic currents are critical in neurodevelopment (Egawa and Fukuda, 2013) and are increased in pathological conditions, such as inflammation (Tonsfeldt et al., 2016). Regulation of GAT activity and trafficking has a dramatic effect on tonic currents, especially those mediated by extrasynaptic $GABA_A$ receptors (Scimemi et al., 2005; Scimemi, 2014a,b). In addition to controlling integration of inputs onto GABAergic neurons, these tonic currents control the coincidence detection window of excitatory inputs onto pyramidal neurons (Sylantyev et al., 2020) and contribute to regulation of dopamine release in the dorsal striatum (Roberts et al., 2020). GAT3 activity in astrocytes regulates release of ATP and adenosine that contributes to heterosynaptic depression in the hippocampus (Boddum et al., 2016), highlighting an additional mechanism for regulating synaptic activity.

DOPAMINE UPTAKE: ONE TRANSPORTER, THREE CURRENTS, MULTIPLE REGULATION SITES

Dopamine uptake via the membrane transporter DAT is stoichiometrically coupled to the co-transport of two Na^+ and one Cl^- ion (**Figure 3**) (Krueger, 1990; McElvain and Schenk, 1992; Gu et al., 1994; Penmatsa et al., 2013, 2015). Voltage-clamp recordings of DAT-mediated currents in *Xenopus* oocytes, however, show that the mean net charge to dopamine ratio is significantly larger than the one predicted by the stoichiometric coupling ratio (Sonders et al., 1997; Ingram et al., 2002). This discrepancy can be accounted for by the fact that DAT, like glutamate and GABA transporters (as well as serotonin and norepinephrine transporters; Bruns et al., 1993; Cammack et al., 1994; Mager et al., 1994; Galli et al., 1995; Jayanthi et al., 2002), also mediates two stoichiometrically uncoupled conductances: one that requires dopamine binding to the transporter, and one that does not and is constitutively active. For simplicity, we refer to them as the uncoupled and the leak conductance, respectively.

It is interesting to note that the concentration of dopamine required for half-maximal transport is ∼580 nM, whereas the one required for activation of the uncoupled current is only ∼35 nM (Ingram et al., 2002). The extracellular concentration of dopamine in the brain has been known to vary on a sub-second time scale due to phasic firing of dopaminergic neurons, and to be modulated by administration of substances of abuse. Until recently, fast-scan cyclic voltammetry (FSCV) has been considered the technique that provides the best combination of temporal resolution, sensitivity and chemical selectivity (Roberts et al., 2013), but even in this case it has been traditionally used to obtain relative, as opposed to absolute values of dopamine concentrations in the brain. In 2018, the development of cellular-scale probes have enabled stable recording of sub-second extracellular dopamine oscillations (Schwerdt et al., 2018). Although the recorded levels of dopamine were specific for each mouse, they ranged between 40–450 nM (Schwerdt et al., 2018). This means that the uncoupled DAT current is likely to be a main contributor to cell excitability and neurotransmitter release in DAT-expressing neurons. The uncoupled DAT-mediated current is carried by chloride and, surprisingly, its activation increases cell excitability in cultured dopaminergic neurons (Ingram et al., 2002; Carvelli et al., 2004).

In physiological conditions, the leak current is carried by K^+ and perhaps H^+ ions. This leak current is voltage-dependent, outward-rectifying and reverses at ∼–10 mV (Sonders et al., 1997). Although its activation does not require ion or agonist binding to the transporter, it can be blocked by dopamine and other DAT ligands. The ability of substrates to block the leak current is not consistently observed among other members of the Na^+/Cl^--dependent cotransporter family, with the exception of GAT1 (Mager et al., 1994; Cammack and Schwartz, 1996;

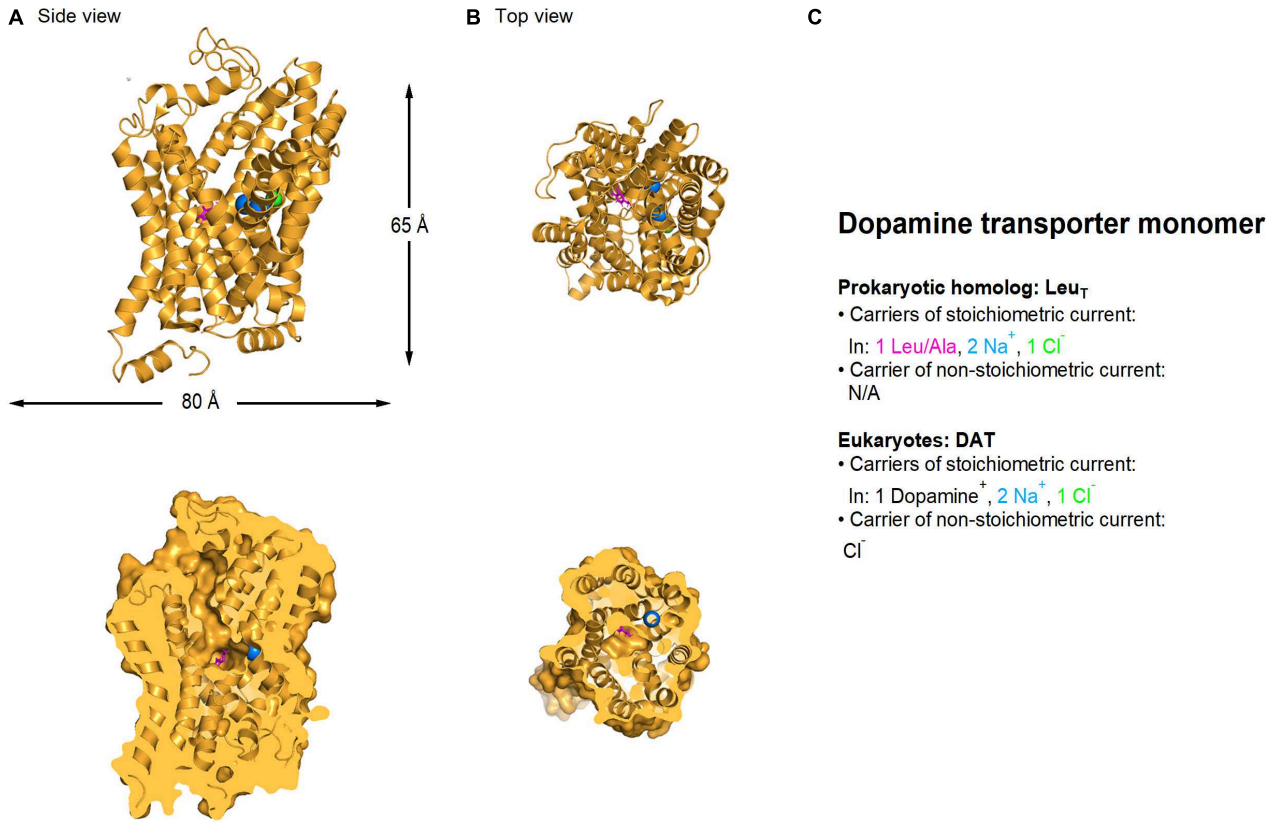

FIGURE 3 | Crystal structure of *Drosophila melanogaster* dDAT dopamine transporter (PDB: 4XP1). **(A)** Side view of the *Drosophila* dopamine transporter parallel to the membrane, using a ribbon (*top*) and a surface representation sliced through the center of the transporter (*bottom*). **(B)** As in A, viewed from the extracellular side of the membrane. L-Dopa (*magenta*), sodium (*blue*) and chloride ions (*green*) are represented as spheres. **(C)** Summary of the main feature of the stoichiometric and non-stoichiometric current mediated by LeuT (prokaryotic dopamine transporter homolog) and DAT transporters in eukaryotes, respectively. Image generated using The PyMOL Molecular Graphics System (Version 2.3.2; Schrödinger, 2010).

MacAulay et al., 2002; Kanner, 2003) and the serotonin (Mager et al., 1994) and norepinephrine transporters (Galli et al., 1995). These findings identify multiple mechanisms through which dopamine transporters can change the membrane potential and the signaling properties of neurons through mechanisms that are distinct from its ability to take up dopamine from the extracellular space.

A summary of current studies on modulation of dopamine transporters listed in PubMed is provided in **Table 3**.

The Pharmacology of Dopamine Transporters

DAT is a target of psychostimulants like cocaine and amphetamine. Cocaine binds to DAT and increases extracellular dopamine levels by blocking its transport activity (Chen and Reith, 2000; Norregaard and Gether, 2001; Goldberg et al., 2003; Torres et al., 2003). In contrast, amphetamine is a substrate for this transporter (Kahlig et al., 2005). The inward transport of amphetamine increases the number of inward-facing transporter binding sites, which results in an increased rate of dopamine efflux through what at first sight may look like an exchange process (Sulzer et al., 1995; Kahlig et al., 2005). In reality, this phenomenon may be more complex, as evidenced by the fact that N-terminus phosphorylation of DAT alters only the amphetamine-induced dopamine efflux without altering dopamine uptake (Khoshbouei et al., 2004). Dopamine and amphetamine are both substrates for DAT, and compete with each other for binding to the transporter (Sulzer et al., 1993; Hoffman et al., 1998). They can both trigger dopamine efflux through reversed uptake, by inverting the electrochemical gradient for Na^+ and Cl^- (Sitte et al., 1998). Whereas dopamine inhibits the DAT channel-like behavior, amphetamine activates it. This effect is not due to differences in the ability of dopamine and amphetamine to change the intracellular Na^+ concentration, because it can still be detected in outside-out patches, where the intracellular Na^+ concentration is controlled (Kahlig et al., 2005).

The Surface Mobility and Cellular Distribution of Dopamine Transporters

Dopamine transporters are monoamine neurotransmitter transporters located in the pre-synaptic terminal of dopaminergic neurons, away from the synaptic area (Nirenberg et al., 1997). These cells are located in the ventral tegmental area and

TABLE 3 | Regulating factors of dopamine transporter Uptake and expression.

Agent	Assay	DAT
Dopamine		
Dopamine	Uptake	(Parker and Cubeddu, 1988) rat striatum slices
Dopamine	Uptake	(Gulley et al., 2002) Xenopus ooc, rat striatum
Dopamine	Uptake	(Gulley et al., 2002) rat NAc
Dopamine	Uptake	(Gorentla and Vaughan, 2005) LLC-PK1
Dopamine	Uptake	(Chi and Reith, 2003) HEK293
Dopamine	Expression	(Chi and Reith, 2003) HEK293
Dopamine	Expression	(Johnson et al., 2005a) rat striatum synapt
Dopamine	Expression	(Furman et al., 2009) N2A, rat striatum synapt (rapid 1 min treatment)
DAT inhibitors		
AMPH	Uptake	(Parker and Cubeddu, 1988) rat striatum slices
AMPH	Uptake	(Sulzer et al., 1993) rat midbrain nrn
AMPH	Uptake	(Wieczorek and Kruk, 1994) rat striatum slices
AMPH	Uptake	(Sulzer et al., 1995) snail dopaminergic nrn
AMPH	Uptake	(Jones et al., 1998) ms striatum slices
AMPH	Uptake	(Anderson et al., 1998) snail dopaminergic nrn
AMPH	Uptake	(Jones et al., 1999) ms striatum
AMPH	Uptake	(Mundorf et al., 1999) PC12
AMPH	Uptake	(Saunders et al., 2000) EM4 HEK293
AMPH	Uptake	(Kahlig et al., 2004) HEK293
AMPH	Uptake	(Gulley et al., 2002) Xenopus ooc
AMPH	Uptake	(Garcia et al., 2005) EM4 HEK293
AMPH	Uptake	(Johnson et al., 2005b) rat striatum slices
AMPH	Uptake	(Williams et al., 2007) rat striatum
AMPH	Uptake	(Johnson et al., 2005a) rat striatum synapt
AMPH	Uptake	(Fischer and Cho, 1979) rat striatum homogenates
AMPH	Uptake	(Lute et al., 2008) ms midbrain nrn
AMPH	Uptake	(Chen et al., 2009) ms striatum
AMPH	Uptake	(Wheeler et al., 2015) primary midbrain nrn
AMPH	Uptake	(Zestos et al., 2016) rat NAc
AMPH	Uptake	(Chen et al., 2009) ms striatum (rapid<90 s treatment)
Cocaine	Uptake	(Pristupa et al., 1998) Sf9
Cocaine	Uptake	(Sandoval et al., 2001) rat striatum synapt
Cocaine	Uptake	(Cervinski et al., 2005) LLC-PK1
Cocaine	Uptake	(Gorentla and Vaughan, 2005) LLC-PK1
Cocaine	Uptake	(Schoffelmeer et al., 2011) rat NAc
Cocaine	Uptake	(Wheeler et al., 2017) rat NAc
GBR12909	Uptake	(Schoffelmeer et al., 2011) rat NAc
GBR12935	Uptake	(Mason et al., 2005) HEK293
4HA	Uptake	(Fischer and Cho, 1979) rat striatum homogenates
METH	Uptake	(Kim et al., 2000) rat striatum synapt
METH	Uptake	(Metzger et al., 2000) rat striatum synapt
METH	Uptake	(Sandoval et al., 2001) rat striatum synapt
METH	Uptake	(Gorentla and Vaughan, 2005) LLC-PK1
METH	Uptake	(Cervinski et al., 2005) LLC-PK1
MDMA	Uptake	(Sandoval et al., 2001) rat striatum synapt
MPD	Uptake	(Sandoval et al., 2001) rat striatum synapt
Nomifensine	Uptake	(Raiteri et al., 1979) rat striatum synapt
AMPH	Expression	(Saunders et al., 2000) EM4 HEK
AMPH	Expression	(Sorkina et al., 2003) PAE
AMPH	Expression	(Garcia et al., 2005) EM4 HEK293
AMPH	Expression	(Kahlig et al., 2004) HEK293
AMPH	Expression	(Chen et al., 2009) ms striatum

(Continued)

TABLE 3 | Continued

Agent	Assay	DAT
AMPH	Expression	(Johnson et al., 2005a) rat striatum synapt
AMPH	Expression	(Boudanova et al., 2008a) PC12
AMPH	Expression	(Hong and Amara, 2013) HEK293, rat embryonic midbrain nrn
AMPH	Expression	(Wheeler et al., 2015) SK-N-SH, ms midbrain nrn
AMPH	Expression	(Johnson et al., 2005a) rat striatum synapt
AMPH	Expression	(Furman et al., 2009) N2A (rapid 1 min treatment)
AMPH	Expression	(Chen et al., 2009) ms striatum (rapid<90 s treatment)
Cocaine	Expression	(Johnson et al., 2005a) rat striatum synapt
GBR12909	Expression	(Gorentla and Vaughan, 2005) LLC-PK1
GBR12935	Expression	(Furman et al., 2009) rat striatum synapt
PKA activators		
8-Br-cAMP	Uptake	(Page et al., 2004) rat striatum synapt
8-Br-cAMP	Uptake	(Pristupa et al., 1998) Sf9
8-Br-cAMP	Uptake	(Copeland et al., 1996) rat striatum synapt
8-Br-cAMP	Uptake	(Page et al., 2004) rat striatum synapt
db-cAMP	Uptake	(Wheeler et al., 2015) SK-N-SH
Forskolin	Uptake	(Daniels and Amara, 1999) MCDK
IBMX	Uptake	(Daniels and Amara, 1999) MCDK
Sp-cAMPS	Uptake	(Pristupa et al., 1998) Sf9
db-cAMP	Expression	(Wheeler et al., 2015) SK-N-SH
PKA inhibitors		
H89	Uptake	(Page et al., 2004) rat striatum synapt
KT5720	Uptake	(Wheeler et al., 2015) SK-N-SH
Rp-cAMPs	Uptake	(Pristupa et al., 1998) Sf9
KT5720	Expression	(Wheeler et al., 2015) SK-N-SH
PKC activators		
DiC8	Uptake	(Copeland et al., 1996) rat striatum synapt
Indolactam V	Uptake	(Vaughan et al., 1997) rat striatum synapt
OAG	Uptake	(Vaughan et al., 1997) rat striatum synapt
PDBu	Uptake	(Zhang et al., 1997) C6 glioma
PMA	Uptake	(Kitayama et al., 1994) COS
PMA	Uptake	(Copeland et al., 1996) rat striatum synapt
PMA	Uptake	(Vaughan et al., 1997) rat striatum synapt
PMA	Uptake	(Huff et al., 1997) LLC-PK1
PMA	Uptake	(Gorentla and Vaughan, 2005) LLC-PK1
PMA	Uptake	(Zhang et al., 1997) C6 glioma
PMA	Uptake	(Zhu et al., 1997) Xenopus ooc
PMA	Uptake	(Pristupa et al., 1998) Sf9
PMA	Uptake	(Melikian and Buckley, 1999) PC12
PMA	Uptake	(Chang et al., 2001) COS
PMA	Uptake	(Granas et al., 2003) HEK293
PMA	Uptake	(Cervinski et al., 2005) LLC-PK1
PMA	Uptake	(Boudanova et al., 2008b) PC12
PMA	Expression	(Zhu et al., 1997) Xenopus ooc
PMA	Expression	(Chang et al., 2001) COS
PMA	Expression	(Pristupa et al., 1998) COS
PMA	Expression	(Gorentla and Vaughan, 2005) LLC-PK1
PMA	Expression	(Pristupa et al., 1998) Sf9
PMA	Expression	(Daniels and Amara, 1999) MCDK
PMA	Expression	(Melikian and Buckley, 1999) PC12
PMA	Expression	(Granas et al., 2003) HEK293
PMA	Expression	(Loder and Melikian, 2003) PC12
PMA	Expression	(Sorkina et al., 2003) PAE

(Continued)

TABLE 3 | Continued

Agent	Assay	DAT
PMA	Expression	(Holton et al., 2005) PC12
PMA	Expression	(Miranda et al., 2007) HeLa
PMA	Expression	(Boudanova et al., 2008b) PC12
PMA	Expression	(Cremona et al., 2011) EM4 HEK, HeLa, ms striatum nrn, ms striatum slices
PMA	Expression	(Navaroli et al., 2011) PC12
PMA	Expression	(Hong and Amara, 2013) HEK293
PMA	Expression	(Eriksen et al., 2009) HEK293
PMA	Expression	(Eriksen et al., 2009) rat midbrain nrn
PKC inhibitors		
BIM-1	Uptake	(Gorentla and Vaughan, 2005) LLC-PK1
BIM-1	Uptake	(Melikian and Buckley, 1999) PC12
BIM-1	Uptake	(Boudanova et al., 2008a) PC12
Chelerythrine	Uptake	(Sandoval et al., 2001) rat striatum synapt
Chelerythrine	Uptake	(Zhang et al., 1997) C6 glioma
Enzastaurin	Uptake	(Zestos et al., 2016) rat striatum synapt
Gö6976	Uptake	(Johnson et al., 2005b) rat striatum slices
LY379196	Uptake	(Johnson et al., 2005b) rat striatum slices
NPC15437	Uptake	(Sandoval et al., 2001) rat striatum synapt
Rottlerin	Uptake	(Johnson et al., 2005b) rat striatum slices
Ruboxistaurin	Uptake	(Zestos et al., 2016) rat striatum synapt
Staurosporine	Uptake	(Huff et al., 1997) LLC-PK1
Staurosporine	Uptake	(Zhang et al., 1997) C6 glioma
Staurosporine	Uptake	(Pristupa et al., 1998) Sf9
Okadaic acid	Uptake	(Copeland et al., 1996) rat striatum synapt
Staurosporine	Uptake	(Daniels and Amara, 1999) MCDK
BIM-1	Expression	(Boudanova et al., 2008a) PC12
PI3K activators		
Insulin	Uptake	(Carvelli et al., 2002) rat striatum synapt, EM4 HEK293
Insulin	Uptake	(Garcia et al., 2005) EM4 HEK293
Insulin	Uptake	(Schoffelmeer et al., 2011) rat NAc
Insulin	Expression	(Carvelli et al., 2002) rat striatum synapt, EM4 HEK293
PI3K inhibitors		
LY294002	Uptake	(Carvelli et al., 2002) rat striatum synapt, EM4 HEK293
LY294002	Expression	(Carvelli et al., 2002) rat striatum synapt, EM4 HEK293
MAPK inhibitors		
UO126	Uptake	(Moron et al., 2003) HeLa
PD98059	Uptake	(Moron et al., 2003) HeLa
PD98059	Expression	(Moron et al., 2003) HeLa
PTK inhibitors		
Genistein	Uptake	(Doolen and Zahniser, 2001) Xenopus ooc
Genistein	Uptake	(Hoover et al., 2007) rat dorsal striatum synapt
Lavendustin A	Uptake	(Doolen and Zahniser, 2001) Xenopus ooc
Tyrphostin	Uptake	(Doolen and Zahniser, 2001) Xenopus ooc
Tyrphostin	Uptake	(Hoover et al., 2007) rat dorsal striatum synapt
Genistein	Expression	(Doolen and Zahniser, 2001) Xenopus ooc
Phosphatase inhibitors		
Okadaic acid	Uptake	(Copeland et al., 1996) rat striatum synapt
Okadaic acid	Uptake	(Vaughan et al., 1997) rat striatum synapt
Okadaic acid	Uptake	(Zhang et al., 1997) C6 glioma
Okadaic acid	Uptake	(Page et al., 2004) rat striatum synapt
Src inhibitors		
PP2	Uptake	(Doolen and Zahniser, 2001) Xenopus ooc

(Continued)

TABLE 3 | Continued

Agent	Assay	DAT
Others		
8-Br-cGMP	Uptake	(Copeland et al., 1996) rat striatum synapt
Corticosterone	Uptake	(Wheeler et al., 2017) rat NAc
CPE	Uptake	(Zhang et al., 2009) HEK293
KN-62	Uptake	(Page et al., 2004) rat striatum synapt
Leptin	Uptake	(Schoffelmeer et al., 2011) rat NAc
mbCD	Uptake	(Jones et al., 2012) HEK293
Mazindol	Uptake	(Gorentla and Vaughan, 2005) LLC-PK1
Monensin	Uptake	(Sulzer et al., 1993) rat midbrain nrn
NH4Cl	Uptake	(Sulzer et al., 1993) rat midbrain nrn
Nystatin	Uptake	(Jones et al., 2012) HEK293
Octopamine	Uptake	(Parker and Cubeddu, 1988) rat striatum slices
PEA	Uptake	(Parker and Cubeddu, 1988) rat striatum slices
PICK1	Uptake	(Torres et al., 2001) HEK293
Tributylamine	Uptake	(Sulzer et al., 1993) rat midbrain nrn
Tyramine	Uptake	(Gulley et al., 2002) Xenopus ooc
Tyramine	Uptake	(Parker and Cubeddu, 1988) rat striatum slices
Trypan blue	Uptake	(Mason et al., 2005) HEK293
Zinc	Uptake	(Jones et al., 2012) HEK293
CPE	Expression	(Zhang et al., 2009) HEK293
mbCD	Expression	(Jones et al., 2012) HEK293
Momensin	Expression	(Sorkina et al., 2005) PAEC
PICK1	Expression	(Torres et al., 2001) HEK293
SKF38393	Expression	(Wheeler et al., 2015) SK-N-SH
Streptozotocin	Expression	(Williams et al., 2007) rat striatum

The table provides a summary of the results obtained in the literature regarding the mechanisms controlling the rate of dopamine uptake and its expression in a variety of animal models and expression systems. The color coding of each cell and abbreviations are as described for ***Table 1****. NAc, nucleus accumbens; AMPH, amphetamine; CPE, carboxypeptidase E; 4HA, 4-Hydroxyamphetamine; IBMX, 3-isobutyl-1-methylxanthine; METH, methamphetamine; MPD, methylphenidate; PEA, phenylethylamine; PP2, protein phosphatase 2.*

substantia nigra, project to the cingulate and medial prefrontal cortex, *nucleus accumbens*, olfactory tubercle, lateral habenula, and *striatum*. Through their axonal projections, dopaminergic neurons control motivation, reward reinforcement and movement, in addition to attention, planning and memory. Therefore, the regulation of DAT function has extensive functional implications for all these behaviors. It is now evident that the role of DAT is not limited to regulating the extracellular concentration of dopamine but is also involved in the homeostatic maintenance of presynaptic function (Torres et al., 2003). Like other membrane proteins, DAT is associated with intracellular proteins that ensure the appropriate location of the transporter in specific domains of the cell membrane at a given time. Accordingly, DAT has been shown to bind to the SNARE protein complex syntaxin 1A (Lee et al., 2004), the PDZ domain protein PICK1 (Torres et al., 2001; Bjerggaard et al., 2004), CaMKII (Fog et al., 2006), and the multiple-LIM-domain-containing adaptor protein HIC-5 (Carneiro et al., 2002).

DAT is equally distributed in and out of rafts (Foster et al., 2008), nanometer-wide and temporally dynamic lipid microdomains enriched in cholesterol, sphingolipids and glycosylphosphatidylinositol (GPI)-anchored proteins (Hancock, 2006). Structural studies of the *Drosophila melanogaster* DAT (dDAT) reveal that cholesterol can bind in a crevice formed by transmembrane domains 5, 7, and 1a, which is thought to prevent the conformational changes required for the transporter to transition from outward-facing to inward-facing (Penmatsa et al., 2013, 2015). This is in agreement with functional studies that show DAT can be regulated by cholesterol, due to its ability to promote an outward-facing conformation of the transporter (Hong and Amara, 2010; Jones et al., 2012).

By using Fluorescence Correlation Spectroscopy (FCS) and FRAP, Adkins et al. (2007) measured the surface diffusion coefficient of DAT in two types of cells: HEK293 and N2a cells. Due to differences in laser beam waist and sampling areas between FRAP and FCS, FCS is better suited to detect fast protein movements within a confined domain, whereas FRAP allows to detect long-range diffusion between domains in the membrane (Adkins et al., 2007). In HEK293 cells, DAT diffuses with a diffusion coefficient of 3.6×10^{-9} cm^2/s, consistent with a relatively freely diffusible protein. This diffusion coefficient is lower in N2a cells, where DAT is partially immobilized ($D < 10^{-10}$ cm^2/s). This difference is likely due to the existence of cell-specific direct or indirect interactions between DAT and cytoskeletal proteins or with membrane rafts. Accordingly, single particle tracking studies confirm that the median diffusion

coefficient for DAT is 1.6×10^{-10} cm^2/s in Flp-In 293 cells (Kovtun et al., 2015).

Overall, these findings indicate that DAT transporters diffuse substantially slower and in a more confined manner than the glutamate transporter GLT-1, probably because of the presence of different types of protein interactions in different membrane transporters or because of the presence/lack of specific interacting substrates (Murphy-Royal et al., 2015).

Transcriptional, Translational, and Post-translational Regulation of Dopamine Transporters

The human DAT gene was first cloned in 1991, and it is localized to chromosome 5p15.3 and has a single transcriptional start site (Kilty et al., 1991; Vandenbergh et al., 1992a,b). DAT has a half-life of about 2 days on the cell membrane, suggesting the existence of dynamic processes of transcriptional and translational regulation (Kimmel et al., 2000; Kahlig and Galli, 2003). Transcription factors like *Nurr1* and *Pitx3* have an expression pattern that match that of dopaminergic neurons, and are known to be crucial for the development, survival and maintenance of midbrain dopaminergic neurons (Lee et al., 2010; Rodriguez-Traver et al., 2016; Salemi et al., 2016). Accordingly, disrupting the *Nurr1* gene alters the development of dopaminergic neurons (Zetterstrom et al., 1997; Castillo et al., 1998; Saucedo-Cardenas et al., 1998). *Nurr1* binds with high-affinity to an NGFI-B responsive element within the promoter regions of DAT and other dopamine-related genes (Sacchetti et al., 1999). The ability of *Nurr1* to increase DAT expression, however, relies on mechanisms that are independent of the NGFI-B responsive element. There are a variety of sequence motifs identified through *in silico* studies, which point to the fact that DAT can be regulated epigenetically via DNA methylation and histone acetylation *in vitro* and *in vivo* (Wang et al., 2007). Like other housekeeping genes, the DAT gene lacks conserved TATA and CAAT boxes (confirming that DAT is susceptible to regulation by histone acetylation), and its core promoter is GC-rich (confirming that DAT expression can be regulated via DNA methylation) (Choi and Kim, 2008).

These discoveries prompted a number of biochemical and mutagenesis studies on heterologous expression systems, which led to the identification of key structural features and functional domains of the transporter. A major breakthrough occurred when the first X-ray crystal structure of the bacterial leucine transporter $LeuT_{Aa}$, which shares 20–25% homology with all monoamine transporters was solved at 1.65 Å resolution (Yamashita et al., 2005). This was followed by the structure of *Drosophila melanogaster* DAT, which shares 50–55% homology with monoamine transporters (Penmatsa et al., 2013, 2015; Wang et al., 2015). Together, these studies suggest that all monoamine transporters have 12 α-helix spanning domains and an alternating access substrate translocation mechanism (Kristensen et al., 2011). Despite the structural similarity of the core transmembrane regions of all monoamine transporters, their extracellular loops, N- and C-termini differ significantly in length and sequence (Kristensen et al., 2011). This is important because these regions are the site of post-translational modifications and can be the site of protein–protein interactions that control transporter localization, stability and activity (Aggarwal and Mortensen, 2017). Post-translational modifications, binding partner interactions, modulation by cholesterol and membrane raft associations are all capable of modulating DAT activity and ultimately dopamine clearance from the extracellular space.

The N-terminus of the DAT protein is subject to phosphorylation and ubiquitination (Karam and Javitch, 2018). Although five serine residues at positions 2, 4, 7, 12, 13 have been identified as targets for phosphorylation by PKC, the only verified phosphorylation site is Ser7 (Moritz et al., 2013). The localization of these sites at the distal end of a long and flexible domain suggests that these residues may be also regulated by partner interactions, but these effects have not been demonstrated. A second verified phosphorylation site is Thr53, which is followed by a Pro residue, making it specific for proline-directed kinases such as ERK. Thr53 is also flanked by an SH3 domain, which is a ligand for protein scaffolding (Saksela and Permi, 2012). In between these two phosphorylation sites, Lys27 is a residue that undergoes ubiquitination catalyzed by the ubiquitin E3 ligases *Nedd4-2* and *Parkin*. This modification is increased by PKC activation and contributes to promote DAT endocytosis (Hong and Amara, 2010; Vina-Vilaseca and Sorkin, 2010). The N-terminal domain also contains binding sites for the regulatory partners syntaxin 1 (res 1–33, which reduces dopamine uptake) and D2 dopamine receptors (res. 1–15) (Lee et al., 2007; Binda et al., 2008; Carvelli et al., 2008). On the C-terminal domain of the DAT protein, Cys580 provides an *S*-palmitoylation site, and a FREK motif at residues 587–590 binds the small Ras-like GTPase Rin1 and contributes to PKC-mediated endocytosis (Boudanova et al., 2008b; Navaroli et al., 2011). Other regulatory domains in the C-terminal region include binding sites for CaMK (res. 612–617) and α-synuclein (res. 606–620) (Lee et al., 2001; Moszczynska et al., 2007). The C-terminal domain also contains a PDZ domain-binding sequence, where interactions with scaffolding proteins like PICK1 occur. Notably, these interactions are neither necessary nor sufficient for surface targeting of DAT, and have yet unidentified functional consequences (Bjerggaard et al., 2004). Other members of the "DAT interactome" include PP2Ac (Baumann et al., 2000), Hic-5 (Carneiro et al., 2002), RACK (Lee et al., 2004), D_2 dopamine receptors (Bolan et al., 2007), flotillin-1 (Cremona et al., 2011), Rin (Navaroli et al., 2011), and the k-opioid receptor (Kivell et al., 2014; Bermingham and Blakely, 2016).

The regulatory mechanisms described so far make it easy to spot that protein kinases like PKC, one of the best characterized regulatory proteins for DAT, can regulate dopamine uptake through a variety of processes, including an endocytotic mechanism driven by the phosphorylation of DAT accessory proteins, a kinetic down-regulation mediated by Ser7 phosphorylation, and an increased dopamine efflux mediated by altered surface transporter activity. Together, these modifications allow PKC to reduce dopamine uptake. The actions of PKC are opposite to those induced by palmitoylation, which lead to reduced DAT degradation (Chen et al., 2013). It is important

to keep in mind that the primary sites of PKC-stimulated phosphorylation are the membrane rafts, the microdomains rich in cholesterol and sphingolipids. Therefore, changing PKC-mediated phosphorylation of DAT can affect its raft distribution and protein interactions. In contrast to PKC, ERK provides a tonic mechanism to increase dopamine uptake perhaps via phosphorylation of Thr53 (Foster et al., 2012). In addition to PKC and ERK, there is a host of other kinases that are capable of regulating DAT activity, including PKA, PKG, CaMKII, MAPK, PI3K/Akt and tyrosine kinases. PKCβ may also be involved in the mechanism of D_2 receptor regulation of DAT by ERK (Chen et al., 2013).

Physiological Roles of Dopamine Transporters

DAT regulates extracellular concentrations of the neuromodulator dopamine and thus, subsequent activation of dopamine receptors that can enhance or inhibit neurons. DAT is the target of psychoactive and psychotherapeutic drugs such as methylphenidate and amphetamines that are used in treatment of attention deficit and hyperactivity disorder (ADHD) symptoms, as well as drugs of abuse (Schmitt et al., 2013; German et al., 2015). Genetic variants of SLC6A3, the gene encoding DAT in humans, have been identified in patients with neuropsychiatric, neurodevelopmental and neurodegenerative disorders (Mazei-Robison et al., 2005; Serretti and Mandelli, 2008; Mick and Faraone, 2009; Sakrikar et al., 2012; Bowton et al., 2014; Hansen et al., 2014; Mergy et al., 2014; Herborg et al., 2018; Campbell et al., 2019; DiCarlo et al., 2019). Studies of these variants have observed deficits in uptake, transporter-associated currents, trafficking and regulation (Gowrishankar et al., 2014). Further studies of these mutants should give more insight into the complex regulation of dopamine-modulated circuits. An intriguing new area is the role that DAT plays in transport of ligands that act on the trace amine-associated receptor subtype 1 (Taar1), an intracellularly localized G protein-coupled receptor that can, in turn, regulate internalization of both the DAT and EAAT3 in dopaminergic neurons (Underhill et al., 2014, 2019), enhancing extrasynaptic glutamate signaling (Li et al., 2017). Taar1 is known to regulate monoaminergic signaling and dysregulation of TAAR1 signaling may play important roles in neuropsychiatric disorders (Schwartz et al., 2018; Dodd et al., 2020).

CONCLUSION

Transporters for excitatory, inhibitory, and modulatory neurotransmitters like glutamate, GABA and dopamine are complex molecular machines that do much more than act as vacuums that clear neurotransmitters out of the extracellular space. This complexity arises in part from the core biophysical properties of these transporters, which are capable of generating different types of ionic currents. The additional levels of complexity comes from the fact that their residence time on the membrane, their trafficking from intracellular compartments and their kinetics can be modulated at different levels, including transcriptional, epigenetic, translational and post-translational levels. All these forms of modulation can change across species, cell types and brain regions. Since these regulatory mechanisms also change over time, their efficacy likely follows the metabolic state of a given neuron or astrocyte. The knowledge accumulated over the last few years and the growth of novel experimental approaches will undoubtedly provide new insights into cell-specific changes in the way the activity of neurotransmitter transporters can control cell excitability and metabolism across the brain.

AUTHOR CONTRIBUTIONS

RMR and SLI wrote the manuscript. AS wrote the manuscript and coordinated the investigative team. All authors contributed to the article and approved the submitted version.

FUNDING

This work was supported by the Australian National Health and Medical Research Council Project grant APP1164494 to RMR, NIH grant R01 DA042565 to SLI, and NSF grants IOS1655365 and IOS2011998 to AS.

ACKNOWLEDGMENTS

We performed detailed PubMed searches to include information listed in **Tables 1–3**. We apologize to authors of any work we might have missed.

REFERENCES

Adkins, E. M., Samuvel, D. J., Fog, J. U., Eriksen, J., Jayanthi, L. D., Vaegter, C. B., et al. (2007). Membrane mobility and microdomain association of the dopamine transporter studied with fluorescence correlation spectroscopy and fluorescence recovery after photobleaching. *Biochemistry* 46, 10484–10497. doi: 10.1021/bi700429z

Adolph, O., Koster, S., Rath, M., Georgieff, M., Weigt, H. U., Engele, J., et al. (2007). Rapid increase of glial glutamate uptake via blockade of the protein kinase A pathway. *Glia* 55, 1699–1707. doi: 10.1002/glia.20583

Aggarwal, S., and Mortensen, O. V. (2017). Overview of monoamine transporters. *Curr. Protoc. Pharmacol.* 79, 12.16.1–12.16.17. doi: 10.1002/cpph.32

Al Awabdh, S., Gupta-Agarwal, S., Sheehan, D. F., Muir, J., Norkett, R., Twelvetrees, A. E., et al. (2016). Neuronal activity mediated regulation of glutamate transporter GLT-1 surface diffusion in rat astrocytes in dissociated and slice cultures. *Glia* 64, 1252–1264. doi: 10.1002/glia.22997

Anderson, B. B., Chen, G., Gutman, D. A., and Ewing, A. G. (1998). Dopamine levels of two classes of vesicles are differentially depleted by amphetamine. *Brain Res.* 788, 294–301. doi: 10.1016/s0006-8993(98)00040-7

Anderson, C. M., and Swanson, R. A. (2000). Astrocyte glutamate transport: review of properties, regulation, and physiological functions. *Glia* 32, 1–14. doi: 10.1002/1098-1136(200010)32:1<1::aid-glia10>3.0.co;2-w

Anderson, J. G., Cooney, P. T., and Erikson, K. M. (2007). Brain manganese accumulation is inversely related to gamma-amino butyric acid uptake in male and female rats. *Toxicol. Sci.* 95, 188–195. doi: 10.1093/toxsci/kfl130

Anderson, J. G., Fordahl, S. C., Cooney, P. T., Weaver, T. L., Colyer, C. L., and Erikson, K. M. (2008). Manganese exposure alters extracellular GABA, GABA receptor and transporter protein and mRNA levels in the developing rat brain. *Neurotoxicology* 29, 1044–1053. doi: 10.1016/j.neuro.2008.08.002

Arriza, J. L., Fairman, W. A., Wadiche, J. I., Murdoch, G. H., Kavanaugh, M. P., and Amara, S. G. (1994). Functional comparisons of three glutamate transporter subtypes cloned from human motor cortex. *J. Neurosci.* 14, 5559–5569. doi: 10.1523/jneurosci.14-09-05559.1994

Assaife-Lopes, N., Sousa, V. C., Pereira, D. B., Ribeiro, J. A., Chao, M. V., and Sebastiao, A. M. (2010). Activation of adenosine A2A receptors induces TrkB translocation and increases BDNF-mediated phospho-TrkB localization in lipid rafts: implications for neuromodulation. *J. Neurosci.* 30, 8468–8480. doi: 10.1523/jneurosci.5695-09.2010

Bagley, E. E., Gerke, M. B., Vaughan, C. W., Hack, S. P., and Christie, M. J. (2005). GABA transporter currents activated by protein kinase A excite midbrain neurons during opioid withdrawal. *Neuron* 45, 433–445. doi: 10.1016/j.neuron.2004.12.049

Bagley, E. E., Hacker, J., Chefer, V. I., Mallet, C., McNally, G. P., Chieng, B. C., et al. (2011). Drug-induced GABA transporter currents enhance GABA release to induce opioid withdrawal behaviors. *Nat. Neurosci.* 14, 1548–1554. doi: 10.1038/nn.2940

Bahena-Trujillo, R., and Arias-Montano, J. A. (1999). [3H] gamma-aminobutyric acid transport in rat substantia nigra pars reticulata synaptosomes: pharmacological characterization and phorbol ester-induced inhibition. *Neurosci. Lett.* 274, 119–122. doi: 10.1016/s0304-3940(99)00692-8

Bailey, C. G., Ryan, R. M., Thoeng, A. D., Ng, C., King, K., Vanslambrouck, J. M., et al. (2011). Loss-of-function mutations in the glutamate transporter SLC1A1 cause human dicarboxylic aminoaciduria. *J. Clin. Invest.* 121, 446–453. doi: 10.1172/jci44474

Barakat, L., and Bordey, A. (2002). GAT-1 and reversible GABA transport in Bergmann glia in slices. *J. Neurophysiol.* 88, 1407–1419. doi: 10.1152/jn.2002.88.3.1407

Barbaresi, P., Gazzanelli, G., and Malatesta, M. (2001). gamma-Aminobutyric acid transporters in the cat periaqueductal gray: a light and electron microscopic immunocytochemical study. *J. Comp. Neurol.* 429, 337–354. doi: 10.1002/1096-9861(20000108)429:2<337::aid-cne12>3.0.co;2-z

Bassan, M., Liu, H., Madsen, K. L., Armsen, W., Zhou, J., Desilva, T., et al. (2008). Interaction between the glutamate transporter GLT1b and the synaptic PDZ domain protein PICK1. *Eur. J. Neurosci.* 27, 66–82. doi: 10.1111/j.1460-9568.2007.05986.x

Baumann, M. H., Ayestas, M. A., Dersch, C. M., Brockington, A., Rice, K. C., and Rothman, R. B. (2000). Effects of phentermine and fenfluramine on extracellular dopamine and serotonin in rat nucleus accumbens: therapeutic implications. *Synapse* 36, 102–113. doi: 10.1002/(sici)1098-2396(200005)36:2<102::aid-syn3>3.0.co;2-#

Beckman, M. L., Bernstein, E. M., and Quick, M. W. (1998). Protein kinase C regulates the interaction between a GABA transporter and syntaxin 1A. *J. Neurosci.* 18, 6103–6112. doi: 10.1523/jneurosci.18-16-06103.1998

Beckman, M. L., Bernstein, E. M., and Quick, M. W. (1999). Multiple G protein-coupled receptors initiate protein kinase C redistribution of GABA transporters in hippocampal neurons. *J. Neurosci.* 19:RC9.

Behrens, P. F., Franz, P., Woodman, B., Lindenberg, K. S., and Landwehrmeyer, G. B. (2002). Impaired glutamate transport and glutamate-glutamine cycling: downstream effects of the Huntington mutation. *Brain* 125, 1908–1922. doi: 10.1093/brain/awf180

Bellini, S., Fleming, K. E., De, M., McCauley, J. P., Petroccione, M. A., D'Brant, L. Y., et al. (2018). Neuronal glutamate transporters control dopaminergic signaling and compulsive behaviors. *J. Neurosci.* 38, 937–961. doi: 10.1523/jneurosci.1906-17.2017

Benediktsson, A. M., Marrs, G. S., Tu, J. C., Worley, P. F., Rothstein, J. D., Bergles, D. E., et al. (2012). Neuronal activity regulates glutamate transporter dynamics in developing astrocytes. *Glia* 60, 175–188. doi: 10.1002/glia.21249

Berger, U. V., DeSilva, T. M., Chen, W., and Rosenberg, P. A. (2005). Cellular and subcellular mRNA localization of glutamate transporter isoforms GLT1a and GLT1b in rat brain by in situ hybridization. *J. Comp. Neurol.* 492, 78–89. doi: 10.1002/cne.20737

Bergles, D. E., Tzingounis, A. V., and Jahr, C. E. (2002). Comparison of coupled and uncoupled currents during glutamate uptake by GLT-1 transporters. *J. Neurosci.* 22, 10153–10162. doi: 10.1523/jneurosci.22-23-10153.2002

Bermingham, D. P., and Blakely, R. D. (2016). Kinase-dependent regulation of monoamine neurotransmitter transporters. *Pharmacol. Rev.* 68, 888–953. doi: 10.1124/pr.115.012260

Bernabe, A., Mendez, J. A., Hernandez-Kelly, L. C., and Ortega, A. (2003). Regulation of the Na+-dependent glutamate/aspartate transporter in rodent cerebellar astrocytes. *Neurochem. Res.* 28, 1843–1849.

Bernardinelli, Y., Randall, J., Janett, E., Nikonenko, I., Konig, S., Jones, E. V., et al. (2014). Activity-dependent structural plasticity of perisynaptic astrocytic domains promotes excitatory synapse stability. *Curr. Biol.* 24, 1679–1688. doi: 10.1016/j.cub.2014.06.025

Bernstein, E. M., and Quick, M. W. (1999). Regulation of gamma-aminobutyric acid (GABA) transporters by extracellular GABA. *J. Biol. Chem.* 274, 889–895. doi: 10.1074/jbc.274.2.889

Berry, C. B., Hayes, D., Murphy, A., Wiessner, M., Rauen, T., and McBean, G. J. (2005). Differential modulation of the glutamate transporters GLT1, GLAST and EAAC1 by docosahexaenoic acid. *Brain Res.* 1037, 123–133. doi: 10.1016/j.brainres.2005.01.008

Bhat, S., El-Kasaby, A., Freissmuth, M., and Sucic, S. (2020). Functional and biochemical consequences of disease variants in neurotransmitter transporters: a special emphasis on folding and trafficking deficits. *Pharmacol. Ther.* 2020:107785. doi: 10.1016/j.pharmthera.2020.107785

Binda, F., Dipace, C., Bowton, E., Robertson, S. D., Lute, B. J., Fog, J. U., et al. (2008). Syntaxin 1A interaction with the dopamine transporter promotes amphetamine-induced dopamine efflux. *Mol. Pharmacol.* 74, 1101–1108. doi: 10.1124/mol.108.048447

Bjerggaard, C., Fog, J. U., Hastrup, H., Madsen, K., Loland, C. J., Javitch, J. A., et al. (2004). Surface targeting of the dopamine transporter involves discrete epitopes in the distal C terminus but does not require canonical PDZ domain interactions. *J. Neurosci.* 24, 7024–7036. doi: 10.1523/jneurosci.1863-04.2004

Boddum, K., Jensen, T. P., Magloire, V., Kristiansen, U., Rusakov, D. A., Pavlov, I., et al. (2016). Astrocytic GABA transporter activity modulates excitatory neurotransmission. *Nat. Commun.* 7:13572.

Bohmer, C., Philippin, M., Rajamanickam, J., Mack, A., Broer, S., Palmada, M., et al. (2004). Stimulation of the EAAT4 glutamate transporter by SGK protein kinase isoforms and PKB. *Biochem. Biophys. Res. Commun.* 324, 1242–1248. doi: 10.1016/j.bbrc.2004.09.193

Bolan, E. A., Kivell, B., Jaligam, V., Oz, M., Jayanthi, L. D., Han, Y., et al. (2007). D2 receptors regulate dopamine transporter function via an extracellular signal-regulated kinases 1 and 2-dependent and phosphoinositide 3 kinase-independent mechanism. *Mol. Pharmacol.* 71, 1222–1232. doi: 10.1124/mol.106.027763

Boudanova, E., Navaroli, D. M., and Melikian, H. E. (2008a). Amphetamine-induced decreases in dopamine transporter surface expression are protein kinase C-independent. *Neuropharmacology* 54, 605–612. doi: 10.1016/j.neuropharm.2007.11.007

Boudanova, E., Navaroli, D. M., Stevens, Z., and Melikian, H. E. (2008b). Dopamine transporter endocytic determinants: carboxy terminal residues critical for basal and PKC-stimulated internalization. *Mol. Cell Neurosci.* 39, 211–217. doi: 10.1016/j.mcn.2008.06.011

Boudker, O., Ryan, R. M., Yernool, D., Shimamoto, K., and Gouaux, E. (2007). Coupling substrate and ion binding to extracellular gate of a sodium-dependent aspartate transporter. *Nature* 445, 387–393. doi: 10.1038/nature05455

Bowton, E., Saunders, C., Reddy, I. A., Campbell, N. G., Hamilton, P. J., Henry, L. K., et al. (2014). SLC6A3 coding variant Ala559Val found in two autism probands alters dopamine transporter function and trafficking. *Transl. Psychiatry* 4:e464. doi: 10.1038/tp.2014.90

Brosnan, J. T., and Brosnan, M. E. (2013). Glutamate: a truly functional amino acid. *Amino Acids* 45, 413–418. doi: 10.1007/s00726-012-1280-4

Bruijn, L. I., Becher, M. W., Lee, M. K., Anderson, K. L., Jenkins, N. A., Copeland, N. G., et al. (1997). ALS-linked SOD1 mutant G85R mediates damage to astrocytes and promotes rapidly progressive disease with SOD1-containing inclusions. *Neuron* 18, 327–338. doi: 10.1016/s0896-6273(00)80272-x

Bruns, D., Engert, F., and Lux, H. D. (1993). A fast activating presynaptic reuptake current during serotonergic transmission in identified neurons of Hirudo. *Neuron* 10, 559–572. doi: 10.1016/0896-6273(93)90159-o

Bull, N. D., and Barnett, N. L. (2002). Antagonists of protein kinase C inhibit rat retinal glutamate transport activity in situ. *J. Neurochem.* 81, 472–480. doi: 10.1046/j.1471-4159.2002.00819.x

Butchbach, M. E., Tian, G., Guo, H., and Lin, C. L. (2004). Association of excitatory amino acid transporters, especially EAAT2, with cholesterol-rich lipid raft

microdomains: importance for excitatory amino acid transporter localization and function. *J. Biol. Chem.* 279, 34388–34396. doi: 10.1074/jbc.m403938200

Cammack, J. N., Rakhilin, S. V., and Schwartz, E. A. (1994). A GABA transporter operates asymmetrically and with variable stoichiometry. *Neuron* 13, 949–960. doi: 10.1016/0896-6273(94)90260-7

Cammack, J. N., and Schwartz, E. A. (1996). Channel behavior in a gamma-aminobutyrate transporter. *Proc. Natl. Acad. Sci. U.S.A.* 93, 723–727. doi: 10.1073/pnas.93.2.723

Campbell, N. G., Shekar, A., Aguilar, J. I., Peng, D., Navratna, V., Yang, D., et al. (2019). Structural, functional, and behavioral insights of dopamine dysfunction revealed by a deletion in SLC6A3. *Proc. Natl. Acad. Sci. U.S.A.* 116, 3853–3862. doi: 10.1073/pnas.1816247116

Canul-Tec, J. C., Assal, R., Cirri, E., Legrand, P., Brier, S., Chamot-Rooke, J., et al. (2017). Structure and allosteric inhibition of excitatory amino acid transporter 1. *Nature* 544, 446–451. doi: 10.1038/nature22064

Carneiro, A. M., Ingram, S. L., Beaulieu, J. M., Sweeney, A., Amara, S. G., Thomas, S. M., et al. (2002). The multiple LIM domain-containing adaptor protein Hic-5 synaptically colocalizes and interacts with the dopamine transporter. *J. Neurosci.* 22, 7045–7054. doi: 10.1523/jneurosci.22-16-07045.2002

Carvelli, L., Blakely, R. D., and DeFelice, L. J. (2008). Dopamine transporter/syntaxin 1A interactions regulate transporter channel activity and dopaminergic synaptic transmission. *Proc. Natl. Acad. Sci. U.S.A.* 105, 14192–14197. doi: 10.1073/pnas.0802214105

Carvelli, L., McDonald, P. W., Blakely, R. D., and DeFelice, L. J. (2004). Dopamine transporters depolarize neurons by a channel mechanism. *Proc. Natl. Acad. Sci. U.S.A.* 101, 16046–16051. doi: 10.1073/pnas.0403299101

Carvelli, L., Moron, J. A., Kahlig, K. M., Ferrer, J. V., Sen, N., Lechleiter, J. D., et al. (2002). PI 3-kinase regulation of dopamine uptake. *J. Neurochem.* 81, 859–869. doi: 10.1046/j.1471-4159.2002.00892.x

Casado, M., Bendahan, A., Zafra, F., Danbolt, N. C., Aragon, C., Gimenez, C., et al. (1993). Phosphorylation and modulation of brain glutamate transporters by protein kinase C. *J. Biol. Chem.* 268, 27313–27317. doi: 10.1016/s0021-9258(19)74251-3

Castillo, S. O., Baffi, J. S., Palkovits, M., Goldstein, D. S., Kopin, I. J., Witta, J., et al. (1998). Dopamine biosynthesis is selectively abolished in substantia nigra/ventral tegmental area but not in hypothalamic neurons in mice with targeted disruption of the Nurr1 gene. *Mol. Cell Neurosci.* 11, 36–46. doi: 10.1006/mcne.1998.0673

Cater, R. J., Vandenberg, R. J., and Ryan, R. M. (2014). The domain interface of the human glutamate transporter EAAT1 mediates chloride permeation. *Biophys. J.* 107, 621–629. doi: 10.1016/j.bpj.2014.05.046

Cater, R. J., Vandenberg, R. J., and Ryan, R. M. (2016). Tuning the ion selectivity of glutamate transporter-associated uncoupled conductances. *J. Gen. Physiol.* 148, 13–24. doi: 10.1085/jgp.201511556

Cervinski, M. A., Foster, J. D., and Vaughan, R. A. (2005). Psychoactive substrates stimulate dopamine transporter phosphorylation and down-regulation by cocaine-sensitive and protein kinase C-dependent mechanisms. *J. Biol. Chem.* 280, 40442–40449. doi: 10.1074/jbc.m501969200

Chan, P. H., Kerlan, R., and Fishman, R. A. (1983). Reductions of gamma-aminobutyric acid and glutamate uptake and (Na+ + K+)-ATPase activity in brain slices and synaptosomes by arachidonic acid. *J. Neurochem.* 40, 309–316. doi: 10.1111/j.1471-4159.1983.tb11284.x

Chang, M. Y., Lee, S. H., Kim, J. H., Lee, K. H., Kim, Y. S., Son, H., et al. (2001). Protein kinase C-mediated functional regulation of dopamine transporter is not achieved by direct phosphorylation of the dopamine transporter protein. *J. Neurochem.* 77, 754–761. doi: 10.1046/j.1471-4159.2001.00284.x

Chaudhry, F. A., Lehre, K. P., van Lookeren Campagne, M., Ottersen, O. P., Danbolt, N. C., and Storm-Mathisen, J. (1995). Glutamate transporters in glial plasma membranes: highly differentiated localizations revealed by quantitative ultrastructural immunocytochemistry. *Neuron* 15, 711–720. doi: 10.1016/0896-6273(95)90158-2

Chen, I., Pant, S., Wu, Q., Cater, R., Sobti, M., Vandenberg, R. J., et al. (2021). Glutamate transporters contain a conserved chloride channel with two hydrophobic gates. *bioRxiv* [Preprint], doi: 10.1101/2020.05.25.115360

Chen, N., and Reith, M. E. (2000). Structure and function of the dopamine transporter. *Eur. J. Pharmacol.* 405, 329–339.

Chen, R., Daining, C. P., Sun, H., Fraser, R., Stokes, S. L., Leitges, M., et al. (2013). Protein kinase Cbeta is a modulator of the dopamine D2 autoreceptor-activated trafficking of the dopamine transporter. *J. Neurochem.* 125, 663–672. doi: 10.1111/jnc.12229

Chen, R., Furman, C. A., Zhang, M., Kim, M. N., Gereau, R. W. T., Leitges, M., et al. (2009). Protein kinase Cbeta is a critical regulator of dopamine transporter trafficking and regulates the behavioral response to amphetamine in mice. *J. Pharmacol. Exp. Ther.* 328, 912–920. doi: 10.1124/jpet.108.147959

Chen, T., Tanaka, M., Wang, Y., Sha, S., Furuya, K., Chen, L., et al. (2017). Neurosteroid dehydroepiandrosterone enhances activity and trafficking of astrocytic GLT-1 via sigma1 receptor-mediated PKC activation in the hippocampal dentate gyrus of rats. *Glia* 65, 1491–1503. doi: 10.1002/glia.23175

Chen, W., Aoki, C., Mahadomrongkul, V., Gruber, C. E., Wang, G. J., Blitzblau, R., et al. (2002). Expression of a variant form of the glutamate transporter GLT1 in neuronal cultures and in neurons and astrocytes in the rat brain. *J. Neurosci.* 22, 2142–2152. doi: 10.1523/jneurosci.22-06-02142.2002

Chen, W., Mahadomrongkul, V., Berger, U. V., Bassan, M., DeSilva, T., Tanaka, K., et al. (2004). The glutamate transporter GLT1a is expressed in excitatory axon terminals of mature hippocampal neurons. *J. Neurosci.* 24, 1136–1148. doi: 10.1523/jneurosci.1586-03.2004

Cheng, C., Glover, G., Banker, G., and Amara, S. G. (2002). A novel sorting motif in the glutamate transporter excitatory amino acid transporter 3 directs its targeting in Madin-Darby canine kidney cells and hippocampal neurons. *J. Neurosci.* 22, 10643–10652. doi: 10.1523/jneurosci.22-24-10643.2002

Cheng, M. H., Torres-Salazar, D., Gonzalez-Suarez, A. D., Amara, S. G., and Bahar, I. (2017). Substrate transport and anion permeation proceed through distinct pathways in glutamate transporters. *eLife* 6:e25850.

Chi, L., and Reith, M. E. (2003). Substrate-induced trafficking of the dopamine transporter in heterologously expressing cells and in rat striatal synaptosomal preparations. *J. Pharmacol. Exp. Ther.* 307, 729–736. doi: 10.1124/jpet.103.055095

Chiu, C. S., Jensen, K., Sokolova, I., Wang, D., Li, M., Deshpande, P., et al. (2002). Number, density, and surface/cytoplasmic distribution of GABA transporters at presynaptic structures of knock-in mice carrying GABA transporter subtype 1-green fluorescent protein fusions. *J. Neurosci.* 22, 10251–10266. doi: 10.1523/jneurosci.22-23-10251.2002

Chivukula, A. S., Suslova, M., Kortzak, D., Kovermann, P., and Fahlke, C. (2020). Functional consequences of SLC1A3 mutations associated with episodic ataxia 6. *Hum. Mutat.* 41, 1892–1905. doi: 10.1002/humu.24089

Choi, J. K., and Kim, Y. J. (2008). Epigenetic regulation and the variability of gene expression. *Nat. Genet.* 40, 141–147. doi: 10.1038/ng.2007.58

Choi, K. D., Jen, J. C., Choi, S. Y., Shin, J. H., Kim, H. S., Kim, H. J., et al. (2017). Late-onset episodic ataxia associated with SLC1A3 mutation. *J. Hum. Genet.* 62, 443–446. doi: 10.1038/jhg.2016.137

Chowdhury, H. H., Kreft, M., and Zorec, R. (2002). Rapid insulin-induced exocytosis in white rat adipocytes. *Pflugers Arch.* 445, 352–356. doi: 10.1007/s00424-002-0938-2

Clark, J. A., Deutch, A. Y., Gallipoli, P. Z., and Amara, S. G. (1992). Functional expression and CNS distribution of a beta-alanine-sensitive neuronal GABA transporter. *Neuron* 9, 337–348. doi: 10.1016/0896-6273(92)90172-a

Conradt, M., and Stoffel, W. (1997). Inhibition of the high-affinity brain glutamate transporter GLAST-1 via direct phosphorylation. *J. Neurochem.* 68, 1244–1251. doi: 10.1046/j.1471-4159.1997.68031244.x

Conradt, M., Storck, T., and Stoffel, W. (1995). Localization of N-glycosylation sites and functional role of the carbohydrate units of GLAST-1, a cloned rat brain L-glutamate/L-aspartate transporter. *Eur. J. Biochem.* 229, 682–687. doi: 10.1111/j.1432-1033.1995.0682j.x

Copeland, B. J., Vogelsberg, V., Neff, N. H., and Hadjiconstantinou, M. (1996). Protein kinase C activators decrease dopamine uptake into striatal synaptosomes. *J. Pharmacol. Exp. Ther.* 277, 1527–1532.

Cordeiro, J. M., Meireles, S. M., Vale, M. G., Oliveira, C. R., and Goncalves, P. P. (2000). Ca(2+) regulation of the carrier-mediated gamma-aminobutyric acid release from isolated synaptic plasma membrane vesicles. *Neurosci. Res.* 38, 385–395. doi: 10.1016/s0168-0102(00)00193-0

Corey, J. L., Davidson, N., Lester, H. A., Brecha, N., and Quick, M. W. (1994). Protein kinase C modulates the activity of a cloned gamma-aminobutyric acid transporter expressed in *Xenopus oocytes* via regulated subcellular

redistribution of the transporter. *J. Biol. Chem.* 269, 14759–14767. doi: 10.1016/s0021-9258(17)36690-5

Cremona, M. L., Matthies, H. J., Pau, K., Bowton, E., Speed, N., Lute, B. J., et al. (2011). Flotillin-1 is essential for PKC-triggered endocytosis and membrane microdomain localization of DAT. *Nat. Neurosci.* 14, 469–477. doi: 10.1038/nn.2781

Cristovao-Ferreira, S., Navarro, G., Brugarolas, M., Perez-Capote, K., Vaz, S. H., Fattorini, G., et al. (2013). A1R-A2AR heteromers coupled to Gs and G i/0 proteins modulate GABA transport into astrocytes. *Purinerg. Signal.* 9, 433–449. doi: 10.1007/s11302-013-9364-5

Cristovao-Ferreira, S., Vaz, S. H., Ribeiro, J. A., and Sebastiao, A. M. (2009). Adenosine A2A receptors enhance GABA transport into nerve terminals by restraining PKC inhibition of GAT-1. *J. Neurochem.* 109, 336–347. doi: 10.1111/j.1471-4159.2009.05963.x

Dabir, D. V., Robinson, M. B., Swanson, E., Zhang, B., Trojanowski, J. Q., Lee, V. M., et al. (2006). Impaired glutamate transport in a mouse model of tau pathology in astrocytes. *J. Neurosci.* 26, 644–654. doi: 10.1523/jneurosci.3861-05.2006

Dall'Igna, O. P., Bobermin, L. D., Souza, D. O., and Quincozes-Santos, A. (2013). Riluzole increases glutamate uptake by cultured C6 astroglial cells. *Int. J. Dev. Neurosci.* 31, 482–486. doi: 10.1016/j.ijdevneu.2013.06.002

Danbolt, N. C. (2001). Glutamate uptake. *Prog. Neurobiol.* 65, 1–105.

Danbolt, N. C., Storm-Mathisen, J., and Kanner, B. I. (1992). An [Na+ + K+]coupled L-glutamate transporter purified from rat brain is located in glial cell processes. *Neuroscience* 51, 295–310. doi: 10.1016/0306-4522(92)90316-t

Daniels, G. M., and Amara, S. G. (1999). Regulated trafficking of the human dopamine transporter. Clathrin-mediated internalization and lysosomal degradation in response to phorbol esters. *J. Biol. Chem.* 274, 35794–35801. doi: 10.1074/jbc.274.50.35794

Davis, K. E., Straff, D. J., Weinstein, E. A., Bannerman, P. G., Correale, D. M., Rothstein, J. D., et al. (1998). Multiple signaling pathways regulate cell surface expression and activity of the excitatory amino acid carrier 1 subtype of Glu transporter in C6 glioma. *J. Neurosci.* 18, 2475–2485. doi: 10.1523/jneurosci.18-07-02475.1998

Dehnes, Y., Chaudhry, F. A., Ullensvang, K., Lehre, K. P., Storm-Mathisen, J., and Danbolt, N. C. (1998). The glutamate transporter EAAT4 in rat cerebellar Purkinje cells: a glutamate-gated chloride channel concentrated near the synapse in parts of the dendritic membrane facing astroglia. *J. Neurosci.* 18, 3606–3619. doi: 10.1523/jneurosci.18-10-03606.1998

Deken, S. L., Beckman, M. L., Boos, L., and Quick, M. W. (2000). Transport rates of GABA transporters: regulation by the N-terminal domain and syntaxin 1A. *Nat. Neurosci.* 3, 998–1003. doi: 10.1038/79939

Deken, S. L., Wang, D., and Quick, M. W. (2003). Plasma membrane GABA transporters reside on distinct vesicles and undergo rapid regulated recycling. *J. Neurosci.* 23, 1563–1568. doi: 10.1523/jneurosci.23-05-01563.2003

Delgado-Acevedo, C., Estay, S. F., Radke, A. K., Sengupta, A., Escobar, A. P., Henriquez-Belmar, F., et al. (2019). Behavioral and synaptic alterations relevant to obsessive-compulsive disorder in mice with increased EAAT3 expression. *Neuropsychopharmacology* 44, 1163–1173. doi: 10.1038/s41386-018-0302-7

DiCarlo, G. E., Aguilar, J. I., Matthies, H. J., Harrison, F. E., Bundschuh, K. E., West, A., et al. (2019). Autism-linked dopamine transporter mutation alters striatal dopamine neurotransmission and dopamine-dependent behaviors. *J. Clin. Invest.* 129, 3407–3419. doi: 10.1172/jci127411

Divito, C. B., Borowski, J. E., Glasgow, N. G., Gonzalez-Suarez, A. D., Torres-Salazar, D., Johnson, J. W., et al. (2017). Glial and neuronal glutamate transporters differ in the Na(+) requirements for activation of the substrate-independent anion conductance. *Front. Mol. Neurosci.* 10:150. doi: 10.3389/fnmol.2017.00150

Dodd, S., Carvalho, A. F., Puri, B. K., Maes, M., Bortolasci, C. C., Morris, G., et al. (2020). Trace amine-associated receptor 1 (TAAR1): a new drug target for psychiatry? *Neurosci. Biobehav. Rev.* 120, 537–541. doi: 10.1016/j.neubiorev.2020.09.028

Doolen, S., and Zahniser, N. R. (2001). Protein tyrosine kinase inhibitors alter human dopamine transporter activity in *Xenopus oocytes*. *J. Pharmacol. Exp. Ther.* 296, 931–938.

Dowd, L. A., and Robinson, M. B. (1996). Rapid stimulation of EAAC1-mediated Na+-dependent L-glutamate transport activity in C6 glioma cells by phorbol ester. *J. Neurochem.* 67, 508–516. doi: 10.1046/j.1471-4159.1996.67020508.x

Drejer, J., Meier, E., and Schousboe, A. (1983). Novel neuron-related regulatory mechanisms for astrocytic glutamate and GABA high affinity uptake. *Neurosci. Lett.* 37, 301–306. doi: 10.1016/0304-3940(83)90448-2

Eckstein-Ludwig, U., Fei, J., and Schwarz, W. (1999). Inhibition of uptake, steady-state currents, and transient charge movements generated by the neuronal GABA transporter by various anticonvulsant drugs. *Br. J. Pharmacol.* 128, 92–102. doi: 10.1038/sj.bjp.0702794

Egawa, K., and Fukuda, A. (2013). Pathophysiological power of improper tonic GABA(A) conductances in mature and immature models. *Front. Neural Circ.* 7:170. doi: 10.3389/fncir.2013.00170

Eliasof, S., and Jahr, C. E. (1996). Retinal glial cell glutamate transporter is coupled to an anionic conductance. *Proc. Natl. Acad. Sci. U.S.A.* 93, 4153–4158. doi: 10.1073/pnas.93.9.4153

Eriksen, J., Rasmussen, S. G., Rasmussen, T. N., Vaegter, C. B., Cha, J. H., Zou, M. F., et al. (2009). Visualization of dopamine transporter trafficking in live neurons by use of fluorescent cocaine analogs. *J. Neurosci.* 29, 6794–6808. doi: 10.1523/jneurosci.4177-08.2009

Espinoza-Rojo, M., Lopez-Bayghen, E., and Ortega, A. (2000). GLAST: gene expression regulation by phorbol esters. *Neuroreport* 11, 2827–2832. doi: 10.1097/00001756-200008210-00043

Fairman, W. A., Vandenberg, R. J., Arriza, J. L., Kavanaugh, M. P., and Amara, S. G. (1995). An excitatory amino-acid transporter with properties of a ligand-gated chloride channel. *Nature* 375, 599–603. doi: 10.1038/375599a0

Fan, H. P., Fan, F. J., Bao, L., and Pei, G. (2006). SNAP-25/syntaxin 1A complex functionally modulates neurotransmitter gamma-aminobutyric acid reuptake. *J. Biol. Chem.* 281, 28174–28184. doi: 10.1074/jbc.m601382200

Fan, S., Xian, X., Li, L., Yao, X., Hu, Y., Zhang, M., et al. (2018). Ceftriaxone improves cognitive function and upregulates GLT-1-related glutamate-glutamine cycle in APP/PS1 mice. *J. Alzheimers Dis.* 66, 1731–1743. doi: 10.3233/jad-180708

Fang, H., Huang, Y., and Zuo, Z. (2006). Enhancement of substrate-gated Cl-currents via rat glutamate transporter EAAT4 by PMA. *Am. J. Physiol. Cell Physiol.* 290, C1334–C1340.

Fang, Q., Hu, W. W., Wang, X. F., Yang, Y., Lou, G. D., Jin, M. M., et al. (2014). Histamine up-regulates astrocytic glutamate transporter 1 and protects neurons against ischemic injury. *Neuropharmacology* 77, 156–166. doi: 10.1016/j.neuropharm.2013.06.012

Farhan, H., Korkhov, V. M., Paulitschke, V., Dorostkar, M. M., Scholze, P., Kudlacek, O., et al. (2004). Two discontinuous segments in the carboxyl terminus are required for membrane targeting of the rat gamma-aminobutyric acid transporter-1 (GAT1). *J. Biol. Chem.* 279, 28553–28563. doi: 10.1074/jbc.m307325200

Fattorini, G., Melone, M., and Conti, F. (2020). A reappraisal of GAT-1 localization in Neocortex. *Front. Cell Neurosci.* 14:9. doi: 10.3389/fncel.2020.00009

Ferrer-Martinez, A., Felipe, A., Nicholson, B., Casado, J., Pastor-Anglada, M., and McGivan, J. (1995). Induction of the high-affinity Na(+)-dependent glutamate transport system XAG- by hypertonic stress in the renal epithelial cell line NBL-1. *Biochem. J.* 310(Pt 2), 689–692. doi: 10.1042/bj3100689

Figiel, M., Maucher, T., Rozyczka, J., Bayatti, N., and Engele, J. (2003). Regulation of glial glutamate transporter expression by growth factors. *Exp. Neurol.* 183, 124–135. doi: 10.1016/s0014-4886(03)00134-1

Fischer, J. F., and Cho, A. K. (1979). Chemical release of dopamine from striatal homogenates: evidence for an exchange diffusion model. *J. Pharmacol. Exp. Ther.* 208, 203–209.

Fischer, K. D., Houston, A. C. W., Desai, R. I., Doyle, M. R., Bergman, J., Mian, M., et al. (2018). Behavioral phenotyping and dopamine dynamics in mice with conditional deletion of the glutamate transporter GLT-1 in neurons: resistance to the acute locomotor effects of amphetamine. *Psychopharmacology* 235, 1371–1387. doi: 10.1007/s00213-018-4848-1

Fog, J. U., Khoshbouei, H., Holy, M., Owens, W. A., Vaegter, C. B., Sen, N., et al. (2006). Calmodulin kinase II interacts with the dopamine transporter C terminus to regulate amphetamine-induced reverse transport. *Neuron* 51, 417–429. doi: 10.1016/j.neuron.2006.06.028

Foster, J. D., Adkins, S. D., Lever, J. R., and Vaughan, R. A. (2008). Phorbol ester induced trafficking-independent regulation and enhanced phosphorylation of the dopamine transporter associated with membrane rafts and cholesterol. *J. Neurochem.* 105, 1683–1699. doi: 10.1111/j.1471-4159.2008.05262.x

Foster, J. D., Yang, J. W., Moritz, A. E., Challasivakanaka, S., Smith, M. A., Holy, M., et al. (2012). Dopamine transporter phosphorylation site threonine 53 regulates substrate reuptake and amphetamine-stimulated efflux. *J. Biol. Chem.* 287, 29702–29712. doi: 10.1074/jbc.m112.367706

Fournier, K. M., Gonzalez, M. I., and Robinson, M. B. (2004). Rapid trafficking of the neuronal glutamate transporter, EAAC1: evidence for distinct trafficking pathways differentially regulated by protein kinase C and platelet-derived growth factor. *J. Biol. Chem.* 279, 34505–34513. doi: 10.1074/jbc.m404032200

Furman, C. A., Chen, R., Guptaroy, B., Zhang, M., Holz, R. W., and Gnegy, M. (2009). Dopamine and amphetamine rapidly increase dopamine transporter trafficking to the surface: live-cell imaging using total internal reflection fluorescence microscopy. *J. Neurosci.* 29, 3328–3336. doi: 10.1523/jneurosci.5386-08.2009

Furness, D. N., Dehnes, Y., Akhtar, A. Q., Rossi, D. J., Hamann, M., Grutle, N. J., et al. (2008). A quantitative assessment of glutamate uptake into hippocampal synaptic terminals and astrocytes: new insights into a neuronal role for excitatory amino acid transporter 2 (EAAT2). *Neuroscience* 157, 80–94. doi: 10.1016/j.neuroscience.2008.08.043

Galli, A., DeFelice, L. J., Duke, B. J., Moore, K. R., and Blakely, R. D. (1995). Sodium-dependent norepinephrine-induced currents in norepinephrine-transporter-transfected HEK-293 cells blocked by cocaine and antidepressants. *J. Exp. Biol.* 198, 2197–2212.

Gamboa, C., and Ortega, A. (2002). Insulin-like growth factor-1 increases activity and surface levels of the GLAST subtype of glutamate transporter. *Neurochem. Int.* 40, 397–403. doi: 10.1016/s0197-0186(01)00106-1

Ganel, R., and Crosson, C. E. (1998). Modulation of human glutamate transporter activity by phorbol ester. *J. Neurochem.* 70, 993–1000. doi: 10.1046/j.1471-4159.1998.70030993.x

Garaeva, A. A., Guskov, A., Slotboom, D. J., and Paulino, C. (2019). A one-gate elevator mechanism for the human neutral amino acid transporter ASCT2. *Nat. Commun.* 10:3427.

Garaeva, A. A., Oostergetel, G. T., Gati, C., Guskov, A., Paulino, C., and Slotboom, D. J. (2018). Cryo-EM structure of the human neutral amino acid transporter ASCT2. *Nat. Struct. Mol. Biol.* 25, 515–521. doi: 10.1038/s41594-018-0076-y

Garcia, B. G., Wei, Y., Moron, J. A., Lin, R. Z., Javitch, J. A., and Galli, A. (2005). Akt is essential for insulin modulation of amphetamine-induced human dopamine transporter cell-surface redistribution. *Mol. Pharmacol.* 68, 102–109. doi: 10.1124/mol.104.009092

Garcia-Tardon, N., Gonzalez-Gonzalez, I. M., Martinez-Villarreal, J., Fernandez-Sanchez, E., Gimenez, C., and Zafra, F. (2012). Protein kinase C (PKC)-promoted endocytosis of glutamate transporter GLT-1 requires ubiquitin ligase Nedd4-2-dependent ubiquitination but not phosphorylation. *J. Biol. Chem.* 287, 19177–19187. doi: 10.1074/jbc.m112.355909

Gavrilov, N., Golyagina, I., Brazhe, A., Scimemi, A., Turlapov, V., and Semyanov, A. (2018). Astrocytic coverage of dendritic spines, dendritic shafts, and axonal boutons in hippocampal neuropil. *Front. Cell Neurosci.* 12:248. doi: 10.3389/fncel.2018.00248

Geerlings, A., Nunez, E., Lopez-Corcuera, B., and Aragon, C. (2001). Calcium- and syntaxin 1-mediated trafficking of the neuronal glycine transporter GLYT2. *J. Biol. Chem.* 276, 17584–17590. doi: 10.1074/jbc.m010602200

Gegelashvili, G., Civenni, G., Racagni, G., Danbolt, N. C., Schousboe, I., and Schousboe, A. (1996). Glutamate receptor agonists up-regulate glutamate transporter GLAST in astrocytes. *Neuroreport* 8, 261–265. doi: 10.1097/00001756-199612200-00052

Gegelashvili, G., and Schousboe, A. (1997). High affinity glutamate transporters: regulation of expression and activity. *Mol. Pharmacol.* 52, 6–15. doi: 10.1124/mol.52.1.6

Genoud, C., Quairiaux, C., Steiner, P., Hirling, H., Welker, E., and Knott, G. W. (2006). Plasticity of astrocytic coverage and glutamate transporter expression in adult mouse cortex. *PLoS Biol.* 4:e343. doi: 10.1371/journal.pbio.0040343

German, C. L., Baladi, M. G., McFadden, L. M., Hanson, G. R., and Fleckenstein, A. E. (2015). Regulation of the dopamine and vesicular monoamine transporters: pharmacological targets and implications for disease. *Pharmacol. Rev.* 67, 1005–1024. doi: 10.1124/pr.114.010397

Ginsberg, S. D., Martin, L. J., and Rothstein, J. D. (1995). Regional deafferentation down-regulates subtypes of glutamate transporter proteins. *J. Neurochem.* 65, 2800–2803. doi: 10.1046/j.1471-4159.1995.65062800.x

Goldberg, N. R., Beuming, T., Soyer, O. S., Goldstein, R. A., Weinstein, H., and Javitch, J. A. (2003). Probing conformational changes in neurotransmitter transporters: a structural context. *Eur. J. Pharmacol.* 479, 3–12. doi: 10.1016/j.ejphar.2003.08.052

Goncalves, P. P., Carvalho, A. P., and Vale, M. G. (1997). Regulation of [gamma-3H]aminobutyric acid transport by Ca^{2+} in isolated synaptic plasma membrane vesicles. *Brain Res. Mol. Brain Res.* 51, 106–114. doi: 10.1016/s0169-328x(97)00223-4

Goncalves, P. P., Meireles, S. M., and Vale, M. G. (1999). Regulation of the gamma-aminobutyric acid transporter activity by protein phosphatases in synaptic plasma membranes. *Neurosci. Res.* 33, 41–47. doi: 10.1016/s0168-0102(98)00107-2

Gonzalez, M. I., Kazanietz, M. G., and Robinson, M. B. (2002). Regulation of the neuronal glutamate transporter excitatory amino acid carrier-1 (EAAC1) by different protein kinase C subtypes. *Mol. Pharmacol.* 62, 901–910. doi: 10.1124/mol.62.4.901

Gonzalez, M. I., Lopez-Colom, A. M., and Ortega, A. (1999). Sodium-dependent glutamate transport in Muller glial cells: regulation by phorbol esters. *Brain Res.* 831, 140–145. doi: 10.1016/s0006-8993(99)01438-9

Gonzalez-Gonzalez, I. M., Garcia-Tardon, N., Cubelos, B., Gimenez, C., and Zafra, F. (2008a). The glutamate transporter GLT1b interacts with the scaffold protein PSD-95. *J. Neurochem.* 105, 1834–1848. doi: 10.1111/j.1471-4159.2008.05281.x

Gonzalez-Gonzalez, I. M., Garcia-Tardon, N., Gimenez, C., and Zafra, F. (2008b). PKC-dependent endocytosis of the GLT1 glutamate transporter depends on ubiquitylation of lysines located in a C-terminal cluster. *Glia* 56, 963–974. doi: 10.1002/glia.20670

Goodspeed, K., Pérez-Palma, E., Iqbal, S., Cooper, D., Scimemi, A., Johannesen, K. M., et al. (2020). Current knowledge of SLC6A1-related neurodevelopmental disorders. *Brain Commun.* 2:fcaa170.

Gorentla, B. K., and Vaughan, R. A. (2005). Differential effects of dopamine and psychoactive drugs on dopamine transporter phosphorylation and regulation. *Neuropharmacology* 49, 759–768. doi: 10.1016/j.neuropharm.2005.08.011

Gowrishankar, R., Hahn, M. K., and Blakely, R. D. (2014). Good riddance to dopamine: roles for the dopamine transporter in synaptic function and dopamine-associated brain disorders. *Neurochem. Int.* 73, 42–48. doi: 10.1016/j.neuint.2013.10.016

Granas, C., Ferrer, J., Loland, C. J., Javitch, J. A., and Gether, U. (2003). N-terminal truncation of the dopamine transporter abolishes phorbol ester- and substance P receptor-stimulated phosphorylation without impairing transporter internalization. *J. Biol. Chem.* 278, 4990–5000. doi: 10.1074/jbc.m205058200

Grewer, C., Balani, P., Weidenfeller, C., Bartusel, T., Tao, Z., and Rauen, T. (2005). Individual subunits of the glutamate transporter EAAC1 homotrimer function independently of each other. *Biochemistry* 44, 11913–11923. doi: 10.1021/bi050987n

Grewer, C., Madani Mobarekeh, S. A., Watzke, N., Rauen, T., and Schaper, K. (2001). Substrate translocation kinetics of excitatory amino acid carrier 1 probed with laser-pulse photolysis of a new photolabile precursor of D-aspartic acid. *Biochemistry* 40, 232–240. doi: 10.1021/bi0015919

Grewer, C., and Rauen, T. (2005). Electrogenic glutamate transporters in the CNS: molecular mechanism, pre-steady-state kinetics, and their impact on synaptic signaling. *J. Membr. Biol.* 203, 1–20. doi: 10.1007/s00232-004-0731-6

Grewer, C., Watzke, N., Wiessner, M., and Rauen, T. (2000). Glutamate translocation of the neuronal glutamate transporter EAAC1 occurs within milliseconds. *Proc. Natl. Acad. Sci. U.S.A.* 97, 9706–9711. doi: 10.1073/pnas.160170397

Gu, H., Wall, S. C., and Rudnick, G. (1994). Stable expression of biogenic amine transporters reveals differences in inhibitor sensitivity, kinetics, and ion dependence. *J. Biol. Chem.* 269, 7124–7130. doi: 10.1016/s0021-9258(17)37256-3

Guillet, B. A., Velly, L. J., Canolle, B., Masmejean, F. M., Nieoullon, A. L., and Pisano, P. (2005). Differential regulation by protein kinases of activity and cell surface expression of glutamate transporters in neuron-enriched cultures. *Neurochem. Int.* 46, 337–346. doi: 10.1016/j.neuint.2004.10.006

Gulley, J. M., Doolen, S., and Zahniser, N. R. (2002). Brief, repeated exposure to substrates down-regulates dopamine transporter function in *Xenopus oocytes* in vitro and rat dorsal striatum in vivo. *J. Neurochem.* 83, 400–411. doi: 10.1046/j.1471-4159.2002.01133.x

Guskov, A., Jensen, S., Faustino, I., Marrink, S. J., and Slotboom, D. J. (2016). Coupled binding mechanism of three sodium ions and aspartate in the glutamate transporter homologue GltTk. *Nat. Commun.* 7:13420.

Hagiwara, T., Tanaka, K., Takai, S., Maeno-Hikichi, Y., Mukainaka, Y., and Wada, K. (1996). Genomic organization, promoter analysis, and chromosomal localization of the gene for the mouse glial high-affinity glutamate transporter Slc1a3. *Genomics* 33, 508–515. doi: 10.1006/geno.1996.0226

Hancock, J. F. (2006). Lipid rafts: contentious only from simplistic standpoints. *Nat. Rev. Mol. Cell Biol.* 7, 456–462. doi: 10.1038/nrm1925

Hansen, F. H., Skjørringe, T., Yasmeen, S., Arends, N. V., Sahai, M. A., Erreger, K., et al. (2014). Missense dopamine transporter mutations associate with adult parkinsonism and ADHD. *J. Clin. Invest.* 124, 3107–3120. doi: 10.1172/jci73778

Harsing, L. G. Jr., Solyom, S., and Salamon, C. (2001). The role of glycineB binding site and glycine transporter (GlyT1) in the regulation of [3H]GABA and [3H]glycine release in the rat brain. *Neurochem. Res.* 26, 915–923.

Haugeto, O., Ullensvang, K., Levy, L. M., Chaudhry, F. A., Honore, T., Nielsen, M., et al. (1996). Brain glutamate transporter proteins form homomultimers. *J. Biol. Chem.* 271, 27715–27722. doi: 10.1074/jbc.271.44.27715

Hefendehl, J. K., LeDue, J., Ko, R. W., Mahler, J., Murphy, T. H., and MacVicar, B. A. (2016). Mapping synaptic glutamate transporter dysfunction in vivo to regions surrounding Abeta plaques by iGluSnFR two-photon imaging. *Nat. Commun.* 7:13441.

Hepp, R., Perraut, M., Chasserot-Golaz, S., Galli, T., Aunis, D., Langley, K., et al. (1999). Cultured glial cells express the SNAP-25 analogue SNAP-23. *Glia* 27, 181–187. doi: 10.1002/(sici)1098-1136(199908)27:2<181::aid-glia8>3.0.co;2-9

Herborg, F., Andreassen, T. F., Berlin, F., Loland, C. J., and Gether, U. (2018). Neuropsychiatric disease-associated genetic variants of the dopamine transporter display heterogeneous molecular phenotypes. *J. Biol. Chem.* 293, 7250–7262. doi: 10.1074/jbc.RA118.001753

Herde, M. K., Bohmbach, K., Domingos, C., Vana, N., Komorowska-Muller, J. A., Passlick, S., et al. (2020). Local efficacy of glutamate uptake decreases with synapse size. *Cell Rep.* 32:108182. doi: 10.1016/j.celrep.2020.108182

Hertz, L., Bock, E., and Schousboe, A. (1978). GFA content, glutamate uptake and activity of glutamate metabolizing enzymes in differentiating mouse astrocytes in primary cultures. *Dev. Neurosci.* 1, 226–238. doi: 10.1159/000112577

Heshmati, M., Christoffel, D. J., LeClair, K., Cathomas, F., Golden, S. A., Aleyasin, H., et al. (2020). Depression and social defeat stress are associated with inhibitory synaptic changes in the nucleus accumbens. *J. Neurosci.* 40, 6228–6233. doi: 10.1523/jneurosci.2568-19.2020

Higuera-Matas, A., Miguens, M., Coria, S. M., Assis, M. A., Borcel, E., del Olmo, N., et al. (2012). Sex-specific disturbances of the glutamate/GABA balance in the hippocampus of adult rats subjected to adolescent cannabinoid exposure. *Neuropharmacology* 62, 1975–1984. doi: 10.1016/j.neuropharm.2011.12.028

Hoffman, A. F., Lupica, C. R., and Gerhardt, G. A. (1998). Dopamine transporter activity in the substantia nigra and striatum assessed by high-speed chronoamperometric recordings in brain slices. *J. Pharmacol. Exp. Ther.* 287, 487–496.

Hofmann, K., Duker, M., Fink, T., Lichter, P., and Stoffel, W. (1994). Human neutral amino acid transporter ASCT1: structure of the gene (SLC1A4) and localization to chromosome 2p13-p15. *Genomics* 24, 20–26. doi: 10.1006/geno.1994.1577

Holmseth, S., Scott, H. A., Real, K., Lehre, K. P., Leergaard, T. B., Bjaalie, J. G., et al. (2009). The concentrations and distributions of three C-terminal variants of the GLT1 (EAAT2; slc1a2) glutamate transporter protein in rat brain tissue suggest differential regulation. *Neuroscience* 162, 1055–1071. doi: 10.1016/j.neuroscience.2009.03.048

Holton, K. L., Loder, M. K., and Melikian, H. E. (2005). Nonclassical, distinct endocytic signals dictate constitutive and PKC-regulated neurotransmitter transporter internalization. *Nat. Neurosci.* 8, 881–888. doi: 10.1038/nn1478

Hong, W. C., and Amara, S. G. (2010). Membrane cholesterol modulates the outward facing conformation of the dopamine transporter and alters cocaine binding. *J. Biol. Chem.* 285, 32616–32626. doi: 10.1074/jbc.m110.150565

Hong, W. C., and Amara, S. G. (2013). Differential targeting of the dopamine transporter to recycling or degradative pathways during amphetamine- or PKC-regulated endocytosis in dopamine neurons. *FASEB J.* 27, 2995–3007. doi: 10.1096/fj.12-218727

Hoover, B. R., Everett, C. V., Sorkin, A., and Zahniser, N. R. (2007). Rapid regulation of dopamine transporters by tyrosine kinases in rat neuronal preparations. *J. Neurochem.* 101, 1258–1271. doi: 10.1111/j.1471-4159.2007.04522.x

Horton, N., and Quick, M. W. (2001). Syntaxin 1A up-regulates GABA transporter expression by subcellular redistribution. *Mol. Membr. Biol.* 18, 39–44. doi: 10.1080/09687680010029383

Hu, J., Fei, J., Reutter, W., and Fan, H. (2011). Involvement of sialic acid in the regulation of gamma–aminobutyric acid uptake activity of gamma-aminobutyric acid transporter 1. *Glycobiology* 21, 329–339. doi: 10.1093/glycob/cwq166

Hu, J., and Quick, M. W. (2008). Substrate-mediated regulation of gamma-aminobutyric acid transporter 1 in rat brain. *Neuropharmacology* 54, 309–318. doi: 10.1016/j.neuropharm.2007.09.013

Huang, H. T., Liao, C. K., Chiu, W. T., and Tzeng, S. F. (2017). Ligands of peroxisome proliferator-activated receptor-alpha promote glutamate transporter-1 endocytosis in astrocytes. *Int. J. Biochem. Cell Biol.* 86, 42–53. doi: 10.1016/j.biocel.2017.03.008

Hudson, B. D., Hebert, T. E., and Kelly, M. E. (2010). Physical and functional interaction between CB1 cannabinoid receptors and beta2-adrenoceptors. *Br. J. Pharmacol.* 160, 627–642. doi: 10.1111/j.1476-5381.2010.00681.x

Huff, R. A., Vaughan, R. A., Kuhar, M. J., and Uhl, G. R. (1997). Phorbol esters increase dopamine transporter phosphorylation and decrease transport Vmax. *J. Neurochem.* 68, 225–232. doi: 10.1046/j.1471-4159.1997.68010225.x

Imoukhuede, P. I., Moss, F. J., Michael, D. J., Chow, R. H., and Lester, H. A. (2009). Ezrin mediates tethering of the gamma-aminobutyric acid transporter GAT1 to actin filaments via a C-terminal PDZ-interacting domain. *Biophys. J.* 96, 2949–2960. doi: 10.1016/j.bpj.2008.11.070

Ingram, S. L., Prasad, B. M., and Amara, S. G. (2002). Dopamine transporter-mediated conductances increase excitability of midbrain dopamine neurons. *Nat. Neurosci.* 5, 971–978. doi: 10.1038/nn920

Jacob, C. P., Koutsilieri, E., Bartl, J., Neuen-Jacob, E., Arzberger, T., Zander, N., et al. (2007). Alterations in expression of glutamatergic transporters and receptors in sporadic Alzheimer's disease. *J. Alzheimers Dis.* 11, 97–116. doi: 10.3233/jad-2007-11113

Jansson, L. C., Louhivuori, L., Wigren, H. K., Nordstrom, T., Louhivuori, V., Castren, M. L., et al. (2013). Effect of glutamate receptor antagonists on migrating neural progenitor cells. *Eur. J. Neurosci.* 37, 1369–1382. doi: 10.1111/ejn.12152

Jayanthi, L. D., Vargas, G., and DeFelice, L. J. (2002). Characterization of cocaine and antidepressant-sensitive norepinephrine transporters in rat placental trophoblasts. *Br. J. Pharmacol.* 135, 1927–1934. doi: 10.1038/sj.bjp.0704658

Ji, Y. F., Xu, S. M., Zhu, J., Wang, X. X., and Shen, Y. (2011). Insulin increases glutamate transporter GLT1 in cultured astrocytes. *Biochem. Biophys. Res. Commun.* 405, 691–696. doi: 10.1016/j.bbrc.2011.01.105

Ji, Y. F., Zhou, L., Xie, Y. J., Xu, S. M., Zhu, J., Teng, P., et al. (2013). Upregulation of glutamate transporter GLT-1 by mTOR-Akt-NF-small ka, CyrillicB cascade in astrocytic oxygen-glucose deprivation. *Glia* 61, 1959–1975. doi: 10.1002/glia.22566

Jiang, N. W., Wang, D. J., Xie, Y. J., Zhou, L., Su, L. D., Li, H., et al. (2016). Downregulation of glutamate transporter EAAT4 by conditional knockout of rheb1 in Cerebellar Purkinje cells. *Cerebellum* 15, 314–321. doi: 10.1007/s12311-015-0701-9

Johnson, L. A., Furman, C. A., Zhang, M., Guptaroy, B., and Gnegy, M. E. (2005a). Rapid delivery of the dopamine transporter to the plasmalemmal membrane upon amphetamine stimulation. *Neuropharmacology* 49, 750–758. doi: 10.1016/j.neuropharm.2005.08.018

Johnson, L. A., Guptaroy, B., Lund, D., Shamban, S., and Gnegy, M. E. (2005b). Regulation of amphetamine-stimulated dopamine efflux by protein kinase C beta. *J. Biol. Chem.* 280, 10914–10919. doi: 10.1074/jbc.m413887200

Jones, K. T., Zhen, J., and Reith, M. E. (2012). Importance of cholesterol in dopamine transporter function. *J. Neurochem.* 123, 700–715. doi: 10.1111/jnc.12007

Jones, S. R., Gainetdinov, R. R., Wightman, R. M., and Caron, M. G. (1998). Mechanisms of amphetamine action revealed in mice lacking the dopamine transporter. *J. Neurosci.* 18, 1979–1986. doi: 10.1523/jneurosci.18-06-01979.1998

Jones, S. R., Joseph, J. D., Barak, L. S., Caron, M. G., and Wightman, R. M. (1999). Dopamine neuronal transport kinetics and effects of amphetamine. *J. Neurochem.* 73, 2406–2414. doi: 10.1046/j.1471-4159.1999.0732406.x

Kahlig, K. M., Binda, F., Khoshbouei, H., Blakely, R. D., McMahon, D. G., Javitch, J. A., et al. (2005). Amphetamine induces dopamine efflux through a dopamine transporter channel. *Proc. Natl. Acad. Sci. U.S.A.* 102, 3495–3500. doi: 10.1073/pnas.0407737102

Kahlig, K. M., and Galli, A. (2003). Regulation of dopamine transporter function and plasma membrane expression by dopamine, amphetamine, and cocaine. *Eur. J. Pharmacol.* 479, 153–158. doi: 10.1016/j.ejphar.2003.08.065

Kahlig, K. M., Javitch, J. A., and Galli, A. (2004). Amphetamine regulation of dopamine transport. Combined measurements of transporter currents and transporter imaging support the endocytosis of an active carrier. *J. Biol. Chem.* 279, 8966–8975.

Kalandadze, A., Wu, Y., and Robinson, M. B. (2002). Protein kinase C activation decreases cell surface expression of the GLT-1 subtype of glutamate transporter. Requirement of a carboxyl-terminal domain and partial dependence on serine 486. *J. Biol. Chem.* 277, 45741–45750. doi: 10.1074/jbc.m203771200

Kang, M., Ryu, J., Kim, J. H., Na, H., Zuo, Z., and Do, S. H. (2010). Corticosterone decreases the activity of rat glutamate transporter type 3 expressed in *Xenopus oocytes*. *Steroids* 75, 1113–1118. doi: 10.1016/j.steroids.2010.07.003

Kanner, B. I. (2003). Transmembrane domain I of the gamma-aminobutyric acid transporter GAT-1 plays a crucial role in the transition between cation leak and transport modes. *J. Biol. Chem.* 278, 3705–3712. doi: 10.1074/jbc.m210525200

Karam, C. S., and Javitch, J. A. (2018). Phosphorylation of the amino terminus of the dopamine transporter: regulatory mechanisms and implications for amphetamine action. *Adv. Pharmacol.* 82, 205–234. doi: 10.1016/bs.apha.2017.09.002

Karatas-Wulf, U., Koepsell, H., Bergert, M., Sonnekes, S., and Kugler, P. (2009). Protein kinase C-dependent trafficking of glutamate transporters excitatory amino acid carrier 1 and glutamate transporter 1b in cultured cerebellar granule cells. *Neuroscience* 161, 794–805. doi: 10.1016/j.neuroscience.2009.04.017

Karki, P., Webb, A., Smith, K., Johnson, J. Jr., Lee, K., Son, D. S., et al. (2014). Yin Yang 1 is a repressor of glutamate transporter EAAT2, and it mediates manganese-induced decrease of EAAT2 expression in astrocytes. *Mol. Cell Biol.* 34, 1280–1289. doi: 10.1128/mcb.01176-13

Karylowski, O., Zeigerer, A., Cohen, A., and McGraw, T. E. (2004). GLUT4 is retained by an intracellular cycle of vesicle formation and fusion with endosomes. *Mol. Biol. Cell* 15, 870–882. doi: 10.1091/mbc.e03-07-0517

Kerkerian, L., Dusticier, N., and Nieoullon, A. (1987). Modulatory effect of dopamine on high-affinity glutamate uptake in the rat striatum. *J. Neurochem.* 48, 1301–1306. doi: 10.1111/j.1471-4159.1987.tb05661.x

Keynan, S., and Kanner, B. I. (1988). gamma-Aminobutyric acid transport in reconstituted preparations from rat brain: coupled sodium and chloride fluxes. *Biochemistry* 27, 12–17. doi: 10.1021/bi00401a003

Khoshbouei, H., Sen, N., Guptaroy, B., Johnson, L., Lund, D., Gnegy, M. E., et al. (2004). N-terminal phosphorylation of the dopamine transporter is required for amphetamine-induced efflux. *PLoS Biol.* 2:E78. doi: 10.1371/journal.pbio.0020078

Kilty, J. E., Lorang, D., and Amara, S. G. (1991). Cloning and expression of a cocaine-sensitive rat dopamine transporter. *Science* 254, 578–579. doi: 10.1126/science.1948035

Kim, D. U., Kim, M. K., Cho, Y. W., Kim, Y. S., Kim, W. J., Lee, M. G., et al. (2011). Association of a synonymous GAT3 polymorphism with antiepileptic drug pharmacoresistance. *J. Hum. Genet.* 56, 640–646. doi: 10.1038/jhg.2011.73

Kim, S., Westphalen, R., Callahan, B., Hatzidimitriou, G., Yuan, J., and Ricaurte, G. A. (2000). Toward development of an in vitro model of methamphetamine-induced dopamine nerve terminal toxicity. *J. Pharmacol. Exp. Ther.* 293, 625–633.

Kimmel, H. L., Carroll, F. I., and Kuhar, M. J. (2000). Dopamine transporter synthesis and degradation rate in rat striatum and nucleus accumbens using RTI-76. *Neuropharmacology* 39, 578–585. doi: 10.1016/s0028-3908(99)00160-4

Kinney, G. A. (2005). GAT-3 transporters regulate inhibition in the neocortex. *J, Neurophysiol.* 94, 4533–4537. doi: 10.1152/jn.00420.2005

Kitayama, S., Dohi, T., and Uhl, G. R. (1994). Phorbol esters alter functions of the expressed dopamine transporter. *Eur. J. Pharmacol.* 268, 115–119. doi: 10.1016/0922-4106(94)90180-5

Kivell, B., Uzelac, Z., Sundaramurthy, S., Rajamanickam, J., Ewald, A., Chefer, V., et al. (2014). Salvinorin A regulates dopamine transporter function via a kappa opioid receptor and ERK1/2-dependent mechanism. *Neuropharmacology* 86, 228–240. doi: 10.1016/j.neuropharm.2014.07.016

Koch, H. P., Brown, R. L., and Larsson, H. P. (2007). The glutamate-activated anion conductance in excitatory amino acid transporters is gated independently by the individual subunits. *J. Neurosci.* 27, 2943–2947. doi: 10.1523/jneurosci.0118-07.2007

Kolen, B., Kortzak, D., Franzen, A., and Fahlke, C. (2020). An amino-terminal point mutation increases EAAT2 anion currents without affecting glutamate transport rates. *J. Biol. Chem.* 295, 14936–14947. doi: 10.1074/jbc.ra120.013704

Kovtun, O., Sakrikar, D., Tomlinson, I. D., Chang, J. C., Arzeta-Ferrer, X., Blakely, R. D., et al. (2015). Single-quantum-dot tracking reveals altered membrane dynamics of an attention-deficit/hyperactivity-disorder-derived dopamine transporter coding variant. *ACS Chem. Neurosci.* 6, 526–534. doi: 10.1021/cn500202c

Kristensen, A. S., Andersen, J., Jorgensen, T. N., Sorensen, L., Eriksen, J., Loland, C. J., et al. (2011). SLC6 neurotransmitter transporters: structure, function, and regulation. *Pharmacol. Rev.* 63, 585–640.

Krueger, B. K. (1990). Kinetics and block of dopamine uptake in synaptosomes from rat caudate nucleus. *J. Neurochem.* 55, 260–267. doi: 10.1111/j.1471-4159.1990.tb08847.x

Laughlin, T. M., Tram, K. V., Wilcox, G. L., and Birnbaum, A. K. (2002). Comparison of antiepileptic drugs tiagabine, lamotrigine, and gabapentin in mouse models of acute, prolonged, and chronic nociception. *J. Pharmacol. Exp. Ther.* 302, 1168–1175. doi: 10.1124/jpet.302.3.1168

Law, R. M., Stafford, A., and Quick, M. W. (2000). Functional regulation of gamma-aminobutyric acid transporters by direct tyrosine phosphorylation. *J. Biol. Chem.* 275, 23986–23991. doi: 10.1074/jbc.m910283199

Leary, G. P., Holley, D. C., Stone, E. F., Lyda, B. R., Kalachev, L. V., and Kavanaugh, M. P. (2011). The central cavity in trimeric glutamate transporters restricts ligand diffusion. *Proc. Natl. Acad. Sci. U.S.A.* 108, 14980–14985. doi: 10.1073/pnas.1108785108

Leary, G. P., Stone, E. F., Holley, D. C., and Kavanaugh, M. P. (2007). The glutamate and chloride permeation pathways are colocalized in individual neuronal glutamate transporter subunits. *J. Neurosci.* 27, 2938–2942. doi: 10.1523/jneurosci.4851-06.2007

Lee, F. J., Liu, F., Pristupa, Z. B., and Niznik, H. B. (2001). Direct binding and functional coupling of alpha-synuclein to the dopamine transporters accelerate dopamine-induced apoptosis. *FASEB J.* 15, 916–926. doi: 10.1096/fsb2fj000334com

Lee, F. J., Pei, L., Moszczynska, A., Vukusic, B., Fletcher, P. J., and Liu, F. (2007). Dopamine transporter cell surface localization facilitated by a direct interaction with the dopamine D2 receptor. *EMBO J.* 26, 2127–2136. doi: 10.1038/sj.emboj.7601656

Lee, G., Huang, Y., Washington, J. M., Briggs, N. W., and Zuo, Z. (2005). Carbamazepine enhances the activity of glutamate transporter type 3 via phosphatidylinositol 3-kinase. *Epilepsy Res.* 66, 145–153. doi: 10.1016/j.eplepsyres.2005.08.003

Lee, H. S., Bae, E. J., Yi, S. H., Shim, J. W., Jo, A. Y., Kang, J. S., et al. (2010). Foxa2 and Nurr1 synergistically yield A9 nigral dopamine neurons exhibiting improved differentiation, function, and cell survival. *Stem Cells* 28, 501–512.

Lee, K. H., Kim, M. Y., Kim, D. H., and Lee, Y. S. (2004). Syntaxin 1A and receptor for activated C kinase interact with the N-terminal region of human dopamine transporter. *Neurochem. Res.* 29, 1405–1409. doi: 10.1023/b:nere.0000026404.08779.43

Lehre, K. P., and Danbolt, N. C. (1998). The number of glutamate transporter subtype molecules at glutamatergic synapses: chemical and stereological quantification in young adult rat brain. *J. Neurosci.* 18, 8751–8757. doi: 10.1523/jneurosci.18-21-08751.1998

Lehre, K. P., Levy, L. M., Ottersen, O. P., Storm-Mathisen, J., and Danbolt, N. C. (1995). Differential expression of two glial glutamate transporters in the rat brain: quantitative and immunocytochemical observations. *J. Neurosci.* 15, 1835–1853. doi: 10.1523/jneurosci.15-03-01835.1995

Leng, K., Li, E., Eser, R., Piergies, A., Sit, R., Tan, M., et al. (2021). Molecular characterization of selectively vulnerable neurons in Alzheimer's disease. *Nat. Neurosci.* 24, 276–287.

Leonova, J., Thorlin, T., Aberg, N. D., Eriksson, P. S., Ronnback, L., and Hansson, E. (2001). Endothelin-1 decreases glutamate uptake in primary cultured rat astrocytes. *Am. J. Physiol. Cell Physiol.* 281, C1495–C1503.

Levy, L., Lehre, K., Walaas, S., Storm-Mathisen, J., and Danbolt, N. (1995). Down-regulation of glial glutamate transporters after glutamatergic denervation in the rat brain. *Eur. J. Neurosci.* 7, 2036–2041. doi: 10.1111/j.1460-9568.1995.tb00626.x

Levy, L. M., Lehre, K. P., Rolstad, B., and Danbolt, N. C. (1993). A monoclonal antibody raised against an [Na(+)+K+]coupled L-glutamate transporter purified from rat brain confirms glial cell localization. *FEBS Lett.* 317, 79–84. doi: 10.1016/0014-5793(93)81495-l

Levy, L. M., Warr, O., and Attwell, D. (1998). Stoichiometry of the glial glutamate transporter GLT-1 expressed inducibly in a Chinese hamster ovary cell line selected for low endogenous Na+-dependent glutamate uptake. *J. Neurosci.* 18, 9620–9628. doi: 10.1523/jneurosci.18-23-09620.1998

Li, L. B., Toan, S. V., Zelenaia, O., Watson, D. J., Wolfe, J. H., Rothstein, J. D., et al. (2006). Regulation of astrocytic glutamate transporter expression by Akt: evidence for a selective transcriptional effect on the GLT-1/EAAT2 subtype. *J. Neurochem.* 97, 759–771. doi: 10.1111/j.1471-4159.2006.03743.x

Li, M. H., Underhill, S. M., Reed, C., Phillips, T. J., Amara, S. G., and Ingram, S. L. (2017). Amphetamine and methamphetamine increase NMDAR-GluN2B synaptic currents in midbrain dopamine neurons. *Neuropsychopharmacology* 42, 1539–1547. doi: 10.1038/npp.2016.278

Li, S., Mallory, M., Alford, M., Tanaka, S., and Masliah, E. (1997). Glutamate transporter alterations in Alzheimer disease are possibly associated with abnormal APP expression. *J. Neuropathol. Exp. Neurol.* 56, 901–911. doi: 10.1097/00005072-199708000-00008

Lim, S. K., Park, M. J., Jung, H. K., Park, A. Y., Kim, D. I., Kim, J. C., et al. (2008). Bradykinin stimulates glutamate uptake via both B1R and B2R activation in a human retinal pigment epithelial cells. *Life Sci.* 83, 761–770. doi: 10.1016/j.lfs.2008.09.014

Lin, C. L., Tzingounis, A. V., Jin, L., Furuta, A., Kavanaugh, M. P., and Rothstein, J. D. (1998). Molecular cloning and expression of the rat EAAT4 glutamate transporter subtype. *Brain Res. Mol. Brain Res.* 63, 174–179. doi: 10.1016/s0169-328x(98)00256-3

Loder, M. K., and Melikian, H. E. (2003). The dopamine transporter constitutively internalizes and recycles in a protein kinase C-regulated manner in stably transfected PC12 cell lines. *J. Biol. Chem.* 278, 22168–22174. doi: 10.1074/jbc.m301845200

Lu, C.-C., and Hilgemann, D. W. (1999). GAT1 (GABA: Na+: Cl–) cotransport function: steady state studies in giant Xenopus oocyte membrane patches. *J. Gen. Physiol.* 114, 429–444. doi: 10.1085/jgp.114.3.429

Lushnikova, I., Skibo, G., Muller, D., and Nikonenko, I. (2009). Synaptic potentiation induces increased glial coverage of excitatory synapses in CA1 hippocampus. *Hippocampus* 19, 753–762. doi: 10.1002/hipo.20551

Lute, B. J., Khoshbouei, H., Saunders, C., Sen, N., Lin, R. Z., Javitch, J. A., et al. (2008). PI3K signaling supports amphetamine-induced dopamine efflux. *Biochem. Biophys. Res. Commun.* 372, 656–661. doi: 10.1016/j.bbrc.2008.05.091

MacAulay, N., Zeuthen, T., and Gether, U. (2002). Conformational basis for the Li(+)-induced leak current in the rat gamma-aminobutyric acid (GABA) transporter-1. *J. Physiol.* 544, 447–458. doi: 10.1113/jphysiol.2002.022897

Mager, S., Min, C., Henry, D. J., Chavkin, C., Hoffman, B. J., Davidson, N., et al. (1994). Conducting states of a mammalian serotonin transporter. *Neuron* 12, 845–859. doi: 10.1016/0896-6273(94)90337-9

Mager, S., Naeve, J., Quick, M., Labarca, C., Davidson, N., and Lester, H. A. (1993). Steady states, charge movements, and rates for a cloned GABA transporter expressed in *Xenopus oocytes*. *Neuron* 10, 177–188. doi: 10.1016/0896-6273(93)90309-f

Malik, A. R., and Willnow, T. E. (2019). Excitatory amino acid transporters in physiology and disorders of the central nervous system. *Int. J. Mol. Sci.* 20:5671. doi: 10.3390/ijms20225671

Maragakis, N. J., Dykes-Hoberg, M., and Rothstein, J. D. (2004). Altered expression of the glutamate transporter EAAT2b in neurological disease. *Ann. Neurol.* 55, 469–477. doi: 10.1002/ana.20003

Martinez-Lozada, Z., Guillem, A. M., and Robinson, M. B. (2016). Transcriptional regulation of glutamate transporters: from extracellular signals to transcription factors. *Adv. Pharmacol.* 76, 103–145.

Martins, R. S., de Freitas, I. G., Sathler, M. F., Martins, V., Schitine, C. S., da Silva Sampaio, L., et al. (2018). Beta-adrenergic receptor activation increases GABA uptake in adolescent mice frontal cortex: Modulation by cannabinoid receptor agonist WIN55,212-2. *Neurochem. Int.* 120, 182–190. doi: 10.1016/j.neuint.2018.08.011

Mason, J. N., Farmer, H., Tomlinson, I. D., Schwartz, J. W., Savchenko, V., DeFelice, L. J., et al. (2005). Novel fluorescence-based approaches for the study of biogenic amine transporter localization, activity, and regulation. *J. Neurosci. Methods* 143, 3–25. doi: 10.1016/j.jneumeth.2004.09.028

Matsusaki, M., Kishida, A., Stainton, N., Ansell, C. W. G., and Akashi, M. (2001). Synthesis and characterization of novel biodegradable polymers composed of hydroxycinnamic acid and D,L-lactic acid. *J. Appl. Polym. Sci.* 82, 2357–2364. doi: 10.1002/app.2085

Matthews, E. Jr., Rahnama-Vaghef, A., and Eskandari, S. (2009). Inhibitors of the γ-aminobutyric acid transporter 1 (GAT1) do not reveal a channel mode of conduction. *Neurochem. Intern.* 55, 732–740. doi: 10.1016/j.neuint.2009.07.005

Mazei-Robison, M. S., Couch, R. S., Shelton, R. C., Stein, M. A., and Blakely, R. D. (2005). Sequence variation in the human dopamine transporter gene in children with attention deficit hyperactivity disorder. *Neuropharmacology* 49, 724–736. doi: 10.1016/j.neuropharm.2005.08.003

McElvain, J. S., and Schenk, J. O. (1992). A multisubstrate mechanism of striatal dopamine uptake and its inhibition by cocaine. *Biochem. Pharmacol.* 43, 2189–2199. doi: 10.1016/0006-2952(92)90178-l

McGeer, P., McGeer, E., Scherer, U., and Singh, K. (1977). A glutamatergic corticostriatal path? *Brain Res.* 128, 369–373. doi: 10.1016/0006-8993(77)91003-4

McHugh, E. M., Zhu, W., Milgram, S., and Mager, S. (2004). The GABA transporter GAT1 and the MAGUK protein Pals1: interaction, uptake modulation, and coexpression in the brain. *Mol. Cell Neurosci.* 26, 406–417. doi: 10.1016/j.mcn.2004.03.006

McNair, L. F., Andersen, J. V., Aldana, B. I., Hohnholt, M. C., Nissen, J. D., Sun, Y., et al. (2019). Deletion of neuronal GLT-1 in mice reveals its role in synaptic glutamate homeostasis and mitochondrial function. *J. Neurosci.* 39, 4847–4863. doi: 10.1523/jneurosci.0894-18.2019

McNair, L. F., Andersen, J. V., Nissen, J. D., Sun, Y., Fischer, K. D., Hodgson, N. W., et al. (2020). Conditional knockout of GLT-1 in neurons leads to alterations in aspartate homeostasis and synaptic mitochondrial metabolism in Striatum and Hippocampus. *Neurochem. Res.* 45, 1420–1437. doi: 10.1007/s11064-020-03000-7

Medvedev, N., Popov, V., Henneberger, C., Kraev, I., Rusakov, D. A., and Stewart, M. G. (2014). Glia selectively approach synapses on thin dendritic spines. *Philos. Trans. R. Soc. Lond. B Biol. Sci.* 369:20140047. doi: 10.1098/rstb.2014.0047

Melikian, H. E., and Buckley, K. M. (1999). Membrane trafficking regulates the activity of the human dopamine transporter. *J. Neurosci.* 19, 7699–7710. doi: 10.1523/jneurosci.19-18-07699.1999

Melone, M., Barbaresi, P., Fattorini, G., and Conti, F. (2005). Neuronal localization of the GABA transporter GAT-3 in human cerebral cortex: a procedural artifact? *J. Chem. Neuroanat.* 30, 45–54. doi: 10.1016/j.jchemneu.2005.04.002

Melone, M., Bellesi, M., and Conti, F. (2009). Synaptic localization of GLT-1a in the rat somatic sensory cortex. *Glia* 57, 108–117. doi: 10.1002/glia.20744

Melone, M., Bellesi, M., Ducati, A., Iacoangeli, M., and Conti, F. (2011). Cellular and synaptic localization of EAAT2a in human cerebral cortex. *Front. Neuroanat.* 4:151. doi: 10.3389/fnana.2010.00151

Melone, M., Ciappelloni, S., and Conti, F. (2015). A quantitative analysis of cellular and synaptic localization of GAT-1 and GAT-3 in rat neocortex. *Brain Struct. Funct.* 220, 885–897. doi: 10.1007/s00429-013-0690-8

Melone, M., Ciriachi, C., Pietrobon, D., and Conti, F. (2019). Heterogeneity of Astrocytic and neuronal GLT-1 at cortical excitatory synapses, as revealed by its colocalization with Na+/K+-ATPase alpha isoforms. *Cereb. Cortex* 29, 3331–3350. doi: 10.1093/cercor/bhy203

Melone, M., Cozzi, A., Pellegrini-Giampietro, D. E., and Conti, F. (2003). Transient focal ischemia triggers neuronal expression of GAT-3 in the rat perilesional cortex. *Neurobiol. Dis.* 14, 120–132. doi: 10.1016/s0969-9961(03)00042-1

Mergy, M. A., Gowrishankar, R., Davis, G. L., Jessen, T. N., Wright, J., Stanwood, G. D., et al. (2014). Genetic targeting of the amphetamine and methylphenidate-sensitive dopamine transporter: on the path to an animal model of attention-deficit hyperactivity disorder. *Neurochem. Int.* 73, 56–70. doi: 10.1016/j.neuint.2013.11.009

Metzger, R. R., Haughey, H. M., Wilkins, D. G., Gibb, J. W., Hanson, G. R., and Fleckenstein, A. E. (2000). Methamphetamine-induced rapid decrease in dopamine transporter function: role of dopamine and hyperthermia. *J. Pharmacol. Exp. Ther.* 295, 1077–1085.

Meyer, T., Speer, A., Meyer, B., Sitte, W., Kuther, G., and Ludolph, A. C. (1996). The glial glutamate transporter complementary DNA in patients with amyotrophic lateral sclerosis. *Ann. Neurol.* 40, 456–459. doi: 10.1002/ana.410400317

Michaluk, P. H., Heller, J., and Rusakov, D. A. (2020). Rapid recycling of glutamate transporters on the astroglial surface. *bioRxiv* [Preprint], doi: 10.1101/2020.11.08.373233v1

Mick, E., and Faraone, S. V. (2009). Family and genetic association studies of bipolar disorder in children. *Child Adolesc. Psychiatr. Clin. N. Am.* 18, 441–453. doi: 10.1016/j.chc.2008.11.008

Mim, C., Balani, P., Rauen, T., and Grewer, C. (2005). The glutamate transporter subtypes EAAT4 and EAATs 1-3 transport glutamate with dramatically different kinetics and voltage dependence but share a common uptake mechanism. *J. Gen. Physiol.* 126, 571–589. doi: 10.1085/jgp.200509365

Minelli, A., Barbaresi, P., Reimer, R. J., Edwards, R. H., and Conti, F. (2001). The glial glutamate transporter GLT-1 is localized both in the vicinity of and at distance from axon terminals in the rat cerebral cortex. *Neuroscience* 108, 51–59. doi: 10.1016/s0306-4522(01)00375-x

Miranda, M., Dionne, K. R., Sorkina, T., and Sorkin, A. (2007). Three ubiquitin conjugation sites in the amino terminus of the dopamine transporter mediate protein kinase C-dependent endocytosis of the transporter. *Mol. Biol. Cell* 18, 313–323. doi: 10.1091/mbc.e06-08-0704

Mitrovic, A. D., Plesko, F., and Vandenberg, R. J. (2001). Zn(2+) inhibits the anion conductance of the glutamate transporter EEAT4. *J. Biol. Chem.* 276, 26071–26076. doi: 10.1074/jbc.m011318200

Mookherjee, P., Green, P. S., Watson, G. S., Marques, M. A., Tanaka, K., Meeker, K. D., et al. (2011). GLT-1 loss accelerates cognitive deficit onset in an Alzheimer's disease animal model. *J. Alzheimers Dis.* 26, 447–455. doi: 10.3233/jad-2011-110503

Moritz, A. E., Foster, J. D., Gorentla, B. K., Mazei-Robison, M. S., Yang, J. W., Sitte, H. H., et al. (2013). Phosphorylation of dopamine transporter serine 7 modulates cocaine analog binding. *J. Biol. Chem.* 288, 20–32. doi: 10.1074/jbc.m112.407874

Moron, J. A., Zakharova, I., Ferrer, J. V., Merrill, G. A., Hope, B., Lafer, E. M., et al. (2003). Mitogen-activated protein kinase regulates dopamine transporter surface expression and dopamine transport capacity. *J. Neurosci.* 23, 8480–8488. doi: 10.1523/jneurosci.23-24-08480.2003

Moss, F. J., Imoukhuede, P. I., Scott, K., Hu, J., Jankowsky, J. L., Quick, M. W., et al. (2009). GABA transporter function, oligomerization state, and anchoring: correlates with subcellularly resolved FRET. *J. Gen. Physiol.* 134, 489–521. doi: 10.1085/jgp.200910314

Moszczynska, A., Saleh, J., Zhang, H., Vukusic, B., Lee, F. J., and Liu, F. (2007). Parkin disrupts the alpha-synuclein/dopamine transporter interaction: consequences toward dopamine-induced toxicity. *J. Mol. Neurosci.* 32, 217–227. doi: 10.1007/s12031-007-0037-0

Mukainaka, Y., Tanaka, K., Hagiwara, T., and Wada, K. (1995). Molecular cloning of two glutamate transporter subtypes from mouse brain. *Biochim. Biophys. Acta* 1244, 233–237. doi: 10.1016/0304-4165(95)00062-g

Mundorf, M. L., Hochstetler, S. E., and Wightman, R. M. (1999). Amine weak bases disrupt vesicular storage and promote exocytosis in chromaffin cells. *J. Neurochem.* 73, 2397–2405. doi: 10.1046/j.1471-4159.1999.0732397.x

Murphy-Royal, C., Dupuis, J. P., Varela, J. A., Panatier, A., Pinson, B., Baufreton, J., et al. (2015). Surface diffusion of astrocytic glutamate transporters shapes synaptic transmission. *Nat. Neurosci.* 18, 219–226. doi: 10.1038/nn.3901

Nakayama, T., Kawakami, H., Tanaka, K., and Nakamura, S. (1996). Expression of three glutamate transporter subtype mRNAs in human brain regions and peripheral tissues. *Brain Res. Mol. Brain Res.* 36, 189–192. doi: 10.1016/0169-328x(95)00297-6

Navaroli, D. M., Stevens, Z. H., Uzelac, Z., Gabriel, L., King, M. J., Lifshitz, L. M., et al. (2011). The plasma membrane-associated GTPase Rin interacts with the dopamine transporter and is required for protein kinase C-regulated dopamine transporter trafficking. *J. Neurosci.* 31, 13758–13770. doi: 10.1523/jneurosci.2649-11.2011

Nirenberg, M. J., Chan, J., Pohorille, A., Vaughan, R. A., Uhl, G. R., Kuhar, M. J., et al. (1997). The dopamine transporter: comparative ultrastructure of dopaminergic axons in limbic and motor compartments of the nucleus accumbens. *J. Neurosci.* 17, 6899–6907. doi: 10.1523/jneurosci.17-18-06899.1997

Norregaard, L., and Gether, U. (2001). The monoamine neurotransmitter transporters: structure, conformational changes and molecular gating. *Curr. Opin. Drug Discov. Dev.* 4, 591–601.

O'Donovan, S. M., Sullivan, C. R., and McCullumsmith, R. E. (2017). The role of glutamate transporters in the pathophysiology of neuropsychiatric disorders. *NPJ Schizophr.* 3:32.

Otis, T. S., and Kavanaugh, M. P. (2000). Isolation of current components and partial reaction cycles in the glial glutamate transporter EAAT2. *J. Neurosci.* 20, 2749–2757. doi: 10.1523/jneurosci.20-08-02749.2000

Padovano, V., Massari, S., Mazzucchelli, S., and Pietrini, G. (2009). PKC induces internalization and retention of the EAAC1 glutamate transporter in recycling endosomes of MDCK cells. *Am. J. Physiol. Cell Physiol.* 297, C835–C844.

Page, G., Barc-Pain, S., Pontcharraud, R., Cante, A., Piriou, A., and Barrier, L. (2004). The up-regulation of the striatal dopamine transporter's activity by cAMP is PKA-, CaMK II- and phosphatase-dependent. *Neurochem. Int.* 45, 627–632. doi: 10.1016/j.neuint.2004.04.002

Pakulska, W. (2007). Influence of tiagabine on the antinociceptive action of morphine, metamizole and indomethacin in mice. *Acta Pol. Pharm.* 64, 263–270.

Palos, T. P., Ramachandran, B., Boado, R., and Howard, B. D. (1996). Rat C6 and human astrocytic tumor cells express a neuronal type of glutamate transporter. *Brain Res. Mol. Brain Res.* 37, 297–303. doi: 10.1016/0169-328x(95)00331-l

Parinejad, N., Peco, E., Ferreira, T., Stacey, S. M., and van Meyel, D. J. (2016). Disruption of an EAAT-mediated chloride channel in a *Drosophila* model of Ataxia. *J. Neurosci.* 36, 7640–7647. doi: 10.1523/jneurosci.0197-16.2016

Park, H. Y., Kim, J. H., Zuo, Z., and Do, S. H. (2008). Ethanol increases the activity of rat excitatory amino acid transporter type 4 expressed in *Xenopus oocytes*: role of protein kinase C and phosphatidylinositol 3-kinase. *Alcohol. Clin. Exp. Res.* 32, 348–354. doi: 10.1111/j.1530-0277.2007.00577.x

Park, S. J., Shin, H. J., Gu, B. W., Woo, K. I., Zuo, Z., Do, S. H., et al. (2015). Desflurane increased the activity of excitatory amino-acid carrier 1 (EAAC1) expressed in *Xenopus oocytes*. *Eur. J. Pharmacol.* 757, 84–89. doi: 10.1016/j.ejphar.2015.03.058

Parker, E. M., and Cubeddu, L. X. (1988). Comparative effects of amphetamine, phenylethylamine and related drugs on dopamine efflux, dopamine uptake and mazindol binding. *J. Pharmacol. Exp. Ther.* 245, 199–210.

Parpura, V., Fang, Y., Basarsky, T., Jahn, R., and Haydon, P. G. (1995). Expression of synaptobrevin II, cellubrevin and syntaxin but not SNAP-25 in cultured astrocytes. *FEBS Lett.* 377, 489–492. doi: 10.1016/0014-5793(95)01401-2

Patrushev, I., Gavrilov, N., Turlapov, V., and Semyanov, A. (2013). Subcellular location of astrocytic calcium stores favors extrasynaptic neuron-astrocyte communication. *Cell Calc.* 54, 343–349. doi: 10.1016/j.ceca.2013.08.003

Peacey, E., Miller, C. C., Dunlop, J., and Rattray, M. (2009). The four major N- and C-terminal splice variants of the excitatory amino acid transporter GLT-1 form cell surface homomeric and heteromeric assemblies. *Mol. Pharmacol.* 75, 1062–1073. doi: 10.1124/mol.108.052829

Peghini, P., Janzen, J., and Stoffel, W. (1997). Glutamate transporter EAAC-1-deficient mice develop dicarboxylic aminoaciduria and behavioral abnormalities but no neurodegeneration. *EMBO J.* 16, 3822–3832. doi: 10.1093/emboj/16.13.3822

Penmatsa, A., Wang, K. H., and Gouaux, E. (2013). X-ray structure of dopamine transporter elucidates antidepressant mechanism. *Nature* 503, 85–90. doi: 10.1038/nature12533

Penmatsa, A., Wang, K. H., and Gouaux, E. (2015). X-ray structures of *Drosophila* dopamine transporter in complex with Nisoxetine and Reboxetine. *Nat. Struct. Mol. Biol.* 22, 506–508. doi: 10.1038/nsmb.3029

Perego, C., Di Cairano, E. S., Ballabio, M., and Magnaghi, V. (2012). Neurosteroid allopregnanolone regulates EAAC1-mediated glutamate uptake and triggers actin changes in Schwann cells. *J. Cell Physiol.* 227, 1740–1751. doi: 10.1002/jcp.22898

Perez-Alvarez, A., Navarrete, M., Covelo, A., Martin, E. D., and Araque, A. (2014). Structural and functional plasticity of astrocyte processes and dendritic spine interactions. *J. Neurosci.* 34, 12738–12744. doi: 10.1523/jneurosci.2401-14.2014

Petr, G. T., Sun, Y., Frederick, N. M., Zhou, Y., Dhamne, S. C., Hameed, M. Q., et al. (2015). Conditional deletion of the glutamate transporter GLT-1 reveals

that astrocytic GLT-1 protects against fatal epilepsy while neuronal GLT-1 contributes significantly to glutamate uptake into synaptosomes. *J. Neurosci.* 35, 5187–5201. doi: 10.1523/jneurosci.4255-14.2015

Piani, D., Frei, K., Pfister, H. W., and Fontana, A. (1993). Glutamate uptake by astrocytes is inhibited by reactive oxygen intermediates but not by other macrophage-derived molecules including cytokines, leukotrienes or platelet-activating factor. *J. Neuroimmunol.* 48, 99–104. doi: 10.1016/0165-5728(93)90063-5

Picaud, S., Larsson, H. P., Wellis, D. P., Lecar, H., and Werblin, F. (1995). Cone photoreceptors respond to their own glutamate release in the tiger salamander. *Proc. Natl. Acad. Sci. U.S.A.* 92, 9417–9421. doi: 10.1073/pnas.92.20.9417

Pines, G., Danbolt, N. C., Bjoras, M., Zhang, Y., Bendahan, A., Eide, L., et al. (1992). Cloning and expression of a rat brain L-glutamate transporter. *Nature* 360, 464–467.

Plachez, C., Danbolt, N. C., and Recasens, M. (2000). Transient expression of the glial glutamate transporters GLAST and GLT in hippocampal neurons in primary culture. *J. Neurosci. Res.* 59, 587–593. doi: 10.1002/(sici)1097-4547(20000301)59:5<587::aid-jnr1>3.0.co;2-l

Pogun, S., Dawson, V., and Kuhar, M. J. (1994). Nitric oxide inhibits 3H-glutamate transport in synaptosomes. *Synapse* 18, 21–26. doi: 10.1002/syn.890180104

Pogun, S., and Kuhar, M. J. (1994). Regulation of neurotransmitter reuptake by nitric oxide. *Ann. N.Y. Acad. Sci.* 738, 305–315. doi: 10.1111/j.1749-6632.1994.tb21816.x

Porton, B., Greenberg, B. D., Askland, K., Serra, L. M., Gesmonde, J., Rudnick, G., et al. (2013). Isoforms of the neuronal glutamate transporter gene, SLC1A1/EAAC1, negatively modulate glutamate uptake: relevance to obsessive-compulsive disorder. *Transl. Psychiatry* 3:e259. doi: 10.1038/tp.2013.35

Pristupa, Z. B., McConkey, F., Liu, F., Man, H. Y., Lee, F. J., Wang, Y. T., et al. (1998). Protein kinase-mediated bidirectional trafficking and functional regulation of the human dopamine transporter. *Synapse* 30, 79–87. doi: 10.1002/(sici)1098-2396(199809)30:1<79::aid-syn10>3.0.co;2-k

Quick, M. W., Corey, J. L., Davidson, N., and Lester, H. A. (1997). Second messengers, trafficking-related proteins, and amino acid residues that contribute to the functional regulation of the rat brain GABA transporter GAT1. *J. Neurosci.* 17, 2967–2979. doi: 10.1523/jneurosci.17-09-02967.1997

Radian, R., and Kanner, B. I. (1983). Stoichiometry of sodium- and chloride-coupled gamma-aminobutyric acid transport by synaptic plasma membrane vesicles isolated from rat brain. *Biochemistry* 22, 1236–1241. doi: 10.1021/bi00274a038

Raiteri, L., Stigliani, S., Zedda, L., Raiteri, M., and Bonanno, G. (2002). Multiple mechanisms of transmitter release evoked by "pathologically" elevated extracellular [K+]: involvement of transporter reversal and mitochondrial calcium. *J. Neurochem.* 80, 706–714. doi: 10.1046/j.0022-3042.2001.00750.x

Raiteri, M., Cerrito, F., Cervoni, A. M., and Levi, G. (1979). Dopamine can be released by two mechanisms differentially affected by the dopamine transport inhibitor nomifensine. *J. Pharmacol. Exp. Ther.* 208, 195–202.

Rauen, T., and Kanner, B. I. (1994). Localization of the glutamate transporter GLT-1 in rat and macaque monkey retinae. *Neurosci. Lett.* 169, 137–140. doi: 10.1016/0304-3940(94)90375-1

Rauen, T., Wiessner, M., Sullivan, R., Lee, A., and Pow, D. V. (2004). A new GLT1 splice variant: cloning and immunolocalization of GLT1c in the mammalian retina and brain. *Neurochem. Int.* 45, 1095–1106. doi: 10.1016/j.neuint.2004.04.006

Reyes, N., Ginter, C., and Boudker, O. (2009). Transport mechanism of a bacterial homologue of glutamate transporters. *Nature* 462, 880–885. doi: 10.1038/nature08616

Richerson, G. B., and Wu, Y. (2004). Role of the GABA transporter in epilepsy. *Adv. Exp. Med. Biol.* 548, 76–91. doi: 10.1007/978-1-4757-6376-8_6

Rimmele, T. S., and Rosenberg, P. A. (2016). GLT-1: the elusive presynaptic glutamate transporter. *Neurochem. Int.* 98, 19–28. doi: 10.1016/j.neuint.2016.04.010

Rivera, C., Voipio, J., Payne, J. A., Ruusuvuori, E., Lahtinen, H., Lamsa, K., et al. (1999). The K+/Cl- co-transporter KCC2 renders GABA hyperpolarizing during neuronal maturation. *Nature* 397, 251–255. doi: 10.1038/16697

Roberts, B. M., Doig, N. M., Brimblecombe, K. R., Lopes, E. F., Siddorn, R. E., Threlfell, S., et al. (2020). GABA uptake transporters support dopamine release in dorsal striatum with maladaptive downregulation in a parkinsonism model. *Nat. Commun.* 11:4958.

Roberts, J. G., Lugo-Morales, L. Z., Loziuk, P. L., and Sombers, L. A. (2013). Real-time chemical measurements of dopamine release in the brain. *Methods Mol. Biol.* 964, 275–294. doi: 10.1007/978-1-62703-251-3_16

Robinson, M. B. (2002). Regulated trafficking of neurotransmitter transporters: common notes but different melodies. *J. Neurochem.* 80, 1–11. doi: 10.1046/j.0022-3042.2001.00698.x

Rodriguez-Traver, E., Solis, O., Diaz-Guerra, E., Ortiz, O., Vergano-Vera, E., Mendez-Gomez, H. R., et al. (2016). Role of Nurr1 in the generation and differentiation of dopaminergic neurons from stem cells. *Neurotox Res.* 30, 14–31. doi: 10.1007/s12640-015-9586-0

Roginski, R., Choudhury, K., Marone, M., and Geller, H. (1993). Molecular characterization and expression of a rat-brain glutamate transporter CDNA. *Anesthesiology* 79:A787.

Romero, J., de Miguel, R., Ramos, J. A., and Fernandez-Ruiz, J. J. (1998). The activation of cannabinoid receptors in striatonigral GABAergic neurons inhibited GABA uptake. *Life Sci.* 62, 351–363. doi: 10.1016/s0024-3205(97)01117-x

Rosenblum, L. T., and Trotti, D. (2017). EAAT2 and the molecular signature of amyotrophic lateral sclerosis. *Adv. Neurobiol.* 16, 117–136. doi: 10.1007/978-3-319-55769-4_6

Rothstein, J. D., Dykes-Hoberg, M., Pardo, C. A., Bristol, L. A., Jin, L., Kuncl, R. W., et al. (1996). Knockout of glutamate transporters reveals a major role for astroglial transport in excitotoxicity and clearance of glutamate. *Neuron* 16, 675–686. doi: 10.1016/s0896-6273(00)80086-0

Rothstein, J. D., Martin, L., Levey, A. I., Dykes-Hoberg, M., Jin, L., Wu, D., et al. (1994). Localization of neuronal and glial glutamate transporters. *Neuron* 13, 713–725. doi: 10.1016/0896-6273(94)90038-8

Rothstein, J. D., Van Kammen, M., Levey, A. I., Martin, L. J., and Kuncl, R. W. (1995). Selective loss of glial glutamate transporter GLT-1 in amyotrophic lateral sclerosis. *Ann. Neurol.* 38, 73–84. doi: 10.1002/ana.410380114

Ryan, R. M., and Mindell, J. A. (2007). The uncoupled chloride conductance of a bacterial glutamate transporter homolog. *Nat. Struct. Mol. Biol.* 14, 365–371. doi: 10.1038/nsmb1230

Ryan, R. M., Mitrovic, A. D., and Vandenberg, R. J. (2004). The chloride permeation pathway of a glutamate transporter and its proximity to the glutamate translocation pathway. *J. Biol. Chem.* 279, 20742–20751. doi: 10.1074/jbc.m304433200

Ryan, R. M., and Vandenberg, R. J. (2016). Elevating the alternating-access model. *Nat. Struct. Mol. Biol.* 23, 187–189. doi: 10.1038/nsmb.3179

Sacchetti, P., Brownschidle, L. A., Granneman, J. G., and Bannon, M. J. (1999). Characterization of the 5′-flanking region of the human dopamine transporter gene. *Brain Res. Mol. Brain Res.* 74, 167–174. doi: 10.1016/s0169-328x(99)00275-2

Sakrikar, D., Mazei-Robison, M. S., Mergy, M. A., Richtand, N. W., Han, Q., Hamilton, P. J., et al. (2012). Attention deficit/hyperactivity disorder-derived coding variation in the dopamine transporter disrupts microdomain targeting and trafficking regulation. *J. Neurosci.* 32, 5385–5397. doi: 10.1523/jneurosci.6033-11.2012

Saksela, K., and Permi, P. (2012). SH3 domain ligand binding: what's the consensus and where's the specificity? *FEBS Lett.* 586, 2609–2614. doi: 10.1016/j.febslet.2012.04.042

Salat, K., and Kulig, K. (2011). GABA transporters as targets for new drugs. *Future Med. Chem.* 3, 211–222. doi: 10.4155/fmc.10.298

Salat, K., Podkowa, A., Malikowska, N., Kern, F., Pabel, J., Wojcieszak, E., et al. (2017). Novel, highly potent and in vivo active inhibitor of GABA transporter subtype 1 with anticonvulsant, anxiolytic, antidepressant and antinociceptive properties. *Neuropharmacology* 113, 331–342. doi: 10.1016/j.neuropharm.2016.10.019

Salemi, S., Baktash, P., Rajaei, B., Noori, M., Amini, H., Shamsara, M., et al. (2016). Efficient generation of dopaminergic-like neurons by overexpression of Nurr1 and Pitx3 in mouse induced pluripotent stem cells. *Neurosci. Lett.* 626, 126–134. doi: 10.1016/j.neulet.2016.05.032

Sandoval, V., Riddle, E. L., Ugarte, Y. V., Hanson, G. R., and Fleckenstein, A. E. (2001). Methamphetamine-induced rapid and reversible changes in dopamine transporter function: an in vitro model. *J. Neurosci.* 21, 1413–1419. doi: 10.1523/jneurosci.21-04-01413.2001

Saucedo-Cardenas, O., Quintana-Hau, J. D., Le, W. D., Smidt, M. P., Cox, J. J., De Mayo, F., et al. (1998). Nurr1 is essential for the induction of the dopaminergic phenotype and the survival of ventral mesencephalic late dopaminergic precursor neurons. *Proc. Natl. Acad. Sci. U.S.A.* 95, 4013–4018. doi: 10.1073/pnas.95.7.4013

Saunders, C., Ferrer, J. V., Shi, L., Chen, J., Merrill, G., Lamb, M. E., et al. (2000). Amphetamine-induced loss of human dopamine transporter activity: an internalization-dependent and cocaine-sensitive mechanism. *Proc. Natl. Acad. Sci. U.S.A.* 97, 6850–6855. doi: 10.1073/pnas.110035297

Schallier, A., Smolders, I., Van Dam, D., Loyens, E., De Deyn, P. P., Michotte, A., et al. (2011). Region- and age-specific changes in glutamate transport in the AbetaPP23 mouse model for Alzheimer's disease. *J. Alzheimers Dis.* 24, 287–300. doi: 10.3233/jad-2011-101005

Schikorski, T., and Stevens, C. F. (1997). Quantitative ultrastructural analysis of hippocampal excitatory synapses. *J. Neurosci.* 17, 5858–5867. doi: 10.1523/jneurosci.17-15-05858.1997

Schitine, C. S., Mendez-Flores, O. G., Santos, L. E., Ornelas, I., Calaza, K. C., Perez-Toledo, K., et al. (2015). Functional plasticity of GAT-3 in avian Muller cells is regulated by neurons via a glutamatergic input. *Neurochem. Int.* 82, 42–51. doi: 10.1016/j.neuint.2015.02.004

Schmitt, A., Asan, E., Lesch, K. P., and Kugler, P. (2002). A splice variant of glutamate transporter GLT1/EAAT2 expressed in neurons: cloning and localization in rat nervous system. *Neuroscience* 109, 45–61. doi: 10.1016/s0306-4522(01)00451-1

Schmitt, A., Asan, E., Puschel, B., Jons, T., and Kugler, P. (1996). Expression of the glutamate transporter GLT1 in neural cells of the rat central nervous system: non-radioactive in situ hybridization and comparative immunocytochemistry. *Neuroscience* 71, 989–1004. doi: 10.1016/0306-4522(95)00477-7

Schmitt, K. C., Rothman, R. B., and Reith, M. E. (2013). Nonclassical pharmacology of the dopamine transporter: atypical inhibitors, allosteric modulators, and partial substrates. *J. Pharmacol. Exp. Ther.* 346, 2–10. doi: 10.1124/jpet.111.191056

Schoffelmeer, A. N., Drukarch, B., De Vries, T. J., Hogenboom, F., Schetters, D., and Pattij, T. (2011). Insulin modulates cocaine-sensitive monoamine transporter function and impulsive behavior. *J. Neurosci.* 31, 1284–1291. doi: 10.1523/jneurosci.3779-10.2011

Schrödinger, L. L. C. (2010). *The PyMOL molecular graphics system*. Version 1:5.

Schwartz, M. D., Canales, J. J., Zucchi, R., Espinoza, S., Sukhanov, I., and Gainetdinov, R. R. (2018). Trace amine-associated receptor 1: a multimodal therapeutic target for neuropsychiatric diseases. *Expert Opin. Ther. Targets* 22, 513–526. doi: 10.1080/14728222.2018.1480723

Schwerdt, H. N., Zhang, E., Kim, M. J., Yoshida, T., Stanwicks, L., Amemori, S., et al. (2018). Cellular-scale probes enable stable chronic subsecond monitoring of dopamine neurochemicals in a rodent model. *Commun. Biol.* 1:144.

Scimemi, A. (2014a). Plasticity of GABA transporters: an unconventional route to shape inhibitory synaptic transmission. *Front. Cell Neurosci.* 8:128. doi: 10.3389/fncel.2014.00128

Scimemi, A. (2014b). Structure, function, and plasticity of GABA transporters. *Front. Cell. Neurosci.* 8:161. doi: 10.3389/fncel.2014.00161

Scimemi, A., Fine, A., Kullmann, D. M., and Rusakov, D. A. (2004). NR2B-containing receptors mediate cross talk among hippocampal synapses. *J. Neurosci.* 24, 4767–4777. doi: 10.1523/jneurosci.0364-04.2004

Scimemi, A., Meabon, J. S., Woltjer, R. L., Sullivan, J. M., Diamond, J. S., and Cook, D. G. (2013). Amyloid-beta1-42 slows clearance of synaptically released glutamate by mislocalizing astrocytic GLT-1. *J. Neurosci.* 33, 5312–5318. doi: 10.1523/jneurosci.5274-12.2013

Scimemi, A., Semyanov, A., Sperk, G., Kullmann, D. M., and Walker, M. C. (2005). Multiple and plastic receptors mediate tonic GABA(A) receptor currents in the hippocampus. *J. Neurosci.* 25, 10016–10024. doi: 10.1523/jneurosci.2520-05.2005

Scimemi, A., Tian, H., and Diamond, J. S. (2009). Neuronal transporters regulate glutamate clearance, NMDA receptor activation, and synaptic plasticity in the hippocampus. *J. Neurosci.* 29, 14581–14595. doi: 10.1523/jneurosci.4845-09.2009

Scopelliti, A. J., Font, J., Vandenberg, R. J., Boudker, O., and Ryan, R. M. (2018). Structural characterisation reveals insights into substrate recognition by the glutamine transporter ASCT2/SLC1A5. *Nat. Commun.* 9:38.

Scott, H. A., Gebhardt, F. M., Mitrovic, A. D., Vandenberg, R. J., and Dodd, P. R. (2011). Glutamate transporter variants reduce glutamate uptake in Alzheimer's disease. *Neurobiol. Aging* 32, 553.e551-e511.

Seal, R. P., and Amara, S. G. (1999). Excitatory amino acid transporters: a family in flux. *Annu. Rev. Pharmacol. Toxicol.* 39, 431–456. doi: 10.1146/annurev.pharmtox.39.1.431

Seal, R. P., Shigeri, Y., Eliasof, S., Leighton, B. H., and Amara, S. G. (2001). Sulfhydryl modification of V449C in the glutamate transporter EAAT1 abolishes substrate transport but not the substrate-gated anion conductance. *Proc. Natl. Acad. Sci. U.S.A.* 98, 15324–15329. doi: 10.1073/pnas.011400198

Serretti, A., and Mandelli, L. (2008). The genetics of bipolar disorder: genome 'hot regions,' genes, new potential candidates and future directions. *Mol. Psychiatry* 13, 742–771. doi: 10.1038/mp.2008.29

Sharma, A., Kazim, S. F., Larson, C. S., Ramakrishnan, A., Gray, J. D., McEwen, B. S., et al. (2019). Divergent roles of astrocytic versus neuronal EAAT2 deficiency on cognition and overlap with aging and Alzheimer's molecular signatures. *Proc. Natl. Acad. Sci. U.S.A.* 116, 21800–21811. doi: 10.1073/pnas.1903566116

Sheldon, A. L., Gonzalez, M. I., Krizman-Genda, E. N., Susarla, B. T., and Robinson, M. B. (2008). Ubiquitination-mediated internalization and degradation of the astroglial glutamate transporter, GLT-1. *Neurochem. Int.* 53, 296–308. doi: 10.1016/j.neuint.2008.07.010

Shifman, M. (1991). The effect of gangliosides upon recovery of aspartate/glutamatergic synapses in striatum after lesions of the rat sensorimotor cortex. *Brain Res.* 568, 323–324. doi: 10.1016/0006-8993(91)91419-2

Shin, J. W., Nguyen, K. T., Pow, D. V., Knight, T., Buljan, V., Bennett, M. R., et al. (2009). Distribution of glutamate transporter GLAST in membranes of cultured astrocytes in the presence of glutamate transport substrates and ATP. *Neurochem. Res.* 34, 1758–1766. doi: 10.1007/s11064-009-9982-z

Sieber, S. A., and Marahiel, M. A. (2005). Molecular mechanisms underlying nonribosomal peptide synthesis: approaches to new antibiotics. *Chem. Rev.* 105, 715–738. doi: 10.1021/cr0301191

Sims, K. D., Straff, D. J., and Robinson, M. B. (2000). Platelet-derived growth factor rapidly increases activity and cell surface expression of the EAAC1 subtype of glutamate transporter through activation of phosphatidylinositol 3-kinase. *J. Biol. Chem.* 275, 5228–5237. doi: 10.1074/jbc.275.7.5228

Sitcheran, R., Gupta, P., Fisher, P. B., and Baldwin, A. S. (2005). Positive and negative regulation of EAAT2 by NF-kappaB: a role for N-myc in TNFalpha-controlled repression. *EMBO J.* 24, 510–520. doi: 10.1038/sj.emboj.7600555

Sitte, H. H., Huck, S., Reither, H., Boehm, S., Singer, E. A., and Pifl, C. (1998). Carrier-mediated release, transport rates, and charge transfer induced by amphetamine, tyramine, and dopamine in mammalian cells transfected with the human dopamine transporter. *J. Neurochem.* 71, 1289–1297. doi: 10.1046/j.1471-4159.1998.71031289.x

Sogaard, R., Borre, L., Braunstein, T. H., Madsen, K. L., and MacAulay, N. (2013). Functional modulation of the glutamate transporter variant GLT1b by the PDZ domain protein PICK1. *J. Biol. Chem.* 288, 20195–20207. doi: 10.1074/jbc.m113.471128

Sonders, M. S., and Amara, S. G. (1996). Channels in transporters. *Curr. Opin. Neurobiol.* 6, 294–302.

Sonders, M. S., Zhu, S. J., Zahniser, N. R., Kavanaugh, M. P., and Amara, S. G. (1997). Multiple ionic conductances of the human dopamine transporter: the actions of dopamine and psychostimulants. *J. Neurosci.* 17, 960–974. doi: 10.1523/jneurosci.17-03-00960.1997

Sorkina, T., Doolen, S., Galperin, E., Zahniser, N. R., and Sorkin, A. (2003). Oligomerization of dopamine transporters visualized in living cells by fluorescence resonance energy transfer microscopy. *J. Biol. Chem.* 278, 28274–28283. doi: 10.1074/jbc.m210652200

Sorkina, T., Hoover, B. R., Zahniser, N. R., and Sorkin, A. (2005). Constitutive and protein kinase C-induced internalization of the dopamine transporter is mediated by a clathrin-dependent mechanism. *Traffic* 6, 157–170. doi: 10.1111/j.1600-0854.2005.00259.x

Stenovec, M., Kreft, M., Grilc, S., Pangrsic, T., and Zorec, R. (2008). EAAT2 density at the astrocyte plasma membrane and Ca(2 +)-regulated exocytosis. *Mol. Membr. Biol.* 25, 203–215. doi: 10.1080/09687680701790925

Stoffel, W., Sasse, J., Duker, M., Muller, R., Hofmann, K., Fink, T., et al. (1996). Human high affinity, Na(+)-dependent L-glutamate/L-aspartate transporter

GLAST-1 (EAAT-1): gene structure and localization to chromosome 5p11-p12. *FEBS Lett.* 386, 189–193. doi: 10.1016/0014-5793(96)00424-3

Su, Z. Z., Leszczyniecka, M., Kang, D. C., Sarkar, D., Chao, W., Volsky, D. J., et al. (2003). Insights into glutamate transport regulation in human astrocytes: cloning of the promoter for excitatory amino acid transporter 2 (EAAT2). *Proc. Natl. Acad. Sci. U.S.A.* 100, 1955–1960. doi: 10.1073/pnas.0136555100

Sullivan, R., Rauen, T., Fischer, F., Wiessner, M., Grewer, C., Bicho, A., et al. (2004). Cloning, transport properties, and differential localization of two splice variants of GLT-1 in the rat CNS: implications for CNS glutamate homeostasis. *Glia* 45, 155–169. doi: 10.1002/glia.10317

Sulzer, D., Chen, T. K., Lau, Y. Y., Kristensen, H., Rayport, S., and Ewing, A. (1995). Amphetamine redistributes dopamine from synaptic vesicles to the cytosol and promotes reverse transport. *J. Neurosci.* 15, 4102–4108. doi: 10.1523/jneurosci.15-05-04102.1995

Sulzer, D., Maidment, N. T., and Rayport, S. (1993). Amphetamine and other weak bases act to promote reverse transport of dopamine in ventral midbrain neurons. *J. Neurochem.* 60, 527–535. doi: 10.1111/j.1471-4159.1993.tb03181.x

Susarla, B. T., and Robinson, M. B. (2003). Rottlerin, an inhibitor of protein kinase Cdelta (PKCdelta), inhibits astrocytic glutamate transport activity and reduces GLAST immunoreactivity by a mechanism that appears to be PKCdelta-independent. *J. Neurochem.* 86, 635–645. doi: 10.1046/j.1471-4159.2003.01886.x

Susarla, B. T., and Robinson, M. B. (2008). Internalization and degradation of the glutamate transporter GLT-1 in response to phorbol ester. *Neurochem. Int.* 52, 709–722. doi: 10.1016/j.neuint.2007.08.020

Susarla, B. T., Seal, R. P., Zelenaia, O., Watson, D. J., Wolfe, J. H., Amara, S. G., et al. (2004). Differential regulation of GLAST immunoreactivity and activity by protein kinase C: evidence for modification of amino and carboxyl termini. *J. Neurochem.* 91, 1151–1163. doi: 10.1111/j.1471-4159.2004.02791.x

Swanson, R. A., Liu, J., Miller, J. W., Rothstein, J. D., Farrell, K., Stein, B. A., et al. (1997). Neuronal regulation of glutamate transporter subtype expression in astrocytes. *J. Neurosci.* 17, 932–940. doi: 10.1523/jneurosci.17-03-00932.1997

Sylantyev, S., Savtchenko, L. P., O'Neill, N., and Rusakov, D. A. (2020). Extracellular GABA waves regulate coincidence detection in excitatory circuits. *J. Physiol.* 598, 4047–4062. doi: 10.1113/jp279744

Tai, Y. H., Wang, Y. H., Tsai, R. Y., Wang, J. J., Tao, P. L., Liu, T. M., et al. (2007). Amitriptyline preserves morphine's antinociceptive effect by regulating the glutamate transporter GLAST and GLT-1 trafficking and excitatory amino acids concentration in morphine-tolerant rats. *Pain* 129, 343–354. doi: 10.1016/j.pain.2007.01.031

Tan, J., Zelenaia, O., Correale, D., Rothstein, J. D., and Robinson, M. B. (1999). Expression of the GLT-1 subtype of Na+-dependent glutamate transporter: pharmacological characterization and lack of regulation by protein kinase C. *J. Pharmacol. Exp. Ther.* 289, 1600–1610.

Tanaka, K. (1993). Cloning and expression of a glutamate transporter from mouse brain. *Neurosci. Lett.* 159, 183–186. doi: 10.1016/0304-3940(93)90829-a

Tebano, M. T., Martire, A., Potenza, R. L., Gro, C., Pepponi, R., Armida, M., et al. (2008). Adenosine A(2A) receptors are required for normal BDNF levels and BDNF-induced potentiation of synaptic transmission in the mouse hippocampus. *J. Neurochem.* 104, 279–286.

Tian, Y., Kapatos, G., Granneman, J. G., and Bannon, M. J. (1994). Dopamine and gamma-aminobutyric acid transporters: differential regulation by agents that promote phosphorylation. *Neurosci. Lett.* 173, 143–146. doi: 10.1016/0304-3940(94)90169-4

Todorov, A. A., Kolchev, C. B., and Todorov, A. B. (2005). Tiagabine and gabapentin for the management of chronic pain. *Clin. J. Pain* 21, 358–361. doi: 10.1097/01.ajp.0000110637.14355.77

Tonsfeldt, K. J., Suchland, K. L., Beeson, K. A., Lowe, J. D., Li, M. H., and Ingram, S. L. (2016). Sex Differences in GABAA signaling in the periaqueductal gray induced by persistent inflammation. *J. Neurosci.* 36, 1669–1681. doi: 10.1523/jneurosci.1928-15.2016

Torp, R., Danbolt, N. C., Babaie, E., Bjoras, M., Seeberg, E., Storm-Mathisen, J., et al. (1994). Differential expression of two glial glutamate transporters in the rat brain: an in situ hybridization study. *Eur. J. Neurosci.* 6, 936–942. doi: 10.1111/j.1460-9568.1994.tb00587.x

Torp, R., Hoover, F., Danbolt, N. C., Storm-Mathisen, J., and Ottersen, O. P. (1997). Differential distribution of the glutamate transporters GLT1 and rEAAC1 in rat cerebral cortex and thalamus: an in situ hybridization analysis. *Anat. Embryol.* 195, 317–326. doi: 10.1007/s004290050051

Torres, G. E., Gainetdinov, R. R., and Caron, M. G. (2003). Plasma membrane monoamine transporters: structure, regulation and function. *Nat. Rev. Neurosci.* 4, 13–25. doi: 10.1038/nrn1008

Torres, G. E., Yao, W. D., Mohn, A. R., Quan, H., Kim, K. M., Levey, A. I., et al. (2001). Functional interaction between monoamine plasma membrane transporters and the synaptic PDZ domain-containing protein PICK1. *Neuron* 30, 121–134. doi: 10.1016/s0896-6273(01)00267-7

Torres-Salazar, D., and Fahlke, C. (2007). Neuronal glutamate transporters vary in substrate transport rate but not in unitary anion channel conductance. *J. Biol. Chem.* 282, 34719–34726. doi: 10.1074/jbc.m704118200

Trotti, D., Peng, J. B., Dunlop, J., and Hediger, M. A. (2001). Inhibition of the glutamate transporter EAAC1 expressed in *Xenopus oocytes* by phorbol esters. *Brain Res.* 914, 196–203. doi: 10.1016/s0006-8993(01)02802-5

Trotti, D., Volterra, A., Lehre, K. P., Rossi, D., Gjesdal, O., Racagni, G., et al. (1995). Arachidonic acid inhibits a purified and reconstituted glutamate transporter directly from the water phase and not via the phospholipid membrane. *J. Biol. Chem.* 270, 9890–9895. doi: 10.1074/jbc.270.17.9890

Tzingounis, A. V., and Wadiche, J. I. (2007). Glutamate transporters: confining runaway excitation by shaping synaptic transmission. *Nat. Rev. Neurosci.* 8, 935–947. doi: 10.1038/nrn2274

Underhill, S. M., Ingram, S. L., Ahmari, S. E., Veenstra-VanderWeele, J., and Amara, S. G. (2019). Neuronal excitatory amino acid transporter EAAT3: emerging functions in health and disease. *Neurochem. Int.* 123, 69–76. doi: 10.1016/j.neuint.2018.05.012

Underhill, S. M., Wheeler, D. S., and Amara, S. G. (2015). Differential regulation of two isoforms of the glial glutamate transporter EAAT2 by DLG1 and CaMKII. *J. Neurosci.* 35, 5260–5270. doi: 10.1523/jneurosci.4365-14.2015

Underhill, S. M., Wheeler, D. S., Li, M., Watts, S. D., Ingram, S. L., and Amara, S. G. (2014). Amphetamine modulates excitatory neurotransmission through endocytosis of the glutamate transporter EAAT3 in dopamine neurons. *Neuron* 83, 404–416. doi: 10.1016/j.neuron.2014.05.043

Untiet, V., Kovermann, P., Gerkau, N. J., Gensch, T., Rose, C. R., and Fahlke, C. (2017). Glutamate transporter-associated anion channels adjust intracellular chloride concentrations during glial maturation. *Glia* 65, 388–400. doi: 10.1002/glia.23098

Vandenbergh, D. J., Persico, A. M., Hawkins, A. L., Griffin, C. A., Li, X., Jabs, E. W., et al. (1992a). Human dopamine transporter gene (DAT1) maps to chromosome 5p15.3 and displays a VNTR. *Genomics* 14, 1104–1106. doi: 10.1016/s0888-7543(05)80138-7

Vandenbergh, D. J., Persico, A. M., and Uhl, G. R. (1992b). A human dopamine transporter cDNA predicts reduced glycosylation, displays a novel repetitive element and provides racially-dimorphic TaqI RFLPs. *Brain Res. Mol. Brain Res.* 15, 161–166. doi: 10.1016/0169-328x(92)90165-8

Vaughan, R. A., Huff, R. A., Uhl, G. R., and Kuhar, M. J. (1997). Protein kinase C-mediated phosphorylation and functional regulation of dopamine transporters in striatal synaptosomes. *J. Biol. Chem.* 272, 15541–15546. doi: 10.1074/jbc.272.24.15541

Vaz, S. H., Cristovao-Ferreira, S., Ribeiro, J. A., and Sebastiao, A. M. (2008). Brain-derived neurotrophic factor inhibits GABA uptake by the rat hippocampal nerve terminals. *Brain Res.* 1219, 19–25. doi: 10.1016/j.brainres.2008.04.008

Vaz, S. H., Jorgensen, T. N., Cristovao-Ferreira, S., Duflot, S., Ribeiro, J. A., Gether, U., et al. (2011). Brain-derived neurotrophic factor (BDNF) enhances GABA transport by modulating the trafficking of GABA transporter-1 (GAT-1) from the plasma membrane of rat cortical astrocytes. *J. Biol. Chem.* 286, 40464–40476. doi: 10.1074/jbc.m111.232009

Venderova, K., Brown, T. M., and Brotchie, J. M. (2005). Differential effects of endocannabinoids on [(3)H]-GABA uptake in the rat *Globus pallidus*. *Exp. Neurol.* 194, 284–287. doi: 10.1016/j.expneurol.2005.02.012

Ventura, R., and Harris, K. M. (1999). Three-dimensional relationships between hippocampal synapses and astrocytes. *J. Neurosci.* 19, 6897–6906. doi: 10.1523/jneurosci.19-16-06897.1999

Verdon, G., and Boudker, O. (2012). Crystal structure of an asymmetric trimer of a bacterial glutamate transporter homolog. *Nat. Struct. Mol. Biol.* 19, 355–357. doi: 10.1038/nsmb.2233

Veruki, M. L., Morkve, S. H., and Hartveit, E. (2006). Activation of a presynaptic glutamate transporter regulates synaptic transmission through electrical signaling. *Nat. Neurosci.* 9, 1388–1396. doi: 10.1038/nn1793

Vina-Vilaseca, A., and Sorkin, A. (2010). Lysine 63-linked polyubiquitination of the dopamine transporter requires WW3 and WW4 domains of Nedd4-2 and UBE2D ubiquitin-conjugating enzymes. *J. Biol. Chem.* 285, 7645–7656. doi: 10.1074/jbc.m109.058990

Voisin, P., Viratelle, O., Girault, J. M., Morrison-Bogorad, M., and Labouesse, J. (1993). Plasticity of astroglial glutamate and γ-Aminobutyric acid uptake in cell cultures derived from postnatal mouse cerebellum. *J. Neurochem.* 60, 114–127. doi: 10.1111/j.1471-4159.1993.tb05829.x

Volterra, A., Trotti, D., Cassutti, P., Tromba, C., Galimberti, R., Lecchi, P., et al. (1992). A role for the arachidonic acid cascade in fast synaptic modulation: ion channels and transmitter uptake systems as target proteins. *Adv. Exp. Med. Biol.* 318, 147–158. doi: 10.1007/978-1-4615-3426-6_13

Volterra, A., Trotti, D., and Racagni, G. (1994a). Glutamate uptake is inhibited by arachidonic acid and oxygen radicals via two distinct and additive mechanisms. *Mol. Pharmacol.* 46, 986–992.

Volterra, A., Trotti, D., Tromba, C., Floridi, S., and Racagni, G. (1994b). Glutamate uptake inhibition by oxygen free radicals in rat cortical astrocytes. *J. Neurosci.* 14, 2924–2932. doi: 10.1523/jneurosci.14-05-02924.1994

Voutsinos, B., Dutuit, M., Reboul, A., Fevre-Montange, M., Bernard, A., Trouillas, P., et al. (1998). Serotoninergic control of the activity and expression of glial GABA transporters in the rat cerebellum. *Glia* 23, 45–60. doi: 10.1002/(sici)1098-1136(199805)23:1<45::aid-glia5>3.0.co;2-3

Wadiche, J. I., Amara, S. G., and Kavanaugh, M. P. (1995a). Ion fluxes associated with excitatory amino acid transport. *Neuron* 15, 721–728. doi: 10.1016/0896-6273(95)90159-0

Wadiche, J. I., Arriza, J. L., Amara, S. G., and Kavanaugh, M. P. (1995b). Kinetics of a human glutamate transporter. *Neuron* 14, 1019–1027. doi: 10.1016/0896-6273(95)90340-2

Wadiche, J. I., and Jahr, C. E. (2005). Patterned expression of Purkinje cell glutamate transporters controls synaptic plasticity. *Nat. Neurosci.* 8, 1329–1334. doi: 10.1038/nn1539

Wadiche, J. I., and Kavanaugh, M. P. (1998). Macroscopic and microscopic properties of a cloned glutamate transporter/chloride channel. *J. Neurosci.* 18, 7650–7661. doi: 10.1523/jneurosci.18-19-07650.1998

Walker, M. C., and van der Donk, W. A. (2016). The many roles of glutamate in metabolism. *J. Ind. Microbiol. Biotechnol.* 43, 419–430. doi: 10.1007/s10295-015-1665-y

Wang, D., Deken, S. L., Whitworth, T. L., and Quick, M. W. (2003). Syntaxin 1A inhibits GABA flux, efflux, and exchange mediated by the rat brain GABA transporter GAT1. *Mol. Pharmacol.* 64, 905–913. doi: 10.1124/mol.64.4.905

Wang, Z., Li, W., Mitchell, C. K., and Carter-Dawson, L. (2003). Activation of protein kinase C reduces GLAST in the plasma membrane of rat Muller cells in primary culture. *Vis. Neurosci.* 20, 611–619. doi: 10.1017/s0952523803206039

Wang, D., and Quick, M. W. (2005). Trafficking of the plasma membrane gamma-aminobutyric acid transporter GAT1. Size and rates of an acutely recycling pool. *J. Biol. Chem.* 280, 18703–18709. doi: 10.1074/jbc.m500381200

Wang, J., Michelhaugh, S. K., and Bannon, M. J. (2007). Valproate robustly increases Sp transcription factor-mediated expression of the dopamine transporter gene within dopamine cells. *Eur. J. Neurosci.* 25, 1982–1986. doi: 10.1111/j.1460-9568.2007.05460.x

Wang, K. H., Penmatsa, A., and Gouaux, E. (2015). Neurotransmitter and psychostimulant recognition by the dopamine transporter. *Nature* 521, 322–327. doi: 10.1038/nature14431

Wang, X., and Boudker, O. (2020). Large domain movements through the lipid bilayer mediate substrate release and inhibition of glutamate transporters. *eLife* 9:e58417.

Wang, Y., Lu, S., Qu, Z., Wu, L., and Wang, Y. (2017). Sonic hedgehog induces GLT-1 degradation via PKC delta to suppress its transporter activities. *Neuroscience* 365, 217–225. doi: 10.1016/j.neuroscience.2017.09.051

Watzke, N., Bamberg, E., and Grewer, C. (2001). Early intermediates in the transport cycle of the neuronal excitatory amino acid carrier EAAC1. *J. Gen. Physiol.* 117, 547–562. doi: 10.1085/jgp.117.6.547

Watzke, N., and Grewer, C. (2001). The anion conductance of the glutamate transporter EAAC1 depends on the direction of glutamate transport. *FEBS Lett.* 503, 121–125. doi: 10.1016/s0014-5793(01)02715-6

Wenzel, J., Lammert, G., Meyer, U., and Krug, M. (1991). The influence of long-term potentiation on the spatial relationship between astrocyte processes and potentiated synapses in the dentate gyrus neuropil of rat brain. *Brain Res.* 560, 122–131. doi: 10.1016/0006-8993(91)91222-m

Wheeler, D. S., Ebben, A. L., Kurtoglu, B., Lovell, M. E., Bohn, A. T., Jasek, I. A., et al. (2017). Corticosterone regulates both naturally occurring and cocaine-induced dopamine signaling by selectively decreasing dopamine uptake. *Eur. J. Neurosci.* 46, 2638–2646. doi: 10.1111/ejn.13730

Wheeler, D. S., Underhill, S. M., Stolz, D. B., Murdoch, G. H., Thiels, E., Romero, G., et al. (2015). Amphetamine activates Rho GTPase signaling to mediate dopamine transporter internalization and acute behavioral effects of amphetamine. *Proc. Natl. Acad. Sci. U.S.A.* 112, E7138–E7147.

Whitworth, T. L., and Quick, M. W. (2001). Upregulation of gamma-aminobutyric acid transporter expression: role of alkylated gamma-aminobutyric acid derivatives. *Biochem. Soc. Trans.* 29, 736–741. doi: 10.1042/bst0290736

Wieczorek, W. J., and Kruk, Z. L. (1994). Differential action of (+)-amphetamine on electrically evoked dopamine overflow in rat brain slices containing corpus striatum and nucleus accumbens. *Br. J. Pharmacol.* 111, 829–836. doi: 10.1111/j.1476-5381.1994.tb14813.x

Williams, J. M., Owens, W. A., Turner, G. H., Saunders, C., Dipace, C., Blakely, R. D., et al. (2007). Hypoinsulinemia regulates amphetamine-induced reverse transport of dopamine. *PLoS Biol.* 5:e274. doi: 10.1371/journal.pbio.0050274

Wilson, J. M., Khabazian, I., Pow, D. V., Craig, U. K., and Shaw, C. A. (2003). Decrease in glial glutamate transporter variants and excitatory amino acid receptor down-regulation in a murine model of ALS-PDC. *Neuromolecul. Med.* 3, 105–118. doi: 10.1385/nmm:3:2:105

Winter, N., Kovermann, P., and Fahlke, C. (2012). A point mutation associated with episodic ataxia 6 increases glutamate transporter anion currents. *Brain* 135, 3416–3425. doi: 10.1093/brain/aws255

Witcher, M. R., Kirov, S. A., and Harris, K. M. (2007). Plasticity of perisynaptic astroglia during synaptogenesis in the mature rat hippocampus. *Glia* 55, 13–23. doi: 10.1002/glia.20415

Witcher, M. R., Park, Y. D., Lee, M. R., Sharma, S., Harris, K. M., and Kirov, S. A. (2010). Three-dimensional relationships between perisynaptic astroglia and human hippocampal synapses. *Glia* 58, 572–587.

Woo, T. U., Whitehead, R. E., Melchitzky, D. S., and Lewis, D. A. (1998). A subclass of prefrontal gamma-aminobutyric acid axon terminals are selectively altered in schizophrenia. *Proc. Natl. Acad. Sci. U.S.A.* 95, 5341–5346. doi: 10.1073/pnas.95.9.5341

Wu, X., Kihara, T., Akaike, A., Niidome, T., and Sugimoto, H. (2010). PI3K/Akt/mTOR signaling regulates glutamate transporter 1 in astrocytes. *Biochem. Biophys. Res. Commun.* 393, 514–518. doi: 10.1016/j.bbrc.2010.02.038

Wu, Y., Wang, W., Diez-Sampedro, A., and Richerson, G. B. (2007). Nonvesicular inhibitory neurotransmission via reversal of the GABA transporter GAT-1. *Neuron* 56, 851–865. doi: 10.1016/j.neuron.2007.10.021

Wu, Y., Wang, W., and Richerson, G. B. (2003). Vigabatrin induces tonic inhibition via GABA transporter reversal without increasing vesicular GABA release. *J. Neurophysiol.* 89, 2021–2034. doi: 10.1152/jn.00856.2002

Xie, Y. Y., Qu, J., Zhou, L., Lv, N., Gong, J. E., Cao, Y. Z., et al. (2017). Lack of association between SLC6A11 genetic polymorphisms and drug resistant epilepsy in chinese han population. *Clin. Lab.* 63, 1113–1120.

Xu, Y. F., Cai, Y. Q., Cai, G. Q., Jiang, J., Sheng, Z. J., Wang, Z. G., et al. (2008). Hypoalgesia in mice lacking GABA transporter subtype 1. *J. Neurosci. Res.* 86, 465–470. doi: 10.1002/jnr.21499

Yamashita, A., Singh, S. K., Kawate, T., Jin, Y., and Gouaux, E. (2005). Crystal structure of a bacterial homologue of Na+/Cl–dependent neurotransmitter transporters. *Nature* 437, 215–223. doi: 10.1038/nature03978

Yan, X., Yadav, R., Gao, M., and Weng, H. R. (2014). Interleukin-1 beta enhances endocytosis of glial glutamate transporters in the spinal dorsal horn through activating protein kinase C. *Glia* 62, 1093–1109. doi: 10.1002/glia.22665

Yan, X. X., Cariaga, W. A., and Ribak, C. E. (1997). Immunoreactivity for GABA plasma membrane transporter, GAT-1, in the developing rat cerebral cortex: transient presence in the somata of neocortical and hippocampal neurons. *Brain Res. Dev. Brain Res.* 99, 1–19. doi: 10.1016/s0165-3806(96)00192-7

Yan, X. X., and Ribak, C. E. (1998). Developmental expression of gamma-aminobutyric acid transporters (GAT-1 and GAT-3) in the rat cerebellum: evidence for a transient presence of GAT-1 in Purkinje cells. *Brain Res. Dev. Brain Res.* 111, 253–269. doi: 10.1016/s0165-3806(98)00144-8

Yang, Y., Kinney, G. A., Spain, W. J., Breitner, J. C., and Cook, D. G. (2004). Presenilin-1 and intracellular calcium stores regulate neuronal glutamate uptake. *J. Neurochem.* 88, 1361–1372. doi: 10.1046/j.1471-4159.2003.02279.x

Yernool, D., Boudker, O., Jin, Y., and Gouaux, E. (2004). Structure of a glutamate transporter homologue from *Pyrococcus horikoshii*. *Nature* 431, 811–818. doi: 10.1038/nature03018

Yoo, S. Y., Kim, J. H., Do, S. H., and Zuo, Z. (2008). Inhibition of the activity of excitatory amino acid transporter 4 expressed in *Xenopus oocytes* after chronic exposure to ethanol. *Alcohol. Clin. Exp. Res.* 32, 1292–1298. doi: 10.1111/j.1530-0277.2008.00697.x

Yu, X., Plotnikova, O., Bonin, P. D., Subashi, T. A., McLellan, T. J., Dumlao, D., et al. (2019). Cryo-EM structures of the human glutamine transporter SLC1A5 (ASCT2) in the outward-facing conformation. *eLife* 8:e48120.

Zeigerer, A., McBrayer, M. K., and McGraw, T. E. (2004). Insulin stimulation of GLUT4 exocytosis, but not its inhibition of endocytosis, is dependent on RabGAP AS160. *Mol. Biol. Cell* 15, 4406–4415. doi: 10.1091/mbc.e04-04-0333

Zelenaia, O., Schlag, B. D., Gochenauer, G. E., Ganel, R., Song, W., Beesley, J. S., et al. (2000). Epidermal growth factor receptor agonists increase expression of glutamate transporter GLT-1 in astrocytes through pathways dependent on phosphatidylinositol 3-kinase and transcription factor NF-kappaB. *Mol. Pharmacol.* 57, 667–678. doi: 10.1124/mol.57.4.667

Zerangue, N., Arriza, J. L., Amara, S. G., and Kavanaugh, M. P. (1995). Differential modulation of human glutamate transporter subtypes by Arachidonic acid. *J. Biol. Chem.* 270, 6433–6435. doi: 10.1074/jbc.270.12.6433

Zerangue, N., and Kavanaugh, M. P. (1996). Flux coupling in a neuronal glutamate transporter. *Nature* 383, 634–637. doi: 10.1038/383634a0

Zestos, A. G., Mikelman, S. R., Kennedy, R. T., and Gnegy, M. E. (2016). PKCbeta inhibitors attenuate amphetamine-stimulated dopamine efflux. *ACS Chem. Neurosci.* 7, 757–766. doi: 10.1021/acschemneuro.6b00028

Zetterstrom, R. H., Solomin, L., Jansson, L., Hoffer, B. J., Olson, L., and Perlmann, T. (1997). Dopamine neuron agenesis in Nurr1-deficient mice. *Science* 276, 248–250. doi: 10.1126/science.276.5310.248

Zhang, H., Li, S., Wang, M., Vukusic, B., Pristupa, Z. B., and Liu, F. (2009). Regulation of dopamine transporter activity by carboxypeptidase E. *Mol. Brain* 2:10. doi: 10.1186/1756-6606-2-10

Zhang, L., Coffey, L. L., and Reith, M. E. (1997). Regulation of the functional activity of the human dopamine transporter by protein kinase C. *Biochem. Pharmacol.* 53, 677–688. doi: 10.1016/s0006-2952(96)00898-2

Zhang, L., Li, L., Wang, B., Qian, D. M., Song, X. X., and Hu, M. (2014). HCMV induces dysregulation of glutamate uptake and transporter expression in human fetal astrocytes. *Neurochem. Res.* 39, 2407–2418. doi: 10.1007/s11064-014-1445-5

Zhang, Q., Fukuda, M., Van Bockstaele, E., Pascual, O., and Haydon, P. G. (2004). Synaptotagmin IV regulates glial glutamate release. *Proc. Natl. Acad. Sci. U.S.A.* 101, 9441–9446. doi: 10.1073/pnas.0401960101

Zhou, J., and Sutherland, M. L. (2004). Glutamate transporter cluster formation in astrocytic processes regulates glutamate uptake activity. *J. Neurosci.* 24, 6301–6306. doi: 10.1523/jneurosci.1404-04.2004

Zhu, S. J., Kavanaugh, M. P., Sonders, M. S., Amara, S. G., and Zahniser, N. R. (1997). Activation of protein kinase C inhibits uptake, currents and binding associated with the human dopamine transporter expressed in *Xenopus oocytes*. *J. Pharmacol. Exp. Ther.* 282, 1358–1365.

Zike, I. D., Chohan, M. O., Kopelman, J. M., Krasnow, E. N., Flicker, D., Nautiyal, K. M., et al. (2017). OCD candidate gene SLC1A1/EAAT3 impacts basal ganglia-mediated activity and stereotypic behavior. *Proc. Natl. Acad. Sci. U.S.A.* 114, 5719–5724. doi: 10.1073/pnas.1701736114

Zschocke, J., Bayatti, N., Clement, A. M., Witan, H., Figiel, M., Engele, J., et al. (2005). Differential promotion of glutamate transporter expression and function by glucocorticoids in astrocytes from various brain regions. *J. Biol. Chem.* 280, 34924–34932. doi: 10.1074/jbc.m502581200

Conflict of Interest: The authors declare that the research was conducted in the absence of any commercial or financial relationships that could be construed as a potential conflict of interest.

frontiers in Cellular Neuroscience

ORIGINAL RESEARCH
published: 15 April 2021
doi: 10.3389/fncel.2021.658244

Striatal Dopamine Transporter Function Is Facilitated by Converging Biology of α-Synuclein and Cholesterol

Sarah Threlfell[1,2], Amir Saeid Mohammadi[3], Brent J. Ryan[1,2], Natalie Connor-Robson[1,2], Nicola J. Platt[1], Rishi Anand[1], Florence Serres[4], Trevor Sharp[4], Nora Bengoa-Vergniory[1,2], Richard Wade-Martins[1,2], Andrew Ewing[5], Stephanie J. Cragg[1,2†] and Katherine R. Brimblecombe[1,2*†]*

[1]Department of Physiology, Anatomy and Genetics, University of Oxford, Oxford, United Kingdom, [2]Oxford Parkinson's Disease Centre, Medical Sciences Division, University of Oxford, Oxford, United Kingdom, [3]Department of Chemistry and Chemical Engineering, Chalmers University of Technology, Gothenburg, Sweden, [4]University Department of Pharmacology, University of Oxford, Oxford, United Kingdom, [5]Department of Chemistry and Molecular Biology, University of Gothenburg, Gothenburg, Sweden

Striatal dopamine transporters (DAT) powerfully regulate dopamine signaling, and can contribute risk to degeneration in Parkinson's disease (PD). DATs can interact with the neuronal protein α-synuclein, which is associated with the etiology and molecular pathology of idiopathic and familial PD. Here, we tested whether DAT function in governing dopamine (DA) uptake and release is modified in a human-α-synuclein-overexpressing (*SNCA*-OVX) transgenic mouse model of early PD. Using fast-scan cyclic voltammetry (FCV) in *ex vivo* acute striatal slices to detect DA release, and biochemical assays, we show that several aspects of DAT function are promoted in *SNCA*-OVX mice. Compared to background control α-synuclein-null mice (*Snca*-null), the *SNCA*-OVX mice have elevated DA uptake rates, and more pronounced effects of DAT inhibitors on evoked extracellular DA concentrations ($[DA]_o$) and on short-term plasticity (STP) in DA release, indicating DATs play a greater role in limiting DA release and in driving STP. We found that DAT membrane levels and radioligand binding sites correlated with α-synuclein level. Furthermore, DAT function in *Snca*-null and *SNCA*-OVX mice could also be promoted by applying cholesterol, and using Tof-SIMS we found genotype-differences in striatal lipids, with lower striatal cholesterol in *SNCA*-OVX mice. An inhibitor of cholesterol efflux transporter ABCA1 or a cholesterol chelator in *SNCA*-OVX mice reduced the effects of DAT-inhibitors on evoked $[DA]_o$. Together these data indicate that human α-synuclein in a mouse model of PD promotes striatal DAT function, in a manner supported by extracellular cholesterol, suggesting converging biology of α-synuclein and cholesterol that regulates DAT function and could impact DA function and PD pathophysiology.

Keywords: dopamine transporter (DAT), alpha-synuclein (SNCA), cholesterol, striatum, Parkinson's disease, early stage parkinsonism, dopamine uptake, galactoceramide

OPEN ACCESS

Edited by:
Annalisa Scimemi, University at Albany, United States

Reviewed by:
Aurelio Galli, University of Alabama at Birmingham, United States
Sara Raulerson Jones, Wake Forest School of Medicine, United States

***Correspondence:**
Katherine R. Brimblecombe katherine.brimblecombe@dpag.ox.ac.uk
Stephanie J. Cragg stephanie.cragg@dpag.ox.ac.uk

†These authors share last authorship

Specialty section:
This article was submitted to Cellular Neurophysiology, a section of the journal Frontiers in Cellular Neuroscience

Received: *25 January 2021*
Accepted: *22 March 2021*
Published: *15 April 2021*

Citation:
Threlfell S, Mohammadi AS, Ryan BJ, Connor-Robson N, Platt NJ, Anand R, Serres F, Sharp T, Bengoa-Vergniory N, Wade-Martins R, Ewing A, Cragg SJ and Brimblecombe KR (2021) Striatal Dopamine Transporter Function Is Facilitated by Converging Biology of α-Synuclein and Cholesterol. Front. Cell. Neurosci. 15:658244. doi: 10.3389/fncel.2021.658244

INTRODUCTION

Striatal dopamine (DA) release is regulated by mechanisms that drive activity in midbrain DA neurons in conjunction with mechanisms in striatum that act on and within DA axons (Sulzer et al., 2016). DA uptake transporters (DATs) on DA axons clear striatal DA from the extracellular space to spatially and temporally limit DA signaling (Cragg and Rice, 2004). In addition, it has become evident that striatal DATs also regulate the underlying process of DA release. Inhibition of DATs with pharmacological inhibitors not only limits the uptake but also promotes the amount of DA released (John and Jones, 2007) through a synapsin-dependent pathway (Venton et al., 2006; Kile et al., 2010) suggesting that the DAT limits vesicular mobilization for release. In addition, DATs regulate the short-term dynamic plasticity of DA release, promoting subsequent release at short inter-pulse intervals (IPIs) corresponding to high frequency firing, and limiting subsequent release at longer IPIs corresponding to low frequency firing (Condon et al., 2019).

Besides their role in regulating DA release and uptake, DATs are implicated in the etiology of Parkinson's disease (PD). DATs offer a route of entry to DA neurons-of environmental toxins e.g., MPTP, pesticides (Lehmensiek et al., 2006; Ritz et al., 2009), and higher DAT expression and DAT: VMAT ratios promote oxidative stress *via* dopamine oxidation and consequent dopamine neuron loss (Miller et al., 1999; Masoud et al., 2015). Variations in the *DAT/SLC6A3* gene that are associated with PD susceptibility increase the expression of striatal DAT (van de Giessen et al., 2009; Richter et al., 2017). Furthermore, the DAT is electrogenic, offering depolarizing currents, which can be uncoupled from translocation of DA (Sonders et al., 1997), and so contribute to a metabolic burden, requiring ATP to re-establish ion gradients across the axonal membrane (Pissadaki and Bolam, 2013).

DAT function is regulated by post-translational modifications and lipid- and protein-binding partners (Vaughan and Foster, 2013), including α-synuclein (Lee et al., 2001) and cholesterol (Jones et al., 2012). DATs co-localize with α-synuclein in human post-mortem tissue (Bellucci et al., 2011) and many aspects of the DAT are reported to be affected by α-synuclein, including surface expression, internalization, DA translocation, and sensitivity to ligands. However, there is a lack of consensus about the impact of α-synuclein on DAT function, with conflicting evidence showing that DAT function can be enhanced (Lee et al., 2001; Chadchankar et al., 2011), decreased (Wersinger and Sidhu, 2003; Swant et al., 2011; Lundblad et al., 2012), or remains unaffected (Abeliovich et al., 2000). This lack of consensus might reflect the differing experimental preparations, assays and aspect of DAT function explored, and also might arise from the different structural forms (monomeric, oligomeric or fibrillary, soluble or aggregated) of α-synuclein that might be differently present (Alegre-Abarrategui et al., 2019) and have different pathophysiological outcomes. Determining the structural form and binding partners of α-synuclein is non-trivial and has been reviewed elsewhere (Alegre-Abarrategui et al., 2019; Alza et al., 2019). In addition, α-synuclein is in an equilibrium between cytosolic and membrane-bound states and cholesterol has been shown to affect the position of this equilibrium (Man et al., 2020). Cholesterol is a key component of highly curved membranes including synaptic vesicles, which α-synuclein can associate with (Galvagnion, 2017).

Here, we assessed whether DAT function is modified in the *SNCA*-OVX mouse model of early PD relative to *Snca*-null background control mice. *SNCA*-OVX mice are devoid of mouse α-synuclein but overexpress human wild-type α-synuclein at disease-relevant levels modeling *SNCA* locus multiplication seen in PD (Singleton et al., 2003). They show early deficits in DA release prior to DA cell loss, behavioral deficits in old age (Janezic et al., 2013), and progressive α-synuclein oligomerization with age compared to *Snca*-null mice (Bengoa-Vergniory et al., 2020) but in the absence of aggregation (Janezic et al., 2013). The control *Snca*-null mice do not differ from wild-type mice in DA release levels using our stimulation protocols (Senior et al., 2008). We assessed whether the *SNCA*-OVX PD model has altered DAT function in DA release or uptake by the DAT, and explored a potential point of convergence with cholesterol biology, using fast-scan cyclic voltammetry, molecular biology and ToF-SIMS.

MATERIALS AND METHODS

Mice

All procedures were conducted in accordance with the United Kingdom Animals (Scientific Procedures) Act of 1986 and approved by the local ethical review panel at the Department of Physiology, Anatomy and Genetics, University of Oxford. *SNCA*-OVX mice (B6.Cg-Tg(*SNCA*)OVX37Rwm Snca^{tm1Rosl}/J; Jackson Laboratories stock no. 023837) are BAC-transgenic mice that overexpress human α-synuclein from the *SNCA* genomic locus at Parkinson's disease-relevant levels, and are back-crossed onto a mouse α-synuclein-null (*Snca*-null) background. *SNCA*-OVX and their litter-mate *Snca*-null background control mice were produced as described previously (Janezic et al., 2013). Mice were age-(3–20 months) and sex-matched throughout. Data from male and female mice were combined given there were no apparent differences between the effects of cocaine on DA release between the sexes in both genotypes (**Supplementary Figure 5**). DAT-Cre mice (DAT^{IRESCRE}Jax stock number 006660) were homozygote 4-month old males, generated by crossing heterozygous mice.

Proximity Ligation Assay (PLA)

DAT:α-synuclein PLA experiments were carried out using Duolink® *in situ* kits supplied by Sigma Aldrich according to the manufacturer's instructions, and an α-synuclein antibody (syn4D6 ab1903, Abcam), and a DAT antibody (ab5990, Abcam). Briefly, the conjugates were prepared using the DuoLink® Probemaker kit by incubating 20 μl of each antibody (1 mg/ml) with the Probemaker activated oligonucleotide (Plus and Minus respectively) and conjugation buffer and leaving it overnight at room temperature. Conjugates were incubated with Probemaker stop solution for 30 min at room temperature and then suspended in Probemaker storage buffer. Paraffin-embedded tissue was prepared for fluorescent PLA® by dewaxing in

xylene and histoclear, rehydrating *via* graded alcohols, blocking endogenous peroxidases with 10% H_2O_2 for 15 min at room temperature, followed by antigen retrieval using microwave heat (10 min total) and citrate buffer pH 6 (ab93678, Abcam). All samples were incubated in Duolink® block solution for 1 h at 37°C, followed by conjugates diluted in Duolink® PLA diluent (both DAT and α-synuclein 1:100) overnight at 4°C. After washing in TBS + 0.05% Tween 20, samples were incubated with Duolink® ligation solutions and ligase for 1 h at 37°C, before washing and incubation with Duolink® amplification reagents and polymerase for 2.5 h at 37°C. Samples were then washed with Duolink® wash buffer B and mounted/coverslipped with Fluorsave (Calbiochem). Images were blindly acquired at three distinct sites in dorso-medial, dorso-mid and dorso-lateral striatum from a single 5 μm coronal section per mouse, and puncta were automatically counted with ImageJ. Three mice per genotype were assessed.

DAT Immunofluorescence

Paraffin-embedded mouse brains from *SNCA*-OVX and *Snca*-null mice were sectioned to 5 μm. Paraffin-embedded tissue was prepared for immunofluorescence by dewaxing in xylene and histoclear, rehydrating *via* graded alcohols, blocking endogenous peroxidases with 10% H_2O_2 for 15 min at room temperature, followed by antigen retrieval using microwave heat (10 min total) and citrate buffer pH 6 (ab93678, Abcam). The tissue was blocked for 1 h at room temp (TBS containing 1 M glycine, 10% normal goat serum and 0.1% Triton) prior to incubating in DAT primary antibody (rat anti-DAT; ab5990, Abcam) overnight at 4°C. Following washes in TBS + 0.1% Triton, the tissue was incubated in secondary antibody (Alexa Fluor 488 Goat anti-rat, Life Technologies) for 1 h at room temperature. Sections were then washed and coverslipped with Fluorsave™ (Calbiochem). Images were taken blindly in dorso-mid, dorso-medial and dorso-lateral striatum from two coronal sections, three mice per genotype were quantified automatically with ImageJ.

3H-Cocaine Autoradiography

Mice (three per group; 3–4 months old) were sacrificed by cervical dislocation and the brains immediately collected and snap-frozen in isopentane. Coronal sections (20 μm) were sectioned on a cryostat at the level of the striatum (plates 18–24; Franklin and Paxinos, 2004), thaw-mounted onto gelatinized slides, and stored at −80°C until use. Slides were defrosted and air-dried at room temperature before being pre-incubated for 10 min in an ice-cold PBS buffer (150 mM NaCl, 10 mM $NaHPO_4$, pH7.4). Slides were then incubated at 4°C for 30 min in a PBS buffer containing [^{3}H]-cocaine (1 μM; Perkin Elmer). Non-specific binding was determined in presence of GBR 12935 (1 μM). After incubation, slides were washed twice in ice-cold PBS and left to dry. Slides were then put in contact with film (Kodak MR) for 6 weeks. Densitometric analysis of the autoradiograms was performed against 3H-microscales (Amersham, UK) using a computerized imaging system (MCID Core, version 7.0, Interfocus Imaging Limited, UK) and subsequently normalized to *Snca*-null.

Western Blots

Protein extraction and Western analysis was performed as previously described (Janezic et al., 2013). Striatal tissue was homogenized in PBS (pH 7.4) containing 1% Igepal CA-630, 0.1% SDS, 0.5% sodium deoxycholate, and protease inhibitor mixture using a Tissue Tearor (Biospec Products, Inc.). Protein content was quantified using a BCA assay kit (Sigma) and proteins were analyzed by Western blotting under reducing, non-denaturing conditions. Primary antibodies used were: mouse anti-alpha synuclein 1:500 (Abcam ab1903) and rat anti-DAT 1:1,000 (Millipore; mab369) and anti-beta actin (HRP-conjugated) antibody (Abcam ab49900) at 1:50,000. Bands were visualized using horseradish peroxidase-conjugated goat anti-mouse or goat anti-rat IgG (Bio-Rad) and the chemiluminescent ECL+ kit (GE Healthcare) or immobilon ECL (Millipore). Bands were quantified using ImageJ software.

Fast-Scan Cyclic Voltammetry

Sex- and age-matched adult mice (3–20 months) were killed *via* cervical dislocation and the brains were removed quickly on ice and transferred into ice-cold oxygenated HEPES-based buffer) in mM: 120 NaCl, 20 $NaHCO_3$, 6.7 HEPES acid, 5KCL, 3.3 HEPES salt, 2 $CaCl_2$, 2 $MgSO_4$, 1.2 K_2PO_4 and 10 glucose) saturated with 95%O_2/5% CO_2. Three-hundred micrometer coronal slices containing striatum (+1.1 to +1.4 mm anterior of Bregma; Franklin and Paxinos, 2004) were taken and left to recover at room temperature in HEPES-based bugger for at least 1 h prior to transferring to recording chamber and to aCSF (in mM: 124 NaCl, 62 $NaHCo_3$, 3.8 KCl, 2.4 $CaCl_2$, 1.3 $MgSO_4$, 1.3 KH_2PO_4 and 10 glucose) saturated with 95% O_2/5% CO_2 for recording. Slices were warmed to 32°C and carbon fiber microelectrode (CFM) inserted into non recording site for charging for 30 min prior to recording.

Carbon-fiber microelectrodes were manufactured in-house using borosilicate glass (GC200F-10, Harvard Apparatus) and epoxy-free carbon fiber (7 μm diameter; Goodfellow). Voltage waveform (−0.7 V to +1.3 V) was scanned at 8 Hz at 800 V/s across the recording CFM and switched out of circuit between scans using a Millar Voltammeter as described previously (Threlfell et al., 2010, 2012).

Single recording sites in either dorsomedial or dorsolateral caudate putamen (CPu) were selected and multiple stimulation paradigms were delivered in a pseudo-random order with 2.5 min intervals between stimulations. Following a period of recording to establish a stable baseline in control or drug conditions, at least three repeats of each stimuli were made within a given condition—e.g., aCSF control or drug. These repeats were then averaged within an experiment and normalized and averaged across different animals to obtain a mean effect of a drug. At least three animals per experiment were used (*N*).

To assess dopamine reuptake kinetics in *SNCA*-OVX and *Snca*-null we used two different approaches. We used exponential decay curve fits and Michaelis-Menten models to fit the falling phases of evoked DA transients using GraphPad Prism 6.0. Exponential curve fits were applied to individual transients concentration-matched between genotypes, and fitted over 1 s to extract rate constants, *k*. Conditions designed to maximize $[DA]_o$

and thereby approach levels that might approach V_{max} were train stimuli of 20 pulses at 100 Hz delivered in the presence of K_v^+-channel blocker 4-AP (100 μM), nicotinic acetylcholine receptor blocker DHβE (1 μM) and D2 receptor antagonist L-741,626 (1 μM).

In experiments applying cholesterol, slices were pre-incubated for 1 h in water soluble (ws)-cholesterol (50 μg/ml) or vehicle (methyl-β-cyclodextrin; 1 mM) prior to transferring to the recording chamber. For probucol treated experiments, slices were incubated in probucol (5 μM) or DMSO vehicle control for 30 min then transferred to recording chamber with probucol (5 μM) present in the superfusate throughout recording. For nystatin treated experiments slices were incubated in nystatin (25 or 100 μg/ml) or vehicle control (DMSO) for 30 min and then transferred to recording chamber due to potential interactions with the CFM.

Drugs

Dihydro-β-erythroidine (DHβE), nomifensine maleate salt, GBR 12935, L-741,626, 4-Aminopyridine and nystatin were purchased from Tocris Bioscience. Cocaine, methyl-β-cyclodextrin and ws-cholesterol were purchased from Sigma–Aldrich. Nystatin was purchased from Abcam. Drugs were dissolved in distilled water, DMSO (GBR 12935, L-741,626, probucol and nystatin) or 0.1 M HCl (nomifensine) to make stock aliquots at 1,000–10,000× final concentrations and stored at −20°C until required. Stock aliquots were diluted with oxygenated aCSF to the final concentration immediately before use. Nystatin and methyl-β-cyclodextrin and ws-cholesterol were prepared fresh prior to each use.

Secondary Ion Mass Spectrometry (Tof-SIMS)

Frozen brain samples were sectioned at −20°C to 6 μm thickness and the slices containing both CPu and NAc were mounted on ITO glass slides. The brain tissue samples were stored in capped containers at −80°C until SIMS analysis. The sections were dehydrated in a vacuum desiccator for 30 min. ToF-SIMS analysis was performed using a J105 3D mass spectrometry imaging instrument (Ionoptika, Limited, U.K.). The instrument was equipped with a continuous 40 keV primary gas cluster ion beam (GCIB) to analyze the samples and clusters of CO_2 gas (AGA, Sweden) with a nominal size of 6,000 [$(CO_2)_{6,000}^+$] were utilized as the primary analysis ion beam. The ion dose density was kept below the static limit (1×10^{13} ions/cm^2), in order to minimize surface damage. Spectra were obtained over a mass range of 100–1,000 Da and the mass resolution was approximately 5,000–8,000 in the range of intact phospholipids. In order to perform statistical analysis and comparison between *SNCA*-OVX and *Snca*-null mice, data were collected from three animals per genotype and from four slices per mouse. Data were normalized to the total ion counts obtained in the measured mass range.

Statistical Analysis

All data are expressed as means ± SEM (unless otherwise stated) and the sample size, n = technical repeats and N = number of animals. The number of animals in each data set was ≥3. Parametric tests were used for data sets with equal variances and passed normality tests (D'Agostino and Pearson normality test). Subsequently, comparisons for differences in means were assessed using unpaired *t*-tests, or Mann–Whitney tests or one- or two-way ANOVAs with *post hoc* Sidak's multiple comparison tests using GraphPad Prism 6.0. Michaelis–Menten fits used GraphPad Prism.

RESULTS

DAT Function Is Potentiated by α-Synuclein

In mice expressing human α-synuclein on a mouse α-synuclein-null background (*SNCA*-OVX; Janezic et al., 2013), we used fast-scan cyclic voltammetry to test whether α-synuclein expression affected properties of DA release in *ex vivo* slices that are regulated by DAT. Initially, we ensured that we could replicate previously published finding that striatal DA release is impaired in *SNCA*-OVX compared to *Snca*-null mice by 3 months—(Janezic et al., 2013). In control conditions, $[DA]_o$ release evoked by a single local electrical pulse in the dorsal striatum was 34% lower in *SNCA*-OVX compared to *Snca*-null (**Figures 1A,B**, 1.69 ± 0.11 μM vs. 2.57 ± 0.20 μM), in line with previous findings. Local electrical stimuli evoke DA release by direct depolarization of DA axons and indirectly by activating nAChRs on DA axons following evoked ACh release from cholinergic interneurons (Cachope et al., 2012; Threlfell et al., 2012; Wang et al., 2014). Therefore, we also tested whether the DA deficit in *SNCA*-OVX mice is present when the ACh-driven portion of DA release is prevented. In the presence of nAChR antagonism (DHβE 1 μM), levels of $[DA]_o$ evoked by a single electrical pulse were lower than in drug-free media as previously published (Rice and Cragg, 2004), and, remained 34% lower in *SNCA*-OVX vs. *Snca*-null mice (**Figures 1A,B**, 0.37 ± 0.03 μM vs. 0.69 ± 0.05 μM).

Next, we explored DA uptake kinetics using several approaches. We first extracted decay constants, k, from single-phase exponential decay curves fitted to concentration-matched $[DA]_o$ transients evoked by either single pulse or stimulation protocols that drive elevated $[DA]_o$ (20p 100 Hz in DHβE, 4AP, L741–626). k was significantly greater in *SNCA*-OVX than *Snca*-null mice indicating faster uptake kinetics, for both stimulus protocols when analyzed either separately (**Figure 1C**) or in combination (**Figures 1D,E**). Second, we constructed a Michaelis–Menten-like plot, of the maximum decay rate (V) found on falling transients plotted vs. $[DA]_o$ and found that both V_{max} and K_m of the best-fit curves were greater in *SNCA*-OVX than *Snca*-null mice (**Figure 1F**, V_{max}: 11.8 vs. 7.2 μM/s; K_m: 4.0 vs. 1.8 μM). We then tested whether the altered DAT function in *SNCA*-OVX was reflected by differential effects of DAT inhibition on $[DA]_o$. Indeed, inhibition of DAT with either cocaine (5 μM), GBR 12935 (10 μM) or nomifensine (10 μM) resulted in a greater enhancement of evoked $[DA]_o$ in *SNCA*-OVX vs. *Snca*-null mice (**Figures 1G,H**). We explored whether the changes to DAT function might be an adaptation

to, or conversely arise independently from, a deficit in evoked DA release levels in *SNCA*-OVX mice (Janezic et al., 2013) as chronic DA levels can impact DAT function (Calipari et al., 2013; Siciliano et al., 2018; Brodnik et al., 2020). In particular we tested whether the effect of cocaine was greater in *SNCA*-OVX vs. *Snca*-null mice in the NAc where, in contrast to dorsal striatum, there is no deficit in evoked $[DA]_o$ (Janezic et al., 2013), and found that the effect of cocaine on 1p-evoked $[DA]_o$ was similarly enhanced in NAc of *SNCA*-OVX mice (**Supplementary Figure 1**) indicating that altered DAT function in *SNCA*-OVX mice occurs is not due to a DA release deficit.

In addition, we have recently shown that the DAT is a powerful regulator of short-term plasticity in DA release, whereby the DAT promotes a strong inverse relationship between $[DA]_o$ released at a subsequently paired pulse (paired-pulse ratio) and interpulse interval (IPI; Condon et al., 2019). We tested whether elevated DAT function in *SNCA*-OVX resulted in this relationship being promoted. Indeed, we found a slightly steeper inverse relationship between paired-pulse ratio and IPI in *SNCA*-OVX vs. *Snca*-null (**Figure 1I**; in the presence of nicotinic receptor antagonism to prevent the confounding effects of ACh (Rice and Cragg, 2004). In turn, for short bursts of 4 pulses, there was a steeper relationship between frequency and evoked $[DA]_o$ in *SNCA*-OVX vs. *Snca*-null (**Figure 1J**). These differences between genotypes were ameliorated by cocaine (**Figures 1I,J**), which weakened the relationship of $[DA]_o$ to IPI and frequency in both genotypes, as seen previously in wild-type mice (Condon et al., 2019).

DAT Availability Is Increased by α-Synuclein

To understand the enhanced DAT function in *SNCA*-OVX striatum we explored how DATs and α-synuclein interact. Using a proximal ligation assay (PLA) we identified that DATs form a close spatial arrangement with α-synuclein (<40 nm) in *SNCA*-OVX mice (**Figures 2A,B**), supporting the hypothesis that α-synuclein and DAT associate. We tested whether α-synuclein expression increased DAT levels using western blot. However, under reducing conditions we found no difference in total striatal DAT levels between wild-type mice (*Snca*-wt), *Snca*-null, or *SNCA*-OVX mice (**Figures 2C,D**). To validate these data, and in particular, as a positive control for the ability of western blotting to detect differences in DAT levels, we confirmed that we could detect the lower DAT levels seen in DAT-$Cre^{+/+}$ mice compared to controls (Bäckman et al., 2006). In parallel with these low levels of DAT we confirmed in DAT-Cre mice that uptake rates for released DA were correspondingly low and that there were only modest effects of cocaine on peak $[DA]_o$ and paired-pulse ratios detected with FCV (**Supplementary Figures S2A,B**). Consequently, the elevated DAT function in *SNCA*-OVX mice seems not due to different level of total DAT, suggesting that DAT function might be affected at the level of the cell surface. We tested whether α-synuclein could be revealed to modify the levels of DAT levels under more native conditions using two different assays. We immunolabeled DAT in striatum and found greater levels of DAT-immunoreactivity in *SNCA*-OVX vs. *Snca*-null striatum (**Figures 2E,F**). We also used autoradiography with [^{3}H]-cocaine to determine the relative density of striatal DAT binding sites, and found levels to be about 2.5 times higher in *SNCA*-OVX mice compared to *Snca*-null mice, with intermediate levels seen in wild-type mice *Snca*-wt; **Figures 2G,H**). The relative level of transporter binding, *SNCA*-OVX > *Snca*-wt > *Snca*-null tallies with the order of relative effect size of cocaine on increasing peak 1p-evoked $[DA]_o$ seen with cocaine in these genotypes in our hands, which is respectively 2.5-fold in *SNCA*-OVX > 2-fold in wild-types (Condon et al., 2019) > and 1.8-fold in *Snca*-null (**Figure 1**). These differences between *SNCA*-OVX and *Snca*-wt mice also correlate with the relative expression levels of pan-species α-synuclein, whereby *SNCA*-OVX expresses human α-synuclein at 2-fold the level of mouse α-synuclein seen in *Snca*-wt mice (**Figure 2I**), as previously published (Janezic et al., 2013). Together these data illustrate that DAT and α-synuclein form a close spatial interaction and that α-synuclein promotes DAT availability to bind its ligand.

Cholesterol Promotes DAT Function

There is a complex reciprocal relationship between α-synuclein and cholesterol, whereby cholesterol can influence α-synuclein levels and structural forms, and cholesterol levels have been reported to depend on α-synuclein expression (Barceló-Coblijn et al., 2006; Don et al., 2014; Ronzitti et al., 2014; Mazzulli et al., 2016; Galvagnion, 2017; Hsiao et al., 2017; Alecu and Bennett, 2019) and furthermore, somewhat analogously to our findings with α-synuclein and DAT function, cholesterol has been shown to promote ligand binding to DAT (Hong and Amara, 2010; Morissette et al., 2018) and enhance DA transport (Jones et al., 2012; Morissette et al., 2018). We therefore explored whether there is converging biology between α-synuclein and cholesterol and DAT function in *SNCA*-OVX mice. Firstly, we tested whether applied cholesterol could phenocopy the effect of α-synuclein level on DAT function. Application of water-soluble cholesterol (50 μg/ml) decreased $[DA]_o$ evoked by a single pulse in *Snca*-null mice (**Figure 3A**), and increased the rate constant *k* for exponential curve-fits to the falling phase of concentration-matched transients, indicating that applied cholesterol increases DA clearance (**Figure 3B**, *k*, 2.54 vs. 3.14 s^{-1}, $P < 0.0001$). Furthermore, applied cholesterol enhanced the effect of cocaine on peak $[DA]_o$ evoked by a single pulse in *Snca*-null mice (**Figure 3C**) and also in *SNCA*-OVX mice (**Figure 3D**). There was no difference in the effect of cocaine between vehicle and drug free conditions (**Supplementary Figure 3**). To explore whether cholesterol levels might be modified in *SNCA*-OVX mice, we measured cholesterol content of striatal tissue membranes using ToF-SIMS. We found that levels of cholesterol in *SNCA*-OVX mice were significantly lower than those in *Snca*-null mice, whereas levels of galactosylceremide (32:1) were higher (**Figures 3E,F**), which was not due to any difference in glucocerebrosidase (GBA) activity, unlike previous findings (Galvagnion, 2017; **Supplementary Figure 4**).

The finding that cholesterol content is lower in *SNCA*-OVX mice might at first seem counterintuitive, given that DAT function is enhanced in *SNCA*-OVX mice and by application of ws-cholesterol. However, these findings would be consistent

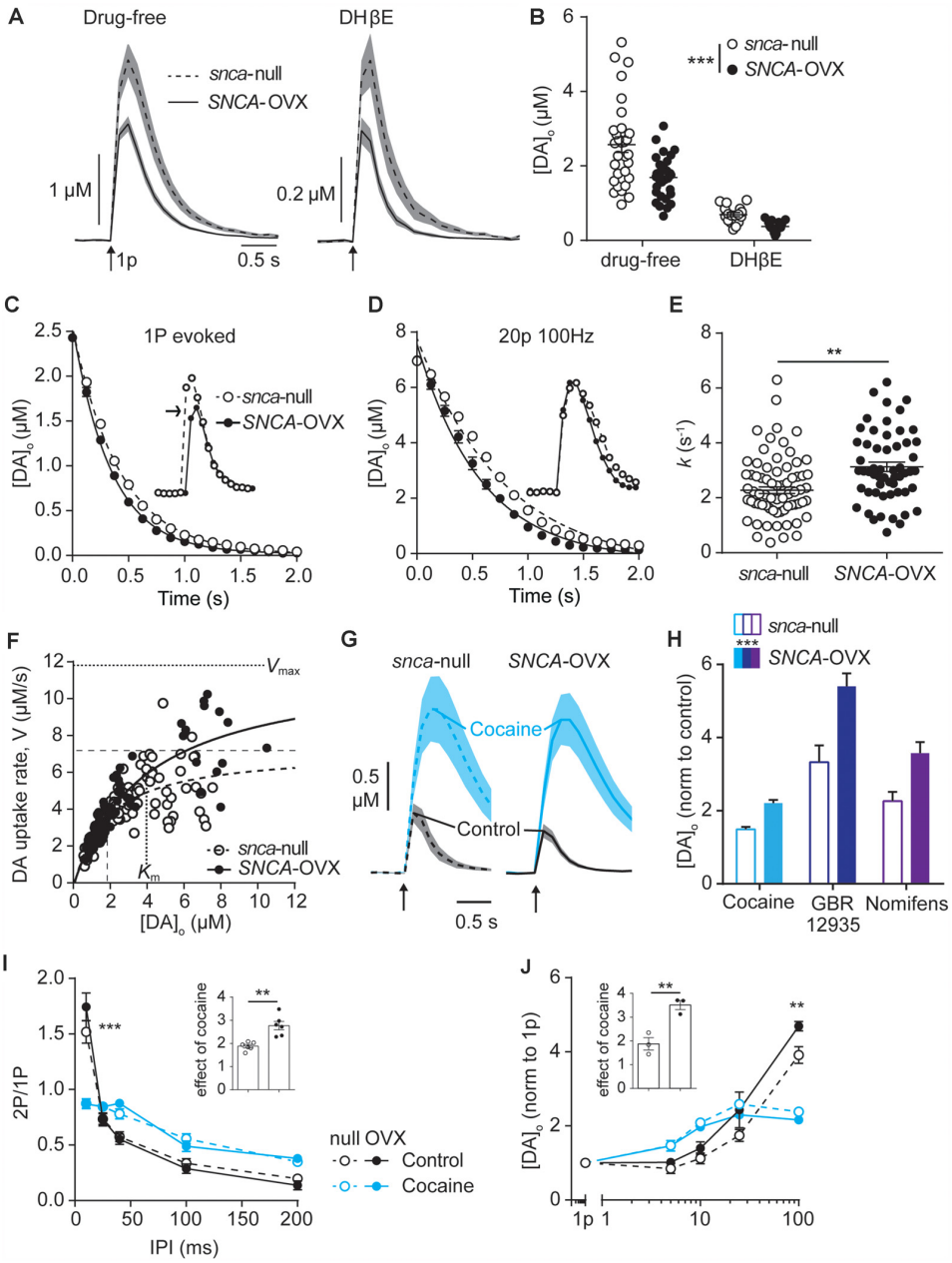

FIGURE 1 | Dopamine transporters (DAT) function is potentiated by α-synuclein. **(A)** Mean $[DA]_o \pm$ SEM (*shaded*) evoked by single pulses (*arrow*) vs. time in caudate putamen (CPu) of *Snca*-null (dashed line) and *SNCA*-OVX (solid line) mice in drug-free conditions (*left*) or DHβE (*right*). **(B)** Summary of peak evoked $[DA]_o$. ***$P < 0.001$, two-way ANOVA main effect of genotype: $F_{(1,90)} = 14.54$, $P = 0.0003$; drug x genotype interaction: $F_{(1,90)} = 3.19$, $P = 0.078$. **(C,D)** One-phase exponential decay curve fits for falling phases of the mean of concentration-matched $[DA]_o$ transients evoked by a single pulse **(C)** or 20p 20 Hz in the presence of DHBE (1 μM), 4-aminopyridine (100 μM), L-741,626 (1 μM) **(D)**, for *Snca*-null and *SNCA*-OVX mice. *Insets*, transients offset to allow for concentration-matching *(arrow)*. Comparison of *k*, *Snca*-null vs. *SNCA*-OVX: 1p, 2.39 vs. 2.92, $F_{(1,825)} = 64.5$, $P < 0.0001$; 20p, 1.29 vs. 1.73, $F_{(1,842)} = 53.01$, $P < 0.0001$. **(E)** Summary of *k* (s^{-1}) calculated for all transients, 2.34 vs. 3.13, $t_{(123)} = 3.35$, **$P = 0.0011$. **(F)** Maximum decay rates seen for each transient vs. $[DA]_o$ at that rate for *Snca*-null (unfilled) and *SNCA*-OVX (filled). Unconstrained Michelis–Menten curve-fits for null (*dashed*) and *SNCA*-OVX (solid). V_{max} and K_m are indicated by horizontal and vertical lines. $V_{max} = 7.20$ vs. 11.84 μM/s, $K_m = 1.82$ vs. 3.97 μM, comparison of fits: $F_{(2,181)} = 15.75$, $P < 0.001$, $R^2 = 0.52$ and 0.80. **(G)** Mean $[DA]_o$ (μM) ± SEM vs. time evoked by single pulses (*arrow*) in CPu, before cocaine (control, black line) and in the presence of cocaine (blue, 5 μM). **(H)** Summary of effects of DAT inhibitors cocaine, GBR 12935 and nomifensine on 1p-evoked $[DA]_o$ in *Snca*-null and *SNCA*-OVX, two-way ANOVA: effect of drug, $F_{(2,28)} = 18.63$, $P < 0.0001$; effect of genotype, $F_{(1,28)} = 18.67$, $P = 0.0002$; genotype x cocaine interaction, $F_{(2,28)} = 0.91$, $P = 0.41$. **(I)** Paired-pulse ratios (PPR) for $[DA]_o$ vs. inter-pulse interval (IPI) in control conditions (DHβE; *black*), and with cocaine (*blue*) in *Snca*-null (unfilled) and *SNCA*-OVX (filled). Two-way ANOVA: condition x IPI interaction, $F_{(12,100)} = 137.9$, $P < 0.0001$, Sidak's post-test ***$P < 0.001$. **(J)** Peak $[DA]_o$ (normalized to condition 1p) ± SEM vs. frequency for 4p trains (5–100 Hz) in control (in the presence of DHβE; *black*) and cocaine (*blue*) in *Snca*-null (unfilled) and *SNCA*-OVX (filled). Two-way ANOVA: condition x frequency interaction, $F_{(12,40)} = 19.56$, $P < 0.0001$, Sidak's posttest: ***$P < 0.001$. Insets, normalized effect of cocaine on 1p-evoked release for these datasets.

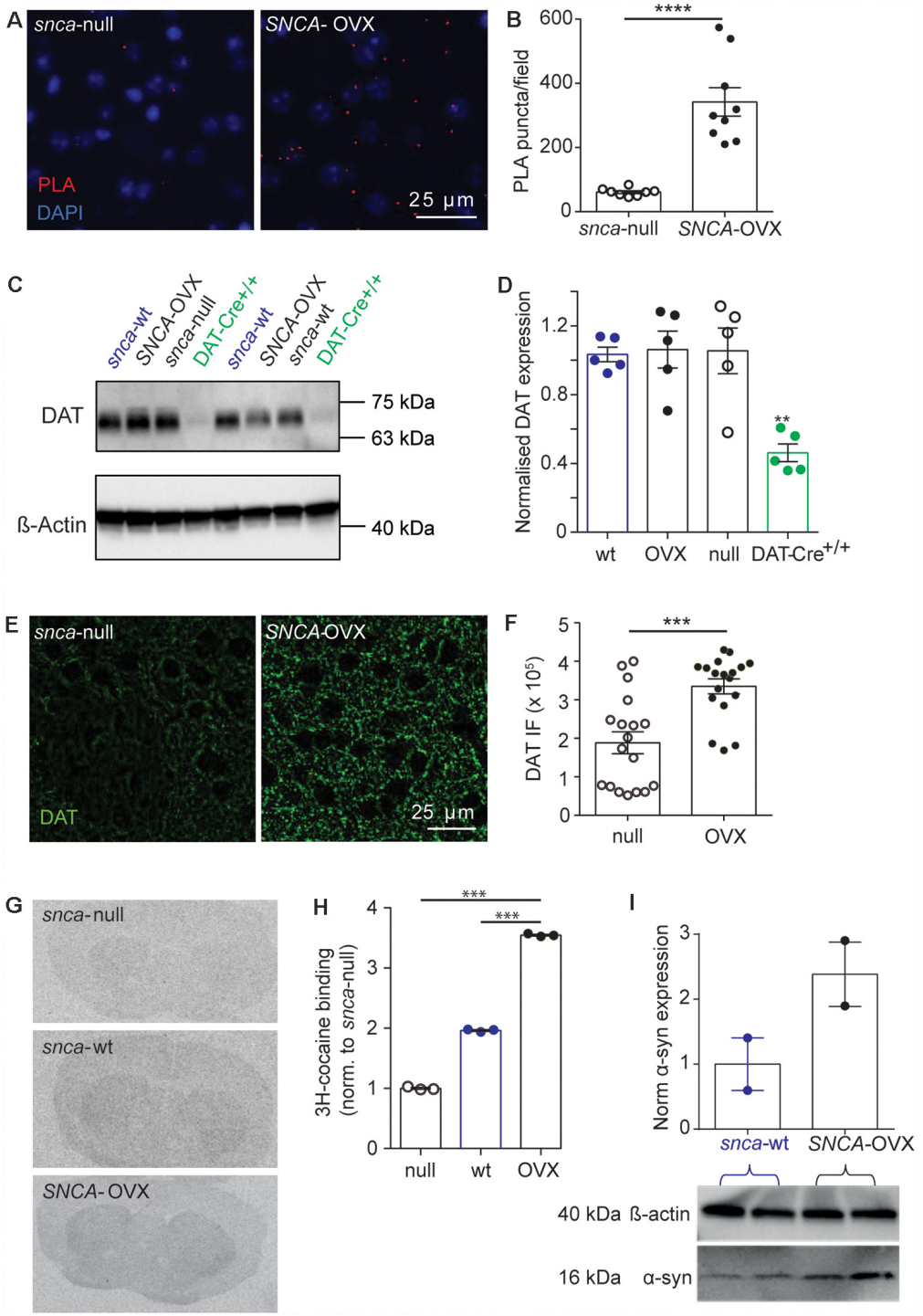

FIGURE 2 | DAT availability is promoted by α-synuclein. **(A)** Representative images of PLA puncta (DAT: syn-PLA, *red*) and DAPI (*blue)* in dorsal striatum of *Snca*-null and *SNCA*-OVX mice. Scale bar, 25 µm. **(B)** Quantification of density of DAT: α-synuclein PLA puncta. Unpaired *t*-test with Welch's correction for unequal variances, $t_{(8.156)} = 6.285$, $n = 9$ samples, $N = 3$ animals, $^{****}P < 0.0001$. **(C)** Example Western blots from striatal homogenates showing glycosylated DAT band (70 kDa), and actin band (42 kDa). **(D)** DAT levels (relative to actin) in *Snca*-wt, *Snca*-null, *SNCA*-OVX and DAT-Cre$^{+/+}$ mice. One-way ANOVA: $F_{(3,16)} = 1.03$, $P = 0.001$. *Post hoc* Dunnett's multiple comparisons test, C57BL/6J vs. DAT-Cre+/+, $^{**}P < 0.01$. **(E)** Representative images of DAT immunofluorescence (IF) in dorsal striatum. Scale bar, 25 µm. **(F)** Quantification of DAT IF. Unpaired *t*-test, $t_{(34)} = 4.29$, $^{***}P = 0.0001$, $n = 18$, $N = 3$. **(G)** Representative autoradiograms demonstrating the distribution of ^{3}H-cocaine binding sites. **(H)** Mean ± SEM ^{3}H-cocaine binding sites in striatum. One-way ANOVA: $F_{(3,7)} = 2.47$, *post hoc* Dunnett's comparisons tests for genotype, $N = 3$ per genotype, $^{***}P < 0.001$. **(I)** Western blot from striatal homogenates showing pan-species α-synuclein band (16 kDa) and actin band (42 kDa) with normalized quantification of α-synuclein expression, from *Snca*-wt and *SNCA*-OVX. $N = 2$ animals.

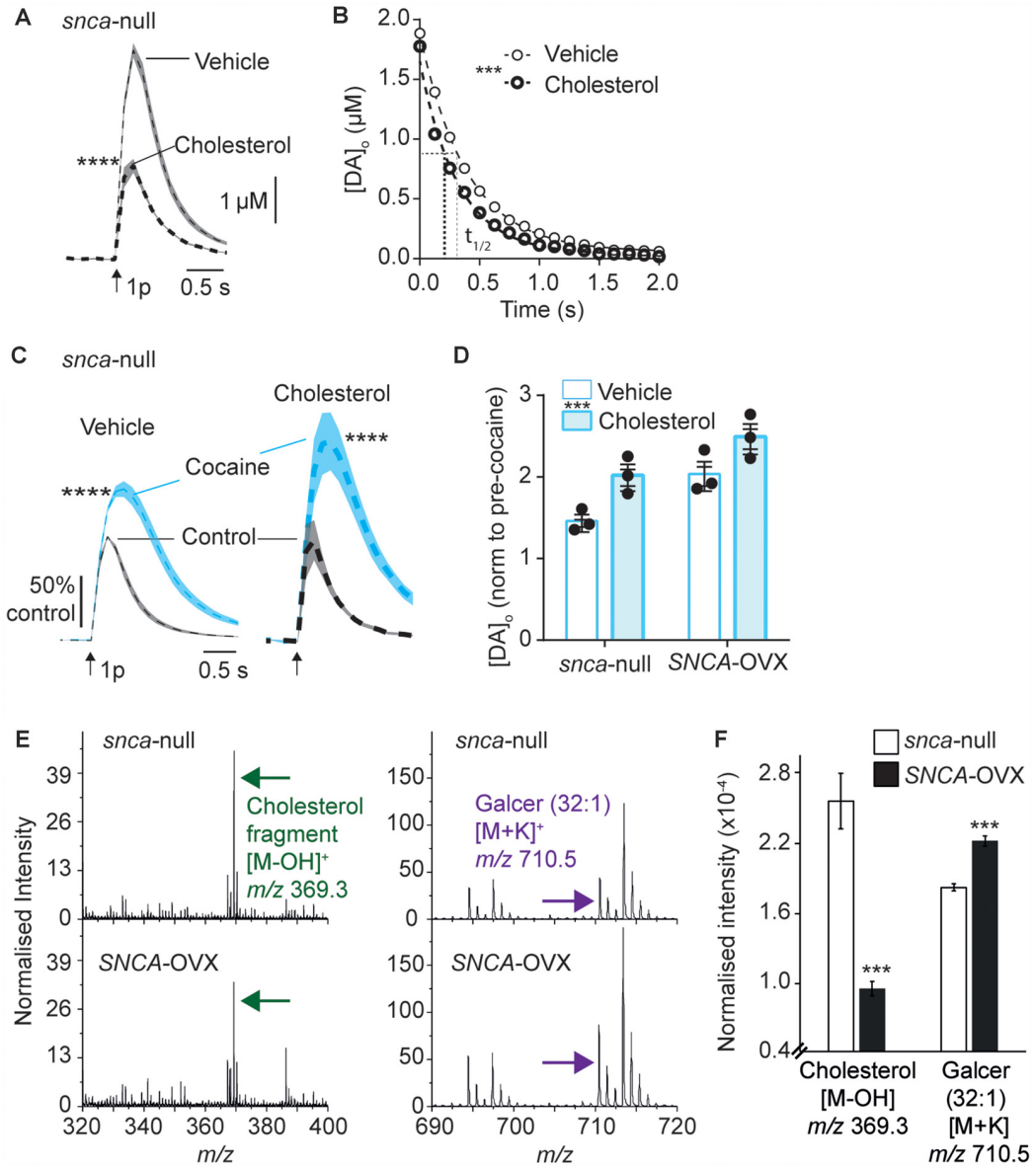

FIGURE 3 | Applied cholesterol potentiates DAT function. **(A)** Mean $[DA]_o$ ± SEM vs. time evoked by single pulses (*arrow*) in CPu from *Snca*-null mice incubated in vehicle or ws-cholesterol. $^{****}P < 0.0001$. **(B)** One-phase exponential decay curve fits for falling phases of mean $[DA]_o$ transients concentration-matched. k (s^{-1}) 2.54 (vehicle) vs. 3.14 (cholesterol), half-lives ($t_{(1/2)}$) are indicated by for vehicle (fine line) and cholesterol (thick dotted), $F_{(1,617)} = 46.4$, $^{***}P < 0.0001$. **(C)** Mean $[DA]_o$ (normalized to control conditions) ± SEM vs. time evoked by single pulses (*arrow*) in CPu of *Snca* -null mice, in control (*black*) and in the presence of cocaine (*blue*) from slices incubated in vehicle or cholesterol. $^{****}P < 0.0001$. **(D)** Summary of effects of cocaine on mean peak $[DA]_o$ ± SEM, normalized to pre-cocaine condition. Two-way ANOVA: effect of cholesterol, $F_{(1,8)} = 14.9$, $^{***}P = 0.005$; effect of genotype, $F_{(1,8)} = 15.8$, $P = 0.004$; Genotype x cocaine interaction, $F_{(1,8)} = 0.15$, $P = 0.70$. **(E)** Secondary ion mass spectrometry (SIMS) analyses of *Snca* -null (top) and *SNCA*-OVX (bottom) striatum groups obtained from the striatum region of brain tissue in positive ion mode. Cholesterol (green arrow) and galactosylceramide (*galcer*; purple arrow) signal intensity (normalized to the number of selected pixels for the spectrum). **(F)** Statistical comparison of striatal lipid species cholesterol and galcer (32:1). In SNCA−/− (unfilled bars) and *SCNA*-OVX (filled bars) Mean ± SEM (normalized to the total ion count). 2-sample *T*-test, $n = 12$, $^{***}P < 0.001$.

with α-synuclein (soluble monomeric and oligomeric forms) being able to potentiate cholesterol efflux, *via* the ATP-binding cassette (ABC) transporter ABCA1 (Hsiao et al., 2017). Elevated cholesterol efflux could reduce cellular cholesterol level, consistent with the low cellular cholesterol content seen in *SNCA*-OVX measured by ToF-SIMS, and cholesterol efflux could promote extracellular cholesterol, consistent with elevated DAT function seen in *SNCA*-OVX mice. To test whether elevated DAT function in *SNCA*-OVX mice is due to enhanced extracellular cholesterol we tested whether an inhibitor of ABCA1 activity (probucol, 5 µM) could decrease the effect of cocaine in peak $[DA]_o$. After incubation of striatal slices from *SNCA*-

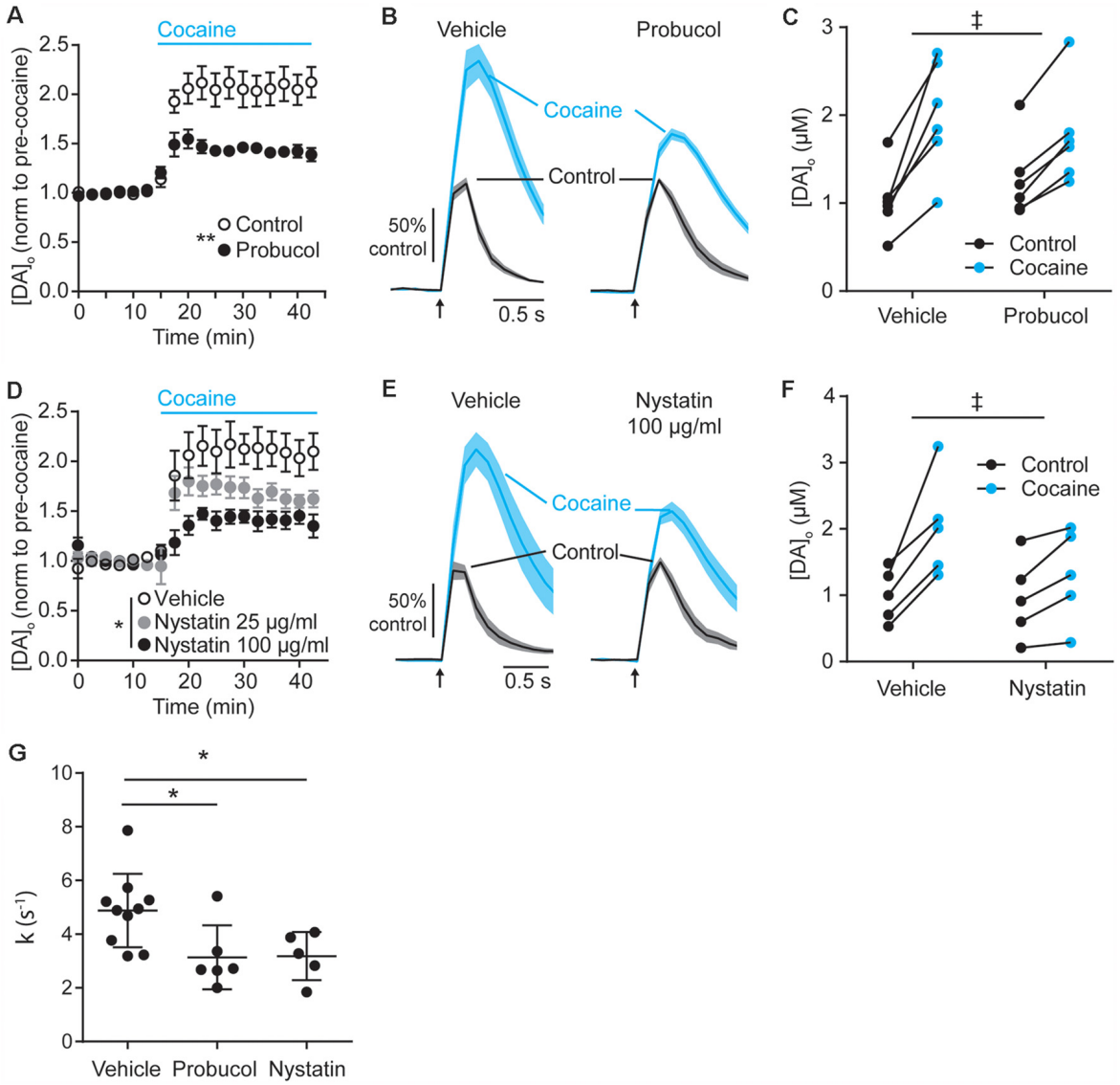

FIGURE 4 | Decreasing extracellular cholesterol in *SNCA*-OVX striatum decreases DAT control of DA release. **(A–D)** Mean peak $[DA]_o$ ± SEM evoked by 1p vs. time (min) in CPu of *SNCA*-OVX mice incubated in vehicle control (unfilled circles) or **(A)** Probucol (black), **(D)** Nystatin 25 μg/ml (gray), or 100 μg/ml (black). Cocaine (5 μM) added at 12.5 min (blue bar). Two-way ANOVAs: **(A)** repeated measures for time, time x probucol interaction, $F_{(17,170)} = 10.13$, $P < 0.0001$; effect of probucol, $F_{(1,10)} = 14.19$, $^{**}P = 0.0037$. **(D)** time x nystatin interaction, $F_{(34,204)} = 4.95$, $P < 0.0001$; effect of nystatin, $F_{(2,12)} = 5.98$, $^{*}P = 0.016$. **(B–E)** Mean $[DA]_o$ (normalized to control conditions) ± SEM (shaded) vs. time evoked by single pulses (*arrow*) in CPu of *SNCA*-OVX mice from slices incubated in vehicle or **(C)** probucol (5 μM) or **(E)** nystatin 100 μg/ml (thick line) in control condition (black) or with cocaine (blue). **(C–F)** $[DA]_o$ before and after cocaine from slices treated with vehicle and **(C)** probucol or **(F)** nystatin 100 μg/ml. Two-way ANOVA, repeated measures by cocaine treatment: **(C)** probucol x cocaine interaction, $F_{(1,10)} = 6.51$, $^{‡}P = 0.029$; **(F)** nystatin x cocaine interaction, $F_{(1,8)} = 7.16$, $^{‡}P = 0.028$. **(G)** Summary of k (s^{-1}) for averaged falling phase transients in vehicle, probucol, or nystatin. One-way ANOVA: $F_{(2,18)} = 5.17$, $P = 0.017$, Dunnett's post-tests: vehicle vs. probucol, $^{*}P = 0.024$; vehicle vs. nystatin, $^{*}P = 0.038$.

OVX mice in probucol, we found that the effect of cocaine was less than in vehicle-treated slices (**Figures 4A–C**). In addition, we tested whether nystatin (25–100 μg/ml), which chelates extracellular/sequesters lipid raft cholesterol, could also decrease the effect of cocaine. Indeed, nystatin, decreased the effect of cocaine on peak $[DA]_o$ in a concentration-dependent manner (**Figures 4D–F**), and both nystatin and probucol led to a significant slowing of the falling phases of DA transients (**Figure 4G**). Together these data support the hypothesis that α-synuclein potentiates DAT function *via* its ability to potentiate cholesterol efflux *via* the ABCA1 transporter, leading to an elevation in extracellular cholesterol that in turn potentiates DAT function.

DISCUSSION

Here, we report that striatal DAT function is enhanced in the *SNCA*-OVX mouse model of PD, compared to *Snca-*

null background controls. Furthermore, we show changes to cholesterol and other lipid levels, that can directly impact DAT function. These findings demonstrate that the intersecting biologies of α-synuclein and cholesterol can powerfully regulate DAT function.

In *SNCA*-OVX mice, we found close spatial localization of α-synuclein and DAT, and increased DAT function in several aspects relative to *Snca*-null controls. DAT function in wild-type mice represented an intermediate level between the extremes of *SNCA*-OVX and *Snca*-null mice. Extracellular DA clearance kinetics were enhanced, the effects of DAT inhibitors on peak $[DA]_o$ were promoted, and there was enhanced facilitation of DA release at short IPIs in *SNCA*-OVX mice. Correspondingly, we found evidence of elevated membrane DAT levels, from *in situ* autoradiography and DAT-immunocytochemistry, but not greater total DAT expression. We found that both the V_{max} and K_m for DA uptake were greater than in *Snca*-null control mice. These data therefore indicate that α-synuclein is promoting DAT availability, and also changing DA binding. These outcomes could also potentially be driven by an increase in forward trafficking of DAT to the membrane, a decrease in reverse trafficking and/or a change in conformation, including the relative outward- vs. inward-facing DAT. Our findings that K_m appears increased in *SNCA*-OVX mice in addition to V_{max}, appears to indicate that α-synuclein not only increases the number of DA-translocation sites, but also affects how DA binds to DAT. One candidate explanation might be an underlying change to the stoichiometry of DATs e.g., an increase in monomeric/oligomeric (dimer or tetramer) ratio, which was not assessed here but is known to affect the number of actively translocating DAT units and their availability to bind substrate (Gur et al., 2017; Zhen and Reith, 2018). Interestingly, cholesterol has been shown to affect how DA binds to DAT by promoting an outward facing confirmation (Hong and Amara, 2010; Jones et al., 2012). Intriguingly, our lipid analyses identified significantly lower levels of cellular cholesterol in *SNCA*-OVX mice, which is consistent with a report that soluble monomeric α-synuclein promotes cholesterol efflux, *via* the ABCA1 transporter (Hsiao et al., 2017). Potentially, the level of ceramide and cholesterol are related in a way that an increasing level of ceramide at the cell membrane promotes the release of cholesterol to the extracellular space, resulting in a lower level of cholesterol at the cell membrane (Mohammadi et al., 2018). Cholesterol efflux *via* ABCA1 transporter can occur from neurons or astrocytes (Lee et al., 2020). Correspondingly, we found that probucol, which decreases ABCA1 transporter function, or a cholesterol chelator, decreased the effect of cocaine on elevating peak evoked $[DA]_o$. These findings together suggest that the elevated DAT function in *SNCA*-OVX mice is dependent on extracellular cholesterol, reflected in reduced membrane cholesterol levels. This hypothesis should be explored in future work and in other PD models.

These findings support a converging biology of α-synuclein, cholesterol and DAT, but the precise mechanism is still to be characterized. DATs are subject to extensive post-translation modifications (phosphorylation, palmitoylation, glycosylation, ubiquitination), express many regulatory binding domains (CRAC, SH3) and associate with other molecular regulators of DA release (D2Rs, RIM, synt-1; Vaughan and Foster, 2013). Both cholesterol and α-synuclein have scope to affect many of these parameters both directly and indirectly e.g., α-synuclein and cholesterol affecting VGCC function (Ronzitti et al., 2014), which in turn interacts with DAT function (Kile et al., 2010; Cameron et al., 2015). Furthermore, although DAT expression is restricted to DA axons, cholesterol and α-synuclein are more ubiquitous. Therefore, our observed effects of α-synuclein induced cholesterol efflux might involve other interacting striatal cellular networks, neuronal and non-neuronal.

The overall up-regulation of DAT function in *SNCA*-OVX mice also offers insights into another previous observation in this mouse model. DATs can apparently limit the recruitment of vesicles for release (Venton et al., 2006; Kile et al., 2010), and we have previously shown that vesicles within DA axons in *SNCA*-OVX mice are less dispersed and more tightly clustered, and that DA releasability is restricted (Janezic et al., 2013). Elevated DAT function could be a mechanism that contributes to this redistribution of DA vesicles and limited DA release.

We note that the increases to DAT function in *SNCA*-OVX mice, compared to background control mice, also similar parallel effects of knocking down a different protein in DA neurons, the Ca^{2+} binding protein calbindin-D28k (calb1; Brimblecombe et al., 2019). Calb1 expression in midbrain DA neurons is negatively correlated with vulnerability to degeneration in PD, being lower in SN neurons that are more vulnerable. A multiple hit hypothesis has been suggested for driving DA neuron degeneration in PD, arising from hits that include α-synuclein burden, Ca^{2+} burden and oxidative stress due to DA load after uptake (Sulzer, 2007; Mosharov et al., 2009; Post et al., 2018; Surmeier, 2018). We speculate that the enhanced DA uptake rates caused by α-synuclein could have important implications for pathology in Parkinson's. For example, increased DA uptake would decrease the extracellular availability of DA for acting on post-synaptic targets, exacerbating the effects of a deficit in DA release. Furthermore, elevated DAT function might increase intracellular levels of DA and provide an additional source of oxidative stress due to production of toxic metabolites, especially if coupled with low VMAT levels (Miller et al., 1999; Masoud et al., 2015). Our findings that both cholesterol and α-synuclein function are linked to DA uptake biology, indicate that the pathological gain of each individual hit will not act independently, but co-operatively through biological interactions.

In conclusion, we show that human α-synuclein promotes multiple facets of the ways in which DATs regulate DA release and extracellular levels, through mechanisms that depend on extracellular cholesterol. The interacting biology of α-synuclein, cholesterol and DATs leads to changes to DAT function and DA signaling in this mouse model of PD that will diminish DA output, and could potentiate the burden of cytosolic DA, potentially promoting vulnerability to degeneration.

DATA AVAILABILITY STATEMENT

The raw data supporting the conclusions of this article will be made available by the authors, without undue reservation.

ETHICS STATEMENT

The animal study was reviewed and approved by University of Oxford DPAG/EP AWERB.

AUTHOR CONTRIBUTIONS

KB, ST, and SC conceived the study. ST, AM, BR, NC-R, NP, RA, FS, TS, NB-V, and KB acquired and analyzed data. RW-M, AE, and TS contributed resources and commented on the manuscript. KB and SC co-wrote the manuscript. All authors contributed to the article and approved the submitted version.

FUNDING

The work was funded by grant support from Parkinson's UK (J-1403; G-1803). RA was supported by an MRC-iCASE award. NP was supported by an MRC-DTA Studentship.

SUPPLEMENTARY MATERIAL

The Supplementary Material for this article can be found online at: https://www.frontiersin.org/articles/10.3389/fncel.2021.658244/full#supplementary-material.

REFERENCES

Abeliovich, A., Schmitz, Y., Fariñas, I., Choi-Lundberg, D., Ho, W. H., Castillo, P. E., et al. (2000). Mice lacking α-synuclein display functional deficits in the nigrostriatal dopamine system. *Neuron* 25, 239–252. doi: 10.1016/s0896-6273(00)80886-7

Alecu, I., and Bennett, S. A. L. (2019). Dysregulated lipid metabolism and its role in α-synucleinopathy in Parkinson's disease. *Front. Neurosci.* 13:328. doi: 10.3389/fnins.2019.00328

Alegre-Abarrategui, J., Brimblecombe, K. R., Roberts, R. F., Velentza-Almpani, E., Tilley, B. S., Bengoa-Vergniory, N., et al. (2019). Selective vulnerability in α-synucleinopathies. *Acta Neuropathol.* 138, 681–704. doi: 10.1007/s00401-019-02010-2

Alza, N. P., Iglesias González, P. A., Conde, M. A., Uranga, R. M., and Salvador, G. A. (2019). Lipids at the crossroad of α-synuclein function and dysfunction: biological and pathological implications. *Front. Cell. Neurosci.* 13:175. doi: 10.3389/fncel.2019.00175

Bäckman, C. M., Malik, N., Zhang, Y., Shan, L., Grinberg, A., Hoffer, B. J., et al. (2006). Characterization of a mouse strain expressing Cre recombinase from the 3' untranslated region of the dopamine transporter locus. *Genesis* 44, 383–390. doi: 10.1002/dvg.20228

Barceló-Coblijn, G., Golovko, M. Y., Weinhofer, I., Berger, J., and Murphy, E. J. (2006). Brain neutral lipids mass is increased in α-synuclein gene-ablated mice. *J. Neurochem.* 101, 132–141. doi: 10.5435/JAAOS-D-17-00026

Bellucci, A., Navarria, L., Falarti, E., Zaltieri, M., Bono, F., Collo, G., et al. (2011). Redistribution of DAT/α-synuclein complexes visualized by "*in situ*" proximity ligation assay in transgenic mice modeling early Parkinson's disease. *PLoS One* 6:e27959. doi: 10.1371/journal.pone.0027959

Bengoa-Vergniory, N., Faggiani, E., Ramos-Gonzalez, P., Kirkiz, E., Connor-Robson, N., Brown, L. V., et al. (2020). CLR01 protects dopaminergic neurons *in vitro* and in mouse models of Parkinson's disease. *Nat. Commun.* 11:4885. doi: 10.1038/s41467-020-18689-x

Brimblecombe, K. R., Vietti-Michelina, S., Platt, N. J., Kastli, R., Hnieno, A., Gracie, C. J., et al. (2019). Calbindin-D28K limits dopamine release in ventral but not dorsal striatum by regulating Ca^{2+} availability and dopamine transporter function. *ACS Chem. Neurosci.* 10, 3419–3426. doi: 10.1021/acschemneuro.9b00325

Brodnik, Z. D., Xu, W., Batra, A., Lewandowski, S. I., Ruiz, C. M., Mortensen, O. V., et al. (2020). Chemogenetic manipulation of dopamine neurons dictates cocaine potency at distal dopamine transporters. *J. Neurosci.* 40, 8767–8779. doi: 10.1523/JNEUROSCI.0894-20.2020

Cachope, R., Mateo, Y., Mathur, B. N., Irving, J., Wang, H.-L., Morales, M., et al. (2012). Selective activation of cholinergic interneurons enhances accumbal phasic dopamine release: setting the tone for reward processing. *Cell Rep.* 2, 33–41. doi: 10.1016/j.celrep.2012.05.011

Calipari, E. S., Ferris, M. J., Salahpour, A., Caron, M. G., and Jones, S. R. (2013). Methylphenidate amplifies the potency and reinforcing effects of amphetamines by increasing dopamine transporter expression. *Nat. Commun.* 4:2720. doi: 10.1038/ncomms3720

Cameron, K. N., Solis, E. Jr., Ruchala, I., De Felice, L. J., and Eltit, J. M. (2015). Amphetamine activates calcium channels through dopamine transporter-mediated depolarization. *Cell Calcium* 58, 457–466. doi: 10.1016/j.ceca.2015.06.013

Chadchankar, H., Ihalainen, J., Tanila, H., and Yavich, L. (2011). Decreased reuptake of dopamine in the dorsal striatum in the absence of α-synuclein. *Brain Res.* 1382, 37–44. doi: 10.1016/j.brainres.2011.01.064

Condon, M. D., Platt, N. J., Zhang, Y.-F., Roberts, B. M., Clements, M. A., Vietti-Michelina, S., et al. (2019). Plasticity in striatal dopamine release is governed by release-independent depression and the dopamine transporter. *Nat. Commun.* 10:4263. doi: 10.1038/s41467-019-12264-9

Cragg, S. J., and Rice, M. E. (2004). DAncing past the DAT at a DA synapse. *Trends Neurosci.* 27, 270–277. doi: 10.1016/j.tins.2004.03.011

Don, A. S., Hsiao, J.-H. T., Bleasel, J. M., Couttas, T. A., Halliday, G. M., and Kim, W. S. (2014). Altered lipid levels provide evidence for myelin dysfunction in multiple system atrophy. *Acta Neuropathol. Commun.* 2:150. doi: 10.1186/s40478-014-0150-6

Franklin, K. B. J., and Paxinos, G. (2004). *Mouse Brain in Stereotaxic Coordinates.* San Diego, CA: Academic Press.

Galvagnion, C. (2017). The Role of lipids interacting with α-synuclein in the pathogenesis of Parkinson's disease. *J. Parkinsons Dis.* 7, 433–450. doi: 10.3233/JPD-171103

Gur, M., Cheng, M. H., Zomot, E., and Bahar, I. (2017). Effect of dimerization on the dynamics of neurotransmitter:sodium symporters. *J. Phys. Chem. B* 121, 3657–3666. doi: 10.1021/acs.jpcb.6b09876

Hong, W. C., and Amara, S. G. (2010). Membrane cholesterol modulates the outward facing conformation of the dopamine transporter and alters cocaine binding. *J. Biol. Chem.* 285, 32616–32626. doi: 10.1074/jbc.M110.150565

Hsiao, J.-H. T., Halliday, G. M., and Kim, W. S. (2017). α-synuclein regulates neuronal cholesterol efflux. *Molecules* 22:1769. doi: 10.3390/molecules22101769

Janezic, S., Threlfell, S., Dodson, P. D. P. D., Dowie, M. J. M. J., Taylor, T. N., Potgieter, D., et al. (2013). Deficits in dopaminergic transmission precede neuron loss and dysfunction in a new Parkinson model. *Proc. Natl. Acad. Sci. U S A* 110, E4016–E4025. doi: 10.1073/pnas.1309143110

John, C. E., and Jones, S. R. (2007). Voltammetric characterization of the effect of monoamine uptake inhibitors and releasers on dopamine and serotonin uptake in mouse caudate-putamen and substantia nigra slices. *Neuropharmacology* 52, 1596–1605. doi: 10.1016/j.neuropharm.2007.03.004

Jones, K. T., Zhen, J., and Reith, M. E. A. (2012). Importance of cholesterol in dopamine transporter function. *J. Neurochem.* 123, 700–715. doi: 10.1111/jnc.12007

Kile, B. M., Guillot, T. S., Venton, B. J., Wetsel, W. C., Augustine, G. J., and Wightman, R. M. (2010). Synapsins differentially control dopamine and serotonin release. *J. Neurosci.* 30, 9762–9770. doi: 10.1523/JNEUROSCI.2071-09.2010

Lee, F. J. S., Lie, F., Pristupa, Z. B., and Niznik, H. B. (2001). Direct binding and functional coupling of α-synuclein to the dopamine transporters accelerate

dopamine-induced apoptosis. *FASEB J.* 15, 916–926. doi: 10.1096/fj.00-0334com

Lee, J. A., Hall, B., Allsop, J., Alqarni, R., and Allen, S. P. (2020). Lipid metabolism in astrocytic structure and function. *Semin. Cell Dev. Biol.* doi: 10.1016/j.semcdb.2020.07.017 [Epub ahead of print].

Lehmensiek, V., Tan, E.-M., Liebau, S., Lenk, T., Zettlmeisl, H., Schwarz, J., et al. (2006). Dopamine transporter-mediated cytotoxicity of 6-hydroxydopamine *in vitro* depends on expression of mutant α-synucleins related to Parkinson's disease. *Neurochem. Int.* 48, 329–340. doi: 10.1016/j.neuint.2005.11.008

Lundblad, M., Decressac, M., Mattsson, B., and Bjorklund, A. (2012). Impaired neurotransmission caused by overexpression of α-synuclein in nigral dopamine neurons. *Proc. Natl. Acad. Sci. U S A* 109, 3213–3219. doi: 10.1073/pnas.1200575109

Man, W. K., De Simone, A., Barritt, J. D., Vendruscolo, M., Dobson, C. M., and Fusco, G. (2020). A role of cholesterol in modulating the binding of α-synuclein to synaptic-like vesicles. *Front. Neurosci.* 14:18. doi: 10.3389/fnins.2020.00018

Masoud, S. T., Vecchio, L. M., Bergeron, Y., Hossain, M. M., Nguyen, L. T., Bermejo, M. K., et al. (2015). Increased expression of the dopamine transporter leads to loss of dopamine neurons, oxidative stress and l-DOPA reversible motor deficits. *Neurobiol. Dis.* 74, 66–75. doi: 10.1016/j.nbd.2014.10.016

Mazzulli, J. R., Zunke, F., Isacson, O., Studer, L., and Krainc, D. (2016). α-synuclein-induced lysosomal dysfunction occurs through disruptions in protein trafficking in human midbrain synucleinopathy models. *Proc. Natl. Acad. Sci. U S A* 113, 1931–1936. doi: 10.1073/pnas.1520335113

Miller, G. W., Gainetdinov, R. R., Levey, A. I., and Caron, M. G. (1999). Dopamine transporters and neuronal injury. *Trends Pharmacol. Sci.* 20, 424–429. doi: 10.1016/s0165-6147(99)01379-6

Mohammadi, A. S., Li, X., and Ewing, A. G. (2018). Mass spectrometry imaging suggests that cisplatin affects exocytotic release by alteration of cell membrane lipids. *Anal. Chem.* 90, 8509–8516. doi: 10.1021/acs.analchem.8b01395

Morissette, M., Morin, N., Rouillard, C., and Di Paolo, T. (2018). Membrane cholesterol removal and replenishment affect rat and monkey brain monoamine transporters. *Neuropharmacology* 133, 289–306. doi: 10.1016/j.neuropharm.2018.01.039

Mosharov, E. V., Larsen, K. E., Kanter, E., Phillips, K. A., Wilson, K., Schmitz, Y., et al. (2009). Interplay between cytosolic dopamine, calcium and α-synuclein causes selective death of substantia nigra neurons. *Neuron* 62, 218–229. doi: 10.1016/j.neuron.2009.01.033

Pissadaki, E. K., and Bolam, J. P. (2013). The energy cost of action potential propagation in dopamine neurons: clues to susceptibility in Parkinson's disease. *Front. Comput. Neurosci.* 7:13. doi: 10.3389/fncom.2013.00013

Post, M. R., Lieberman, O. J., and Mosharov, E. V. (2018). Can interactions between α-synuclein, dopamine and calcium explain selective neurodegeneration in Parkinson's disease? *Front. Neurosci.* 12:161. doi: 10.3389/fnins.2018.00161

Rice, M. E., and Cragg, S. J. (2004). Nicotine amplifies reward-related dopamine signals in striatum. *Nat. Neurosci.* 7, 583–584. doi: 10.1038/nn1244

Richter, F., Gabby, L., McDowell, K. A., Mulligan, C. K., De La Rosa, K., Sioshansi, P. C., et al. (2017). Effects of decreased dopamine transporter levels on nigrostriatal neurons and paraquat/maneb toxicity in mice. *Neurobiol. Aging* 51, 54–66. doi: 10.1016/j.neurobiolaging.2016.11.015

Ritz, B. R., Manthripragada, A. D., Costello, S., Lincoln, S. J., Farrer, M. J., Cockburn, M., et al. (2009). Dopamine transporter genetic variants and pesticides in Parkinson's disease. *Environ. Health Perspect.* 117, 964–969. doi: 10.1289/ehp.0800277

Ronzitti, G., Bucci, G., Emanuele, M., Leo, D., Sotnikova, T. D., Mus, L. V., et al. (2014). Exogenous α-synuclein decreases raft partitioning of Cav2.2 channels inducing dopamine release. *J. Neurosci.* 34, 10603–10615. doi: 10.1523/JNEUROSCI.0608-14.2014

Senior, S. L., Ninkina, N., Deacon, R., Bannerman, D., Buchman, V. L., Cragg, S. J., et al. (2008). Increased striatal dopamine release and hyperdopaminergic-like behavior in mice lacking both α-synuclein and γ-synuclein. *Eur. J. Neurosci.* 27, 947–957. doi: 10.1111/j.1460-9568.2008.06055.x

Siciliano, C. A., Saha, K., Calipari, E. S., Fordahl, S. C., Chen, R., Khoshbouei, H., et al. (2018). Amphetamine reverses escalated cocaine intake *via* restoration of dopamine transporter conformation. *J. Neurosci.* 38, 484–497. doi: 10.1523/JNEUROSCI.2604-17.2017

Singleton, A. B., Farrer, M., Johnson, J., Singleton, A., Hague, S., Kachergus, J., et al. (2003). α-Synuclein locus triplication causes Parkinson's disease. *Science* 302:841. doi: 10.1126/science.1090278

Sonders, M. S., Zhu, S. J., Zahniser, N. R., Kavanaugh, M. P., and Amara, S. G. (1997). Multiple ionic conductances of the human dopamine transporter: the actions of dopamine and psychostimulants. *J. Neurosci.* 17, 960–974. doi: 10.1523/JNEUROSCI.17-03-00960.1997

Sulzer, D. (2007). Multiple hit hypotheses for dopamine neuron loss in Parkinson's disease. *Trends Neurosci.* 30, 244–250. doi: 10.1016/j.tins.2007.03.009

Sulzer, D., Cragg, S. J., and Rice, M. E. (2016). Striatal dopamine neurotransmission: regulation of release and uptake. *Basal Ganglia* 6, 123–148. doi: 10.1016/j.baga.2016.02.001

Surmeier, D. J. (2018). Determinants of dopaminergic neuron loss in Parkinson's disease. *FEBS J.* 285, 3657–3668. doi: 10.1111/febs.14607

Swant, J., Goodwin, J. S., North, A., Ali, A. A., Gamble-George, J., Chirwa, S., et al. (2011). α-synuclein stimulates a dopamine transporter-dependent chloride current and modulates the activity of the transporter. *J. Biol. Chem.* 286, 43933–43943. doi: 10.1074/jbc.M111.241232

Threlfell, S., Clements, M. A., Khodai, T., Pienaar, I. S., Exley, R., Wess, J., et al. (2010). Striatal muscarinic receptors promote activity dependence of dopamine transmission *via* distinct receptor subtypes on cholinergic interneurons in ventral versus dorsal striatum. *J. Neurosci.* 30, 3398–3408. doi: 10.1523/JNEUROSCI.5620-09.2010

Threlfell, S., Lalic, T., Platt, N. J., Jennings, K. A., Deisseroth, K., and Cragg, S. J. (2012). Striatal dopamine release is triggered by synchronized activity in cholinergic interneurons. *Neuron* 75, 58–64. doi: 10.1016/j.neuron.2012.04.038

van de Giessen, E. M., de Win, M. M. L., Tanck, M. W. T., van den Brink, W., Baas, F., and Booij, J. (2009). Striatal dopamine transporter availability associated with polymorphisms in the dopamine transporter gene SLC6A3. *J. Nucl. Med.* 50, 45–52. doi: 10.2967/jnumed.108.053652

Vaughan, R. A., and Foster, J. D. (2013). Mechanisms of dopamine transporter regulation in normal and disease states. *Trends Pharmacol. Sci.* 34, 489–496. doi: 10.1016/j.tips.2013.07.005

Venton, B. J., Seipel, A. T., Phillips, P. E. M., Wetsel, W. C., Gitler, D., Greengard, P., et al. (2006). Cocaine increases dopamine release by mobilization of a synapsin-dependent reserve pool. *J. Neurosci.* 26, 3206–3209. doi: 10.1523/JNEUROSCI.4901-04.2006

Wang, L., Zhang, X., Xu, H., Zhou, L., Jiao, R., Liu, W., et al. (2014). Temporal components of cholinergic terminal to dopaminergic terminal transmission in dorsal striatum slices of mice. *J. Physiol.* 592, 3559–3576. doi: 10.1113/jphysiol.2014.271825

Wersinger, C., and Sidhu, A. (2003). Attenuation of dopamine transporter activity by α-synuclein. *Neurosci. Lett.* 340, 189–192. doi: 10.1016/s0304-3940(03)00097-1

Zhen, J., and Reith, M. E. A. (2018). Functional properties of dopamine transporter oligomers after copper linking. *J. Neurochem.* 144, 162–171. doi: 10.1111/jnc.14259

Conflict of Interest: The authors declare that the research was conducted in the absence of any commercial or financial relationships that could be construed as a potential conflict of interest.

frontiers in Cellular Neuroscience

REVIEW
published: 06 May 2021
doi: 10.3389/fncel.2021.662859

EAAT5 Glutamate Transporter-Mediated Inhibition in the Vertebrate Retina

Peter D. Lukasiewcz[1,2]*, *Gregory W. Bligard*[1] and *James D. DeBrecht*[1]

[1] Department of Ophthalmology & Visual Sciences, Washington University School of Medicine in St. Louis, St. Louis, MO, United States, [2] Department of Neuroscience, Washington University School of Medicine in St. Louis, St. Louis, MO, United States

Glutamate transporters typically remove glutamate from the synaptic cleft. In addition, all glutamate transporters have a chloride channel, which is opened upon glutamate binding to the transporter. There are five types of glutamate transporter (EAATs 1–5, excitatory amino acid transporters), which have distinct chloride conductances. Some EAATs that have low chloride conductances, remove glutamate from the synaptic cleft most effectively (e.g., EAAT1). By contrast, EAATs that have high chloride conductances, remove glutamate less effectively (e.g., EAAT5). We have studied EAAT5 in the retina. In the retina, light activates a chloride current, mediated by the glutamate activation of EAAT5. EAAT5 is not a significant contributor to lateral inhibition in the retina. Instead, it is the main source of autoinhibition to rod bipolar cells (RBCs). EAAT5-mediated inhibition has a substantial effect on synaptic transmission from RBCs to downstream retinal neurons.

Keywords: EAAT5, glutamate, transporter, retina, inhibition, light-response

OPEN ACCESS

Edited by:
Annalisa Scimemi, University at Albany, United States

Reviewed by:
Christoph Fahlke, Julich-Forschungszentrum, Helmholtz-Verband Deutscher Forschungszentren (HZ), Germany
Andrés E. Chávez, Universidad de Valparaiso, Chile

***Correspondence:**
Peter D. Lukasiewcz
lukasiewicz@wustl.edu

Specialty section:
This article was submitted to Cellular Neurophysiology, a section of the journal Frontiers in Cellular Neuroscience

Received: *01 February 2021*
Accepted: *19 March 2021*
Published: *06 May 2021*

Citation:
Lukasiewcz PD, Bligard GW and DeBrecht JD (2021) EAAT5 Glutamate Transporter-Mediated Inhibition in the Vertebrate Retina. Front. Cell. Neurosci. 15:662859. doi: 10.3389/fncel.2021.662859

INTRODUCTION

Glutamate is not enzymatically broken down. Thus, the uptake of glutamate from the synapse terminates the glutamate signal. Typically, the glutamate signaling ends by the rapid diffusion of glutamate from the synapse. Subsequent glutamate reuptake into glia and neurons clears released glutamate from the synapse, ultimately terminating the glutamate-evoked, excitatory signal. Generally, glial glutamate transporters play a larger role than neuronal glutamate transporters in clearing glutamate from the synapse and terminating the excitatory signal in retina and the brain (Higgs and Lukasiewicz, 1999; Amara and Fontana, 2002).

There are five subtypes of EAATs 1–5, excitatory amino acid transporters (for reviews, see Amara and Fontana, 2002; Vandenberg and Ryan, 2013; Fahlke et al., 2016). Glutamate transporters are found on glia and neurons (see **Figure 1**). The isoforms, EAAT1–2 are primarily considered glial transporters and EAAT3–5 are primarily considered neuronal glutamate transporters (Amara and Fontana, 2002; Vandenberg and Ryan, 2013). There are exceptions to this general rule; EAAT2 is found on some retinal and brain neurons and EAAT5 is found on some retinal glia (Eliasof et al., 1998; Petr et al., 2015; Rimmele and Rosenberg, 2016).

All EAATs have two functions, they can bind and clear glutamate and they can function as anion channels (Fahlke et al., 2016). EAATs 1–3 clear glutamate from the synapse effectively but have relatively small anion conductances. EAATs 4 and 5 clear glutamate from the synapse relatively inefficiently (compared to EAATs 1–3), but they have large anion conductances (Fairman et al., 1995; Arriza et al., 1997; Fahlke et al., 2016). Machtens et al. (2015) describe the molecular mechanisms that form the anion conductance by EAATs.

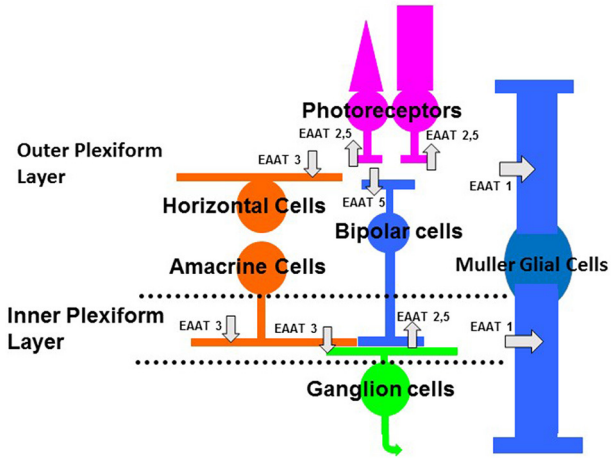

FIGURE 1 | Schematic of the vertebrate retina showing the main classes of neurons and glia. Photoreceptors (rods, on right, and cones, on left) provide input to bipolar cells and horizontal cells. Synaptic contacts between photoreceptor and their post-synaptic targets occur in the outer plexiform layer. Bipolar cells, which relay information between photoreceptors and ganglion cells, provide input to amacrine cells and ganglion cells. Horizontal cells and amacrine cells are laterally ranging cells that modulate the flow of visual information in the outer and inner plexiform layers, respectively. The Muller cell is the main glial cell in the retina, spanning the entire retina thickness, from photoreceptors to ganglion cell axons. Glutamate transporters are indicated by the gray arrows. The subtypes of EAATs or glutamate transporters and the cell types on which they are located (see text for more explanation) are indicated in the schematic. Some glutamate transporters or EAATs are located on photoreceptors and bipolar cells, where they act as glutamate receptors that gate anion conductances (EAAT5) (Picaud et al., 1995b; Veruki et al., 2006). Glutamate transporters (EAAT1) are also on Muller cells, where they take up glutamate and terminate the excitatory signal (Higgs and Lukasiewicz, 1999).

This review focuses on the vertebrate retina. There are several isoforms of EAATs in the retina (Rauen, 2000). EAATs 1–3 are found on both glial cells and neurons and are efficient transporters of glutamate, but mediate a small chloride current (if at all). EAATs 1–3 are found in the retina. EAAT1 is primarily localized in the Muller glial cell (Rauen et al., 1996; Lehre et al., 1997; Pow and Barnett, 1999; Sarthy et al., 2005), as indicated in **Figure 1**. EAAT2 is found in photoreceptors and in bipolar cells (Rauen and Kanner, 1994; Eliasof et al., 1998), as shown in **Figure 1**. EAAT2 is also a presynaptic EAAT in the brain (Petr et al., 2015; Rimmele and Rosenberg, 2016). EAAT3 is found in the inner retina (Rauen et al., 1996; Schultz and Stell, 1996; Schniepp et al., 2004). There is EAAT3 immunocytochemical labeling of horizontal cells, amacrine cells, and ganglion cells (**Figure 1**). EAATs 4 and 5 mediate large chloride conductances (Fairman et al., 1995; Arriza et al., 1997), but only EAAT5 is found in the neurons and Muller cells of the retina (Arriza et al., 1997; Ward et al., 2004). EAAT4 immuno-labeling is not found in neurons or Muller glial cells of the retina (Ward et al., 2004). EAAT5, by contrast, mediates a large chloride current, is found almost exclusively in the retina (Arriza et al., 1997) and is the focus of this review (see **Figure 1**). Because glutamate binding to this isoform of EAAT gates a chloride conductance that mediates inhibition, EAAT5 affects visual processing in the retina, as noted below.

Numerous groups have studied EAAT5's role in visual processing at the photoreceptor and bipolar cell outputs (Eliasof and Werblin, 1993; Picaud et al., 1995b; Grant and Werblin, 1996; Palmer et al., 2003; Rabl et al., 2003; Veruki et al., 2006; Wersinger et al., 2006; Ichinose and Lukasiewicz, 2012; Bligard et al., 2020). EAAT4 is not found in the neurons or Muller glial cells of the retina, based on Northern blot experiments (Eliasof et al., 1998) or immunohistochemistry (Ward et al., 2004) and likely does not play a role in retinal processing. Thus, EAAT5, which mediates a large chloride conductance, is found almost exclusively in the retina and affects visual processing in the both synaptic layers of the retina, is the focus of this review.

CLONING THE EAAT5 TRANSPORTER

The EAATs were first cloned and expressed in oocytes by the Amara group (Amara and Fontana, 2002). The last EAAT cloned was EAAT5 by Arriza et al. (1997). This isoform was found to have a large chloride ion conductance associated with it. Northern blots showed that it was found primarily in retina (Arriza et al., 1997). Subsequent studies by Eliasof et al. (1998) showed the expression of EAATs in the salamander retina. EAAT5 immuno-signals were found in photoreceptors, Muller glial cells, and bipolar cells (Eliasof et al., 1998) (**Figure 1**). Functional studies, at the time, suggested that it has pre-synaptic and post-synaptic roles in photoreceptors and bipolar cells, respectively (Grant and Dowling, 1995; Picaud et al., 1995b; Grant and Werblin, 1996).

There is no EAAT5-specific antagonist or EAAT5 knockout animal. EAAT5 transporters' location and functions have been attributed to the use of EAAT5-specific antibodies (Eliasof et al., 1998; Wersinger et al., 2006). Additionally, EAAT5 was cloned from the human retina (Arriza et al., 1997), where it is found primarily by Northern blot analysis. EAAT5 also mediates a large chloride conductance, when heterologously expressed in frog oocytes (Arriza et al., 1997; Eliasof et al., 1998). Finally, the neurons or Muller glia of the retina do not express EAAT4, the other isoform with a large chloride conductance (Fairman et al., 1995). Thus, it is inferred that the large chloride conductance that is mediated by an EAAT is the EAAT5 transporter.

The roles of glutamate transporters in signaling have been well-studied in the retina (Picaud et al., 1995b; Grant and Werblin, 1996; Higgs and Lukasiewicz, 1999; Palmer et al., 2003; Wersinger et al., 2006; Ichinose and Lukasiewicz, 2012). In particular, variants of the glutamate transporters with large anion conductances have been investigated in retina. Typically, chloride mediates the anion current. Signaling in both synaptic layers, the outer plexiform layer, where photoreceptors make synaptic contacts with bipolar and horizontal cells, and the inner plexiform layer, where bipolar cells make synaptic contacts with amacrine and ganglion cells, EAATs shape the excitatory signal (**Figure 1**). **Figure 1** shows a schematic view of EAATs found in the retina. EAAT5 is found in the outer plexiform layer on several neuronal types. It is found presynaptically on rod and

cone photoreceptor terminals (Picaud et al., 1995a; Grant and Werblin, 1996). In addition, it is found post-synaptically on the dendrites of teleost fish ON bipolar cells (Grant and Dowling, 1995).

In mammals and fish, EAAT5 is found on the synaptic terminals of ON bipolar cells, which depolarize to increments of light (Palmer et al., 2003; Veruki et al., 2006; Wersinger et al., 2006; Ichinose and Lukasiewicz, 2012; Bligard et al., 2020). In mammals, EAAT5 is only found on the synaptic terminals of rod bipolar cells, but not on the terminals of cone bipolar cells at the inner plexiform layer (Veruki et al., 2006; Wersinger et al., 2006; Ichinose and Lukasiewicz, 2012; Bligard et al., 2020). Thus, EAAT5 may modulate the rod signaling pathway in mammalian retina, but not the cone signaling pathways.

EAAT5'S FUNCTIONAL ROLE IN ROD AND CONE PHOTORECEPTORS

Does EAAT5 signaling play a functional role in the retina? In the outer retina, EAAT5 is found in the outer plexiform layer on both rod and cone photoreceptor terminals (Picaud et al., 1995b; Grant and Werblin, 1996). Glutamate that is released from rod and cone photoreceptors activates that EAAT5, negatively feeding back, activating a chloride conductance, inhibiting the photoreceptor and reducing the further release of glutamate. In these cases (primarily in lower vertebrates), ECl is more negative than the photoreceptor membrane potential. Thus, activation of the EAAT5 gated chloride conductance results in a hyperpolarization of the photoreceptor and a reduction in the rate of release of glutamate. Rabl et al. (2003) show that activation of EAATs on rods reduces calcium currents, which in turn reduces glutamate release. Postsynaptic partners of photoreceptors, such as off bipolar cells and horizontal cells, are depolarized by glutamate. Activation of the EAAT5 chloride conductance would limit the depolarization in these postsynaptic, retinal neurons. In some mammals, ECl is more positive than the cone resting potential. Thus, EAAT5 activation results in a depolarization and an increase in release of glutamate. Szmajda and Devries (2011) showed that glutamate can spill over and activate neighboring cones, causing them to depolarize when EAAT5 is activated on neighboring cones. The depolarization of neighboring cones by the activation of EAAT5 may act to prime them, allowing them to respond more effectively to darkness (cones are depolarized in the dark and hyperpolarized by light).

EAAT5 ROLE ON FISH BIPOLAR CELL DENDRITES

EAAT5 is also found post-synaptically on white perch ON bipolar cell dendrites (Grant and Dowling, 1995) (**Figure 1**). Note that these dendritically localized transporter gated anion channels have not been found in all vertebrate retinas, primarily only fish. ON bipolar cell dendrites contact photoreceptors. Thus, changes in the release of glutamate affect glutamate responses that are mediated by ON bipolar cell dendrites. Grant and Dowling (1995) reported that the cone inputs, but not the rod inputs, were mediated by a glutamate-activated chloride conductance. Pharmacological evidence indicated that this conductance had the properties of a glutamate transporter. It was not affected by ligands that typically activate or block known glutamate receptors. It was likely an EAAT5 glutamate transporter because it exhibited a chloride conductance and was sensitive to glutamate transporter-specific ligands. The rod input, by contrast, was mediated by the more conventional mGluR6 receptors (as in other vertebrate retinas). Glutamate binding to the mGluR6 receptor closed a non-specific cation conductance that is mediated by TRPM1 channels (Koike et al., 2009; Morgans et al., 2009, 2010), hyperpolarizing the bipolar cell (Slaughter and Miller, 1981). These fish neurons are mixed bipolar cells that receive inputs from both rod and cones. The rod input (increased glutamate release in the dark) results in the glutamate activation of mGluR6 receptors, the closing of a non-specific cation TRPM1 channel, and a hyperpolarization of the ON bipolar cell. By contrast, the cone input results in glutamate activation of transporter-mediated chloride conductance and the hyperpolarization of the white perch, ON bipolar cell (Grant and Dowling, 1995). Thus, rod and cone inputs to the carp ON bipolar cell both hyperpolarize the ON bipolar cell in darkness, but they do so by distinct functional mechanisms.

Similar results have been reported for mouse ON bipolar cell dendrites (Tse et al., 2014). Tse et al. (2014) claim that a component of the mouse ON bipolar cell response is mediated by an EAAT-like conductance, as in fish. However, when many components of the mGluR6 and TRPM1 complex are eliminated, they have no ON bipolar responses (Dryja et al., 2005; Gregg et al., 2007; Koike et al., 2009; Morgans et al., 2009). This would suggest that the transporter conductance described by Tse et al. (2014) plays little or no role in ON bipolar cell signaling in mouse. The role of an EAAT conductance on mouse on bipolar cells remains unclear.

EAAT5'S FUNCTION ROLE AT THE INNER PLEXIFORM LAYER

EAAT5 is also located on the synaptic terminals of fish bipolar cells and mammalian rod bipolar cells, the outputs of bipolar cells, which contact amacrine and ganglion cells (**Figure 1**). Palmer et al. (2003) showed that EAATs are present at fish ON bipolar cells. They found that EAAT activation elicited a current in isolated, fish synaptic terminals. The authors showed that the pharmacology of the anion current was consistent with an EAAT and not conventional glutamate, GABA, or glycine receptors. The magnitude of the EAAT anion current correlated with glutamate release (glutamate activates the anion conductance), which was assessed with capacitance measurements (glutamate vesicle fusion resulted in capacitance increases).

EAAT5 transporters are found not only on the bipolar cell terminals of fish ON bipolar cells but also on retinal bipolar cells of mammals. Wersinger et al. (2006) showed that EAAT5 transporters are present on the terminals of rat, rod bipolar cells. This special type of ON bipolar cell mediates rod signaling, relaying rod photoreceptor signals to AII or rod amacrine cells.

Depolarization of the rod bipolar cells elicited glutamate release and activated EAAT5 transporters. This chloride current, was inhibitory and novel. As with some photoreceptors (see above), activation of EAAT5 causes negative feedback in rod bipolar cells, reducing the further release of glutamate by activating a chloride conductance and reducing excitatory signaling. This current was not affected by GABA or glycine receptor antagonists but was reduced by the glutamate transporter blocker TBOA. Thus, as with teleost fish, this was a novel, inhibitory chloride current that was not mediated by a conventional inhibitory neurotransmitter, such as GABA or glycine, which have been shown to mediate amacrine cell inhibition to bipolar cells (Chavez et al., 2006, 2010; Eggers and Lukasiewicz, 2006; Chavez and Diamond, 2008). Instead, as in fish, this new form of inhibition was presumably mediated by an EAAT5 transporter.

Around the same time as the Wersinger et al. (2006) and Veruki et al. (2006) also showed in rat retina that glutamate transporters mediated a novel inhibition, which was independent of GABA and glycine. Using dual recordings, they showed that glutamate release spilled over and activated neighboring rod bipolar cells. Additional experiments show that the transporter-mediated inhibition affected transmission from the rod bipolar cell to postsynaptic targets. Thus, transporter-mediated inhibition, like conventional inhibition, reduced signaling to postsynaptic neurons. So, transporter-mediated anion conductances modulate retinal signaling, in addition to conventional inhibitory neurotransmitters, such as GABA.

TRANSPORTERS MEDIATE LIGHT-EVOKED SIGNALING IN RETINA

Light-evoked signaling is also affected by transporter-mediated inhibition (Ichinose and Lukasiewicz, 2012). As noted by Veruki et al. (2006), spillover occurred between neighboring rod bipolar cells. Two spatially defined types of light-evoked inhibition occurred. Transporter-mediated inhibition is spatially restricted to spillover between nearby bipolar cells (∼100 microns). By contrast, conventional inhibition, mediated by GABA and glycine, was mediated by amacrine cells and had a larger spatial extent (>500 microns). Activation of the transporter with puffs of D-aspartate reduced the light-evoked bipolar responses and blockade of the transporter current with TBOA enhanced the light-evoked bipolar response (Ichinose and Lukasiewicz, 2012). Note that TBOA (threo-beta-benyloxyaspartate) is a general blocker of EAATs (Shimamoto et al., 1998). A specific EAAT5 blocker does not exist, as noted above.

Blockade of transporter currents with TBOA enhanced exocytosis. Activation of the transporter currents with D-aspartate reduced exocytosis. Taken together, light-evoked signaling from rod bipolar cells is modulated by transporter-mediated inhibition. Thus, the light-evoked output of rod bipolar cells is affected not only by conventional inhibition from GABAergic and glycinergic amacrine cells but also by inhibition caused by the activation of EAAT5. The extent of light-evoked inhibition attributed to transporters is relatively local (<100 microns) and caused by glutamate spillover from neighboring rod bipolar cells. Conventional inhibition, by contrast, occurs over a wider lateral extent (∼500 microns) and is mediated by wide field amacrine cells.

Rod bipolar cells receive two types of conventional GABA-mediated inhibition, reciprocal, feedback inhibition (with a narrow spatial extent) and wide-field, lateral inhibition (with a wide spatial extent) (Chavez et al., 2006, 2010). Transporters also mediate a form of feedback inhibition; glutamate released from rod bipolar cells feeds back and activates EAAT5 transporters, which inhibit the rod bipolar cell (Palmer et al., 2003; Veruki et al., 2006; Wersinger et al., 2006; Ichinose and Lukasiewicz, 2012). As with photoreceptors, described above, activation of the glutamate transporter limits the release of additional glutamate by transporter-mediated inhibition. Most of the feedback to rod bipolar cells was mediated by transporter (Bligard et al., 2020). By contrast, all of the wide-field lateral inhibition was mediated by GABA, released from amacrine cell contacts with rod bipolar cell (Eggers and Lukasiewicz, 2006; Chavez et al., 2010; Ichinose and Lukasiewicz, 2012; Bligard et al., 2020). Why do two forms of feedback inhibition exist at rod bipolar cells? It turns out that the two forms of feedback inhibition have distinct time courses. Conventional, GABAergic feedback is fast (both onset and offset) and transporter-mediated feedback is slow (both onset and offset).

In silico modeling by Bligard et al. (2020) showed that both the fast, GABA-mediated feedback and the slow transporter-mediated feedback were so that the transmitter release from the rod bipolar cell was optimal (not too large or too little). Either form of feedback alone could suffice to keep transmitter release optimal, but the amount of either form of feedback need to be increased many fold to attain this. The two forms of feedback, with different time courses, complemented each other and were necessary for optimal transmitter release from the rod bipolar cell. Thus, the combination of the quick and transient GABA feedback with the slower and more sustained transporter feedback were optimal for modulating both the initial and prolonged phases of transmit release from rod bipolar cells.

The EAATS, especially EAAT5 (Arriza et al., 1997) and EAAT4 (Fairman et al., 1995), act as an anion channel that can be gated by glutamate. In the retina, EAAT5 is the predominant transporter with anion channel properties (Arriza et al., 1997; Eliasof et al., 1998). EAAT5 is found on photoreceptors and rod bipolar cells (Wersinger et al., 2006) where it can be activated by glutamate that is released from these neurons (Picaud et al., 1995b; Grant and Werblin, 1996; Veruki et al., 2006; Wersinger et al., 2006; Ichinose and Lukasiewicz, 2012; Bligard et al., 2020). The EAAT5 transporter can be activated by light and, when activated, can affect visual processing in the retina (Ichinose and Lukasiewicz, 2012; Bligard et al., 2020).

Works by Gameiro et al. (2011) and Schneider et al. (2014) heterologously expressed EAAT5 and found that, in contrast to Veruki et al. (2006), the transporter-mediated chloride current was smaller and slower. The findings using heterologous expression systems suggest that EAAT5 does not mediate chloride currents in retina. It is unclear why the properties of native and heterologously expressed EAAT5 are different. Native and heterologously expressed behaviors are not always

identical. This is the case with heterologously expressed and native neurotransmitter receptors (Parker et al., 2003). It is possible that an intracellular or an extracellular factor present in the native case is not present in the expressed case, accounting for the differences.

SUMMARY

EAAT5 is found in most vertebrate retinas. Functional studies have been performed on amphibian, teleost fish, and mammals. EAAT5 was initially cloned from the human retina (Arriza et al., 1997). EAAT5 gates an anion conductance (Arriza et al., 1997). This transporter-gated conductance shapes the release of glutamate from photoreceptors and bipolar cells. This form of inhibition (in most cases) modulates visual processing in both the first and second synaptic layers of the retina. Because the signal that gates the transporter-mediated conductance is spatially limited (typically to spillover transmission to nearby neurons), this form of inhibition is typically limited to local feedback. GABA and other conventional neurotransmitters mediate longer range-wide field inhibition (Eggers and Lukasiewicz, 2006; Chavez and Diamond, 2008; Chavez et al., 2010). Bipolar cells receive two types of feedback inhibition at their terminals (Wersinger et al., 2006; Bligard et al., 2020). The rapid, transient feedback that is mediated by synaptic GABA is complemented by the slow, sustained feedback inhibition that is mediated by EAAT5 to optimally control signaling between mammalian rod bipolar cells and their postsynaptic targets.

There is still some uncertainty about the native anion channel gated by glutamate's interaction with EAATs. Most of the literature suggests that EAAT5 is the native anion channel gated by glutamate (Arriza et al., 1997; Eliasof et al., 1998). However, results from heterologously expressed EAAT5 show functional differences (Gameiro et al., 2011; Schneider et al., 2014). The differences in EAAT5 function could be attributed to processes in the native tissue that are not present in expression systems. Boehmer et al. (2005) show that EAAT5 function may be regulated by kinases. Additional work is needed in the regulation of EAATS in the retina.

It is also possible that another EAAT contributes to retinal processing. This is suggested by the functional differences between heterologously expressed EAAT5 (Gameiro et al., 2011) and the putative native EAAT5 (Veruki et al., 2006). It is still not fully understood what the roles of EAATs are in visual processing.

AUTHOR CONTRIBUTIONS

All authors contributed to manuscript, read, and approved the submitted version.

FUNDING

This work was supported by the National Eye Institute Grant EY08922 (PL), EY013360 (GB), EY02687, and Research to Prevent Blindness (W.U. Dept. Ophthalmology).

REFERENCES

Amara, S. G., and Fontana, A. C. (2002). Excitatory amino acid transporters: keeping up with glutamate. *Neurochem. Int*. 41, 313–318. doi: 10.1016/S0197-0186(02)00018-9

Arriza, J. L., Eliasof, S., Kavanaugh, M. P., and Amara, S. G. (1997). Excitatory amino acid transporter 5, a retinal glutamate transporter coupled to a chloride conductance. *Proc. Natl. Acad. Sci. U. S. A.* 94, 4155–4160. doi: 10.1073/pnas.94.8.4155

Bligard, G. W., DeBrecht, J., Smith, R. G., and Lukasiewicz, P. D. (2020). Light-evoked glutamate transporter EAAT5 activation coordinates with conventional feedback inhibition to control rod bipolar cell output. *J. Neurophysiol*. 123, 1828–1837. doi: 10.1152/jn.00527.2019

Boehmer, C., Rajamanickam, J., Schniepp, R., Kohler, K., Wulff, P., Kuhl, D., et al. (2005). Regulation of the excitatory amino acid transporter EAAT5 by the serum and glucocorticoid dependent kinases SGK1 and SGK3. *Biochem. Biophys. Res. Commun*. 329, 738–742. doi: 10.1016/j.bbrc.2005.02.035

Chavez, A. E., and Diamond, J. S. (2008). Diverse mechanisms underlie glycinergic feedback transmission onto rod bipolar cells in rat retina. *J. Neurosci*. 28, 7919–7928. doi: 10.1523/JNEUROSCI.0784-08.2008

Chavez, A. E., Grimes, W. N., and Diamond, J. S. (2010). Mechanisms underlying lateral GABAergic feedback onto rod bipolar cells in rat retina. *J. Neurosci*. 30, 2330–2339. doi: 10.1523/JNEUROSCI.5574-09.2010

Chavez, A. E., Singer, J. H., and Diamond, J. S. (2006). Fast neurotransmitter release triggered by Ca influx through AMPA-type glutamate receptors. *Nature* 443, 705–708. doi: 10.1038/nature05123

Dryja, T. P., McGee, T. L., Berson, E. L., Fishman, G. A., Sandberg, M. A., Alexander, K. R., et al. (2005). Night blindness and abnormal cone electroretinogram ON responses in patients with mutations in the GRM6 gene encoding mGluR6. *Proc. Natl. Acad. Sci. U. S. A.* 102, 4884–4889. doi: 10.1073/pnas.0501233102

Eggers, E. D., and Lukasiewicz, P. D. (2006). GABAA, GABAC and glycine receptor-mediated inhibition differentially affects light-evoked signaling from mouse retinal rod bipolar cells. *J. Physiol*. 572, 215–225. doi: 10.1113/jphysiol.2005.103648

Eliasof, S., Arriza, J. L., Leighton, B. H., Kavenaugh, M. P., and Amara, S. G. (1998). Excitatory amino acid transporters of the salamander retina: identification, localization and function. *J. Neurosci*. 18, 698–712. doi: 10.1523/JNEUROSCI.18-02-00698.1998

Eliasof, S., and Werblin, F. (1993). Characterization of the glutmate transporter in retinal cones of the tiger salamander. *J. Neurosci*. 13, 402–411. doi: 10.1523/JNEUROSCI.13-01-00402.1993

Fahlke, C., Kortzak, D., and Machtens, J. P. (2016). Molecular physiology of EAAT anion channels. *Pflugers Arch*. 468, 491–502. doi: 10.1007/s00424-015-1768-3

Fairman, W. A., Vandenberg, R. J., Arriza, J. L., Kavanaught, M. P., and Amara, S. G. (1995). An excitatory amino-acid transporter with properties of a ligand-gated chloride channel. *Nature* 375, 599–603. doi: 10.1038/375599a0

Gameiro, A., Braams, S., Rauen, T., and Grewer, C. (2011). The discovery of slowness: low-capacity transport and slow anion channel gating by the glutamate transporter EAAT5. *Biophys. J*. 100, 2623–2632. doi: 10.1016/j.bpj.2011.04.034

Grant, G. B., and Dowling, J. E. (1995). A glutamate-activated chloride current in cone-driven ON bipolar cells of the white perch retina. *J. Neurosci*. 15, 3852–3862. doi: 10.1523/JNEUROSCI.15-05-03852.1995

Grant, G. B., and Werblin, F. S. (1996). A glutamate-elicited chloride current with transporter-like properties in rod photoreceptors of the tiger salamander. *Vis. Neurosci*. 13, 135–144. doi: 10.1017/S0952523800007185

Gregg, R. G., Kamermans, M., Klooster, J., Lukasiewicz, P. D., Peachey, N. S., Vessey, K. A., et al. (2007). Nyctalopin expression in retinal bipolar cells restores visual function in a mouse model of complete X-linked congenital stationary night blindness. *J. Neurophysiol*. 98, 3023–3033. doi: 10.1152/jn.00608.2007

Higgs, M. H., and Lukasiewicz, P. D. (1999). Glutamate uptake limits synaptic excitation of retinal ganglion cells. *J. Neurosci.* 19, 3691–3700. doi: 10.1523/JNEUROSCI.19-10-03691.1999

Ichinose, T., and Lukasiewicz, P. D. (2012). The mode of retinal presynaptic inhibition switches with light intensity. *J. Neurosci.* 32, 4360–4371. doi: 10.1523/JNEUROSCI.5645-11.2012

Koike, C., Obara, T., Uriu, Y., Numata, T., Sanuki, R., Miyata, K., et al. (2009). TRPM1 is a component of the retinal ON bipolar cell transduction channel in the mGluR6 cascade. *Proc. Natl. Acad. Sci. U. S. A.* 107, 332–337. doi: 10.1073/pnas.0912730107

Lehre, K. P., Davanger, S., and Danbolt, N. C. (1997). Localization of the glutamate transporter protein GLAST in rat retina. *Brain Res.* 744, 129–137. doi: 10.1016/S0006-8993(96)01022-0

Machtens, J. P., Kortzak, D., Lansche, C., Leinenweber, A., Kilian, P., Begemann, B., et al. (2015). Mechanisms of anion conduction by coupled glutamate transporters. *Cell* 160, 542–553. doi: 10.1016/j.cell.2014.12.035

Morgans, C. W., Brown, R. L., and Duvoisin, R. M. (2010). TRPM1: the endpoint of the mGluR6 signal transduction cascade in retinal ON-bipolar cells. *BioEssays* 32, 609–614. doi: 10.1002/bies.200900198

Morgans, C. W., Zhang, J., Jeffrey, B. G., Nelson, S. M., Burke, N. S., Duvoisin, R. M., et al. (2009). TRPM1 is required for the depolarizing light response in retinal ON-bipolar cells. *Proc. Natl. Acad. Sci. U. S. A.* 106, 19174–19178. doi: 10.1073/pnas.0908711106

Palmer, M. J., Taschenberger, H., Hull, C., Tremere, L., and von Gersdorff, H. (2003). Synaptic activation of presynaptic glutamate transporter currents in nerve terminals. *J. Neurosci.* 23, 4831–4841. doi: 10.1523/JNEUROSCI.23-12-04831.2003

Parker, J. C., Sarkar, D., Quick, M. W., and Lester, R. A. (2003). Interactions of atropine with heterologously expressed and native alpha 3 subunit-containing nicotinic acetylcholine receptors. *Br. J. Pharmacol.* 138, 801–810. doi: 10.1038/sj.bjp.0705124

Petr, G. T., Sun, Y., Frederick, N. M., Zhou, Y., Dhamne, S. C., Hameed, M. Q., et al. (2015). Conditional deletion of the glutamate transporter GLT-1 reveals that astrocytic GLT-1 protects against fatal epilepsy while neuronal GLT-1 contributes significantly to glutamate uptake into synaptosomes. *J. Neurosci.* 35, 5187–5201. doi: 10.1523/JNEUROSCI.4255-14.2015

Picaud, S. A., Larsson, H. P., Grant, G. B., Lecar, H., and Werblin, F. S. (1995b). Glutamate-gated chloride channel with glutamate-transporter-like properties in cone photoreceptors of the tiger salamander. *J. Neurophysiol.* 74, 1760–1771. doi: 10.1152/jn.1995.74.4.1760

Picaud, S. A., Larsson, H. P., Wellis, D. P., Lecar, H., and Werblin, F. (1995a). Cone photoreceptors respond to their own glutamate release in the tiger salamander. *Proc. Natl. Acad. Sci. U. S. A.* 92, 9417–9421. doi: 10.1073/pnas.92.20.9417

Pow, D. V., and Barnett, N. L. (1999). Changing patterns of spatial buffering of glutamate in developing rat retinae are mediated by the Muller cell glutamate transporter GLAST. *Cell Tissue Res.* 297, 57–66. doi: 10.1007/s004410051333

Rabl, K., Bryson, E. J., and Thoreson, W. B. (2003). Activation of glutamate transporters in rods inhibits presynaptic calcium currents. *Vis. Neurosci.* 20, 557–566. doi: 10.1017/S0952523803205095

Rauen, T. (2000). Diversity of glutamate transporter expression and function in the mammalian retina. *Amino Acids* 19, 53–62. doi: 10.1007/s007260070033

Rauen, T., and Kanner, B. I. (1994). Localization of the glutamate transporter GLT-1 in rat and macaque monkey retinae. *Neurosci. Lett.* 169, 137–140. doi: 10.1016/0304-3940(94)90375-1

Rauen, T., Rothstein, J. D., and Wässle, H. (1996). Differential expression of three glutamate transporter subtypes in the rat retina. *Cell Tissue Res.* 286, 325–336. doi: 10.1007/s004410050702

Rimmele, T. S., and Rosenberg, P. A. (2016). GLT-1: the elusive presynaptic glutamate transporter. *Neurochem. Int.* 98, 19–28. doi: 10.1016/j.neuint.2016.04.010

Sarthy, V. P., Pignataro, L., Pannicke, T., Weick, M., Reichenbach, A., Harada, T., et al. (2005). Glutamate transport by retinal Muller cells in glutamate/aspartate transporter-knockout mice. *Glia* 49, 184–196. doi: 10.1002/glia.20097

Schneider, N., Cordeiro, S., Machtens, J.-P., Braams, S., Rauen, T., and Fahlke, C. (2014). Functional properties of the retinal glutamate transporters GLT-1c and EAAT5. *J. Biol. Chem.* 289, 1815–1824. doi: 10.1074/jbc.M113.517177

Schniepp, R., Kohler, K., Ladewig, T., Guenther, E., Henke, G., Palmada, M., et al. (2004). Retinal colocalization and in vitro interaction of the glutamate transporter EAAT3 and the serum- and glucocorticoid-inducible kinase SGK1 [correction]. *Invest. Ophthalmol. Vis. Sci.* 45, 1442–1449. doi: 10.1167/iovs.03-0062

Schultz, K., and Stell, W. K. (1996). Immunocytochemical localization of the high-affinity glutamate transporter, EAAC1, in the retina of representative vertebrate species. *Neurosci. Lett.* 211, 191–194. doi: 10.1016/0304-3940(96)12762-2

Shimamoto, K., Lebrun, B., Yasuda-Kamatani, Y., Sakaitani, M., Shigeri, Y., Yumoto, N., et al. (1998). DL-threo-beta-benzyloxyaspartate, a potent blocker of excitatory amino acid transporters. *Mol. Pharmacol.* 53, 195–201. doi: 10.1124/mol.53.2.195

Slaughter, M. M., and Miller, R. F. (1981). 2-amino-4-phosphonobutyric acid: a new pharmacological tool for retina research. *Science* 211, 182–185. doi: 10.1126/science.6255566

Szmajda, B. A., and Devries, S. H. (2011). Glutamate spillover between mammalian cone photoreceptors. *J. Neurosci.* 31, 13431–13441. doi: 10.1523/JNEUROSCI.2105-11.2011

Tse, D. Y., Chung, I., and Wu, S. M. (2014). Possible roles of glutamate transporter EAAT5 in mouse cone depolarizing bipolar cell light responses. *Vision Res.* 103, 63–74. doi: 10.1016/j.visres.2014.06.005

Vandenberg, R. J., and Ryan, R. M. (2013). Mechanisms of glutamate transport. *Physiol. Rev.* 93, 1621–1657. doi: 10.1152/physrev.00007.2013

Veruki, M. L., Mørkve, S. H., and Hartveit, E. (2006). Activation of a presynaptic glutamate transporter regulates synaptic transmission through electrical signaling. *Nat. Neurosci.* 9, 1388–1396. doi: 10.1038/nn1793

Ward, M. M., Jobling, A. I., Puthussery, T., Foster, L. E., and Fletcher, E. L. (2004). Localization and expression of the glutamate transporter, excitatory amino acid transporter 4, within astrocytes of the rat retina. *Cell Tissue Res.* 315, 305–310. doi: 10.1007/s00441-003-0849-3

Wersinger, E., Schwab, Y., Sahel, J.-A., Rendon, A., Pow, D. V., Picaud, S., et al. (2006). The glutamate transporter EAAT5 works as a presynaptic receptor in mouse rod bipolar cells. *J. Physiol.* 577, 221–234. doi: 10.1113/jphysiol.2006.118281

Conflict of Interest: The authors declare that the research was conducted in the absence of any commercial or financial relationships that could be construed as a potential conflict of interest.

frontiers in Cellular Neuroscience

ORIGINAL RESEARCH
published: 10 May 2021
doi: 10.3389/fncel.2021.673782

Investigating the Mechanism of Sodium Binding to SERT Using Direct Simulations

*Dániel Szöllősi and Thomas Stockner**

Institute of Pharmacology, Center for Physiology and Pharmacology, Medical University of Vienna, Vienna, Austria

The serotonin transporter (SERT) terminates neurotransmission by transporting serotonin from the synapse into the pre-synaptic nerve terminal. Altered SERT function leads to several neurological diseases including depression, anxiety, mood disorders, and attention deficit hyperactivity disorders (ADHD). Accordingly SERT is the target for their pharmacological treatments, but also targeted by multiple drugs of abuse. Transport of serotonin by SERT is energized by the transmembrane electrochemical gradient of sodium. We used extensive molecular dynamics simulations to investigate the process of sodium binding to SERT, which is the first step in the transport cycle that leads to serotonin uptake. Comparing data from 51 independent simulations, we find a remarkably well-defined path for sodium entry and could identify two transient binding sites, while observing binding kinetics that are comparable to experimental data. Importantly, the structure and dynamics of the sodium binding sites indicate that sodium binding is accompanied by an induced-fit mechanism that leads to new conformations and reduces local dynamics.

Keywords: human serotonin transporter, sodium binding, kinetics, sodium binding pathway, molecular dynamics simulations, SERT

OPEN ACCESS

Edited by:
Renae Ryan,
The University of Sydney, Australia

Reviewed by:
Anders Skov Kristensen,
University of Copenhagen, Denmark
Mary Hongying Cheng,
University of Pittsburgh,
United States

***Correspondence:**
Thomas Stockner
thomas.stockner@meduniwien.ac.at

Specialty section:
This article was submitted to Cellular Neurophysiology, a section of the journal Frontiers in Cellular Neuroscience

Received: *28 February 2021*
Accepted: *14 April 2021*
Published: *10 May 2021*

Citation:
Szöllősi D and Stockner T (2021) Investigating the Mechanism of Sodium Binding to SERT Using Direct Simulations. Front. Cell. Neurosci. 15:673782. doi: 10.3389/fncel.2021.673782

INTRODUCTION

The function of the serotonin transporter (SERT) is to terminate neurotransmission by reuptake of serotonin (5HT) from the synapse into the pre-synaptic nerve terminal. Dysfunction of SERT has been implicated in several neurological diseases including depression, anxiety, mood disorders, and attention deficit hyperactivity disorders (ADHD; Freissmuth et al., 2017). Moreover, drugs of abuse like cocaine or amphetamine interfere with normal SERT function and lead to depletion of the 5HT pools in the pre-synaptic nerve terminal (Hilber et al., 2005).

The structure of SERT has been resolved in the outward-open, outward-occluded, and inward-open conformation (Coleman et al., 2016, 2019). The sodium binding sites were first identified in the homologous bacterial small amino acid transporter LeuT (Yamashita et al., 2005), which also revealed the conserved fold of this transporter family. The substrate binding site (labeled S1) is located in the center of the transporter, halfway through the membrane. The transport cycle leading to 5HT uptake is initiated by binding of substrate and co-transported ions to the outward-open conformation. Full assembly of the transport complex consisting of bound ions and 5HT leads first to 5HT occlusion in the substrate binding site S1, followed by a transition to the inward-open conformation from which substrate

and ions are released into the cytosol. Return to the outward-open state is facilitated by binding of a potassium ion or a proton (Nelson and Rudnick, 1979; Hasenhuetl et al., 2016).

An energy source is necessary for facilitating uphill transport, to guaranty directionality and for enabling efficient neurotransmitter clearance by reuptake (Grouleff et al., 2015). SERT belongs to the SLC6 protein family which uses the transmembrane electrochemical gradient of sodium as a primary energy source (Chen et al., 2004). Strict coupling is required between binding of substrate and ions and the key conformational changes of the transport cycle, thereby allowing for efficient transport and initiating transport only once the transport complex has assembled (Tavoulari et al., 2016). Several studies showed that sodium binding stabilizes the outward-open conformation, thereby preventing futile cycling events (Claxton et al., 2010; Zhao and Noskov, 2011; Zhao et al., 2011; Stolzenberg et al., 2015; Tavoulari et al., 2016; Coleman et al., 2019; Li et al., 2019). The high external sodium concentration of 150 mM ensures that the two sodium binding sites are filled, as the K_M of sodium for serotonin transport is 25 mM (Quick, 2003). Moreover, a positive cooperativity between sodium and substrate binding was observed that strongly increases the affinity of 5HT to SERT (Chen and Reith, 2003; Hasenhuetl et al., 2018).

The sodium binding sites (referred to as NA1 for site 1 and NA2 for site 2, see **Figure 1**) of SERT are sodium selective (Felts et al., 2014), a property shared with LeuT (Yamashita et al., 2005; Noskov and Roux, 2008; Zhao and Noskov, 2011). Accordingly, transport is not sustained by other monovalent ions, while mutations of the ion coordinating residues reduce transport activity (Tavoulari et al., 2009; Andersen et al., 2010; Felts et al., 2014). Structures of SLC6 transporters suggest that NA1 and NA2 have distinct roles, with NA1 mainly responsible for substrate binding, while the ion in NA2 is important for stabilization of the outward-open state (Grouleff et al., 2015; Coleman et al., 2019). Solvation of sodium in NA2 is suggested to be important for the transition to the inward-open state (Forrest et al., 2008; Zhao and Noskov, 2011; Borre et al., 2014; Razavi et al., 2017). Simulations investigating the effect of bound ions started with bound ions or investigated the ion-free state (Zhao and Noskov, 2011; Grouleff et al., 2015; Zomot et al., 2015; Razavi et al., 2017; Li et al., 2019).

Kinetic models of the transport cycle, largely build on electrophysiological measurements, predict a sodium association rate constant of 10^6 to 10^7 $M^{-1}s^{-1}$ (Hasenhuetl et al., 2016, 2018; Burtscher et al., 2019) to the chloride bound outward-open SERT, therefore indicating that at physiological conditions the sodium binding is fast enough (nanosecond to microsecond time-range) to be amendable for direct investigation using molecular dynamics simulation. Starting from a set of 51 SERT structure in the outward-open conformations, extracted from a 0.5 μs long simulation of a sodium free SERT, we simulated sodium binding in 51 independent 150 ns long trajectories (**Figure 1**), resulting in 8 μs of total simulation time. Sodium binds to at least one of the sodium binding sites in the majority of simulations. We find a transient binding site at the extracellular gate (R104–E493) that acts as initial engagement site with the vestibule of SERT. Sodium enters fast into the vestibule, attracted by a strong negative electrostatic field created by SERT that protrudes into the extracellular medium to facilitate sodium attraction. Before reaching the NA1 and NA2 sites, sodium binds to a second temporary interaction site in the S1 just outside NA1 and NA2. Analyses of the geometries of NA1 and NA2 reveal that their local structures are dynamic in the absence of sodium. The change in geometry of NA1 and NA2 upon sodium binding is reminiscent of an induced-fit mechanism that leads to a more compact, well-defined, and rigid conformation.

MATERIALS AND METHODS

We selected the outward-open human SERT crystal structure (PDB ID: 5I71; Coleman et al., 2016) to investigate sodium binding. Missing side chains and the originally absent Cl^- ion were positioned using MODELLER 9.20 (Shen and Sali, 2006; Webb and Sali, 2014) creating 100 structures. The best model based on the DOPE score was used for simulations.

The all atom model was converted into a coarse grain representation of the MARTINI force field (Monticelli et al., 2008; de Jong et al., 2013; Wassenaar et al., 2015) and inserted in a 1-palmitoyl-2-oleoylphosphatidylcholine: cholesterol containing membrane (POPC:CHOL 70:30 mol%; van Meer, 1998). The system was solvated in water and 150 mM NaCl. The coarse-grain system was simulated for 1 μs while restraining the protein structure to allow the membrane to accommodate the transporter and to equilibrate around SERT. After membrane equilibration, the coarse-grained system was converted to an all-atom representation (Wassenaar et al., 2014) and the original SERT model replaced the converted protein model to avoid spurious local structural problems induced by the double coordinate conversion of the protocol. Possible atom overlaps between reinserted transporter and the relaxed environment were relaxed using the *membed* procedure (Wolf et al., 2010). We used the amber ff99SB-ILDN force field (Lindorff-Larsen et al., 2010) to describe SERT, ions and the solvent, and Slipid (Jämbeck and Lyubartsev, 2012, 2013) for POPC and cholesterol. Residue Glu508 was protonated as suggested by structural analysis of the SERT crystal structure (Coleman et al., 2016). All simulations were carried out with GROMACS version 2019.2 (Abraham et al., 2015). The final assembled system was energy-minimized and equilibrated in four steps of 2.5 ns, each by stepwise releasing the position restraints (1,000, 100, 10, 1 kJ/mol/nm) that are active on the Cα atoms and the bound Cl^-. The production run was carried for 500 ns after removing all position restraints. The temperature was maintained at 310 K using the v-rescale (τ = 0.5 ps) thermostat (Bussi et al., 2007), while separately coupling protein, membrane, and solvent. Pressure was maintained at 1 bar using the Parrinello-Rahman barostat (Parrinello and Rahman, 1981) in a semiisotropic manner and applying a coupling constant of 20.1 ps. Long range electrostatic interactions were described using the smooth particle mesh Ewald method (Darden et al., 1993) applying a cutoff of 0.9 nm. The van der Waals interactions were described using the Lennard Jones potentials applying a cutoff of 0.9 nm. Long-range corrections for energy and pressure were applied. Coordinates of all atoms were recorded every 5 ps.

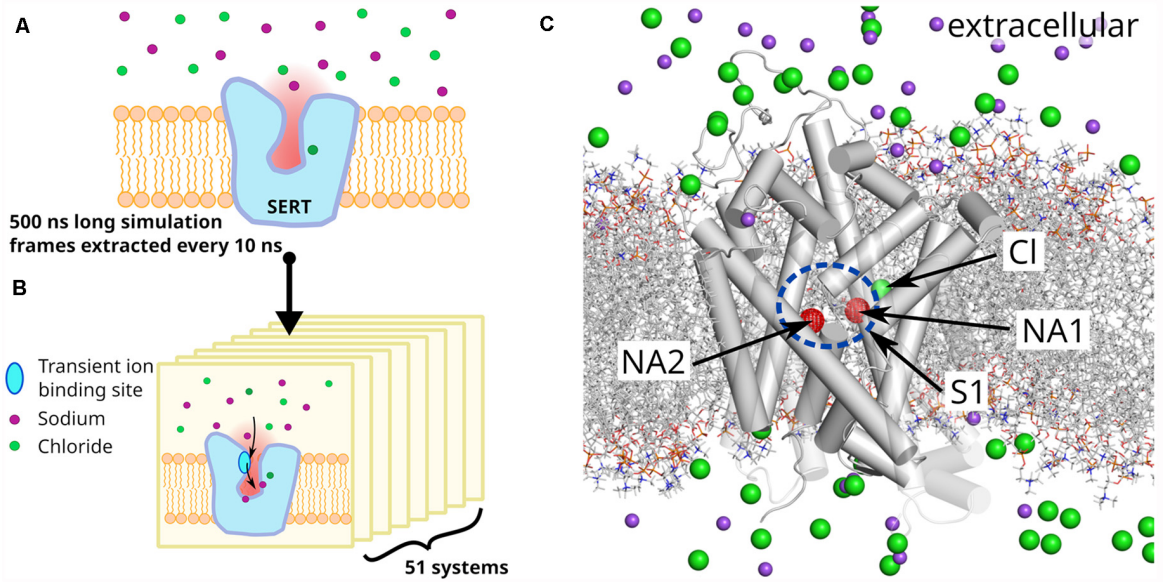

FIGURE 1 | System and system setup. **(A)** A 500 ns long unbiased simulation of serotonin transporter (SERT) in the absence of bound sodium ions was carried out to prepare a set of starting systems. **(B)** Fifty-one snapshots separated by 10 ns were extracted and sodium ions removed, if present in the outer vestibule. All systems were independently simulated for 150 ns. **(C)** Representative starting structure of a selected SERT snapshot, showing sodium (purple) and chloride (green) ions as spheres and highlighting the sodium binding sites NA1 and NA2 by red spheres. The substrate binding site S1 is indicated by a blue ellipse. The lipid membrane is represented by gray dashed lines. NA1 is formed by TM1, TM6 and TM7, NA2 by TM1 and TM8. Temporary binding sites are formed by D326, E493, and E494 from which E493 is part of the extracellular gate (EC) with R104.

The complete set of parameters of the production run can be found in the **Supplementary Materials**. The resulting trajectory was used as parent trajectory to extract starting structures for the sodium binding simulations, namely taking a snapshot every 10 ns including time = 0 ns, providing 51 starting structures, after removing the sodium ion that entered the substrate binding pocket S1. The resulting 51 systems were simulated for 150 ns with the same simulation parameters as the parent trajectories.

Figures and statistical analyses were generated by the GROMACS package, R, and python scripts using the MD Analysis package, v0.19.2 (Michaud-Agrawal et al., 2011; Gowers et al., 2016). For visualization VMD (Humphrey et al., 1996) v1.9.3 and Pymol v1.8.4 were used.

RESULTS

Sodium Binding Kinetics

The aim of this study is to investigate the binding of sodium ions to SERT. To prepare starting structures, we performed a 500 ns long equilibrium simulation of SERT that has a chloride ion bound to the chloride binding site, while the sodium binding sites NA1 and NA2 are empty. SERT is embedded in an equilibrated 1-palmitoyl-2-oleoylphosphatidylcholine: cholesterol (POPC:CHOL) membrane in a 70:30 molar ratio, while the solvent contains 150 mM NaCl. The goal of this initial simulation is to obtain representative SERT conformations. From this 500 ns long equilibrium trajectory, we extract a snapshot every 10 ns, obtaining 51 systems or replicates (**Figure 1**). Any sodium ion that entered the vestibule during the 500 ns long preparatory simulation is removed and reinserted randomly into the bulk solvent. An independent simulation of 150 ns was carried out for each of these 51 systems.

We define the extracellular salt bridge between residue R104 on TM1 and residue E493 on TM10 as the structural cut-off for identifying any sodium ion to reside within the vestibule, as once passing this salt bridge, sodium ions typically remain within the vestibule. The salt bridge is part of the extracellular gate (EC) in the SLC6 family (Yamashita et al., 2005), which in SERT consists of the salt bridge (R104-E493) and the hydrophobic lid (F335, I172, Y176) that together seal the S1 from the extracellular side if SERT is inward-facing (Coleman et al., 2016). These simulations show rapid sodium entry into the outer vestibule of SERT with a mono-exponential time dependency and a half-value entry time of 5.7 ns (**Figure 2A**), and every system contains at least one sodium ion in the outer vestibule after 22.2 ns (**Figure 2D**).

Binding to NA1 and NA2 is slower. Sodium enters NA1 (**Figure 2B**) in 27 of the 51 simulations (150 ns each), while binding to NA2 is in 15 simulations (**Figure 2C**). **Figure 2** shows the binding kinetics of the complete dataset. By fitting a mono-exponential curve to the data we find a binding constant of $4.2{\cdot}10^7$ $M^{-1}s^{-1}$ for NA1 (**Figure 2E**) and $1.9{\cdot}10^7$ $M^{-1}s^{-1}$ for NA2 (**Figure 2F**). The first order rate constant for sodium binding to both NA1 and NA2 is $9.8{\cdot}10^6$ $M^{-1}s^{-1}$. The rate constants detected in these simulations are in reasonable agreement with the experimental data-derived kinetic models that predict a sodium binding rate constant to both sodium

binding sites between 10^6 and 10^7 $M^{-1}s^{-1}$ (Hasenhuetl et al., 2016, 2018; Burtscher et al., 2019). Interestingly, in eight out of the nine simulations when sodium binds to both sodium binding sites, NA2 is filled before NA1. In the majority of trajectories which display sodium binding to NA2, this event is followed by sodium binding to NA1. In contrast, initial binding of sodium to NA1 is followed rarely (1 case) by sodium binding to NA2, suggesting that binding of sodium to one sodium binding site might affect binding to the other sodium binding site.

The systems which bind sodium ions are randomly distributed among the 51 trajectories, therefore indicating that the conformations extracted from the 500 ns long parent simulation do not have a conformational bias. A structural change occurring during the preparatory 500 ns simulation that could affect and/or modulate sodium binding would also create a distinct pattern of sodium binding events among the 51 trajectories that deviates from a random distribution. We observe chloride unbinding in a few simulations, whereby it is leaving its binding site through the empty NA1 site, followed by fast diffusion through the vestibule into the extracellular bulk solvent. The binding of sodium to NA1 could not be observed in any of these systems, suggesting that the presence of a bound chloride is necessary for sodium binding to NA1.

The Path of Sodium Through the Outer Vestibule

Next, we investigate the path that sodium takes through the outer vestibule. For the analysis, we fit all trajectories to a reference frame (starting conformation of the first trajectory) using Cα atoms, which allows us to average the entire dataset. To identify the areas of frequent sodium encounters, we create a 3D spatial density map of sodium positions averaged over the 51 trajectories, which therefore is a histogram of encountered sodium positions over the entire dataset (**Figure 3A**). In the extracellular space, this histogram represents an average density of the randomly diffusing sodium ions, in the outer vestibule the density is associated with the path that sodium takes to reach the S1, while in the S1 the density is linked to the areas of most frequent encounters of sodium before binding to NA1 or NA2. We find that the sodium ions are attracted to SERT at its extracellular site, as the sodium concentration above the outer vestibule is larger than the average density in the extracellular solution (initial enrichment zone). An initial recruitment zone exists in the extracellular vestibule above the outer salt bridge. It is located next to residue D328 that attracts sodium ions by its negative charge, thereby locally increasing the concentration and thus promoting sodium binding to SERT. Experimental data have shown that mutations of D328 affect sodium binding (Kortagere et al., 2013). Directly at the salt bridge between R104 and E493 (**Figure 3A**) at the EC gate a transient sodium binding site exist, to which the ions typically remain bound for a short period of time before moving further towards the S1 substrate binding site (**Figure 3**). The width of the largest sodium density (**Figure 3A**) is comparable to the size of a sodium ion, while the density indicates that the transient binding site is extended vertically along the outer vestibule, suggesting that this dynamic binding zone attracts sodium ions for promoting their transition towards the substrate binding site S1. This sodium binding zone is dynamic, as: (i) sodium ions are not bound to a specific position similar to NA1 and NA2, but move within this zone and (ii) because sodium ions remain bound for only a short period of time, consistent with a low affinity site.

The largest density of sodium ions is observed in the S1 and in the NA1 and NA2 sites. We find that sodium ions reside for some time just outside the NA1 and NA2 binding sites before final binding. Important to note that in two simulations a third sodium was present at the S1 site. This increasing sodium density towards NA1 and NA2 is indicative of a force generated by SERT that attracts sodium ions. **Figure 3B** shows water density and therefore indicates the size of the outer vestibule. A comparison between the density of sodium and the area occupied by water shows that sodium spreads through most of the volume of the outer vestibule. An important exception seems to be the region surrounding R104. While the positive charge of the arginine will create a repulsive force acting on the positively charged sodium ions, the extracellular salt-bridge partner E493 and the adjacent E494 are highly attractive and form the temporary sodium binding site. While reaching to most of the vestibule volume, the density of sodium occupancy suggests that sodium follows a preferred path through the vestibule.

Complementary to the relative sodium density, we quantified the average displacement of sodium ions by taking a snapshot every 10 ps, averaged over the 51 trajectories. **Figure 3C** shows the average displacement of sodium ions mapped to the starting position of the first of the two consecutive frames. In the vestibule, the average displacement is smaller as compared to the extracellular solutions, showing that the velocity of sodium diffusion is lower within the vestibule. Sodium displacement is not equally reduced throughout the outer vestibule. The regions of very low displacement of 7.5 nm/ns or smaller are associated with the regions of high sodium density because a sodium ion remains in this region of higher density for a longer time. A comparison between sodium density (**Figure 3A**) and average sodium displacement (**Figure 3C**) indicates that high sodium density and small displacements are not fully correlated. This is most evident at the transient sodium binding site at the EC gate and in the region connecting it to the S1. The upper part of the high sodium density at the outer gate shows high sodium displacement, which is consistent with repeated fast sodium entering and leaving the region. In contrast, at the lower end of the transient sodium binding site at the EC gate, the average sodium displacement is very low (5–7.5 nm/ns), indicative of a more specific ion binding site, which nevertheless remains transient. This data indicates that sodium becomes first dynamically recruited from the extracellular medium and is guided towards the transient binding site at the EC gate. The region between this transient sodium binding site and the S1 substrate binding site shows an increased displacement of 10 nm/ns. The same region overlaps partially with high sodium density in the S1, showing that at the upper end of the S1 the average movement of sodium is relatively fast. In contrast to these fast movements, in the S1 regions juxtaposed to NA1 and NA2, movements of sodium ions are below 3 nm/ns, indicative

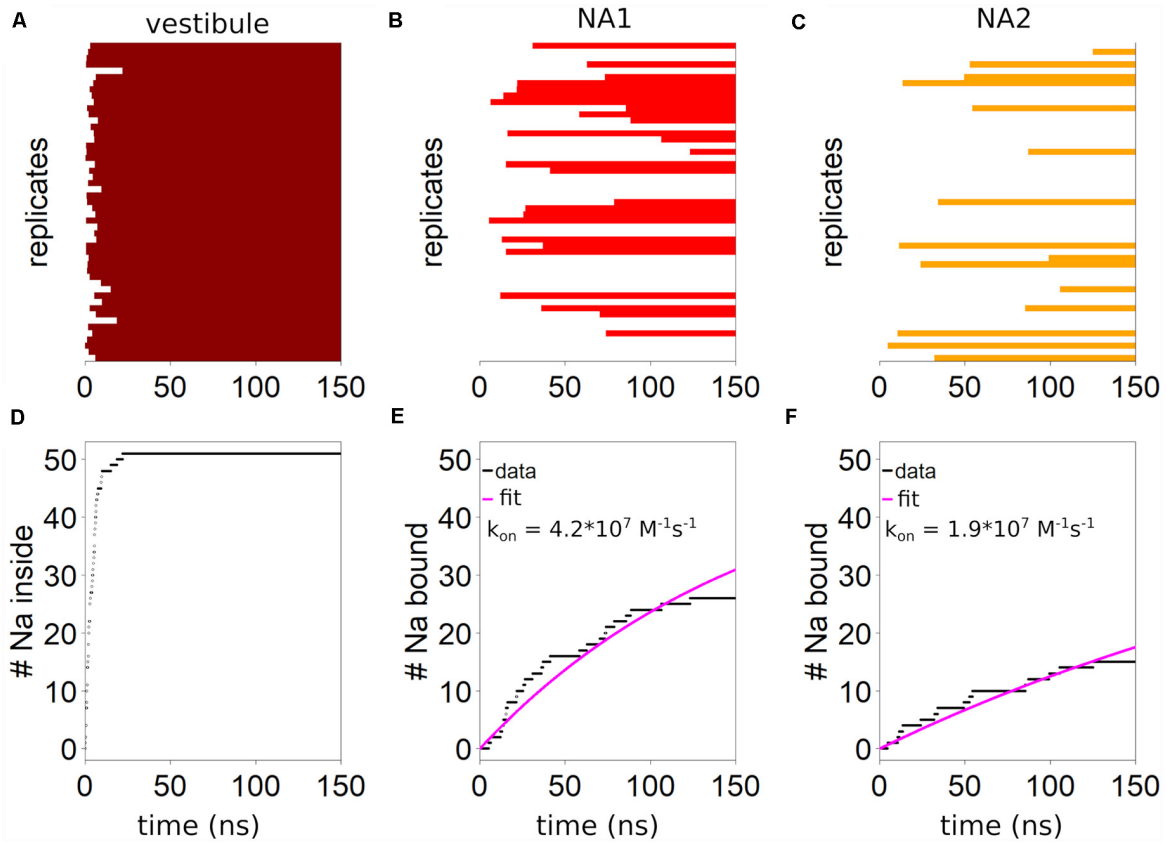

FIGURE 2 | Kinetics of sodium binding. The presence of at least one sodium ion **(A)** in the vestibule is indicated by a horizontal dark red bar for the 51 simulations or replicates. The outer salt bridge between R104 and E493 is defined as the boundary for being within the outer vestibule. **(B)** Binding of sodium to NA1 is indicated by red horizontal bars. **(C)** The presence of sodium in NA2 is symbolized by orange bars. Cumulative number of trajectories (replicates) showing **(D)** sodium ions entering the vestibule, **(E)** bind to NA1 or **(F)** to NA2. Estimation of the first order rate constant of sodium binding by fitting an exponential equation of the form: $y = A \cdot (51\text{-}e^{-bt})$, with the pre-factor constrained to 51 assuming all conformations are capable of binding.

of an increasingly strong attracted sodium. Sodium ions remain associated to these temporary sites for some time before entering NA1 or NA2. Similar sites have been identified in the bacterial homolog LeuT (Zomot et al., 2015).

Binding of Sodium to the Binding Sites NA1 and NA2

Sodium ions entering NA1 and NA2 are the final steps of binding to SERT. **Figure 2** shows that the binding kinetics are similar, the association rate to NA1 being faster than to NA2. The binding of ligands to proteins is typically associated with structural changes. The mode of these structural changes can range from conformational selection (Monod et al., 1965), where a pre-existing conformation is selected by the ligand, to an induced-fit mechanism (Koshland et al., 1966), in which the protein assumes a new conformation upon ligand binding. To identify and quantify the structural change in NA1 and NA2 upon sodium binding, we defined a structural measure of the sodium binding site and correlated these with sodium association. Sodium is coordinated by several oxygen atoms from the SERT backbone and side chains. **Figures 4A,E** show a structural legend of the used measures, which consists of the average distance between all sodium coordinating atoms of SERT (NA1: A96-O, D98-CG, N101-OD, S336-O, S336-OH, N368-OD; NA2: G94-O, V97-O, and L434-O) and their center of mass. This average distance represents a quantification of the compactness of NA1 and NA2. The center of mass coincides well with the position of bound sodium ions if present.

Figures 4B,F show a representative time course of the compactness of NA1 and NA2 of one simulation. Respective plots for all other systems that bind sodium ions can be found in **Supplementary Figures 1,2**. The average distance between oxygen atoms is larger before sodium binding, while sodium binding marks a steep drop in the average distance. **Figures 4C,G** show an overview of all simulations as a violin plot, which summarizes all observed distances and represents the relative probability by the respective width. Trajectories are separated between pre- (blue) and post- (red) sodium binding, if sodium enters the sodium binding site, with the black bar indicating the compactness at the moment of sodium binding. The trajectories are sorted according to the time point of sodium entering

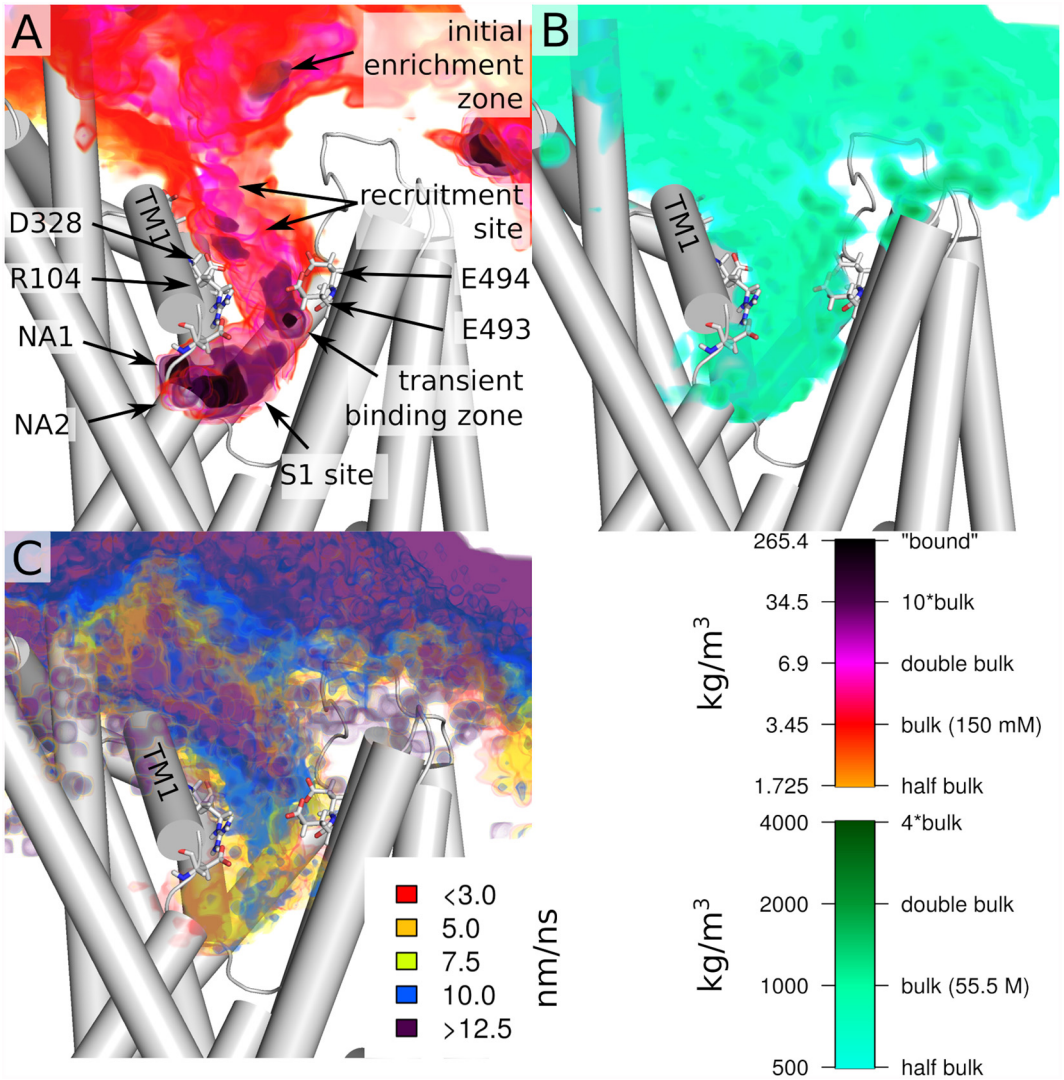

FIGURE 3 | Overview of the entry path of sodium ions. **(A)** Spatial density of sodium ion and **(B)** water at the protein extracellular interface and in the outer vestibule. **(C)** Velocity of sodium ion movements (displacement) at the extracellular interface and in the outer vestibule. All values are shown as colored volumes together with the starting structure of the first replica. Values are averages of all 51 trajectories, which were initially fitted by their Cα atoms. Trajectories were analyzed every 5 ps for the spatial densities and every 10 ps for displacement. The spatial grids have a resolution of 0.1 nm.

the sodium binding site according to **Figure 2**. The NA1 is on average by 0.1 nm more open in the absence of sodium (**Figure 4C**), while the variability of the compactness of the NA1 site is larger in the absence of sodium as compared to the sodium-bound state. The compactness of NA1 at the moment of sodium entry (black bar) is between the average pre- and post-sodium binding state. The range of compactness values at the moment of sodium entry indicates that no specific geometry or compactness of the sodium binding site(s) is required. Importantly, the values indicate that sodium enters when the apo state is particularly compact. Similar observations also apply to NA2 (**Figure 4G**), as the binding site is more compact in the presence of sodium, while the time point of sodium entry is associated with an NA2 size that is small for the apo state.

To more directly compare the geometries of the sodium binding sites across the 51 trajectories, we measured the root mean square deviation (RMSD) of the same sodium coordinating residues in Cartesian space. **Figures 4D,H** show a comparison of all simulations vs. all simulations, sorted according to **Figures 4C,G**. The squares on the diagonal of the matrix represent a structural comparison of structures of one simulation to all other structures of the same simulation, while the off-diagonal squares measure similarity between different simulations. The big dark violet block at the lower end of **Figures 4D,H** shows very similar values along the diagonal and for the off-diagonal squares after sodium binding. This big block includes all trajectories that show sodium binding. Sodium enters the binding site right at the beginning of the simulations in the first trajectories at the lower-left corner,

while the moment of sodium entry continues shifting to later time points according to trajectory sorting. The respective time points are shown in **Figure 2**. RMSD values consistently change from high values to low values, once sodium binds. The RMSD plot complements the compactness measure and shows that the same local sodium bound conformation keep being reached after binding.

The situation is different for the simulations, which did not show sodium binding: the RMSD values show that the geometry is variable (off-diagonal elements have low or high RMSD values) with some trajectories being similar to each other while differing from others. Almost all trajectories differ from the sodium-bound conformation, the few exceptions showing that the sodium-bound-like geometry can be reached in the absence of sodium, but also indicates that such a state is rare. A very similar pattern can be observed for NA2, as binding of sodium promotes a well-defined conformation, while sodium-free state samples multiple conformations. However, the overall variability is smaller.

Electric Field in the Vestibule

The density analysis (**Figure 3**) shows an above-average sodium density in the outer vestibule and in the adjacent solvent. To investigate if SERT would generate a negative electrostatic field that could attract the positively charged sodium ions, we quantified the electrostatic potential and the field lines generated by SERT using the adaptive Poisson-Boltzmann solver (APBS; Baker et al., 2001; Dolinsky et al., 2004). Consistent with the increased local sodium density, SERT creates a strong negative electrostatic potential in the outer vestibule with the field lines reaching into the solvent adjacent to the entry site at the outer vestibule (**Figure 5**). The strength of the field is a function of the ion-binding state of SERT. The electrostatic field lines and thus the field gradient reaches from the S1 to the extracellular solvent in the apo state of SERT (**Figure 5A**). The field is even stronger in the presence of the chloride ion (**Figure 5B**), while in the presence of sodium ions bound to NA1 and NA2 the gradient of the electrostatic field is weaker. These data indicate that SERT exerts an attractive force for sodium ions to reach the S1 and for binding to NA1 and NA2. The residual negative potential and the residual field gradient after sodium binding indicates that SERT can still attract 5HT by electrostatic interactions.

DISCUSSION

The binding and co-transport of extracellular sodium into the cell and the movement downhill its electrochemical gradient is the primary determinant for driving the transport cycle of SERT (Chen et al., 2004). This electrochemical gradient of sodium leads under physiological conditions to the transport of 5HT into cells even during cellular conditions where the transport is uphill the 5HT chemical gradient (Grouleff et al., 2015). The binding of sodium ions stabilizes the outward-open conformation of SERT (Claxton et al., 2010; Zhao and Noskov, 2011; Zhao et al., 2011; Stolzenberg et al., 2015; Tavoulari et al., 2016; Coleman et al., 2019; Li et al., 2019) and strongly increases the affinity of the substrate 5HT, while transport occurs only once the complex between SERT, 5HT and the co-transported ions is established (Masson et al., 1999; Felts et al., 2014; Tavoulari et al., 2016). Stabilization of substrate in the S1 was linked to NA1, as in LeuT the substrate interacts directly with the sodium ion in NA1 (Yamashita et al., 2005; Grouleff et al., 2015; Coleman et al., 2019), while in the monoamine transporters, the sodium ion in NA1 positions the sidechain of the adjacent aspartate (D98 in SERT) to interact with the amino groups of the substrate (Wang et al., 2015; Coleman et al., 2016, 2019). The main role of the sodium ion bound to NA2 is to stabilize the closed intracellular gate and thus the outward-open conformation (Zhao and Noskov, 2011; Zhao et al., 2012; Khelashvili et al., 2015; Tavoulari et al., 2016; Razavi et al., 2017; LeVine et al., 2018).

In this study, we investigate the first step of the transport cycle, which is the binding of sodium ions to the outward-open conformation of SERT in the presence of chloride ions, as experimental data indicate that chloride remains continuously bound throughout the transport cycle (Buchmayer et al., 2013; Hasenhuetl et al., 2016). We find that the structure of SERT is optimized for an efficient recruitment of sodium ions into the open vestibule and observe an association rate constant (k_{on}) of $9.8{\cdot}10^6$ $M^{-1}s^{-1}$, which is in good agreement with experimentally observed rate constants (Hasenhuetl et al., 2016, 2018; Burtscher et al., 2019). The fast binding is induced by the strong electrostatic field of SERT, which has a negative sign in the outer vestibule and guides the positively charged sodium ions into the S1. The computationally identified rate constant should be considered an upper estimate, because in simulations the starting structure of SERT is already in a sodium binding competent conformation, while the experimental procedure of the electrophysiological measurements provides a more complex readout, which is convoluted by conformational changes of SERT. The situation is less clear for LeuT, as sodium, which has a low mM affinity for LeuT (Zhao et al., 2010), was stably bound to NA2 in most simulations (Zhao et al., 2012; Tavoulari et al., 2016), but was also found to dissociate from LeuT through the outer vestibule in one study (Zomot et al., 2015).

The binding of sodium ions to SERT is a multilayered process: sodium ions become initially attracted to a binding zone outside the extracellular salt bridge that serves as an initial recruitment zone for positively charged ions thereby increasing their local concentration. The most important residue in this recruitment zone is D328. A mutation of this residue was shown to decrease the affinity of amphetamines and to reduce amphetamine-mediated efflux (Kortagere et al., 2013). Mutation of the corresponding residue in the dopamine transporter (D313) was shown to decrease the affinity for dopamine, which was suggested to be an indirect effect that is caused by a reduced accessibility of sodium ions for reaching the sodium binding sites (Chen and Reith, 2003).

At the extracellular gate, we find a transient sodium binding site, which shows a high propensity to attract sodium ions

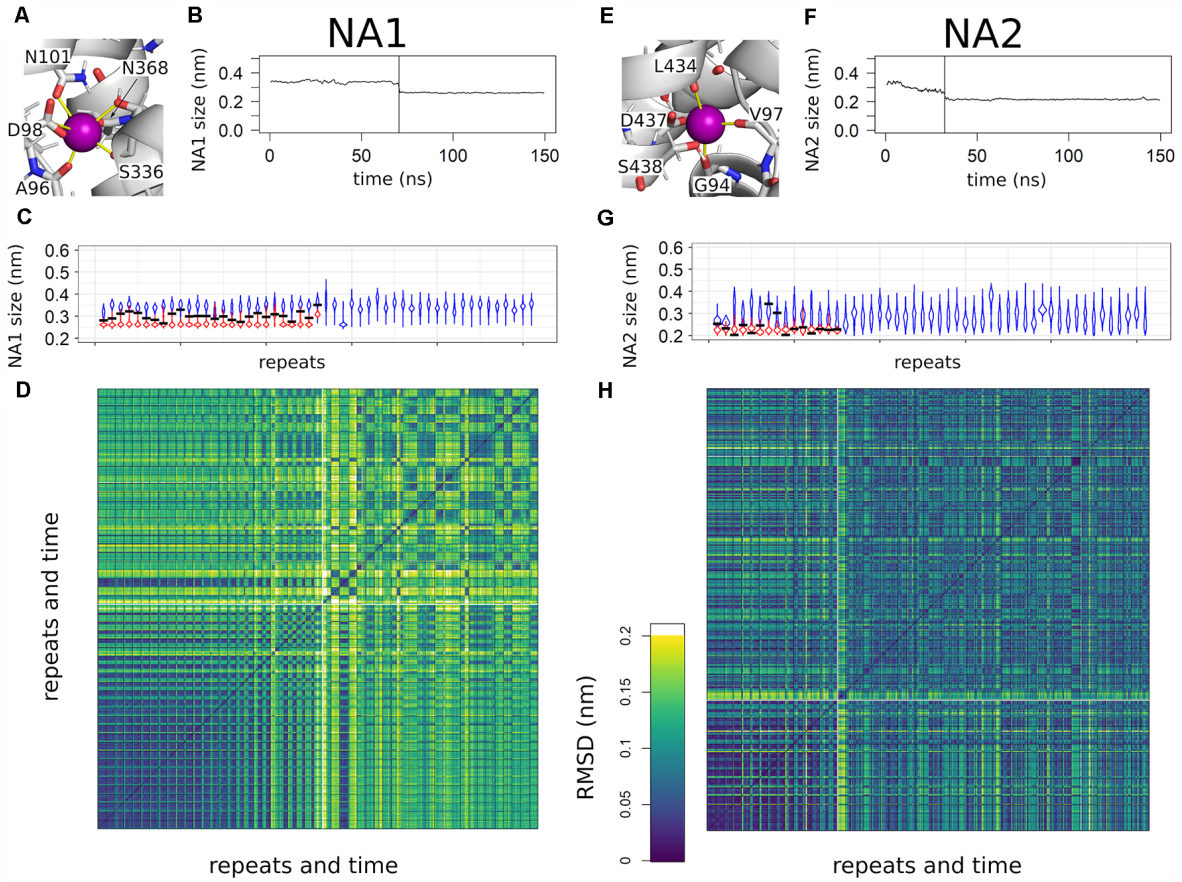

FIGURE 4 | Overview of sodium binding to NA1 and NA2. **(A,E)** Close up to NA1 and NA2. Distances used for the compactness measurement are highlighted by yellow lines. The same binding atoms are also used for the root mean square deviation (RMSD) analyses. **(B,F)** A representative example for the change in the compactness upon sodium binding. The time point of sodium entering NA1 or NA2 is highlighted by a vertical line. Curves are smoothed by a 1 ns running average. **(C,G)** Violin plots of the binding site compactness for all simulations sorted according to the time point of sodium binding to NA1 or NA2, respectively. In case of a sodium binding event, the trajectory was divided at the time of sodium binding. The violin in blue represents the pre-bound state and the violin in red shows the compactness after binding. The compactness at the time point of sodium binding is highlighted by a horizontal black line. The temporal resolution of the distance analysis was 100 ps. **(D,H)** RMSD analysis of all simulations sorted as in panels **(C,G)** of the atoms used for measuring NA1 and NA2 compactness. The boundaries between individual simulations are indicated by a black grid, while the white lines are used to separate simulations that show sodium binding from simulations in which sodium does not bind to SERT. Temporal resolution for the RMSD matrix was 10 ns.

that were initially recruited to the zone next to D328. Despite simulations showing high local ion density, sodium ions did not remain bound for very long to this site next to the glutamate residues 493 and 494. A weak sodium binding affinity seems mechanistic important because preventing any interference with proper assembly of the transport complex consisting of ion- and 5HT-bound SERT. If in contrast, this site would represent a strong sodium binding site halfway to the S1, it would be detrimental for transport, because preventing or at least slowing the processes of sodium and 5HT binding. Importantly, the narrow shape of the outer vestibule at the extracellular gate provides sodium ions with only two escape routes: unbinding towards the extracellular space or proceeding towards S1. The direction of the electrostatic field lines pointing towards the more negative S1 ensures that sodium ions move more likely towards NA1 and NA2 if the sites are not yet sodium bound.

In the last step before stably binding to SERT, sodium ions associate with a second transient binding site in the S1 juxtaposed to the NA1 and the NA2 sites. A comparable behavior was observed in LeuT (Zomot et al., 2015). This second transient binding site coincides with the position of positively charged nitrogen atoms of substrates and inhibitors as observed in structures of dDAT and hSERT (Wang et al., 2015; Coleman et al., 2016), suggesting that it has a dual role: (i) to serve as a transient site to efficiently recruit sodium ions; and (ii) to form an interaction site for the positive changed nitrogen of the monoamine substrate 5HT.

Structural changes induced by ligand binding have frequently been described as following an induced-fit mechanism (Koshland et al., 1966) or conformation selection (Monod et al., 1965), which represent extreme views of structural adaptations of proteins to the presence of ligands. The conformational changes associated with sodium binding to NA1 and NA2 suggest an

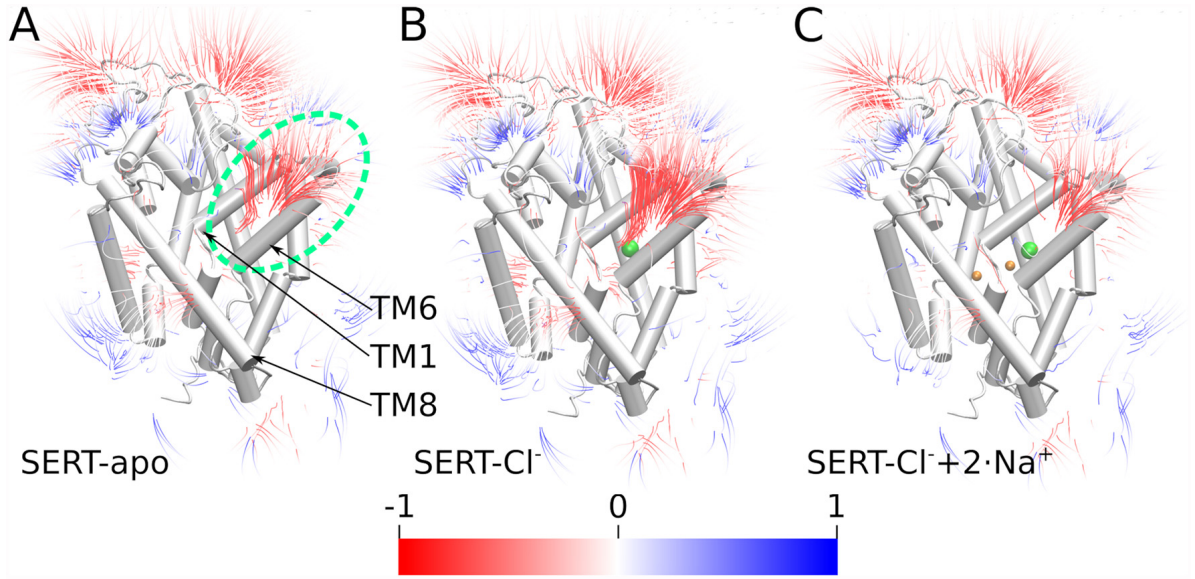

FIGURE 5 | Electrostatic gradients and fields. Electrostatic potential field lines solved by the adaptive Poisson-Boltzmann solver (APBS) of the outward-open SERT of **(A)** the apo state, **(B)** SERT with bound Cl^-, **(C)** SERT with bound Cl^- and Na^+ ions; the green dashed ellipse highlights the outer vestibule. Field lines are colored by potential with a color gradient form red through white till blue representing a scale from −1 to 1 (kT/e). Field strength more negative than −1 is red while values above 1 are blue.

overall induced-fit mechanism (**Figure 4**), as NA1 and NA2 are more compact in the presence of sodium. The situation is particularly clear for NA1, which is very dynamic and wide open in the absence of sodium, but also NA2 shows a comparable behavior. The time point of sodium association correlates with a very compact geometry of NA1 in the absence of sodium. Such a selective binding process would be consistent with a conformational selection as sodium ions seem to select a particular conformation for their association. At the same time, the NA1 compacts further once a sodium ion is bound. This becomes apparent in **Figure 4** as NA1 becomes more compact after sodium binding, thus a clear indication of an induced-fit effect. Together these data indicate that the structural arrangement of NA1 might be a combination of an initial conformational selection followed by an induced-fit condensation. The driving forces for compacting the NA1 site are most likely electrostatic attractions between sodium and the coordinating oxygen atoms of SERT that carry partial negative charges. Water molecules occupy NA1 and NA2 if their site are not binding a sodium ion. The neutral water molecule, which is slightly bigger than a sodium ion, cannot lead to the same electrostatic attractions, while also unable to form hydrogen bonds with all potential interaction partners. For the initial conformational selection, similar arguments may apply: (i) initial stabilization of sodium is more efficient, if the site is more compact, (ii) while the presence of water molecules might be energetically less favorable if the site is more compact.

Beyond the core three carbonyl backbone oxygen atoms of residues G94, V97, and L434 of NA2, the side chains of D437 and S438 contribute to complete the NA2 site. Their interaction with the bound sodium ion is more dynamic and can be replaced by a water-bridged interaction. The conformation of S438 is associated with sodium entry, because the side chain needs to rotate for allowing initial sodium association, thereby forming a small barrier which could explain the slower association rate as compared to NA1. The side chain of residue D437 is partially solvated in our simulations as also observed in other studies (Zhao and Noskov, 2011; Khelashvili et al., 2015; Tavoulari et al., 2016; Razavi et al., 2017; LeVine et al., 2018). These water molecules reach residue D437 from the intracellular side; it is, therefore, conceivable that water interactions with and the dynamics of the side chain of residue D437 are associated with the transition towards the inward-facing state. Both residues (D437 and S438) are not essential for protein function as their mutation does not affect the surface expression of SERT, while transport activity is reduced between 15% and 93%, depending on the identity of the mutation (Felts et al., 2014). These data therefore suggest that the three backbone carbonyl oxygen atoms are essential for sodium binding, while the side chains of D437 and S438 have a secondary role in NA2 function.

In conclusion, our large-scale simulation approach to directly study the association of sodium ions reveal that SERT creates a strong electrostatic field that reaches into the extracellular milieu and attracts positively charged ions towards their binding sites. The data show that specific sites for sodium interactions exist within the outer vestibule which are transient enough to support efficient recruitment and transition of sodium ions. The binding of the sodium ions to the NA1 and the NA2 sites is associated with local structural changes that consist of an

initial conformation selection followed by an electrostatic driven induced-fit process.

DATA AVAILABILITY STATEMENT

The raw data supporting the conclusions of this article will be made available by the authors, without undue reservation.

AUTHOR CONTRIBUTIONS

DS and TS contributed in the conception of the work, the design of data analysis, the interpretation of the results, and drafted the manuscript. DS performed the simulations, data collection, and developed the analysis code. TS provided funding and supervised the work. All authors contributed to the article and approved the submitted version.

FUNDING

The research underlying the current publication has been supported by the Austrian Science Fund (FWF) stand-alone grant P 32017 to TS.

ACKNOWLEDGMENTS

The results presented have been achieved using the Vienna Scientific Cluster (VSC).

SUPPLEMENTARY MATERIAL

The Supplementary Material for this article can be found online at: https://www.frontiersin.org/articles/10.3389/fncel.2021.673782/full#supplementary-material.

REFERENCES

Abraham, M. J., Murtola, T., Schulz, R., Páll, S., Smith, J. C., Hess, B., et al. (2015). GROMACS: high performance molecular simulations through multi-level parallelism from laptops to supercomputers. *SoftwareX* 1–2, 19–25. doi: 10.1016/j.softx.2015.06.001

Andersen, J., Olsen, L., Hansen, K. B., Taboureau, O., Jørgensen, F. S., Jørgensen, A. M., et al. (2010). Mutational mapping and modeling of the binding site for (S)-citalopram in the human serotonin transporter. *J. Biol. Chem.* 285, 2051–2063. doi: 10.1074/jbc.M109.072587

Baker, N. A., Sept, D., Joseph, S., Holst, M. J., and McCammon, J. A. (2001). Electrostatics of nanosystems: application to microtubules and the ribosome. *Proc. Natl. Acad. Sci. U S A* 98, 10037–10041. doi: 10.1073/pnas.181342398

Borre, L., Andreassen, T. F., Shi, L., Weinstein, H., and Gether, U. (2014). The second sodium site in the dopamine transporter controls cation permeation and is regulated by chloride. *J. Biol. Chem.* 289, 25764–25773. doi: 10.1074/jbc.M114.574269

Buchmayer, F., Schicker, K., Steinkellner, T., Geier, P., Stubiger, G., Hamilton, P. J., et al. (2013). Amphetamine actions at the serotonin transporter rely on the availability of phosphatidylinositol-4,5-bisphosphate. *Proc. Natl. Acad. Sci. U S A* 110, 11642–11647. doi: 10.1073/pnas.1220552110

Burtscher, V., Schicker, K., Freissmuth, M., and Sandtner, W. (2019). Kinetic models of secondary active transporters. *Int. J. Mol. Sci.* 20:5365. doi: 10.3390/ijms20215365

Bussi, G., Donadio, D., and Parrinello, M. (2007). Canonical sampling through velocity rescaling. *J. Chem. Phys.* 126:014101. doi: 10.1063/1.2408420

Chen, N., and Reith, M. E. A. (2003). Na+ and the substrate permeation pathway in dopamine transporters. *Eur. J. Pharmacol.* 479, 213–221. doi: 10.1016/j.ejphar.2003.08.070

Chen, N.-H., Reith, M. E. A., and Quick, M. W. (2004). Synaptic uptake and beyond: the sodium- and chloride-dependent neurotransmitter transporter family SLC6. *Pflugers Arch.* 447, 519–531. doi: 10.1007/s00424-003-1064-5

Claxton, D. P., Quick, M., Shi, L., de Carvalho, F. D., Weinstein, H., Javitch, J. A., et al. (2010). Ion/substrate-dependent conformational dynamics of a bacterial homolog of neurotransmitter:sodium symporters. *Nat. Struct. Mol. Biol.* 17, 822–829. doi: 10.1038/nsmb.1854

Coleman, J. A., Green, E. M., and Gouaux, E. (2016). X-ray structures and mechanism of the human serotonin transporter. *Nature* 532, 334–339. doi: 10.1038/nature17629

Coleman, J. A., Yang, D., Zhao, Z., Wen, P.-C., Yoshioka, C., Tajkhorshid, E., et al. (2019). Serotonin transporter-ibogaine complexes illuminate mechanisms of inhibition and transport. *Nature* 569, 141–145. doi: 10.1038/s41586-019-1135-1

Darden, T., York, D., and Pedersen, L. (1993). Particle mesh ewald: an N ·log (N) method for Ewald sums in large systems. *J. Chem. Phys.* 98, 10089–10092. doi: 10.1063/1.464397

de Jong, D. H., Singh, G., Bennett, W. F. D., Arnarez, C., Wassenaar, T. A., Schäfer, L. V., et al. (2013). Improved parameters for the martini coarse-grained protein force field. *J. Chem. Theory Comput.* 9, 687–697. doi: 10.1021/ct300646g

Dolinsky, T. J., Nielsen, J. E., McCammon, J. A., and Baker, N. A. (2004). PDB2PQR: an automated pipeline for the setup of Poisson-Boltzmann electrostatics calculations. *Nucleic Acids Res.* 32, W665–W667. doi: 10.1093/nar/gkh381

Felts, B., Pramod, A. B., Sandtner, W., Burbach, N., Bulling, S., Sitte, H. H., et al. (2014). The two Na+ sites in the human serotonin transporter play distinct roles in the ion coupling and electrogenicity of transport. *J. Biol. Chem.* 289, 1825–1840. doi: 10.1074/jbc.M113.504654

Forrest, L. R., Zhang, Y.-W., Jacobs, M. T., Gesmonde, J., Xie, L., Honig, B. H., et al. (2008). Mechanism for alternating access in neurotransmitter transporters. *Proc. Natl. Acad. Sci. U S A* 105, 10338–10343. doi: 10.1073/pnas.0804659105

Freissmuth, M., Stockner, T., and Sucic, S. (2017). SLC6 transporter folding diseases and pharmacochaperoning. *Handb. Exp. Pharmacol.* 245, 249–270. doi: 10.1007/164_2017_71

Gowers, R., Linke, M., Barnoud, J., Reddy, T., Melo, M., Seyler, S., et al. (2016). "MDAnalysis: a python package for the rapid analysis of molecular dynamics simulations," in *Proceedings of the 15th Python in Science Conference, Vol. 32* (Austin, TX), 98–105.

Grouleff, J., Ladefoged, L. K., Koldsø, H., and Schiøtt, B. (2015). Monoamine transporters: insights from molecular dynamics simulations. *Front. Pharmacol.* 6:235. doi: 10.3389/fphar.2015.00235

Hasenhuetl, P. S., Bhat, S., Mayer, F. P., Sitte, H. H., Freissmuth, M., and Sandtner, W. (2018). A kinetic account for amphetamine-induced monoamine release. *J. Gen. Physiol.* 150, 431–451. doi: 10.1085/jgp.201711915

Hasenhuetl, P. S., Freissmuth, M., and Sandtner, W. (2016). Electrogenic binding of intracellular cations defines a kinetic decision point in the transport cycle of the human serotonin transporter. *J. Biol. Chem.* 291, 25864–25876. doi: 10.1074/jbc.M116.753319

Hilber, B., Scholze, P., Dorostkar, M. M., Sandtner, W., Holy, M., Boehm, S., et al. (2005). Serotonin-transporter mediated efflux: a pharmacological analysis of amphetamines and non-amphetamines. *Neuropharmacology* 49, 811–819. doi: 10.1016/j.neuropharm.2005.08.008

Humphrey, W., Dalke, A., and Schulten, K. (1996). VMD: visual molecular dynamics. *J. Mol. Graph.* 14, 33–38. doi: 10.1016/0263-7855(96)00018-5

Jämbeck, J. P. M., and Lyubartsev, A. P. (2012). An extension and further validation of an all-atomistic force field for biological membranes. *J. Chem. Theory Comput.* 8, 2938–2948. doi: 10.1021/ct300342n

Jämbeck, J. P. M., and Lyubartsev, A. P. (2013). Another piece of the membrane puzzle: extending slipids further. *J. Chem. Theory Comput.* 9, 774–784. doi: 10.1021/ct300777p

Khelashvili, G., Stanley, N., Sahai, M. A., Medina, J., LeVine, M. V., Shi, L., et al. (2015). Spontaneous inward opening of the dopamine transporter is triggered

by PIP 2 -regulated dynamics of the N-terminus. *ACS Chem. Neurosci.* 6, 1825–1837. doi: 10.1021/acschemneuro.5b00179

Kortagere, S., Fontana, A. C. K., Rose, D. R., and Mortensen, O. V. (2013). Identification of an allosteric modulator of the serotonin transporter with novel mechanism of action. *Neuropharmacology* 72, 282–290. doi: 10.1016/j.neuropharm.2013.04.026

Koshland, D. E. Jr., Némethy, G., and Filmer, D. (1966). Comparison of experimental binding data and theoretical models in proteins containing subunits. *Biochemistry* 5, 365–385. doi: 10.1021/bi00865a047

LeVine, M. V., Cuendet, M. A., Razavi, A. M., Khelashvili, G., and Weinstein, H. (2018). Thermodynamic coupling function analysis of allosteric mechanisms in the human dopamine transporter. *Biophys. J.* 114, 10–14. doi: 10.1016/j.bpj.2017.10.030

Li, J., Zhao, Z., and Tajkhorshid, E. (2019). Locking two rigid-body bundles in an outward-facing conformation: the ion-coupling mechanism in a LeuT-fold transporter. *Sci. Rep.* 9:19479. doi: 10.1038/s41598-019-55722-6

Lindorff-Larsen, K., Piana, S., Palmo, K., Maragakis, P., Klepeis, J. L., Dror, R. O., et al. (2010). Improved side-chain torsion potentials for the Amber ff99SB protein force field. *Proteins* 78, 1950–1958. doi: 10.1002/prot.22711

Masson, J., Sagné, C., Hamon, M., and El Mestikawy, S. (1999). Neurotransmitter transporters in the central nervous system. *Pharmacol. Rev.* 51, 439–464.

Michaud-Agrawal, N., Denning, E. J., Woolf, T. B., and Beckstein, O. (2011). MDAnalysis: a toolkit for the analysis of molecular dynamics simulations. *J. Comput. Chem.* 32, 2319–2327. doi: 10.1002/jcc.21787

Monod, J., Wyman, J., and Changeux, J.-P. (1965). On the nature of allosteric transitions: a plausible model. *J. Mol. Biol.* 12, 88–118. doi: 10.1016/s0022-2836(65)80285-6

Monticelli, L., Kandasamy, S. K., Periole, X., Larson, R. G., Tieleman, D. P., and Marrink, S.-J. (2008). The MARTINI coarse-grained force field: extension to proteins. *J. Chem. Theory Comput.* 4, 819–834. doi: 10.1021/ct700324x

Nelson, P. J., and Rudnick, G. (1979). Coupling between platelet 5-hydroxytryptamine and potassium transport. *J. Biol. Chem.* 254, 10084–10089. doi: 10.1016/s0021-9258(19)86675-9

Noskov, S. Y., and Roux, B. (2008). Control of ion selectivity in LeuT: two Na+ binding sites with two different mechanisms. *J. Mol. Biol.* 377, 804–818. doi: 10.1016/j.jmb.2008.01.015

Parrinello, M., and Rahman, A. (1981). Polymorphic transitions in single crystals: a new molecular dynamics method. *J. Appl. Phys.* 52, 7182–7190. doi: 10.1063/1.328693

Quick, M. W. (2003). Regulating the conducting states of a mammalian serotonin transporter. *Neuron* 40, 537–549. doi: 10.1016/s0896-6273(03)00605-6

Razavi, A. M., Khelashvili, G., and Weinstein, H. (2017). A markov state-based quantitative kinetic model of sodium release from the dopamine transporter. *Sci. Rep.* 7:40076. doi: 10.1038/srep40076

Shen, M., and Sali, A. (2006). Statistical potential for assessment and prediction of protein structures. *Protein Sci.* 15, 2507–2524. doi: 10.1110/ps.062416606

Stolzenberg, S., Quick, M., Zhao, C., Gotfryd, K., Khelashvili, G., Gether, U., et al. (2015). Mechanism of the association between Na+ binding and conformations at the intracellular gate in neurotransmitter:sodium symporters. *J. Biol. Chem.* 290, 13992–14003. doi: 10.1074/jbc.M114.625343

Tavoulari, S., Forrest, L. R., and Rudnick, G. (2009). Fluoxetine (Prozac) binding to serotonin transporter is modulated by chloride and conformational changes. *J. Neurosci.* 29, 9635–9643. doi: 10.1523/JNEUROSCI.0440-09.2009

Tavoulari, S., Margheritis, E., Nagarajan, A., DeWitt, D. C., Zhang, Y.-W., Rosado, E., et al. (2016). Two Na+ sites control conformational change in a neurotransmitter transporter homolog. *J. Biol. Chem.* 291, 1456–1471. doi: 10.1074/jbc.M115.692012

van Meer, G. (1998). Lipids of the Golgi membrane. *Trends Cell Biol.* 8, 29–33. doi: 10.1016/s0962-8924(97)01196-3

Wang, K. H., Penmatsa, A., and Gouaux, E. (2015). Neurotransmitter and psychostimulant recognition by the dopamine transporter. *Nature* 521, 322–327. doi: 10.1038/nature14431

Wassenaar, T. A., Ingólfsson, H. I., Böckmann, R. A., Tieleman, D. P., and Marrink, S. J. (2015). Computational lipidomics with insane: a versatile tool for generating custom membranes for molecular simulations. *J. Chem. Theory Comput.* 11, 2144–2155. doi: 10.1021/acs.jctc.5b00209

Wassenaar, T. A., Pluhackova, K., Böckmann, R. A., Marrink, S. J., and Tieleman, D. P. (2014). Going backward: a flexible geometric approach to reverse transformation from coarse grained to atomistic models. *J. Chem. Theory Comput.* 10, 676–690. doi: 10.1021/ct400617g

Webb, B., and Sali, A. (2014). Protein structure modeling with MODELLER. *Methods Mol. Biol.* 1137, 1–15. doi: 10.1007/978-1-4939-0366-5_1

Wolf, M. G., Hoefling, M., Aponte-Santamaría, C., Grubmüller, H., and Groenhof, G. (2010). g_membed: efficient insertion of a membrane protein into an equilibrated lipid bilayer with minimal perturbation. *J. Comput. Chem.* 31, 2169–2174. doi: 10.1002/jcc.21507

Yamashita, A., Singh, S. K., Kawate, T., Jin, Y., and Gouaux, E. (2005). Crystal structure of a bacterial homologue of Na+/Cl—dependent neurotransmitter transporters. *Nature* 437, 215–223. doi: 10.1038/nature03978

Zhao, C., and Noskov, S. Y. (2011). The role of local hydration and hydrogen-bonding dynamics in ion and solute release from ion-coupled secondary transporters. *Biochemistry* 50, 1848–1856. doi: 10.1021/bi101454f

Zhao, C., Stolzenberg, S., Gracia, L., Weinstein, H., Noskov, S., and Shi, L. (2012). Ion-controlled conformational dynamics in the outward-open transition from an occluded state of LeuT. *Biophys. J.* 103, 878–888. doi: 10.1016/j.bpj.2012.07.044

Zhao, Y., Terry, D. S., Shi, L., Quick, M., Weinstein, H., Blanchard, S. C., et al. (2011). Substrate-modulated gating dynamics in a Na+-coupled neurotransmitter transporter homologue. *Nature* 474, 109–113. doi: 10.1038/nature09971

Zhao, Y., Terry, D., Shi, L., Weinstein, H., Blanchard, S. C., and Javitch, J. A. (2010). Single-molecule dynamics of gating in a neurotransmitter transporter homologue. *Nature* 465, 188–193. doi: 10.1038/nature09057

Zomot, E., Gur, M., and Bahar, I. (2015). Microseconds simulations reveal a new sodium-binding site and the mechanism of sodium-coupled substrate uptake by LeuT. *J. Biol. Chem.* 290, 544–555. doi: 10.1074/jbc.M114.617555

Conflict of Interest: The authors declare that the research was conducted in the absence of any commercial or financial relationships that could be construed as a potential conflict of interest.

frontiers in Cellular Neuroscience

REVIEW
published: 03 June 2021
doi: 10.3389/fncel.2021.677563

Rare Opportunities for Insights Into Serotonergic Contributions to Brain and Bowel Disorders: Studies of the SERT Ala56 Mouse

Samantha E. Stilley[1] *and Randy D. Blakely*[1,2]*

[1]*Department of Biomedical Science, Charles E. Schmidt College of Medicine, Florida Atlantic University, Boca Raton, FL, United States,* [2]*Brain Institute, Florida Atlantic University, Jupiter, FL, United States*

Altered structure, expression, and regulation of the presynaptic serotonin (5-HT) transporter (SERT) have been associated with multiple neurobehavioral disorders, including mood disorders, obsessive-compulsive disorder (OCD), and autism spectrum disorder (ASD). Opportunities to investigate mechanistic links supporting these associations were spurred with the identification of multiple, rare human SERT coding variants in a study that established a male-specific linkage of ASD to a linkage marker on chromosome 17 which encompassed the location of the SERT gene (*SLC6A4*). We have explored the most common of these variants, SERT Ala56, *in vitro* and *in vivo*. Results support a tonic elevation of 5-HT transport activity in transfected cells and human lymphoblasts by the variant *in vitro* that leads to an increased 5-HT clearance rate *in vivo* when studied in the SERT Ala56 mouse model, along with altered sensitivity to SERT regulatory signaling pathways. Importantly, hyperserotonemia, or an elevated whole blood 5-HT, level, was found in SERT Ala56 mice, reproducing a well-replicated trait observed in a significant fraction of ASD subjects. Additionally, we found multiple biochemical, physiological, and behavioral alterations in the SERT Ala56 mice that can be analogized to those observed in ASD and its medical comorbidities. The similarity of the functional impact of the SERT Ala56 variant to the consequences of p38α MAPK activation, ascribed to the induction of a biased conformation of the transporter toward an outward-facing conformation, has resulted in successful efforts to restore normal behavioral and bowel function *via* pharmacological and genetic p38α MAPK targeting. Moreover, the ability of the inflammatory cytokine IL-1β to enhance SERT activity *via* a p38α MAPK-dependent pathway suggests that the SERT Ala56 conformation mimics that of a chronic inflammatory state, supporting findings in ASD of elevated inflammatory cytokine levels. In this report, we review studies of the SERT Ala56 variant, discussing opportunities for continued insight into how chronically altered synaptic 5-HT homeostasis can drive reversible, functional perturbations in 5-HT sensitive pathways in the brain and periphery, and how targeting the SERT regulome, particularly through activating pathways such as those involving IL-1β/p38α MAPK, may be of benefit for neurobehavioral disorders, including ASD.

Keywords: serotonin, autism, SERT, SERT Ala56 mouse, p38α MAPK, immune, IL-1β

OPEN ACCESS

Edited by:
Susan L. Ingram, Oregon Health and Science University, United States

Reviewed by:
Mariano Soiza-Reilly, Molecular Biology and Neurosciences (IFIBYNE), Argentina
Amy Eshleman, VA Portland Health Care System, United States

***Correspondence:**
Randy D. Blakely
rblakely@health.fau.edu

Specialty section:
This article was submitted to Cellular Neurophysiology, a section of the journal Frontiers in Cellular Neuroscience

Received: *07 March 2021*
Accepted: *27 April 2021*
Published: *03 June 2021*

Citation:
Stilley SE and Blakely RD (2021) Rare Opportunities for Insights Into Serotonergic Contributions to Brain and Bowel Disorders: Studies of the SERT Ala56 Mouse. Front. Cell. Neurosci. 15:677563. doi: 10.3389/fncel.2021.677563

INTRODUCTION: SEROTONERGIC CONNECTIONS TO ASD

Infantile autism was first described by Leo Kanner, who reported the behavioral features of 11 children who were unable to engage with others socially or to understand the intent of those around them, preferring aloneness as well as sameness (Kanner, 1943). Kanner also noticed that these traits seemed to be ones the children were born with, rather than developing over time. Today, what Kanner referred to as autism is recognized to exemplify significant phenotypic heterogeneity, in keeping with a formal diagnosis of autism spectrum disorder (ASD). Given its heterogeneity of presentation and traits that can be seen in other disorders, ASD can only be formally diagnosed through rigorous behavioral assessments, with two domains of deficits recognized by the fifth edition of the Diagnostic and Statistical Manual of Mental Disorders (DSM-5). These domains are described as exhibiting: (1) persistent deficits in social communication and social interaction across multiple contexts; and (2) restricted, repetitive patterns of behavior, interests, or activities. For diagnosis, these symptoms must be present in the early developmental period and lead to clinically significant impairment in social, occupational, or other important areas of current functioning, with features not better explained by intellectual disability or global developmental delay (American Psychiatric Association., 2000). Symptoms often appear before 3 years of age and are lifelong, leading to a very high socioeconomic burden for parents and other caregivers. ASD is a widely prevalent disease affecting 1 in 54 children and is more common in boys (Merikangas and Alsamy, 2020). Because the definition and diagnostic labeling of ASD has changed since its original description, we will use the term ASD in this review, doing so with the clear recognition that this term was not used in the earlier studies we note.

With little understanding of the basis of ASD at the time of discovery, a potentially exciting lead appeared with the finding that some patients presented with high levels of serotonin (5-HT) in the blood, or hyperserotonemia (Schain and Freedman, 1961). Blood 5-HT derives from enterochromaffin cells that release the amine for local actions, but which is also released into the enteric circulation, where it first encounters platelets that express high levels of the high-affinity, antidepressant-sensitive 5-HT transporter (SERT; Erspamer and Asero, 1952; Anderson et al., 1987). Because free 5-HT in the blood is rapidly metabolized and cleared from the blood, and platelet number has not been found to be elevated, the hyperserotonemia of ASD is believed to represent elevated platelet stores of 5-HT (Veenstra-VanderWeele et al., 2009). Hyperserotonemia can be identified in approximately 30% of ASD patients and to date, remains the most reproducible biomarker associated with ASD (Pagan et al., 2021). However, the presence of the trait in some individuals that do not meet criteria for ASD (Takahashi et al., 1976a,b; Hanna et al., 1991) and its lack of representation in a majority of ASD subjects precludes hyperserotonemia from being diagnostically determinative. It is reported that hyperserotonemia of ASD is more common in boys than in girls (Shuffrey et al., 2017), as is ASD, suggesting a connection to mechanisms that support pathophysiology, though exact mechanisms remain ill-defined. Further evidence that altered 5-HT homeostasis or sensitivity plays a role in ASD derives from studies demonstrating that 5-HT selective reuptake inhibitors mitigate symptoms of receptiveness and aggressiveness in ASD subjects (Mehlinger et al., 1990; Todd, 1991; Cook et al., 1992; Cook and Leventhal, 1996), though the core features of ASD are not overcome (King et al., 2009). Notably, when 5-HT levels are depleted using tryptophan depletion, ASD symptoms are worsened (McDougle et al., 1993, 1996).

Familial relationships of hyperserotonemia have been reported (Leventhal et al., 1990) though whether this indicates common heritability or environmental influence is not clear. However, findings report that affected siblings with ASD have higher levels of serotonin than an affected ASD subject without another sibling that is affected, supporting heritability (Piven et al., 1991). Indeed, further studies provided evidence that blood 5-HT level is a highly heritable trait (Leventhal et al., 1990; Weiss et al., 2005; Muller et al., 2016), indicating that the changes found in hyperserotonemic ASD subjects may have identifiable genetic determinants. Because platelets do not synthesize 5-HT but acquire it from the bloodstream *via* SERT, and because a single gene expresses SERT found in both the brain and platelets (Lesch et al., 1993; Ramamoorthy et al., 1993) the transporter has been a major focus for models seeking to connect hyperserotonemia to ASD (Rotman et al., 1980; Piven et al., 1991; Cook and Leventhal, 1996).

Evidence of 5-HT (Wallace and Lauder, 1983) and SERT (Altamura et al., 2007; Chen et al., 2015) actions during brain development has bolstered considerations of the transporter as relevant for neurodevelopmental disorders such as ASD. During development, SERT is expressed in glutamatergic thalamocortical axons and influences sensory map architecture. SERT knock-out in these neurons but not in serotonergic neurons causes lasting changes in sensory map architecture (Chen et al., 2015). Changes in the thalamocortical projections could contribute to sensory hypersensitivity that is seen in individuals with ASD and other neurodevelopmental disorders (Chen et al., 2015). Significant effects of 5-HT manipulations on fetal neurogenesis have also been noted (Lauder and Krebs, 1978). 5-HT synthesis, quantity, and receptor binding sites are highest during development and are then reduced around puberty (Chugani et al., 1999). Interestingly, the temporal profile of developmental 5-HT synthesis appears altered in ASD patients, consistent with a developmental disturbance in 5-HT homeostasis in these children (Chugani et al., 1999). With the cloning of rodent SERTs (Blakely et al., 1991; Hoffman et al., 1991; Chang et al., 1996) and the availability of gene expression and antibody probes to localize sites of SERT mRNA and protein expression in rodents, we (Schroeter and Blakely, 1996) and others (Hansson et al., 1998; Lebrand et al., 1998, 2006) found significant expression of the transporter occurring in mouse and brain serotonergic neurons in the midgestational embryo, with transient expression in non-serotonergic neurons. The non-serotonergic sites include glutamategeric thalamocortical neurons (Hansson et al., 1998) and prefrontal cortex (PFC)

neurons (Soiza-Reilly et al., 2019) where expression continues into the early postnatal period. Moreover, Chen and colleagues have shown that early developmental SERT expression in glutamatergic thalamocortical neurons is critical for proper development of somatosensory cortex (Chen et al., 2015) whereas Soiza-Reilly and coworkers demonstrated a requirement for developmental SERT expression by PFC neurons in the establishment of normal excitability of dorsal raphe neurons (5-HT and non 5-HT) and behavioral responses to stress. Lastly, work by Bonnin and colleagues demonstrated that significant levels of 5-HT exist in the developing mouse forebrain prior to the region's enervation by serotonergic axons, derived from the placenta (Bonnin et al., 2011) speaking to even earlier roles for 5-HT in brain development. Together, these studies argue strongly that a focus on adult-onset mood disorders in considering a role for SERT in neurobehavioral disorders is myopic, with a more developmental disorder orientation reasonable in the light of the aforementioned links of 5-HT and SERT to ASD.

SERT: FROM GENE TO GENETIC STUDIES OF ASD

As alluded to above, the vast majority of studies considering a role for SERT in pathophysiological states concern a role in mood and anxiety disorders and 5-HT uptake attenuation by 5-HT-selective reuptake inhibitors (SSRIs; Montgomery, 1995; Owens and Nemeroff, 1998). This body of work encouraged our efforts to clone human SERT cDNA (Ramamoorthy et al., 1993) and implement chromosomal *in situ* hybridization to provide evidence for a single locus for the cognate gene (*SLC6A4*) at 17q11.2, a finding subsequently validated by the Human Genome Project. The predicted sequence of human SERT and its evolutionary variants suggests a transporter protein structure comprised of 12 transmembrane domains (TMs) with intracellular NH2 and COOH termini. This prediction has been amply verified through biochemical studies and most importantly through the generation of high-resolution X-ray crystal structures of human SERT in different conformations bound to 5-HT and antagonists (Coleman et al., 2016, 2019; Coleman and Gouaux, 2018). The sequence encoding human SERT protein is actually a small fraction of the size of the *SLC6A4* gene (∼2 kb vs. ∼40 kb), with significant opportunities for noncoding regulation at the genomic and mRNA level (Bradley and Blakely, 1997; Murphy and Moya, 2011). Two common, non-coding polymorphisms in the *SLC6A4* gene have been the subject of many studies seeking to link SERT expression to genetic variation and neurobehavioral disorders, an intron 2 variable nucleotide tandem repeat (STin2; Lesch et al., 1994) and a promoter region insertion-deletion polymorphism (5-HTTLPR; Lesch et al., 1996) In relation to ASD, previous studies have suggested that no significant relationship between these polymorphisms and ASD can be established and it is unlikely that they play a significant role in the susceptibility to ASD (Betancur et al., 2002; Huang and Santangelo, 2008). However, other studies have reported that these polymorphisms increase the risk for hyperserotonemia in autistic patients, which and therefore may contribute to behavioral manifestations in a subset of subjects (Coutinho et al., 2004; Jaiswal et al., 2015).

RARE OPPORTUNITIES TO ASSESS A SEROTONERGIC CONTRIBUTION TO ASD: SERT CODING VARIATION

Mechanistic insights concerning the impact of common (or rare) non-coding genetic variation *in vivo* can be particularly challenging given a lack of evolutionary conservation that is often seen when moving from human to model systems such as mouse or rat and difficulties in developing *in vitro* models, particularly considering the large size of many genes, including most of the transporters found in the SLC6 transporter family. In contrast, the identification of disease-associated coding variation presents a particularly important opportunity to identify functional impact as the sites within a protein where such variation is found are often highly conserved and can be both studied *in vitro* using mutant cDNAs and *in vivo* through simple codon substitutions. Initial searches for common, disease-associated coding variation in *SLC6A4* failed to indicate common coding variation that could be linked to neurobehavioral disorders including unipolar depression, bipolar disorder (Lesch et al., 1995) and obsessive-compulsive disorder (OCD; Altemus et al., 1996) with a single instance of a coding variant (Leu255Met) found among 67 subjects with major depression (Di Bella et al., 1996) or an additional 74 with OCD, and, due to its rarity and location distant from presumed functional domains, was not further characterized. Consistent with these findings, a much larger analysis of GenBank deposited cDNA sequences revealed nine *SLC6A4*-associated coding variants in 450 subjects, although each was found in single individuals, with the exception of an N-terminal-localized Gly56Ala substitution found in four subjects (frequency = 0.009; Glatt et al., 2001). In general, consistent findings of an exceedingly low frequency of coding variation in the *SLC6A4* gene encouraged the focus on association studies that could be pursued with much more common promoter and intronic variation.

Undeterred by the rarity of SERT coding variation, or perhaps prescient that such variation, if disease-associated, might contribute to disorders presenting with a more heterogenous phenotype, Murphy's group pursued sequencing of families presenting with multiple members who exhibit a spectrum of neurobehavioral disorders including OCD, AS (Asperger's syndrome), anorexia and substance use disorders (Ozaki et al., 2003). Multiple affected individuals from two unrelated families were found to express a SERT Ile425Val coding variant, modifying a highly conserved position in the eighth transmembrane domain, and resulting in elevated 5-HT transport activity in transfected COS-7 cells (Kilic et al., 2003). Wendland and colleagues (Wendland et al., 2008) pursued a much larger case-control study of functional variants in OCD and found none to carry the 425Val variant, indicating that the disorder, like other neuropsychiatric disorders, is etiologically heterogeneous. Similar conclusions were reached from a large multicenter family genotyping study, where three individuals out

of 1241 individuals were found to carry the Val425 variant, two with OCD diagnoses, though none transmitted the variant to their six affected children (Voyiaziakis et al., 2011), suggesting that the variant, though functional *in vitro*, may not act deterministically *in vivo*, at least in subjects with a highly defined OCD diagnosis. Regardless, the findings by Ozaki et al. of SERT coding variation noted above raised the possibility that consideration of phenotypes within broad spectrum disorders like ASD, or across diagnostically distinct disorders, particularly those with OCD-like traits, might be more likely to present with functionally penetrant transporter mutations.

Sutcliffe's group (McCauley et al., 2004) pursued linkage studies in 137 families bearing ASD offspring, identifying a significant male-specific signal at 17q11.2, an area containing the *SLC6A4* gene. These findings were of interest as *SLC6A4* had previously been identified with a male-specific linkage to whole blood 5-HT levels at 17q (Weiss et al., 2005). The *ITGB3* gene, encoding the β3 subunit of the fibrinogen receptor (integrin αIIbβ3) that is highly expressed on platelets, is localized to 17q21.3, and was also identified in the Weiss et al study as a quantitative trait locus (QTL) for whole blood 5-HT. Interestingly, Carneiro and colleagues demonstrated that SERT and integrin αIIbβ3 can be isolated in a physical complex in platelets (Carneiro et al., 2008) and that fibrinogen produces SERT activation *via* a p38 MAPK pathway. Moreover when the *Itgb3* gene is manipulated in mice, 5-HT synapse density is altered (Dohn et al., 2017), as is synaptosomal 5-HT uptake (Mazalouskas et al., 2015), and ASD-like behaviors emerge (Dohn et al., 2017).

When again referring to the linkage study of McCauley et al. (2004) an increased linkage was seen in the 70 families of this collection possessing probands that exhibited rigid-compulsive traits (RCTs), with an absence of linkage evident in families lacking probands with RCTs, consistent with a model of different genes contributing to the varying traits of ASD (e.g., development and use of language, social behavior dysfunction, sensory aversion, RCTs). Only nominal association with these traits was seen for the 5-HTTLPR (short allele), suggesting that if mutations in *SLC6A4* contributed to the linkage, a model of over-transmission of heterogeneous, functional alleles was more plausible. In an expanded set of 341 families (Sutcliffe et al., 2005), the group reinforced the 17q11.2 linkage finding and its sex-dependence, with linkage at this region eliminated when families with at least one affected female (FC) were analyzed separately and strengthened when considering families with only male probands (MO) (**Figure 1A**). In evaluating families most contributing to the linkage, four SERT coding variants (familial transmission of three variants noted in **Figures 1B–D**), and 15 other novel noncoding variants, were identified, with a fifth coding variant identified in an expanded set of families (**Figure 1E**). Given the low frequency of coding variants exhibited by the *SLC6A4* gene, the abundance of such variants in the Sutcliffe et al. study deserved further scrutiny. The most common of the coding variants identified was the Gly56Ala substitution that had been previously identified (Glatt et al., 2001). Although relatively few in number, the Ala56 encoding allele was found to be associated with ASD in the assembled families, was more frequent in affected males, and was over-transmitted to offspring with ASD. Subjects expressing this variant were enriched for traits of altered interpretation of social intent, RCTs, and sensory aversion when compared to the full ASD group (Sutcliffe et al., 2005). It should be noted that Sakurai and colleagues, using a large–scale screening approach with a different family structure, also identified G56A in 4/350 cases (Sakurai et al., 2008), a difference in frequency not different from controls. The other substitutions identified in the Sutcliffe et al.'s (2005) study included Ile425Leu, Phe465Leu, Leu550Val, and Lys605Asn, all occurring at highly conserved positions. The identification of the Leu425 coding variant is particularly striking given the prior (Ozaki et al., 2003) and subsequent findings of the Val425 variant (Moya et al., 2013) in subjects with OCD traits and Tourette's Disorder traits.

Given the overall rarity of the SERT coding variants identified in ASD or phenotypically somewhat related disorders (ASD and OCD both presenting with RCTs) and their conditional penetrance *in vivo*, the degree to which they speak to serotonergic dysfunction in these disorders rests significantly on their ability to alter SERT function, and ultimately, 5-HT signaling and behavior. Sutcliffe and colleagues (Sutcliffe et al., 2005) reported that the SERT Ala56 variant conferred elevated 5-HT uptake activity to lymphoblasts derived from ASD subjects in the linkage study, with homozygous carriers exhibiting the highest activity (**Figure 1F**). Similar elevations of lymphoblast 5-HT uptake could be shown in studies with the other coding variants noted, with no significant differences found in glutamate uptake (Prasad et al., 2009). Heterologous expression studies (Prasad et al., 2005, 2009; Sutcliffe et al., 2005) revealed that Ala56, as well as the Leu or Val425, Leu465, and Val550 variants, demonstrate increased 5-HT uptake compared to wildtype SERT (Ye and Blakely, 2011). These findings indicate that the variants themselves confer uptake elevations, rather than other aspects of the lymphoblast environment. All variants, except Ala56, demonstrated elevated surface SERT expression (Prasad et al., 2005, 2009). SERT Ala56 appears to achieve elevated 5-HT uptake stimulation through catalytic activation, derived from a decreased 5-HT K_M. *In toto*, these findings led to the hypothesis that reduced synaptic 5-HT availability during development may impact risk for the development of ASD traits (Ye and Blakely, 2011). Subsequent studies have confirmed this and shown that a maternal SERT Ala56 genotype affects offspring forebrain 5-HT levels and broadens the thalamocortical axon projections (Muller et al., 2017). Thus, the suggestion that SERT coding variation impacts brain development, given the evidence of genetic linkage and functional consequences to 5-HT uptake, dovetails with the identified embryonic expression of SERT, and that 5-HT serves as an axonal guidance molecule in the developing brain (Haydon et al., 1984; Bonnin et al., 2007).

ELEVATION OF SERT ACTIVITY BY ACTIVATION OF PKG AND p38α MAPK-LINKED PATHWAYS

Findings that SERT coding variation identified in ASD subjects impacts SERT activity raise questions as to how SERT naturally

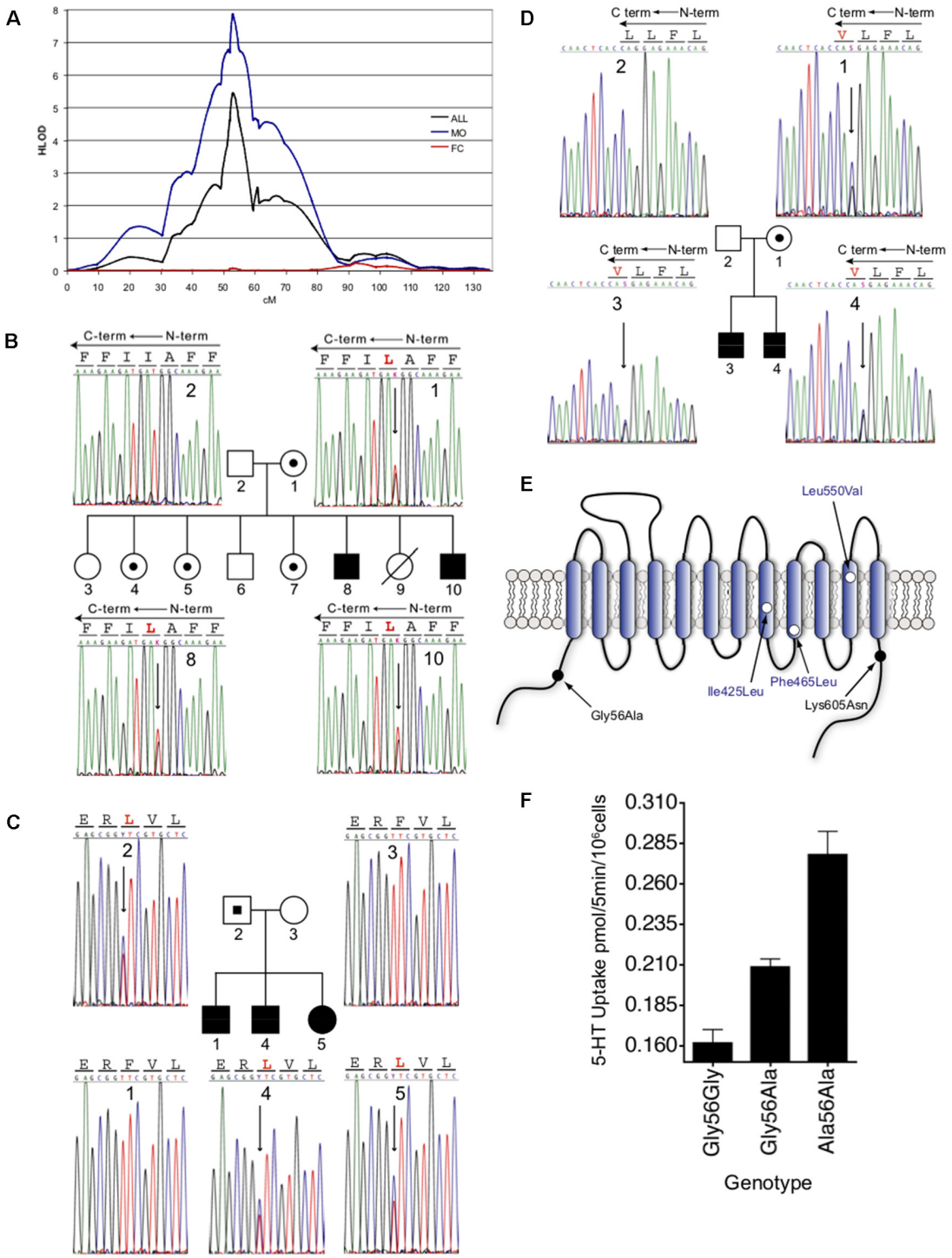

FIGURE 1 | Male-biased linkage of autism and novel coding variants at the 17q11.2 *SLC6A4* locus. **(A)**. Male-biased linkage of autism to 17q11.2. Multipoint linkage analysis on chromosome 17 is shown for the overall 341-family data set (*black line*), 202 MO families (*blue line*), or the remaining 138 FC families (*red line*). HLOD scores were calculated under a recessive model and were plotted as a function of marker position in centimorgans (cM) along chromosome 17. **(B–D)** Sequence detection of novel nonsynonymous *SLC6A4* variants in families with autism. Sequence-based detection is shown for each of the three novel coding variants, with corresponding pedigrees. **(B)** Ile425Leu. **(C)** Phe465Leu. **(D)** Leu550Val. Blackened circles or squares reflect individuals with an autism diagnosis, unblackened circles or squares reflect individuals without autism, and allele carriers without autism are indicated by small blackened circles or squares within the larger pedigree symbol. Electropherogram data is shown in either sense **(B)** or antisense **(A,C)** orientations, with corresponding coding sequence. Antisense

(*Continued*)

FIGURE 1 | Continued
sequences **(A,C)** indicate the reversed orientation of amino acid codons, represented by lines across each three-base sequence. Variant amino acids are shown in red, and corresponding heterozygous sequence changes are indicated by an arrow. Individual numbers in the respective pedigrees correspond to numbers within each of the sequence frames. **(E)** Schematic representation of the 5-HT transporter. Amino acid substitutions are indicated by location within transmembrane or cytoplasmic domains. **(F)** Dosage-dependent elevated 5-HT transporter activity of Ala56-encoded SERT in native lymphoblastoid cells. Lymphocytes genotype-matched at 5-HTTLPR (L/L) and the intron 2 VNTR (10/10) and bearing Gly/Gly, Gly/Ala, or Ala/Ala encoding genotypes at residue 56 were assayed for [^{3}H]5-HT transport activity. Three independent experiments were performed in triplicate for each line, and the combined basal uptake data were plotted. Figure from Sutcliffe et al. (2005).

changes functional state or is regulated in its routing to and from the cell surface. Significant research has revealed that SERT activity and surface activity can be rapidly and independently regulated by multiple G protein-coupled receptors and protein kinases (Ramamoorthy et al., 2011; Bermingham and Blakely, 2016). These include protein kinase C (PKC; Qian et al., 1997; Jayanthi et al., 2005), protein kinase G (PKG; Zhu et al., 2004; Ramamoorthy et al., 2007; Chang et al., 2012), and p38 MAPK (Zhu et al., 2004, 2006; Prasad et al., 2005). Activation of PKC results in an internalization of SERT which results in blunted serotonin uptake (Qian et al., 1997). PKC activators rapidly, and in a concentration-dependent manner, elevate basal hSERT phosphorylation. Protein phosphatases are also regulators of SERT, as initially shown with studies of PP1/2A inhibitors that downregulate 5HT transport and elevate phosphorylation (Ramamoorthy et al., 1998). These studies led to studies demonstrating a complex formed between SERT and PP2A (Bauman et al., 2000). PKG have been shown to increase cell surface SERT protein, increase phosphorylation, and increase SERT uptake (Zhu et al., 2004). Importantly, PKG and p38 MAPK regulatory pathways have been found to lie downstream of multiple cell surface receptors. Specifically, adenosine A3 receptors (A3ARs) have been found to induce a rapid increase in SERT activity, mediated by PKG-dependent surface trafficking as well as by PKG- and p38 MAPK-dependent catalytic activation in RBL-2H3 cells (Zhu et al., 2004, 2007) and serotonergic nerve terminals (Zhu et al., 2007). The pro-inflammatory cytokine IL-1β has been found to rapidly activate cell surface SERT proteins catalytically *in vitro* and *in vivo via* IL-1R1 receptors (Zhu et al., 2006) providing a link between innate immune system activation and changes in serotonergic signaling, just one of the paths of cross-talk between the immune system and 5-HT signaling (Baganz and Blakely, 2013). This IL-1R1 dependent activation of SERT involves an IL-1R1 to p38α MAPK signaling pathway and can be induced rapidly (1 h) in the brain by peripheral innate immune system activation by i.p. lipopolysaccharide (LPS; **Figure 2**; Zhu et al., 2010). Conditional deletion of p38α MAPK in serotonin neurons results in a loss of the ability of peripheral LPS to stimulate brain SERT as well as to trigger SSRI-sensitive despair-like behavior as well as anxiety-like traits (Baganz et al., 2015).

ALTERED SENSITIVITY OF SERT CODING VARIANTS TO PKG AND p38α MAPK SIGNALING

To gain a broader understanding of the functional impact of human SERT coding variation, Prasad and colleagues (Prasad et al., 2005) sought evidence of 5-HT transport changes associated with the known variants at the time. Several variants were found to cause an elevation in 5-HT uptake in transfected HeLa cells, including SERT Ala56 as noted above, and one substitution, Pro339Leu, was found to confer reduced transport uptake. The latter variant to our knowledge remains unassociated with a clinical phenotype. Given the evidence that a majority of SERT coding variants identified in ASD subjects demonstrate elevated 5-HT uptake in transfected cells, as well as in lymphoblasts of carriers (Prasad et al., 2009), and that SERT can be naturally stimulated *via* PKG and p38 MAPK-linked pathways, Prasad probed SERT variants to determine whether basal transport differences might reflect altered regulatory mechanisms. Multiple variants were found to display elevated SERT function in transfected HeLa cells due to either elevated surface expression (e.g., SERT Val425) or enhanced catalytic function (e.g., SERT Ala56; Prasad et al., 2005). Importantly, these variants also displayed either blunted or absent PKG- and p38 MAPK-mediated stimulation. Recently, Quinlan et al. (2019) provided evidence, using limited proteolysis approaches, cysteine accessibility studies, and fluorescence resonance energy transfer (FRET), that both the SERT Ala56 and Asn605 variants stabilize an open-outward conformation that can explain a constitutive shift to a higher-affinity state for 5-HT (**Figure 3**). SERT Ala56 also displays significantly reduced sensitivity to protein phosphatase 2A (PP2A) antagonists (Prasad et al., 2009) which may reflect the loss of PP2A complex subunits from SERT Ala56 described in recent proteomic studies (Quinlan et al., 2019). SERT exhibits changes in lateral surface mobility when regulated through PKG/p38MAPK pathways, though these changes do not appear to relocate it away from membrane rafts (Chang et al., 2012), suggesting a local untethering from associated proteins that allows for increased conformational flexibility and enhanced 5-HT transport, as seen with gain of function SERT mutants. When SERT Ala56 and SERT Leu425 are stably transfected from the same genomic locus in CHO cells, both variants display kinetic features consistent with catalytic activation (Prasad et al., 2009), consistent with findings of Kilic and Rudnick in the initial studies of the SERT Val425 variant (Kilic et al., 2003). We suggest that the surface elevation we observe with SERT Val425 expression in transfected Hela cells of elevated basal surface expression (Prasad et al., 2005), vs. the enhanced catalytic function observed for the same variant in transfected COS-7 cells (Kilic et al., 2003) derives from the relatively lower levels of expression achieved in the HeLa model vs. the COS-7 model, where significantly high expression is achieved, saturating membrane trafficking pathways, allowing only catalytic activation to occur. This idea is consistent with a model whereby normally enhanced SERT trafficking to the

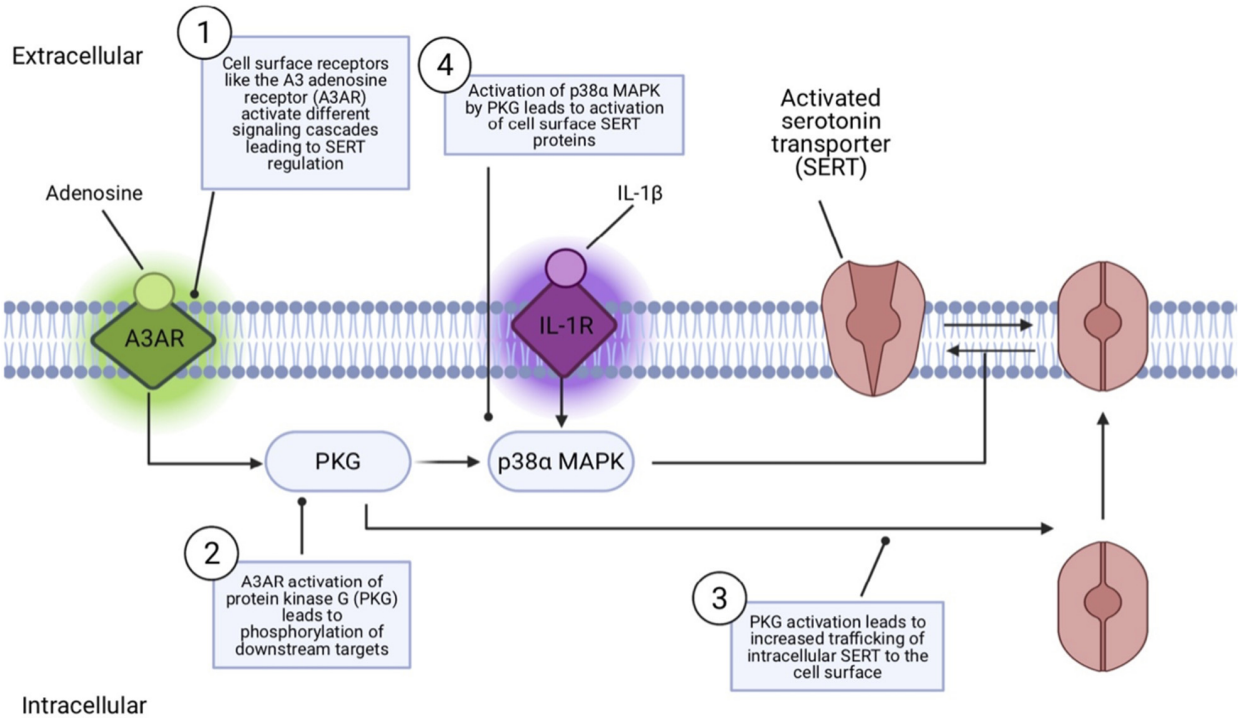

FIGURE 2 | Model of receptor-mediated SERT regulation. Cell surface receptors like the adenosine receptor (A3AR) can regulate SERT *via* a protein kinase G (PKG) pathway that can both mobilize intracellular SERT proteins to move to the cell surface and, *via* a second, p38α MAPK-linked pathway, activate surface transporters to rapidly increase 5-HT transport rates. IL-1R stimulation by the inflammatory cytokine Il-1β can lead to SERT activation *via* PKG-independent p38α MAPK stimulation, without impacting SERT surface trafficking.

surface is followed rapidly by catalytic activation, driven by stabilization of an outward-facing conformation (Blakely et al., 2005), and where coding variants that lead to excess 5-HT uptake do so by driving the transporter to the membrane and/or driving an outward conformation without extrinsic kinase-activating stimuli.

IN VIVO EVIDENCE OF A FUNCTIONAL IMPACT OF SERT Ala56 IN KNOCK-IN MICE

To more definitively establish a physiologically relevant, functional impact of the SERT Ala56 variant *in vivo*, Veenstra-VanderWeele and coworkers generated SERT Ala56 knock-in mice with homologous recombination approaches in embryonic stem cells (Veenstra-VanderWeele et al., 2009). Homozygous knock-in Ala56 mice demonstrate normal growth rates and fertility and display no gross sensorimotor deficits. As predicted by transfected cell studies, the SERT Ala56 mutation does not impact SERT protein levels as compared to wildtype littermates born from heterozygous parents (Veenstra-VanderWeele et al., 2012). Also, similar to previous findings in transfected cells, these studies revealed that SERT Ala56 phosphorylation is significantly elevated in midbrain synaptosomes under basal conditions. Moreover, activation of PKG with 8-Bromo-cGMP (8-Br-cGMP) fails to augment SERT Ala56 synaptosomal phosphorylation, whereas phosphorylation of wildtype SERT is significantly elevated. Additionally, treatment of SERT Ala56 synaptosomes with a p38 MAPK inhibitor normalizes the SERT Ala56 phosphorylation levels to that of wildtype SERT, in support of a hyperphosphorylated state of SERT Ala56 stimulated by a PKG-dependent p38 MAPK pathway. Whereas studies with SERT Ala56 synaptosomes failed to demonstrate the expected increase in basal SERT activity, studies using *in vivo* high-speed chronoamperometry revealed a significantly elevated hippocampal 5-HT clearance rate, suggesting that preparation of synaptosomes disrupts the mechanisms by which elevated SERT phosphorylation is translated into a change in catalytic function, possibly a result of cytoskeletal changes. Loose-patch recordings of dorsal raphe 5-HT neurons in midbrain slices from SERT Ala56 mice also revealed reduced basal firing rates *ex vivo*. Should these reductions occur *in vivo*, the Ala56 variant may reduce synaptic 5-HT by both decreased 5-HT release as well as enhanced 5-HT clearance. As SERT knockout mice demonstrate reductions in sensitivity of multiple 5-HT receptors (Fox et al., 2008), in keeping with excess 5-HT mediated receptor downregulation, a constitutively-imposed increased rate of 5-HT clearance is expected to increase the sensitivity of 5-HT receptors. Indeed, SERT Ala56 mice display increased sensitivity of 5-HT_{1A} and $5\text{-HT}_{2A/2C}$ receptors when probed *in vitro* and *in vivo* (Veenstra-VanderWeele et al., 2012). With respect to 5-HT_{1A} receptor hypersensitivity, which we demonstrated in

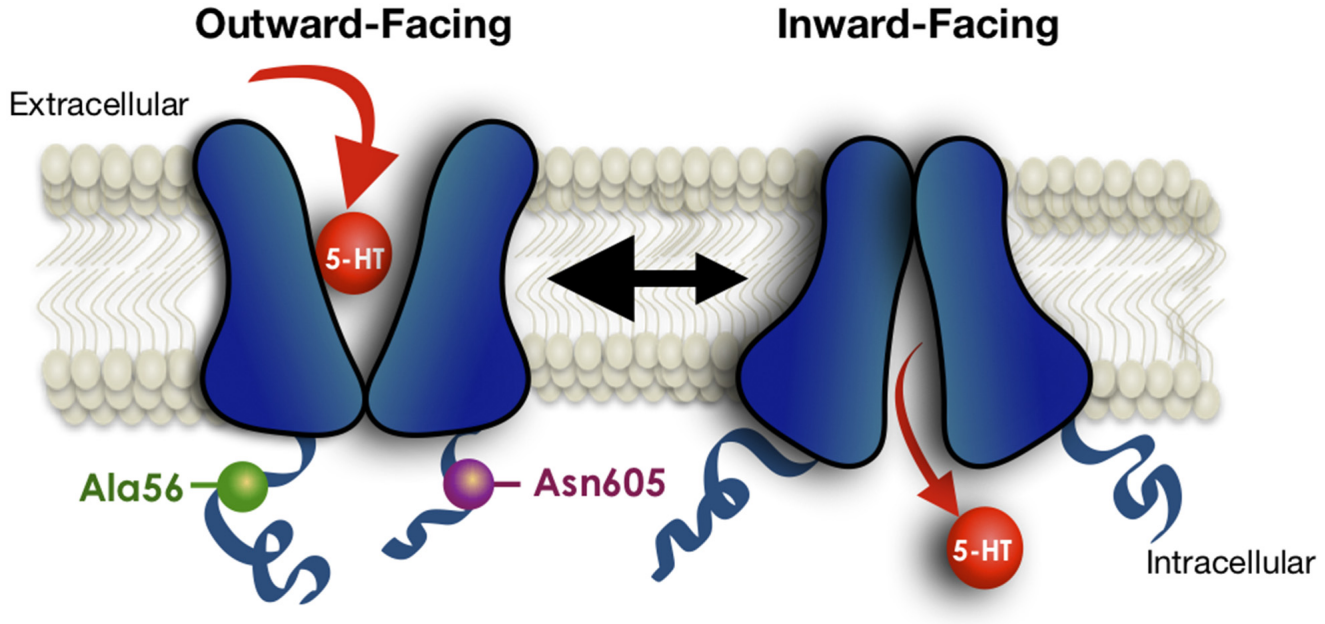

FIGURE 3 | Schematic indicating conformational bias of SERT Ala56 and Asn605 relative to WT SERT. Limited proteolysis, fluorescence resonance energy transfer (FRET), and cysteine-accessibility studies indicate that the Ala56 and Asn605 coding variants impose conformation that leading to a more outward-facing conformation of the transporter, facilitating access of 5-HT to the substrate-binding site under resting conditions. Modified from Quinlan et al. (2019).

the SERT Ala56 by monitoring hypothermia in response to the 5-HT_{1A} receptor agonist 8-OH-DPAT, we suspect that hypersensitivity of this receptor also explains the decreased firing of 5-HT neurons recorded in acute brain slices due to increased auto-inhibitory feedback. More recent studies also indicate SERT Ala56-mediated changes in 5-HT_{1B} receptor expression (O'Reilly et al., 2021). These findings provide a clear example of how a modest change in SERT structure can be amplified through changes in the multiple receptors and signaling cascades that support the actions of 5-HT *in vivo*.

BIOCHEMICAL AND BEHAVIORAL ALTERATIONS IN THE SERT Ala56 MOUSE

As noted earlier, hyperserotonemia is a well-replicated finding in a significant subset of subjects with ASD, with elevated SERT expression or activity one path to increasing platelet levels of 5-HT. SERT Ala56 mice demonstrate hyperserotonemia in comparison to their wildtype littermates (Veenstra-VanderWeele et al., 2012), the first time, to our knowledge, that this biomarker was established *in vivo* from a heritable human mutation. Most importantly, SERT Ala56 mice display behavioral changes that can be analogized to those observed in ASD. With respect to changes in language acquisition and communication ASD phenotypes, SERT Ala56 pups demonstrate reduced ultrasonic vocalization compared to wildtype siblings when separated from the mother. The mutant mice also demonstrate diminished social preference in the three-chamber test and social withdrawal in the tube test. Finally, SERT Ala56 mice display abnormal repetitive behavior, indicated by repeated cycling to the top of their cage, registered in an automated system as increased "hanging bouts" (Veenstra-VanderWeele et al., 2012). In keeping with evidence of altered sensory integration in ASD (Siemann et al., 2017, 2020), additional studies have revealed a reduced ability of SERT Ala56 mice to integrate multiple sensory cues to facilitate operant responding for reward (Siemann et al., 2017). In humans, SERT Ala56 is found in unaffected as well as ASD subjects, likely reflecting the nature of complex diseases, in which many genes each contribute small amounts of risk, and thus additional genetic background influences diagnosis or penetrance of the disease. A similar phenomenon likely underlies changes in SERT Ala56-induced phenotypes when the variant is expressed in mice on different genetic backgrounds (Kerr et al., 2013). The initial studies with SERT Ala56 mice were performed with the Ala56 variant expressed on a 129S6/S4 hybrid background. Unlike the reduced sociability evident for SERT Ala56 in the three-chamber test in these studies, no difference with wildtype littermates was observed in social preference when the variant was expressed on a C57BL/6 background (Kerr et al., 2013). However, social withdrawal in the tube test was observed on either genetic background. As another example, whereas reduced pup vocalizations of SERT Ala56 pups upon maternal separation were observed with the variant on the 129S6/S4 background, *elevated* ultrasonic vocalizations were found for Ala56 pups on a C57BI6/J background. Even further complexity is evident. The maternal genotype of the SERT Ala56 pups appears to impact the penetrance of the SERT Ala56 allele, revealed in biochemical and neurodevelopment comparisons of offspring derived from heterozygous vs.

homozygous mothers (Muller et al., 2017). Together, these findings demonstrate a remarkable, context-dependent impact on SERT Ala56 effects, both in terms of direction and penetrance. Such examples are to be expected for a complex disorder like ASD where combinations of genetic changes of small effect drive risk in many subjects.

CHANGES IN BOWEL FUNCTION IN SERT Ala56 MICE

A common medical comorbidity of ASD is gastrointestinal (GI) dysfunction (McElhanon et al., 2014), with evidence supporting RCTs associated with functional constipation (Marler et al., 2017). The basis for the association of GI symptoms in people with ASD is unclear; however, alterations in the gut-brain axis, the connection of the enteric nervous system (ENS) and CNS may provide some answers (Israelyan and Margolis, 2019). This connection is modulated, in part, through the intrinsic gut 5-HT neuronal system (Gershon, 2013). Additionally, as previously mentioned, 5-HT in the bloodstream is derived from intestinal enterochromaffin cells. Serotonergic neurons of the ENS regulate gut motility as well as the development of the ENS. Changes in gut microbiota can also influence 5-HT availability in the periphery (O'Mahony et al., 2015). SERT Ala56 mice have been found to display diminished colonic transit and electrical wave propagation (Robson et al., 2018), thought to derive from a diminished density of late-born enteric neuronal subsets that can influence gut function and epithelial structure (Margolis et al., 2016). Remarkably, these effects can be reversed by maternal and fetal treatment with the 5-HT_4 receptor agonist prucalopride (Margolis et al., 2016), consistent with the developmental deficit in synaptic 5-HT signaling in the gut of SERT Ala56 mice, just as predicted for the CNS.

GENETIC AND PHARMACOLOGICAL REVERSAL OF PHYSIOLOGICAL, BEHAVIORAL AND GI ALTERATIONS IN SERT Ala56 MICE

As reviewed above, SERT Ala56 protein *in vitro* and *in vivo* is hyperphosphorylated through a p38 MAPK-dependent pathway. Four genes (α, β, γ, δ) encode isoforms of p38 MAPK. Each of these has a broad tissue distribution and multiple mechanisms of regulation. Previously, we identified that pharmacological blockade of p38 MAPK with SB203580 eliminates the ability of the adenosine A3 receptor to stimulate SERT (Zhu et al., 2004) as well as activation of SERT by the proinflammatory cytokines IL-1β and TNF-α (Zhu et al., 2006). Further work demonstrated that peripheral administration of LPS can rapidly elevate SERT activity *in vivo* through an IL-1 receptor and p38 MAPK-dependent manner (Zhu et al., 2010). Through conditional elimination of p38α MAPK, we demonstrated a requirement for the alpha isoform in serotonergic neurons in LPS-induced SERT stimulation and despair behavior (Baganz et al., 2015), adding evidence for synaptic roles of the kinase (Falcicchia et al., 2020). The implication of the p38α MAPK isoform in SERT regulation encouraged us to consider targeting p38α MAPK to overcome the altered traits of the SERT Ala56 mouse. Fortunately, Watterson's group had recently generated isoform-selective, CNS-penetrant, p38α MAPK inhibitors (Roy et al., 2019), typified by MW150. Remarkably, after only 1 week of daily i.p. administration of MW150 (Robson et al., 2018), the constitutively elevated hippocampal 5-HT clearance imposed by the SERT Ala56 variant was normalized (**Figure 4**). Moreover, such treatments normalized multiple pharmacological, behavioral, and GI alterations seen in adult SERT Ala56 mice. Importantly, conditional genetic elimination of serotonergic p38α MAPK in 5-HT neurons, as seen with the rescue of anxiety and despair behavior following LPS treatment, rescued social behavior deficits in the tube test. Together, these findings raise the possibility that some aspects of ASD in some people may be treatable through the use of p38α MAPK inhibitors. The fact that pharmacological inhibition of p38α MAPK can normalize SERT Ala56-induced phenotypes in adult animals suggests also that the circuits modulated by altered 5-HT clearance retain plasticity into adulthood, and indicates that medications based on MW150 may be of benefit to adults on the spectrum.

FUTURE DIRECTIONS

Significant evidence now exists to support a physical and functional perturbation of transporter function by the SERT Ala56 mutation, though there remains much to learn about the variant. Understanding the temporal emergence of traits evident in adult SERT Ala56 mice warrants pursuit. Elevated 5-HT clearance induced by the variant has been shown to have the capacity to diminish 5-HT signaling, leading to physiological and behavioral consequences. Given the reversibility of some of these traits with pharmacological manipulations of adult mice, many of these changes appear to influence traits with significant plasticity, including aspects of gut dysfunction that appear to derive from poor, 5-HT dependent development of enteric neural networks. We also do not yet know whether the effects of MW150 are long–lasting after drug discontinuation or can be sustained through chronic administration. Other mouse models of ASD that demonstrate serotonergic dysfunction, particularly those that may feature neuroinflammatory changes, should be explored for utility. Of course, studies in humans to define the safety, tolerability, and efficacy of MW150 are needed and then possibly can be used for individuals with ASD. Our suspicion, given the heterogeneity of ASD, and the highly focused mouse model with which we have tested MW150, is that it will be important to stratify subjects for possible treatment by a relevant biomarker or trait, perhaps hyperserotonemia or RCTs. Gut dysfunction may be a medical comorbidity of ASD that can be treated with agents such as MW150, given our success with the drug in the SERT Ala56 model. As SERT is expressed in both the brain and the gut, it remains possible that certain behavioral traits observed in the SERT Ala56 mice have their origin through primary changes in gut function, possibly through alterations in the microbiome. Animals where the SERT Ala56 mutation is restricted to the brain or periphery are under development and are needed to address

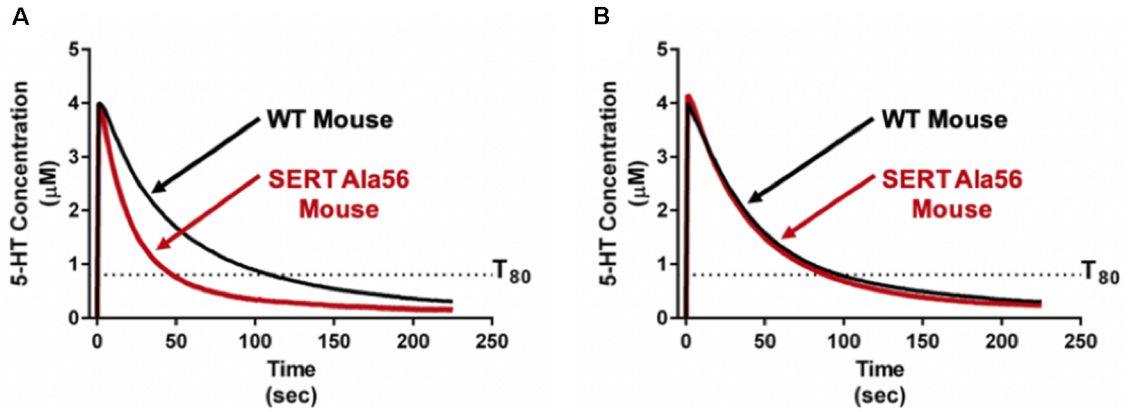

FIGURE 4 | Pharmacological p38α MAPK inhibitor administration normalizes *in vivo* hippocampal 5-HT clearance rates in SERT Ala56 mice. **(A)** SERT Ala56 mice exhibit an elevated rate of hippocampal 5-HT clearance as compared to their SERT Gly56 counterparts when assessed by high-speed *in vivo* chronoamperometry. **(B)** Increased 5-HT clearance rate of SERT Ala56 mice is normalized to WT rates by repeated p38α MAPK inhibition with MW150 (5 mg/kg, QD, i.p. × 7 days). Figure adapted from Robson et al. (2018).

this issue. In SERT Ala56 mice, and in the other models discussed above, insufficient attention has been given to the impact of sex as a biological variable. Autism is more common in males than females and evidence indicates that hyperserotonemia is also more common in boys than girls with ASD (Shuffrey et al., 2017), reinforcing our use nearly exclusively of males to date in studies of SERT Ala56 mice. As we have found that peripheral and central 5-HT levels are under the control of different genetic programs in male and female mice (Ye et al., 2014), as has been found in humans (Weiss et al., 2005), we expect that the strength and direction of serotonergic changes with the SERT Ala56 variant or other models of serotonergic dysfunction will be illuminating of potential therapeutic relevance. Last, an extensive network of mRNAs (O'Reilly et al., 2021) and proteins (Quinlan et al., 2020) are altered in the context of SERT Ala56, remarkable given the modest nature of the coding substitution, though reinforcing a functional impact of the variant *in vivo*. Further mining of these networks may provide additional opportunities for insights into disease risk and treatment.

Although not studied nearly to the same extent, it is reasonable to expect that other SERT coding variants found to induce SERT hyperfunction *in vitro* would also lead to enhanced SERT-mediated 5-HT clearance and its attendant physiological and behavioral traits when expressed *in vivo*. The degree to which these effects will be modified by genetic background, in the mouse or man, remains to be seen but is likely given the modulatory vs. deterministic nature of 5-HT signaling. By no means does evidence from our studies of rare SERT variants indicate that SERT plays a deterministic role in ASD or even the underlying serotonergic contributions to traits altered in the disorder. However, it is also not unreasonable to consider that multiple sources of ASD risk, genetic or environmental, may impact core or comorbid features of ASD through changes in serotonergic signaling. Support for this idea has recently been provided by studies in the Malenka lab using a 16p11.2 syntenic deletion mouse model of ASD (Walsh et al., 2018). Individuals with this recurrent microdeletion, encompassing approximately 25 genes, were not reported to show distinguishing features that indicate a specific subtype of ASD, though they were noted to more generally display behavioral difficulties involving aggression and overactivity (Kumar et al., 2007). Interestingly, a majority of the genes impacted by the microdeletion were found to associate with a single functional network whose hub gene (TNF), while not residing in the deletion, is an inflammatory cytokine that Zhu et al. (2006) found to positively regulate SERT. In their work, Walsh and colleagues demonstrated deficits in 5-HT secretion in the nucleus accumbens of mice with a 5-HT neuron-specific 16p11.2 deletion to diminished social interactions and that could be rescued by optogenetic stimulation of 5-HT projections to this region, as well as by pharmacological activation of accumbens $5HT_{1B}$ receptors. Future work with other mouse models of ASD, particularly those demonstrating altered social behavior and/or repetitive behavior should explore opportunities for the rescue of deficits using optogenetic, chemogenetic, or pharmacological manipulation of 5-HT pathways. Recently, we described an altered recovery of SERT-associated proteins in midbrain extracts of SERT Ala56 mice (Quinlan et al., 2020) including a number of ASD linked proteins (**Figure 5**). These findings suggest that findings with of rare SERT variants may speak to SERT-dependent serotonergic signaling alterations of more common, deterministic ASD genes. Further work to specify SERT protein complexes that participate in serotonergic signaling modulation may uncover novel molecular determinants of risk for ASD and opportunities for therapeutics. A case in point may be our report of ASD-associated A3 adenosine receptor coding variants whose properties include changes in SERT association and an inability to extinguish PKG-dependent SERT regulation (Campbell et al., 2013). Perhaps CNS penetrant, A3 adenosine receptor-specific antagonists might prove of value for some people with ASD. A biomarker and potential therapeutic that is receiving an

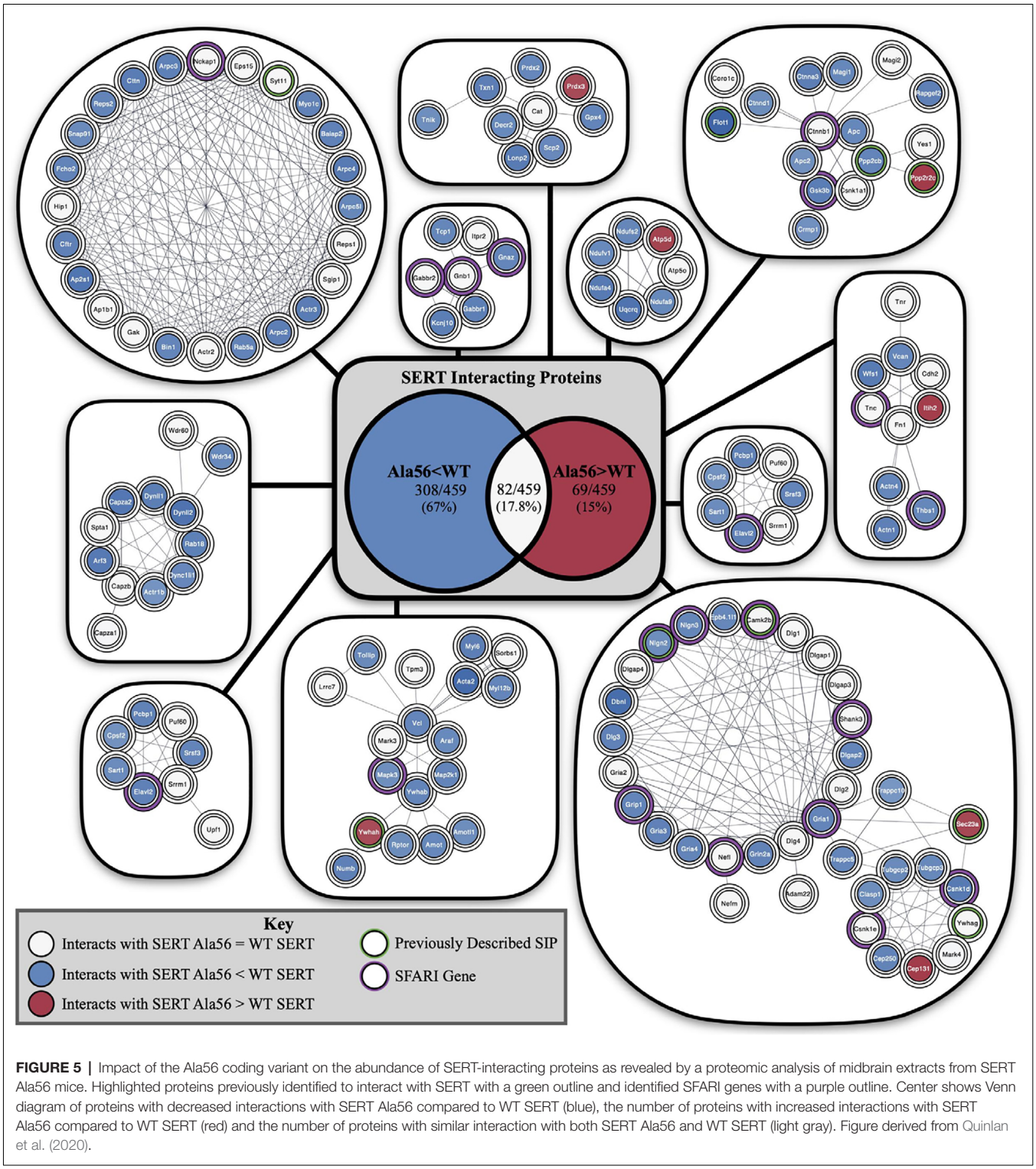

FIGURE 5 | Impact of the Ala56 coding variant on the abundance of SERT-interacting proteins as revealed by a proteomic analysis of midbrain extracts from SERT Ala56 mice. Highlighted proteins previously identified to interact with SERT with a green outline and identified SFARI genes with a purple outline. Center shows Venn diagram of proteins with decreased interactions with SERT Ala56 compared to WT SERT (blue), the number of proteins with increased interactions with SERT Ala56 compared to WT SERT (red) and the number of proteins with similar interaction with both SERT Ala56 and WT SERT (light gray). Figure derived from Quinlan et al. (2020).

increasing amount of attention in ASD is oxytocin, and, in humans, Hammock and colleagues have shown levels that negatively correlated with 5-HT. A negative correlation is also seen in oxytocin receptor (*Oxtr)* knockout mice (Hammock et al., 2012).

Our work on SERT coding variants associated with ASD has reinforced our interest in the neurobehavioral impact of PKG and p38α MAPK regulation of SERT in neurobehavioral disorders. In particular, the ability of activation of innate immune signaling pathways to drive SERT hyperfunction and

associated behavioral traits *in vivo* suggests new opportunities to target neurobehavioral disorders linked to perturbed 5-HT signaling. Increasingly, we recognize the interplay of immunity and brain development and function, a bidirectional flow that is regulated in both directions by 5-HT (Baganz and Blakely, 2013). Significant evidence indicates that altered innate immunity, favoring a pro-inflammatory state, underlies depression, anxiety, and other mood disturbances, which many models suggest derives from alterations in functional coupling of neural circuits (Raison and Miller, 2011; Felger et al., 2016). We believe that 5-HT and pro-inflammatory signaling are more intertwined than we have understood, made all the more evident by the findings that CNS 5-HT neurons are a significant site of expression in the CNS of receptors for Il-1β (Cunningham et al., 1992; Liu et al., 2019). Early life stress and its induction by limited maternal care may be treatable through consideration of how stress and inflammation impact 5-HT signaling. Maternal immune activation (MIA) can be modeled in rodents and has demonstrated traits in offspring reminiscent of the core symptoms of ASD (Malkova et al., 2012). Whether with respect to developmental disorders or the mood disorders that too often plague us in maturity, we suspect we will continue to learn how genetic and environmental stresses mediate their unwanted effects on the brain and behavior for some time to come.

AUTHOR CONTRIBUTIONS

SS and RB wrote the manuscript. All authors contributed to the article and approved the submitted version.

FUNDING

RB and SS were supported by National Institute of Mental Health Award MH094527.

ACKNOWLEDGMENTS

We thank Dr. Maureen Hahn for her careful reading and editing of the manuscript.

REFERENCES

Altamura, C., Dell'Acqua, M., Moessner, R., Murphy, D., Lesch, K., and Persico, A. M. (2007). Altered neocortical cell density and layer thickness in serotonin transporter knockout mice: a quantitation study. *Cereb. cortex* 17, 1394–1401. doi: 10.1093/cercor/bhl051

Altemus, M., Murphy, D. L., Greenberg, B., and Lesch, K. P. (1996). Intact coding region of the serotonin transporter gene in obsessive–compulsive disorder. *Am. J. Med. Genet.* 67, 409–411. doi: 10.1002/(SICI)1096-8628(19960726)67:4<409::AID-AJMG16>3.0.CO;2-N

American Psychiatric Association. (2000). *Diagnostic And Statistical Manual Of Mental Disorders-Text Revision (DSM-IV-TR; 4th edition).* Washington, D.C.: American Psychiatric Association Press, Inc.

Anderson, G. M., Feibel, F. C., and Cohen, D. J. (1987). Determination of serotonin in whole blood, platelet-rich plasma, platelet-poor plasma and plasma ultrafiltrate. *Life Sci.* 40, 1063–1070. doi: 10.1016/0024-3205(87)90568-6

Baganz, N. L., and Blakely, R. D. (2013). A dialogue between the immune system and brain, spoken in the language of serotonin. *ACS Chem. Neurosci.* 4, 48–63. doi: 10.1021/cn300186b

Baganz, N., Lindler, K., Zhu, C., Smith, J., Robson, M., Iwamoto, H., et al. (2015). A requirement of serotonergic p38α mitogen-activated protein kinase for peripheral immune system activation of CNS serotonin uptake and serotonin-linked behaviors. *Transl. Psychiatry* 5, e671–e671. doi: 10.1038/tp.2015.168

Bauman, A. L., Apparsundaram, S., Ramamoorthy, S., Wadzinski, B. E., Vaughan, R. A., and Blakely, R. D. (2000). Cocaine and antidepressant-sensitive biogenic amine transporters exist in regulated complexes with protein phosphatase 2A. *J. Neurosci.* 20, 7571–7578. doi: 10.1523/JNEUROSCI.20-20-07571.2000

Bermingham, D. P., and Blakely, R. D. (2016). Kinase-dependent regulation of monoamine neurotransmitter transporters. *Pharmacol. Rev.* 68, 888–953. doi: 10.1124/pr.115.012260

Betancur, C., Corbex, M., Spielewoy, C., Philippe, A., Laplanche, J.-L., Launay, J.-M., et al. (2002). Serotonin transporter gene polymorphisms and hyperserotonemia in autistic disorder. *Mol. Psychiatry* 7, 67–71. doi: 10.1038/sj/mp/4000923

Blakely, R. D., Berson, H. E., Fremeau, R. T., Caron, M. G., Peek, M. M., Prince, H. K., et al. (1991). Cloning and expression of a functional serotonin transporter from rat brain. *Nature* 354, 66–70. doi: 10.1038/354066a0

Blakely, R. D., DeFelice, L. J., and Galli, A. (2005). Biogenic amine neurotransmitter transporters: just when you thought you knew them. *Physiology* 20, 225–231. doi: 10.1152/physiol.00013.2005

Bonnin, A., Goeden, N., Chen, K., Wilson, M. L., King, J., Shih, J. C., et al. (2011). A transient placental source of serotonin for the fetal forebrain. *Nature* 472, 347–350. doi: 10.1038/nature09972

Bonnin, A., Torii, M., Wang, L., Rakic, P., and Levitt, P. (2007). Serotonin modulates the response of embryonic thalamocortical axons to netrin-1. *Nat. Neurosci.* 10, 588–597. doi: 10.1038/nn1896

Bradley, C. C., and Blakely, R. D. (1997). Alternative splicing of the human serotonin transporter gene. *J. Neurochem.* 69, 1356–1367. doi: 10.1046/j.1471-4159.1997.69041356.x

Campbell, N. G., Zhu, C.-B., Lindler, K. M., Yaspan, B. L., Kistner-Griffin, E., Hewlett, W. A., et al. (2013). Rare coding variants of the adenosine A3 receptor are increased in autism: on the trail of the serotonin transporter regulome. *Mol. Autism* 4:28. doi: 10.1186/2040-2392-4-28

Carneiro, A. M., Cook, E. H., Murphy, D. L., and Blakely, R. D. (2008). Interactions between integrin alphaIIbbeta3 and the serotonin transporter regulate serotonin transport and platelet aggregation in mice and humans. *J. Clin. Invest.* 118, 1544–1552. doi: 10.1172/JCI33374

Chang, A. S., Chang, S. M., Starnes, D. M., Schroeter, S., Bauman, A. L., and Blakely, R. D. (1996). Cloning and expression of the mouse serotonin transporter. *Mol. Brain Res.* 43, 185–192. doi: 10.1016/s0169-328x(96)00172-6

Chang, J. C., Tomlinson, I. D., Warnement, M. R., Ustione, A., Carneiro, A. M., Piston, D. W., et al. (2012). Single molecule analysis of serotonin transporter regulation using antagonist-conjugated quantum dots reveals restricted, p38 MAPK-dependent mobilization underlying uptake activation. *J. Neurosci.* 32, 8919–8929. doi: 10.1523/JNEUROSCI.0048-12.2012

Chen, X., Ye, R., Gargus, J. J., Blakely, R. D., Dobrenis, K., and Sze, J. Y. (2015). Disruption of transient serotonin accumulation by non-serotonin-producing neurons impairs cortical map development. *Cell Rep.* 10, 346–358. doi: 10.1016/j.celrep.2014.12.033

Chugani, D. C., Muzik, O., Behen, M., Rothermel, R., Janisse, J. J., Lee, J., et al. (1999). Developmental changes in brain serotonin synthesis capacity in autistic and nonautistic children. *Ann. Neurol.* 45, 287–295. doi: 10.1002/1531-8249(199903)45:3<287::aid-ana3>3.0.co;2-9

Coleman, J. A., and Gouaux, E. (2018). Structural basis for recognition of diverse antidepressants by the human serotonin transporter. *Nat. Struct. Mol. Biol.* 25, 170–175. doi: 10.1038/s41594-018-0026-8

Coleman, J. A., Green, E. M., and Gouaux, E. (2016). X-ray structures and mechanism of the human serotonin transporter. *Nature* 532, 334–339. doi: 10.1038/nature17629

Coleman, J. A., Yang, D., Zhao, Z., Wen, P. C., Yoshioka, C., Tajkhorshid, E., et al. (2019). Serotonin transporter-ibogaine complexes illuminate mechanisms of inhibition and transport. *Nature* 569, 141–145. doi: 10.1038/s41586-019-1135-1

Cook, E., and Leventhal, B. L. (1996). The serotonin system in autism. *Curr. Opin. Pediatr.* 8, 348–354. doi: 10.1097/00008480-199608000-00008

Cook, E. H., Jr., Rowlett, R., Jaselskis, C., and Leventhal, B. L. (1992). Fluoxetine treatment of children and adults with autistic disorder and mental retardation. *J. Am. Acad. Child Adolesc. Psychiatry* 31, 739–745. doi: 10.1097/00004583-199207000-00024

Coutinho, A., Oliveira, G., Morgadinho, T., Fesel, C., Macedo, T., Bento, C., et al. (2004). Variants of the serotonin transporter gene (SLC6A4) significantly contribute to hyperserotonemia in autism. *Mol. Psychiatry* 9, 264–271. doi: 10.1038/sj.mp.4001409

Cunningham, E. T. Jr., Wada, E., Carter, D. B., Tracey, D. E., Battey, J. E., and De Souza, E. B. (1992). *In situ* histochemical localization of type I interleukin-1 receptor messenger RNA in the central nervous system, pituitary, and adrenal gland of the mouse. *J. Neurosci.* 12, 1101–1114. doi: 10.1523/JNEUROSCI.12-03-01101.1992

Di Bella, D., Catalano, M., Balling, U., Smeraldi, E., and Lesch, K. P. (1996). Systematic screening for mutations in the coding region of the human serotonin transporter (5-HTT) gene using PCR and DGGE. *Am. J. Med. Genet.* 67, 541–545. doi: 10.1002/(SICI)1096-8628(19961122)67:6<541::AID-AJMG5>3.0.CO;2-K

Dohn, M. R., Kooker, C. G., Bastarache, L., Jessen, T., Rinaldi, C., Varney, S., et al. (2017). The gain-of-function integrin β3 pro33 variant alters the serotonin system in the mouse brain. *J. Neurosci.* 37, 11271–11284. doi: 10.1523/JNEUROSCI.1482-17.2017

Erspamer, V., and Asero, B. (1952). Identification of enteramine, the specific hormone of the enterochromaffin cell system, as 5-hydroxytryptamine. *Nature* 169, 800–801. doi: 10.1038/169800b0

Falcicchia, C., Tozzi, F., Arancio, O., Watterson, D. M., and Origlia, N. (2020). Involvement of p38 MAPK in synaptic function and dysfunction. *Int. J. Mol. Sci.* 21:5624. doi: 10.3390/ijms21165624

Felger, J. C., Li, Z., Haroon, E., Woolwine, B. J., Jung, M. Y., Hu, X., et al. (2016). Inflammation is associated with decreased functional connectivity within corticostriatal reward circuitry in depression. *Mol. Psychiatry* 21, 1358–1365. doi: 10.1038/mp.2015.168

Fox, M. A., Jensen, C. L., French, H. T., Stein, A. R., Huang, S.-J., Tolliver, T. J., et al. (2008). Neurochemical, behavioral and physiological effects of pharmacologically enhanced serotonin levels in serotonin transporter (SERT)-deficient mice. *Psychopharmacology* 201, 203–218. doi: 10.1007/s00213-008-1268-7

Gershon, M. D. (2013). 5-Hydroxytryptamine (serotonin) in the gastrointestinal tract. *Curr Opin. Endocrinol. Diabetes Obes.* 20:14. doi: 10.1097/MED.0b013e32835bc703

Glatt, C. E., DeYoung, J. A., Delgado, S., Service, S. K., Giacomini, K. M., Edwards, R. H., et al. (2001). Screening a large reference sample to identify very low frequency sequence variants: comparisons between two genes. *Nat. Genet.* 27, 435–438. doi: 10.1038/86948

Hammock, E., Veenstra-VanderWeele, J., Yan, Z., Kerr, T. M., Morris, M., Anderson, G. M., et al. (2012). Examining autism spectrum disorders by biomarkers: example from the oxytocin and serotonin systems. *J. Am. Acad. Child Adolesc. Psychiatry* 51, 712.e1–721.e1. doi: 10.1016/j.jaac.2012.04.010

Hanna, G. L., Yuwiler, A., and Cantwell, D. P. (1991). Whole blood serotonin in juvenile obsessive-compulsive disorder. *Biol. Psychiatry* 29, 738–744. doi: 10.1016/0006-3223(91)90193-p

Hansson, S., Mezey, E., and Hoffman, B. (1998). Serotonin transporter messenger RNA in the developing rat brain: early expression in serotonergic neurons and transient expression in non-serotonergic neurons. *Neuroscience* 83, 1185–1201. doi: 10.1016/s0306-4522(97)00444-2

Haydon, P., McCobb, D., and Kater, S. (1984). Serotonin selectively inhibits growth cone motility and synaptogenesis of specific identified neurons. *Science* 226, 561–564. doi: 10.1126/science.6093252

Hoffman, B. J., Mezey, E., and Brownstein, M. J. (1991). Cloning of a serotonin transporter affected by antidepressants. *Science* 254, 579–580. doi: 10.1126/science.1948036

Huang, C. H., and Santangelo, S. L. (2008). Autism and serotonin transporter gene polymorphisms: A systematic review and meta-analysis. *Am. J. Med. Genet. B Neuropsychiatr. Genet.* 147, 903–913. doi: 10.1002/ajmg.b.30720

Israelyan, N., and Margolis, K. G. (2019). Reprint of: serotonin as a link between the gut-brain-microbiome axis in autism spectrum disorders. *Pharmacol. Res.* 140, 115–120. doi: 10.1016/j.phrs.2018.12.023

Jaiswal, P., Guhathakurta, S., Singh, A. S., Verma, D., Pandey, M., Varghese, M., et al. (2015). SLC6A4 markers modulate platelet 5-HT level and specific behaviors of autism: a study from an Indian population. *Prog. Neuropsychopharmacol. Biol. Psychiatry* 56, 196–206. doi: 10.1016/j.pnpbp.2014.09.004

Jayanthi, L. D., Samuvel, D. J., Blakely, R. D., and Ramamoorthy, S. (2005). Evidence for biphasic effects of protein kinase C on serotonin transporter function, endocytosis and phosphorylation. *Mol. Pharmacol.* 67, 2077–2087. doi: 10.1124/mol.104.009555

Kanner, L. (1943). Autistic disturbances of affective contact. *Nerv. Child* 2, 217–250.

Kerr, T. M., Muller, C. L., Miah, M., Jetter, C. S., Pfeiffer, R., Shah, C., et al. (2013). Genetic background modulates phenotypes of serotonin transporter Ala56 knock-in mice. *Mol. Autism* 4:35. doi: 10.1186/2040-2392-4-35

Kilic, F., Murphy, D. L., and Rudnick, G. (2003). A human serotonin transporter mutation causes constitutive activation of transport activity. *Mol. Pharmacol.* 64, 440–446. doi: 10.1124/mol.64.2.440

King, B. H., Hollander, E., Sikich, L., McCracken, J. T., Scahill, L., Bregman, J. D., et al. (2009). Lack of efficacy of citalopram in children with autism spectrum disorders and high levels of repetitive behavior: citalopram ineffective in children with autism. *Arch. Gen. Psychiatry* 66, 583–590. doi: 10.1001/archgenpsychiatry.2009.30

Kumar, R. A., KaraMohamed, S., Sudi, J., Conrad, D. F., Brune, C., Badner, J. A., et al. (2007). Recurrent 16p11.2 microdeletions in autism. *Hum. Mol. Genet.* 17, 628–638. doi: 10.1093/hmg/ddm376

Lauder, J. M., and Krebs, H. (1978). Serotonin as a differentiation signal in early neurogenesis. *Dev. Neurosci.* 1, 15–30. doi: 10.1159/000112549

Lebrand, C., Cases, O., Wehrlé, R., Blakely, R. D., Edwards, R. H., and Gaspar, P. (1998). Transient developmental expression of monoamine transporters in the rodent forebrain. *J. Comp. Neurol.* 401, 506–524.

Lebrand, C., Gaspar, P., Nicolas, D., and Hornung, J. (2006). Transitory uptake of serotonin in the developing sensory pathways of the common marmoset. *J. Comp. Neurol.* 499, 677–689. doi: 10.1002/cne.21137

Lesch, K. P., Balling, U., Gross, J., Strauss, K., Wolozin, B. L., Murphy, D. L., et al. (1994). Organization of the human serotonin transporter gene. *J. Neural Transm. Gen. Sect.* 95, 157–162. doi: 10.1007/BF01276434

Lesch, K.-P., Bengel, D., Heils, A., Sabol, S. Z., Greenberg, B. D., Petri, S., et al. (1996). Association of anxiety-related traits with a polymorphism in the serotonin transporter gene regulatory region. *Science* 274, 1527–1531. doi: 10.1126/science.274.5292.1527

Lesch, K. P., Gross, J., Franzek, E., Wolozin, B. L., Riederer, P., and Murphy, D. L. (1995). Primary structure of the serotonin transporter in unipolar depression and bipolar disorder. *Biol. Psychiatry* 37, 215–223. doi: 10.1016/0006-3223(94)00147-U

Lesch, K. P., Wolozin, B. L., Murphy, D. L., and Reiderer, P. (1993). Primary structure of the human platelet serotonin uptake site: identity with the brain serotonin transporter. *J. Neurochem.* 60, 2319–2322. doi: 10.1111/j.1471-4159.1993.tb03522.x

Leventhal, B. L., Cook, E. H., Jr., Morford, M., Ravitz, A., and Freedman, D. X. (1990). Relationships of whole blood serotonin and plasma norepinephrine within families. *J. Autism Dev. Disord.* 20, 499–511. doi: 10.1007/BF02216055

Liu, X., Nemeth, D. P., McKim, D. B., Zhu, L., DiSabato, D. J., Berdysz, O., et al. (2019). Cell-type-specific interleukin 1 receptor 1 signaling in the brain regulates distinct neuroimmune activities. *Immunity* 50, 317–333.e316.doi: 10.1016/j.immuni.2018.12.012

Malkova, N. V., Collin, Z. Y., Hsiao, E. Y., Moore, M. J., and Patterson, P. H. (2012). Maternal immune activation yields offspring displaying mouse versions of the three core symptoms of autism. *Brain Behav. Immun.* 26, 607–616. doi: 10.1016/j.bbi.2012.01.011

Margolis, K. G., Li, Z., Stevanovic, K., Saurman, V., Israelyan, N., Anderson, G. M., et al. (2016). Serotonin transporter variant drives preventable gastrointestinal abnormalities in development and function. *J. Clin. Invest.* 126, 2221–2235. doi: 10.1172/JCI84877

Marler, S., Ferguson, B. J., Lee, E. B., Peters, B., Williams, K. C., McDonnell, E., et al. (2017). Association of rigid-compulsive behavior with functional

constipation in autism spectrum disorder. *J. Autism Dev. Disord.* 47, 1673–1681. doi: 10.1007/s10803-017-3084-6

Mazalouskas, M., Jessen, T., Varney, S., Sutcliffe, J. S., Veenstra-VanderWeele, J., Cook, E. H., et al. (2015). Integrin β3 haploinsufficiency modulates serotonin transport and antidepressant-sensitive behavior in mice. *Neuropsychopharmacology* 40, 2015–2024. doi: 10.1038/npp.2015.51

McCauley, J. L., Olson, L., Dowd, M., Amin, T., Steele, A., Blakely, R., et al. (2004). Linkage and association analysis at the serotonin transporter (SLC6A4) locus in a rigid-compulsive subset of autism. *Am. J. Med. Genet. B Neuropsychiatr. Genet.* 127, 104–112. doi: 10.1002/ajmg.b.20151

McDougle, C. J., Naylor, S. T., Goodman, W. K., Volkmar, F. R., Cohen, D. J., Price, L. H.. (1993). Acute tryptophan depletion in autistic disorder: a controlled case study. *Biol. Psychiatry* 33, 547–550. doi: doi: 10.1016/0006-3223(93)90011-2

McDougle, C. J., Naylor, S. T., Cohen, D. J., Aghajanian, G. K., Heninger, G. R., Price, L. H. (1996). Effects of tryptophan depletion in drug-free adults with autistic disorder. *Arch. Gen. Psychiatry* 53, 993–1000. doi: 10.1001/archpsyc.1996.01830110029004

McElhanon, B. O., McCracken, C., Karpen, S., and Sharp, W. G. (2014). Gastrointestinal symptoms in autism spectrum disorder: a meta-analysis. *Pediatrics* 133, 872–883. doi: 10.1542/peds.2013-3995

Mehlinger, R., Scheftner, W. A., and Poznanski, E. (1990). Fluoxetine and autism. *J. Am. Acad. Child Adolesc. Psychiatry* 29:985. doi: 10.1097/00004583-199011000-00032

Merikangas, A. K. and Alsamy, L. (2020). Using the tools of genetic epidemiology to understand sex differences in neuropsychiatric disorders. *Genes, Brain and Behav.* 19:e12660. doi: 10.1111/gbb.12660

Montgomery, S. A. (1995). Selective serotonin reuptake inhibitors in the acute treatment of depression. *J. Psychopharmacol.* 12, 15–19. doi: 10.1177/026988119801200304l

Moya, P. R., Wendland, J. R., Rubenstein, L. M., Timpano, K. R., Heiman, G. A., Tischfield, J. A., et al. (2013). Common and rare alleles of the serotonin transporter gene, SLC6A4, associated with Tourette's disorder. *Mov. Disord.* 28, 1263–1270. doi: 10.1002/mds.25460

Muller, C. L., Anacker, A. M., Rogers, T. D., Goeden, N., Keller, E. H., Forsberg, C. G., et al. (2017). Impact of maternal serotonin transporter genotype on placental serotonin, fetal forebrain serotonin and neurodevelopment. *Neuropsychopharmacology* 42, 427–436. doi: 10.1038/npp.2016.166

Muller, C. L., Anacker, A. M. J., and Veenstra-VanderWeele, J. (2016). The serotonin system in autism spectrum disorder: from biomarker to animal models. *Neuroscience* 321, 24–41. doi: 10.1016/j.neuroscience.2015.11.010

Murphy, D. L., and Moya, P. R. (2011). Human serotonin transporter gene (SLC6A4) variants: their contributions to understanding pharmacogenomic and other functional G×G and G×E differences in health and disease. *Curr. Opin. Pharmacol.* 11, 3–10. doi: 10.1016/j.coph.2011.02.008

O'Mahony, S. M., Clarke, G., Borre, Y., Dinan, T., and Cryan, J. (2015). Serotonin, tryptophan metabolism and the brain-gut-microbiome axis. *Behav. Brain Res.* 277, 32–48. doi: 10.1515/jbcpp-2020-0338

O'Reilly, K. C., Connor, M., Pierson, J., Shuffrey, L. C., Blakely, R. D., Ahmari, S. E., et al. (2021). Serotonin 5-HT(1B) receptor-mediated behavior and binding in mice with the overactive and dysregulated serotonin transporter Ala56 variant. *Psychopharmacology (Berl)* 238, 1111–1120. doi: 10.1007/s00213-020-05758-8

Owens, M. J., and Nemeroff, C. B. (1998). The serotonin transporter and depression. *Depress. Anxiety* 8, 5–12.

Ozaki, N., Goldman, D., Kaye, W., Plotnicov, K., Greenberg, B., Lappalainen, J., et al. (2003). Serotonin transporter missense mutation associated with a complex neuropsychiatric phenotype. *Mol. Psychiatry* 8, 933–936. doi: 10.1038/sj.mp.4001365

Pagan, C., Benabou, M., Leblond, C., Cliquet, F., Mathieu, A., Lemière, N., et al. (2021). Decreased phenol sulfotransferase activities associated with hyperserotonemia in autism spectrum disorders. *Transl. Psychiatry* 11, 1–11. doi: 10.1038/s41398-020-01125-5

Piven, J., Tsai, G. C., Nehme, E., Coyle, J. T., Chase, G. A., and Folstein, S. E. (1991). Platelet serotonin, a possible marker for familial autism. *J. Autism Dev. Disord.* 21, 51–59. doi: 10.1007/BF02206997

Prasad, H. C., Steiner, J. A., Sutcliffe, J. S., and Blakely, R. D. (2009). Enhanced activity of human serotonin transporter variants associated with autism. *Philos. Trans. R. Soc. Lond. B Biol. Sci.* 364, 163–173. doi: 10.1098/rstb.2008.0143

Prasad, H. C., Zhu, C.-B., McCauley, J. L., Samuvel, D. J., Ramamoorthy, S., Shelton, R. C., et al. (2005). Human serotonin transporter variants display altered sensitivity to protein kinase G and p38 mitogen-activated protein kinase. *Proc. Natl. Acad. Sci. U S A* 102, 11545–11550. doi: 10.1073/pnas.0501432102

Qian, Y., Galli, A., Ramamoorthy, S., Risso, S., DeFelice, L. J., and Blakely, R. D. (1997). Protein kinase C activation regulates human serotonin transporters in HEK-293 cells *via* altered cell surface expression. *J. Neurosci.* 17, 45–57. doi: 10.1523/JNEUROSCI.17-01-00045.1997

Quinlan, M. A., Krout, D., Katamish, R. M., Robson, M. J., Nettesheim, C., Gresch, P. J., et al. (2019). Human serotonin transporter coding variation establishes conformational bias with functional consequences. *ACS Chem. Neurosci.* 10, 3249–3260. doi: 10.1021/acschemneuro.8b00689

Quinlan, M. A., Robson, M. J., Ye, R., Rose, K. L., Schey, K. L., and Blakely, R. D. (2020). *Ex vivo* quantitative proteomic analysis of serotonin transporter interactome: network impact of the SERT Ala56 coding variant. *Front. Mol. Neurosci.* 13:89. doi: 10.3389/fnmol.2020.00089

Raison, C. L., and Miller, A. H. (2011). Is depression an inflammatory disorder? *Curr. Psychiatry Rep.* 13, 467–475. doi: 10.1007/s11920-011-0232-0

Ramamoorthy, S., Bauman, A. L., Moore, K. R., Han, H., Yang-Feng, T., Chang, A. S., et al. (1993). Antidepressant-and cocaine-sensitive human serotonin transporter: molecular cloning, expression and chromosomal localization. *Proc. Natl. Acad. Sci. U S A* 90, 2542–2546. doi: 10.1073/pnas.90.6.2542

Ramamoorthy, S., Giovanetti, E., Qian, Y., and Blakely, R. D. (1998). Phosphorylation and regulation of antidepressant-sensitive serotonin transporters. *J. Biol. Chem.* 273, 2458–2466. doi: 10.1074/jbc.273.4.2458

Ramamoorthy, S., Samuvel, D. J., Buck, E. R., Rudnick, G., and Jayanthi, L. D. (2007). Phosphorylation of threonine residue 276 is required for acute regulation of serotonin transporter by cyclic GMP. *J. Biol. Chem.* 282, 11639–11647. doi: 10.1074/jbc.M611353200

Ramamoorthy, S., Shippenberg, T. S., and Jayanthi, L. D. (2011). Regulation of monoamine transporters: role of transporter phosphorylation. *Pharmacol. Ther.* 129, 220–238. doi: 10.1016/j.pharmthera.2010.09.009

Robson, M. J., Quinlan, M. A., Margolis, K. G., Gajewski-Kurdziel, P. A., Veenstra-VanderWeele, J., Gershon, M. D., et al. (2018). p38α MAPK signaling drives pharmacologically reversible brain and gastrointestinal phenotypes in the SERT Ala56 mouse. *Proc. Natl. Acad. Sci. U S A* 115, E10245–E10254. doi: 10.1073/pnas.1809137115

Rotman, A., Caplan, R., and Szekely, G. A. (1980). Platelet uptake of serotonin in psychotic children. *Psychopharmacology* 67, 245–248. doi: 10.1007/BF00431264

Roy, S. M., Minasov, G., Arancio, O., Chico, L. W., Van Eldik, L. J., Anderson, W. F., et al. (2019). A selective and brain penetrant p38αMAPK inhibitor candidate for neurologic and neuropsychiatric disorders that attenuates neuroinflammation and cognitive dysfunction. *J. Med. Chem.* 62, 5298–5311. doi: 10.1021/acs.jmedchem.9b00058

Sakurai, T., Reichert, J., Hoffman, E. J., Cai, G., Jones, H. B., Faham, M., et al. (2008). A large-scale screen for coding variants in SERT/SLC6A4 in autism spectrum disorders. *Autism Res.* 1, 251–257. doi: 10.1002/aur.30

Schain, R. J., and Freedman, D. X. (1961). Studies on 5-hydroxyindole metabolism in autistic and other mentally retarded children. *J. Pediatr.* 58, 315–320. doi: 10.1016/s0022-3476(61)80261-8

Schroeter, S., and Blakely, R. D. (1996). Drug targets in the embryo: studies on the cocaine-and antidepressant-sensitive serotonin transporter. *Ann. N Y Acad. Sci.* 801, 239–255. doi: 10.1111/j.1749-6632.1996.tb17446.x

Shuffrey, L. C., Guter, S. J., Delaney, S., Jacob, S., Anderson, G. M., Sutcliffe, J. S., et al. (2017). Is there sexual dimorphism of hyperserotonemia in autism spectrum disorder? *Autism Res.* 10, 1417–1423. doi: 10.1002/aur.1791

Siemann, J., Muller, C., Forsberg, C., Blakely, R., Veenstra-VanderWeele, J., and Wallace, M. (2017). An autism-associated serotonin transporter

variant disrupts multisensory processing. *Transl. Psychiatry* 7, e1067–e1067. doi: 10.1038/tp.2017.17

Siemann, J. K., Veenstra-VanderWeele, J., and Wallace, M. T. (2020). Approaches to understanding multisensory dysfunction in autism spectrum disorder. *Autism Res.* 13, 1430–1449. doi: 10.1002/aur.2375

Soiza-Reilly, M., Meye, F. J., Olusakin, J., Telley, L., Petit, E., Chen, X., et al. (2019). SSRIs target prefrontal to raphe circuits during development modulating synaptic connectivity and emotional behavior. *Mol. Psychiatry* 24, 726–745. doi: 10.1038/s41380-018-0260-9

Sutcliffe, J. S., Delahanty, R. J., Prasad, H. C., McCauley, J. L., Han, Q., Jiang, L., et al. (2005). Allelic heterogeneity at the serotonin transporter locus (SLC6A4) confers susceptibility to autism and rigid-compulsive behaviors. *Am J. Hum. Genet.* 77, 265–279. doi: 10.1086/432648

Takahashi, S., Kanai, H., and Miyamoto, Y. (1976a). Reassessment of elevated serotonin levels in blood platelets in early infantile autism. *J. Autism Child. Schizophr.* 6, 317–326. doi: 10.1007/BF01537909

Takahashi, W., Reichert, E. R., Fung, G. C., and Hokama, Y. (1976b). Acute phase proteins and pesticide exposure. *Life Sci.* 19, 1645–1651. doi: 10.1016/0024-3205(76)90069-2

Todd, R. D. (1991). Fluoxetine in autism. *Am. J. Psychiatry* 148:1089. doi: 10.1176/ajp.148.8.1089b

Veenstra-VanderWeele, J., Jessen, T. N., Thompson, B. J., Carter, M., Prasad, H. C., Steiner, J. A., et al. (2009). Modeling rare gene variation to gain insight into the oldest biomarker in autism: construction of the serotonin transporter Gly56Ala knock-in mouse. *J. Neurodev. Disord.* 1, 158–171. doi: 10.1007/s11689-009-9020-0

Veenstra-VanderWeele, J., Muller, C. L., Iwamoto, H., Sauer, J. E., Owens, W. A., Shah, C. R., et al. (2012). Autism gene variant causes hyperserotonemia, serotonin receptor hypersensitivity, social impairment and repetitive behavior. *Proc. Natl. Acad. Sci. U S A* 109, 5469–5474. doi: 10.1073/pnas.1112345109

Voyiaziakis, E., Evgrafov, O., Li, D., Yoon, H.-J., Tabares, P., Samuels, J., et al. (2011). Association of SLC6A4 variants with obsessive-compulsive disorder in a large multicenter US family study. *Mol. Psychiatry* 16, 108–120. doi: 10.1038/mp.2009.100

Wallace, J. A., and Lauder, J. M. (1983). Development of the serotonergic system in the rat embryo: an immunocytochemical study. *Brain Res. Bull.* 10, 459–479. doi: 10.1016/0361-9230(83)90144-2

Walsh, J. J., Christoffel, D. J., Heifets, B. D., Ben-Dor, G. A., Selimbeyoglu, A., Hung, L. W., et al. (2018). 5-HT release in nucleus accumbens rescues social deficits in mouse autism model. *Nature* 560, 589–594. doi: 10.1038/s41586-018-0416-4

Weiss, L. A., Abney, M., Cook Jr, E. H., and Ober, C. (2005). Sex-specific genetic architecture of whole blood serotonin levels. *Am J. Hum. Genet.* 76, 33–41. doi: 10.1086/426697

Wendland, J. R., DeGuzman, T. B., McMahon, F., Rudnick, G., Detera-Wadleigh, S. D., and Murphy, D. L. (2008). SERT Ileu425Val in autism, asperger syndrome and obsessive–compulsive disorder. *Psychiatr. Genet.* 18, 31–39. doi: 10.1097/YPG.0b013e3282f08a06

Ye, R., and Blakely, R. (2011). Natural and engineered coding variation in antidepressant-sensitive serotonin transporters. *Neuroscience* 197, 28–36. doi: 10.1016/j.neuroscience.2011.08.056

Ye, R., Carneiro, A. M., Airey, D., Sanders?Bush, E., Williams, R. W., Lu, L., et al. (2014). Evaluation of heritable determinants of blood and brain serotonin homeostasis using recombinant inbred mice. *Genes Brain Behav.* 13, 247–260. doi: 10.1111/gbb.12092

Zhu, C. B., Blakely, R. D., and Hewlett, W. A. (2006). The proinflammatory cytokines interleukin-1beta and tumor necrosis factor-alpha activate serotonin transporters. *Neuropsychopharmacology* 31, 2121–2131. doi: 10.1038/sj.npp.1301029

Zhu, C.-B., Hewlett, W. A., Feoktistov, I., Biaggioni, I., and Blakely, R. D. (2004). Adenosine receptor, protein kinase G and p38 mitogen-activated protein kinase-dependent up-regulation of serotonin transporters involves both transporter trafficking and activation. *Mol. Pharmacol.* 65, 1462–1474. doi: 10.1124/mol.65.6.1462

Zhu, C.-B., Lindler, K. M., Owens, A. W., Daws, L. C., Blakely, R. D., and Hewlett, W. A. (2010). Interleukin-1 receptor activation by systemic lipopolysaccharide induces behavioral despair linked to MAPK regulation of CNS serotonin transporters. *Neuropsychopharmacology* 35, 2510–2520. doi: 10.1038/npp.2010.116

Zhu, C. B., Steiner, J. A., Munn, J. L., Daws, L. C., Hewlett, W. A., and Blakely, R. D. (2007). Rapid stimulation of presynaptic serotonin transport by a3 adenosine receptors. *J. Pharmacol. Exp. Ther.* 322, 332–340. doi: 10.1124/jpet.107.121665

Conflict of Interest: The authors declare that the research was conducted in the absence of any commercial or financial relationships that could be construed as a potential conflict of interest.

frontiers in Cellular Neuroscience

ORIGINAL RESEARCH
published: 21 June 2021
doi: 10.3389/fncel.2021.661478

Altered Grooming Syntax and Amphetamine-Induced Dopamine Release in EAAT3 Overexpressing Mice

Angélica P. Escobar[1,2], Jonathan Martínez-Pinto[2,3], Francisco Silva-Olivares[2,3], Ramón Sotomayor-Zárate[2,3] and Pablo R. Moya[1,2]**

[1] Facultad de Ciencias, Centro Interdisciplinario de Neurociencia de Valparaíso (CINV), Universidad de Valparaíso, Valparaiso, Chile, [2] Facultad de Ciencias, Instituto de Fisiología, Universidad de Valparaíso, Valparaiso, Chile, [3] Facultad de Ciencias, Centro de Neurobiología y Fisiopatología Integrativa (CENFI), Universidad de Valparaíso, Valparaiso, Chile

The excitatory amino acid transporter EAAT3 plays an important role in the neuronal uptake of glutamate regulating the activation of glutamate receptors. Polymorphisms in the gene-encoding EAAT3 have been associated with obsessive–compulsive disorder (OCD), although the mechanisms underlying this relationship are still unknown. We recently reported that mice with increased EAAT3 expression in forebrain neurons (EAAT3^{glo}/CMKII) display behavioral and synaptic features relevant to OCD, including increased grooming, higher anxiety-like behavior and altered cortico-striatal synaptic function. The dopamine neurotransmitter system is implicated in ritualistic behaviors. Indeed, dopaminergic neurons express EAAT3, and mice lacking EAAT3 exhibit decreased dopamine release and decreased expression of the dopamine D1 receptor. Moreover, EAAT3 plays a role on the effect of the psychostimulant amphetamine. As such, we sought to determine if the OCD-like behavior in EAAT3^{glo}/CMKII mice is accompanied by altered nigro-striatal dopaminergic transmission. The aim of this study was to analyze dopamine transmission both in basal conditions and after an acute challenge of amphetamine, using behavioral, neurochemical, molecular, and cellular approaches. We found that in basal conditions, EAAT3^{glo}/CMKII mice performed more grooming events and that they remained in phase 1 of the grooming chain syntax compared with control littermates. Administration of amphetamine increased the number of grooming events in control mice, while EAAT3^{glo}/CMKII mice remain unaffected. Interestingly, the grooming syntax of amphetamine-control mice resembled that of EAAT3^{glo}/CMKII mice in basal conditions. Using *in vivo* microdialysis, we found decreased basal dopamine levels in EAAT3^{glo}/CMKII compared with control mice. Unexpectedly, we found that after acute amphetamine, EAAT3^{glo}/CMKII mice had a higher release of dopamine compared with that of control mice, suggesting that EAAT3 overexpression leads to increased dopamine releasability. To determine postsynaptic effect of EAAT3 overexpression over dopamine transmission, we performed Western blot analysis of dopaminergic proteins and found that EAAT3^{glo}/CMKII mice have higher expression of D2 receptors, suggesting a higher inhibition of the indirect striatal

OPEN ACCESS

Edited by:
Renae Ryan,
The University of Sydney, Australia

Reviewed by:
Suzanne Underhill,
National Institutes of Health (NIH), United States
Amy J. Ramsey,
University of Toronto, Canada

***Correspondence:**
Angélica P. Escobar
angelica.escobar@uv.cl
Pablo R. Moya
pablo.moya@uv.cl

Specialty section:
This article was submitted to Cellular Neurophysiology, a section of the journal Frontiers in Cellular Neuroscience

Received: *30 January 2021*
Accepted: *17 May 2021*
Published: *21 June 2021*

Citation:
Escobar AP, Martínez-Pinto J, Silva-Olivares F, Sotomayor-Zárate R and Moya PR (2021) Altered Grooming Syntax and Amphetamine-Induced Dopamine Release in EAAT3 Overexpressing Mice. Front. Cell. Neurosci. 15:661478. doi: 10.3389/fncel.2021.661478

pathway. Together, the data indicate that EAAT3 overexpression impacts on dopamine transmission, making dopamine neurons more sensitive to the effect of amphetamine and leading to a disbalance between the direct and indirect striatal pathways that favors the performance of repetitive behaviors.

Keywords: EAAT3, EAAC1, *SLC1A1*, dopamine receptor, obsessive–compulsive disorder, microdialysis, striatum, amphetamine

INTRODUCTION

Obsessive–compulsive disorder (OCD) is a psychiatric illness characterized by the performance of repetitive behaviors (compulsions) and the presence of intrusive, anxiety-generating thoughts (obsessions) that affects 2–3% worldwide (Grabe et al., 2000; Angst et al., 2004; Bienvenu et al., 2012). A brain circuit largely implicated in OCD is the cortico-striato-thalamo-cortical loop (CSTC), where an imbalance between the efferent pathways of the striatum (either an overactivation of the striatal direct pathway or an inhibition of the indirect pathway) would lead to repetitive behaviors (Saxena and Rauch, 2000; Saxena et al., 2001). Importantly, the activity of the striatal pathways and its dorsolateral and ventral portions are modulated by dopamine (DA) projections from the ventral tegmental area (VTA) and the substantia nigra *pars compacta* (SNc). At the neurochemical level, striatal alterations on DA release as well as on the expression levels of DA receptors could lead to an imbalance in the fine-tuned regulation of the direct and indirect pathways, contributing to the development of compulsive behaviors. Interestingly, altered expression of DA system proteins in the striatum have been reported in neuroimaging studies of OCD (Denys et al., 2004; Hesse et al., 2005; Moresco et al., 2007). In animals, the DA transporter (DAT) knockdown mice shows an increase in DA extracellular level in the striatum and a repetitive grooming behavior (Berridge et al., 2005). On the other hand, the repeated activation of DA type 2 receptors (D2Rs) produces compulsive checking behavior in rats (Szechtman et al., 1998; Escobar et al., 2015) and mice (Asaoka et al., 2019; Sun et al., 2019). These findings reinforce the notion that altered DA neurotransmission may be involved in the development of repetitive behaviors, a cardinal trait in OCD.

Dysfunctions in glutamate system have also been suggested to contribute to the OCD etiology; for detailed reviews, please see Grados et al. (2013), Escobar et al. (2019), and Robbins et al. (2019). Human genetic studies suggest a role for the *SLC1A1* gene encoding the neuronal excitatory amino acid transporter 3 (EAAT3) in OCD (Arnold et al., 2006; Dickel et al., 2006; Wendland et al., 2009; Wu et al., 2013). EAAT3 is expressed postsynaptically in GABA, glutamate, and DA neurons (Coco et al., 1997; Conti et al., 1998; Sidiropoulou et al., 2001; Underhill et al., 2014), buffering glutamate extracellular levels to regulate the activation of AMPA and NMDA receptors (Scimemi et al., 2009; Jarzylo and Man, 2012; Underhill et al., 2014; Delgado-Acevedo et al., 2019).

Mouse models lacking EAAT3 expression have reported dissimilar results in regard to OCD-like behavior. EAAT3 heterozygous mice were found to have no behavioral or neurochemical alterations relevant to OCD (González et al., 2017). In EAAT3 knockout (KO) mice, early studies found no alterations in anxiety or compulsive-like behaviors at 6–8 weeks old but reported a reduction in self-grooming behavior at 10–12 months old (Aoyama et al., 2006), while a recent study found increased grooming in EAAT3 KO mice at an early age, from postnatal day 14 to 35 (Bellini et al., 2018). Using a different EAAT3 KO mouse model, Zike and colleagues reported a reduction in grooming behavior at 2- to 4-month-old mice (Zike et al., 2017). Based on genetic findings of *SLC1A1* gene variants associated with OCD in a large case-control study and that correlated with higher EAAT3 expression in human brain tissue (Wendland et al., 2009), we recently developed a transgenic model with increased EAAT3 expression in principal forebrain neurons (EAAT3^{glo}/CMKII) (Delgado-Acevedo et al., 2019). EAAT3^{glo}/CMKII mice display increased anxiety and compulsive behaviors as well as deficits in cortico-striatal synaptic function, demonstrating that EAAT3 overexpression could be related to the pathophysiology of OCD (Delgado-Acevedo et al., 2019).

Interestingly, EAAT3 is known to impact dopamine neurotransmission. For example, EAAT3 KO mice show a reduction in DA type 1 receptor (D1R) expression and reduced basal DA extracellular levels in the striatum (Zike et al., 2017), suggesting that the decreased grooming behavior found in this model could be a consequence of a decreased activation of the D1R-direct striatal pathway (Zike et al., 2017). In addition, striatal DA release induced by amphetamine and a concomitant grooming behavior are reduced in EAAT3 KO compared with control mice (Zike et al., 2017). On the other hand, Bellini et al. reported an increase in striatal D1R expression in EAAT3 KO mice, which is correlated with higher grooming behavior (Bellini et al., 2018). EAAT3 is expressed in DA neurons (Sidiropoulou et al., 2001; Underhill et al., 2014; Li et al., 2017), and it has been suggested as a neuroprotective effect in late adulthood, since a reduction in EAAT3 expression is related to a reduced number of DA neurons (Berman et al., 2011). Furthermore, it has been shown that the pharmacological effect of amphetamine is mediated by EAAT3 because amphetamine induces the internalization of EAAT3 in DA neurons and potentiates synaptic excitatory glutamate currents (Underhill et al., 2014; Li et al., 2017). Thus, the EAAT3 expression level might regulate the activity of dopaminergic neurons (Li et al., 2017), ultimately impacting on DA release. As dopamine neurons express calcium/calmodulin-dependent kinase 2 promoter (CMKII) (Wang et al., 2013) and the fact that EAAT3^{glo}/CMKII mice exhibit OCD-like behaviors (Delgado-Acevedo et al., 2019), we sought to determine if EAAT3 overexpression impacts on DA system by analyzing neurochemical, molecular,

and behavioral parameters in basal conditions as well as by amphetamine challenge.

MATERIALS AND METHODS

Animals

EAAT3^{glo}/CMKII is a double transgenic mouse line that overexpresses EAAT3 under the control of CMKII using a cre-LoxP system (Delgado-Acevedo et al., 2019). EAAT3^{glo} littermate mice lacking CMKII-cre were used as controls. Mice were housed in the animal care facility at the Facultad de Ciencias, Universidad de Valparaiso, under the care of a veterinarian. Mice were housed in groups of two to five per cage with food and water *ad libitum*, in a light–dark cycle of 12 h (lights on at 7:00 a.m.) in a room with controlled temperature and humidity. Behavioral and surgical procedures were done in mice 3–5 months old. In order to reduce the number of animals used, mice were first tested in behavioral procedures and after at least 14 days to allow for amphetamine washout; *in vivo* microdialysis, immunohistochemistry, or molecular assays were performed in the same animals. All procedures were performed according to the NIH Guidelines and approved by the institutional Bioethics Committee of the Universidad de Valparaiso (BEA138-19).

Drugs

Amphetamine sulfate was donated by Laboratorio Chile S.A. (Santiago, Chile), and it was dissolved in saline solution at a concentration of 1.5 mg/ml. The dose of amphetamine for behavioral and neurochemical experiments was 5.0 mg/kg subcutaneously (s.c.).

Behavior

All behavioral procedures were performed in a behavioral room between 9:00 and 14:00 h. Mice were handled for 20 min each day for three consecutive days to allow habituation. Before the behavioral test, mice were acclimated to the behavioral room at least for 1 h. All experiments were performed in blind to the animal's genotype, and the equipment was cleaned with 5% ethanol solution before and after each test.

Locomotor Activity

Mice were placed in the center of an open field arena (40 × 40 × 35 cm high), and basal horizontal locomotor activity was recorded for 45 min. Next, a single dose of amphetamine (5 mg/kg, s.c.) was administered, and activity was recorded for an additional 45 min. Locomotor activity parameters were recorded and analyzed using Noldus Ethovision XT (Noldus Information Technology, Leesburg, VA, United States). Also, from the first 5 min of recording, the time and frequency in the center of the arena (20 × 20 cm) were determined to evaluate anxiety-like behavior. EAAT3^{glo} n = 11 (6M, 5F); EAAT3^{glo}/CMKII n = 8 (5M, 3F).

Grooming

Mice were placed in a clear plexiglass cylinder, 20-cm diameter and 30-cm high, and recorded using a video camera placed in front of the cylinder. Grooming was recorded in basal conditions for 10 min. Immediately after, mice received a single dose of amphetamine challenge (5 mg/kg, s.c.) and were returned to its home-cage for 35 min. Then the mice were placed back in the clean cylinder, and grooming behavior was recorded for the next 10 min; this was done to properly compare the drug exposure time to the locomotor activity experiments. Grooming behavior (number of events and time spent in grooming) was analyzed manually. Each grooming event was classified according to the grooming phase reached (Cromwell et al., 1998; Berridge et al., 2005; Kalueff et al., 2007). Briefly, the grooming chain syntax consists of four patterns of grooming movements: phase 1 consists of a series of ellipse-shaped movements around the nose; phase 2 is defined as a series of movements made by one paw that reach the mystacial vibrissae to below the eye, phase 3 is a series of movements made by both paws simultaneously reaching the ears, and phase 4 is a sustained movement of body licking (Berridge et al., 2005; Kalueff et al., 2007). EAAT3^{glo} n = 7 (4M, 3F); EAAT3^{glo}/CMKII n = 9 (3M, 6F).

In vivo Microdialysis in Anesthetized Mice

Mice were first anesthetized with isofluorane (3% in 0.5 L/min airflow) in an induction chamber, and then placed in a stereotaxic apparatus with a mask to maintain anesthesia for all the experiment (1–2% isofluorane in 0.5 L/min, airflow) using an animal anesthesia system (model 510, RWD Life Science Co. Ltd., Shenzhen, China). Body temperature was maintained at 37°C. Craniotomy was made according to the following stereotaxic in mm: AP: 1.0, ML: 1.5, according to Paxinos Mouse Brain Atlas. A microdialysis probe (length 2 mm, 0.26 mm diameter, 6 kDa, CMA-11, Harvard Apparatus) was lowered to reach 1.8 mm under the dura, covering the dorsal striatum. The microdialysis probe was continuously perfused with Krebs solution (120 mM NaCl, 2.4 mM KCl, 1.2 mM $CaCl_2$, 0.9 mM NaH_2PO_4, and 1.4 mM Na_2HPO_4, pH 7.4) at a flow of 2 μl/min with a syringe pump. Sample collection started after a 60-min stabilization period. Samples were obtained every 15 min, received in 5.0 μl of perchloric acid solution (0.2 N) and maintained in ice until the end of the experiment. To better compare with the protocol used in behavioral tests, three baseline samples were first obtained, then animals received an amphetamine injection (s.c.), and three samples were collected. By the end of the experiment, samples were kept at −80°C until further analysis. Mice were decapitated under anesthesia, their brains removed, fixed in paraformaldehyde solution (4%), and sliced every 50 μm in a cryostat (Leica apparatus). Slices were stained with cresyl violet for *post hoc* verification of probe location under the light microscope. Only data coming from correct probe placement in the striatum were used for further analysis. EAAT3^{glo} n = 7 (5M, 2F); EAAT3^{glo}/CMKII n = 9 (5M, 4F).

Analysis of Striatal Dialysate

Ten microliters of each dialysate sample were injected to the HPLC-ED system with the following equipment: An isocratic pump (model PU-2080 Plus, Jasco Co., Ltd., Tokyo, Japan), a

C18 column (model Kromasil 100-3.5-C18, AkzoNobel, Bohus, Sweden), and an electrochemical detector (set at 650 mV, 0.5 nA; model LC-4C, BAS, West Lafayette, IN, United States). The mobile phase, containing 0.1 M NaH_2PO_4, 1.0 mM 1-octanesulfonic acid, 1.0 mM EDTA, 1.0% ($^v/_v$) tetrahydrofuran, and 8.0% ($^v/_v$) CH_3CN (pH 3.4) was pumped at a flow rate of 125 ml/min. DA extracellular levels were assessed by comparing the respective peak area and elution time of the sample with a reference standard, and the quantification was performed using a calibration curve for each neurotransmitter (Program ChromPass, Jasco Co., Ltd., Tokyo, Japan). In these conditions, the retention time for dopamine was 9.5 min.

Identification and Quantification of Dopamine Neurons in the Substantia Nigra *Pars compacta*

Dopamine neurons of the SNc were identified by immunostaining for tyrosine hydroxylase (TH). Mice were anesthetized with a mixture of ketamine/xylazine (50/5 mg/kg, respectively) and cardiacly perfused with 50 ml of PBS followed by 50 ml of 4% paraformaldehyde. The brains were removed and postfixed over night with 4% paraformaldehyde and then changed to a solution of 30% sucrose in PBS. Serial 30-μm-thick slices were obtained in a cryostat (Leica Biosystems, IL, United States) spanning the rostrocaudal range of the SNc and recovered every six slices in the same well of a six multiwell plate. Immunostaining for TH was made with rabbit anti-tyrosine-hydroxylase (657012, Merck Millipore, Darmstadt, Germany), diluted at 1:5,000, and incubated overnight at 4°C in 1% horse serum, 0.03% triton in PBS. Donkey anti-rabbit Cy3 (711165152, Jackson Labs, Bar Harbor, ME, United States) diluted at 1:1,000 was used as secondary antibody and incubated for 1 h in the same solution as primary antibody. After three consecutive rinses with PBS, slices were incubated with DAPI (Thermo Fisher Scientific, Waltham, MA, United States) 300 nM for 5 min and then mounted with Fluromount mounting medium (Sigma-Aldrich, St. Louis, MO, United States). Pictures of SNc sections were obtained using a confocal microscope (Nikon) using a 20 × objective with a resolution of 1,024 × 1,024 pixels, and with z steps of 2 μm. TH cells were counted only if the nucleus was fully covered by the z sections. Z-stacks were collapsed in a single image, and cells were counted using the cell counter plugin of image J and then standardized by the area in mm^2. EAAT3^{glo} $n = 7$ (3M, 4F); EAAT3^{glo}/CMKII $n = 11$ (8M,3F).

Quantification of Striatal Dopamine Proteins

Mice were anesthetized with isofluorane in a hermetic saturated chamber, and the brains were quickly removed and rinsed in ice-cold PBS 1 ×. The dorsal striatum was obtained by dissecting a 2-mm-thick slice and immediately stored at −80°C until protein extraction. Proteins were extracted in RIPA lysis buffer with protease inhibitor cocktail. Protein samples (30 μg) were separated by SDS-PAGE on 10% polyacrylamide gels under denaturing conditions (4% stacking gel, 10% resolving gel). Proteins were transferred to nitrocellulose membrane (Cat# 88018, 0.45-μm pore, Thermo Scientific™, Rockford, IL, United States) at 350 mA for 1.5 h. Non-specific sites of membrane binding were blocked with 5% skim milk in T-TBS (0.1% Tween-20, 20 mM TBS, 137 mM NaCl) for 1 h at room temperature. Primary antibodies for immunodetection of dopamine system proteins were selected based on previously published data: 1:1,000 of rabbit anti-D1R (AB1765P, Merck Millipore, Darmstadt, Germany) (Huang et al., 1992; Graham et al., 2015); 1:1,000 of rabbit anti-D2R (AB5084P, Merck Millipore, Darmstadt, Germany) (Galvan et al., 2014; Graham et al., 2015); 1:10,000 of rabbit anti-TH (657012, Merck Millipore, Darmstadt, Germany) (Espinosa et al., 2016); 1:2,000 of rabbit anti-DAT (434-DATEL2, Phosphosolutions, Aurora, CO, United States) (Dib et al., 2018; Alonso et al., 2021). Rabbit anti-GAPDH (G9545, Sigma-Aldrich, St. Louis, MO, United States) at 1:10,000 was used as loading control. As secondary antibody, donkey anti-rabbit conjugated with HRP (711036152, Jackson Immunoresearch Laboratories, Baltimore, MD, United States) diluted 1:5,000 was used. For chemiluminescent detection, we used EZ-ECL kit (SuperSignal™ Femto, Thermo Scientific, Rockford, IL, United States), and the images of the membranes were obtained using a benchtop darkroom (EpiChemi^3 Darkroom, UVP, Upland, CA, United States). The images were analyzed using Image-J™ software. EAAT3^{glo} $n = 4$; EAAT3^{glo}/CMKII $n = 4$.

Analysis and Statistics

Locomotor activity and dopamine release were analyzed by two-way repeated measures ANOVA (group × time) followed by Bonferroni posttest. The percentage of grooming events in each phase of grooming chain syntax was analyzed by two-way repeated measures ANOVA (group × phase) followed by Sidak's multiple comparisons test. Number of grooming events, time spent in grooming behavior, number of dopamine neurons, and levels of dopaminergic proteins were analyzed by unpaired *t*-test. Data are reported as mean ± SEM. Statistical analysis was done using GraphPad Prism v6.0 (GraphPad Software, San Diego, CA, United States), and $p < 0.05$ was considered statistically significant.

RESULTS

Increased Spontaneous Grooming Behavior in EAAT3^{glo}/CMKII Mice Is Accompanied by an Altered Syntax and It Is Insensitive to Amphetamine

We tested whether EAAT3 overexpression leads to changes in grooming structure evaluating this behavior in trials of 10 min. EAAT3^{glo}/CMKII mice showed increased number of spontaneous grooming events compared with control littermates (EAAT3^{glo} 5.7 ± 1.6 events, $N = 7$; EAAT3^{glo}/CMKII 20.4 ± 4.6 events, $N = 9$. $P = 0.0187$, according to unpaired *t*-test). However, the time spent in grooming was not different between groups (EAAT3^{glo} 6.238 ± 1.529 s, $N = 7$; EAAT3^{glo}/CMKII 8.950 ± 1.564 s, $N = 10$. $p = 0.2509$, according to unpaired

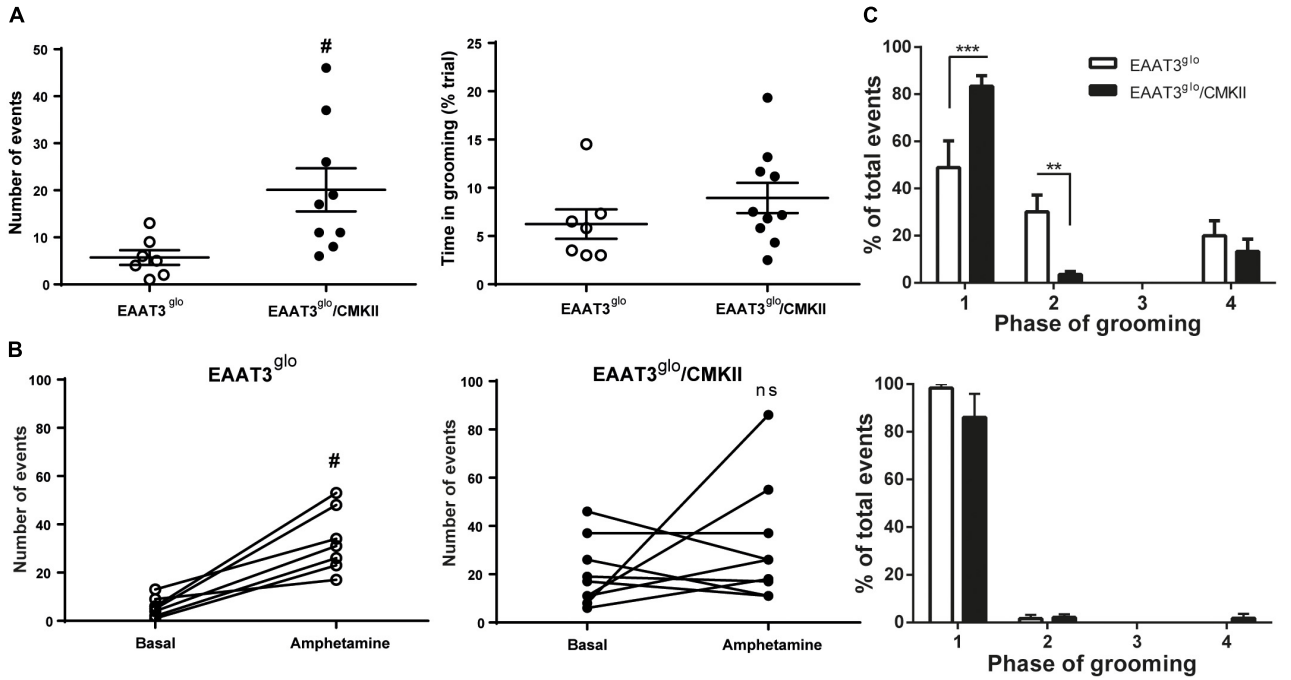

FIGURE 1 | Grooming behavior is increased and its chain syntax altered in EAAT3^{glo}/CMKII mice. Mice were placed in a cylindrical transparent plexiglass container, and its grooming behavior was video recorded for 10 min in basal conditions and after an acute injection of amphetamine [5 mg/kg subcutaneously (s.c.)]. Analysis of grooming was made by an experimenter blind to the genotype of the mice. **(A)** Comparison of grooming behavior between EAAT3^{glo} and EAAT3^{glo}/CMKII mice in basal conditions. **(B)** Number of grooming events in basal conditions paired with the number of grooming events after acute administration of amphetamine in EAAT3^{glo} (left) and EAAT3^{glo}/CMKII (right) mice. **(C)** Distribution of grooming events in the phases of the grooming-chain syntax in basal (upper panel) and after amphetamine administration (lower panel). EAAT3^{glo} $n = 7$ (4M, 3F); EAAT3^{glo}/CMKII $n = 9$ (3M, 6F). $^{**}p < 0.01$, $^{***}p > 0.001$, according to two-way ANOVA and Sidak's multiple comparison test. $^{\#}p = 0.0187$, according to unpaired t-test.

t-test) (**Figure 1A**) suggesting that the duration of individual grooming bouts should be shorter in EAAT3^{glo}/CMKII mice. We assessed then if EAAT3 overexpression leads to a change in the grooming chain syntax (**Figure 1C**, upper panel). We found that both EAAT3^{glo}/CMKII and EAAT3^{glo} mice have a higher proportion of events at phases 1 and 2, and a low proportion of events reaching phase 4 [grooming phase: $F_{(3,\ 60)} = 58.38$, $p < 0.0001$; genotype: $F_{(1,\ 60)} = 0.006677$, $p = 0.9351$; interaction: $F_{(3,\ 60)} = 11.57$, $p < 0.0001$; two-way ANOVA]. Interestingly, EAAT3^{glo}/CMKII mice have a significantly higher proportion of events in phase 1 and a lower proportion in phase 2 compared with controls (phase 1: $p < 0.0001$; phase 2: $p < 0.01$. Sidak's multiple comparisons test), suggesting that EAAT3-overexpressing mice get stuck on the initiation phase of grooming without completing the full behavior. To assess whether amphetamine has a differential effect on grooming due to increased EAAT3 expression, we acutely administered amphetamine (5.0 mg/kg) to EAAT3^{glo}/CMKII and control mice. Interestingly, amphetamine significantly increased the number of grooming events only in controls (EAAT3^{glo}: basal events 5.71 ± 1.57, amphetamine events 33.14 ± 4.96; $p = 0.0156$, paired t-test), while no significant effect was observed in EAAT3-overexpressing mice (EAAT3^{glo}/CMKII: basal events 20.11 ± 4.58, amphetamine events 31.89 ± 8.20; $p = 0.5781$, paired t-test) (**Figure 1B**). Moreover, the syntax chain of grooming phases was shifted in control EAAT3^{glo} mice toward almost all events classified in phase 1, resembling what happens with EAAT3^{glo}/CMKII mice in basal conditions. On the other hand, EAAT3^{glo}/CMKII was maintained in phase 1 [grooming phase: $F_{(3,\ 60)} = 215.0$; $p < 0.0001$; genotype: $F_{(1.\ 60)} = 0.6450$; $p = 0.4251$; interaction: $F_{(3,\ 60)} = 1.125$; $p = 0.3462$; two-way ANOVA], while multiple comparisons test did not show any difference between genotypes (**Figure 1B**, bottom panel). Together, the data suggest that EAAT3 overexpression converts grooming from a spontaneous behavior to an "amphetamine-like" behavior.

Amphetamine-Induced Increase in Locomotor Activity Is Not Modified by EAAT3 Overexpression

We wondered whether increased EAAT3 expression influences the amphetamine-induced locomotor behavior. To assess this, we measured locomotor activity in an open-field arena in basal conditions and after amphetamine administration. We also analyzed the first 5 min in the arena to evaluate anxiety. As we previously reported (Delgado-Acevedo et al., 2019), EAAT3^{glo}/CMKII mice spent significantly less time in the open area of the arena (EAAT3^{glo}: 52.55 ± 11.33 s, $N = 11$; EAAT3^{glo}/CMKII: 19.38 ± 4.89 s, $N = 8$; $p = 0.0300$,

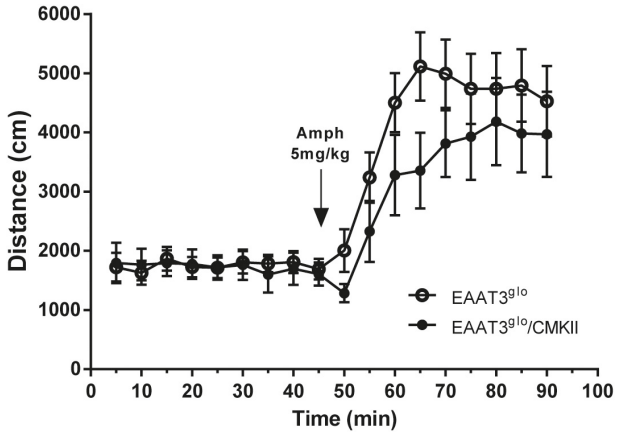

FIGURE 2 | Basal and amphetamine-induced locomotion is unaltered in EAAT3^{glo}/CMKII mice. Mice were placed in an open-field arena (40 × 40 × 35 cm) and their horizontal trajectory was video recorded in basal conditions and after acute amphetamine (5 mg/kg s.c.). Graph shows the cumulative distance traveled by mice in 5 min blocks during 45 min before and after amphetamine. EAAT3^{glo} n = 11 (6M, 5F); EAAT3^{glo}/CMKII n = 8 (5M, 3F).

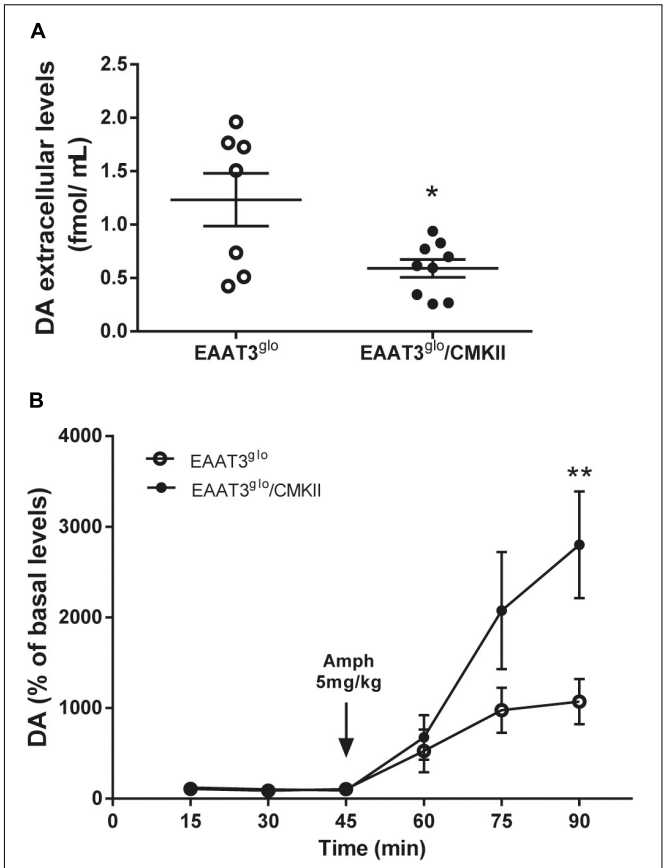

FIGURE 3 | Decreased basal dopamine (DA), but enhanced amphetamine-induced DA levels in EAAT3^{glo}/CMKII mice. *In vivo* microdialysis was done in the striatum of anesthetized mice. Samples were collected every 15 min; three samples were taken in basal conditions and after acute administration of amphetamine (5 mg/kg s.c.). **(A)** Basal DA extracellular concentration in the striatum. Graph shows the average of the three samples taken for basal DA concentration. *p = 0.0163 according to unpaired t-test. **(B)** Temporal course of amphetamine-induced DA release. Data are expressed as percentage of basal DA levels. **$p < 0.01$ according to two-way ANOVA and Bonferroni's posttest. EAAT3^{glo} n = 7 (5M, 2F); EAAT3^{glo}/CMKII n = 9 (5M, 4F).

unpaired t-test), indicating increased anxiety-like behavior (**Supplementary Figure 1**). As shown in **Figure 2**, spontaneous locomotor activity was not modified by EAAT3 overexpression as basal locomotor activity was similar between genotypes. Amphetamine administration significantly increased locomotor activity to the same extent in both genotypes, although maximal locomotor effect was delayed by 15 min in EAAT3^{glo}/CMKII mice in comparison with EAAT3^{glo} [time: $F_{(17,\ 306)} = 16.14$; $p < 0.0001$; genotype: $F_{(1,\ 306)} = 10.81$; $p = 0.0011$; interaction: $F_{(17,\ 306)} = 0.7600$. $p = 0.7387$; two-way ANOVA]. Together, the data indicate that the increased basal grooming observed in EAAT3^{glo}/CMKII mice is not associated with modifications in horizontal locomotor activity and that although amphetamine does not affect grooming, the induction of locomotion is preserved in this mouse model.

Decreased Basal Dopamine Release and Increased Amphetamine-Induced Dopamine Release in EAAT3-Overexpressing Mice

To evaluate whether behavioral effects of EAAT3 overexpression are correlated with modifications on dopaminergic transmission, we performed *in vivo* brain microdialysis experiments in the striatum in basal conditions and after an amphetamine challenge. We carried out microdialysis experiments in isofluorane-anesthetized mice. We used isofluorane because it induces a stable level of anesthesia during an extended period. As urethane, it does not modify dopamine dynamics (Sabeti et al., 2003; Brodnik and España, 2015). We did not observe any difference in sensitivity to induce anesthesia between genotypes, as every mouse needed around 3% isofluorane in 0.5 L/min of airflow for induction and between 1 and 2% isofluorane in 0.5 L/min airflow for maintenance. We found that basal dopamine release was reduced in EAAT3^{glo}/CMKII mice compared with controls (EAAT3^{glo}: 1.233 ± 0.247 fmol/µl, N = 7; EAAT3^{glo}/CMKII: 0.5912 ± 0.08, N = 9; p = 0.0163, unpaired t-test) (**Figure 3A**). This indicates that the increased grooming behavior in these mice and its alteration of the chain syntax are accompanied by reductions in tonic DA release. Acute amphetamine administration increased dopamine extracellular levels in both groups. Surprisingly, this increase was significantly higher in EAAT3^{glo}/CMKII mice in comparison with their control littermates [time: $F_{(5,\ 84)} = 12.99$, $p < 0.0001$; genotype: $F_{(1,\ 84)} = 7.410$, $p = 0.0079$; interaction: $F_{(5,\ 84)} = 2.703$, $p = 0.0258$; two-way ANOVA (**Figure 3B**)]. *Post hoc* test revealed that the enhanced DA release in EAAT3^{glo}/CMKII mice reached significance 45 min after amphetamine administration (min 90, $p < 0.001$, Bonferroni's posttest). Overall, the data indicate that the lack of effect of amphetamine on grooming behavior

of EAAT3^{glo}/CMKII mice is not associated with a decreased ability of amphetamine to release DA, but rather to unexpectedly sensitize DA release, suggesting that cellular mechanisms arise to set the grooming behavior of EAAT3^{glo}/CMKII at a maximum point so that this behavior cannot be higher even though DA release increases.

EAAT3-Overexpressing Mice Have Increased Expression of DA Type 2 Receptors in the Striatum

It has been reported that EAAT3 KO mice have fewer DA neurons at 12 months old (Berman et al., 2011) but not at 3 months old (Berman et al., 2011; Zike et al., 2017). Thus, it is possible that EAAT3 overexpression impacts on the number of these midbrain neurons. To address this question, we performed immunohistochemistry and counted the number of TH-positive neurons in serial sections of the SNc. As shown in **Figure 4**, EAAT3^{glo}/CMKII and control mice have the same number of DA neurons per area in the SNc (EAAT3^{glo}: 160.5 ± 16.2, $N = 7$; EAAT3^{glo}/CMKII: 155.0 ± 13.4, $N = 11$; $p = 0.5134$), indicating that increased DA release by amphetamine is not due to the presence of more DA neurons. We then assessed the expression DA system proteins in the striatum, the target area of DA neurons from SNc. As shown in **Figure 5**, similar levels of expression were found for D1R, DAT, and TH between EAAT3^{glo}/CMKII and control mice. Interestingly, we found that the expression of D2R was significantly higher in EAAT3^{glo}/CMKII mice (EAAT3^{glo}: 0.2050 ± 0.0248, $N = 4$; EAAT3^{glo}/CMKII: 0.2988 ± 0.0288, $N = 4$; $p = 0.0490$), suggesting that EAAT3 overexpression is related to an imbalance between D1R direct and D2R indirect-striatal pathways.

DISCUSSION

In this work, we characterized the behavioral, neurochemical, and molecular components of the dopamine system in basal conditions and after acute administration of amphetamine in EAAT3glo/CMKII, a recently developed mouse model that overexpresses the neuronal glutamate transporter EAAT3 in principal forebrain neurons. In addition to replicate previous data showing increased grooming behavior (Delgado-Acevedo et al., 2019), we found that acute amphetamine administration does not further stimulate this behavior. Interestingly, most of the spontaneous grooming events of EAAT3^{glo}/CMKII mice remain in phase 1, without progressing to the next stages of the chain syntax (Cromwell et al., 1998; Berridge et al., 2005; Kalueff et al., 2007). In control mice, amphetamine administration induced an increase in grooming events and a shift toward phase 1 of the grooming chain syntax. Together, the data suggest that EAAT3 overexpression alters grooming rendering it similar to an amphetamine-like behavior. Despite the increased spontaneous grooming behavior, basal dopamine levels were decreased in EAAT3^{glo}/CMKII mice. Surprisingly, amphetamine administration induced a higher release of dopamine in this model. At the molecular level, EAAT3 overexpression induced an increase of the expression of dopamine D2R in the striatum. Overall, the data suggest that the increased EAAT3 expression impacts on dopamine system indicating that the increased and altered syntax of grooming is accompanied by a decreased tonic release of dopamine in the striatum and enhanced expression of dopamine receptors in the indirect striatal pathway. On the other hand, the increased EAAT3 expression sensitizes the response of DA neurons to amphetamine.

We previously reported that EAAT3^{glo}/CMKII mice display increased repetitive (including grooming) and anxiety-like behaviors as well as altered corticostriatal synaptic function (Delgado-Acevedo et al., 2019). In the present work, we found that the increased spontaneous grooming behavior is due to increased number of grooming bouts that mostly remain in phase 1 of the grooming-chain syntax (Kalueff et al., 2007), without completing the entire sequence (**Figures 1A,C**). This suggest that the increased EAAT3 expression impacts mechanisms that facilitate the initiation of grooming, while at same time, it shunts the progression to the following phases of this behavior. The execution of a complete grooming behavior relies on the integrity of dopamine nigrostriatal neurotransmission (Berridge, 1989; Berridge et al., 2005). Indeed, depletion of dopamine in the nigrostriatal pathway by injection of 6-OHDA as well as ablation of dopamine D1 receptor (D1R) disrupt grooming behavior (Berridge, 1989; Cromwell et al., 1998; Pelosi et al., 2015). EAAT3 is expressed in dopamine neurons (Plaitakis and Shashidharan, 2000; Sidiropoulou et al., 2001; Berman et al., 2011; Underhill et al., 2014) where its ablation causes modifications on this system including a decrease in the number of dopamine neurons in the SNc (Berman et al., 2011), decreased basal dopamine levels (Zike et al., 2017), and expression of D1R in the striatum (Bellini et al., 2018). Thus, we hypothesized that EAAT3 overexpression might modify basal dopamine transmission to underlie increased grooming behavior. Microdialysis experiments in the striatum show decreased basal dopamine levels and increased expression of D2R in EAAT3^{glo}/CMKII mice compared with controls (**Figures 3A**, **5**). Low basal DA levels have been also reported in other preclinical models of compulsive-checking behavior induced by repeated administration of the D2R agonist, quinpirole (Koeltzow et al., 2003; De Haas et al., 2011; Escobar et al., 2015, 2017). A decreased level of basal dopamine is not explained by less dopamine neurons as the number of TH-positive neurons was not modified by EAAT3 overexpression (**Figure 4**). Our results suggest that by increasing EAAT3 expression in midbrain dopamine neurons, local somatic levels of glutamate are reduced, therefore, reducing the firing of DA neurons. Interestingly, striatal dopamine depletion induced by 6-OHDA injection did not reduce the number of grooming bouts, but its progression to following phases of the grooming-chain syntax (Berridge, 1989). Thus, it is possible that reduced levels of striatal DA contribute to the alterations in grooming behavior found in EAAT3^{glo}/CMKII mice.

Based on our previous findings of increased grooming in EAAT3^{glo}/CMKII mice, our present work focused on the characterization of dopamine neurons in the SNc, where no changes were found in the number of TH-positive neurons. However, we did not evaluate alterations in VTA. In this

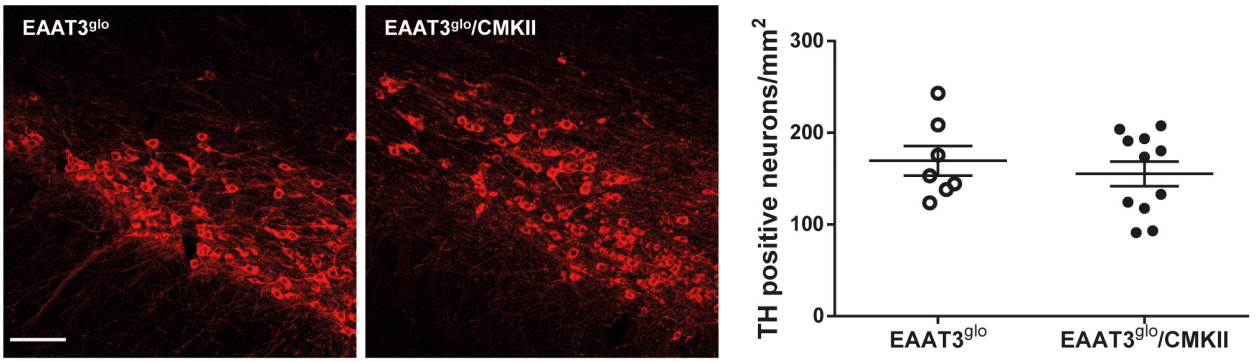

FIGURE 4 | The number of DA neurons is preserved in EAAT3^{glo}/CMKII mice. Immunohistochemistry was made against tyrosine hydroxylase (TH) in 30-μm-thick coronal sections spanning the rostrocaudal axis containing the substantia nigra pars compacta (SNc); the number of TH-positive neurons was quantified and standardized by area in mm^2. Images depict 10 × representative maximum intensity projections of flattened z-stack pictures. Scale bar: 50 μm. EAAT3^{glo} n = 7 (3M, 4F); EAAT3^{glo}/CMKII n = 11 (8M, 3F).

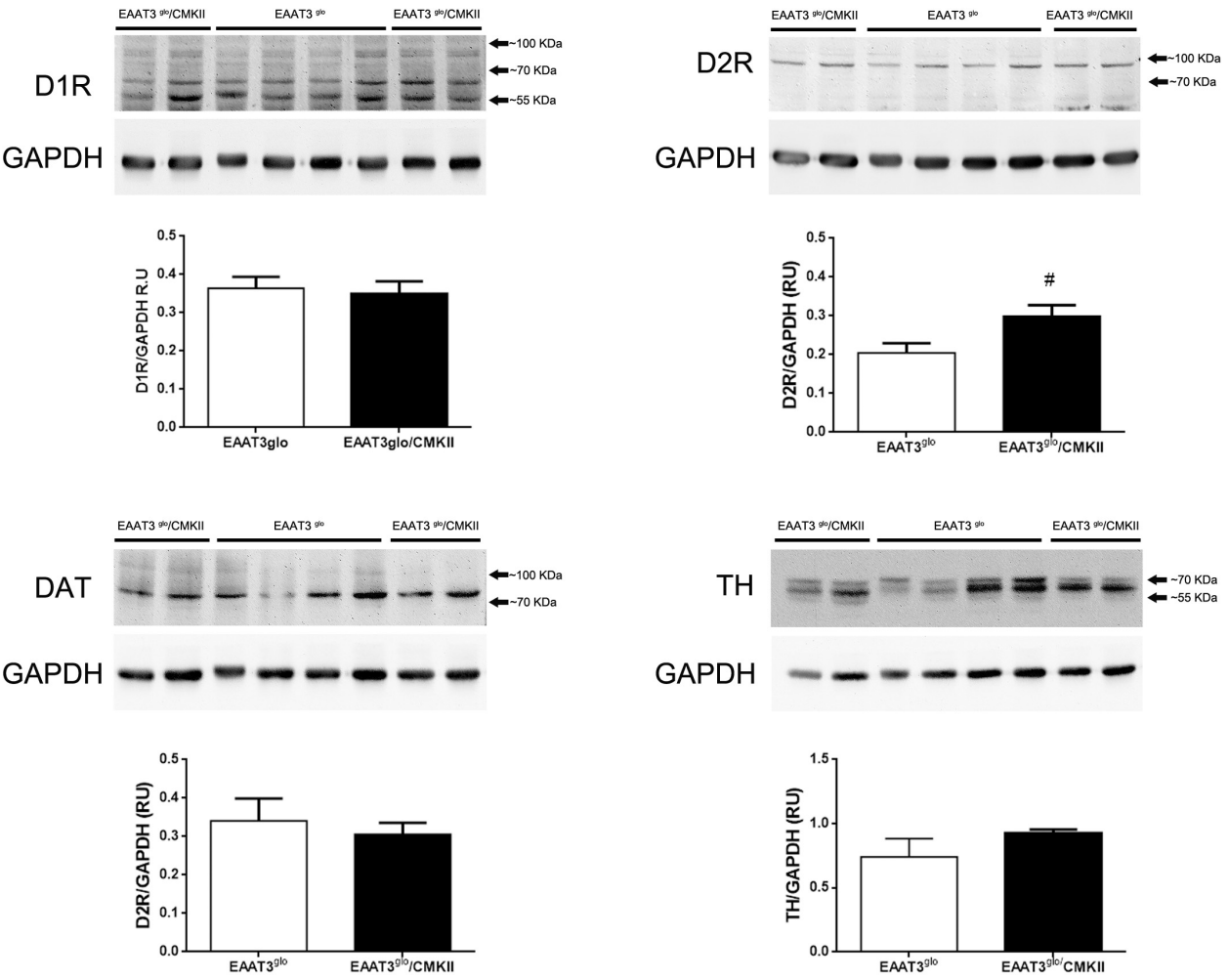

FIGURE 5 | Increased expression of DA D2R in the striatum of EAAT3^{glo}/CMKII mice. Thirty micrograms of striatal protein extracts was processed for the immunodetection and quantification of proteins of the dopaminergic system. Western blot images show the individual bands of protein samples obtained from four mice per group; protein band quantification is depicted below. #p = 0.0286, according to unpaired t-test. EAAT3^{glo} n = 4; EAAT3^{glo}/CMKII n = 4.

regard, the reduced number of dopamine neurons in the SNc of EAAT3 KO mice, reported by Berman and colleagues, was only evident in aged (1 year old), but not in younger (3- to 6-month old) mice (Berman et al., 2011), and it was restored by the administration of N-acetylcysteine, indicating that the effect was due to the lack of cysteine uptake via EAAT3 and an enhancement of the cumulative oxidative damage over time. Using animals at a similar age than in our study, Zike and colleagues found no changes in the number of dopamine neurons of SNc or VTA (Zike et al., 2017). Future experiments should address the impact of EAAT3 overexpression on the number of dopamine neurons in the VTA and mesocorticolimbic function in EAAT3^{glo}/CMKII mice.

We found increased expression of D2R in the striatum of EAAT3^{glo}/CMKII mice (**Figure 5**). D2R has two splicing variants, the short (D2RS) isoform is present presynaptically at dopamine terminals, while the long (D2RL) is present postsynaptically at medium spiny neurons of the indirect pathway (Sesack et al., 1994; Usiello et al., 2000). In this work, we quantified the expression of total D2R; therefore, we could not unravel if the increased EAAT3 expression has a differential impact on D2R isoforms. When activated, D2RS decreases dopamine levels by increasing dopamine reuptake and by decreasing the synthesis and firing of dopamine neurons (Carlson et al., 1986; Napier et al., 1986; Lacey et al., 1987; O'Hara et al., 1996). Thus, an enhanced D2RS expression could explain the reduced basal DA level observed in our mouse model. Whether an increase in D2R triggers a reduction in basal DA, or if the reduced DA triggers a homeostatic increase in D2R remains to be investigated. On the other hand, increased expression of D2RL isoform should be reflected on behavioral traits. Upon activation, D2RL inhibits the activity MSNs of indirect pathway leading to movement facilitation. Therefore, increasing the expression of this receptor could magnify or induce repetitive movements. Indeed, repeated activation of D2R induces sensitization of locomotor activity and compulsive-like behaviors in rats and mice (Szechtman et al., 1998, 2017; Escobar et al., 2015; Asaoka et al., 2019; Sun et al., 2019), which is paralleled with an increased expression of D2R in the high-affinity state (Perreault et al., 2007). Moreover, Deer and C58 mice lines, which naturally develop repetitive-like movements, have a decreased neuronal activity of the indirect pathway (Tanimura et al., 2010), which is restored upon concomitant administration of a D2R antagonist, an adenosine 2A receptor agonist and a mGluR5 receptor-positive allosteric modulator that are able to alleviate the increased repetitive behavior (Muehlmann et al., 2020). To the best of our knowledge, there are no studies addressing grooming syntax in Deer or C58 mice.

Other neurotransmitter systems could also be impacted by EAAT3 overexpression and contribute to the phenotype of EAAT3^{glo}/CMKII mice. In particular, EAAT3 is known to be present in norepinephrine neurons, where amphetamine also stimulates its endocytosis (Underhill et al., 2020). Future studies should investigate potential alterations in norepinephrine as well as serotonin neurotransmission in EAAT3^{glo}/CMKII mice, based on the effectiveness of the current pharmacotherapy targeting these neurotransmitter systems in humans.

Together, the data indicate that chronic inhibition of the indirect striatal pathway triggers the development of compulsive-like behavior and suggest that the increased expression of D2R could mediate the development of the altered grooming behavior observed in the EAAT3^{glo}/CMKII mice. Additionally, increased grooming behavior can be ascribed to the enhanced contribution of GluN2B containing NMDA receptors (Delgado-Acevedo et al., 2019). Indeed, antagonism of NMDA receptors reduced grooming and other repetitive behaviors in rodents prenatally exposed to valproic acid, an animal model of autism (Kang and Kim, 2015; Kim et al., 2017). Therefore, it is plausible to hypothesize that the alteration in GluN2B–NMDA receptor, together with reduced basal DA and enhanced D2R expression, impacts on an augmented and structurally different grooming behavior.

It is known that EAAT3 mediates the effect of the psychostimulant amphetamine on the dopamine system. Acute amphetamine induces a decrease in the surface expression of EAAT3 in midbrain dopamine neurons, which enhance glutamate receptors currents (Underhill et al., 2014; Li et al., 2017). Moreover, amphetamine administration to EAAT3 KO mice induces a lower increase in locomotion and grooming behavior and a lower increase in dopamine extracellular levels compared with controls (Zike et al., 2017). We found that, in EAAT3^{glo}/CMKII mice, amphetamine induced an increase in locomotor activity that was similar to control mice; however, amphetamine increased grooming only in control mice, enhancing the total number of events and their distribution to phase 1 of the grooming chain syntax. EAAT3^{glo}/CMKII mice challenged with amphetamine remained on the same number and phase of grooming events, indicating that increased EAAT3 expression triggers a "ceiling" effect on grooming. Contrary to its behavioral effect, amphetamine induced a significantly higher increase in extracellular dopamine levels in EAAT3^{glo}/CMKII mice compared with controls, indicating that EAAT3 overexpression renders dopamine neurons more responsive to amphetamine, triggering a higher dopamine releasability in the striatum. This result is surprising given the known parallel between higher dopamine extracellular levels with increased locomotion and stereotypy (Pierce and Kalivas, 1997; Kwiatkowski et al., 2019), suggesting that increased EAAT3 overexpression induces glutamatergic mechanisms that affect behavior in response to higher dopamine release. The exposure of dopamine neurons to amphetamine induces the endocytosis of DAT and EAAT3, a phenomenon dependent of the activation of the small GTPase *RhoA* and protein kinase A (PKA) (Underhill et al., 2014). The underlying mechanism includes the entry of amphetamine thorough DAT (Underhill et al., 2014) and the binding to the trace amine-associated receptor, TAAR1, an intracellular G protein-coupled receptor that activates these signaling pathways (Underhill et al., 2021). The decrease in the surface expression of DAT should contribute to the effects of amphetamine to enhance local dopamine extracellular levels. In the same direction, the amphetamine-driven decrease in surface EAAT3 increases local extracellular glutamate and augments the amplitude of NMDA eEPSCs (Underhill et al., 2014), particularly GluN2B-containing NMDA receptors (Li et al., 2017). It is

possible that in EAAT3^{glo}/CMKII mice, the challenge with amphetamine induces the endocytosis of more EAAT3 units compared with controls; this could be sensed by cells as a higher increase in glutamate extracellular levels, which would influence on the level of activation of NMDA receptors. Importantly, activation of NMDA receptors induces and controls the duration and frequency of burst firing in dopamine neurons (Johnson et al., 1992; Chergui et al., 1993; Pearlstein et al., 2015). Burst firing determines phasic and transient increases in dopamine release in target areas that determines salient stimuli. Recently, it has been shown that a single burst of electrical stimulation of midbrain dopamine neurons induces a long-lasting dopamine release in the striatum, which is measurable by microdialysis experiments (Lohani et al., 2018). Together, the data suggest that the enhanced release of dopamine in the striatum seen in EAAT3^{glo}/CMKII mice can also be explained by modifications of glutamate transmission that would lead to a facilitation of phasic activity of dopamine neurons, indicating that the levels of EAAT3 in midbrain dopamine neurons could impact on their firing mode and, by doing so, influence the dopamine transmission in target areas and ultimately behavior.

CONCLUSION

In conclusion, in this study, we found that EAAT3 overexpression impacts on dopamine transmission with pre- and postsynaptic effects in the striatum. These modifications could underlie some of the compulsive behaviors observed in EAAT3^{glo}/CMKII mice and points to EAAT3 as a key mediator in the interplay between dopamine and glutamate transmission.

DATA AVAILABILITY STATEMENT

The raw data supporting the conclusions of this article will be made available by the authors, without undue reservation.

ETHICS STATEMENT

The animal study was reviewed and approved by Bioethics Committee of the Universidad de Valparaiso Protocol No. BEA138-19.

AUTHOR CONTRIBUTIONS

AE and PRM conceived and designed the study. AE, JM-P, and FS-O performed the experiments, collected, and analyzed the data. AE wrote the first manuscript. PRM and RS-Z wrote sections of the manuscript. All authors participated in the manuscript revision as well as read and approved the submitted version.

FUNDING

This work was supported by FONDECYT Grant N°3190843 to AE, N° 1190833 to PRM, and N°120-0474 to RS-Z and Millennium Institute CINV Grant ICM-ANID ICN09-022 to AE and PRM.

SUPPLEMENTARY MATERIAL

The Supplementary Material for this article can be found online at: https://www.frontiersin.org/articles/10.3389/fncel.2021.661478/full#supplementary-material

Supplementary Figure 1 | EAAT3^{glo}/CMKII mice show anxiety-like behavior. Mice were placed in an open-field arena (40 × 40 × 35 cm) and allowed to freely explore for 5 min. The time spend in center (20 × 20 cm) was analyzed. $P = 0.03$, according to unpaired T-test. EAAT3^{glo} $n = 11$ (6M, 5F); EAAT3^{glo}/CMKII $n = 8$ (5M, 3F).

REFERENCES

Alonso, I. P., Pino, J. A., Kortagere, S., Torres, G. E., and España, R. A. (2021). Dopamine transporter function fluctuates across sleep/wake state: potential impact for addiction. *Neuropsychopharmacology* 46, 699–708. doi: 10.1038/s41386-020-00879-2

Angst, J., Gamma, A., Endrass, J., Goodwin, R., Ajdacic, V., Eich, D., et al. (2004). Obsessive-compulsive severity spectrum in the community: prevalence, comorbidity, and course. *Eur. Arch. Psychiatry Clin. Neurosci.* 254, 156–164. doi: 10.1007/s00406-004-0459-4

Aoyama, K., Suh, S. W., Hamby, A. M., Liu, J., Chan, W. Y., Chen, Y., et al. (2006). Neuronal glutathione deficiency and age-dependent neurodegeneration in the EAAC1 deficient mouse. *Nat. Neurosci.* 9, 119–126. doi: 10.1038/nn1609

Arnold, P. D., Sicard, T., Burroughs, E., Richter, M. A., and Kennedy, J. L. (2006). Glutamate transporter gene SLC1A1 associated with obsessive-compulsive disorder. *Arch. Gen. Psychiatry* 63, 769–776. doi: 10.1001/archpsyc.63.7.769

Asaoka, N., Nishitani, N., Kinoshita, H., Nagai, Y., Hatakama, H., Nagayasu, K., et al. (2019). An adenosine A_{2A} receptor antagonist improves multiple symptoms of repeated quinpirole-induced psychosis. *eNeuro* 6:ENEURO.0366-18.2019. doi: 10.1523/ENEURO.0366-18.2019

Bellini, S., Fleming, K. E., De, M., McCauley, J. P., Petroccione, M. A., D'Brant, L. Y., et al. (2018). Neuronal glutamate transporters control dopaminergic signaling and compulsive behaviors. *J. Neurosci.* 38, 937–961. doi: 10.1523/JNEUROSCI.1906-17.2017

Berman, A. E., Chan, W. Y., Brennan, A. M., Reyes, R. C., Adler, B. L., Suh, S. W., et al. (2011). N-acetylcysteine prevents loss of dopaminergic neurons in the EAAC1 -/- mouse. *Ann. Neurol.* 69, 509–520. doi: 10.1002/ana.22162

Berridge, K. C. (1989). Substantia nigra 6-OHDA lesions mimic striatopallidal disruption of syntactic grooming chains: a neural systems analysis of sequence control. *Psychobiology* 17, 377–385. doi: 10.3758/BF03337797

Berridge, K. C., Aldridge, J. W., Houchard, K. R., and Zhuang, X. (2005). Sequential super-stereotypy of an instinctive fixed action pattern in hyper-dopaminergic mutant mice: a model of obsessive compulsive disorder and Tourette's. *BMC Biol.* 3:4. doi: 10.1186/1741-7007-3-4

Bienvenu, O. J., Samuels, J. F., Wuyek, L. A., Liang, K. Y., Wang, Y., Grados, M. A., et al. (2012). Is obsessive–compulsive disorder an anxiety disorder, and what, if any, are spectrum conditions? A family study perspective. *Psychol. Med.* 42, 1–13. doi: 10.1017/S0033291711000742

Brodnik, Z. D., and España, R. A. (2015). Dopamine uptake dynamics are preserved under isoflurane anesthesia. *Neurosci. Lett.* 606, 129–134. doi: 10.1016/j.neulet.2015.08.046

Carlson, J. H., Bergstrom, D. A., and Walters, J. R. (1986). Neurophysiological evidence that D-1 dopamine receptor blockade attenuates postsynaptic but not

autoreceptor-mediated effects of dopamine agonists. *Eur. J. Pharmacol.* 123, 237–251. doi: 10.1016/0014-2999(86)90665-5

Chergui, K., Charléty, P. J., Akaoka, H., Saunier, C. F., Brunet, J. L., Buda, M., et al. (1993). Tonic activation of NMDA receptors causes spontaneous burst discharge of rat midbrain dopamine neurons in vivo. *Eur. J. Neurosci.* 5, 137–144. doi: 10.1111/j.1460-9568.1993.tb00479.x

Coco, S., Verderio, C., Trotti, D., Rothstein, J. D., Volterra, A., and Matteoli, M. (1997). Non-synaptic localization of the glutamate transporter EAAC1 in cultured hippocampal neurons. *Eur. J. Neurosci.* 9, 1902–1910. doi: 10.1111/j.1460-9568.1997.tb00757.x

Conti, F., DeBiasi, S., Minelli, A., Rothstein, J. D., and Melone, M. (1998). EAAC1, a high-affinity glutamate tranporter, is localized to astrocytes and gabaergic neurons besides pyramidal cells in the rat cerebral cortex. *Cereb. Cortex* 8, 108–116. doi: 10.1093/cercor/8.2.108

Cromwell, H. C., Berridge, K. C., Drago, J., and Levine, M. S. (1998). Action sequencing is impaired in D $_{1A}$ -deficient mutant mice. *Eur. J. Neurosci.* 10, 2426–2432. doi: 10.1046/j.1460-9568.1998.00250.x

De Haas, R., Nijdam, A., Westra, T. A., Kas, M. J. H., and Westenberg, H. G. M. (2011). Behavioral pattern analysis and dopamine release in quinpirole-induced repetitive behavior in rats. *J. Psychopharmacol.* 25, 1712–1719. doi: 10.1177/0269881110389093

Delgado-Acevedo, C., Estay, S. F., Radke, A. K., Sengupta, A., Escobar, A. P., Henríquez-Belmar, F., et al. (2019). Behavioral and synaptic alterations relevant to obsessive-compulsive disorder in mice with increased EAAT3 expression. *Neuropsychopharmacology* 44, 1163–1173. doi: 10.1038/s41386-018-0302-7

Denys, D., Van Der Wee, N., Janssen, J., De Geus, F., and Westenberg, H. G. M. (2004). Low level of dopaminergic D2 receptor binding in obsessive-compulsive disorder. *Biol. Psychiatry* 55, 1041–1045. doi: 10.1016/j.biopsych.2004.01.023

Dib, T., Martínez-Pinto, J., Reyes-Parada, M., Torres, G. E., and Sotomayor-Zárate, R. (2018). Neonatal programming with testosterone propionate reduces dopamine transporter expression in nucleus accumbens and methylphenidate-induced locomotor activity in adult female rats. *Behav. Brain Res.* 346, 80–85. doi: 10.1016/j.bbr.2017.12.001

Dickel, D. E., Veenstra-VanderWeele, J., Cox, N. J., Wu, X., Fischer, D. J., Van Etten-Lee, M., et al. (2006). Association testing of the positional and functional candidate gene SLC1A1/EAAC1 in early-onset obsessive-compulsive disorder. *Arch. Gen. Psychiatry* 63, 778–785. doi: 10.1001/archpsyc.63.7.778

Escobar, A. P., Cornejo, F. A., Olivares-Costa, M., González, M., Fuentealba, J. A., Gysling, K., et al. (2015). Reduced dopamine and glutamate neurotransmission in the nucleus accumbens of quinpirole-sensitized rats hints at inhibitory D2 autoreceptor function. *J. Neurochem.* 134, 1081–1090. doi: 10.1111/jnc.13209

Escobar, A. P., González, M. P., Meza, R. C., Noches, V., Henny, P., Gysling, K., et al. (2017). Mechanisms of kappa opioid receptor potentiation of dopamine D2 receptor function in quinpirole-induced locomotor sensitization in rats. *Int. J. Neuropsychopharmacol.* 20, 660–669. doi: 10.1093/ijnp/pyx042

Escobar, A. P., Wendland, J. R., Chávez, A. E., and Moya, P. R. (2019). The neuronal glutamate transporter EAAT3 in obsessive-compulsive disorder. *Front. Pharmacol.* 10:1362. doi: 10.3389/fphar.2019.01362

Espinosa, P., Silva, R. A., Sanguinetti, N. K., Venegas, F. C., Riquelme, R., Gonzalez, L. F., et al. (2016). Programming of dopaminergic neurons by neonatal sex hormone exposure: effects on dopamine content and tyrosine hydroxylase expression in adult male rats. *Neural Plast.* 2016:4569785. doi: 10.1155/2016/4569785

Galvan, A., Hu, X., Rommelfanger, K. S., Pare, J. F., Khan, Z. U., Smith, Y., et al. (2014). Localization and function of dopamine receptors in the subthalamic nucleus of normal and parkinsonian monkeys. *J. Neurophysiol.* 112, 467–479. doi: 10.1152/jn.00849.2013

González, L. F., Henríquez-Belmar, F., Delgado-Acevedo, C., Cisternas-Olmedo, M., Arriagada, G., Sotomayor-Zárate, R., et al. (2017). Neurochemical and behavioral characterization of neuronal glutamate transporter EAAT3 heterozygous mice. *Biol. Res.* 50:29. doi: 10.1186/s40659-017-0138-3

Grabe, H. J., Meyer, C., Hapke, U., Rumpf, H. J., Freyberger, H. J., Dilling, H., et al. (2000). Prevalence, quality of life and psychosocial function in obsessive-compulsive disorder and subclinical obsessive-compulsive disorder in northern Germany. *Eur. Arch. Psychiatry Clin. Neurosci.* 250, 262–268. doi: 10.1007/s004060070017

Grados, M. A., Specht, M. W., Sung, H.-M., and Fortune, D. (2013). Glutamate drugs and pharmacogenetics of OCD: a pathway-based exploratory approach. *Expert Opin. Drug Discov.* 8, 1515–1527. doi: 10.1517/17460441.2013.845553

Graham, M. D., Gardner Gregory, J., Hussain, D., Brake, W. G., and Pfaus, J. G. (2015). Ovarian steroids alter dopamine receptor populations in the medial preoptic area of female rats: implications for sexual motivation, desire, and behaviour. *Eur. J. Neurosci.* 42, 3138–3148. doi: 10.1111/ejn.13121

Hesse, S., Müller, U., Lincke, T., Barthel, H., Villmann, T., Angermeyer, M. C., et al. (2005). Serotonin and dopamine transporter imaging in patients with obsessive-compulsive disorder. *Psychiatry Res. Neuroimaging* 140, 63–72. doi: 10.1016/j.pscychresns.2005.07.002

Huang, Q., Zhou, D., Chase, K., Gusella, J. F., Aronin, N., and Difiglia, M. (1992). Immunohistochemical localization of the D1 dopamine receptor in rat brain reveals its axonal transport, pre- And postsynaptic localization, and prevalence in the basal ganglia, limbic system, and thalamic reticular nucleus. *Proc. Natl. Acad. Sci. U.S.A.* 89, 11988–11992. doi: 10.1073/pnas.89.24.11988

Jarzylo, L. A., and Man, H.-Y. (2012). Parasynaptic NMDA receptor signaling couples neuronal glutamate transporter function to AMPA receptor synaptic distribution and stability. *J. Neurosci.* 32, 2552–2563. doi: 10.1523/JNEUROSCI.3237-11.2012

Johnson, S. W., Seutin, V., and North, R. A. (1992). Burst firing in dopamine neurons induced by N-methyl-D-aspartate: role of electrogenic sodium pump. *Science* 258, 665–667. doi: 10.1126/science.1329209

Kalueff, A. V., Wayne Aldridge, J., Laporte, J. L., Murphy, D. L., and Tuohimaa, P. (2007). Analyzing grooming microstructure in neurobehavioral experiments. *Nat. Protoc.* 2, 2538–2544. doi: 10.1038/nprot.2007.367

Kang, J., and Kim, E. (2015). Suppression of NMDA receptor function in mice prenatally exposed to valproic acid improves social deficits and repetitive behaviors. *Front. Mol. Neurosci.* 8:17. doi: 10.3389/fnmol.2015.00017

Kim, J. W., Seung, H., Kim, K. C., Gonzales, E. L. T., Oh, H. A., Yang, S. M., et al. (2017). Agmatine rescues autistic behaviors in the valproic acid-induced animal model of autism. *Neuropharmacology* 113(Pt. A), 71–81. doi: 10.1016/j.neuropharm.2016.09.014

Koeltzow, T. E., Austin, J. D., and Vezina, P. (2003). Behavioral sensitization to quinpirole is not associated with increased nucleus accumbens dopamine overflow. *Neuropharmacology* 44, 102–110. doi: 10.1016/s0028-3908(02)00328-3

Kwiatkowski, M. A., Hellemann, G., Sugar, C. A., Cope, Z. A., Minassian, A., Perry, W., et al. (2019). Dopamine transporter knockdown mice in the behavioral pattern monitor: a robust, reproducible model for mania-relevant behaviors. *Pharmacol. Biochem. Behav.* 178, 42–50. doi: 10.1016/j.pbb.2017.12.007

Lacey, M. G., Mercuri, N. B., and North, R. A. (1987). Dopamine acts on D2 receptors to increase potassium conductance in neurones of the rat substantia nigra zona compacta. *J. Physiol.* 392, 397–416. doi: 10.1113/jphysiol.1987.sp016787

Li, M. H., Underhill, S. M., Reed, C., Phillips, T. J., Amara, S. G., and Ingram, S. L. (2017). Amphetamine and methamphetamine increase NMDAR-GluN2B synaptic currents in midbrain dopamine neurons. *Neuropsychopharmacology* 42, 1539–1547. doi: 10.1038/npp.2016.278

Lohani, S., Martig, A. K., Underhill, S. M., DeFrancesco, A., Roberts, M. J., Rinaman, L., et al. (2018). Burst activation of dopamine neurons produces prolonged post-burst availability of actively released dopamine. *Neuropsychopharmacology* 43, 2083–2092. doi: 10.1038/s41386-018-0088-7

Moresco, R. M., Pietra, L., Henin, M., Panzacchi, A., Locatelli, M., Bonaldi, L., et al. (2007). Fluvoxamine treatment and D2 receptors: a pet study on OCD drug-naïve patients. *Neuropsychopharmacology* 32, 197–205. doi: 10.1038/sj.npp.1301199

Muehlmann, A. M., Maletz, S., King, M. A., and Lewis, M. H. (2020). Pharmacological targeting of striatal indirect pathway neurons improves subthalamic nucleus dysfunction and reduces repetitive behaviors in C58 mice. *Behav. Brain Res.* 391:112708. doi: 10.1016/j.bbr.2020.112708

Napier, T. C., Givens, B. S., Schulz, D. W., Bunney, B. S., Breese, G. R., and Mailman, R. B. (1986). SCH23390 effects on apomorphine-induced responses of nigral dopaminergic neurons. *J. Pharmacol. Exp. Ther.* 236, 838–845.

O'Hara, C. M., Uhland-Smith, A., O'Malley, K. L., and Todd, R. D. (1996). Inhibition of dopamine synthesis by dopamine D2 and D3 but not D4 receptors. *J. Pharmacol. Exp. Ther.* 277, 186–192.

Pearlstein, E., Gouty-Colomer, L.-A., Michel, F. J., Cloarec, R., and Hammond, C. (2015). Glutamatergic synaptic currents of nigral dopaminergic neurons follow a postnatal developmental sequence. *Front. Cell. Neurosci.* 9:210. doi: 10.3389/fncel.2015.00210

Pelosi, A., Girault, J. A., and Hervé, D. (2015). Unilateral lesion of dopamine neurons induces grooming asymmetry in the mouse. *PLoS One* 10:e0137185. doi: 10.1371/journal.pone.0137185

Perreault, M. L., Seeman, P., and Szechtman, H. (2007). Kappa-opioid receptor stimulation quickens pathogenesis of compulsive checking in the quinpirole sensitization model of obsessive-compulsive disorder (OCD). *Behav. Neurosci.* 121, 976–991. doi: 10.1037/0735-7044.121.5.976

Pierce, R. C., and Kalivas, P. W. (1997). A circuitry model of the expression of behavioral sensitization to amphetamine-like psychostimulants. *Brain Res. Brain Res. Rev.* 25, 192–216. doi: 10.1016/s0165-0173(97)00021-0

Plaitakis, A., and Shashidharan, P. (2000). Glutamate transport and metabolism in dopaminergic neurons of substantia nigra: implications for the pathogenesis of Parkinson& apos disease. *J. Neurol.* 247(Suppl. 2), II25–II35. doi: 10.1007/PL00007757

Robbins, T. W., Vaghi, M. M., and Banca, P. (2019). Obsessive-compulsive disorder: puzzles and prospects. *Neuron* 102, 27–47. doi: 10.1016/j.neuron.2019.01.046

Sabeti, J., Gerhardt, G. A., and Zahniser, N. R. (2003). Chloral hydrate and ethanol, but not urethane, alter the clearance of exogenous dopamine recorded by chronoamperometry in striatum of unrestrained rats. *Neurosci. Lett.* 343, 9–12. doi: 10.1016/S0304-3940(03)00301-X

Saxena, S., and Rauch, S. L. (2000). Functional neuroimaging and the neuroanatomy of obsessive-compulsive disorder. *Psychiatric Clin. North Am.* 23, 563–586. doi: 10.1016/s0193-953x(05)70181-7

Saxena, S., Bota, R. G., and Brody, A. (2001). Brain-behavior relationships in obsessive-compulsive disorder. *Semin. Clin. Neuropsychiatry* 6, 82–101. doi: 10.1053/scnp.2001.21833

Scimemi, A., Tian, H., and Diamond, J. S. (2009). Neuronal transporters regulate glutamate clearance, NMDA receptor activation, and synaptic plasticity in the hippocampus. *J. Neurosci.* 29, 14581–14595. doi: 10.1523/JNEUROSCI.4845-09.2009

Sesack, S. R., Aoki, C., and Pickel, V. M. (1994). Ultrastructural localization of D2 receptor-like immunoreactivity in midbrain dopamine neurons and their striatal targets. *J. Neurosci.* 14, 88–106. doi: 10.1523/jneurosci.14-01-00088.1994

Sidiropoulou, K., Chao, S., Lu, W., and Wolf, M. E. (2001). Amphetamine administration does not alter protein levels of the GLT-1 and EAAC1 glutamate transporter subtypes in rat midbrain, nucleus accumbens, striatum, or prefrontal cortex. *Brain Res. Mol. Brain Res.* 90, 187–192. doi: 10.1016/s0169-328x(01)00110-3

Sun, T., Song, Z., Tian, Y., Tian, W., Zhu, C., Ji, G., et al. (2019). Basolateral amygdala input to the medial prefrontal cortex controls obsessive-compulsive disorder-like checking behavior. *Proc. Natl. Acad. Sci. U.S.A.* 116, 3799–3804. doi: 10.1073/pnas.1814292116

Szechtman, H., Ahmari, S. E., Beninger, R. J., Eilam, D., Harvey, B. H., Edemann-Callesen, H., et al. (2017). Obsessive-compulsive disorder: insights from animal models. *Neurosci. Biobehav. Rev.* 76, 254–279. doi: 10.1016/j.neubiorev.2016.04.019

Szechtman, H., Sulis, W., and Eilam, D. (1998). Quinpirole induces compulsive checking behavior in rats: a potential animal model of obsessive-compulsive disorder (OCD). *Behav. Neurosci.* 112, 1475–1485. doi: 10.1037/0735-7044.112.6.1475

Tanimura, Y., Vaziri, S., and Lewis, M. H. (2010). Indirect basal ganglia pathway mediation of repetitive behavior: attenuation by adenosine receptor agonists. *Behav. Brain Res.* 210, 116–122. doi: 10.1016/j.bbr.2010.02.030

Underhill, S. M., Colt, M. S., and Amara, S. G. (2020). Amphetamine stimulates endocytosis of the norepinephrine and neuronal glutamate transporters in cultured locus coeruleus neurons. *Neurochem. Res.* 45, 1410–1419. doi: 10.1007/s11064-019-02939-6

Underhill, S. M., Hullihen, P. D., Chen, J., Fenollar-Ferrer, C., Rizzo, M. A., Ingram, S. L., et al. (2021). Amphetamines signal through intracellular TAAR1 receptors coupled to Gα13 and GαS in discrete subcellular domains. *Mol. Psychiatry* 26, 1208–1223. doi: 10.1038/s41380-019-0469-2

Underhill, S. M., Wheeler, D. S., Li, M., Watts, S. D., Ingram, S. L., and Amara, S. G. (2014). Amphetamine modulates excitatory neurotransmission through endocytosis of the glutamate transporter EAAT3 in dopamine neurons. *Neuron* 83, 404–416. doi: 10.1016/j.neuron.2014.05.043

Usiello, A., Baik, J.-H., Rougé-Pont, F., Picetti, R., Dierich, A., LeMeur, M., et al. (2000). Distinct functions of the two isoforms of dopamine D2 receptors. *Nature* 408, 199–203. doi: 10.1038/35041572

Wang, X., Zhang, C., Szábo, G., and Sun, Q. Q. (2013). Distribution of CaMKIIα expression in the brain in vivo, studied by CaMKIIα-GFP mice. *Brain Res.* 1518, 9–25. doi: 10.1016/j.brainres.2013.04.042

Wendland, J. R., Moya, P. R., Timpano, K. R., Anavitarte, A. P., Kruse, M. R., Wheaton, M. G., et al. (2009). A haplotype containing quantitative trait loci for SLC1A1 gene expression and its association with obsessive-compulsive disorder. *Arch. Gen. Psychiatry* 66:408. doi: 10.1001/archgenpsychiatry.2009.6

Wu, H., Wang, X., Yu, S., Wang, D., Chen, J., Jiang, K., et al. (2013). Association of the candidate gene SLC1A1 and obsessive–compulsive disorder in Han ChinesePopulation. *Psychiatry Res.* 209, 737–739. doi: 10.1016/j.psychres.2012.12.016

Zike, I. D., Chohan, M. O., Kopelman, J. M., Krasnow, E. N., Flicker, D., Nautiyal, K. M., et al. (2017). OCD candidate gene SLC1A1 /EAAT3 impacts basal ganglia-mediated activity and stereotypic behavior. *Proc. Natl. Acad. Sci. U.S.A.* 114, 5719–5724. doi: 10.1073/pnas.1701736114

Conflict of Interest: The authors declare that the research was conducted in the absence of any commercial or financial relationships that could be construed as a potential conflict of interest.

frontiers in Cellular Neuroscience

ORIGINAL RESEARCH
published: 12 July 2021
doi: 10.3389/fncel.2021.682460

A Computational Study of Astrocytic GABA Release at the Glutamatergic Synapse: EAAT-2 and GAT-3 Coupled Dynamics

Bronac Flanagan, Liam McDaid, John Joseph Wade, Marinus Toman, KongFatt Wong-Lin and Jim Harkin*

Intelligent Systems Research Centre, Ulster University, Derry, United Kingdom

OPEN ACCESS

Edited by:
Annalisa Scimemi, University at Albany, United States

Reviewed by:
Maurizio De Pittà, Basque Center for Applied Mathematics, Spain
Leonid Savtchenko, University College London, United Kingdom

***Correspondence:**
Bronac Flanagan
b.flanagan@ulster.ac.uk

Specialty section:
This article was submitted to Non-Neuronal Cells, a section of the journal Frontiers in Cellular Neuroscience

Received: *18 March 2021*
Accepted: *15 June 2021*
Published: *12 July 2021*

Citation:
Flanagan B, McDaid L, Wade JJ, Toman M, Wong-Lin K and Harkin J (2021) A Computational Study of Astrocytic GABA Release at the Glutamatergic Synapse: EAAT-2 and GAT-3 Coupled Dynamics. Front. Cell. Neurosci. 15:682460. doi: 10.3389/fncel.2021.682460

Neurotransmitter dynamics within neuronal synapses can be controlled by astrocytes and reflect key contributors to neuronal activity. In particular, Glutamate (Glu) released by activated neurons is predominantly removed from the synaptic space by perisynaptic astrocytic transporters EAAT-2 (GLT-1). In previous work, we showed that the time course of Glu transport is affected by ionic concentration gradients either side of the astrocytic membrane and has the propensity for influencing postsynaptic neuronal excitability. Experimental findings co-localize GABA transporters GAT-3 with EAAT-2 on the perisynaptic astrocytic membrane. While these transporters are unlikely to facilitate the uptake of synaptic GABA, this paper presents simulation results which demonstrate the coupling of EAAT-2 and GAT-3, giving rise to the ionic-dependent reversed transport of GAT-3. The resulting efflux of GABA from the astrocyte to the synaptic space reflects an important astrocytic mechanism for modulation of hyperexcitability. Key results also illustrate an astrocytic-mediated modulation of synaptic neuronal excitation by released GABA at the glutamatergic synapse.

Keywords: astrocyte, sodium-signaling, neurotransmission, synapse, glutamate, GABA

INTRODUCTION

Glutamate (Glu) and γ-aminobutyric acid (GABA) are the brain's most prevalent excitatory and inhibitory neurotransmitters, respectively (Petroff, 2002). Exposure of neurons expressing appropriate excitatory ionotropic receptors, including *N*-methyl-D-aspartate receptors (NMDA-Rs) and α-amino-3-hydroxy-5-methyl-4-isoxazolepropionic acid receptors (AMPA-Rs), to Glu can result in an influx of cations elevating the neuronal membrane potential toward the firing threshold (Meldrum, 2000). Conversely, the exposure of neurons expressing GABA ionotropic receptors ($GABA_A$-Rs) to GABA can result in a hyperpolarising current, decreasing the neuronal membrane potential away from the firing threshold (Sigel and Steinmann, 2012). As the metabolism

of Glu and GABA is an intracellular process, these neurotransmitters must be rapidly removed from the extracellular space (ECS) by their corresponding transporters, to avoid the over-exposure of the agonist to the excitatory and inhibitory ionotropic receptors (Petroff, 2002). Broadly speaking on a network level, a balance between excitation and inhibition is necessary for normal brain activity (Fellin et al., 2006). Moreover, imbalance of excitatory/inhibitory transmission is believed to underlie such conditions as epilepsy (Clasadonte and Haydon, 2012; Coulter and Steinhäuser, 2015), autism spectrum disorders (Pizzarelli and Cherubini, 2011), schizophrenia (Coyle, 2004) and Alzheimer's disease (Robinson, 2000). In particular, studies have indicated altered Glu and GABA concentrations within focal seizure sites (During and Spencer, 1993; Petroff, 2002), favoring excitatory neuronal behavior over inhibition.

In previous work (Flanagan et al., 2018) the effects of synaptic glutamatergic dynamics on postsynaptic firing were explored, where it was found that an increased astrocytic Glu content was sufficient to slow synaptic Glu clearance due to reduced driving force across the excitatory amino-acid transporter 2 (EAAT-2, homologue of GLT-1). Altered sodium (Na^+) and calcium (Ca^{2+}) dynamics within the astrocyte were also found and are attributed to variations in the EAAT-2 currents.

A strong extracellular-to-intracellular Na^+ concentration gradient is imperative for a range of homeostatic functions, including neurotransmitter transport (Kirischuk et al., 2012; Verkhratsky and Nedergaard, 2018). The influx of Glu across the astrocytic membrane, against a large ($\sim 10^6$ times) concentration gradient, by EAAT-2 requires the concerted transport of $3Na^+$ and $1H^+$ and counter-transport of $1K^+$ for each Glu ion (Zerangue and Kavanaugh, 1996). Due to its Na^+-dependence, the reversal potential of the EAAT-2 lies well above the astrocytic resting membrane potential of ~ -80 mV (Verkhratsky and Nedergaard, 2018), ensuring the astrocytic influx of Glu upon synaptic Glu release.

In contrast, the reversal potential of GABA transporter type-3 (GAT-3) approximates to the astrocytic membrane potential and is also dependent on co-transport substrate (Na^+ and Cl^-) concentrations at equilibrium. Where the clearance of synaptic-released Glu appears as a predominantly astrocytic function (Danbolt, 2001), synaptic-released GABA is mostly retaken by the releasing neuron and subsequently recycled into vesicles (Hertz et al., 1999; Schousboe et al., 2014). As the GABA concentration in the ECS close to the astrocyte would be unlikely to increase based on this synaptic self-recovery of neurotransmitter, the direction of GABA transport by GAT-3 transporter is highly sensitive to fluctuations in astrocytic and extracellular ionic concentrations. In other words, the development of an astrocytic [Na^+] microdomain (Breslin et al., 2018) may be sufficient to prompt the release of GABA into the ECS by disturbing the electrochemical potential of the transporter and eliciting an efflux of transporter substrates from the astrocyte. In particular, EAAT-2 activation has been observed experimentally to initiate the GAT-3-mediated release of GABA (Héja et al., 2012), believed to modulate tonic neuronal inhibition through the action of $GABA_A$-Rs (Rossi et al., 2003; Farrant and Nusser, 2005; Héja et al., 2012). Considering this observation, the co-localization of the major Glu and GABA transporters, EAAT-2 and GAT-3, respectively, on the astrocytic membrane (Minelli et al., 1996; Héja et al., 2012; Kirischuk et al., 2012) may indicate a finely balanced excitatory-inhibitory mechanism: the uptake of Glu coupled to the astrocytic release of cytoplasmic GABA (Héja et al., 2012).

Traditionally, the classification of neuronal synapses was determined by the presynaptic neuron-released neurotransmitter (O'Rourke et al., 2012), for example, the presynaptic neuron of a glutamatergic synapse would release Glu by activity-induced exocytosis (Kandel et al., 2012). Consequently, computational models of neuron-astrocyte synapses consider neuronal and astrocytic activity as a function of neuronal-released neurotransmitter (Bentzen et al., 2009; Allam et al., 2012; Tewari and Majumdar, 2012; Li et al., 2016; Hübel et al., 2017). The neurotransmitter almost exclusively modeled at the tripartite synapse is Glu (Manninen et al., 2018), and the possibility of a secondary neurotransmitter at the same synapse has hitherto been ignored. The significance and novelty of this paper lies in the fact that it explores the astrocyte-mediated symbiosis of two neurotransmitters, Glu and GABA, at the glutamatergic synapse with a view to creating a more complete view of ionic dynamics at the tripartite synapses.

Furthermore, this paper considers the electrochemical potentials of both EAAT-2 and GAT-3 proteins with a view to (a) explain experimentally observed phenomena, (b) explore the effectiveness of this balance where astrocytic Glu concentrations are elevated and (c) predict the effects of this balance for postsynaptic neuron activity.

MATERIALS AND METHODS

To consider the effects of synaptic neurotransmitter fluxes, namely the presynaptic and postsynaptic neuronal synaptic-driven dynamics, the model in **Figure 1** was considered. The model extends a previously developed framework (Flanagan et al., 2018) to characterize tripartite synapse signaling, to include GABAergic signaling as well. A pulsed depolarizing current of 5 $\mu A/cm^2$ was applied for 50 s to the presynaptic neuronal membrane, generating a presynaptic neuronal 10 Hz firing rate. Consideration was also given to the influence of astrocytic Glu content, in line with previous simulation (Flanagan et al., 2018), specifically in the transport of Glu across the astrocytic membrane. To achieve this, the basal astrocytic [Glu] of 1.5 mM and 5 mM were chosen to represent the bounds of the physiological range (Attwell et al., 1993) and the basal astrocytic [Glu] of 10 mM hypothesized pathological state (Flanagan et al., 2018), following glutamine synthetase downregulation (Eid et al., 2008; Perez et al., 2012). At each neuronal spike, Glu and K^+ were released from the presynaptic neuron into the synaptic cleft. The model was also simulated with the exclusion of GAT-3 to act as a control in determining the role of EAAT-2-induced GAT-3 transport at the neuronal synapse. The key ions considered were Na^+, K^+, Glu, Ca^{2+} and GABA.

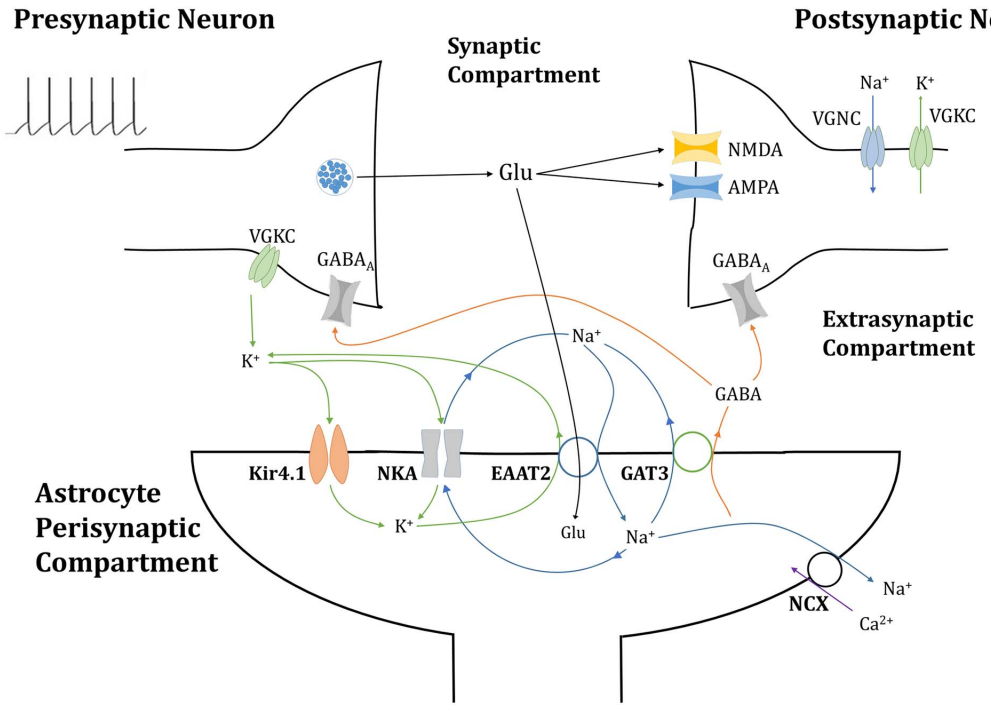

FIGURE 1 | Tripartite glutamatergic synapse compartment model: consisting of neuronal, synaptic, and astrocytic compartments, within which ionic concentrations are dynamic and neuronal membrane currents respond to neurotransmitter-mediated ionotropic currents (not to scale). Glutamate (Glu) neurotransmitter is released into the synapse by the presynaptic neuron in a membrane potential-dependent mechanism, where it activates neurotransmitter-gated ionotropic receptors NMDA and AMPA channels located on the postsynaptic neuron. This postsynaptic membrane activity triggers the activation of voltage-gated sodium (Na^+) and potassium (K^+) channels (VGNC and VGKC, respectively), also located on the postsynaptic neuronal membrane. Synaptic Glu is exclusively taken up by astrocytic membrane-bound excitatory amino acid transporter 2 (EAAT2), along with synaptic Na^+ and the counter-transport of astrocytic K^+. The influx of Na^+ into the astrocytic compartment triggers the release of GABA (and Na^+) through GABA transporter type 3 (GAT3), into the synaptic compartment, where it activated inhibitory ionotropic $GABA_A$ receptors located both on the pre- and postsynaptic neuronal membranes. Synaptic K^+ transport is completed with the inclusion of inwardly rectifying K^+ channels (Kir4.1) and the Na^+/K^+ ATPase transporter (NKA). Na^+ dynamics are completed by the NKA and reversible Na^+/Ca^{2+} exchanger (NCX).

Presynaptic Membrane and Neurotransmitter Dynamics

The presynaptic neuron is modeled using a Hodgkin-Huxley-based (Hodgkin and Huxley, 1952; Golomb et al., 2006) description for voltage-gated Na^+ and K^+ dynamics. The presynaptic membrane potential uses the formalism.

$$C_M \frac{dV_{m,pre}}{dt} = -(I_{Na,Preneuron} + I_{K,Preneuron} + I_{L,Preneuron} + I_{PreGABAA} + I_{app}) \quad (1)$$

where $I_{Na,Preneuron}$, $I_{K,Preneuron}$ and $I_{L,Preneuron}$ reflect voltage-gated Na^+, K^+ and leak presynaptic currents, respectively, and are described in **Table 1** with parameters enumerated in **Table 2**. $I_{PreGABAA}$ is the $GABA_A$ mediated current in response to synaptic astrocyte-released GABA, see below, and I_{app} is an applied stimulus.

To improve upon previous work (Flanagan et al., 2018), a more realistic description of synaptic resources was accounted for to preserve biological realism. To this end, the model adopts the Tsodyks-Markram model (Tsodyks et al., 1998) description for the use of synaptic resources within a facilitating synapse, so that any alteration of the neuronal activity would be directly influenced by the GABA-induced inhibition rather than the nature of the synapse model. This model describes the fraction of recovered resources (x), active resources (y) and inactive resources (z) using the model scheme

$$\frac{dx}{dt} = \frac{z}{\tau_r} - Ux\delta\left(t - t_{sp}\right) \quad (2)$$

$$\frac{dy}{dt} = -\frac{y}{\tau_i} + Ux\delta\left(t - t_{sp}\right) \quad (3)$$

$$\frac{dz}{dt} = \frac{y}{\tau_i} - \frac{z}{\tau_r} \quad (4)$$

using parameters detailed in **Table 3**.

In this model the amount of Glu released by the presynaptic neuron is proposed to be proportional to the fraction of active resources (Eq. 3) is scaled by constant parameter of 0.1 mM, chosen to sufficiently perturb the system under all cases, namely to excite the postsynaptic membrane to its firing threshold. At each presynaptic neuronal spike, Glu is released by the presynaptic neuron into the synaptic compartment, along with a small amount of K^+ representing the input to the system.

TABLE 1 | Neuron membrane dynamics.

Membrane currents	Description	Equation(s)	Source
$I_{Na,neuron}$	Voltage-gated Na^+ current	$I_{Na,neuron} = g_{Na,neuron} m_\infty^3 h\,(V_m - E_{Na})$ $E_{Na} = \frac{RT}{F}\ln\left(\frac{Na_{syn}}{Na_{neuron}}\right)$ $m_\infty = \left(1 + e^{\left(-\frac{V_m-(-30)}{9.5}\right)}\right)^{-1}$ $\frac{dh}{dt} = \frac{h_\infty - h}{\tau_h}$ $\tau_h = \left(0.1 + \frac{0.75}{1 + e^{\left(-\frac{V_m-(-40.5)}{-6}\right)}}\right)$ $h_\infty = \left(1 + e^{\left(-\frac{V_m-(-45)}{-7}\right)}\right)^{-1}$	Golomb et al., 2006
$I_{K,neuron}$	Voltage-gated K^+ current	$I_{K,neuron} = g_{k,neuron} n^4\,(V_m - E_K)$ $E_K = \frac{RT}{F}\ln\left(\frac{K_{syn}}{K_{neuron}}\right)$ $\frac{dn}{dt} = \frac{n_\infty - n}{\tau_n}$ $\tau_n = 0.1 + \frac{0.5}{1 + e^{\left(-\frac{V_m-(-27)}{-15}\right)}}$ $n_\infty = \left(1 + e^{-\frac{V_m-(-35)}{10}}\right)^{-1}$	Golomb et al., 2006
$I_{L,N}$	Membrane leak current	$I_{L,N} = g_L\,(V_m - E_L)$	Golomb et al., 2006
I_{NMDA}	NMDA-mediated current	$I_{NMDA} = g_{NMDA} r_{NMDA}\,(V_m - E_{NMDA})\,Mg_V$ $\frac{dr_{NMDA}}{dt} = \alpha_{NMDA}\,[Glu]\,(1 - r_{NMDA}) - \beta_{NMDA} r_{NMDA}$ $Mg_V = \left(1 + e^{\frac{-0.062 V_m MG}{3.57}}\right)^{-1}$	Destexhe et al., 1998
I_{AMPA}	AMPA-mediated current	$I_{AMPA} = g_{AMPA} r_{AMPA}\,(V_m - E_{AMPA})$ $\frac{dr_{AMPA}}{dt} = \alpha_{AMPA}\,[Glu]\,(1 - r_{AMPA}) - \beta_{AMPA} r_{AMPA}$	Destexhe et al., 1998
I_{GABAA}	$GABA_A$-mediated current	$I_{GABAA} = g_{GABAA} r_{GABAA}\,(V_m - E_{GABAA})$ $\frac{dr_{GABAA}}{dt} = \alpha_{GABAA}\,[GABA]\,(1 - r_{GABAA}) - \beta_{GABAA} r_{GABAA}$	Destexhe et al., 1998

Astrocytic Membrane Dynamics

Astrocytic membrane ionic currents, subject to changes in ionic concentrations (Glu, K^+, Na^+, Ca^{2+} and GABA), are then calculated using the following equations

$$I_{Na,ast} = 1.5I_{EAAT} + 3I_{NKA} + 3I_{NCX} + 2I_{GAT} + I_{Na,L} \quad (5)$$

$$I_{K,ast} = -0.5I_{EAAT} + 2I_{NKA} + I_{Kir} + I_{K,L} \quad (6)$$

$$I_{Glu,ast} = -0.5I_{EAAT} + I_{Glu,L} \quad (7)$$

$$I_{Ca,ast} = -2I_{NCX} + I_{Ca,L} \quad (8)$$

$$I_{GABA,ast} = I_{GAT} \quad (9)$$

within this scheme I_{EAAT}, I_{NKA}, I_{NCX}, I_{GAT} and I_{Kir} denote EAAT-2, NKA, Na^+-Ca^{2+} exchanger (NCX), GAT-3 and inwardly rectifying K^+ channel ($Kir_{4.1}$) generated currents, respectively. The inclusion of Na^+, K^+, Glu, and Ca^{2+} leak currents, denoted $I_{Na,L}$, $I_{K,L}$, $I_{Glu,L}$, and $I_{CaL,\,L}$ respectively, provide model stability. Each transport current is calculated using the existing concentration of its corresponding substrate(s), the equations of which are found in **Table 4** and parameters used in the model are contained in **Table 5**. To study the effects of these currents on concentrations alone, the membrane potential of the astrocyte is set to be constant.

Currents are converted to ionic fluxes by Faraday's law, where the change in the astrocytic concentration of ion X is given by

$$\frac{dX_{ast}}{dt} = -\frac{I_{X,ast}}{zF} S_A Vol_A$$
$$\{X = Na^+, K^+, Glu, Ca^{2+}, GABA\} \quad (10)$$

and corresponding change in synaptic concentration given by

$$\frac{dX_{syn}}{dt} = \frac{I_{X,ast}}{zF} S_A Vol_S$$
$$\{X = Na^+, K^+, Glu, Ca^{2+}, GABA\} \quad (11)$$

using the surface area of the peri-synaptic astrocytic membrane (S_A) and volume of astrocyte (Vol_A) and synaptic compartments (Vol_S) as parameters.

Postsynaptic Membrane Dynamics

Synaptic Glu and GABA concentrations are also used to calculated local postsynaptic neuronal membrane dynamics, the neurotransmitters activating corresponding receptors on the postsynaptic terminal, the equations for which are found in **Table 1** and the parameters used in **Table 2**.

The localized effect of these neurotransmitter-driven currents on the postsynaptic neuron are also calculated using a Hodgkin-Huxley-based (Hodgkin and Huxley, 1952; Golomb et al., 2006) description, with the change in the postsynaptic neuron membrane potential (V_m) is thus calculated as the (negative) sum

TABLE 2 | Neuronal membrane model parameters.

Parameter	Description	Value	Units	Source
Vn_{eq}	Resting postsynaptic neuron membrane potential	−71	*mV*	Calculated at equilibrium values
g_{Nan}	Neuronal voltage-gated Na^+ channel conductance	35	$mScm^{-2}$	Hodgkin and Huxley, 1952
g_{kDr}	Neuronal voltage-gated K^+ channel conductance	6	$mScm^{-2}$	Hodgkin and Huxley, 1952
C_m	Neuron capacitance	1	μFcm^{-2}	Hodgkin and Huxley, 1952
g_L	Neuronal leak channel conductance	0.0112	$mScm^{-2}$	Hodgkin and Huxley, 1952
E_L	Neuron leak conductance	−74.6	*mV*	Calculated
g_{NMDA}	Synaptic NMDA-R maximal conductance	0.026	$mScm^{-2}$	Destexhe et al., 1998
g_{AMPA}	Synaptic AMPA-R maximal conductance	0.0145	$mScm^{-2}$	Destexhe et al., 1998
g_{GABAA}	Synaptic GABAA-R maximal conductance	0.0145	$mScm^{-2}$	Destexhe et al., 1998
E_{GABAA}	$GABA_A$ reversal potential	−85	*mV*	Destexhe et al., 1998
E_{AMPA}	AMPA reversal potential	0	*mV*	Destexhe et al., 1998
E_{NMDA}	$GABA_A$ reversal potential	0	*mV*	Destexhe et al., 1998
α_{GABAA}	$GABA_A$ forward rate constant	5×10^2	$M^{-1}msec^{-1}$	Destexhe et al., 1998
α_{AMPA}	AMPA forward rate constant	1.1×10^3	$M^{-1}msec^{-1}$	Destexhe et al., 1998
α_{NMDA}	NMDA forward rate constant	72	$M^{-1}msec^{-1}$	Destexhe et al., 1998
β_{GABAA}	$GABA_A$ backward rate constant	0.72	$msec^{-1}$	Destexhe et al., 1998
β_{AMPA}	AMPA backward rate constant	0.190	$msec^{-1}$	Destexhe et al., 1998
β_{NMDA}	NMDA backward rate constant	6.6×10^{-3}	$msec^{-1}$	Destexhe et al., 1998

TABLE 3 | Presynaptic resource model parameters.

Parameter	Description	Value	Units	Source
τ_i	Synaptic inactivity time constant	0.003	*sec*	Tsodyks et al., 1998
τ_r	Synaptic recovery time constant	0.800	*sec*	Tsodyks et al., 1998
U	Synaptic efficacy utilization fraction	0.5	∼	Tsodyks et al., 1998

of intrinsic voltage-gated Na^+ and K^+ currents, a leak current and synaptic NMDA, AMPA and $GABA_A$ mediated currents (Destexhe et al., 1998) as given by

$$C_M \frac{dV_m}{dt} = -\left(I_{Na,neuron} + I_{K,neuron} + I_{L,neuron} + I_{NMDA} + I_{AMPA} + I_{GABAA}\right). \quad (12)$$

Model Simulation

The simulation uses the forward Euler numerical integration scheme with 0.01 ms time step using MATLAB R2017b. Each time step of the model was considered in three separate settings, where only the initial astrocytic Glu concentration differs, i.e., $[Glu]_{ast,eq}$ = 1.5, 5, and 10 mM and leak conductances are adjusted accordingly so that equilibrium conditions are met initially.

RESULTS

Results are split into two sections: the first considers the resulting ionic changes due to the simulation while the second considers the effects of the neurotransmitter dynamics on the pre- and postsynaptic neuronal membrane. As astrocytes are considered the main controller of ionic homeostasis, this model only considers changes in ionic concentrations due to astrocytic membrane-mediated currents.

Astrocyte-Mediated Neurotransmitter and Ionic Dynamics

EAAT Activation Leads to Increase of Astrocytic $[Na^+]$

In agreement with previously reported findings (Breslin et al., 2018; Flanagan et al., 2018), the activation of EAAT-2 transporter by neuronal-released Glu was sufficient to generate an astrocytic influx of Na^+ within the model containing GAT-3 (**Figure 2A**). This resulted in a decrease in synaptic $[Na^+]$ (**Figure 2A.i**) and a corresponding increase in astrocytic $[Na^+]$ (**Figure 2A.ii**). The simulation was repeated without GAT-3, as a control, and found similar, yet exaggerated results (**Figures 2B.i,ii**). This is expected from the dual effect of decreased EAAT-2-mediated influx, resulting from reduced presynaptic neuronal activity, and the Na^+-dependent efflux of Na^+ through GAT-3. $[K^+]$ increased in the synaptic compartment (**Figures 2A.iii,B.iii**) with neuronal activity and correspondingly decreased in the astrocytic compartment (**Figures 2A.iv,B.iv**). Considering this inverse behavior between intracellular and extracellular concentration change, these results suggest that the astrocytic efflux of K^+ by EAAT-2 dominates over the influx of K^+ by the Na^+/K^+ ATPase (NKA), with a net increase of $[K^+]$ in the cleft. However, the rate of change of $[K^+]$ in both compartments was higher where the model did not include GAT-3 (**Figures 2B.iii,iv**) because the NKA is sensitive to astrocytic $[Na^+]$ and therefore in the absence of GAT-3 a heightened NKA activity results. This generated a more pronounced change in $[K^+]$ in both compartments. Due to the fact this is not a closed system, as K^+ has been injected due to the presynaptic activity, the concentration levels do not return to baseline following the simulation.

EAAT-Mediated $[Na_{ast}]$ Increase Is Sufficient to Reverse GAT-3

The reversal potential of GAT-3 (E_{GAT}) is heavily dependent on the $[Na^+]$ gradient across the astrocytic membrane and, at equilibrium conditions, is close to parity with the astrocytic

TABLE 4 | Astrocyte membrane transporter equations.

Membrane current	Equation(s)	Source
I_{Kir}	$I_{Kir} = g_{kir} * \sqrt{K_{syn}} * (V_a - E_K)$;	Witthoft et al., 2013
I_{NKCC}	$I_{NKCC} = I_{NKCC,max}\, log\left(\left(\frac{Na_{syn}}{Na_{ast}}\right)\left(\frac{K_{syn}}{K_{ast}}\right)\left(\frac{Cl_{syn}}{Cl_{ast}}\right)^2\right)$	Witthoft et al., 2013
I_{NCX}	$I_{NCX} = I_{NCXmax}\left(\left(\frac{Na_{ast}}{Na_{syn}}\right)^3 e^{\frac{\gamma F V_a}{RT}} - \left(\frac{Ca_{ast}}{Ca_{syn}}\right) e^{\frac{(\gamma-1)F V_a}{RT}}\right)$	Schutter and Smolen, 1998
I_{EAAT}	$I_{EAAT} = -\alpha_{EAAT} \cdot e^{-\beta_{EAAT}(V_a - E_{EAAT})}$	
	$E_{EAAT} = \frac{RT}{2F} ln\left(\left(\frac{Na_{syn}}{Na_{ast}}\right)^3 \left(\frac{H_{syn}}{H_{ast}}\right)\left(\frac{Glu_{syn}}{Glu_{ast}}\right)\left(\frac{K_{ast}}{K_{syn}}\right)\right)$	Flanagan et al., 2018
I_{NKA}	$I_{NKA} = I_{NKAmax}\left(\frac{Na_{ast}^{1.5}}{Na_{ast}^{1.5} + K_{Nai}^{1.5}}\right)\left(\frac{K_{syn}}{K_{syn} + K_{Ke}}\right)$	Halnes et al., 2013
I_{GAT}	$I_{GAT} = g_{gat}\,(V\_a - E_{GAT})$;	
	$E_{GAT} = \frac{RT}{F} ln\left(\left(\frac{Na_{syn}}{Na_{ast}}\right)^2 \left(\frac{GABA_{syn}}{GABA_{ast}}\right)\left(\frac{Cl_{syn}}{Cl_{ast}}\right)\right)$	Adapted from Verkhratsky and Nedergaard (2018)
$I_{X,L}$	$I_{X,L} = g_X (V_a - E_X)$	
	$E_X = \frac{RT}{z_X F} ln\left(\frac{X_{out}}{X_{in}}\right) for X = Na_{ast}, K_{ast}, Glu_{ast}, Ca_{ast}$	

TABLE 5 | Astrocytic membrane transporter parameters.

Parameter	Description	Value	Units	Source
F	Faraday's constant	96480	C mol^{-1}	
R	Ideal gas constant	8.3145	J K^{-1} mol^{-1}	
T	Temperature	310	K	
Vol_S	Synaptic Volume	8.5883×10^{-16}	L	Breslin et al., 2018
Vol_A	Astrocytic Volume	1.885×10^{-17}	L	Breslin et al., 2018
S_A	Astrocytic membrane surface area	1.4137×10^{-13}	m^2	Breslin et al., 2018
P_{NKAmax}	Maximal NKA current	0.1081	A m^-2	Adapted from Halnes et al. (2013)
K_{Nai}	NKA affinity for Na^+	1.5	mM	Halnes et al., 2013
K_{Ke}	NKA affinity for K^+	10	mM	Halnes et al., 2013
I_{NCXmax}	NCX max current density	0.01	A m^{-2}	Schutter and Smolen, 1998
γ	NCX partition parameter	0.5	[]	Schutter and Smolen, 1998
α_{EAAT}	EAAT scaling constant	$2 = 10^{-4}$	A m^{-2}	Flanagan et al., 2018
β_{EAAT}	EAAT scaling constant	29.2	V^{-1}	Flanagan et al., 2018
g_{kir}	K^+ conductance	1440	S m^{-2}	Adapted from Witthoft et al. (2013)
E_{Kir}	Reversal potential for Kir4.1	0.025	V	Witthoft et al., 2013
g_{gat}	GAT3 conductance	2.1×10^2	Sm^{-2}	Maximized parameter
z_{Na}	Na^+ valency	+1	[]	
z_K	K^+ valency	+1	[]	
z_{Ca}	Ca^{2+} valency	+2	[]	
z_{Glu}	Glu valency	−1	[]	

membrane potential (Verkhratsky and Nedergaard, 2018). This indicates that the direction of its mediated ionic fluxes is highly sensitive to any change in $[Na^+]$. The reversible nature of the transporter is demonstrated in **Figure 4B**, where a reduction in the transmembrane $[Na^+]$ gradient is sufficient to reduce E_{GAT} to below the astrocytic membrane potential, facilitating the release of its substrates, GABA, Na^+ and Cl^- (not included in this model). Note that the recovery rate of E_{GAT} following activation is markedly faster where astrocytic Glu is lower, which can be attributed to the correlation between EAAT-2 activity and astrocytic [Glu] (Flanagan et al., 2018). EAAT-2 activity increased as astrocytic Glu decreased and thus EAAT-2- mediated influx of Na^+ resulted in heightened NKA activity. This increase in transmembrane currents resulted in a faster recovery of E_{GAT}.

As expected, the inclusion of a GAT-3 transporter restricted astrocytic $[Na^+]$ as the concentration dependent GAT-3 reversal potential dropped below the astrocytic membrane potential, resulting in the net efflux of Na^+ through this transporter. Little difference was recorded in comparison between simulation setups regarding basal astrocytic [Glu], due to the relative size of the Glu-mediated fluxes compared to the magnitude of the ionic concentrations.

Time Course of Synaptic Glutamate Affected by GAT-3 Activity

As with GAT-3 transport, the rate of Glu transport by astrocytic EAAT-2 is largely dependent on the transmembrane $[Na^+]$ gradient (Zerangue and Kavanaugh, 1996; Levy et al., 1998) in

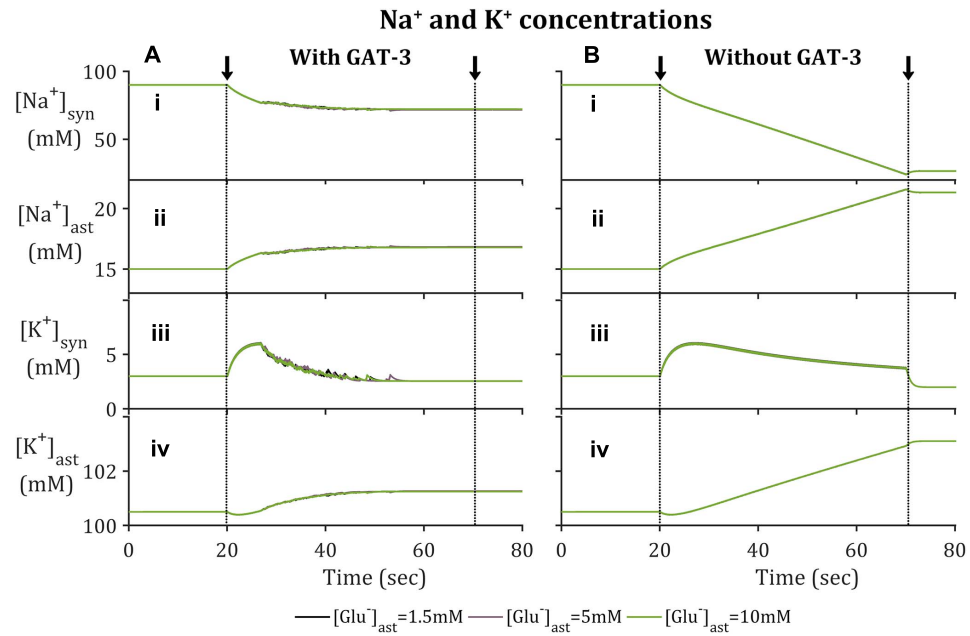

FIGURE 2 | Astrocytic and synaptic concentrations of Na^+ and K^+ where the model **(A)** includes GAT-3 activity and **(B)** where GAT-3 activity is not included; **(i–iv)** describes (respectively) synaptic Na^+, astrocytic $[Na^+]$, synaptic $[K^+]$ and astrocytic $[K^+]$. The results show the ionic concentrations of a simulation in which the presynaptic neuron is subject to an applied current, pulsed at a frequency of 10 Hz over a 50 s window starting at 20 s (window of applied current given by arrows and dashed vertical lines).

addition to the Glu concentration gradient across the astrocytic membrane (Flanagan et al., 2018). In support of previously presented results (Flanagan et al., 2018), increased astrocytic Glu content promotes a longer rate of clearance and higher concentration attainment of synaptic Glu (**Figure 3A.i**), despite the fraction of active synaptic resources (**Figure 3A.ii**) being identical in all cases. This rate of clearance is increased further if GAT-3 is not included (**Figure 3B**) as a result of the heightened shift in $[Na^+]$ and $[K^+]$ transmembrane gradients (**Figure 2**).

Time-Scale of GAT-3-Mediated GABA Release Appropriate for Tonic Inhibition

In contrast to the sharp increase of [Glu] (**Figure 3A**), as implicitly described by neuronal exocytosis, the rate of GABA release by reversed GAT-3 transport is much slower (**Figure 4**), increasing in line with neuronal activity and decreasing slowly as the reversal potential increases above the astrocytic membrane potential. The slow time course of GAT-3 mediated GABA release describes the tonic inhibition described by Rossi et al. (2003); Farrant and Nusser (2005), and Héja et al. (2012). As GAT-3 is predominantly controlled by $[Na^+]$ gradients, and from **Figures 2A.i,ii**, **4**, it can be seen than these differ little due to basal astrocytic [Glu], little difference can be seen in the GAT-3-mediated synaptic [GABA] (**Figure 4A**). Note that the flux of GABA fluctuates a little in line with astrocytic $[Na^+]$, at ∼26 s in the simulation these fluctuations become more pronounced due to the slowing of presynaptic neuronal activity (**Figure 5**) as the GAT-3-mediated efflux of Na^+ attempts to correct the equilibrium concentration gradient (**Figure 4B**). Following the termination of presynaptic firing and Glu-mediated ionic currents, the transmembrane $[Na^+]$ gradient stabilizes (**Figures 2A.i,ii**), resulting in no net release of GABA (**Figure 4A**).

Pre- and Postsynaptic Neuron Membrane Dynamics

Astrocyte-Released GABA Sufficient to Suppress Presynaptic Neuronal Firing

In order to model the longer-term neuronal effects of EAAT-2-GAT-3 coupling, a similar simulation to a previously published study (Flanagan et al., 2018) was performed. The major differences between the former and latter models being the inclusion of GAT-3 transport and more realistic presynaptic firing activity. The presynaptic neuronal membrane dynamics were modeled using a Hodgkin-Huxley formalism. Within this model a pulsed periodic current of 5 $\mu A/cm^2$ was applied, sufficient to initiate a 10 Hz presynaptic neuronal firing for 50 s. In addition to the applied current, the presynaptic neuron is exposed to inhibitory currents mediated by synaptic GABA-activating $GABA_A$ receptors.

From **Figure 5**, the current applied to the presynaptic neuron results in an initial firing frequency of ∼10 Hz. Where synaptic GABA is released by the astrocytic GAT-3 (**Figure 4**) and subsequently activates presynaptic $GABA_A$-Rs; $GABA_A$-mediated currents then compete with the simulated applied current to generate subthreshold presynaptic potentials (**Figure 5A.i**), reducing the presynaptic firing frequency

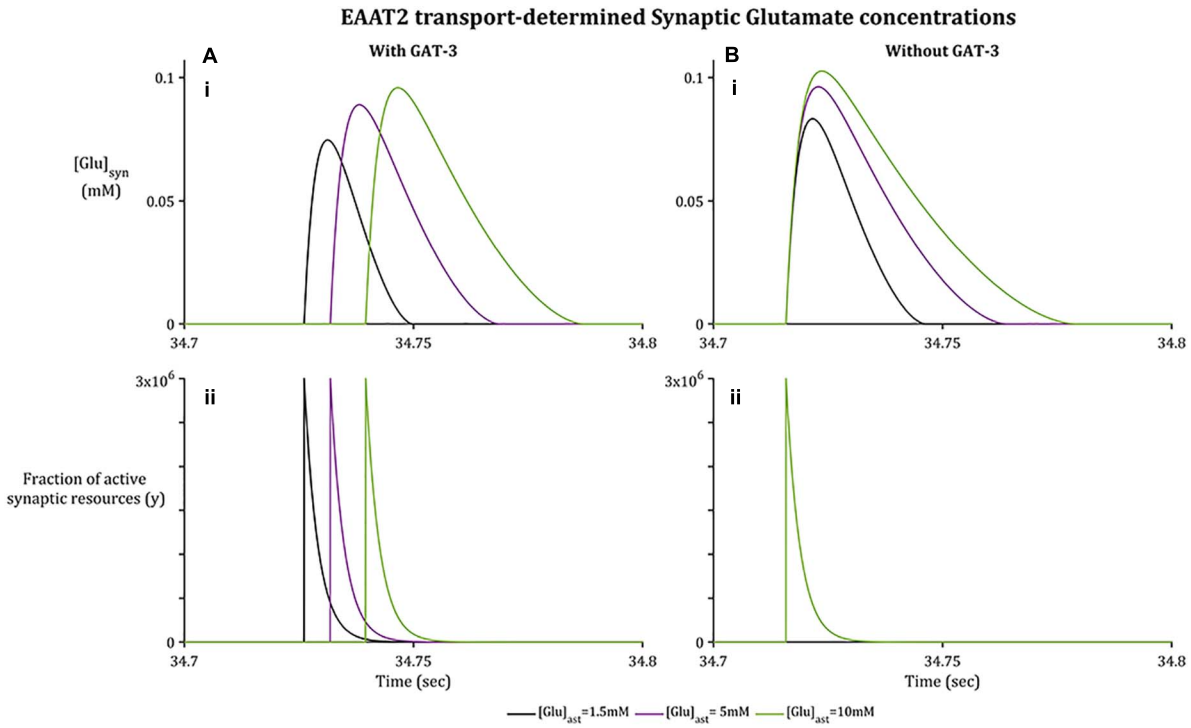

FIGURE 3 | Synaptic [Glu] dynamics for a 0.1 s window within the simulation associated with basal $[Glu]_{ast}$.**(A.i)** shows $[Glu]_{syn}$ increasing to a higher concentration where the basal $[Glu]_{ast}$ is higher, despite the fraction of active synaptic resources **(A.ii)** being identical in all cases. Within **(B.i)**, $[Glu]_{syn}$ increases to a higher concentration again for all $[Glu]_{ast}$ where the GAT3-mediated transport is not included, again despite an identical fraction of active resources **(B.ii)** being released by the presynaptic neuron.

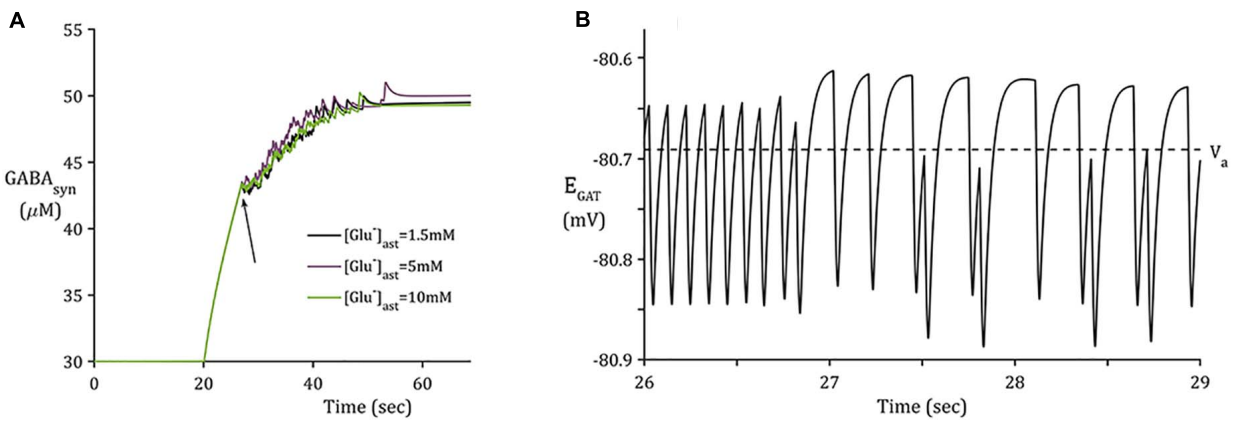

FIGURE 4 | Synaptic GABA dynamics: **(A)** GABA concentration due to GAT-3 activity **(B)** 3-s window of GAT-3 reversal potential for $[Glu]_{ast}$ = 1.5 mM (initial time of window indicated by arrow in panel **(A).**

(**Figure 5B.i**). In contrast, if no GABA is released by astrocytic GAT-3, the presynaptic neuronal firing persists (**Figure 5.ii**).

Postsynaptic Neuronal $GABA_A$-Receptor Activation Mediates Reduction in Hyperexcitability

Besides $GABA_A$ mediated currents, the postsynaptic terminal is subject to Glu-mediated activation of NMDA and AMPA receptors. Higher frequency firing was observed in the postsynaptic neuron (**Figures 6B.i,ii**) where the model does not include GAT-3 activity in comparison to the model containing GAT-3 activity (**Figures 6A.i,ii**). We attribute this to the dual effect of a prolonged synaptic Glu time course and over-activation of NMDA and AMPA-Rs (Flanagan et al., 2018), coupled with the exclusion of GABA-mediated inhibitory currents. Postsynaptic neuronal excitability has been shown to be correlated to time course of synaptic Glu (Flanagan et al., 2018) through activation

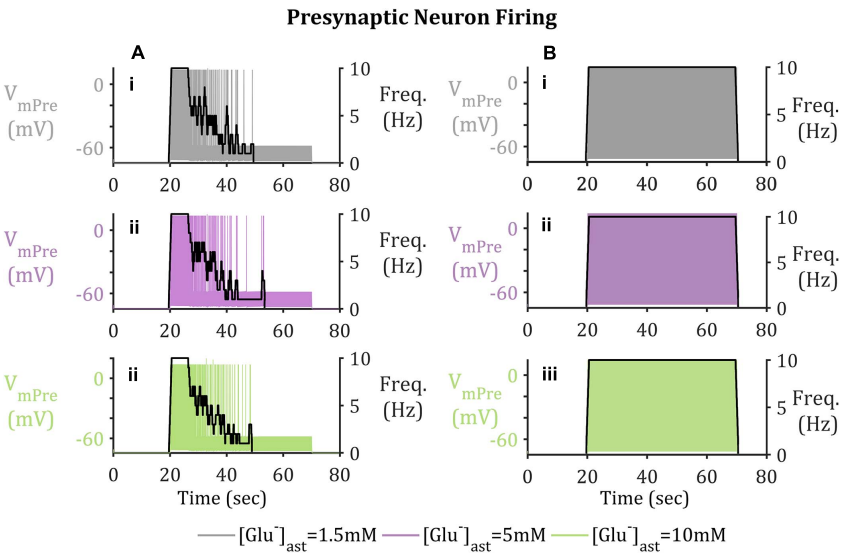

FIGURE 5 | Presynaptic Neuron Membrane Activity **(A)** with and **(B)** without GAT-3-mediated GABA release. Upon activation of the presynaptic neuron by means of a pulsed applied current, Glu released into the synapse triggers the activation of EAAT-2 currents, located on the astrocytic membrane. EAAT-2 transports both Glu and Na^+ into the astrocyte disturbing the equilibrium state of GAT-3, resulting in the release of GABA back to the presynaptic neuron, where upon binding to presynaptic membrane-bound $GABA_A$-Rs inhibits the neuron, even in the presence of a pulsed applied current. **(i–iii)** shows presynaptic neuron membrane potential, overlaid with presynaptic neuron firing frequency (given in black with the right-hand y-axis). Results describe basal **(i)** $[Glu]_{ast}$ = 1.5 mM, **(ii)** $[Glu]_{ast}$ = 5 mM, and **(iii)** $[Glu]_{ast}$ = 10 mM.

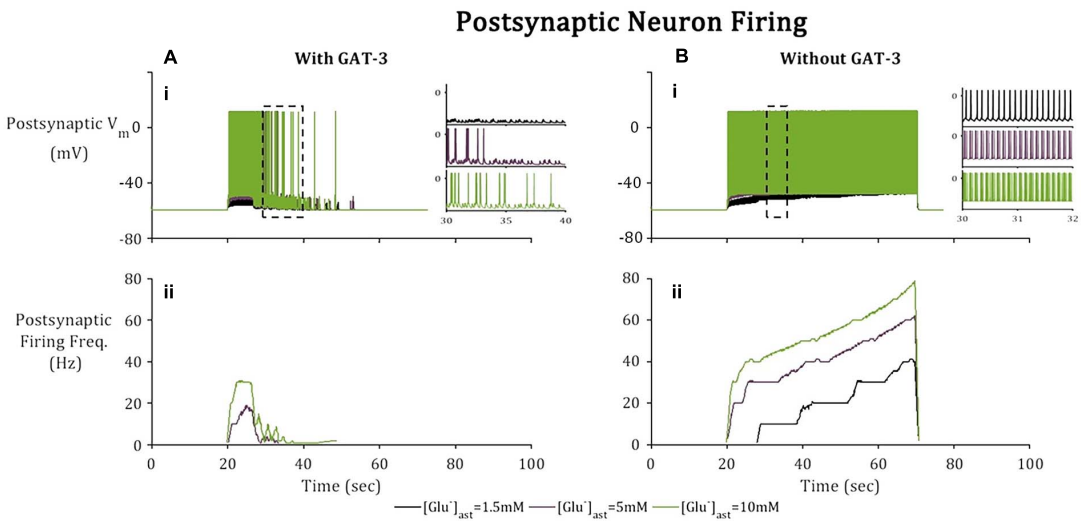

FIGURE 6 | Postsynaptic neuronal activity in model simulation across 3 paradigms, $[Glu]_{ast}$ = 1.5, 5, and 10 mM. Postsynaptic neuronal membrane is subject to **(A)** NMDA, AMPA, and $GABA_A$ mediated currents with inclusion of astrocytic GAT-3-mediated GABA transport and **(B)** where the GAT-3-mediated GABA release has been omitted. **(i)** Postsynaptic neuron membrane potential and **(ii)** firing frequency as a result of an applied current (pulsed at a frequency of 10 Hz over a 50 s window starting at 20 s). All graphs depict firing frequency calculated using a moving average using window size 1 s, 10% overlap). Inset Figs describe 10 s window (left) for each of the basal $[Glu]_{ast}$ and 2 s window (right) for each basal $[Glu]_{ast}$, where the time window was selected according to extent of neuronal activity.

of ionotropic NMDA and AMPA-Rs. Thus, as basal astrocytic [Glu] increased, time course of synaptic Glu increased (**Figure 4**) increasing the postsynaptic firing frequency (**Figure 6**) in both cases (with and without GAT-3).

To consider the effects of astrocytic GAT-3 mediated release of GABA for postsynaptic neuronal activity, three cases were considered; (i) where GABA activates $GABA_A$-mediated inhibitory currents located on both pre- and postsynaptic neuronal membranes (as above) (ii) where GABA activates $GABA_A$ mediated inhibitory currents located on the postsynaptic neuronal membrane alone and (iii) where GAT-3 is not included in the model, as a control. **Figure 7** illustrates the simulation

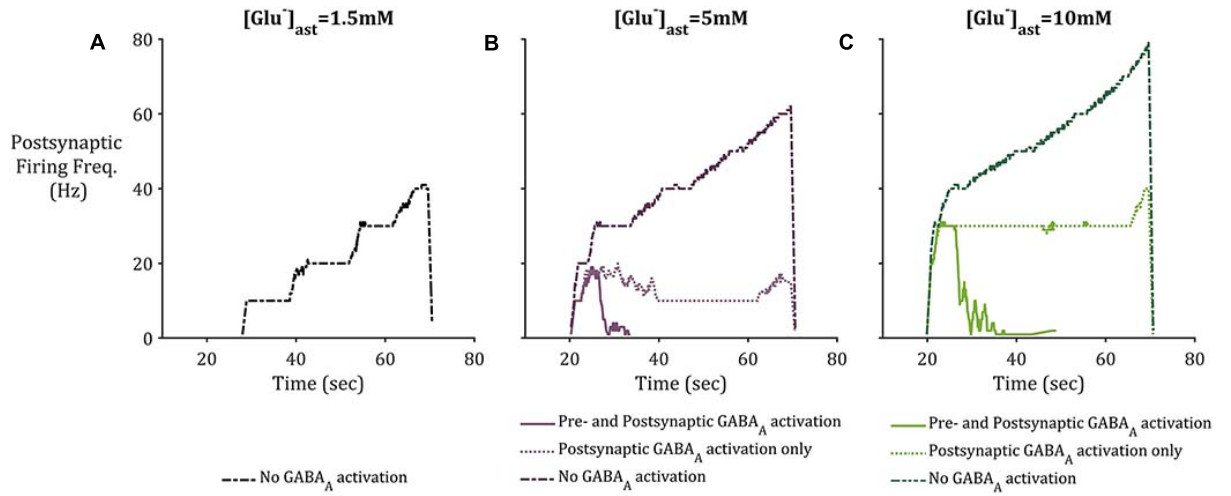

FIGURE 7 | Postsynaptic neuronal firing frequency where **(A)** basal $[Glu]_{ast}$ = 1.5 mM, **(B)** basal $[Glu]_{ast}$ = 5 mM, and **(C)** basal $[Glu]_{ast}$ = 10 mM. Within each plot results from the modeling simulation described above were recorded, where inclusion of astrocytic GAT-3 resulted in GABA-mediated activation of $GABA_A$-Rs are either located on both presynaptic and postsynaptic neuronal membrane (*solid* line), or the postsynaptic neuronal membrane only (*dotted* line). Exclusion of GAT-3 and thus no $GABA_A$-R mediated currents are included as control (*dash-dotted* line). In all cases, the inclusion of GABA dynamics resulted in diminished postsynaptic activity, specifically where [Glu]ast = 1.5 mM, which resulted in no postsynaptic activity where $GABA_A$-R activation was considered.

results using the setup described for each of the basal astrocytic [Glu] of 1.5, 5, and 10 mM. Where astrocytic [Glu] is low, the inclusion of GABA dynamics results in sub- threshold postsynaptic potentials only and thus the firing is completely suppressed (**Figure 7A**) in comparison to where GAT-3 is excluded from the model and thus GABA dynamics and GABA-mediated inhibition are ignored.

In the cases of higher astrocytic [Glu], the inclusion of GABA dynamics in both cases (i) and (ii) is sufficient to not only significantly reduce the firing frequency of the postsynaptic neuron, but also curtail the runaway Glu-mediated excitation of the neuronal membrane, as seen in the dash-dotted lines in **Figures 7B,C**.

DISCUSSION

The effects of astrocytic function and dysfunction on synaptic activity are widely researched areas in both experimental and computational fields. In this study, we focused on one particular recognized function of astrocytes: the control of extracellular Glu and GABA neurotransmitter concentrations by astrocytic transporters.

The experimental observation that astrocytic GABA transporters, GAT-3, respond to Glu mediated EAAT-2 activation (Héja et al., 2009) appears to indicate a synaptic feedback determined by the influx of shared substrate, Na^+. Governed by the reversal potential of GAT-3, this activation mediates the release of GABA from the astrocyte and may modulate a long-lasting tonic inhibition of nearby neurons (Farrant and Nusser, 2005; Héja et al., 2009; Kersanté et al., 2013) as opposed to transient, or phasic, inhibition typically resulting from exocytotic release (Farrant and Nusser, 2005). A model to describe the interaction between EAAT-2 and GAT-3 activity was developed, exploring their effects for synaptic Glu and GABA concentrations and consequential perturbation of both the pre- and postsynaptic neuronal membrane potential.

Within this paper, a simulation sought to explore and explain the interplay of EAAT-2 and GAT-3 transport. Within the simulated time, it was noted that astrocytic GAT-3 released inhibitory neurotransmitter GABA in addition to acting as a non-ATP dependent mechanism for regulating intracellular Na^+: a role traditionally assigned to the NKA which relies directly on ATP availability. Based on the findings of this paper, the proposition of previous experimental study (Héja et al., 2012) is supported, that GAT-3 acts to provide a modulatory effect when faced with excessive synaptic excitation. In addition, the modulatory effect is diminished where astrocytic [Glu] is elevated, as the time course of synaptic Glu is prolonged (Flanagan et al., 2018), thus locally exciting the postsynaptic neuron for longer. Results indicate that astrocyte-released GABA through GAT-3 acting on the postsynaptic neuron alone is also sufficient to suppress postsynaptic neuronal activity. It was noted that presynaptic neuronal inhibition decreases where astrocytic [Glu] is elevated.

As in Flanagan et al. (2018), consideration was taken of the astrocytic [Glu], reflecting the hypothesized effects of astrocytic glutamine synthetase downregulation (Perez et al., 2012) as observed in the focal sites of some epilepsies, particularly mesial temporal lobe epilepsy (MTLE) (Petroff et al., 2002; Eid et al., 2004). Previously reported results (Flanagan et al., 2018) indicate the slowing of synaptic Glu clearance in line with increasing astrocytic [Glu]. This resulted in the over-activation of postsynaptic NMDA and AMPA receptors and thus heightened local postsynaptic neuronal firing frequencies. Within this paper, the inclusion of astrocytic GAT-3 modulates

the postsynaptic firing frequencies despite increased astrocytic Glu content, however, the strength of astrocytic GABA-mediated neuronal inhibition decreases where astrocytic [Glu] is elevated. The implications of this within the context of MTLE would be an ineffective astrocytic GABA-induced synaptic modulation, which would be further impaired by chronic GS downregulation (Hammer et al., 2008), resulting in increased neuronal hyperexcitability and seizure generation.

Although astrocytic-released GABA may act on an extrasynaptic location and the corresponding $GABA_A$-Rs have been seen to have a higher affinity to GABA than their synaptic counterparts (Farrant and Nusser, 2005), this has not been accounted for in this model and remains a direction for future work. In addition, this study took account of neuronal inhibition mediated by the ubiquitous $GABA_A$-Rs due to experimental results demonstrating their fast activating inhibitory effect of neuronal hyperexcitability and epileptiform activity (Mann et al., 2009). These receptors were modeled to counteract the fast-excitatory behavior of NMDA-R and AMPA-R mediated currents. Further developments of this model would also take account of slower $GABA_B$ receptor-activation and their longer-term effects on neuronal hyperexcitability.

DATA AVAILABILITY STATEMENT

The raw data supporting the conclusions of this article will be made available by the authors, without undue reservation.

AUTHOR CONTRIBUTIONS

BF, LM, JW, MT, KW-L, and JH contributed to conception and design of the study. BF wrote the code. BF, LM, and JW wrote the first draft of the manuscript. All authors contributed to manuscript revision, read, and approved the submitted version.

ACKNOWLEDGMENTS

This work acknowledges funding support from Northern Ireland's Department for the Economy.

REFERENCES

Allam, S. L., Ghaderi, V. S., Bouteiller, J.-M. C., Legendre, A., Ambert, N., Greget, R., et al. (2012). A computational model to investigate astrocytic glutamate uptake influence on synaptic transmission and neuronal spiking. *Front. Comput. Neurosci.* 6:70. doi: 10.3389/fncom.2012.00070

Attwell, D., Barbour, B., and Szatkowski, M. (1993). Nonvesicular release of neurotransmitter. *Neuron* 11, 401–407. doi: 10.1016/0896-6273(93)90145-h

Bentzen, N. C. K., Zhabotinsky, A. M., and Laugesen, J. L. (2009). Modeling of glutamate-induced dynamical patterns. *Int. J. Neural Syst.* 19, 395–407. doi: 10.1142/s0129065709002105

Breslin, K., Joseph Wade, J., Wong-Lin, K. F., Harkin, J., Flanagan, B., Van Zalinge, H., et al. (2018). Potassium and sodium microdomains in thin astroglial processes: a computational model study. *PLoS Comput. Biol.* 14:e1006151. doi: 10.1371/journal.pcbi.1006151

Clasadonte, J., and Haydon, P. G. (2012). "Astrocytes and epilepsy," in *Jasper's Basic Mechanisms of the Epilepsies*, 4th Edn, eds J. Noebels, M. Avoli, M. Rogawski, R. Olsen, and A. Delgado-Escueta (New York, NY: Oxford University Press).

Coulter, D. A., and Steinhäuser, C. (2015). Role of astrocytes in epilepsy. *Cold Spring Harb. Perspect. Med.* 5:a022434.

Coyle, J. T. (2004). The GABA-glutamate connection in schizophrenia: which is the proximate cause? *Biochem. Pharmacol.* 68, 1507–1514. doi: 10.1016/j.bcp.2004.07.034

Danbolt, N. C. (2001). Glutamate uptake. *Prog. Neurobiol.* 65, 1–105.

Destexhe, A., Mainen, Z. F., and Sejnowski, T. J. (1998). "Kinetic models of synaptic transmission," in *Methods in Neuronal Modeling: From Ions to Networks*, 2nd Edn, eds C. Koch and I. Segev (Cambridge, MA: Massachusetts Intitute of Technology), 1–25.

During, M. J., and Spencer, D. D. (1993). Extracellular hippocampal glutamate and spontaneous seizure in the conscious human brain. *Lancet* 341, 1607–1610. doi: 10.1016/0140-6736(93)90754-5

Eid, T., Ghosh, A., Wang, Y., Beckström, H., Zaveri, H. P., Lee, T. S. W., et al. (2008). Recurrent seizures and brain pathology after inhibition of glutamine synthetase in the hippocampus in rats. *Brain* 131, 2061–2070. doi: 10.1093/brain/awn133

Eid, T., Thomas, M. J., Spencer, D. D., Rundén-Pran, E., Lai, J. C. K., Malthankar, G. V., et al. (2004). Loss of glutamine synthetase in the human epileptogenic hippocampus: possible mechanism for raised extracellular glutamate in mesial temporal lobe epilepsy. *Lancet* 363, 28–37. doi: 10.1016/s0140-6736(03)15166-5

Farrant, M., and Nusser, Z. (2005). Variations on an inhibitory theme: phasic and tonic activation of GABAA receptors. *Nat. Rev. Neurosci.* 6, 215–229. doi: 10.1038/nrn1625

Fellin, T., Pascual, O., and Haydon, P. G. (2006). Astrocytes coordinate synaptic networks: balanced excitation and inhibition. *Physiology* 21, 208–215. doi: 10.1152/physiol.00161.2005

Flanagan, B., McDaid, L., Wade, J., Wong-Lin, K., and Harkin, J. (2018). A computational study of astrocytic glutamate influence on post-synaptic neuronal excitability. *PLoS Comput. Biol.* 14:e1006040. doi: 10.1371/journal.pcbi.1006040

Golomb, D., Yue, C., and Yaari, Y. (2006). Contribution of persistent Na+ current and M-type K+ current to somatic bursting in CA1 pyramidal cells: combined experimental and modeling study. *J. Neurophysiol.* 96, 1912–1926. doi: 10.1152/jn.00205.2006

Halnes, G., Østby, I., Pettersen, K. H., Omholt, S. W., and Einevoll, G. T. (2013). Electrodiffusive model for astrocytic and neuronal ion concentration dynamics. *PLoS Comput. Biol.* 9:e1003386. doi: 10.1371/journal.pcbi.1003386

Hammer, J., Alvestad, S., Osen, K. K., Skare, Ø, Sonnewald, U., Ottersen, O. P., et al. (2008). Expression of glutamine synthetase and glutamate dehydrogenase in the latent phase and chronic phase in the kainate model of temporal lobe epilepsy. *Glia* 56, 856–868. doi: 10.1002/glia.20659

Héja, L., Barabás, P., Nyitrai, G., Kékesi, K. A., Lasztóczi, B., Toke, O., et al. (2009). Glutamate uptake triggers transporter-mediated GABA release from astrocytes. *PLoS One* 4:e7153. doi: 10.1371/journal.pone.0007153

Héja, L., Nyitrai, G., Kékesi, O., Dobolyi, Á, Szabó, P., Fiáth, R., et al. (2012). Astrocytes convert network excitation to tonic inhibition of neurons. *BMC Biol.* 10:26. doi: 10.1186/1741-7007-10-26

Hertz, L., Dringen, R., Schousboe, A., and Robinson, S. R. (1999). Astrocytes: glutamate producers for neurons. *J. Neurosci. Res.* 57, 417–428. doi: 10.1002/(sici)1097-4547(19990815)57:4<417::aid-jnr1>3.0.co;2-n

Hodgkin, A. L., and Huxley, A. F. (1952). A quantitative description of membrane current and its application to conduction and excitation in nerve. *J. Physiol.* 117, 500–544. doi: 10.1113/jphysiol.1952.sp004764

Hübel, N., Hosseini-Zare, M. S., Žiburkus, J., and Ullah, G. (2017). The role of glutamate in neuronal ion homeostasis: a case study of spreading

depolarization. *PLoS Comput. Biol.* 13:e1005804. doi: 10.1371/journal.pcbi.1005804

Kandel, E. R., Schwartz, J. H., Jessell, T. M., Siegelbaum, S. A., Hudspeth, A. J., and Mack, S. (2012). *Principles of Neural Science*, 5th Edn, eds A. Sydor and H. Lebowitz (New York: McGraw Hill Professional).

Kersanté, F., Rowley, S. C. S., Pavlov, I., Gutièrrez-Mecinas, M., Semyanov, A., Reul, J. M. H. M., et al. (2013). A functional role for both -aminobutyric acid (GABA) transporter-1 and GABA transporter-3 in the modulation of extracellular GABA and GABAergic tonic conductances in the rat hippocampus. *J. Physiol.* 591, 2429–2441. doi: 10.1113/jphysiol.2012.246298

Kirischuk, S., Parpura, V., and Verkhratsky, A. (2012). Sodium dynamics: another key to astroglial excitability? *Trends Neurosci.* 35, 497–506. doi: 10.1016/j.tins.2012.04.003

Levy, L. M., Warr, O., and Attwell, D. (1998). Stoichiometry of the glial glutamate transporter GLT-1 expressed inducibly in a chinese hamster ovary cell line selected for low endogenous Na+-dependent glutamate uptake. *J. Neurosci.* 18, 9620–9628. doi: 10.1523/jneurosci.18-23-09620.1998

Li, J., Tang, J., Ma, J., Du, M., Wang, R., and Wu, Y. (2016). Dynamic transition of neuronal firing induced by abnormal astrocytic glutamate oscillation. *Sci. Rep.* 6:32343.

Mann, E. O., Kohl, M. M., and Paulsen, O. (2009). Distinct roles of GABAA and GABAB receptors in balancing and terminating persistent cortical activity. *J. Neurosci.* 29, 7513–7518. doi: 10.1523/jneurosci.6162-08.2009

Manninen, T., Havela, R., and Linne, M.-L. (2018). Computational models for calcium-mediated astrocyte functions. *Front. Comput. Neurosci.* 12:14. doi: 10.3389/fncom.2018.00014

Meldrum, B. S. (2000). Glutamate as a neurotransmitter in the brain: review of physiology and pathology. *J. Nutr.* 130(4 Suppl.), 1007S–1015S.

Minelli, A., DeBiasi, S., Brecha, N. C., Zuccarello, L. V., and Conti, F. (1996). GAT-3, a high-affinity GABA plasma membrane transporter, is localized to astrocytic processes, and it is not confined to the vicinity of GABAergic synapses in the cerebral cortex. *J. Neurosci.* 16, 6255–6264. doi: 10.1523/jneurosci.16-19-06255.1996

O'Rourke, N. A., Weiler, N. C., Micheva, K. D., and Smith, S. J. (2012). Deep molecular diversity of mammalian synapses: why it matters and how to measure it. *Nat. Rev. Neurosci.* 13, 365–379. doi: 10.1038/nrn3170

Perez, E. L., Lauritzen, F., Wang, Y., Lee, T. S. W., Kang, D., Zaveri, H. P., et al. (2012). Evidence for astrocytes as a potential source of the glutamate excess in temporal lobe epilepsy. *Neurobiol. Dis.* 47, 331–337. doi: 10.1016/j.nbd.2012.05.010

Petroff, O. A. C. (2002). GABA and glutamate in the human brain. *Neuroscientist* 8, 562–573. doi: 10.1177/1073858402238515

Petroff, O. A. C., Errante, L. D., Rothman, D. L., Kim, J. H., and Spencer, D. D. (2002). Glutamate-glutamine cycling in the epileptic human hippocampus. *Epilepsia* 43, 703–710. doi: 10.1046/j.1528-1157.2002.38901.x

Pizzarelli, R., and Cherubini, E. (2011). Alterations of GABAergic signaling in autism spectrum disorders. *Neural Plast.* 2011:297153.

Robinson, S. R. (2000). Neuronal expression of glutamine synthetase in Alzheimer's disease indicates a profound impairment of metabolic interactions with astrocytes. *Neurochem. Int.* 36, 471–482. doi: 10.1016/s0197-0186(99)00150-3

Rossi, D. J., Hamann, M., and Attwell, D. (2003). Multiple modes of GABAergic inhibition of rat cerebellar granule cells. *J. Physiol.* 548(Pt 1), 97–110.

Schousboe, A., Scafidi, S., Bak, L. K., Waagepetersen, H. S., and McKenna, M. C. (2014). "Glutamate metabolism in the brain focusing on astrocytes," in *Glutamate and {ATP} at the Interface of Metabolism and Signaling in the Brain*, eds V. Parpura, A. Schousboe, and A. Verkhratsky (Cham: Springer International Publishing), 13–30.

Schutter, E. D. E., and Smolen, P. (1998). "Calcium dynamics in large neuronal models," in *Methods in Neuronal Modeling: From Ions to Networks*, 2nd Edn, eds C. Koch and I. Segev (Cambridge, MA: Massachusetts Intitute of Technology), 211–250.

Sigel, E., and Steinmann, M. E. (2012). Structure, function, and modulation of GABA(A) receptors. *J. Biol. Chem.* 287, 40224–40231.

Tewari, S. G., and Majumdar, K. K. (2012). A mathematical model of the tripartite synapse: astrocyte-induced synaptic plasticity. *J. Biol. Phys.* 38, 232–236.

Tsodyks, M., Pawelzik, K., and Markram, H. (1998). Neural networks with dynamic synapses. *Neural Comput.* 10, 821–835.

Verkhratsky, A., and Nedergaard, M. (2018). Physiology of astroglia. *Physiol. Rev.* 98, 239–389.

Witthoft, A., Filosa, J. A., and Karniadakis, G. E. (2013). Potassium buffering in the neurovascular unit: models and sensitivity analysis. *Biophys. J.* 105, 2046–2054.

Zerangue, N., and Kavanaugh, M. P. (1996). Flux coupling in a neuronal glutamate transporter. *Nature* 383, 634–637.

Conflict of Interest: The authors declare that the research was conducted in the absence of any commercial or financial relationships that could be construed as a potential conflict of interest.

frontiers in Cellular Neuroscience

BRIEF RESEARCH REPORT
published: 23 July 2021
doi: 10.3389/fncel.2021.707813

Buffering by Transporters Can Spare Geometric Hindrance in Controlling Glutamate Escape

Leonid P. Savtchenko, Kaiyu Zheng and Dmitri A. Rusakov**

UCL Queen Square Institute of Neurology, University College London, London, United Kingdom

The surface of astrocyte processes that often surround excitatory synapses is packed with high-affinity glutamate transporters, largely preventing extrasynaptic glutamate escape. The shape and prevalence of perisynaptic astroglia vary among brain regions, in some cases providing a complete isolation of synaptic connections from the surrounding tissue. The perception has been that the geometry of perisynaptic environment is therefore essential to preventing extrasynaptic glutamate escape. To understand to what degree this notion holds, we modelled brain neuropil as a space filled with a scatter of randomly sized, overlapping spheres representing randomly shaped cellular elements and intercellular lumen. Simulating release and diffusion of glutamate molecules inside the interstitial gaps in this medium showed that high-affinity transporters would efficiently constrain extrasynaptic spread of glutamate even when diffusion passages are relatively open. We thus estimate that, in the hippocampal or cerebellar neuropil, the bulk of glutamate released by a synaptic vesicle is rapidly bound by transporters (or high-affinity target receptors) mainly in close proximity of the synaptic cleft, whether or not certain physiological or pathological events change local tissue geometry.

Keywords: excitatory synapse, glutamate, glutamate spillover, glutamate transporters, astrocyte, perisynaptic astroglial processes, synaptic environment

OPEN ACCESS

Edited by:
Susan L. Ingram,
Oregon Health and Science University, United States

Reviewed by:
Leonid Kalachev,
University of Montana, United States
Gertrudis Perea,
Cajal Institute (CSIC), Spain

****Correspondence:***
Leonid P. Savtchenko
leonid.savtchenko@ucl.ac.uk
Dmitri A. Rusakov
d.rusakov@ucl.ac.uk

Specialty section:
This article was submitted to Cellular Neurophysiology, a section of the journal Frontiers in Cellular Neuroscience

Received: *10 May 2021*
Accepted: *21 June 2021*
Published: *23 July 2021*

Citation:
Savtchenko LP, Zheng K and Rusakov DA (2021) Buffering by Transporters Can Spare Geometric Hindrance in Controlling Glutamate Escape. Front. Cell. Neurosci. 15:707813. doi: 10.3389/fncel.2021.707813

INTRODUCTION

Glutamatergic circuitry of the brain has long been associated with a "wired," one-to-one type of transmission that carries excitatory signals between individual nerve cells. This type of connectivity has provided a basis upon which the computation logic of neural-network learning algorithms was established and benefited from. To ensure that glutamate released into the synaptic cleft does not escape activating its receptors beyond the target cell, excitatory synapses are often surrounded by perisynaptic astrocyte processes (PAPs), part of the sponge-like morphology of brain astroglia. PAPs vary extensively in shape and size, and their membrane surface is densely packed with high-affinity glutamate transporters, among other signalling molecules (reviewed in Heller and Rusakov, 2015; Bazargani and Attwell, 2016; Murphy-Royal et al., 2017; Rose et al., 2017; Verkhratsky and Nedergaard, 2018). At some specialised synaptic connections, PAPs form a comprehensive isolating shield around one or several synaptic contacts (Barbour, 1993; Grosche et al., 1999; Rollenhagen et al., 2007; Borst and Soria van Hoeve, 2012). However, common (small) cortical synapses normally have only a varied fraction of their immediate neuropil environment (20–80%) occupied by PAPs (Spacek and Harris, 1998; Ventura and Harris, 1999; Witcher et al., 2007; Lushnikova et al., 2009; Patrushev et al., 2013; Bernardinelli et al., 2014; Medvedev et al., 2014; Pannasch et al., 2014; Gavrilov et al., 2018; Henneberger et al., 2020). It has often been argued that the synapse has to

be comprehensively surrounded by the transporter-enriched PAPs, to prevent synaptically released glutamate from spilling over to the neighbouring tissue. Whilst the latter would indeed stop glutamate from escaping, whether the commonly observed partial PAP coverage is as effective in this respect has remained uncertain, prompting intense theoretical and experimental exploration of extrasynaptic glutamate escape (Diamond, 2001; Rusakov, 2001; Scimemi et al., 2004; Szapiro and Barbour, 2007; Zheng et al., 2008; Scimemi et al., 2009; Henneberger et al., 2020).

This issue has been somewhat blurred by the "aqueous" connotation arising from the commonly used term "glutamate spillover." In reality, glutamate molecules do not flow or spill over as do liquids. They undergo rapid Brownian diffusion, bouncing off multiple nanoscale obstacles (such as water molecules) millions of times, moving into random directions, in nanoscale steps. Thus, any diffusing glutamate molecule has a chance to encounter a PAP surface populated with high-affinity glutamate transporters. The other issue affecting our perception of extrasynaptic glutamate actions is our understanding of the extracellular space architecture. The classical electron micrographs of fixed brain tissue tend to depict the interstitial space as a system of thin gaps between adjacent cell membranes. It has emerged, however, that in live brain the extracellular space occupies ∼20% of neuropil tissue volume, with interstitial gaps sometimes as wide as 200 nm (Thorne and Nicholson, 2006; Tonnesen et al., 2018; Paviolo et al., 2020). These data suggest that there could be much less geometric hindrance to diffusion in the brain neuropil than commonly perceived. Our aim was therefore to understand better, in comparative terms, the roles of geometric hindrance and of glutamate transporter binding in regulating extrasynaptic escape of glutamate, as predicted by physics. To this end, we explored detailed Monte Carlo simulations of particle diffusion and (transporter) binding in complex, quasi-randomly shaped geometries representing the extracellular space.

METHODS

Monte Carlo Simulations of Particle Diffusion

Monte Carlo algorithms for particle diffusion were designed and run with MATLAB: they were previously described in detail, and tested and constrained using various experimental settings (Savtchenko et al., 2013, 2021; Sylantyev et al., 2013). The simulation arena was a 3 μm wide cube, with 2,000 particles "released" instantaneously at the centre. Particles positioned at time t at point $r_i(x, y, z)$ were moved, over time step Δt, to point $r_{i+1}(x + 2\delta_x\Delta_{1D}, y + 2\delta_y\Delta_{1D}, z + 2\delta_z\Delta_{1D})$ where Δ_{1D} stands for the mean square displacement in the Einstein's diffusion equation for 1D Brownian motion $\Delta_{1D}^2 = 2D\Delta t$, $D = 0.65\ \mu m^2/ms$ is the glutamate diffusion coefficient in the interstitial space (Zheng et al., 2017), and $\delta_{x|y|z}$ denotes a "delta-correlated" (independently seeded, uncorrelated) uniform random number from the (−1, 1) range. The latter ensures that Brownian particles are equally likely to move into either direction whereas scale factor 2 for δ gives the average elementary displacement in x-y-z either $-\Delta_{1D}$ or $+\Delta_{1D}$. This algorithm provided the duty-cycle translational particle movements in a contiguous 3D space, over all directions with varied 3D steps, rather than over the rectangular 3D-lattice vertices used by us and many others previously. The randomness of the displacement vector helped avoid occasional numerical deadlocks for particles trapped near the space dead-ends formed by aggregated overlapped spheres. The time step Δt (usually < 0.1 μs) was set to be small enough to prevent particles from "tunnelling" through the smallest obstacles, and the actual value of D was verified at regular intervals.

The interaction with obstacles was simulated either as an elastic collision, or as a permanent bond (the catchment layer of ± 3 nm of the sphere surface, comparable with the maximal elementary displacement Δ_{1D}), with the probability as indicated. Because the characteristic diffusion time from the centre to the arena boundary (<1 ms) was much shorter than the time constant of glutamate unbinding from glial glutamate transporter (GLT1 type), particle binding to the spheres on the millisecond scale was set as permanent.

Simulating Sphere-Filled Space Representing Brain Neuropil

There were at least two reasons to believe that randomly sized overlapping spheres would be a more realistic representation of neuropil compared to regular lattices of regular shapes, a tissue model used extensively by us and others previously. Firstly, multiple intersecting spheres give randomly shaped and randomly sized cellular elements and extracellular channels, as opposed to uniform or regular structures. Secondly, this approach provides a mixture of concave and convex shapes, including "diffusion dead-ends" which are considered an important trait of brain neuropil (Hrabe et al., 2004). Both features therefore reflect reality better than do regular lattices.

Filling the space with overlapping spheres followed the routines described in detail previously (Savtchenko et al., 2021). In brief, the key parameter controlling this procedure was the volume fraction β occupied by the spheres: β = 1-α where α commonly stands for medium porosity, such as the volume fraction of the extracellular space in brain tissue. The β-value was calculated by (a) scattering 10^5 test points uniformly randomly throughout the arena, and (b) calculating the proportion of the point falling outside the spheres. We verified that increasing the number of such test points to 10^6 altered β by < 1%, pointing to asymptotic accuracy.

To fill the space with overlapping spheres that have a distributed size, we generated random co-ordinates of sphere centroids across the arena, and the random radius value for each sphere, in accord with the designated diameter distribution, which in our case was uniformly random between 20 and 100 nm. The initial number of spheres was estimated based on their average volume and the average size (to give the required β-value), and we left the co-ordinate origin unoccupied by any sphere. The space-filling cycle was repeated, with adjusted sphere numbers, until β approached the required value with ∼5% accuracy.

Our initial tests revealed that introducing transporter binding effectively restricted free particle movement across the simulated arena within ∼1 ms. We therefore limited simulated time to 1 ms.

Computing Environment

Monte Carlo simulations were run on a dedicated 8-node BEOWULF-style diskless PC cluster running under the Gentoo LINUX operating system (kernel 4.12.12), which was an upgraded, *ad hoc* built version of the cluster described earlier (Zheng et al., 2008). Individual nodes comprised an HP ProLiant DL120 G6 Server containing a quad-core Intel Xeon X3430 processor and 8 GB of DDR3 RAM. Nodes were connected through a NetGear Gigabit Ethernet switch to a master computer that distributes programs and collects the results on its hard disk. Parallelisation and optimisation of the algorithms and program codes were implemented by AMC Bridge LLC (Waltham, MA).

RESULTS

Surface Binding Is Efficient in Curtailing Particle Diffusion Even in Highly Porous Environment

In a porous medium, the diffusion transfer rate scales, at least to a first approximation, with medium porosity α (Tartakovsky and Dentz, 2019), which in the brain represents tissue volume fraction of the extracellular space (Sykova and Nicholson, 2008). Thus, narrowing interstitial passages in the neuropil will slow down escape of glutamate released at the synapse. To understand how this would affect the scatter of glutamate molecules away from the release site, we simulated brain neuropil as a space filled by randomly sized, overlapping spheres representing cellular structures: this procedure formed a porous, randomly shaped medium, with volume fraction β occupied by spheres, or porosity α = 1-β (see section "Methods") (Savtchenko et al., 2021).

For the sake of comparison, we first tracked the fate of 2,000 diffusing particles representing glutamate molecules released in the middle of a 3 μm cube arena, with space porosity of either α = 0.7 or α = 0.2, the latter representing an adult mammalian brain (Thorne and Nicholson, 2006; Tonnesen et al., 2018). The diffusion coefficient for glutamate was set at D = 0.65 μm^2/ms, as measured through diffusion retardation in the interstitial brain space using time-resolved fluorescence anisotropy imaging (Suhling et al., 2015; Zheng et al., 2017). Because the characteristic free-diffusion time over the arena was < 1 ms, our simulations ran for 1 ms. The outcome showed that narrowing diffusion passages by 3.5 times slowed down particle escape, so that the molecular scatter became 1.5–2 times narrower (**Figures 1A,B**).

Next, instead of narrowing the extracellular space, we equipped surfaces of the spheres with the ability to hold diffusing molecules that "bumped" into them. This arrangement reflects the scenario when astroglial surfaces that are densely populated with GLT1 transporters (up to 10^5 μm^{-2}; Lehre and Danbolt, 1998; Lehre and Rusakov, 2002) represent all cell membranes in the nearby neuropil. Again, the time constant characterising

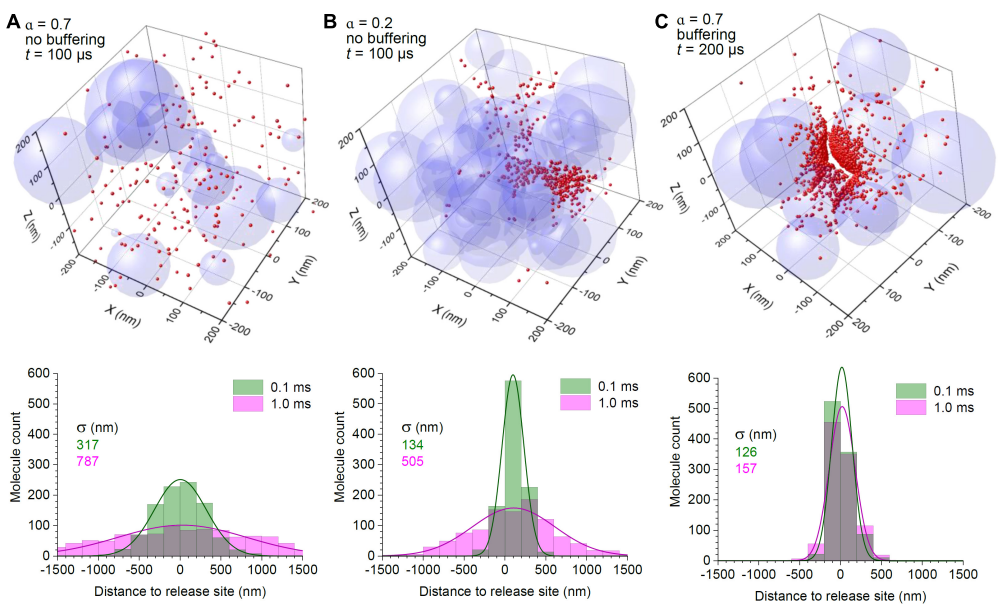

FIGURE 1 | Surface binding to high-affinity transporters provides efficient control of extrasynaptic glutamate escape even in high-porosity tissue. **(A)** 3D graph: A snapshot of the simulated molecular scatter (400 nm wide fragment of the 3 μm wide simulation arena), 0.1 ms after release of 2,000 particles in the centre, with a scatter of overlapping spheres representing 3D obstacles to diffusion; α = 0.7, medium porosity (volume fraction of the free space). Histogram: spatial distribution of diffusing particles across the simulation arena, at two time points post-release, as indicated; solid lines, best-fit Gaussian distribution; σ, distribution dispersion (standard deviation). **(B)** Simulations as in **(A)**, but with medium porosity α = 0.2; note that the particle scatter is skewed because of the asymmetric geometry of diffusion obstacles (sphere aggregates); other notations as in **(A)**. **(C)** Simulations as in **(A)**, but with the particle-surface binding enabled; particle catchment occurs at a distance of ± 3 nm of the surface, to reflect the elementary diffusion displacement Δ_{1D} (see section "Methods"); other notations as in **(A)**.

glutamate unbinding or the glutamate uptake rate for the main glial glutamate transporter GLT1 is much longer than the diffusion time of < 1 ms (Bergles et al., 2002; Savtchenko et al., 2018). Thus, a permanent bond was fully representative of glutamate-transporter interaction on this time scale. Simulations showed that in these conditions the molecules remained within the vicinity of the release site, with little progression of the spread, even though 80% of the medium was available for free diffusion (**Figure 1C**).

Glutamate Escape in Realistic Neuropil

The results above illustrate that, in principle, binding to glutamate transporters could provide an efficient barrier to diffusion even when the diffusion passages are widely open. However, it was important to relate these observations to a set of parameters characteristic of the real brain neuropil. Whilst $\alpha = 0.2$ is thought to faithfully represent brain tissue porosity across regions (Nicholson and Phillips, 1981; Sykova and Nicholson, 2008; Tonnesen et al., 2018), astroglial coverage of synapse varies significantly. Stereological estimates based on quantitative electron microscopy suggest that in the neuropil of the rodent cerebellum (molecular layer) and hippocampus (area CA1), astroglial surfaces represent a ∼30 and 13% fraction, respectively, of all cell membrane surfaces (Lehre and Danbolt, 1998; Lehre and Rusakov, 2002; Savtchenko et al., 2018), whereas in the supraoptic nucleus cortex this fraction could exceed 50% (Pilgrim et al., 1982).

Based on these measurements, we first simulated glutamate release and diffusion in a modelled neuropil with $\alpha = 0.2$ as in **Figure 1B**, but with the probability for individual molecules to be bound by the surface of either 0.3 or 0.13, thus representing the occurrence of transporter-enriched astroglial membranes in the cerebellar molecular layer or hippocampal area CA1, respectively. This approach assumes that the occurrence of astroglial and non-astroglial membranes near excitatory synapses does not follow any regular pattern but is arbitrary, which appears in line with the quantitative analyses of synaptic environment (Lehre and Rusakov, 2002; Patrushev et al., 2013; Medvedev et al., 2014). The other important assumption here is that the numbers of glutamate transporters expressed in perisynaptic astroglial membranes are much higher than the numbers of released glutamate molecules, a relationship consistent with single-vesicle release (Lehre and Danbolt, 1998; Savtchenko et al., 2013). We have also introduced a 320 nm wide, 20 nm thick synaptic cleft (free of transporters) based on the typical dimensions of such clefts at CA3-CA1 synapses (Harris and Stevens, 1989; Harris et al., 1992), centred at the arena co-ordinate origin, coinciding with the glutamate release site.

The results suggest that the bulk of glutamate escaping from cerebellar molecular layer synapses is bound to transporters within ∼100 nm from the cleft, so that virtually all molecules become immobile very rapidly after ∼0.1 ms (**Figure 2A**). In these simulations, the distribution histograms represent all, both free and transporter-bound, molecules, so that the spatiotemporal dynamics of freely diffusing glutamate is reflected in how this distribution changes in time (see section "Discussion"). In the hippocampus, where astroglial presence is three times lower, the glutamate profile does change from 0.1 to 1 ms post-release, allowing for a more widespread "tail" of diffusing molecules, even though the majority of them still remain bound in close proximity to the cleft (**Figure 2B**).

The Effect of Extracellular Space Shrinkage or Expansion

It has long been known that during intense excitatory activity, or in some pathological conditions such as epilepsy or ischemia, the extracellular space of the brain can shrink (Lux et al., 1986; Vorisek and Sykova, 1997; Vargova et al., 2001; Witcher et al., 2010). We have therefore asked whether such changes could significantly affect extrasynaptic escape of glutamate, by repeating our simulations for reduced porosity values. As expected, decreasing tissue porosity α from 0.2 to 0.1 and further to 0.05 led to a lower number of molecules escaping away from the cleft. However, the main feature of glutamate escape, its intense binding in cleft proximity, remained (**Figures 2C,D**).

Finally, we asked what could happen when the extracellular space is significantly expanded, which is thought to be the case during postnatal development (Lehmenkuhler et al., 1993), but also in the human cerebellum (Cragg, 1979). Simulations adopting $\alpha = 0.5$ still indicated perisynaptic binding as a prevalent feature even though glutamate molecules have a significantly wider spread, and a longer free-diffusion span than in cases with lower α (**Figure 3**).

DISCUSSION

Scope and Limitations

It this study we asked which aspects of the perisynaptic environment are prevalent in controlling glutamate escape from excitatory synapses. Our primary purpose was therefore to understand whether geometric hindrance by tissue elements, and high-affinity binding by glutamate transporters, play comparable roles, in this context. The goal was neither to firmly establish the "true" glutamate escape profile for a particular synaptic type nor to expand such claims to various synaptic types featuring varied morphologies. The modelling relied on several basic assumptions, such as (a) single-vesicle glutamate release hence non-saturation of local glutamate transporters, (b) random distribution of glial and non-glial cellular surfaces in the neuropil, with the ratio established purely by the probability of encountering one or the other surface, and (c) negligible binding inside the synaptic cleft (numbers of glutamate receptors much smaller than that of released glutamate molecules). Clearly, these assumptions impose certain interpretability limitations: repetitive synaptic discharges or highly asymmetric occurrence of perisynaptic astroglia may produce a somewhat different dynamic picture of glutamate escape.

Empirical Relevance

Our estimates are generally consistent with the previous theoretical assessments that used alternative modelling

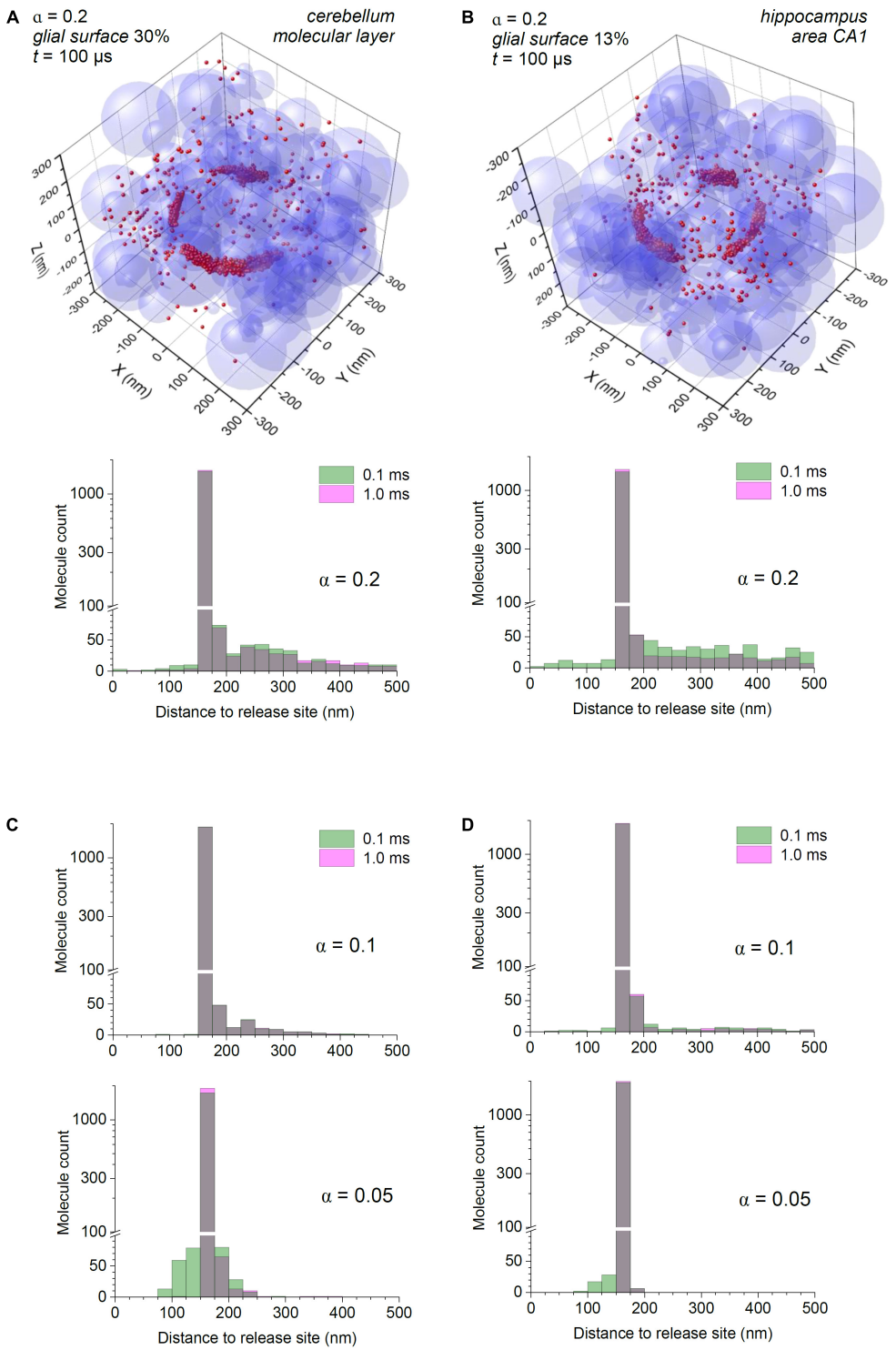

FIGURE 2 | Astroglial high-affinity transporters control the scatter of escaping glutamate molecules in the modelled cerebellar and hippocampal neuropil. **(A)** Simulations as in **Figure 1B**, with the synaptic cleft (diameter 320 nm, height 20 nm) placed in the co-ordinate origin (also glutamate release site); particle-surface binding enabled, for each particle with probability of 0.3 (to mimic 30% chance of encountering cell membranes representing astroglia); medium porosity α = 0.2. Histogram: spatial distribution of glutamate molecules (free and transporter-bound combined) across the simulation arena, at two time points post-release, as indicated; note two scales (one log-scale) of the ordinate. **(B)** Simulations as in **(A)**, with the particle-surface binding enabled, for each particle with probability of 0.13 (to mimic 13% of neuropil cell membranes representing astroglia); other notations as in **(A)**. **(C)** Simulation outcome (molecule distribution histograms) for the model shown **(A)**, but with tissue porosity values α = 0.1 and α = 0.05, as indicated); other notations as in **(A)**. **(D)** Simulation outcome (molecule distribution histograms) for the model shown **(B)**, but with tissue porosity values α = 0.1 and α = 0.05, as indicated); other notations as in **(B)**.

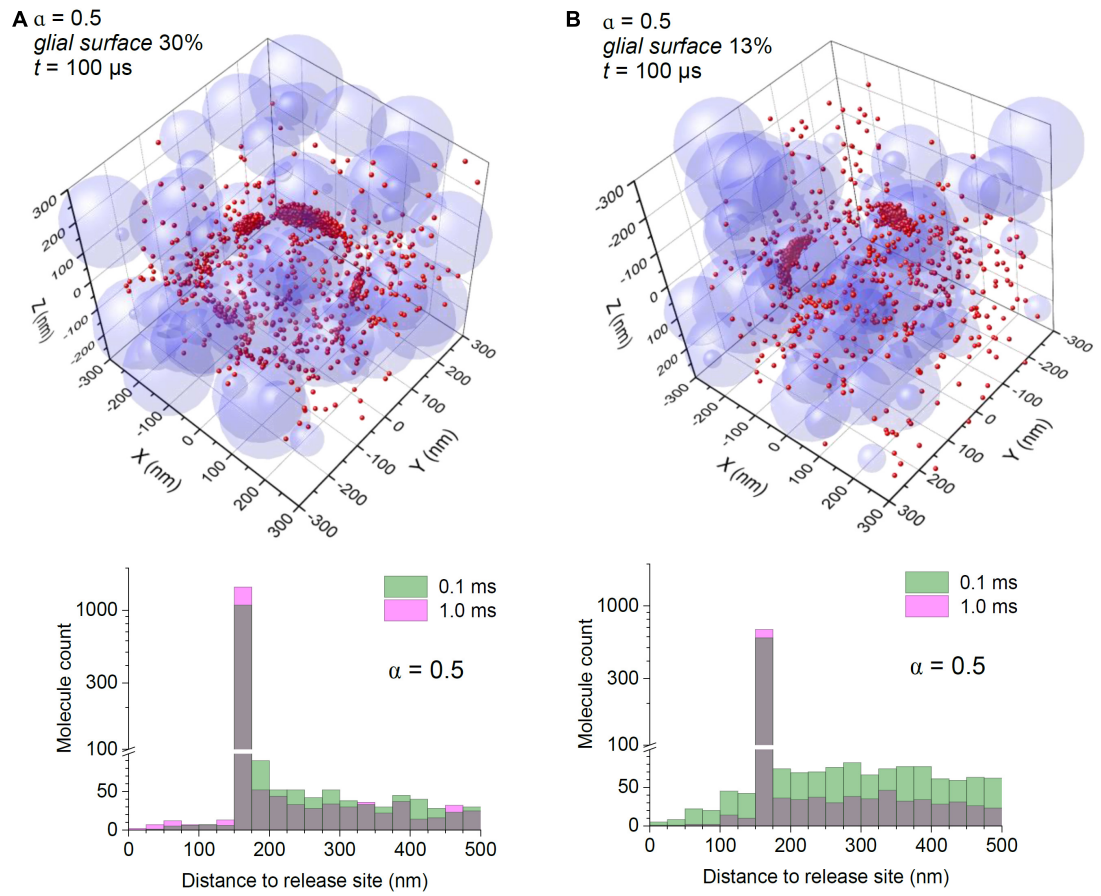

FIGURE 3 | Astroglial high-affinity transporters control the scatter of escaping glutamate molecules under conditions of expanded extracellular space. **(A)** Simulations as in **Figure 2**, with the particle-surface binding enabled, for each particle with probability of 0.3 (to mimic 30% chance of encountering cell membranes representing astroglia); tissue porosity α = 0.5; other notations as in **Figure 2A**. **(B)** Simulations as in **(A)**, but with the particle-surface binding enabled, for each particle with probability of 0.13 (to mimic 13% of neuropil cell membranes representing astroglia); other notations as in **(A)**.

approaches (Scimemi et al., 2004; Zheng et al., 2008; Scimemi et al., 2009; Zheng and Rusakov, 2015; Armbruster et al., 2020) predicting a very rapid fall of free glutamate concentration the cleft. However, the distributions of mainly bound molecules obtained here could be particularly relevant to the experimental measurements of extrasynaptic glutamate escape using optical glutamate sensors (Hires et al., 2008; Jensen et al., 2019; Armbruster et al., 2020; Henneberger et al., 2020). Because such sensors feature the glutamate binding rate on the same scale as do glutamate transporters, one could simply assume that in our simulations a proportion of the binding sites represents glutamate sensors. In this case, the local sensor/transporter concentration ratio would reflect the ratio of glutamate molecules bound to the two respective targets. In other words, assuming no significant difference between the spatial arrangement of either transporters and sensors (e.g., as in the case of astroglia-expressing iGluSnFR), the distribution profiles obtained here for bound glutamate molecules should be equally relevant to sensor-bound molecules.

One may argue that the experimental fluorescence profiles of glutamate-bound iGluSnFR around synapses are much smoother, and with no "voids" indicating the synaptic cleft, compared with the profiles shown here (Jensen et al., 2019). However, this is most likely because fluorescence signal is blurred over the point-spread function of an optical system (~0.4 µm in the *xy* plane and ~1 µm in the *z* direction), and because imaged synapses will have their cleft randomly oriented with respect to the focal plane. Exploring 3D simulation results by mimicking optical projections to match a particular imaging setting should bring theoretical findings closer to a faithful representation of experimental readout.

In this context, one novelty element of the present simulations is tissue modelling that uses randomly sized, randomly positioned intersecting spheres. As explained in the section "Methods," we believe that this approach should provide a fairer representation of brain neuropil than would regular lattices of regular shapes that we and others employed previously. Also, we presented examples of individual trials rather than averaged outcome because "average synapse geometry" is a non-existing entity in which important "outlier" features of perisynaptic architecture could be unduly smoothed out. We therefore considered it intuitively more revealing, in this particular case, to illustrate individual Monte Carlo realisations.

Extracellular Space in Pathology

Our basic results suggest that glutamate transporters can efficiently restrict glutamate diffusion even when the diffusion escape passages are relatively open. As mentioned, dynamic changes of the extracellular space volume, such as its transient or long-term shrinkage, have long been associated with pathological brain conditions such as in epilepsy or stroke (Lux et al., 1986; Vorisek and Sykova, 1997; Sykova, 2001; Vargova et al., 2001; Witcher et al., 2010). At the same time, physiological studies of neurodegenerative diseases, stroke, or addiction have found reduced expression of glial glutamate transporters in brain tissue (Maragakis and Rothstein, 2004; Fontana, 2015; Kruyer et al., 2019), which normally undergo rapid recycling on astroglial surfaces (Michaluk et al., 2021). The present results suggests that, over a wide range of tissue porosities, high-affinity transporters remain the principal factor in curtailing glutamate escape. Thus, the availability of high-affinity glutamate transporters appears a prevalent mechanism to control extrasynaptic actions of glutamate in pathological conditions affecting brain tissue architectonics.

DATA AVAILABILITY STATEMENT

The original contributions presented in the study are included in the article/**Supplementary Material**, further inquiries can be directed to the corresponding author/s.

AUTHOR CONTRIBUTIONS

LS designed and carried out computer simulations. KZ designed and provided cluster computing facilities. DR narrated the study, designed specific tests, and wrote the manuscript. All authors contributed to the article and approved the submitted version.

FUNDING

This work was supported by the Wellcome Trust Principal Fellowship (212251_Z_18_Z), ERC Advanced Grant (323113), and European Commission NEUROTWIN grant (857562), to DR.

ACKNOWLEDGMENTS

Parallelisation and optimisation of the algorithms and program codes were implemented by AMC Bridge LLC (Waltham, MA).

SUPPLEMENTARY MATERIAL

The Supplementary Material for this article can be found online at: https://www.frontiersin.org/articles/10.3389/fncel.2021.707813/full#supplementary-material

REFERENCES

Armbruster, M., Dulla, C. G., and Diamond, J. S. (2020). Effects of fluorescent glutamate indicators on neurotransmitter diffusion and uptake. *Elife* 9:e54441.

Barbour, B. (1993). Synaptic currents evoked in purkinje-cells by stimulating individual granule cells. *Neuron* 11, 759–769. doi: 10.1016/0896-6273(93)90085-6

Bazargani, N., and Attwell, D. (2016). Astrocyte calcium signaling: the third wave. *Nat. Neurosci.* 19, 182–189. doi: 10.1038/nn.4201

Bergles, D. E., Tzingounis, A. V., and Jahr, C. E. (2002). Comparison of coupled and uncoupled currents during glutamate uptake by GLT-1 transporters. *J. Neurosci.* 22, 10153–10162. doi: 10.1523/jneurosci.22-23-10153.2002

Bernardinelli, Y., Muller, D., and Nikonenko, I. (2014). Astrocyte-synapse structural plasticity. *Neural Plast.* 2014:232105.

Borst, J. G., and Soria van Hoeve, J. (2012). The calyx of held synapse: from model synapse to auditory relay. *Annu. Rev. Physiol.* 74, 199–224. doi: 10.1146/annurev-physiol-020911-153236

Cragg, B. (1979). Overcoming the failure of electron-microscopy to preserve the brains extracellular-space. *Trends Neurosci.* 2, 159–161. doi: 10.1016/0166-2236(79)90062-6

Diamond, J. S. (2001). Neuronal glutamate transporters limit activation of NMDA receptors by neurotransmitter spillover on CA1 pyramidal cells. *J. Neurosci.* 21, 8328–8338. doi: 10.1523/jneurosci.21-21-08328.2001

Fontana, A. C. (2015). Current approaches to enhance glutamate transporter function and expression. *J. Neurochem.* 134, 982–1007. doi: 10.1111/jnc.13200

Gavrilov, N., Golyagina, I., Brazhe, A., Scimemi, A., Turlapov, V., and Semyanov, A. (2018). Astrocytic coverage of dendritic spines, dendritic shafts, and axonal boutons in hippocampal neuropil. *Front. Cell Neurosci.* 12:248.

Grosche, J., Matyash, V., Moller, T., Verkhratsky, A., Reichenbach, A., and Kettenmann, H. (1999). Microdomains for neuron-glia interaction: parallel fiber signaling to Bergmann glial cells. *Nat. Neurosci.* 2, 139–143. doi: 10.1038/5692

Harris, K. M., Jensen, F. E., and Tsao, B. (1992). Three-dimensional structure of dendritic spines and synapses in rat hippocampus (CA1) at postnatal day 15 and adult ages: implications for the maturation of synaptic physiology and long-term potentiation. *J. Neurosci.* 12, 2685–2705. doi: 10.1523/jneurosci.12-07-02685.1992

Harris, K. M., and Stevens, J. K. (1989). Dendritic spines of CA 1 pyramidal cells in the rat hippocampus: serial electron microscopy with reference to their biophysical characteristics. *J. Neurosci.* 9, 2982–2997. doi: 10.1523/jneurosci.09-08-02982.1989

Heller, J. P., and Rusakov, D. A. (2015). Morphological plasticity of astroglia: Understanding synaptic microenvironment. *Glia* 63, 2133–2151. doi: 10.1002/glia.22821

Henneberger, C., Bard, L., Panatier, A., Reynolds, J. P., Kopach, O., Medvedev, N. I., et al. (2020). LTP induction boosts glutamate spillover by driving withdrawal of perisynaptic astroglia. *Neuron* 108:e911.

Hires, S. A., Zhu, Y., and Tsien, R. Y. (2008). Optical measurement of synaptic glutamate spillover and reuptake by linker optimized glutamate-sensitive fluorescent reporters. *Proc. Natl. Acad. Sci. U.S.A.* 105, 4411–4416. doi: 10.1073/pnas.0712008105

Hrabe, J., Hrabetova, S., and Segeth, K. (2004). A model of effective diffusion and tortuosity in the extracellular space of the brain. *Biophys. J.* 87, 1606–1617. doi: 10.1529/biophysj.103.039495

Jensen, T. P., Zheng, K. Y., Cole, N., Marvin, J. S., Looger, L. L., and Rusakov, D. A. (2019). Multiplex imaging relates quantal glutamate release to presynaptic Ca2+ homeostasis at multiple synapses in situ. *Nat. Commun.* 10:1414.

Kruyer, A., Scofield, M. D., Wood, D., Reissner, K. J., and Kalivas, P. W. (2019). Heroin cue-evoked astrocytic structural plasticity at nucleus accumbens synapses inhibits heroin seeking. *Biol. Psychiatry* 86, 811–819. doi: 10.1016/j.biopsych.2019.06.026

Lehmenkuhler, A., Sykova, E., Svoboda, J., Zilles, K., and Nicholson, C. (1993). Extracellular-space parameters in the rat neocortex and subcortical white-matter during postnatal-development determined by diffusion analysis. *Neuroscience* 55, 339–351. doi: 10.1016/0306-4522(93)90503-8

Lehre, K. P., and Danbolt, N. C. (1998). The number of glutamate transporter subtype molecules at glutamatergic synapses: chemical and stereological quantification in young adult rat brain. *J. Neurosci.* 18, 8751–8757. doi: 10.1523/jneurosci.18-21-08751.1998

Lehre, K. P., and Rusakov, D. A. (2002). Asymmetry of glia near central synapses favors presynaptically directed glutamate escape. *Biophys. J.* 83, 125–134. doi: 10.1016/s0006-3495(02)75154-0

Lushnikova, I., Skibo, G., Muller, D., and Nikonenko, I. (2009). Synaptic potentiation induces increased glial coverage of excitatory synapses in CA1 hippocampus. *Hippocampus* 19, 753–762. doi: 10.1002/hipo.20551

Lux, H. D., Heinemann, U., and Dietzel, I. (1986). Ionic changes and alterations in the size of the extracellular space during epileptic activity. *Adv. Neurol.* 44, 619–639.

Maragakis, N. J., and Rothstein, J. D. (2004). Glutamate transporters: animal models to neurologic disease. *Neurobiol. Dis.* 15, 461–473. doi: 10.1016/j.nbd.2003.12.007

Medvedev, N., Popov, V., Henneberger, C., Kraev, I., Rusakov, D. A., and Stewart, M. G. (2014). Glia selectively approach synapses on thin dendritic spines. *Philos. Trans. R. Soc. Lond. B Biol. Sci.* 369:20140047. doi: 10.1098/rstb.2014.0047

Michaluk, P., Heller, J. P., and Rusakov, D. A. (2021). Rapid recycling of glutamate transporters on the astroglial surface. *Elife* 10:64714.

Murphy-Royal, C., Dupuis, J., Groc, L., and Oliet, S. H. R. (2017). Astroglial glutamate transporters in the brain: Regulating neurotransmitter homeostasis and synaptic transmission. *J. Neurosci. Res.* 95, 2140–2151. doi: 10.1002/jnr.24029

Nicholson, C., and Phillips, J. M. (1981). Ion diffusion modified by tortuosity and volume fraction in the extracellular micro-environment of the rat cerebellum. *J. Physiol. Lond.* 321, 225–257. doi: 10.1113/jphysiol.1981.sp013981

Pannasch, U., Freche, D., Dallerac, G., Ghezali, G., Escartin, C., Ezan, P., et al. (2014). Connexin 30 sets synaptic strength by controlling astroglial synapse invasion. *Nat. Neurosci* 17, 549–558. doi: 10.1038/nn.3662

Patrushev, I., Gavrilov, N., Turlapov, V., and Semyanov, A. (2013). Subcellular location of astrocytic calcium stores favors extrasynaptic neuron-astrocyte communication. *Cell Calcium* 54, 343–349. doi: 10.1016/j.ceca.2013.08.003

Paviolo, C., Soria, F. N., Ferreira, J. S., Lee, A., Groc, L., Bezard, E., et al. (2020). Nanoscale exploration of the extracellular space in the live brain by combining single carbon nanotube tracking and super-resolution imaging analysis. *Methods* 174, 91–99. doi: 10.1016/j.ymeth.2019.03.005

Pilgrim, C., Reisert, I., and Grab, D. (1982). Volume densities and specific surfaces of neuronal and glial tissue elements in the rat supraoptic nucleus. *J. Comp. Neurol.* 211, 427–431. doi: 10.1002/cne.902110409

Rollenhagen, A., Satzler, K., Rodriguez, E. P., Jonas, P., Frotscher, M., and Lubke, J. H. (2007). Structural determinants of transmission at large hippocampal mossy fiber synapses. *J. Neurosci.* 27, 10434–10444. doi: 10.1523/jneurosci.1946-07.2007

Rose, C. R., Felix, L., Zeug, A., Dietrich, D., Reiner, A., and Henneberger, C. (2017). Astroglial glutamate signaling and uptake in the hippocampus. *Front. Mol. Neurosci.* 10:451.

Rusakov, D. A. (2001). The role of perisynaptic glial sheaths in glutamate spillover and extracellular Ca2+ depletion. *Biophys. J.* 81, 1947–1959. doi: 10.1016/s0006-3495(01)75846-8

Savtchenko, L. P., Bard, L., Jensen, T. P., Reynolds, J. P., Kraev, I., Medvedev, N., et al. (2018). Disentangling astroglial physiology with a realistic cell model in silico. *Nat. Commun.* 9:3554.

Savtchenko, L. P., Sylantyev, S., and Rusakov, D. A. (2013). Central synapses release a resource-efficient amount of glutamate. *Nat. Neurosci.* 16, 10–U163.

Savtchenko, L. P., Zheng, K., and Rusakov, D. A. (2021). Conductance of porous media depends on external electric fields. *Biophys. J.* 120, 1431–1442. doi: 10.1016/j.bpj.2021.02.012

Scimemi, A., Fine, A., Kullmann, D. M., and Rusakov, D. A. (2004). NR2B-containing receptors mediate cross talk among hippocampal synapses. *J. Neurosci.* 24, 4767–4777. doi: 10.1523/jneurosci.0364-04.2004

Scimemi, A., Tian, H., and Diamond, J. S. (2009). Neuronal transporters regulate glutamate clearance. NMDA receptor activation, and synaptic plasticity in the hippocampus. *J. Neurosci.* 29, 14581–14595. doi: 10.1523/jneurosci.4845-09.2009

Spacek, J., and Harris, K. M. (1998). Three-dimensional organization of cell adhesion junctions at synapses and dendritic spines in area CA1 of the rat hippocampus. *J. Comp. Neurol.* 393, 58–68. doi: 10.1002/(sici)1096-9861(19980330)393:1<58::aid-cne6>3.0.co;2-p

Suhling, K., Hirvonen, L. M., Levitt, J. A., Chung, P.-H., Tregidgo, C., Le Marois, A., et al. (2015). Fluorescence lifetime imaging (FLIM): basic concepts and some recent developments. *Med. Photon.* 27, 3–40. doi: 10.1016/j.medpho.2014.12.001

Sykova, E. (2001). Glial diffusion barriers during aging and pathological states. *Prog. Brain Res.* 132, 339–363. doi: 10.1016/s0079-6123(01)32087-3

Sykova, E., and Nicholson, C. (2008). Diffusion in brain extracellular space. *Physiol. Rev.* 88, 1277–1340. doi: 10.1152/physrev.00027.2007

Sylantyev, S., Savtchenko, L. P., Ermolyuk, Y., Michaluk, P., and Rusakov, D. A. (2013). Spike-driven glutamate electrodiffusion triggers synaptic potentiation via a homer-dependent mGluR-NMDAR link. *Neuron* 77, 528–541. doi: 10.1016/j.neuron.2012.11.026

Szapiro, G., and Barbour, B. (2007). Multiple climbing fibers signal to molecular layer interneurons exclusively via glutamate spillover. *Nat. Neurosci.* 10, 735–742. doi: 10.1038/nn1907

Tartakovsky, D. M., and Dentz, M. (2019). Diffusion in Porous Media: Phenomena and Mechanisms. *Transport Porous Media* 130, 105–127. doi: 10.1007/s11242-019-01262-6

Thorne, R. G., and Nicholson, C. (2006). In vivo diffusion analysis with quantum dots and dextrans predicts the width of brain extracellular space. *Proc. Natl. Acad. Sci. U.S.A.* 103, 5567–5572. doi: 10.1073/pnas.0509425103

Tonnesen, J., Inavalli, V. V. G. K., and Nagerl, U. V. (2018). Super-resolution imaging of the extracellular space in living brain tissue. *Cell* 172, 1108–1121. doi: 10.1016/j.cell.2018.02.007

Vargova, L., Jendelova, P., Chvatal, A., and Sykova, E. (2001). Glutamate, NMDA, and AMPA induced changes in extracellular space volume and tortuosity in the rat spinal cord. *J. Cereb. Blood Flow Metab.* 21, 1077–1089. doi: 10.1097/00004647-200109000-00005

Ventura, R., and Harris, K. M. (1999). Three-dimensional relationships between hippocampal synapses and astrocytes. *J. Neurosci.* 19, 6897–6906. doi: 10.1523/jneurosci.19-16-06897.1999

Verkhratsky, A., and Nedergaard, M. (2018). Physiology of astroglia. *Physiol. Rev.* 98, 239–389. doi: 10.1152/physrev.00042.2016

Vorisek, I., and Sykova, E. (1997). Ischemia-induced changes in the extracellular space diffusion parameters, K+, and pH in the developing rat cortex and corpus callosum. *J. Cereb. Blood Flow Metab.* 17, 191–203. doi: 10.1097/00004647-199702000-00009

Witcher, M. R., Kirov, S. A., and Harris, K. M. (2007). Plasticity of perisynaptic astroglia during synaptogenesis in the mature rat hippocampus. *Glia* 55, 13–23. doi: 10.1002/glia.20415

Witcher, M. R., Park, Y. D., Lee, M. R., Sharma, S., Harris, K. M., and Kirov, S. A. (2010). Three-dimensional relationships between perisynaptic astroglia and human hippocampal synapses. *Glia* 58, 572–587.

Zheng, K., and Rusakov, D. A. (2015). Efficient integration of synaptic events by NMDA receptors in three-dimensional neuropil. *Biophys. J.* 108, 2457–2464. doi: 10.1016/j.bpj.2015.04.009

Zheng, K., Scimemi, A., and Rusakov, D. A. (2008). Receptor actions of synaptically released glutamate: the role of transporters on the scale from nanometers to microns. *Biophys. J.* 95, 4584–4596. doi: 10.1529/biophysj.108.129874

Zheng, K. Y., Jensen, T. P., Savtchenko, L. P., Levitt, J. A., Suhling, K., and Rusakov, D. A. (2017). Nanoscale diffusion in the synaptic cleft and beyond measured with time-resolved fluorescence anisotropy imaging. *Sci. Rep.* 7:42022.

Conflict of Interest: The authors declare that the research was conducted in the absence of any commercial or financial relationships that could be construed as a potential conflict of interest.

Publisher's Note: All claims expressed in this article are solely those of the authors and do not necessarily represent those of their affiliated organizations, or those of the publisher, the editors and the reviewers. Any product that may be evaluated in this article, or claim that may be made by its manufacturer, is not guaranteed or endorsed by the publisher.

frontiers in Cellular Neuroscience

ORIGINAL RESEARCH
published: 26 August 2021
doi: 10.3389/fncel.2021.681539

Prolonged Amphetamine Exposures Increase the Endogenous Human Dopamine Receptors 2 at the Cellular Membrane in Cells Lacking the Dopamine Transporter

*Vindhya Nawaratne[1], Sean P. McLaughlin[2], Felix P. Mayer[2], Zayna Gichi[2], Alyssa Mastriano[1] and Lucia Carvelli[1,2]**

[1] Department of Biology, Harriet L. Wilkes Honors College, Florida Atlantic University, Jupiter, FL, United States, [2] Brain Institute, Florida Atlantic University, Jupiter, FL, United States

OPEN ACCESS

Edited by:
Annalisa Scimemi, University at Albany, United States

Reviewed by:
James Foster, University of North Dakota, United States
Claus Loland, University of Copenhagen, Denmark

***Correspondence:**
Lucia Carvelli
lcarvelli@fau.edu

Specialty section:
This article was submitted to Cellular Neurophysiology, a section of the journal Frontiers in Cellular Neuroscience

Received: *16 March 2021*
Accepted: *03 August 2021*
Published: *26 August 2021*

Citation:
Nawaratne V, McLaughlin SP, Mayer FP, Gichi Z, Mastriano A and Carvelli L (2021) Prolonged Amphetamine Exposures Increase the Endogenous Human Dopamine Receptors 2 at the Cellular Membrane in Cells Lacking the Dopamine Transporter. Front. Cell. Neurosci. 15:681539. doi: 10.3389/fncel.2021.681539

The dopamine 2 receptors (D2R) are G-protein coupled receptors expressed both in pre- and post-synaptic terminals that play an important role in mediating the physiological and behavioral effects of amphetamine (Amph). Previous studies have indicated that the effects of Amph at the D2R mainly rely on the ability of Amph to robustly increase extracellular dopamine through the dopamine transporter (DAT). This implies that the effects of Amph on D2R require the neurotransmitter dopamine. However, because of its lipophilic nature, Amph can cross the cellular membrane and thus potentially affect D2R expression independently of dopamine and DAT, *e.g.,* in post-synaptic terminals. Here we used an *in vitro* system to study whether Amph affects total expression, cellular distribution, and function of the human D2R (hD2R), endogenously expressed in HEK293 cells. By performing Western blot experiments, we found that prolonged treatments with 1 or 50 μM Amph cause a significant decrease of the endogenous hD2R in cells transfected with human DAT (hDAT). On the other hand, in cells lacking expression of DAT, quantification of the hD2R-mediated changes in cAMP, biotinylation assays, Western blots and imaging experiments demonstrated an increase of hD2R at the cellular membrane after 15-h treatments with Amph. Moreover, imaging data suggested that barbadin, a specific inhibitor of the βarrestin-βadaptin interaction, blocked the Amph-induced increase of hD2R. Taken together our data suggest that prolonged exposures to Amph decrease or increase the endogenous hD2R at the cellular membrane in HEK293 cells expressing or lacking hDAT, respectively. Considering that this drug is often consumed for prolonged periods, during which tolerance develops, our data suggest that even in absence of DAT or dopamine, Amph can still alter D2R distribution and function.

Keywords: amphetamine, dopamine receptors, G-protein coupled receptors, cAMP, dopamine transporter

INTRODUCTION

Amphetamine (Amph) is a psychostimulant broadly prescribed as long-term therapy for attention deficit hyperactivity disorder (ADHD). Moreover, Amph and Amph-like drugs are commonly abused as recreational drugs and performance enhancers. Despite decades of active research, the exact molecular mechanism(s) of Amph and its analogs remain far from being completely understood. Numerous studies have shown that Amph alters the function of various proteins in the brain, and, among others, proteins linked to the dopamine signaling are major targets. In fact, *in vivo* and *in vitro* experiments have shown that proteins expressed in dopaminergic neurons, such as the dopamine transporter (DAT) and the type 2 dopamine receptors (D2R) are altered during and after Amph treatments (Sulzer, 2011; Ashok et al., 2017). Because dopamine is highly involved in the action of addictive drugs – all drugs of abuse increase synaptic dopamine – it is not surprising that this drug alters the function of DAT and D2R. In fact, these two proteins are key players of dopamine transmission. DAT, for example, by restricting the spatial and temporal action of dopamine and, thus, ensuring fast clearance of extracellular dopamine, is a direct target of Amph. As matter of fact, Amph is a DAT substrate through which Amph gets quick access inside the neurons. The intracellular accumulation of Amph causes several detrimental consequences *e.g.*, reduction of the transporters at the cellular membrane (Saunders et al., 2000), depletion of vesicular dopamine stores and reverse transport of dopamine through DAT (Carvelli et al., 2010; Sulzer, 2011), ultimately causing an increase of DAT- and vesicle-mediated (Daberkow et al., 2013) dopamine release.

Since Amph increases extracellular dopamine, one anticipated consequence of continuous dopamine overflow in the synaptic cleft is the indirect effect of Amph at the dopaminergic receptors. The D2R are located at both pre- and post-synaptic neuronal terminals and the D2R-containing pre-synaptic terminals express DAT as well. Previous findings revealed that the D2R are involved in the reinforcing properties of drugs of abuse (Andrianarivelo et al., 2019), and animals lacking expression of the D2R exhibit reduced Amph-induced behaviors (Carvelli et al., 2010; Solís et al., 2021). Recent studies in human beings also reported that Amph users exhibit significant changes in D2/D3 receptors availability (Ashok et al., 2017). Taken together, these data strongly suggest that the D2R play an important role in mediating the physiological and behavioral changes caused by Amph.

As with most G-protein coupled receptors (GPCR), the activity of the D2R can be regulated by desensitization. Continuous stimulation leads to uncoupling of the receptor from the G-protein, binding to arrestin and receptor internalization (Gainetdinov et al., 2004). While the Amph-induced redistribution of DAT from and to the cell membrane has been well documented (Saunders et al., 2000; Boudanova et al., 2008; Lute et al., 2008; Daberkow et al., 2013; Wheeler et al., 2015), the effects of Amph on D2R redistribution are controversial. For example, some groups have shown an increase in striatal D2R after a 14-day regimen (Levy et al., 1988) or repeated daily treatments (Kilbourna and Dominob, 2011) with Amph, whereas others have found a decrease (Kamata and Rebec, 1984) or no change (Bonhomme et al., 1995). Moreover, Calipari et al. (2014) showed that 5 days of *ad libitum* Amph intake reduced the ability of quinpirole to inhibit dopamine release and, simultaneously, abolished the interaction between the pre-synaptic D2R and the GPCR subunit Gαi2, in rat midbrain, but not in the striatum. These results suggest that Amph affects the D2R located in some, but not all, areas of the brain expressing the D2R (Calipari et al., 2014). The diverging results reported above might reflect the complexity of Amph action, particularly, when this drug is investigated in complex animals such as murine models. For example, the effects of Amph at the D2R located in post-synaptic terminals could be different than those observed in pre-synaptic terminals. To overcome these limitations, we performed a set of experiments to test *in vitro* whether D2R function and distribution were altered following prolonged treatments with physiologically relevant concentrations of Amph. Using a cell line which endogenously expresses human D2R (hD2R), we found that when cells were transfected with hDAT, 15 h of continuous exposure to Amph significantly decreased the expression of endogenous D2R. On the other hand, cells devoid of hDAT exhibited an increase of endogenous D2R in the cellular membrane in absence of dopamine. In these cells, the Amph-induced increase of D2R was confirmed using surface biotinylation assays and confocal microscopy imaging. Also, functional data showed that after D2R activation, the forskolin-mediated cAMP production was significantly decreased in samples treated with Amph for 15 h, again suggesting an increased number of functional D2R at the cellular membrane in cells lacking expression of hDAT and in absence of dopamine. Thus, our results show that Amph, because of its lipophilic nature, might directly affect D2R distribution during prolonged treatments.

MATERIALS AND METHODS

Cell Cultures

Human embryonic kidney 293T (HEK293) cells were cultured in Dulbecco's Modified Eagle's Medium (DMEM; 10569-010, Gibco) supplemented with 10% fetal bovine serum (FBS 16000-4, Gibco) and 1% penicillin/streptomycin (15140-122, Gibco). To confirm the specificity of the D2R antibody or for our cAMP assays, HEK293 cells were transiently transfected with 2.5 μg cDNA of Flag-D2R using TransIT®-LT1 Transfection Reagent (MIR2305, Mirus). The Flag-D2R cDNA was a generous gift from Dr. Jonathan Javitch – Columbia University. Twenty-four hours after transfection, cells were treated with control or Amph for 15 h. HEK293 cells stably expressing hDAT (gift from Randy Blakely – Florida Atlantic University) were additionally supplemented with 250 ug/ml G418 (30-234-Cl, Corning) to maintain the selection pressure. Cells were dissociated using 0.25% trypsin diluted with versene (2 mM EDTA in PBS) and maintained in a humidified incubator with 5% CO_2 at 37°C.

Western Blot Assays

HEK293 cells (0.9 – 1.1 million cells/well) were seeded in 6-well plates. After 24 h, cells were treated with control, 1 or 50 μM

Amph for 15 h, then collected using versene (2 mM EDTA in PBS) and counted. Six million cells from each treatment group were solubilized with 100 μL of lysis buffer (20 mM Hepes pH 7.4, 100 mM NaCl, 1.5 mM MgCl2, 1 mM EDTA, 1 mM EGTA, 0.1% NP40, and proteases/phosphatases inhibitors), passed through a 29-gage needle 25 times and centrifuged for 10 min at 12,000 × *g*. Total amount of proteins in the supernatant was quantified with Pierce™ BCA Protein Assay Kit (23225, Thermo Scientific™). Lysates (30 μg) were denatured with sample buffer containing 20 mM DTT for 1 h, loaded and run on SDS-PAGE gels at 120 V for 2 h and the proteins transferred into PVDF membranes (IPVH00010, Millipore) at 35 V for 16 h at 4°C. The blots were first exposed to the hD2R antibody (1:1000, AB5084P, Sigma-Aldrich) and then detected with an anti-rabbit HRP (1:3000, 65-6120, Invitrogen) and ECL (34577, Thermo Scientific™). The same blots were then probed with a β-actin antibody (1:2000, sc-69879, Santa Cruz) and detected with an anti-mouse IRDye® 680RD (1:10000, 925-68072, LI-COR Biosciences). Images were quantified using Image Studio LI-COR Biosciences. For each gel, sample data were normalized to β-actin bands. Because the amount of D2R with higher molecular weights (75–130 kDa) was more concentrated than those at lower molecular weights (40 kDa), PVDF membranes had different exposure times during band acquisition. This guaranteed a detectable signal for the bands at lower molecular weights, and at the same time, the upper bands were not overexposed.

Confocal Microscopy

Confocal microscopy was performed using a Nikon A1R confocal microscope in the FAU-Brain Institute using a 60× oil-immersion objective and Nikon capture software. HEK293 cells were seeded at 40,000 cells/well in 8 well glass bottom μ-slides (80827, Ibidis) and grown over night. After treating with control, 1 μM or 50 μM Amph with or without 20 μM barbadin for 15 h, cells were fixed for 20 min at room temperature with 3.5% formaldehyde (28906, Thermo Scientific™) prepared in 50% phosphate-buffered saline (PBS), 4% sucrose and 2.5 mM $CaCl_2$. Samples were kept at room temperature for the rest of the experiment. After fixation, cells were washed 3 times with PBS, blocked with 1% BSA in PBS, and stained for 90 min with Anti-Na^+/K^+ ATPase α-1 antibody (05-369, Sigma-Aldrich) diluted to 1:200. Cells were then washed with PBS 3 times to eliminate any unbound antibody and permeabilized with 0.1% saponin and 0.2% BSA in PBS for 30 min. Saponin solution was removed, and cells were incubated for 90 min with the D2R antibody (AB5084P, Sigma-Aldrich) at a final dilution of 1:1000. Samples were washed 3 times with PBS, incubated with anti-mouse Alexa Fluor 405 (A31553, Invitrogen) and anti-rabbit Alexa Fluor 546 (A10040, Invitrogen) secondary antibodies for 30 min. Alexa Fluor 405 and anti-rabbit Alexa Fluor 546 were stimulated using 405 and 561 laser lines, respectively, and detected through DAPI and TRITC filters, respectively. Acquisition of the two fluorophores was done sequentially to prevent cross talk. 2D optical sections of 0.2 or 0.5 μm were acquired using a Nikon A1R HD Galvano scanner. Image deconvolution, figure imaging and fluorescence quantification were performed with FIJI software (ImageJ, NIH). For quantification analysis of the D2R at the cellular membrane and cytoplasm, images of the Na^+/K^+ ATPase antibody (yellow stain) were used to define the cell surface as regions of interest (RoI). These RoI were overlayed onto the images of the same cells labeled with the D2R antibody (cyan stain). Max fluorescence values of the cellular membrane (the RoI) and the cytoplasm (the intracellular region) were measured with ImageJ. Max fluorescence values were used instead of mean fluorescence because some of our cell images (**Figures 2D–K**) exhibited one or more black areas (most likely the nucleus) within the cytoplasm. Inclusion of these black areas in our quantification would have created random artifacts in our analyses. Fluorescence values are reported as the average of at least 3 independent experiments ± SEM.

Cell Surface Biotinylation Assays

After 15-h treatments with/without 1 μM Amph, proteins at the cellular membrane of approximately 8 million HEK293 cells, grown in PDL coated T-75 flasks, were biotinylated with the membrane-impermeant reagent Sulfo-NHS-LC-Biotin (Thermo Fisher, Cat. No 21335) in PBS containing 1 mM $MgCl_2$, 0.1 mM $CaCl_2$ (PBS^{2+}) for 45 min at 4°C. Cells were subsequently washed twice with ice cold PBS^{2+}, lysed in RIPA buffer (supplemented with 1% Triton X-100 and 1% protease inhibitors - Millipore Sigma, Cat No. P8340), and cleared by centrifugation (15 min at 13,000 × *g*). To separate biotinylated proteins from non-biotinylated proteins, 600-1800 ug of total protein were exposed to NeutrAvidin agarose beads (ThermoFisher, Cat No. 29201) for 16 h at 4°C at constant nutation. Prior to the addition of protein, beads were washed 3 times with ice-cold RIPA buffer (supplemented with 1% Triton-X 100 and protease inhibitors). The next day, the supernatant (flow through) was removed from the beads and stored on ice and the beads were washed 3 times with ice-cold RIPA buffer (supplemented with 1% Triton-X 100 and protease inhibitors). Subsequently, proteins were eluted by subjecting the beads to 240 μL of Laemmli sample buffer for 45 min at room temperature on a laboratory agitator (TOMY, MT-360). 220 μL of sample buffer containing proteins obtained from the pulldown, flow through and 15 μg of the corresponding total protein, were separated on SDS-PAGE gels (10% polyacrylamide) for 2 h at 120 V. Finally, protein bands were probed using the same primary/secondary antibodies and conditions as described for our Western blot protocol, except the D2R antibody was used at a 1:200 dilution to compensate for the reduced number of proteins collected in the pulldown.

cAMP Assays

cAMP-Glo™ Assay kit (V1502, Promega) was used to detect intracellular cAMP. HEK293 cells were seeded (900,000 cells/well) in 6-well plates, grown overnight, and transfected with 2.5 μg cDNA of the human Flag-D2R receptor (gift from Johnathan Javitch) using TransIT®-LT1 Transfection Reagent (MIR2305, Mirus). After 24 h, cells were treated with control, 1 μM or 50 μM Amph in absence or presence of 10 nM haloperidol for 15 h. Cells were collected using versene (2 mM EDTA in PBS), resuspended in serum-free media containing 100 μM isobutyl-1-methylxanthine (I5879, Sigma-Aldrich) and 100 μM 4-(3-butoxy-4-methoxybenzyl) imidazolidone

(B8279, Sigma-Aldrich), and plated in a 96-well plate (200,000 cells/well). To stimulate adenylate cyclase, we incubated the cells with 3–100 μM forskolin (F6886, Sigma-Aldrich) in absence or presence of 100 μM of the D2R agonist sumanirole (SML1087, Sigma-Aldrich) for 15 min at 37°C. Cells were lysed following the assay kit's instructions and luminescence was detected following the manufacturer's protocol (cAMP-Glo™ Assay kit). Relative light units were converted to cAMP using a cAMP standard curve and normalized to basal cAMP. Concentration-response curves for forskolin in the absence and presence of sumanirole were fitted with the three-parameter non-linear regression model. Two-way ANOVA with Bonferroni's multiple comparisons test was performed to determine statistical significance.

Dopamine ELISA Assay

An enzyme-linked immunosorbent assay (ELISA, LDN, Nordhorn, Germany) was performed to quantify levels of intracellular dopamine in HEK293 cells. About 4 million cells were grown in DMEM media at 37°C. Cells were detached with 0.25% of trypsin, lysed using radioimmunoprecipitation assay (RIPA) buffer, collected in microcentrifuge tubes and then sonicated for 30 s prior to centrifugation at 13,000 RPM for 1 min. The samples and the provided standards from the kit were pipetted into a 48-well extraction plate and acylated as per the manufacturer's instructions. The resulting supernatant was collected and pipetted into a 96-well microtiter plate for enzymatic conversion, incubated for 2 h and then transferred to pre-coated dopamine microtiter strips. After treating the samples with rabbit dopamine antiserum overnight at 4°C, the antiserum was discarded, then replaced with goat anti-rabbit immunoglobulins. Lastly, a chromogenic substrate was added. Absorbance was measured using a FLUOstar® Omega microplate reader (BMG LABTECH, Orenberg, Germany). A standard curve was generated using a four-parameter logistic regression, and absorbance readings were plotted on the resulting curve to determine dopamine concentrations. Dopamine concentrations reported in the Results section are average of 2 independent experiments ± SEM, and each experiment was done in quadruple.

Statistical Analysis

GraphPad Prism 7.05 was used for statistical analysis and only *p*-values smaller than 0.05 were considered statistically significant. Specific statistical tests are detailed in each graph (see section "Results" or "Figure Legends").

RESULTS

Continuous Exposure to Amphetamine Reduces Endogenous Expression of the Human D2 Receptors in Cells Expressing the Dopamine Transporter

Previous publications have reported conflicting data about the ability of Amph to induce reallocation of the D2R to and from the cellular membrane (Kamata and Rebec, 1984; Levy et al., 1988; Bonhomme et al., 1995; Kilbourna and Dominob, 2011). As most of these experiments were performed using *in vivo* or *ex vivo* preparations, we reasoned simpler preparations, such as cell cultures, might help us clarify these diverging results. We chose to use human embryonic kidney cells (HEK293) because they express endogenous hD2R (Bowton et al., 2010); and, since specific antibodies against these receptors are commercially available, we designed a set of experiments with the goal to quantify changes in endogenous hD2R expression following Amph exposure.

We validated the efficacy of the D2R antibody in our assays by performing parallel experiments where samples from HEK293 cells probed with the hD2R antibody were compared to samples from HEK293 cells transfected with Flag-hD2R and probed with an antibody against the Flag. Similar to previous data obtained in HEK293 cells transfected with D2R (Free et al., 2007), cell lysates from parental HEK293 cells probed with the hD2R antibody showed multiple bands (**Figure 1A**, panel 1). These bands most likely account for D2R monomers, dimers and multimers, and perhaps, also different levels of protein glycosylation (Free et al., 2007). On the other hand, the Flag-hD2R expressing cells probed with the Flag antibody showed two prominent bands, at around 40 and 75 kDa, and a faded smear of bands between 100 and 250 kDa (**Figure 1A**, panel 2). Because the bands at 40 and 75 KD were also present in samples probed with the hD2R antibody (**Figure 1**, compare panels 1,2), we focused our analysis on these two bands which, most likely, represent D2R monomers (40 kDa) and possible dimers (75 kDa) (Free et al., 2007).

D2R and DAT are co-expressed in the pre-synaptic terminals of dopaminergic neurons and transport through DAT is the main route of Amph for fast access into the cytoplasm of these neurons. Thus, we investigated the effects of 15-h Amph exposures on D2R in HEK293 cells, which were previously engineered to stably express hDAT. Western blot experiments demonstrated that cell lysates from hDAT-expressing HEK293 cells exhibit multiple D2R bands arranged in a pattern similar to that observed in HEK293 cells (**Figure 1B**) and, also in these cells, the 40 and 75 kDa bands were detected. Importantly, we found that samples from hDAT-expressing cells treated with 1 or 50 μM Amph for 15 h, exhibited a significant decrease in the 40 kDa band (53.3 ± 11.3 and 41.6 ± 3.9%, respectively) with respect to the control-treated cells (**Figures 1B,C**; one-way ANOVA Dunnett's multiple comparisons test). Similarly, both Amph concentrations reduced the 75 kDa band to 77 ± 7 and 71 ± 5%. These results demonstrate a significant reduction in endogenous hD2R expression following 15-h exposure to 1 or 50 μM Amph in HEK293 cells expressing hDAT.

Continuous Exposure to Amphetamine Increases Endogenous Expression of the Human D2 Receptors in HEK293 Cells Lacking hDAT

The D2R are expressed in pre-synaptic terminals alongside DAT and in post-synaptic terminals which do not express DAT. We investigated if Amph could affect expression of the hD2R in cells lacking DAT expression. Although less effective than

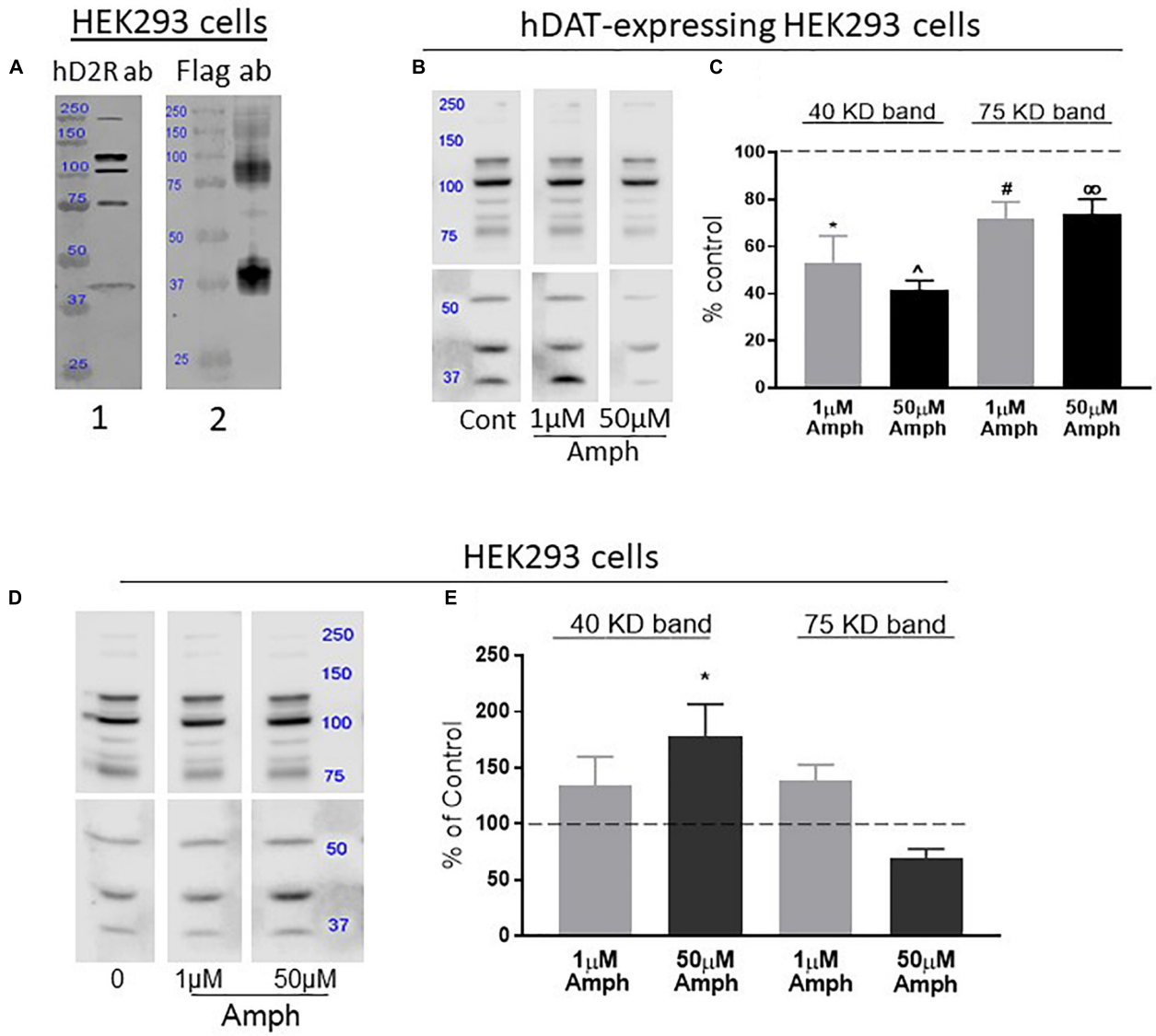

FIGURE 1 | Amphetamine (Amph) decreases the overall expression of the endogenous D2R in cells transfected with hDAT but increases D2R in cells lacking hDAT. **(A)** Antibodies against human D2R identify distinct bands in lysates from HEK293 cells (panel 1). Lysates from HEK293 cells transfected with Flag-D2R and probed with Flag antibodies show two prominent bands at 40 and 75 KD (panel 2). These bands match in size with bands probed with the hD2R antibody in panel 1. **(B)** A representative gel from hDAT-transfected HEK293 cells treated with control, 1 or 50 μM amphetamine (Amph) and immunoblotted with hD2R antibodies is shown, and the average of 4 independent Western blot experiments is plotted in **(C)**. Statistical analysis against control-treated samples was performed using one-way ANOVA Dunnett's multiple comparisons test ($^{*}p = 0.0007$, $^{\wedge}p = 0.0001$, $^{\#}p = 0.01$, $^{\infty}p = 0.03$, each compared to controls). **(D)** A representative gel of samples from HEK293 cells treated with control, 1 or 50 μM Amph and immunoblotted with hD2R antibodies is shown, and the average of 4 independent Western blot experiments is plotted in **(E)**. PVDF membranes from Western blots in **(B,D)** are shown as two halves because different times of exposure to ECL were used. This guaranteed detectable and quantifiable signals at both lower and higher molecular weight bands (see section "Materials and Methods"). Statistical analysis was performed using one-way ANOVA Dunnett's multiple comparisons test ($^{*}p = 0.04$).

via transporter-mediated access, Amph can cross the cellular membrane via diffusion due to its lipophilic nature (Zaczek et al., 1991). Thus, we investigated whether 15-h Amph treatments could affect the endogenous expression of the hD2R receptors in HEK293 cells which do not express hDAT. After treating the cells with control solution, 1 or 50 μM Amph, cell lysates were separated by SDS-PAGE, transfered onto PVDF membranes and probed with hD2R antibodies. Surprisingly, we found that while 1 μM Amph generated a moderate, but not statistically significant, increase of 38 ± 23 and 39 ± 14% at the 40 and 75 kDa bands, respectively, the increase caused by 50 μM Amph at the 40 kDa band was more robust and statistically significant (78 ± 29%; $^{*}p < 0.05$, one-way ANOVA Dunnett's multiple comparisons test; **Figures 1D,E**). No significant change was seen at the 75 kDa band after 15-h treatment with 50 μM Amph. Taken together these results show that 15-h exposure to Amph increases

expression of the endogenous hD2R monomer in cells that do not express hDAT.

Amphetamine Enhances Endogenous D2 Receptors at the Cellular Membrane of Cells Lacking hDAT and in Absence of Dopamine

Our Western blot results (**Figure 1**) show that the effects of Amph at the D2R are dictated by DAT, *i.e.,* cells expressing hDAT exhibit reduction in D2R following prolonged Amph treatments whereas, cells lacking hDAT exhibit an increase of D2R. We were particularly intrigued by the observation that Amph altered the D2R in absence of DAT. Thus, we continued our studies using HEK293 cells which endogenously express the hD2R but not DAT.

While the data shown in **Figures 1D,E** indicate that Amph increases expression of endogenous D2R, it remains elusive whether these changes occurred in specific sub-compartments of the cell, *e.g.,* cellular membrane vs. cytoplasm or both. Using confocal microscopy, we investigated the Amph-induced changes in hD2R expression at the cellular membrane and in the cytoplasm by collecting images from cells stained for hD2R and Na^+/K^+-ATPase. The latter was used as a marker of the cellular membrane. As for our Western blot assays, cells were treated with control solution, 1 or 50 μM Amph for 15 h before being fixed and probed with the two antibodies. Cells exhibited a well-defined Na^+/K^+-ATPase staining which was confined to the cellular membrane (**Figures 2A–F**, yellow stain) and, in accordance with previous publications (Prou et al., 2001), the hD2R antibody revealed puncta all over the cell with most of the puncta located in cytoplasmic compartments (**Figures 2A–F**, cyan stain). The yellow stain of the Na^+/K^+-ATPase was used to identify the area of the cell membrane for quantification analysis of the D2R. Cyan puncta included in this area were selected as D2R in or at closed proximity of the cellular membrane. The cyan puncta outside this area were selected as D2R located in the cytoplasm. **Figures 2A–C** are representative confocal images of 0.2 μm sections from cells treated for 15 h with control (A,D), 1 μM (B,E), or 50 μM (C,F) Amph. **Figures 2D–F** display selected areas (labeled 1–3) from **Figures 2 A–C** respectively, at higher magnification. Magnified images and quantification of fluorescence signals from three independent experiments, showed an increase in D2R at the cellular membrane after 15-h exposure to 1 or 50 μM Amph with respect to controls (**Figure 2J**, left panel. Compare E,F to D). No significant change was measured in the cytoplasm between control- and Amph-treated cells (**Figure 2J**, right panel). It should be noted that our imaging data showed that the 15-h treatment with Amph did not alter the Na^+/K^+-ATPase expression (yellow stain) with respect to control-treated cells (2798 ± 423 and 2353 ± 296 max fluorescence, respectively) suggesting, therefore, that Amph does not alter the expression of every protein at the cellular membrane. Moreover, as previously shown (Ferdous et al., 2020), we did not observe any obvious cytotoxic effect induced by the 15 h treatment with both Amph concentrations. In fact, cell morphology (**Figures 2A–C**) and the number of cells in control-treated samples (14 ± 3 cells/microslide) were comparable to those treated with 1 or 50 μM Amph (13 ± 2 or 13 ± 3 cells/microslide, respectively). Taken together these results show that, in cells lacking expression of hDAT, 15-h exposure to 1 or 50 μM Amph does not affect cell proliferation but causes an increase of endogenous hD2R at the cellular membrane.

For most G-protein coupled receptors, including the D2R, the magnitude of the receptor-mediated signal can be modulated by moving receptors to and from the cellular membrane, a mechanism known as trafficking. Trafficking of clathrin-coated vesicles forming at the cellular membrane (endocytosis) or in intracellular organelles (exocytosis) is one of the major mechanisms used by cells to shuffle proteins at the cellular membrane (Jamieson and Palade, 1971; Pearse, 1976). Among others, β-arrestin and adaptor proteins (AP) are essential proteins for facilitating vesicle budding. Recently, Beautrait et al. (2017) identified a specific drug, barbadin, which prevents the agonist-induced trafficking of G-protein coupled receptors by selectively blocking the interaction between β-arrestin and the AP2 subunit β-adaptin. Thus, we reasoned to test whether the Amph-induced changes at the endogenous D2R could be affected by barbadin. Barbadin treatments did not alter cell morphology (**Figure 2**, compare G–I with A–C) or cell proliferation. In fact, 15 h treatment with barbadin alone or together with 1 or 50 μM Amph yielded the same number of cells (13 ± 2, 15 ± 1, or 12 ± 2 cells/microslide, respectively) with respect to control-treated samples (14 ± 3 cells/microslide). Moreover, barbadin did not change the quantity of D2R with respect to controls at the cellular membrane (682 ± 96 vs. 701 ± 45, respectively), nor in the cytoplasm (782 ± 55 vs. 784 ± 87, respectively). Interestingly though, barbadin completely blocked the Amph-induced increase of D2R at the cellular membrane (left panel in **Figures 2K,G–I**). No change in fluorescence intensity was measured in the cytoplasm after barbadin and Amph treatment (right panel in **Figures 2K,G–I**). Taken together these data demonstrate that Amph enhances D2R at the cellular membrane and inhibition of the β-arrestin/β-adaptin interaction prevents this effect.

Our confocal experiments were replicated consistently over multiple independent experiments. Yet, imaging data are snapshots of a relatively small number of cells and artifacts, such as cell-membrane overlay cannot be excluded. Hence, we supported our studies with a biochemical approach. Biotinylation of cell surface proteins is a technique allowing to discriminate proteins at the cellular membrane from those in the cytoplasm by tagging the surface-expressed proteins with the membrane impermeable reagent Sulfo-NHS-LC-Biotin. We used this technique to further confirm the data collected from our imaging experiments. As the expression of D2R at the cellular membrane is very low with respect to the cytoplasm (Prou et al., 2001), about 8 million cells, pretreated with control or 1 μM Amph, were exposed to Sulfo-NHS-LC-Biotin. This high number of cells, which yielded approximately 1,800 μg of proteins, ensured the detection of D2R at the cell surface. Using avidin beads, we separated biotinylated proteins (proteins at the cell surface) from the proteins in the cytosol. Samples from the biotinylated protein

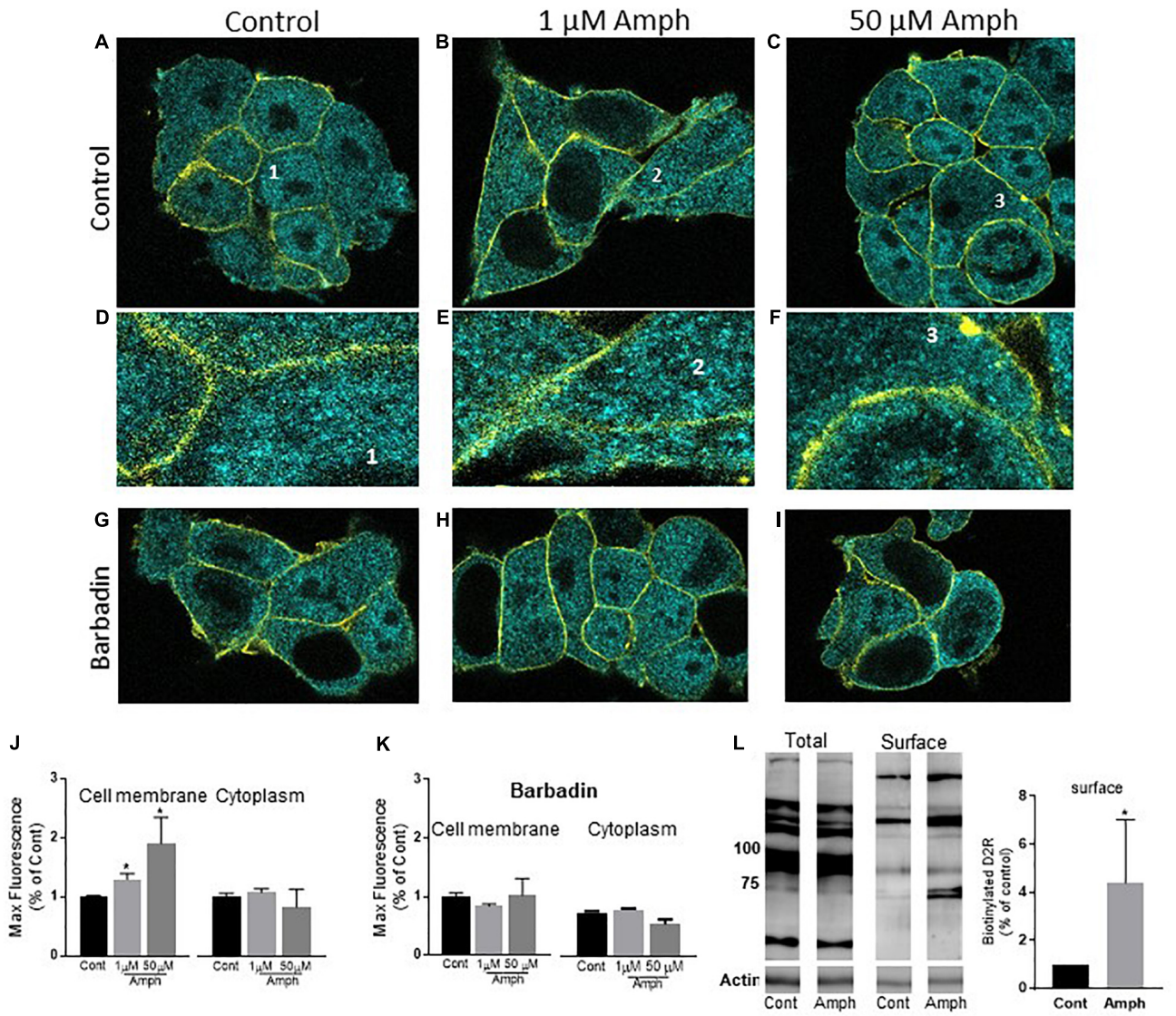

FIGURE 2 | Prolonged amphetamine treatments increase the endogenous hD2R at the cellular membrane in HEK293 cells. **(A–C)** representative confocal images of control **(A)**, 1 **(B)**, or 50 **(C)** μM Amph treated cells shown as 0.2 μm sections for the cyan channel (D2R stain) and the yellow channel (Na^+/K^+-ATPase stain). The latter highlights the cellular membrane of each cell. Details of a single cell from **(A–C)** (1–3) are magnified in **(D–F)**. Representative cells treated with 20 μM barbadin alone or barbadin together with 1 or 50 μM Amph are shown in **(G–I)**, respectively. **(J)** Average of max fluorescence of cyan puncta from 3 independent experiments shows Amph increases D2R at the cellular membrane but not in the cytoplasm (*p = 0.03, one-way ANOVA test). **(K)** Averages from 3 independent experiments show 20 μM barbadin prevents Amph-induced increase of max fluorescence at the cellular membrane. **(L)** Biotinylated samples (Surface) show increased D2R band intensity after 15-h treatment with 1 μM Amph with respect to control treated cells (*p = 0.04, t-test). One representative gel is shown of 4 independent experiments.

fraction were separated by SDS-PAGE and then immunoblotted with the D2R antibody. As shown in **Figure 2L**, 1 μM Amph treatment for 15 h increased the band intensity of the D2R at the cell surface (*p = 0.04; t-test. N = 4). These results, once again, demonstrate that prolonged exposure to low concentrations of Amph enhances the quantity of endogenous D2R at the cellular membrane in HEK293 cells. It is worth noting that our pulldown (membrane surface) samples did not show D2R bands lower than 75 KD (**Figure 2L**, representative gel). This might suggest that only mature (glycosylated) and multimeric D2R reside at the cellular membrane.

Our data show that prolonged treatments with 1 or 50 μM Amph affect hD2R distribution in cells lacking hDAT, thus, suggesting that Amph permeates the cellular membrane of these cells or enters the cells via a DAT-independent mechanism. In this scenario, one could imagine that Amph, after depolarizing these cells, would cause dopamine release into the media and, in turn, dopamine would affect hD2R distribution on the cellular membrane. For this to be true, one should prove that HEK293 cells indeed produce dopamine. We used an Elisa kit (DNL), which is designed for high-sensitive quantification of dopamine, to quantify dopamine in HEK293 cells. Lysed

samples from cells, which were grown and treated following the same conditions as our Western blot and imaging experiments, exhibited a concentration of dopamine that was equivalent or below our blank samples (0.003 ± 0.06 and 0.005 ± 0.02 ng/mL, respectively). Instead, and as expected, our positive control, pure dopamine included in the Elisa kit, showed a concentration of dopamine equal to 5.5 ± 1.5 ng/mL (N = 6). Moreover, our HEK293 cells were grown and treated in media/serum which did not contain dopamine. Taken together, these data demonstrate that the effects of Amph on the D2R are not mediated by dopamine.

Continuous Exposure to Amphetamine Reduces Intracellular cAMP Through the Activation of the D2 Receptors

So far, our data demonstrate that in cells expressing endogenous hD2R but lacking dopamine and hDAT, prolonged exposure to Amph increases hD2R at the cellular membrane (**Figures 1**, **2**). Next, we examined whether the enhancement of the D2R caused by Amph might be of physiological relevance. Because the D2R couple to inhibitory G-protein subunits, which reduce cAMP synthesis by blocking adenylate cyclase, we tested whether the Amph-induced changes at the D2R altered intracellular cAMP production. We could not detect the inhibition of forskolin-mediated cAMP production when we activated the endogenous hD2R, most likely because of the low number of receptors at the membrane. Thus, we transfected our cells with hD2R. As expected, in hD2R transfected cells, stimulation with different concentrations of the adenylate cyclase activator forskolin caused an increase of intracellular cAMP (**Figure 3A**, black circles). Interestingly, 15-h exposure to 1 μM Amph caused a statistically significant decrease of cAMP with respect to cells pretreated with control solution (**Figure 2A** gray squares; p = 0.005, two-way ANOVA test). These results suggest that prolonged Amph exposures reduces the intracellular production of cAMP. However, they did not sufficiently support the conclusion that this effect is mediated by the D2R. Therefore, we tested whether activation of the D2R in cells treated with Amph would produce different levels of cAMP with respect to control-treated cells. After cells were pretreated for 15 h with control, 1 or 50 μM Amph, we thoroughly washed out the drug and treated the cells for 15 min with the D2R agonist sumanirole. We stimulated the D2R with sumanirole because, in contrast to dopamine, this compound is a highly specific D2R agonist (McCall et al., 2005). As shown in **Figures 3B,C**, cells pretreated with 1 or 50 μM Amph exhibited statistically lower levels of intracellular cAMP with respect to cells pretreated with control solution during forskolin activation (p = 0.0001, two-way ANOVA Bonferroni multiple comparison test), whereas sumanirole alone did not cause a statistically different response to forskolin with respect to control treated cells (compare filled circles of **Figure 3B** with A). Importantly, the Amph-induced effect was prevented when haloperidol, a specific D2R antagonist, was co-applied (**Figure 3D**). These results demonstrate that prolonged Amph treatments increase the D2R-induced inhibition of cAMP and, therefore, they suggest that Amph upregulates the D2R and/or increases the number of functional D2R at the cellular membrane.

DISCUSSION

Amphetamine is a psychostimulant broadly used as a performance enhancer and is one of the main drugs prescribed to treat attention deficit disorders. Therapeutical doses of Amph, which are in the range of low μM, improve concentration in people suffering with attention disorders. Amph is also one of the most popular "study drugs" used by college students. Very often though, students end up taking higher doses to extend the benefit of the drug during exam taking or because tolerance develops overtime. The physiological consequences of these higher doses taken for longer and consecutive periods are unknown. Here, we developed an *in vitro* model to study the effects of 15-h exposure to 1 and 50 μM Amph in HEK293 cells. We chose these cells because they endogenously express one of the major targets of Amph, the type 2 dopaminergic receptors (D2R). These receptors play an important role in mediating the physiological and behavioral effects of Amph (Centonze et al., 2001; Seneca et al., 2006; Fan and Hess, 2007; Nelson and Killcross, 2013; Calipari et al., 2014) and, previous reports demonstrated that, in animal models as well as in human studies, D2R expression and function are altered by chronic exposure to Amph (Chen et al., 1999; Calipari et al., 2014; Ashok et al., 2017).

The D2R are expressed in the pre-synaptic terminals, where they colocalize with another major target of Amph, DAT, and in post-synaptic terminals. While it has been suggested that D2R and DAT reciprocally regulate each other (Bolan et al., 2007; Lee et al., 2007; Bertolino et al., 2009), and thus, might cooperatively mediate the effects of Amph, it is not clear if Amph directly alters the D2R in cells lacking expression of DAT. Although less efficiently than via carrier-mediated transport, Amph can cross cellular membranes because of its lipophilicity (Zaczek et al., 1991). Thus, in situations where relatively high concentrations and prolonged exposures to Amph occur, it is reasonable to assume that Amph can affect D2R function in cells lacking expression of DAT in presence or absence of dopamine. For this reason, we investigated whether prolonged Amph exposure altered the endogenous expression of the D2R in HEK293 cells. We recognize that cell cultures do not fully reproduce the physiological conditions seen in *in vivo* models. Nonetheless, they allow us to study the action of a drug in a well-defined pathway without the complexity and interference of other signaling. Moreover, because specific ligands or antibodies capable of discriminating between pre- and post-synaptic D2R do not exist, our model allowed us to reproduce an *in vitro* scenario in which Amph acts at the D2R without the influence of DAT and/or dopamine.

Previous data have suggested that the Amph-induced internalization of D2R was a consequence of the increased extracellular dopamine caused by Amph (Sun et al., 2003). For example, Skinbjerg et al. (2010) showed that Amph causes robust reductions of radioligands binding at the D2R which persisted for several hours (4–24) after the Amph injection. However,

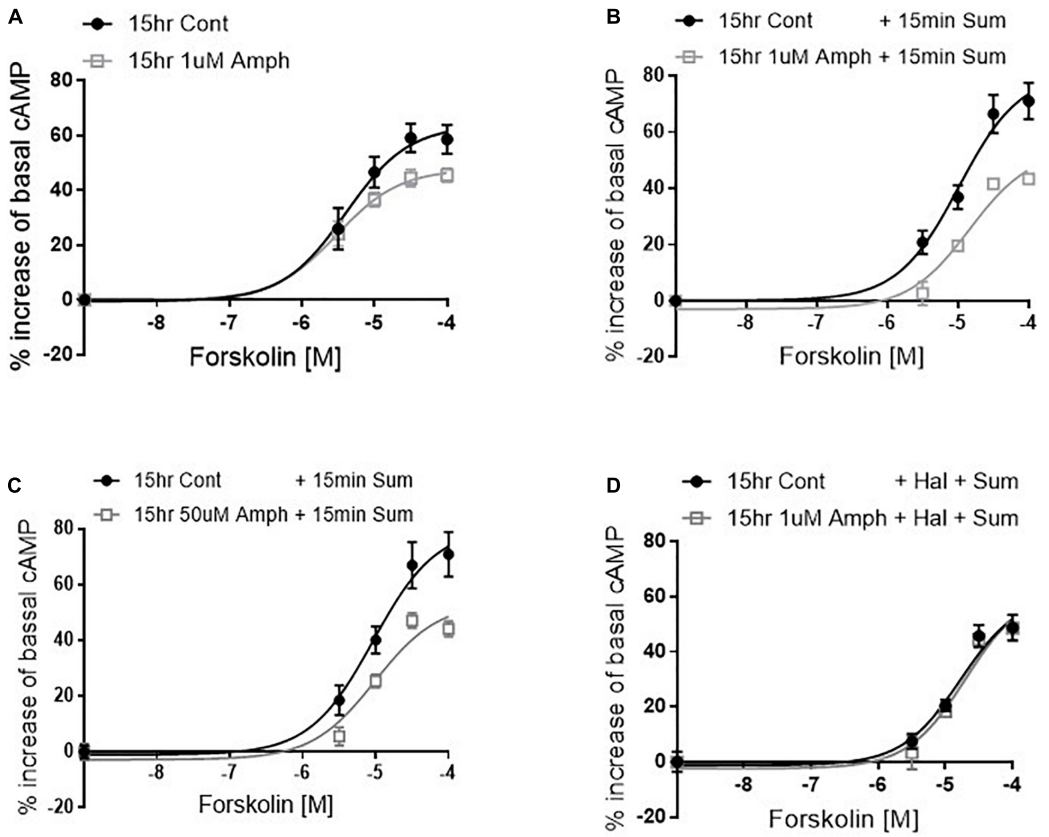

FIGURE 3 | Amphetamine reduces forskolin- and D2R-induced cAMP production. After pretreating cells with control or 1 μM amphetamine (Amph), cells were treated with increasing concentrations of forskolin **(A)**. cAMP production was statistically lower in Amph-pretreated samples with respect to controls ($p = 0.006$). Parallel samples were treated for 15 min with 100 μM sumanirole (Sum) after 15-h pretreatment with control, 1 μM **(B)** or 50 μM **(C)** Amph. Amph significantly reduced cAMP production ($p = 0.0001$). Coincubation of 10 nM haloperidol (Hal) with 1 μM Amph prevented the Sum-induced decrease of cAMP **(D)**. Each graph is the average of 3 independent experiments. Statistical analysis was performed with 2-way ANOVA Bonferroni multiple comparison test.

extracellular dopamine returned to basal levels within 2 h. Hence, it was concluded that the dopamine surge seen after Amph application would induce internalization of the D2R (Skinbjerg et al., 2010). Yet, this study could not discriminate whether the D2R internalization caused by Amph occurred in pre- or post-synaptic cells. Here, we designed an *in vitro* model showing that the effects of Amph on the endogenous D2R are different in parental cells vs. cells transfected with hDAT. Our Western blot data showed that in hDAT-expressing cells, prolonged Amph treatments cause a strong reduction of the endogenous D2R in absence of dopamine. On the other hand, in cells lacking both DAT and dopamine, Amph generated an increase of D2R at the cellular membrane (**Figure 2**). This result was in agreement with previous *in vivo* data showing increased binding potential of the D2R antagonist [^{11}C]raclopride in rats after repeated Amph treatments (Kilbourna and Dominob, 2011). The effect of Amph at the D2R in cells lacking both DAT and dopamine is novel and interesting because it suggests that prolonged use of low concentrations of Amph might directly affect D2R distribution in post-synaptic terminals or in cells expressing D2R but not DAT. Interestingly, we found that blocking the interaction between β-arrestin and β-adaptin, a subunit of the AP2 complex, completely prevented the Amph-induced increase of D2R at the cellular membrane. These data suggest that the recruitment of D2R to the membrane is mediated by clathrin-coated vesicles.

In accordance with data obtained using HEK293 cells transfected with hD2R-Flag (Free et al., 2007), our results show that the hD2R endogenously expressed in these same cells exhibit multiple bands when separated in SDS gels (**Figure 1**) suggesting, therefore, that glycosylation and/or dimerization are integral processes of hD2R expression (Free et al., 2007). Moreover, Free et al. (2007) performed several experiments, and convincingly proved that the bands at 40 and 75 kDa represent un-glycosylated D2R. Interestingly, our results show that these same bands are predominantly affected by the 15-h treatment with Amph. Together these data suggest that lack of glycosylation at the D2R might be required by Amph to affect the expression of the D2R at the cell membrane. Future studies including drugs known to specifically inhibit protein glycosylation will determine whether Amph-induced changes at the D2R are inhibited by blocking D2R glycosylation.

Data collected in this study also suggest that the Amph-induced increase of D2R at the cellular membrane can generate physiological effects since prolonged treatments with Amph

reduced the intracellular concentration of cAMP. D2R couple to G proteins of the Gi/o subfamily which inhibit adenylate cyclase. Consequently, the intracellular concentration of cAMP is reduced upon D2R activation. Thus, it can be assumed that the level of reduction of intracellular cAMP is proportional to the number of activated D2R on the cell membrane. We found that the D2R-mediated changes of intracellular cAMP were increased in cells pretreated with Amph and this effect was prevented by the D2R antagonist haloperidol (**Figure 3**). Again, this observation suggests that prolonged treatments with Amph increase the amount of functional D2R at the cellular membrane. We cannot exclude, though, the possibility that prolonged Amph treatments had a general effect on proteins expression at the cellular membrane. However, this is unlikely since we measured no change in the cell surface staining of Na^+/K^+ ATPase after 15-h Amph treatment.

It is tempting to speculate that Amph mediates its effects at the D2R by acting on different kinases and/or other enzymes in the cytoplasm as previously shown in cells expressing DAT (Lute et al., 2008; Wheeler et al., 2015). However, since we do not have data indicating that Amph, without the dopamine transporter finds its way into the cytoplasm, we cannot sufficiently support this claim in the present study. Alternatively, it is possible that Amph permeates but does not cross the cellular membrane and this would be enough to alter D2R distribution in the lipid bilayer. Future and more specific experiments will elucidate these different possibilities.

The most intuitive conclusion drawn from the present data would be that Amph directly binds to the D2R. However, this seems unlikely because Simmler et al. (2013) have already shown that Amph exhibits low binding affinity ($Ki > 30$ μM) to the hD2R in membrane preparations from HEK293 cells transfected with hD2R. Another important implication of our results is that Amph can potentially alter the dopaminergic signaling without dopamine. This is an important consideration in situations where dopamine depletion occurs, for example, during repeated exposures to high concentrations of Amph (Wagner et al., 1980; Atianjoh et al., 2008).

In conclusion, we have provided evidence that in cells expressing hDAT, prolonged treatments with 1 or 50 μM Amph decreased the endogenous hD2R, whereas, in cells lacking hDAT, Amph increased hD2R at the cellular membrane. Because our results were collected from cells naturally expressing hD2R, and because the concentrations of Amph we used are relevant for human health, we believe our data might be of physiological relevance.

DATA AVAILABILITY STATEMENT

The original contributions presented in the study are included in the article/supplementary material, further inquiries can be directed to the corresponding author.

AUTHOR CONTRIBUTIONS

LC designed the study, analyzed the data, and wrote the manuscript. VN, SPM, FPM, and ZG designed and performed the experiments. AM quantified WB data. All authors contributed to the article and approved the submitted version.

FUNDING

This study was supported by NIH R01 grant (DA042156) to LC.

ACKNOWLEDGMENTS

We thank the two undergraduate students Abigail Canning and Hannah Phelps for their assistance with data acquisition and solutions preparation.

REFERENCES

Andrianarivelo, A., Saint-Jour, E., Walle, R., Trifilieff, P., and Vanhoutte, P. (2019). Modulation and functions of dopamine receptor heteromers in drugs of abuse-induced adaptations. *Neuropharmacology* 152, 42–50. doi: 10.1016/j.neuropharm.2018.12.003

Ashok, A., Mizuno, Y., Volkow, N. D., and Howes, O. D. (2017). Association of Stimulant Use With Dopaminergic Alterations in Users of Cocaine, Amphetamine, or Methamphetamine-A Systematic Review and Meta-analysis. *JAMA Psychiatr.* 74, 511–519. doi: 10.1001/jamapsychiatry.2017.0135

Atianjoh, F., Ladenheim, B., Krasnova, I. N., and Cadet, J. L. (2008). Amphetamine causes dopamine depletion and cell death in the mouse olfactory bulb. *Eur. J. Pharmacol.* 589, 94–97. doi: 10.1016/j.ejphar.2008.05.001

Beautrait, A., Paradis, J. S., Zimmerman, B., Giubilaro, J., Nikolajev, L., Armando, S., et al. (2017). A new inhibitor of the β-arrestin/AP2 endocytic complex reveals interplay between GPCR internalization and signalling. *Nat. Comm.* 8:15054.

Bertolino, A., Fazio, L., Di Giorgio, A., Blasi, G., Romano, R., Taurisano, P., et al. (2009). Genetically determined interaction between the dopamine transporter and the D2 receptor on prefronto-striatal activity and volume in humans. *J. Neurosci.* 29, 1224–1234. doi: 10.1523/jneurosci.4858-08.2009

Bolan, E., Kivell, B., Jaligam, V., Oz, M., Jayanthi, L. D., Han, Y., et al. (2007). D2 receptors regulate dopamine transporter function via an extracellular signal-regulated kinases 1 and 2-dependent and phosphoinositide 3 kinase-independent mechanism. *Mol. Pharmacol.* 71, 1222–1232. doi: 10.1124/mol.106.027763

Bonhomme, N., Cador, M., Stinus, S., Le Moal, M., and Spampinato, U. (1995). Short and long-term changes in dopamine and serotonin receptor binding sites in amphetamine-sensitized rats: a quantitative autoradiographic study. *Brain Res.* 675, 215–223. doi: 10.1016/0006-8993(95)00067-z

Boudanova, E., Navaroli, D. M., and Melikian, H. E. (2008). Amphetamine-induced decreases in dopamine transporter surface expression are protein kinase C-independent. *Neuropharmacology* 54, 605–612. doi: 10.1016/j.neuropharm.2007.11.007

Bowton, E., Saunders, C., Erreger, K., Sakrikar, D., Matthies, H. J., Sen, N., et al. (2010). Dysregulation of dopamine transporters via dopamine D2 autoreceptors triggers anomalous dopamine efflux associated with attention-deficit hyperactivity disorder. *J. Neurosci.* 30, 6048–6057. doi: 10.1523/jneurosci.5094-09.2010

Calipari, E., Sun, H., Eldeeb, K., Luessen, D. J., Feng, X., Howlett, A. C., et al. (2014). Amphetamine self-administration attenuates dopamine D2

autoreceptor function. *Neuropsychopharmacology* 39, 1833–1842. doi: 10.1038/npp.2014.30

Carvelli, L., Matthies, D. S., and Galli, A. (2010). Molecular mechanisms of amphetamine actions in *Caenorhabditis elegans*. *Mol. Pharmacol.* 78, 151–156. doi: 10.1124/mol.109.062703

Centonze, D., Picconi, B., Baunez, C., Borrelli, E., Pisani, A., Bernardi, G., et al. (2001). Cocaine and Amphetamine Depress Striatal GABAergic Synaptic Transmission through D2 Dopamine Receptors. *Neuropsychopharmacology* 26, 164–175. doi: 10.1016/s0893-133x(01)00299-8

Chen, J. C., Su, H. J., Huang, L. I., and Hsieh, M. C. (1999). Reduction in binding and functions of D_2 dopamine receptors in the rat ventral striatum during amphetamine sensitization. *Life Sci.* 64, 343–354. doi: 10.1016/s0024-3205(98)00570-0

Daberkow, D., Brown, H. D., Bunner, K. D., Kraniotis, S. A., Doellman, M. A., Ragozzino, M. E., et al. (2013). Amphetamine paradoxically augments exocytotic dopamine release and phasic dopamine signals. *J. Neurosci.* 33, 452–463. doi: 10.1523/jneurosci.2136-12.2013

Fan, X., and Hess, E. J. (2007). D2-like dopamine receptors mediate the response to amphetamine in a mouse model of ADHD. *Neurobiol. Dis.* 26, 201–211. doi: 10.1016/j.nbd.2006.12.011

Ferdous, N., Kudumala, S., Sossi, S., and Carvelli, L. (2020). Prolonged Amphetamine Treatments Cause Long-Term Decrease of Dopamine Uptake in Cultured Cells. *Neurochem. Res.* 45, 1399–1409. doi: 10.1007/s11064-019-02938-7

Free, B., Hazelwood, L. A., Cabrera, D. M., Spalding, H. N., Namkung, Y., Rankin, M. L., et al. (2007). D1 and D2 dopamine receptor expression is regulated by direct interaction with the chaperone protein calnexin. *J. Biol. Chem.* 282, 21285–21300. doi: 10.1074/jbc.m701555200

Gainetdinov, R. R., Premont, R. T., Bohn, L. M., Lefkowitz, R. J., and Caron, M. G. (2004). Desensitization of G protein-coupled receptors and neuronal functions. *Annu Rev. Neurosci.* 27, 107–144. doi: 10.1146/annurev.neuro.27.070203.144206

Jamieson, J. D., and Palade, G. E. (1971). Synthesis, intracellular transport, and discharge of secretory proteins in stimulated pancreatic exocrine cells. *J. Cell Biol.* 50, 135–158. doi: 10.1083/jcb.50.1.135

Kamata, K., and Rebec, G. V. (1984). Long-term amphetamine treatment attenuates or reverses the depression of neuronal activity produced by dopamine agonists in the ventral tegmental area. *Life Sci.* 34, 2419–2427. doi: 10.1016/0024-3205(84)90431-4

Kilbourna, M. R., and Dominob, E. F. (2011). Increased in vivo [11C]raclopride binding to brain dopamine receptors in amphetamine-treated rats.". *Eur. J. Pharmacol.* 654, 254–257. doi: 10.1016/j.ejphar.2011.01.008

Lee, F., Pei, L., Moszczynska, A., Vukusic, B., Fletcher, P. J., and Liu, F. (2007). Dopamine transporter cell surface localization facilitated by a direct interaction with the dopamine D2 receptor. *EMBO J.* 26, 2127–2136. doi: 10.1038/sj.emboj.7601656

Levy, A., Kim, J. J., and Ellison, G. D. (1988). Chronic amphetamine alters D-2 but not D-1 agonist-induced behavioral responses in rats. *Life Sci.* 43, 1207–1213. doi: 10.1016/0024-3205(88)90210-x

Lute, B., Khoshbouei, H., Saunders, C., Sen, N., Lin, R. Z., Javitch, J. A., et al. (2008). PI3K Signaling Supports Amphetamine-induced Dopamine Efflux. *Biochem. Biophys. Res. Commun.* 372, 656–661. doi: 10.1016/j.bbrc.2008.05.091

McCall, R., Lookingland, K. J., Bédard, P. J., and Huff, R. M. (2005). Sumanirole, a highly dopamine D2-selective receptor agonist: in vitro and in vivo pharmacological characterization and efficacy in animal models of Parkinson's disease. *J. Pharmacol. Exp. Ther.* 314, 1248–1256. doi: 10.1124/jpet.105.084202

Nelson, A., and Killcross, S. (2013). Accelerated habit formation following amphetamine exposure is reversed by D1, but enhanced by D2, receptor antagonists. *Front. Neurosci.* 7:76.

Pearse, B. (1976). Clathrin: a unique protein associated with intracellular transfer of membrane by coated vesicles. *Proc. Natl. Acad. U S A* 73, 1255–1259. doi: 10.1073/pnas.73.4.1255

Prou, D., Gu, W. J., Le Crom, S., Vincent, J. D., Salamero, J., and Vernier, P. (2001). Intracellular retention of the two isoforms of the D(2) dopamine receptor promotes endoplasmic reticulum disruption. *J. Cell Sci.* 114, 3517–3527. doi: 10.1242/jcs.114.19.3517

Saunders, C., Ferrer, J. V., Shi, L., Chen, J., Merrill, G., Lamb, M. E., et al. (2000). Amphetamine-induced loss of human dopamine transporter activity: an internalization-dependent and cocaine-sensitive mechanism. *Proc. Natl. Acad. Sci. U.S.A* 97, 6850–6855. doi: 10.1073/pnas.110035297

Seneca, N., Finnema, S. J., Farde, L., Gulyás, B., Wikström, H. V., Halldin, C., et al. (2006). Effect of amphetamine on dopamine D2 receptor binding in nonhuman primate brain: a comparison of the agonist radioligand [11C]MNPA and antagonist [11C]raclopride. *Synapse* 59, 260–269. doi: 10.1002/syn.20238

Simmler, L., Buser, T. A., Donzelli, M., Schramm, Y., Dieu, L. H., Huwyler, J., et al. (2013). Pharmacological characterization of designer cathinones in vitro. *Br. J. Pharmacol.* 168, 458–470. doi: 10.1111/j.1476-5381.2012.02145.x

Skinbjerg, M., Liow, J. S., Seneca, N., Hong, J., Lu, S., Thorsell, A., et al. (2010). D2 dopamine receptor internalization prolongs the decrease of radioligand binding after amphetamine: a PET study in a receptor internalization-deficient mouse model. *Neuroimage* 50, 1402–1407. doi: 10.1016/j.neuroimage.2010.01.055

Solís, O., García-Sanz, P., Martín, A. B., Granado, N., Sanz-Magro, A., Podlesniy, P., et al. (2021). Behavioral sensitization and cellular responses to psychostimulants are reduced in D2R knockout mice. *Addict. Biol.* 26:1.

Sulzer, D. (2011). How addictive drugs disrupt presynaptic dopamine neurotransmission. *Neuron* 69, 628–649. doi: 10.1016/j.neuron.2011.02.010

Sun, W., Ginovart, N., Ko, F., Seeman, P., and Kapur, S. (2003). In Vivo Evidence for Dopamine-Mediated Internalization of D2-Receptors after Amphetamine: Differential Findings with [3H]Raclopride versus [3H]Spiperone. *Mol. Pharmacol.* 63, 456–462. doi: 10.1124/mol.63.2.456

Wagner, G., Ricaurte, G. A., Johanson, C. E., Schuster, C. R., and Seiden, L. S. (1980). Amphetamine induces depletion of dopamine and loss of dopamine uptake sites in caudate. *Neurology* 30, 547–550. doi: 10.1212/wnl.30.5.547

Wheeler, D., Underhill, S. M., Stolz, D. B., Murdoch, G. H., Thiels, E., Romero, G., et al. (2015). Amphetamine activates Rho GTPase signaling to mediate dopamine transporter internalization and acute behavioral effects of amphetamine. *PNAS* 112:51.

Zaczek, R., Culp, S., and De Souza, E. B. (1991). Interactions of [3H]amphetamine with rat brain synaptosomes. II. Active transport. *J. Pharmacol. Exp. Ther.* 257, 830–835.

Conflict of Interest: The authors declare that the research was conducted in the absence of any commercial or financial relationships that could be construed as a potential conflict of interest.

Publisher's Note: All claims expressed in this article are solely those of the authors and do not necessarily represent those of their affiliated organizations, or those of the publisher, the editors and the reviewers. Any product that may be evaluated in this article, or claim that may be made by its manufacturer, is not guaranteed or endorsed by the publisher.

frontiers in Cellular Neuroscience

ORIGINAL RESEARCH
published: 18 November 2021
doi: 10.3389/fncel.2021.667044

A Novel Biotinylated Homotryptamine Derivative for Quantum Dot Imaging of Serotonin Transporter in Live Cells

*Ian D. Tomlinson[1], Oleg Kovtun[1], Ruben Torres[1,2], Laurel G. Bellocchio[1], Travis Josephs[3] and Sandra J. Rosenthal[1,2,4,5,6,7]**

[1] Department of Chemistry, Vanderbilt University, Nashville, TN, United States, [2] Vanderbilt Institute of Chemical Biology, Vanderbilt University, Nashville, TN, United States, [3] Neuroscience Program, Vanderbilt University, Nashville, TN, United States, [4] Department of Pharmacology, Vanderbilt University, Nashville, TN, United States, [5] Department of Chemical and Biomolecular Engineering, Vanderbilt University, Nashville, TN, United States, [6] Department of Physics and Astronomy, Vanderbilt University, Nashville, TN, United States, [7] Vanderbilt Institute of Nanoscale Science and Engineering, Vanderbilt University, Nashville, TN, United States

OPEN ACCESS

Edited by:
Renae Ryan,
The University of Sydney, Australia

Reviewed by:
Marianne Renner,
Sorbonne Université, France
Ulf Bickmeyer,
Alfred Wegener Institute, Helmholtz Centre for Polar and Marine Research (AWI), Germany

***Correspondence:**
Sandra J. Rosenthal
sandra.j.rosenthal@vanderbilt.edu

Specialty section:
This article was submitted to Cellular Neurophysiology, a section of the journal Frontiers in Cellular Neuroscience

Received: 11 February 2021
Accepted: 19 October 2021
Published: 18 November 2021

Citation:
Tomlinson ID, Kovtun O, Torres R, Bellocchio LG, Josephs T and Rosenthal SJ (2021) A Novel Biotinylated Homotryptamine Derivative for Quantum Dot Imaging of Serotonin Transporter in Live Cells. Front. Cell. Neurosci. 15:667044. doi: 10.3389/fncel.2021.667044

The serotonin transporter (SERT) is the primary target for selective serotonin reuptake inhibitor (SSRI) antidepressants that are thought to exert their therapeutic effects by increasing the synaptic concentration of serotonin. Consequently, probes that can be utilized to study cellular trafficking of SERT are valuable research tools. We have developed a novel ligand (IDT785) that is composed of a SERT antagonist (a tetrahydro pyridyl indole derivative) conjugated to a biotinylated poly ethylene glycol (PEG) via a phenethyl linker. This compound was determined to be biologically active and inhibited SERT-mediated reuptake of IDT307 with the half-maximal inhibitory concentration of 7.2 ± 0.3 μM. We demonstrated that IDT785 enabled quantum dot (QD) labeling of membrane SERT in transfected HEK-293 cultures that could be blocked using the high affinity serotonin reuptake inhibitor paroxetine. Molecular docking studies suggested that IDT785 might be binding to the extracellular vestibule binding site rather than the orthosteric substrate binding site, which could be attributable to the hydrophilicity of the PEG chain and the increased loss of degrees of freedom that would be required to penetrate into the orthosteric binding site. Using IDT785, we were able to study the membrane localization and membrane dynamics of YFP-SERT heterologously expressed in HEK-293 cells and demonstrated that SERT expression was enriched in the membrane edge and in thin cellular protrusions.

Keywords: serotonin transporter, ligand, quantum dot, labeling, single particle tracking

INTRODUCTION

5-hydroxytryptamine (5-HT, serotonin) is a monoamine neurotransmitter involved in the modulation of a myriad of functions in the brain and periphery, including mood, appetite, sleep, memory and learning. The magnitude and duration of serotonin signaling is primarily controlled by rapid clearance of extracellular serotonin via the high-affinity serotonin transporter (SERT;

SLC6A4) (Blakely et al., 1991; Ramamoorthy et al., 1993; Torres et al., 2003). SERT belongs to a family of twelve transmembrane-spanning domain neurotransmitter::sodium symporters (NSS) that harness the electrochemical gradient of Na^+ and Cl^- to translocate substrate through a series of structural rearrangements from outward-open to inward-open conformation (Coleman et al., 2016, 2019, 2020; Cheng and Bahar, 2019). Alterations in SERT activity and expression have been implicated in several neuropsychiatric disorders, including anxiety, autism spectrum disorder (ASD), obsessive-compulsive disorder (OCD), attention deficit/hyperactivity disorder (ADHD), and major depressive disorder (MDD) (Kristensen et al., 2011). Accordingly, SERT is an important pharmacological target for widely prescribed selective serotonin reuptake inhibitors (SSRIs), including paroxetine, citalopram, and fluoxetine (Coleman and Gouaux, 2018), which are used to treat MDD, OCD, and anxiety disorders. Moreover, single nucleotide polymorphisms (SNPs) in the SERT gene can affect the expression, membrane trafficking and activity of the transporter and are enriched in families with neuropsychiatric disorders (Hu et al., 2006; Hahn and Blakely, 2007). SERT activity is tightly regulated at the post-translational level by a complex interplay of kinases, phosphatases, and numerous other SERT interacting proteins (Ramamoorthy et al., 1998; Bermingham and Blakely, 2016; Cooper et al., 2019; Quinlan et al., 2020). Consequently, methodologies that can dissect SERT regulation at the single transporter level represent a promising experimental avenue toward understanding the molecular basis of SERT-associated neuropsychiatric disorders.

Single-molecule fluorescence microscopy is an umbrella term for non-invasive imaging modalities that have emerged in the investigation of transmembrane protein trafficking and regulation, as they can access nanometer spatial and sub-second temporal scales (Rosenthal et al., 2011; Kusumi et al., 2014). Typically, an antibody, a peptide or a derivative of a drug or neurotransmitter are conjugated to a fluorophore and utilized as a probe for optical detection of a membrane protein. The fluorophore is usually separated from the targeting functionality via a spacer arm; this is often required to maintain biological activity of the targeting portion of the probe and may also aid in water solubility. Several dye-conjugated antagonists of neuronal receptors and transporters have been reported in the literature (Madras et al., 1990; Bakthavachalam et al., 1991; Jacobson et al., 1995; Rayport and Sulzer, 1995; Cha et al., 2005; Eriksen et al., 2009; She et al., 2020). However, many commonly used fluorescent dyes have low quantum yields and suboptimal photostability, thereby limiting their utility in experiments that require prolonged monitoring of protein membrane dynamics at video rates (Resch-Genger et al., 2008). Biocompatible colloidal semiconductor quantum dots (QDs) are an attractive alternative to dye fluorophores (Rosenthal et al., 2011). These highly fluorescent semiconductor crystals range in diameter from 2 to 10 nm, have a quantum yield that is significantly larger than many commercial dyes and a narrow, size-tunable, Gaussian emission spectrum. Their large absorption cross section is a continuum above the 1st excitation feature, enabling the use of a single excitation source for multicolor experiments. Many studies using antibody- and peptide-conjugated quantum dots in biological labeling of live cells have been reported (Dahan et al., 2003; Bouzigues et al., 2007; Lee et al., 2017; Bailey et al., 2018). The cornerstone of our QD labeling strategy has been the development of agonist- and antagonist-based fluorescent probes. Unlike the antibody-based approach, such ligand probes do not require a suitable extracellular epitope or an engineered tag in the extracellular domain of the target protein for binding; also, their affinity and binding properties may be modified by the incorporation of simple structural changes into the ligand (Tomlinson et al., 2019). To date, we have successfully developed antagonist-based QD probes to label SERT and other membrane-bound neuronal proteins, including structurally related dopamine transporter (DAT) (Kovtun et al., 2011; Chang et al., 2012b; Kovtun et al., 2015; Rosenthal, 2019; Tomlinson et al., 2019).

Over the past two decades, we have devised several strategies in probe development, including direct attachment of the ligand to a polymer on the QD surface via a covalent bond (Gussin et al., 2006) and ligands that incorporate a biotin moiety for non-covalent binding to streptavidin on the surface of the dot (Kovtun et al., 2011; Tomlinson et al., 2019). We have observed that conjugation of polyethylene glycol (PEG; PEGylation) to the QD surface may be required to overcome non-specific binding to the cell surface (Bentzen et al., 2005) and have incorporated PEG chains into our ligands for this purpose. Currently, we rely on commercially available streptavidin-conjugated QDs that display lower non-specific binding properties. The linker arm of choice in our probes has been a polyethylene glycol (PEG) chain attached to the antagonist via an alkyl spacer, with the biotinylated distal end of the PEG forming the point of attachment to the QD (Tomlinson et al., 2011). Recently, we have observed that the nature of the spacer between the PEG chain and the antagonist can have profound effects on non-specific coverslip binding (Tomlinson et al., 2019). Here, we report synthesis of a novel SERT ligand IDT785 (**Figure 1**) with an electron-rich phenylethyl spacer between the PEG chain and the antagonist. We study its ability to inhibit the human SERT transiently expressed in HEK-293T cells (hSERT), examine specific labeling of hSERT and SERT fused to yellow fluorescent protein (YFP) at the N-terminus with a combination of biotinylated IDT785 streptavidin-conjugated QDs (SavQD), and demonstrate that hSERT surface dynamics may be tracked with IDT785-QD conjugates.

MATERIALS AND METHODS

Chemistry

^{1}H NMR and ^{13}C NMR spectra were obtained on a Brucker AV-400 (400 MHz) NMR spectrometer using deuterated chloroform as the solvent unless otherwise stated. Chemical shifts were expressed in parts per million and were measured relative to tetramethyl silane (TMS). Biotin-PEG-SVA consists of biotin attached to the terminus of poly dispersed PEG5000 whilst the other end of the PEG was terminated with a succinimidyl valerate (SVA) functionality that ultimately forms the point of attachment to the SERT antagonist. This reagent was obtained from Laysan

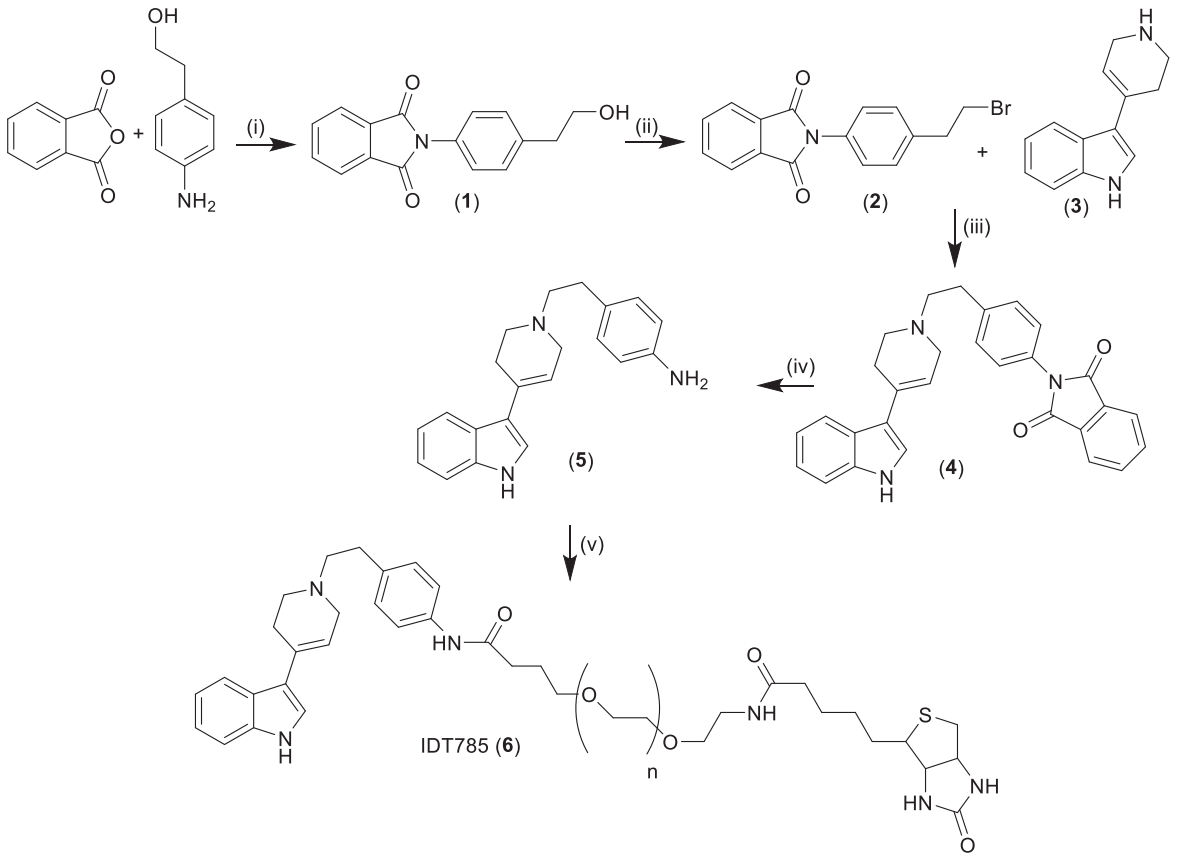

FIGURE 1 | Synthesis of biotinylated SERT ligand IDT785. (i) Pyridine, reflux 18 h, yield = 48%; (ii) PPh_3, triethylamine, methylene chloride, 18 h, yield = 57%; (iii) acetonitrile, triethylamine, reflux, 18 h, yield = 32%; (iv) (a) hydrazine hydrate, ethanol, 1 h, (b) methylene chloride, 18 h, yield = 70%; (v) biotin-PEG5000-SVA, methylene chloride, 18 h. Compounds in bold numbers: (1) = 2-(4-(2-hydroxyethyl)phenyl)isoindoline-1,3-dione, (2) = 2-(4-(2-bromoethyl)phenyl)isoindoline-1,3-dione, (3) = 3-(1,2,3,6-tetrahydropyridin-4-yl)-1*H*-indol, (4) = 2-(4-(2-(4-(1*H*-indol-3-yl)-3,6-dihydropyridin-1(2*H*)-yl)ethyl)phenyl)isoindoline-1,3-dione, (5) = 4-(2-(4-(1*H*-indol-3-yl)-3,6-dihydropyridin-1(2*H*)-yl)ethyl)aniline.

Bio, Arab, AL. The mass of this reagent was assumed to be 5000 Daltons and this was used when calculating the quantities of reagents required to react with it. The progress of all the reactions was monitored by TLC, which was performed on aluminum sheets precoated with silica gel 60 (HF-254, Merck). The developed chromatograms were visualized using UV light (254–365 nm). Sorbtech silica gel (63–200 mesh) was used for preparative column chromatography. IDT307 was synthesized in house as previously described (Blakely et al., 2011). Reagents and solvents for the synthesis of IDT785 were ordered from Sigma Aldrich, Fischer Scientific and VWR, and used without further purification.

Ligand Synthesis

The synthesis of IDT785 is outlined in **Figure 1**. Initially the spacer arm was synthesized by reacting 4-aminophenethyl alcohol with phthalic anhydride to yield the phthalimide (1) in a 48% yield. Then the alcohol was converted to a bromide utilizing an Appel reaction giving the bromide (2) in a 57% yield. The bromo intermediate (2) was coupled to the SERT antagonist (3) via a nucleophilic displacement of the bromide by refluxing in acetonitrile. This gave the phthalimide protected intermediate (4) in a 32% yield. Then the phthalimide protecting group was removed by treatment with hydrazine hydrate resulting in the amino intermediate (5) in a 70% yield. This was coupled to the NHS ester of the biotinylated PEG and the final ligand was purified by size exclusion chromatography on a Sephadex G10 column to yield the final ligand IDT785 (6) which was used without further purification.

2-(4-(2-hydroxyethyl)phenyl)isoindoline-1,3-dione (1)

Phthalic anhydride (6 g, 0.0404 mols) and 4-aminophenethyl alcohol (5.54 g, 0.0404 mols) were mixed in pyridine (150 mL) and heated at reflux with stirring for 18 h (dos Santos et al., 2011). Then the solution was cooled and added to methylene chloride (200 mL). The solution was washed with copper sulfate solution (2 × 100 mL, 10%) then with deionized water (2 × 100 mL) and dried over magnesium sulfate. Then it was filtered and evaporated under reduced pressure. The product was semi purified by column chromatography on silica gel eluted with a gradient system running from ethyl acetate (50%) / hexanes (50%) to ethyl acetate (100%). The resultant semi pure product

was then dissolved in methylene chloride (150 mL) and washed with hydrochloric acid (2M, 2 × 50 mL) and deionized water (2 × 100 mL) to remove unreacted 4-aminophenethyl alcohol. Then it was dried over magnesium sulfate filtered and evaporated to give pure product (1) as a white solid in a 48% yield. ^{1}H NMR ($CDCl_3$) δ 7.99–7.92 (m, 2H), 7.82–7.74 (m, 2H), 7.38 (s, 4H), 3.88 (q, 2H), 2.92 (t, 2H), and 1.66 (brs, 1H); ^{13}C NMR ($CDCl_3$) δ 167.34, 138.76, 134.38, 131.71, 129.92, 129.78, 126.66, 123.72, 63.43, and 38.83.

2-(4-(2-bromoethyl)phenyl)isoindoline-1,3-dione (2)

2-(4-(2-hydroxyethyl)phenyl)isoindoline-1,3-dione (1) (5.2 g, 0.0195 mols) was dissolved in methylene chloride (100 mL) followed by triphenyl phosphine (5.64 g, 0.215 mols). The resultant solution was stirred at ambient temperature and N-bromosuccinimide (3.73 g, 0.0210 mols) was added portion wise, after which stirring was continued for 18 h at ambient temperature. Then the solvent was removed under reduced pressure and the product was purified by column chromatography on silica gel eluted with ethyl acetate (50%) / hexanes (50%) to give 3.7 g of (2) as a white solid in a 57% yield.^{1}H NMR ($CDCl_3$) δ 7.98–7.92 (m, 2H), 7.82–7.78 (m, 2H), 7.42–7.34 (m, 4H), 3.59 (t, 2H), 3.22 (t, 2H); ^{13}C NMR ($CDCl_3$) δ 167.23, 138.80, 134.41, 131.68, 130.38, 129.39, 126.64, 123.74, 39.01, and 32.37.

2-(4-(2-(4-(1*H*-indol-3-yl)-3,6-dihydropyridin-1(2*H*)-yl)ethyl)phenyl)isoindoline-1,3-dione (4)

3-(1,2,3,6-tetrahydropyridin-4-yl)-1*H*-indol (3) was synthesized as previously described (Tomlinson et al., 2005). 2-(4-(2-bromoethyl)phenyl)isoindoline-1,3-dione (2) (3.7 g, 0.0112 mols) was added to dimethylformamide (100 mL). This was followed by 3-(1,2,3,6-tetrahydropyridin-4-yl)-1*H*-indol (3) (2.44 g, 0.0123 mols, and triethylamine (5 mL). The resultant solution was heated at reflux for 18 h, after which it was cooled and the product crystalized out of solution. This was removed by filtration and washed with ethyl acetate to give 1.7 g of (4) in a 32% yield as a yellow solid. ^{1}H NMR (DMSO) δ 11.17 (s, 1H), 8.03–7.87 (m, 5H), 7.50–7.40 (m, 6H), 7.23–7.07 (m, 2H), 6.21 (s, 1H), 3.34 (s, 2H), 2.95 (t, 2H), 2.79–2.74 (m, 4H), 2.60 (s, 2H); ^{13}C NMR (DMSO) δ 201.02, 189.22, 167.13, 136.95, 134.68, 131.58, 129.66, 129.13, 127.21, 123.41, 120.10, 119.57, 119.22, 117.60, 107.17, 59.81, 52.77, 50.02, 41.18, and 32.59.

4-(2-(4-(1*H*-indol-3-yl)-3,6-dihydropyridin-1(2*H*)-yl)ethyl)aniline (5)

2-(4-(2-(4-(1*H*-indol-3-yl)-3,6-dihydropyridin-1(2*H*)-yl)ethyl)phenyl)isoindoline-1,3-dione (**4**) (0.8 g, 0.0018 mols) was added to ethanol (100 mL) and hydrazine hydrate (2 mL) and gently warmed with stirring until a clear yellow solution was obtained. Stirring was continued at ambient temperature for 1 h then the solvent was removed under reduced pressure the residue was added to methylene chloride (100 mL) and stirred at ambient temperature for 18 h. Then the solution was filtered and washed with deionized water (100 mL), dried over magnesium sulfate filtered and evaporated to 0.4 g of product in a 70% yield, that appeared to be pure by NMR and was used in the next step without further purification. ^{1}H NMR ($CDCl_3$) δ 8.26 (s, 1H), 7.90 (d, 1H), 7.37 (d, 1H), 7.26–7.12 (m, 3H), 7.04 (d, 2H), 6.65 (d, 2H), 6.22 (s, 1H), 3.57 (brs, 2H), 3.22 (d, 2H), 2.84–2.50 (m, 8H); ^{13}C NMR ($CDCl_3$) δ 144.42, 136.75, 130.42, 129.71, 129.49, 125.25, 122.13, 121.19, 120.71, 119.97, 119.22, 118.07, 115.30, 111.27, 60.88, 53.15, 50.51, 33.10, and 29.15.

IDT785 (6)

4-(2-(4-(1*H*-indol-3-yl)-3,6-dihydropyridin-1(2*H*)-yl)ethyl)aniline (**5**) (0.05 g, 0.00016 mols) was added to biotin-PEG-SVA (0.1 g, 0.00002 mols) and this mixture was dissolved in methylene chloride. Then triethylamine (2 drops) was added and the solution was stirred at ambient temperature for 18 h. Finally, the solvent was removed under reduced pressure and the product was purified using size exclusion chromatography on Sephadex G10 resin to give 0.08 g of product IDT785 as a white powder.

Materials in Biological Assays

DMEM FluoroBrite Live cell imaging medium, DMEM, fetal bovine serum, penicillin/streptomycin, Lipofectamine 3000, biotin-4-fluorescein (B4F) and QD655Sav (emission max at 655 nm) were purchased from Thermo Fisher Scientific. Poly-D-lysine hydrobromide (mol wt 70,000–150,000), bovine serum albumin (BSA), and paroxetine hydrochloride hemihydrate were purchased from Millipore Sigma. 35-mm uncoated No. 1.5 coverslip-bottomed dishes were purchased from MatTek. pEYFP-C1-hSERT was a gift from Harald Sitte (Addgene plasmid # 70103[1]).

Cell Culture

HEK-293T cells were grown in a complete medium (DMEM with 2 mM glutamine, 10% FBS, 1% pen/strep) in a 37°C incubator with 5% CO_2. Cells were seeded in 0.01 mg/mL poly-D-lysine-coated (1 h at 37°C) MatTek dishes for fluorescence imaging or in uncoated 24-well plates for IDT307 transport assay at an appropriate density to obtain a subconfluent monolayer and grown for 24 h in the complete growth medium. Then the cells were transiently transfected with 500 ng of the appropriate DNA per MatTek dish/well using Lipofectamine 3000 according to the manufacturer's instructions.

IDT307 Transport Assay

HEK-293T cells were seeded in 24-well plates, transfected with 500 ng hSERT pcDNA3 for 24 h, and then incubated with 10 μM IDT307 for 15 min in the presence of increasing concentrations of IDT785. Parallel wells preblocked with 10 μM paroxetine served as a negative control. IDT307 uptake was terminated by aspiration, and adherent HEK-293T cells were then trypsinized, transferred to microfuge tubes, centrifuged at 2500 rpm for 5 min, and resuspended in ice-cold DMEM FluoroBrite. A 100-μL aliquot of the cell suspension corresponding to a single well in a 24-well plate was added to the black-bottom 96-well

[1]http://n2t.net/addgene:70103; RRID:Addgene_70103

plate. IDT307 fluorescence was collected on a BioTek Synergy H4 microplate reader using 480/20 nm excitation, 525/20 nm emission, and a gain of 100. Separately, a 50-μL aliquot of the cell suspension was then added to a coverslip and imaged at 20X (NA 0.4) on an inverted Axiovert 200M epifluorescence microscope using a standard GFP optical configuration.

Molecular Docking

The three-dimensional structures of the docked compounds (paroxetine and IDT785-PEG_2) were prepared in Chem3D 16.0. Docking analysis was performed using UCSF Chimera built-in AutoDock Vina to evaluate the hydrogen bond interaction and their binding affinities. The grid box was defined as 44 × 55 × 68 along the *x*, *y*, and *z* dimension, respectively, with the center *xyz* coordinates (126.823,130.899, and 110.557) at grid resolution of 1 Å for cryo-EM reconstructed ts2-inactive SERT–15B8 Fab–8B6 scFv complex with paroxetine in the outward-open conformation (PDB: 6DZW) to define the binding site for subsequent docking. Prior to docking, ts2-inactive SERT was separated from 15B8 Fab, 8B6 scFv, and paroxetine in UCSF Chimera. The following docking parameters were selected: number of binding modes – 10, exhaustiveness of search – 8, maximum energy difference (kcal/mol) – 3.

Biotin-4-Fluorescein Quenching Assay

In black, flat-bottom 96-well plates, 2 nM QD655Sav was titrated in duplicate wells with biotin-4-fluorescein (B4F) from 3 to 40 nM. Samples were incubated for 1 h at room temp, in the dark, and then fluorescence was measured using a BioTek Synergy H4 microplate reader at 523/13.5 nm with excitation at 494/13.5 nm and an instrument gain of 75. QD655Sav was pre-blocked with either 10 μM IDT785 or 10 μM free biotin for 30 min and then titrated with B4F as previously described. All solutions were prepared in phosphate buffer saline (PBS) without Ca^{2+}/Mg^{2+} (pH 7.4).

QD655Sav Labeling

QD labeling was implemented via a two-step protocol (Chang et al., 2012a; Thal et al., 2020). After the cells were allowed 24 h to achieve transporter expression in MatTek dishes, labeling was carried out by first incubating the cells with IDT785 at 10 μM (or 500 nM for single QD tracking) for 10 min at 37°C. Following three washes with warm DMEM FluoroBrite, cells were then incubated with a 0.1 nM (or 0.05 nM for single QD tracking) QD655Sav diluted in warm DMEM FluoroBrite supplemented with 1% w/w BSA (labeling buffer) for 5 min at room temperature, washed three times with warm DMEM FluoroBrite, and used immediately for time-lapse image series acquisition. In negative control experiments, transfected HEK-293T cells were first blocked with 10 μM paroxetine for at least 10 min and then incubated with IDT785 in the presence of paroxetine.

TIRF Microscopy and Colocalization Analysis

YFP-SERT/QD655 colocalization was imaged in the TIRF mode on a Nikon Eclipse Ti-E inverted microscope equipped with an Andor Zyla 4.2 PLUS sCMOS camera and viewed with an Apo TIRF 60×/1.49 NA oil objective. 488 nm excitation was sourced by a Nikon LU-NV laser unit. YFP-SERT emission was collected with a 525 ± 18 nm emission filter with an exposure time of 500 ms. QD655 signal was collected with a 655 ± 15 nm emission filter with an exposure time of 500 ms. Binary images of YFP-SERT were generated using adaptive thresholding algorithm in Matlab R2017b, the QD centroid positions for a given field of view were overlaid onto the binary YFP-SERT map, and the number/fraction of colocalized QDs for each dual channel field of view acquired were calculated.

Spinning Disk Confocal Microscopy

Time-lapse image series were obtained on an inverted Nikon-Ti Eclipse microscope system equipped with the Yokogawa CSU-X1 spinning disk confocal scanner unit, a heated stage, a 60× oil-immersion Plan Apo 1.4 NA objective, and a back-illuminated sCMOS Prime95B camera. QDs were excited using a 405-nm solid state diode laser (23 mW), and QD655 emission was collected through the 641/150 emission filter. YFP-SERT molecules were excited using the 488-nm line (65 mW), and the YFP emission was collected using the 525/36 emission filter. Single QD tracking was performed at a scan rate of 10 Hz for 1 min at 60× or 100× (Apo TIRF Oil NA 1.49) magnification. SPT data were obtained within 20 min of the final wash step after QD labeling. Cross-section view images of hSERT-transfected HEK-293T were acquired at 100 ms exposure time with 3 × 3 stitching of 512 × pixel sections at 15% overlap.

SIM Microscopy

SIM imaging was performed in single-plane 3D SIM mode on an inverted Nikon SIM microscope equipped Andor DU-897 EMCCD camera, a SR Apo TIRF 100× 1.49 NA oil-immersion objective, and 488 nm (74 mW) solid-state diode lasers used to excite YFP-SERT. Transfected HEK-293T were washed three times with warm DMEM FluoroBrite and imaged in warm DMEM FluoroBrite at room temperature.

Trajectory Reconstruction and Analysis

Image analysis and trajectory construction were performed using ImageJ TrackMate plugin (Jaqaman et al., 2008; Tinevez et al., 2017). Intermittency of QD fluorescence was used to verify that single fluorophores were analyzed, and extracted trajectories were at least 50 frames in length to increase the robustness of statistical analysis (Chang and Rosenthal, 2011, 2013; Kovtun et al., 2020). Trajectories were considered continuous if a blinking QD was rediscovered within a 1 μm distance during the 10-frame time window. For each trajectory, mean square displacement (MSD), $r^2(t)$, was computed as follows:

$$\left\langle r^2\left(n\delta t\right)\right\rangle = \frac{1}{N-n}\sum_{j=0}^{N-n-1}\left\{\left[x\left(j\delta t+n\delta t\right)-x\left(j\delta t\right)\right]^2 + \left[y\left(j\delta t+n\delta t\right)-y\left(j\delta t\right)\right]^2\right\} \quad (1)$$

where δt is the temporal resolution of the acquisition device, $[x(j\delta t), x(j\delta t)]$ is the particle coordinate at t = $j\delta t$, and N is the

number of total frames recorded for an individual particle. Prior to MSD calculations, individual trajectories were reindexed with continuous time vectors to close the gaps caused by blinking and simplify MSD analysis. The diffusion coefficient D_{MLE} was determined through the use of a previously published Maximum Likelihood Estimation (MLE) theoretical framework to maximize performance in accurately calculating D (Michalet and Berglund, 2012). Trajectories with $D_{MLE} < 5 \times 10^{-4}$ $\mu m^2/s$ (equivalent to the 95th percentile value of D_{MLE} derived from the analysis of QDs immobilized on a glass coverslip) were considered immobilized. Additionally, a 2D kernel density was generated for each trajectory using a bivariate kernel density estimator with diagonal bandwidth matrix (Botev et al., 2010), and the vector field corresponding to the x and y components of instantaneous displacements was overlaid onto the 2D kernel density map. The angle θ between two successive vectors $\boldsymbol{u}$ and $\boldsymbol{v}$ was calculated based on the following formula:

$$\cos\theta = \frac{\overrightarrow{u}.\overrightarrow{v}}{\|\overrightarrow{u}\|\|\overrightarrow{v}\|} \quad (2)$$

Relative Deviation Analysis to Classify Trajectory Motion Type

Independently of the motion mode, microscopic diffusion coefficient D_{2-4} was determined by fitting the first 2–4 points of the MSD versus time curves with the equation:

$$\langle r^2(t)\rangle_{2-4} = 4D_{2-4}t + offset \quad (3)$$

Four modes of motion are considered in order to describe the motional behavior of integral membrane proteins in the plasma membrane. These motional modes can be characterized on the basis of the plot of MSD versus time intervals:

(1) Stationary (immobilized) mode, in which a protein displays very little motion.
(2) Simple diffusion mode, in which a protein undergoes simple Brownian motion and its MSD-Δt plot is linear with a slope of 4D.
(3) Directed diffusion mode, in which a protein moves in a direction with a constant drift velocity with superimposed random diffusion with a diffusion coefficient D. In this case, the MSD-Δt plot is parabolic with a differential coefficient of 4D at time 0 (initial slope).
(4) Restricted diffusion mode, in which a protein undergoes Brownian motion within a limited area and cannot escape the area during the observation period ($0 \leq x \leq L_x$, $0 \leq y \leq L_y$). This mode of motion is equivalent to free Brownian diffusion within an infinitely high square well potential. The slope of the MSD-Δt curve at time 0 is again 4D, and the MSD-Δt curve asymptotically approaches ${L_x}^2/6$ and ${L_y}^2/6$ in the x and y directions, respectively.

The MSD-Δt plot shows positive and negative deviations from a straight line with a slope of 4D (in the case of two-dimensional diffusion) for directed diffusion and restricted diffusion, respectively. Larger deviations indicate larger probabilities of non-Brownian diffusion. A parameter for the relative deviation, RD(N, n), is defined as:

$$RD(N, n) = \frac{MSD(N, n)}{4D_{2-4}n\delta t} \quad (4)$$

where *MSD(N, n)* represents MSD determined at a time interval $n\delta t$ from a sequence of N video frames. $4D_{2-4}n\delta t$ is the expected average value of MSD for particles undergoing simple diffusion with a diffusion coefficient of D_{2-4} in two-dimensional space. In the case of simple diffusion, the average *RD(N, n)* should be 1 (Kusumi et al., 1993). Brownian trajectories with a diffusion coefficient of 0.1 $\mu m^2/s$ were generated by random walk simulations using experimentally relevant trajectory lengths (100, 200, 300, 400, 500, and 600 steps) to establish the effective cutoff values of RD at 25 frames (Kovtun et al., 2019). RD values within the 2.5th–97.5th percentile range were taken to represent statistical variations in Brownian motion, and those outside of the range taken as restricted diffusion. A linear least-squares fit to the 2.5th percentile points defined the lower boundary for free diffusion, with trajectories having RD(N,25) below this line classified as restricted. Since YFP-SERT at the plasma membrane should not be actively transported by intracellular processes, directed diffusion represented a small fraction of all trajectories and trajectories with RD(N,25) above the polynomial fit of the 97.5th percentile points were classified as free (Crane and Verkman, 2008).

RESULTS

IDT785 Inhibition of hSERT-mediated IDT307 Uptake

To determine if IDT785 inhibited hSERT uptake function, a fluorescence transport assay was carried out using IDT307 (APP+), a fluorescent substrate for monoamine transporters (Singh et al., 2012; Solis et al., 2012; Beikmann et al., 2013). IDT307 is a twisted intramolecular charge transfer compound (TICT) and only fluoresces once it is transported inside the cell, where it assumes the active (emissive) coplanar conformation by binding to intracellular biomolecules, with a particular preference for nucleic acids enriched in mitochondria and nucleoli (**Figure 2A**; Solis et al., 2012). As expected, hSERT-expressing HEK-293T cells incubated with 10 μM IDT307 for 15 min exhibited characteristic intracellular accumulation of IDT307 most pronounced in the mitochondria and nucleoli, whereas cells pretreated with excess IDT785 (100 μM) and 10 μM paroxetine [SERT binding affinity of ∼70 pM according to Cool et al. (1990)] showed significantly reduced intracellular IDT307 accumulation. Next, the relative half-maximal inhibitory concentration (IC_{50}) of IDT785 for inhibition of IDT307 uptake was determined using the BioTek Synergy H4 microplate reader. Briefly, IDT307 uptake was measured for hSERT-expressing HEK-293T cells incubated in the presence of increasing IDT785 dose or paroxetine (negative control) in duplicate wells (**Figure 2C**). Incubation of hSERT-expressing cells with IDT785 resulted in a concentration-dependent IDT307 uptake inhibition,

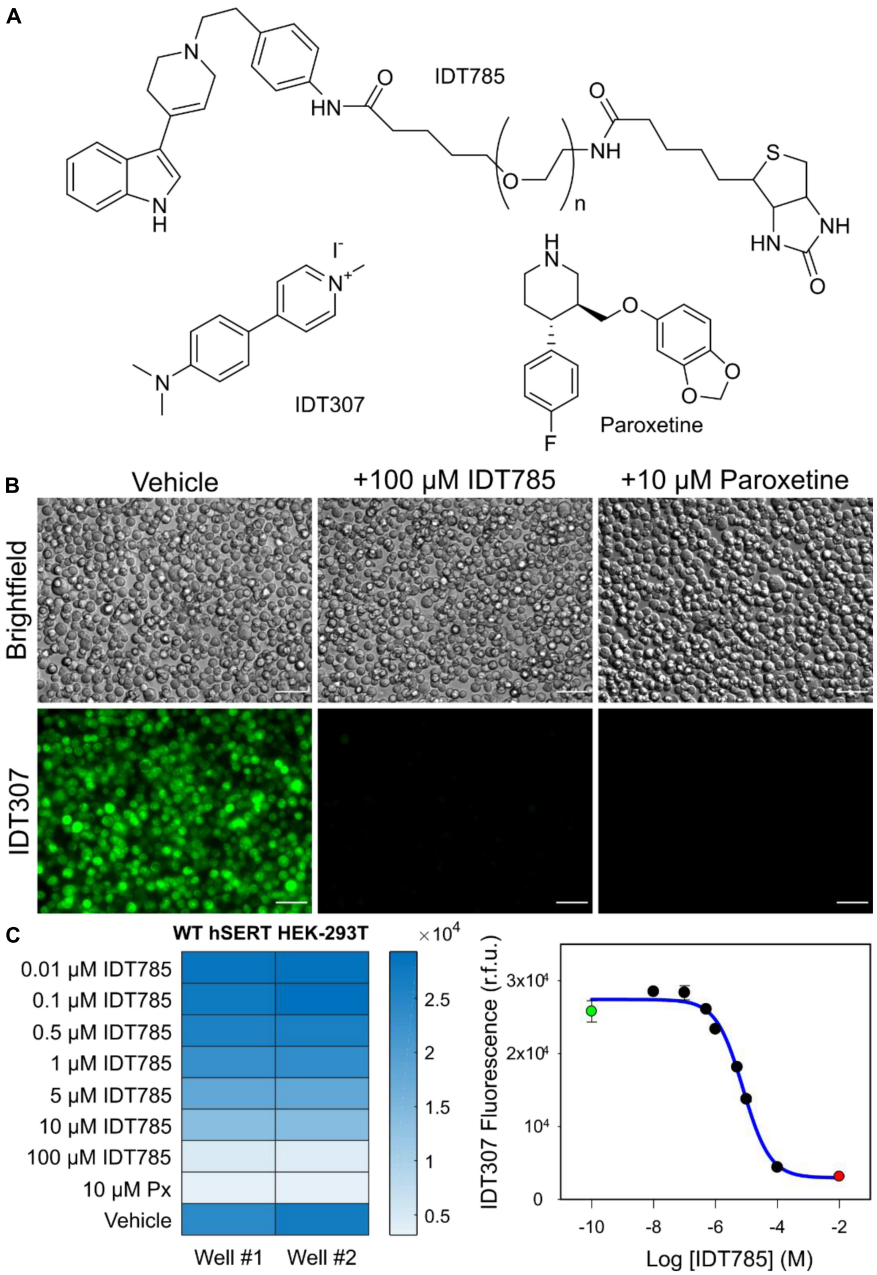

FIGURE 2 | IDT785 inhibits hSERT-mediated IDT307 transport in a dose-dependent manner. **(A)** Structures of compounds used in the IDT307 transport assay are shown. **(B)** Untreated hSERT-expressing HEK-293T cells demonstrated characteristic IDT307 (green) intracellular accumulation, whereas cells pretreated with either 100 μM IDT785 or 10 μM paroxetine showed significantly reduced IDT307 uptake. Scale bar: 50 μm. **(C)** The heat map of microplate reader fluorescence measurements of hSERT-HEK-293T cell suspensions treated with varying IDT785 doses is shown. The relative IC_{50} value of IDT785 for inhibition of IDT307 transport was determined to be 7.2 ± 0.3 μM (mean ± s.e.m.), $n = 3$. IC_{50} was determined by using non-linear regression curve fit for sigmoidal dose response (one-site competition) in Sigma Plot 12. Representative inhibition curve from single experiment is shown here. Data points from unblocked cells (green) and paroxetine-blocked cells (red) were used to establish the top and bottom plateau, respectively.

and the fitted dose-response curve appeared sigmoidal in each independent experiment. IDT307 accumulation in cells treated with 100 μM IDT785 did not reach complete inhibition as defined by paroxetine-treated cells; thus, IDT307 accumulation in paroxetine-treated cells was used as the complete inhibition data point (Weimer et al., 2012). The IC_{50} value was determined to be 7.2 ± 0.3 μM (mean ± s.e.m.) on the basis of three independent experiments, with a representative dose-response curve from a single experiment shown in **Figure 2C**. Our data suggest that although the attachment of spacer-PEG-biotin to the tetrahydropyridine nitrogen atom of the parent drug resulted in a relative reduction of the binding affinity [IC_{50}

of 690 ± 270 nM for 3-(1-methyl-1,2,3,6-tetrahydropyridin-4-yl)-1H-indole; Deskus et al., 2007], IDT785 still possessed biological activity and inhibited hSERT transport function in a dose-dependent manner.

IDT785 Inhibition of QD655Sav-mediated Biotin-4-fluorescein (B4F) Quenching

To determine if the biotin moiety of IDT785 was available for binding to the Sav active site on QD655Sav, a biotin-4-fluorescein (B4F) quenching assay was implemented, previously used to quantify the amount of Sav present on the surface of QDs (Mittal and Bruchez, 2011; Lippert et al., 2016). B4F fluorescence quenching is facilitated through charge transfer from fluorescein to the outward-facing Sav residues, only occurring when they are brought into close proximity by biotin binding (**Figure 3A**). Thus, Sav-mediated B4F quenching can be used in a competition assay format to validate IDT785 biotin binding to QD655Sav. Two fluorescence regimes exist for B4F quenching (Mittal and Bruchez, 2011). The first occurs at low nM B4F concentrations, where B4F quantitatively binds to QD655Sav and B4F fluorescence is significantly reduced. At 4:1 B4F:Sav stoichiometric ration, B4F fluorescence is reduced by up to 88% (Mittal and Bruchez, 2011). Once all biotin-binding sites are occupied with B4F, a second linear concentration-dependent regime is typically observed (**Figure 3B**). As expected, QD655Sav pre-blocked with either 10 μM free biotin or 10 μM biotinylated IDT785 exhibited a linear fluorescence regime at increasing B4F concentrations identical to B4F titration in buffer only (**Figure 3B**), indicating that IDT785 competitively inhibited B4F binding. These data confirmed that the PEG moiety did not interfere with IDT785 biotin terminus binding to Sav presented at the QD surface.

IDT785 Docking to ts2-inactive Outward-Facing SERT

Structural basis for binding of the diverse family of SSRIs to SERT has been under increasing scrutiny. Elegant engineering of thermostable SERT variants has resulted in solved X-ray crystal structures of SERT complexed with various antidepressants, and recent advances in single-particle cryo-EM have shed further light on molecular mechanisms of SERT inhibition by SSRIs (Coleman et al., 2016, 2019, 2020; Coleman and Gouaux, 2018). To gain insight into the interaction of IDT785 drug moiety with SERT, molecular docking was performed for a short version of IDT785 featuring the parent drug, spacer, and the PEG_2 terminus as well as paroxetine (control docking) into the outward-facing ts2-inactive SERT structure (PDB: 6DZW), which was previously solved in complex with paroxetine bound to the orthosteric site using single-particle cryo-EM (Coleman et al., 2019). Molecular docking was carried out using UCSF Chimera 1.4 with AutoDock Vina 1.1.2, and the docked complex for each compound was analyzed on the basis of binding affinity (score in kcal/mol) and hydrogen bond interactions with the amino acid residues within SERT (**Figure 4**). Best-scoring paroxetine binding pose (**Figures 4A–C**) had the binding affinity of −9.8 kcal/mol and docked into the central binding site in good agreement with the reported SERT-bound paroxetine pose shown in purple. Root-mean-square deviation (RMSD) between the reported paroxetine

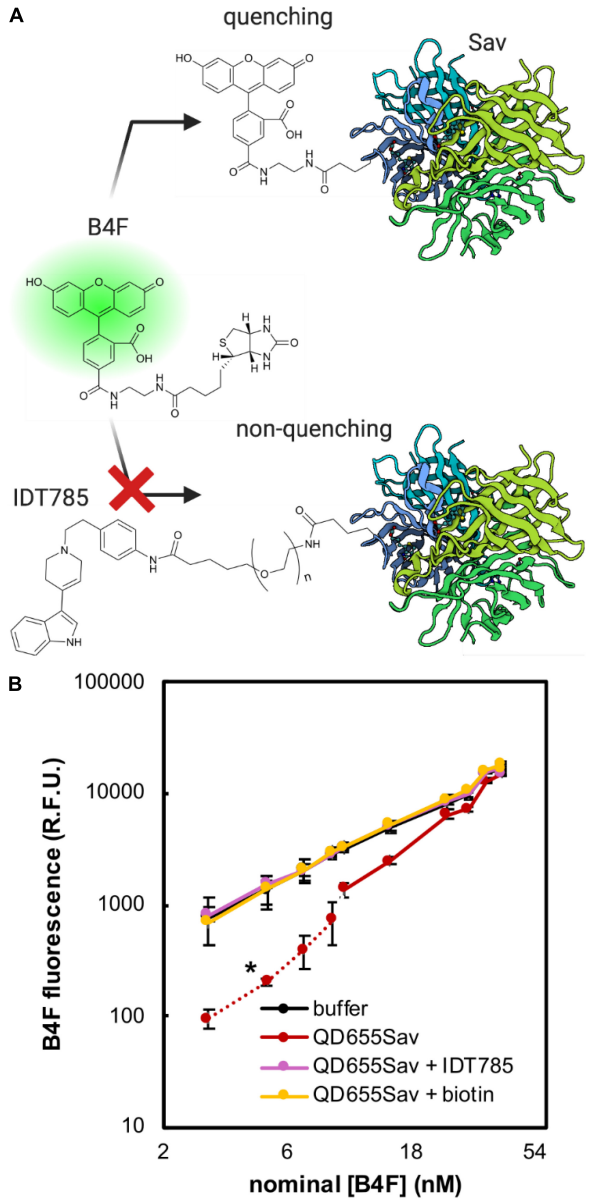

FIGURE 3 | Biotin-4-fluorescein (B4F) quenching assay to validate IDT785 biotin moiety availability. **(A)** Illustration of B4F quenching action. B4F fluorescence is quenched when it binds to streptavidin (Sav) at the QD surface. Pre-blocking QD-bound streptavidin with biotinylated IDT785 prevents B4F from binding, leading to retention of B4F fluorescence. Streptavidin structure was based on the RCSB PDB entry 1SWE. **(B)** Averaged titration profiles of 2 nM QD655Sav with B4F. Dashed red line indicates [B4F] range of strong quenching regime. Once all active sites are filled, fluorescence increases linearly similar to that of buffer (statistical comparison at [B4F] = 3, 5, 7, and 9 nM resulted in $*p < 0.05$, unpaired Student's *t*-test; $n = 4$ fluorescence intensity measurements per data point from 2 independent titrations). Negative controls: (1) QD655Sav pre-blocked with 10 μM IDT785, (2) QD655Sav pre-blocked with 10 μM free biotin, and (3) buffer only without QD655Sav.

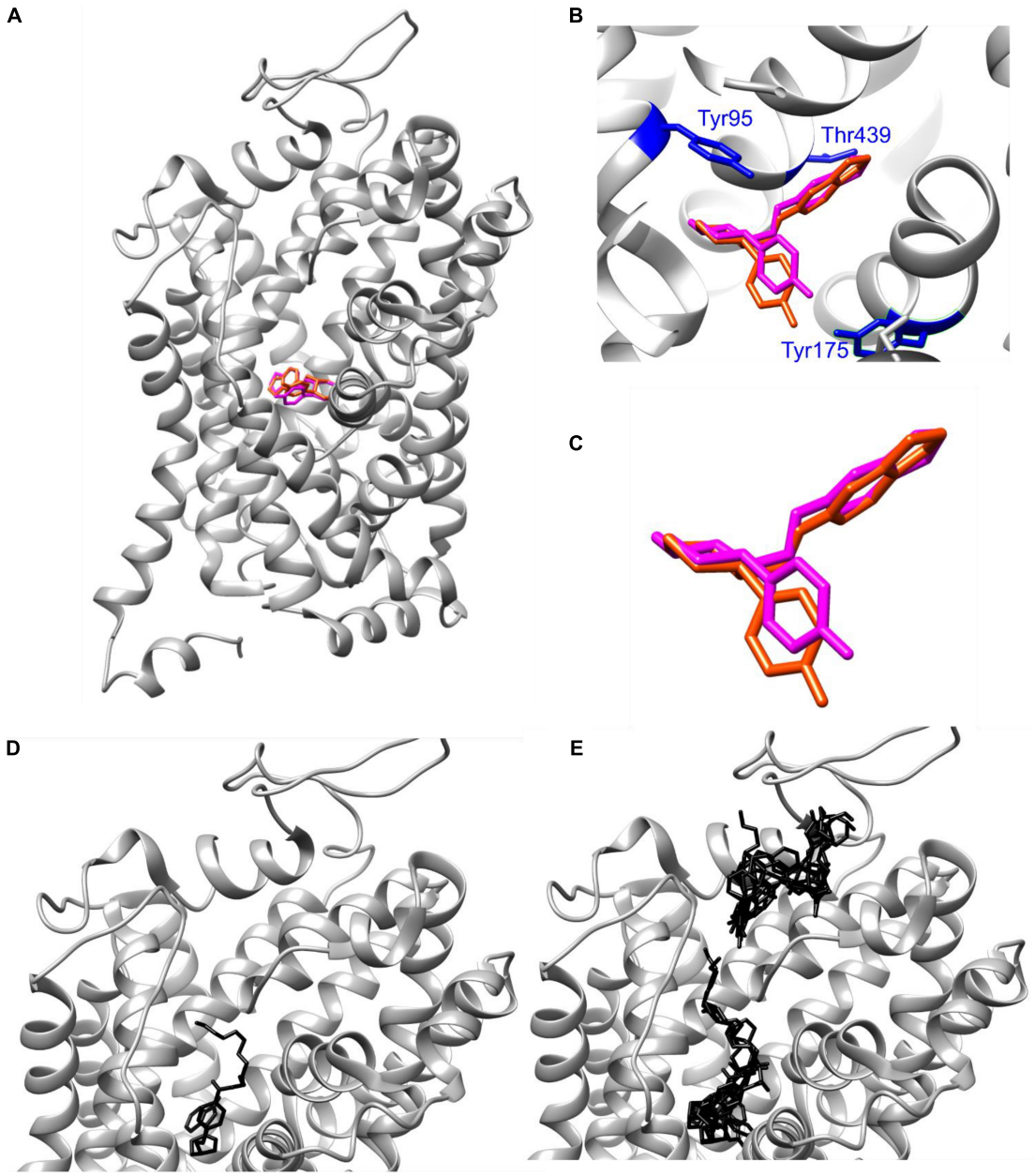

FIGURE 4 | AutoDock Vina docking of paroxetine and IDT785 drug moiety to hSERT. **(A–C)** Poses of paroxetine (magenta) docked via AutoDock Vina into ts2-inactive SERT are compared to the published cryo-EM SERT structure in complex with paroxetine (dark orange) (PDB: 6DZW). **(D)** Best-scoring (–9.8 kcal/mol) pose of PEG_2-spacer-IDT785 docked into ts2-inactive SERT is shown in black, occupying the central binding site with the PEG terminus extending toward the extracellular space. **(E)** Second binding site (range: [–7.6, –7.1] kcal/mol) for PEG_2-spacer-IDT785 was detected within the extracellular region of SERT.

pose and the docked pose in our analysis was calculated to be 0.789Å using open-source DockRMSD (Bell and Zhang, 2019). Hydrogen bond analysis revealed an interaction between the nitrogen atom and Asp98 residue with a distance of 2.327Å as well as Tyr95 with a distance of 2.323Å. Additionally, the benzodioxol oxygen of paroxetine was found to interact with Thr349 with a distance of 3.229Å. Best-scoring IDT785-spacer-PEG_2 pose (**Figure 4D**) had the binding affinity of −9.4 kcal/mol, with the drug moiety occupying the central binding site and the PEG chain extending into the extracellular vestibule. Hydrogen bond analysis revealed amide bond nitrogen interaction with both oxygen atoms (2.259 and 2.299Å) of Glu493, an extracellular gating residue. **Figure 4E** shows all detected IDT785-spacer-PEG_2 conformations docked into SERT structure, with a cluster of lower-scoring poses (binding scores between −7.6 and −7.1 kcal/mol) were located between EL2 and EL4 in the extracellular portion of the transporter. Overall, it appears that IDT785 is able to access the central binding site previously shown

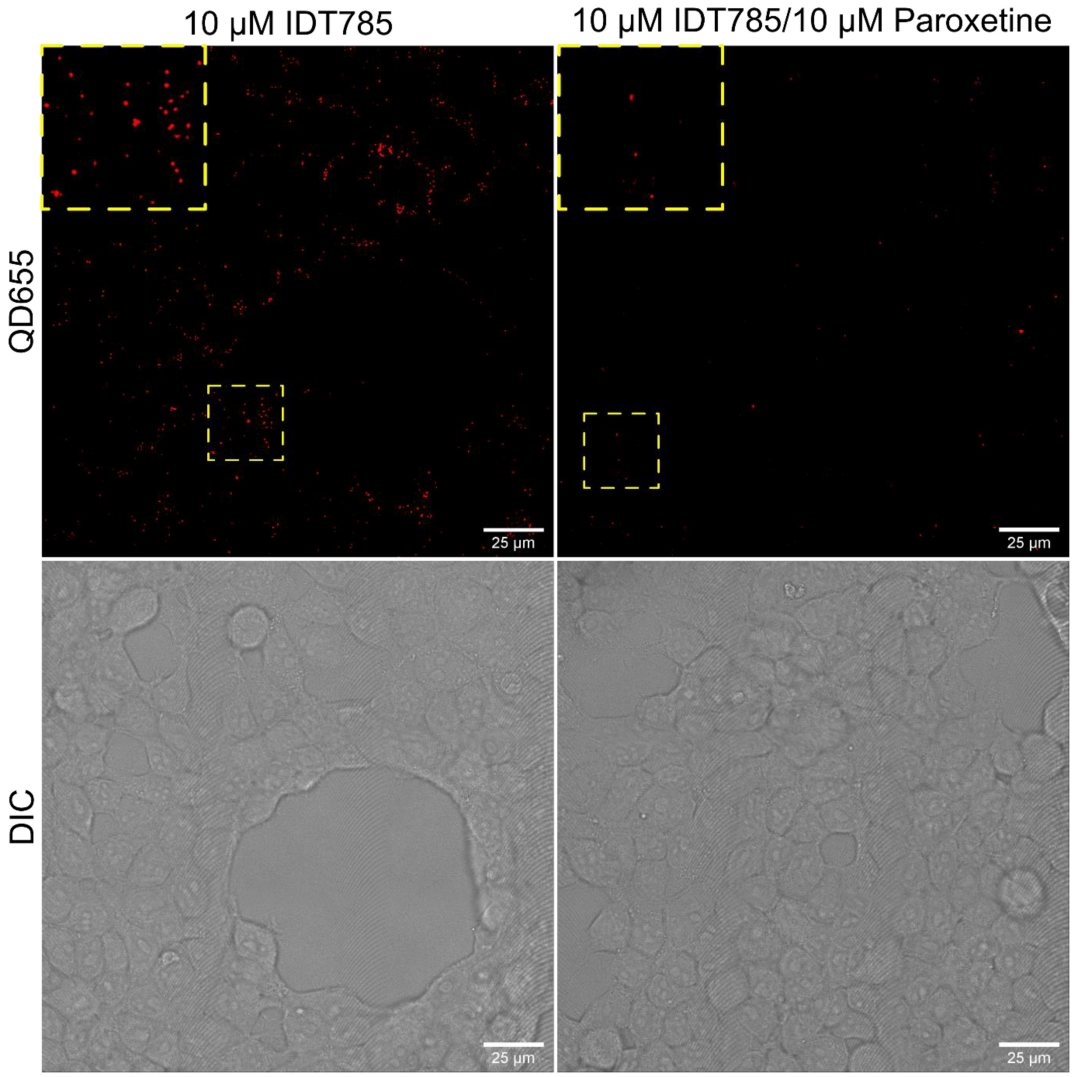

FIGURE 5 | IDT785 enables membrane hSERT labeling with streptavidin-conjugated QDs. Stitched (3 × 3) field of views of hSERT-HEK-293T cells sequentially labeled with 10 μM IDT785 and 0.1 nM QD655Sav (red) in the absence or presence of 10 μM paroxetine were acquired via spinning disk confocal microscope at the depth of ∼5 μm away from the coverslip-membrane interface. Punctate labeling pattern that is reduced in the presence of paroxetine is indicative of specific QD labeling of surface hSERT proteins. Yellow boxes indicate areas shown in the inset squares at digital zoom of ∼2. Scale bar: 25 μm.

to be occupied by paroxetine, although it is unclear whether the addition of a PEG chain impairs the ability of IDT785 to penetrate past the extracellular gate into the orthosteric site.

IDT785-QD Binding to Surface hSERT and YFP-SERT Proteins

After biological activity had been confirmed for both the drug end and the biotin end of IDT785, its ability to enable QD labeling of surface hSERT proteins transiently expressed in HEK-293T cells was evaluated. In a two-step labeling protocol, the cells were labeled first with 10 μM IDT785 for 10 min and then with 0.1 nM QD655Sav for 5 min. QD-labeled cells were imaged on the spinning disk confocal microscope immediately after the last wash step. Stitching 3 × 3 images with 15% overlap at the edges allowed us to capture a large field of view (FOV) of 298 × 298 μm^2 covering tens of cells (**Figure 5**). hSERT-HEK-293T cells preblocked with 10 μM paroxetine and then incubated with 10 μM IDT785 in the presence of 10 μM paroxetine were used as a negative control. A characteristic pattern of QD labeling that appeared to be associated with the membrane edges in the cross-section focal plane was apparent. Cells blocked with paroxetine had considerably fewer bound QD spots indicative of specific hSERT targeting. To obtain a more quantitative measure of QD labeling specificity, HEK-293T cells were transiently transfected with wild-type hSERT tagged with a yellow fluorescent protein at the intracellular N terminus (YFP-SERT) (Sucic et al., 2010; Montgomery et al., 2014). YFP-SERT-expressing cells were labeled with 10 μM IDT785 and 0.1 nM QD655Sav in a two-step protocol, with

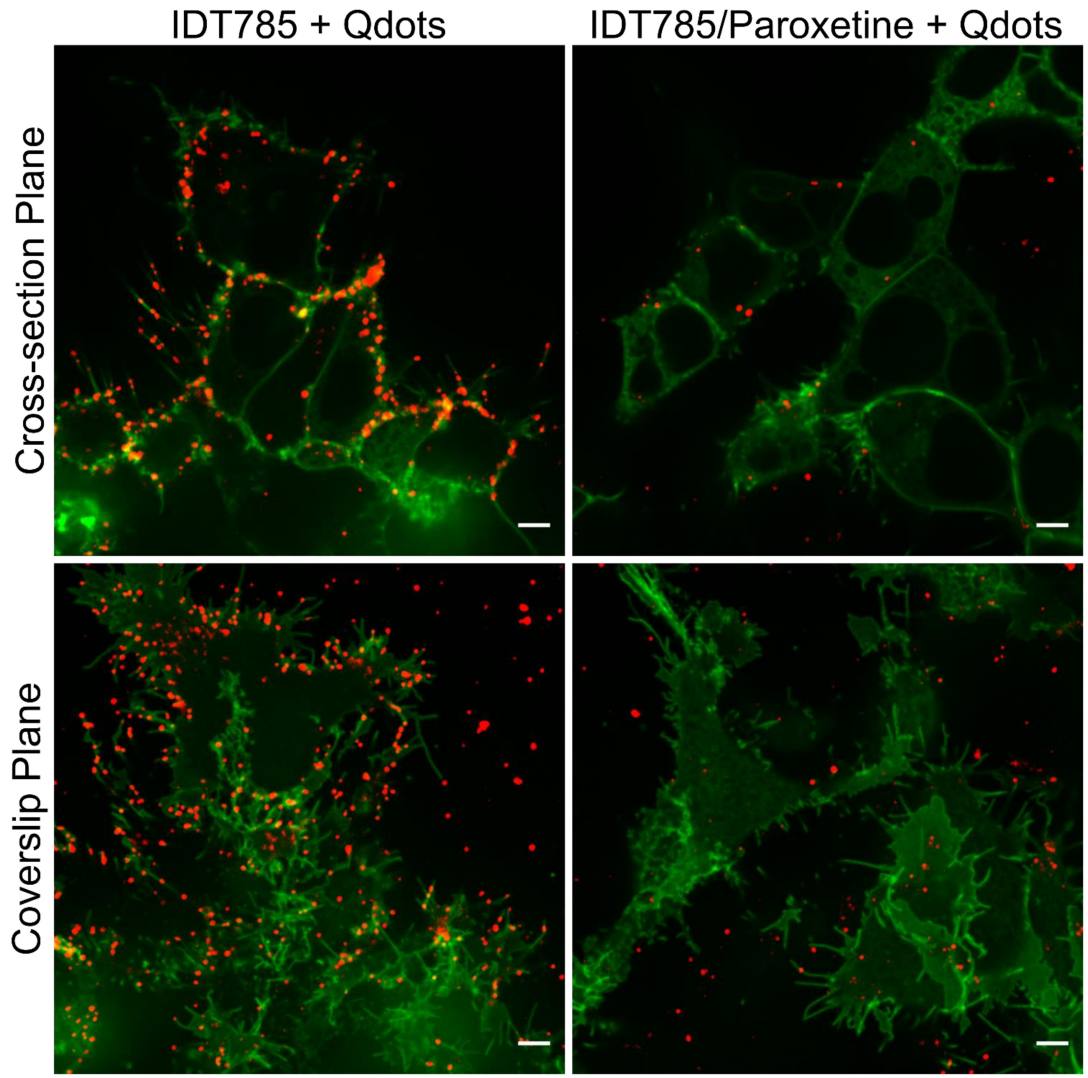

FIGURE 6 | IDT785 enables membrane YFP-SERT labeling with streptavidin-conjugated QDs. Cross-section (~5 μm away from the coverslip) and coverslip images of YFP-SERT-expressing (green) HEK-293T cells sequentially labeled with 10 μM IDT785 and 0.1 nM QD655Sav in the absence or presence of 10 μM paroxetine were acquired via spinning disk confocal microscope. Characteristic membrane-associated QD labeling pattern (red) that is reduced in the presence of paroxetine is readily apparent. Note a small fraction of QDs non-specifically bound to the coverslip outside YFP-SERT membrane regions. Scale bar: 5 μm.

paroxetine-blocked cells serving as a negative control. **Figure 6** shows representative images of the extent of QD labeling of membrane YFP-SERT at the membrane-coverslip interface as well as a few microns away from the coverslip, so that QDs non-specifically adsorbed to the coverslip are omitted (cross-section view). Visual inspection of paroxetine-blocked YFP-SERT-transfected cells revealed considerably lower extent of membrane QD labeling, in agreement with the previous result of untagged wild-type hSERT labeling. However, a fraction of QDs was non-specifically associated with both the plasma membrane and the coverslip surface in paroxetine-blocked cells. Since YFP-SERT appeared to be enriched in the membrane edges and protrusions at the membrane-coverslip interface (**Figures 6**, **7A**; **Supplementary Figure 1**), images of YFP-SERT distribution acquired in the TIRF mode were binarized using adaptive thresholding in Matlab and the colocalization of individual QD centroid positions with YFP-SERT for each acquired field of view (FOV) was determined (**Figure 7B**). The total number of colocalized QDs and the relative fraction of colocalized QDs per acquired FOV were significantly greater for YFP-SERT-expressing cells labeled with IDT785 and QD655Sav in the absence of paroxetine block (**Figure 7C**), thus confirming labeling specificity.

IDT785-enabled Single QD Tracking of YFP-SERT

To track QD-bound YFP-SERT, transfected HEK-293T cells were labeled stepwise with 500 nM IDT785 for 10 min and 0.05 nM QD655Sav for 5 min and imaged for 1 min at 100 ms

exposure time (10 Hz) to record the lateral movement of single QDs. Specificity of QD labeling was confirmed at these conditions by imaging YFP-DAT-transfected HEK-293T cells in parallel (**Supplementary Figure 2**). Representative maximum intensity projection (MIP) image of a 1-min sequence of QD movement overlaid onto YFP-SERT image and corresponding reconstructed QD trajectories are displayed in **Figure 8A**. A range of diffusive behavior was readily apparent from the reconstructed QD trajectory shape. Next, a Relative Deviation (RD) analysis was implemented to classify experimental QD trajectories as freely diffusing or restricted on the basis of mean square displacement (MSD)-Δt curve deviation compared to simulated trajectories undergoing simple Brownian motion (Kusumi et al., 1993; Kovtun et al., 2019). Additionally, QD trajectories diffusing at a rate slower than $D_{\text{cutoff}} = 5 \times 10^{-4}$ $\mu m^2/s$ (95th percentile of diffusion coefficient distribution of QDs dropcast onto a coverslip) were categorized as immobilized (Dahan et al., 2003; Kovtun et al., 2019). **Figure 8B** displays 10 randomly selected trajectories in each category of diffusion type. In total, 40% of QD trajectories (n = 1303) were classified as restricted diffusion, 45% (n = 1435) of QD trajectories were determined to exhibit simple Brownian diffusion, and 15% (n = 471) of QD trajectories were considered to be immobile, comprised of both immobile QD-bound YFP-SERT and QDs non-specifically adsorbed to the coverslip. Time-averaged ensemble MSD-Δt curves of immobilized and restricted QD trajectories exhibited characteristic downward curvature indicative of confined diffusion, whereas MSD-Δt curve for freely diffusing QDs was characterized by linear increase, as expected for a case of simple Brownian diffusion (**Figure 8C**). Analysis of individual trajectories revealed that Brownian trajectories were diffusing laterally at the rate of 0.04 $\mu m^2/s$ (median D_{MLE}) and instantaneous velocity of ~1.3 μm/s, approximately twice the diffusion rate of trajectories classified as restricted (D_{MLE} = 0.019 $\mu m^2/s$) and ~100 × faster than the diffusion rate of immobilized QD pool (**Figures 8D,E**). Overall, IDT785 enabled single QD tracking of YFP-SERT surface dynamics in transfected HEK-293T cells and subsequent classification of distinct motion modes exhibited by individual trajectories at the nanoscale.

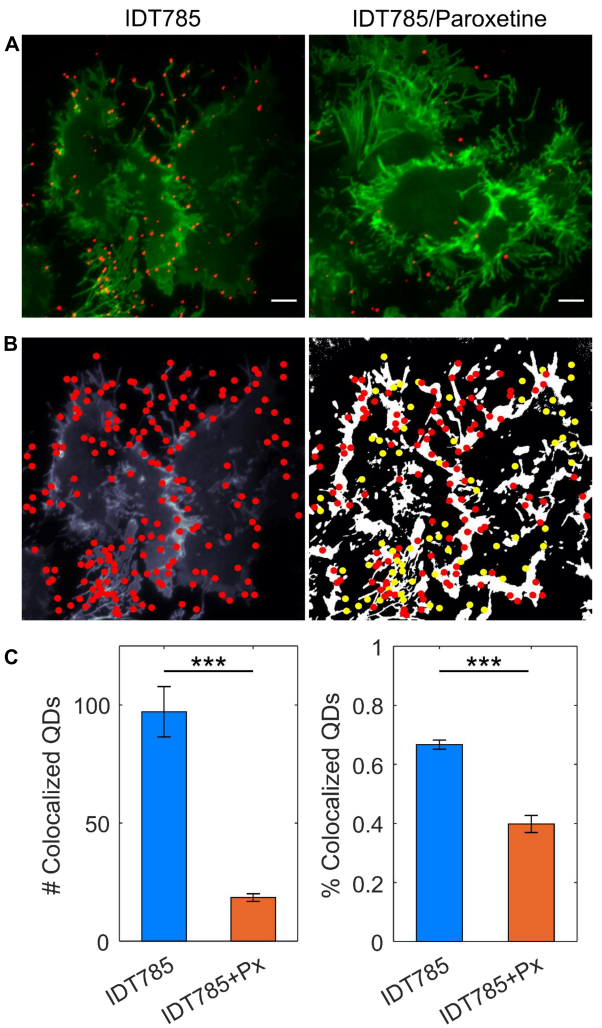

FIGURE 7 | Quantitation of specific QD labeling of YFP-SERT at the membrane-coverslip interface. **(A)** Representative TIRF images of YFP-SERT-HEK-293T cells sequentially labeled with 10 μM IDT785 and 0.1 nM QD655Sav in the absence or presence of 10 μM paroxetine. Scale bar: 5 μm. **(B)** Center positions of individual QDs were estimated with a 2D Gaussian fitting algorithm and overlaid onto binarized maps of YFP-SERT distribution in HEK-293T cells. Colocalization (red) and non-colocalization (yellow) of QDs with YFP-SERT were determined for a given 512 × 512 pixel field of view. **(C)** Number and fraction of colocalized QDs were determined in the absence (n = 17 fields of view; blue) and presence (n = 23 fields of view; orange) of paroxetine. Number of colocalized QDs: 97 ± 10 for IDT785 vs. 18 ± 2 for IDT785+Px; data presented as mean ± s.e.m.; ***$p < 0.0001$, unpaired Student's t-test. Fraction of colocalized QDs: 67 ± 2% for IDT785 vs. 40 ± 3% for IDT785+Px; data presented as mean ± s.e.m.; ***$p < 0.0001$, unpaired Student's t-test.

Protrusion Localization and Membrane Dynamics of YFP-SERT

TIRF imaging to validate ITD785 revealed that YFP-tagged hSERT was enriched in the membrane edges and thin protrusions. Interestingly, converging lines of evidence indicate that neurotransmitter transporters undergo highly specialized sorting, targeting, and retention, which results in a distinct (heterogeneous) surface transporter distribution both *in vitro* and *vivo* (Radian et al., 1990; Minelli et al., 1995; Nirenberg et al., 1997; Zhou et al., 1998; Tao-Cheng and Zhou, 1999; Miner et al., 2000; Steiner et al., 2008; Rao et al., 2012; Montgomery et al., 2014; Block et al., 2015; Caltagarone et al., 2015; Ma et al., 2017; Kaya et al., 2018). In particular, SERT was shown to primarily exist outside the synaptic junctions along the raphe neuron axonal membrane in a highly polarized pattern (Zhou et al., 1998; Tao-Cheng and Zhou, 1999). Catalytically active SERT was reported to preferentially localize to the actin-rich focal adhesions of resting human platelets (Steiner et al., 2008). Moreover, export of both endogenous SERT and heterologously expressed YFP-SERT from the endoplasmic reticulum (ER) is directed toward axonal tracts of cultured rat dorsal raphe neurons (Montgomery et al., 2014). To quantify the extent of YFP-SERT preferential

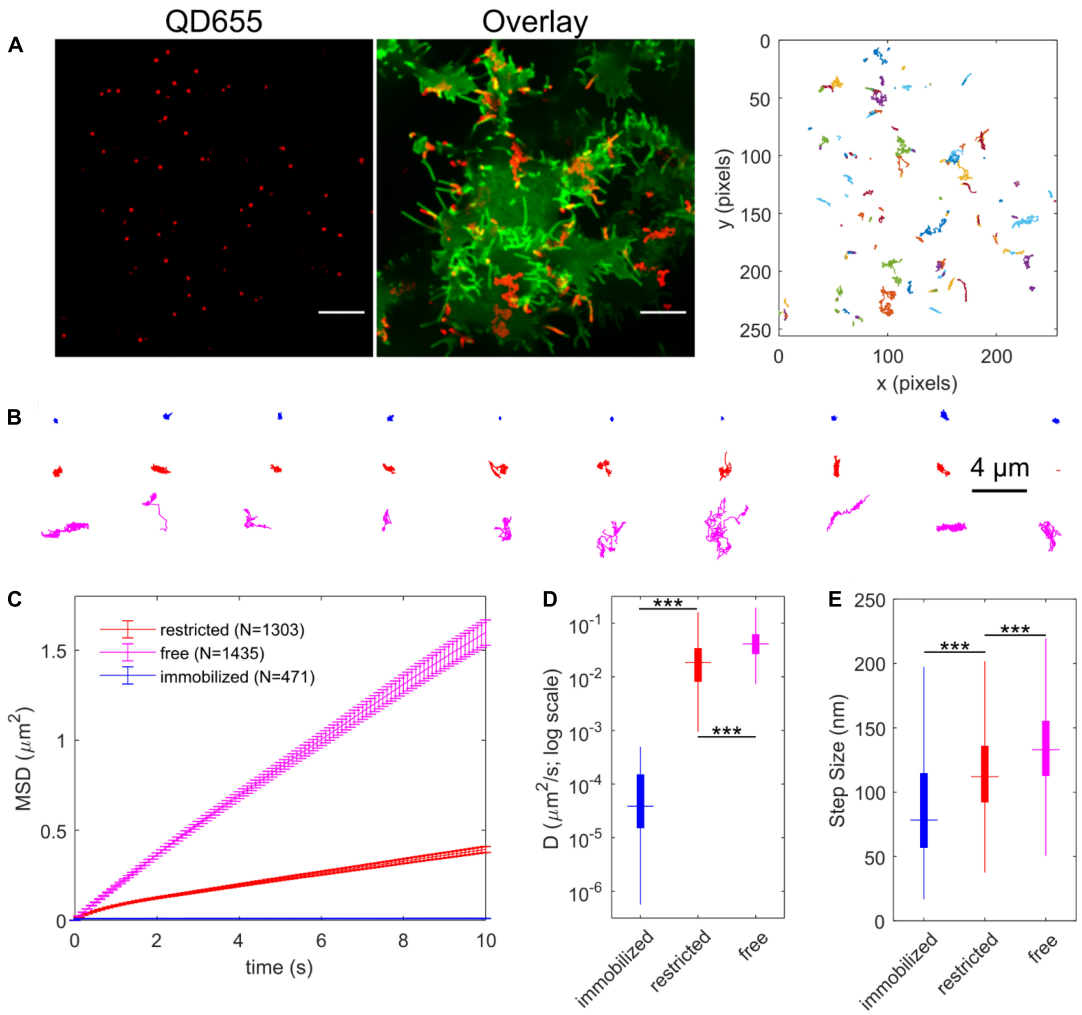

FIGURE 8 | IDT785-QD labeling enables single QD tracking of YFP-SERT in HEK-293T cells. **(A)** Representative spinning disk confocal images show YFP-SERT localization pattern and the corresponding QD labeling. Note the relative increase in YFP-SERT intensity in the protrusions. Scale bar: 10 µm. Middle panel shows maximum intensity projection of QD signal over time (600 frames recorded at 10 Hz) in red overlaid onto YFP-SERT image. Right panel shows reconstructed trajectories corresponding to the tracks apparent in the middle panel. A range of diffusive behavior is readily apparent. **(B)** Relative Deviation (RD) analysis identifies three distinct types of diffusion exhibited by YFP-SERT-QD trajectories. Ten representative trajectories are shown for each diffusion type – immobilized (blue; $D < 5 \times 10^{-4}$ µm^2/s), restricted (red), and free or Brownian (magenta). **(C)** Time-dependent averaged MSD curves are shown for YFP-SERT-QD trajectories that are immobilized (471 tracks from 3 independent experiments; 15% of total), undergo restricted diffusion (1303 tracks from 3 independent experiments; 40%), and undergo free diffusion (1435 tracks from 3 independent experiments; 45%). MSD curves include weighted standard deviation error bars. **(D)** Box plot shows the diffusion coefficient distribution for each diffusion type trajectories. The median value is shown as the colored horizontal line in the box, the 25–75% IQR interval corresponds to the length of the colored box, and whiskers extend to 5 and 95% percentile values. The distributions were compared using the Mann-Whitney *U* test (***$p < 0.001$, immobilized tracks: $D_{median} = 3.9 \times 10^{-5}$ µm^2/s, IQR = [1.5×10^{-5}, 1.5×10^{-4}]; restricted diffusion: $D_{median} = 0.019$ µm^2/s, IQR = [0.008, 0.034]; free diffusion: $D_{median} = 0.041$ µm^2/s, IQR = [0.027, 0.062]). **(E)** Box plot shows the instantaneous step size (per $\Delta t = 100$ ms) distribution for trajectories of each diffusion type. The median value is shown as the colored horizontal line in the box, the 25–75% IQR interval corresponds to the length of the colored box, and whiskers extend to 5 and 95% percentile values. The distributions were compared using the Mann-Whitney *U* test (***$p < 0.001$, immobilized tracks: step $size_{median} = 78$ nm, IQR = [57, 115]; restricted diffusion: step $size_{median} = 112$ nm, IQR = [92, 136]; free diffusion: step $size_{median} = 133$ nm, IQR = [113, 155]).

localization to the edge and protrusion (PE) regions, super-resolved images of YFP-SERT-expressing HEK-293T cells were captured on a structured illumination microscope in a 3D mode (**Figure 9A**). Pronounced peaks in the line intensity profile shown in **Figure 9B** indicate a large increase of the YFP-SERT density in PE membrane regions compared to the flat membrane (FM) zones. The average YFP intensity ratio for PE:FM regions was calculated to be equivalent to approximately 300% enrichment of YFP-SERT in the PE regions, consistent with visually apparent YFP-SERT polarized distribution (**Figure 9C**). Next, at least 100 QD trajectories were manually selected for protrusion- and FM-localized YFP-SERT from time-lapse videos acquired at 100 × magnification for 1 min at 10 Hz for subsequent MSD and diffusion analysis (**Figure 9D**). Motion of QD-labeled YFP-SERT along the protrusions was Brownian in nature, as evidenced by the linear MSD-Δt curve and the

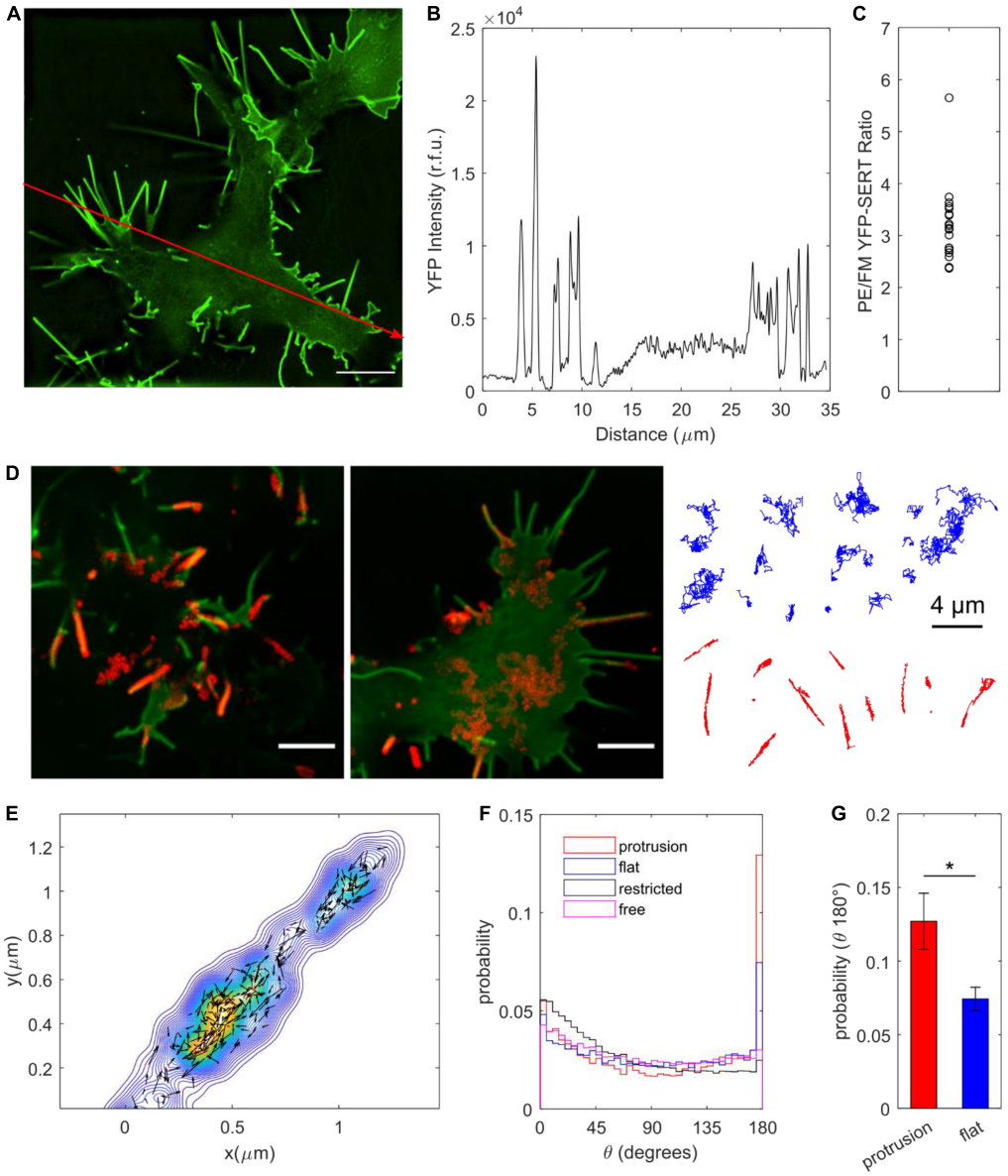

FIGURE 9 | Surface dynamics of YFP-SERT pool localized to the membrane protrusions. **(A)** A representative SIM image demonstrates YFP-SERT localization pattern in transiently transfected HEK-293T cells. Scale bar: 5 μm. **(B)** An intensity line plot corresponding to the red line drawn in **(A)** indicates the presence of high-density YFP-SERT cellular regions localized to the membrane protrusions and membrane edges. **(C)** A scatter plot of the ratio of YFP-SERT intensity in protrusions/edges (PE) vs. flat membrane zones (FM) reveals a ∼300% enrichment of YFP-SERT in PE membrane regions (mean ± s.e.m., PE/FM YFP intensity: 3.2 ± 0.2; data are based on 19 1024 × 1024 reconstructed fields of view acquired in three independent experiments). **(D)** Two representative images demonstrate SERT-QD diffusion in distinct cellular regions – flat membrane (FM) zones and membrane protrusions. Maximum intensity projections of the QD channel of the time-lapse image series (600 frames at 10 Hz, 100×) were overlaid onto YFP-SERT images. Scale bar: 5 μm. Representative trajectories are shown for each membrane region of interest (FM in blue, protrusions in red). **(E)** A representative color-coded bivariate 2D kernel density contour plot corresponds to a single YFP-SERT-QD protrusion trajectory and includes scaled velocity vectors for single-step instantaneous displacements. Bidirectional motion along the protrusion is readily apparent. **(F)** Probability distributions for the angle θ between two successive displacement vectors are displayed for QD trajectories localized to protrusions (n = 64,062 steps) and flat membrane regions (n = 66,072 steps), as well as previously classified trajectories undergoing restricted diffusion (n = 1,045,575 steps) and Brownian diffusion (n = 855,570 steps). θ = 0 degrees corresponds to motion reversal, whereas θ = 180 degrees corresponds to continued progress in a given direction, indicative of unimpeded diffusion. **(G)** Protrusion trajectories (n = 110; red) exhibited greater probability of the calculated θ within the 175–180 degree range compared to flat membrane region trajectories (n = 113; blue) (mean ± s.e.m.; 0.12 ± 0.2 vs. 0.07 ± 0.01; $^*p < 0.05$, unpaired Student's t-test).

median diffusion coefficient of 0.041 $\mu m^2/s$, statistically identical to that of trajectories classified as freely diffusing in the previous section (**Supplementary Figure 3**). Additionally, 2D kernel density contour maps were constructed for individual protrusion trajectories and visualized with overlaid instantaneous velocity vectors in **Figure 9E**. QD-bound YFP-SERT motion along the

protrusion was bidirectional in nature, with frequent direction switching along the major protrusion axis. According to Lam et al. (2019), the higher probability of small angle θ between successive frame-to-frame steps indicates frequent occurrence of directional switching that may be suggestive of diffusion being impeded by submicron-sized compartments. Therefore, the angle θ was calculated for QD-bound YFP-SERT trajectories, with θ = 0° corresponding to direction reversal and θ = 180° indicating unimpeded forward motion (**Figures 9F,G**). The probability of θ in the range of 175–180° for protrusion-localized trajectories was significantly greater than θ in the identical range for FM region-localized trajectories and θ in the range of 0–5° for protrusion-localized trajectories, corroborating that QD-bound YFP-SERT complexes exhibited largely unimpeded diffusion within membrane protrusions. Together, these data further demonstrate that IDT785 readily enables QD-based characterization of YFP-SERT diffusion patterns at the nanoscale.

DISCUSSION

Over the past two decades, ultrastructural electron microscopy and immunofluorescence approaches have revealed a unique pattern of SERT distribution in the plasma membrane in both brain- and periphery-derived cultures (Zhou et al., 1998; Tao-Cheng and Zhou, 1999; Miner et al., 2000; Steiner et al., 2008; Montgomery et al., 2014). The molecular mechanisms that enable optimal SERT positioning for rapid clearance of extracellular serotonin remain largely unknown, and trafficking-dependent regulation of SERT function has been an area of active investigation. The study of SERT trafficking in live cell cultures has been significantly limited by the lack of suitable antibodies that target the extracellular domain of the transporter. To combat this challenge, the Rosenthal laboratory pioneered the use of small-molecule neurotransmitter or antagonist derivatives to enable real-time monitoring of SERT trafficking at the cell surface (Rosenthal et al., 2002; Tomlinson et al., 2011; Chang et al., 2012b). Our current probe design features an attachment of a biotinylated, PEGylated spacer to a transporter-specific antagonist, which can then be readily detected by streptavidin-conjugated QDs and facilitate single QD tracking of transporter membrane dynamics. In this approach, the point of spacer attachment must be carefully chosen to preserve parent antagonist binding affinity for SERT; moreover, the spacer identity is critically important for stabilizing the antidepressant-transporter interaction as well as minimizing non-specific ligand binding to the plasma membrane or coverslip. In particular, our recent report demonstrated that replacing a flexible alkyl (undecyl) spacer with a more rigid, electron-rich, less hydrophobic phenylethyl spacer in the structure of biotinylated D2 dopamine receptor ligand significantly reduced non-specific ligand binding to the coverslip surface (Tomlinson et al., 2019). Thus, our goal in the current study was to incorporate the phenylethyl spacer into the SERT ligand design and determine its effect on parent drug affinity, ligand binding specificity, and consequently the ability to monitor surface SERT dynamics with ligand-conjugated QDs.

Modification of the pyridinyl nitrogen in the parent drug 3-(1,2,3,6-tetrahydropyridin-4-yl)-1H-indole was found to be relatively well-tolerated (Deskus et al., 2007; Tomlinson et al., 2011). The methyl-substituted analog 3-(1-methyl-1,2,3,6-tetrahydropyridin-4-yl)-1H-indole was determined to inhibit [^{3}H]citalopram binding to hSERT in the membrane homogenates of stably transfected HEK-293 cells with the IC_{50} value of 690 ± 270 nM (Deskus et al., 2007). Our concerns were that the steric constraints of the extracellular SERT vestibule might not support the bulkier phenylethyl spacer extending into the extracellular space and slightly lower hydrophobicity of the aromatic ring compared to an alkyl chain might reduce binding stability. To measure the binding affinity of the biotinylated, PEGylated 3-(1-phenethyl-1,2,3,6-tetrahydropyridin-4-yl)-1H-indole (IDT785), an IDT307 (APP+) fluorescent substrate transport assay was employed. IDT307 is actively transported across the membrane via monoamine neurotransmitter transporters (SERT, DAT, NET) as well as organic cation transporters 1–3 (OCT 1–3) and permits rapid characterization of transporter-inhibitor interaction in a 96-well plate format (Duan et al., 2015). The IC_{50} values determined by this method show minimal plate-to-plate or day-to-day variability. hSERT-mediated uptake in transiently transfected HEK-293T cells was effectively inhibited by excess (100 μM) IDT785 and 10 μM paroxetine (negative control) (**Figure 2**), indicating that the phenylethyl spacer did not adversely affect the biological activity of 3-(1,2,3,6-tetrahydropyridin-4-yl)-1H-indole. The IC_{50} of IDT785 was determined to be 7.2 ± 0.3 μM using IDT307-based inhibition assay, comparable to our previously reported compounds based on 3-(1,2,3,6-tetrahydropyridin-4-yl)-1H-indole featuring the undecyl linker (Tomlinson et al., 2011). Admittedly, the IC_{50} of the final biotinylated ligand is quite high and an order of magnitude larger than the IC_{50} of the drug intermediate before the PEGylation step (**Supplementary Figure 4**). Our next goal is to achieve sub-μM affinity before we proceed with SERT tracking experiments in neuronal cultures or intact tissue. At high ligand doses, one might anticipate several potential undesirable off-target effects, including activation of serotonin receptors [the parent drug of IDT785 is a derivative of RU-24969, a preferential 5-HT_{1B} agonist, with a K_i of 0.38 nM, which also displays appreciable affinity for the 5-HT_{1A} receptor (K_i = 2.5 nM) (Aronsen et al., 2014)] or incorporation of the lipophilic moiety of IDT785 into membrane rafts (Erb et al., 2016). These off-target effects can in turn influence SERT surface state by inducing changes in membrane polarization through the activation of membrane ion channels, G protein-mediated stimulation of signaling pathways that control SERT trafficking/phosphorylation/palmitoylation, or local disruption of membrane rafts that are known to stabilize transport-willing SERT conformation. Next, a B4F quenching assay was performed to rule out the possibility (although unlikely) that the PEG chain sterically hindered the availability of the IDT785 biotin end for binding to Sav conjugated to QDs. Quenching of B4F fluorescence upon free Sav or SavQD binding is a well-documented phenomenon, with a nearly 90% B4F fluorescence reduction achieved at B4F:Sav molar ratios ≤ 4:1

(Mittal and Bruchez, 2011; Lippert et al., 2016). Indeed, blocking of QD655Sav with either free biotin or biotinylated IDT785 effectively prevented Sav-mediated B4F quenching, suggesting that the biotin end of IDT785 was readily available for QD655Sav binding (**Figure 3**).

Molecular mechanisms of SSRI interactions with SERT have been of great interest in the pursuit of drugs with greater specificity and fewer adverse side effects. As a result of extensive efforts, X-ray and cryo-EM structures of SSRI-bound SERT are now publicly available (Coleman and Gouaux, 2018). The general consensus is that high-affinity SSRIs occupy the S1 central-binding site composed of subsites A, B, and C and stabilize the transporter in an outward-facing conformation, although ambiguity remains concerning the precise binding poses of SSRIs within S1 (Coleman et al., 2020). A secondary, allosteric site S2 is formed above S1 in the extracellular vestibule of the transporter in the outward-facing conformation, permitting modulation of S1 ligand dissociation kinetics. Previously, docking of 3-(1,2,3,6-tetrahydropyridin-4-yl)-1H-indole derivative to the vestibular binding pocket of hSERT model based on the bacterial homolog LeuT showed that the indole docked deep into the vestibular pocket and the S2 substrate site, whereas tetrahydropyridine N-substituents extended out to the extracellular environment (Nolan et al., 2011). Surprisingly, molecular docking performed via user-friendly Autodock Vina in UCSF Chimera revealed that the best-scoring poses of the parent drug of IDT785 attached to the phenylethyl spacer and a short PEG_2 chain were oriented in such manner that the binding site of the indole moiety overlapped with the central binding site occupied by paroxetine in the cryo-EM SERT structure and the tetrahydropyridine N-substituent extended into the extracellular space, thus supporting the importance of tetrahydropyridine indole portion for SERT binding and consequently enabling capture of extracellular biotin. A separate cluster of lower-scoring binding poses was located in the outer extracellular vestibule partially formed by EL2 and EL4 of SERT. Extending distal PEG_2 spacer to PEG chain with the number of repeat units $n \geq 3$ resulted in a loss of indole access to the central binding site and the best-scoring binding poses (<7 kcal/mol; data not shown) located in the outer extracellular vestibule. This suggests that the introduction of a longer PEG spacer might prevent the indole moiety from accessing deeper into the extracellular vestibule and substrate sites S1 and S2, thus resulting in modest SERT binding affinity as determined in IDT307-based uptake inhibition experiments.

Since biological activity and availability for binding of both ends of IDT785 was verified, the next step was to assess whether IDT785 facilitated specific QD labeling of surface SERT proteins. To this end, wild-type hSERT and YFP-tagged hSERT constructs were transiently expressed in HEK-293T cells and then labeled with biotinylated IDT785 (10 μM or ∼1.4 × its IC_{50} value) and 0.1 nM QD655Sav stepwise; subnanomolar QD concentration was chosen as non-specific binding of commercially available streptavidin-conjugated QDs is well-controlled below 1 nM (Bentzen et al., 2005; Rosenthal et al., 2011) and is thus preferred for single QD tracking assays. Imaging of hSERT-expressing cells revealed sparse QD labeling associated with the plasma membrane that was considerably blocked in the presence of paroxetine (**Figure 5**). This observation was confirmed by imaging of HEK-293T cells transiently expressing YFP-tagged hSERT and incubated with IDT785 and QD655Sav at identical conditions (**Figure 6**). YFP-SERT signal was particularly useful for identifying a fraction of QDs non-specifically adsorbed to the coverslip. Minimal non-specific binding of IDT785-QDs to the coverslip and plasma membrane in paroxetine-blocked cells was observed, likely due to the synergistic effect of the reduced surface area, length and hydrophobicity (logP) of the phenethyl spacer compared to the undecyl linker in our earlier ligands. Interestingly, YFP-SERT was not uniformly distributed in the plasma membrane at the coverslip interface when imaged either via spinning disk confocal microscope (**Figure 6**) or TIRF microscope (**Figure 7**). This phenomenon allowed us to generate binary maps of YFP-SERT cell surface distribution and quantitate the extent of QD labeling specificity by determining individual QD localization to the YFP-SERT-rich membrane regions. As a result, the total number and fraction of detected QDs that were colocalized with YFP-SERT were significantly greater for transfected HEK-293T cells in the absence of paroxetine compared to paroxetine-blocked cells. Quantitative confirmation of labeling specificity at these conditions (10 μM IDT785 for 10 min; 0.1 nM QD655Sav) allowed us to proceed toward single QD tracking experiments.

Single-molecule fluorescence microscopy has revealed that lateral diffusion is a fundamental feature of post-translational regulation of various transmembrane receptors, transporters, and ion channels (Rosenthal et al., 2011; Kusumi et al., 2014; Kovtun et al., 2018). Our previous QD-based studies of SERT surface dynamics demonstrated that endogenous SERT was preferentially compartmentalized to cholesterol-rich microdomains and was readily mobilized in response to cholesterol depletion and phosphorylation of its intracellular domain in immortalized serotonergic rat neurons and cultured rat dorsal raphe neurons (Chang et al., 2012b; Bailey et al., 2018). QD tracking in stably transfected CHO cells showed that the ASD-associated, hyperphosphorylated G56A hSERT variant exhibited ∼40% faster diffusion rate at the cell surface (Kovtun et al., 2018). To demonstrate that IDT785 enables QD tracking of YFP-SERT, HEK-293T expressing YFP-tagged transporters were labeled with a combination of IDT785 (500 nM) and QD655Sav (0.05 nM). QD movement was monitored for 600 frames at the rate of 10 Hz, and single QD trajectories were reconstructed from the acquired time-lapse image series (**Figure 8**). A wide range of diffusive behavior of YFP-SERT was readily evident from the shape of reconstructed QD trajectories, and the RD analysis of MSD-Δt curves in comparison to simulated Brownian motion trajectories showed that 85% of QD trajectories were mobile versus 15% of immobilized QDs, although it was not possible to distinguish QDs non-specifically adsorbed to the coverslip and QDs bound to immobile YFP-SERT (Dahan et al., 2003). The slight majority of mobile QD trajectories exhibited simple Brownian diffusion (45%; median D = 0.04 $\mu m^2/s$), whereas 40% of mobile tracks were determined to undergo restricted diffusion (40%; median D = 0.02 $\mu m^2/s$), consistent with our previous observation that a large pool of endogenous SERT in the neuronal membrane is confined to cholesterol-rich membrane

microdomains (Chang et al., 2012b; Bailey et al., 2018). Naturally, an important question arises - how accurately do QDs measure the rate of lateral diffusion of membrane SERT proteins? In fact, suitability of commercially available QDs for tracking surface dynamics of neuronal receptors and transporters has recently been under scrutiny, as improvements in organic fluorophore photophysics, instrumentation, and stochastic activation-based imaging modalities have simplified implementation of dye-based tracking (Lavis, 2017; Shen et al., 2017). For instance, Lee et al. (2017) discovered that over 90% of AMPA glutamate receptors bound to commercially available QDs (diameter > 20 nm) were extrasynaptic and highly mobile, whereas ∼90% of AMPA receptors labeled with smaller dyes and compact QDs were diffusing in a confined manner in nanodomains within the post-synaptic density (PSD). As another example, Abraham et al. (2017) reported that although QDs could resolve large differences in B cell receptor mobility, larger QDs compared to a small cyanine dye (Cy3) sterically hindered receptor mobility at the cell-coverslip interface, altered the frequency of transitions between fast and slow diffusion states, and reduced the size of transient confinement zones. Recently, ensemble fluorescence recovery after photobleaching (FRAP) measurements performed on monomeric GFP fused to the amino terminus of hSERT heterologously expressed in HEK-293 cells yielded a mobile fraction of 82 ± 8%, with a population diffusion coefficient of 0.151 ± 0.003 $\mu m^2/s$ estimated via direct tracking of individual mGFP-SERT (Anderluh et al., 2017). Single-molecule tracking of mGFP-SERT in transiently transfected CHO cells revealed a major mobile fraction of transporters (85%) characterized by D_1 = 0.30 $\mu m^2/s$ and a minor pool (15%) of mGFP-SERT immobilized during the observation period with D_2 = 0.05 $\mu m^2/s$ (Anderluh et al., 2014). To perform direct comparison, we recorded lateral movement of individual dim YFP-SERT spots in the TIRF mode in HEK-293T cells 6 h post-transfection to ensure low expression density suitable for single molecule tracking. The majority of tracks (63% of 7802 tracks) were determined to be mobile as defined by the previously used $D_{cutoff} = 5 \times 10^{-4}$ $\mu m^2/s$ with a lateral diffusion rate (median D) of 0.07 $\mu m^2/s$ (Δt of 50 ms; **Supplementary Figure 5**). The diffusion rate of the mobile YFP-SERT pool 6 h post-transfection was comparable to that of the mobile QD-tagged YFP-SERT pool imaged ≥ 24 h post-transfection in our study ($D_{median,YFP}$ = 0.066 $\mu m^2/s$ [0.017–0.16 IQR]; $D_{median,Qdot}$ = 0.030 $\mu m^2/s$ [0.015–0.051 IQR]; $^{***}p < 0.001$, Mann-Whitney *U* test). It should be noted that the diffusion coefficient values in our studies were nearly an order of magnitude lower that previously reported average diffusion rates for mGFP-SERT (Anderluh et al., 2014, 2017). Several factors might contribute to the variability in the diffusion rate measurement. Higher photon output per frame at lower acquisition frame rates improves the localization accuracy of slowly moving molecules, resulting in significantly smaller reported diffusion coefficients for slower molecules (Lee et al., 2019). It is also possible that antagonist-conjugated QDs target a membrane pool of YFP-SERT that is "transport-willing" and distinct from tracked YFP-SERT or mGFP-SERT species. In addition to the probe potentially altering the transporter conformational equilibrium, a ligand-based approach may also lead to changes in constitutive transport trafficking to and from the plasma membrane. In fact, SERT was reported to undergo constitutive endocytosis in transfected CAD and HEK-293 cells, with a modest surface loss under basal conditions (up to 10% over 1 h at 37°C) when assessed via internalization assays based on the antibody feeding, surface ELISA, and fluorescent cocaine analog labeling (Rahbek-Clemmensen et al., 2014). However, Kittler et al. demonstrated that antagonists and substrates differentially regulated SERT endocytosis in serotonergic neurons over the course of 4 h (Kittler et al., 2010). In particular, **fluoxetine** led to a dose-dependent internalization of SERT (1 μM: to 63.8 ± 2.5% of control; 10 μM: to 33.9 ± 1.9% of control); **paroxetine** induced a dose-independent downregulation of SERT (500 nM: 75.5 ± 5.9; 10 μM: 66.0 ± 6.7% of control); **sertraline** induced SERT internalization (1 μM: 75.8 ± 2.2%; 5 μM: 61.9 ± 1.8%), while exposure to 50 μM **cocaine** significantly enhanced SERT surface expression (123 ± 3.9%) compared to control levels. Application of substrates led to SERT internalization as follows: **5-HT**, 1 μM: 64.7 ± 2.9% and 10 μM: 57.7 ± 1.9%; **MDMA**, 43.4 ± 1.6%. Additionally, Jørgensen et al. (2014) demonstrated 5-HT-induced reduction in SERT surface expression in both stably transfected HEK-293 cells and cultured raphe serotonergic neurons. When we assessed SERT-bound Qdot localization with respect to the plasma membrane labeled with Cell Mask Deep Red (**Supplementary Figure 6**) during the typical time course of a labeling/tracking experiment, we observed minimal intracellular Qdot accumulation. Thus, minimizing time elapsed between the final wash steps post-labeling and time-lapse image series acquisition likely allows us to capture the surface trafficking events.

Another factor that confounds interpretation of method-to-method differences in SERT diffusion rate is the irregular pattern of YFP-SERT distribution in the plasma membrane of HEK-293T cells observed in our spinning disk confocal and TIRF images. Analysis of SIM images of YFP-SERT distribution corroborated our preliminary observation that YFP-SERT density was markedly increased in the membrane edges and protrusions (**Figure 9**). This phenomenon is similar to conformation-dependent preferential accumulation of dopamine transporter in membrane protrusions (filopodia) that was previously observed in several neuronal and non-neuronal heterologous expression hosts (Caltagarone et al., 2015; Kovtun et al., 2019). QD tracking of YFP-SERT localized to membrane protrusions revealed a simple Brownian, unrestricted pattern of diffusion that resembles surface dynamics of the extrasynaptic pool of neuronal receptors (Maynard and Triller, 2019). Physiological significance of SERT preferential targeting to protrusions and its unhindered lateral mobility within these regions is unclear. Ultrastructural studies demonstrated that SERT primarily resided in the extrasynaptic compartments along the axonal projections in the vicinity of asymmetric synapses (Zhou et al., 1998; Tao-Cheng and Zhou, 1999; Miner et al., 2000); thus, to draw parallels with our state-of-the-art knowledge of neuronal receptor surface dynamics, lateral mobility might represent a yet unappreciated dynamic mechanism of SERT delivery and stabilization in the vicinity of synaptic junctions *in vivo*, where SERT is optimally positioned to clear synaptically released serotonin.

In conclusion, this work presents synthesis, extensive characterization, and QD-based imaging application of a novel biotinylated, PEGylated 3-(1-phenylethyl-1,2,3,6-tetrahydropyridin-4-yl)-1H-indole (IDT785) ligand. Biological activity of IDT785 was demonstrated by its ability to inhibit hSERT-mediated IDT307 uptake with IC_{50} = 7.2 ± 0.3 μM and through the efficient capture of its biotin terminus by streptavidin-conjugated QDs in solution. As a result, IDT785 enabled specific QD labeling of surface WT and YFP-tagged SERT proteins heterologously expressed in HEK-293T cells. IDT785-based single QD tracking of YFP-SERT membrane dynamics allowed classification of the membrane pool of transporters into distinct fractions undergoing simple Brownian, restricted, or immobilized diffusion. Moreover, IDT785-enabled QD tracking resulted in characterization of membrane diffusion of YFP-SERT proteins preferentially localized to the membrane edges and protrusions in HEK-293T cells. Our next goals are (1) to determine whether IDT785 structure can be optimized to achieve sub-μM SERT binding affinity and (2) to evaluate if IDT785 enables specific QD labeling and tracking of endogenous SERT proteins. Overall, our work provides a generalizable blueprint for developing and rigorous characterization of biotinylated ligands that enable QD-based detection of transmembrane neuronal proteins. Our ultimate goal is to implement this approach in the native neuronal context, and we anticipate further synthetic optimizations toward the development of a high-affinity, specific, compact Qdot probe that would allow us to detect SERT and to monitor its surface dynamics *in situ*. We envision that tracking SERT in intact tissue would shed light on intrinsic differences in spatially segregated compartments of raphe 5-HT neurons, which display highly branched axonal processes with numerous axonal-like varicosities. We are particularly interested in SERT diffusion with respect to the axon initial segment that may serve as a physical barrier to separate somatodendritic and axonal SERT pools. We also aim to answer the question whether stimulation is capable of inducing transient SERT stabilization in the vicinity of presynaptic boutons, ultimately leading to altered 5-HT clearance rates.

DATA AVAILABILITY STATEMENT

The raw data supporting the conclusions of this article will be made available by the authors, without undue reservation.

AUTHOR CONTRIBUTIONS

IT, OK, RT, LB, and TJ performed the experiments and analyzed data. IT, OK, RT, LB, and SR conceived the study, designed the experiments, and wrote the manuscript. All authors contributed to the article and approved the submitted version.

FUNDING

RT was supported by the CBI training grant (NIH 5T32GM065086-18). Fluorescence microscopy experiments were performed in part through the use of the Vanderbilt Cell Imaging Shared Resource (supported by NIH grants CA68485, DK20593, DK58404, DK59637, and EY08126). Nikon TIRF microscope was obtained through NIH S10 grant OD018075 01A to Sam Wells.

ACKNOWLEDGMENTS

We would like to thank Randy Blakely for providing WT hSERT-pcDNA3 plasmid vector and David Wright for the use of BioTek Synergy H4 microplate reader housed in the Wright laboratory.

SUPPLEMENTARY MATERIAL

The Supplementary Material for this article can be found online at: https://www.frontiersin.org/articles/10.3389/fncel.2021.667044/full#supplementary-material

REFERENCES

Abraham, L., Lu, H. Y., Falcão, R. C., Scurll, J., Jou, T., Irwin, B., et al. (2017). Limitations of Qdot labelling compared to directly-conjugated probes for single particle tracking of B cell receptor mobility. *Sci. Rep.* 7:11379. doi: 10.1038/s41598-017-11563-9

Anderluh, A., Hofmaier, T., Klotzsch, E., Kudlacek, O., Stockner, T., Sitte, H. H., et al. (2017). Direct PIP2 binding mediates stable oligomer formation of the serotonin transporter. *Nat. Commun.* 8:14089. doi: 10.1038/ncomms14089

Anderluh, A., Klotzsch, E., Ries, J., Reismann, A. W. A. F., Weber, S., Fölser, M., et al. (2014). Tracking single serotonin transporter molecules at the endoplasmic reticulum and plasma membrane. *Biophys. J.* 106, L33–L35. doi: 10.1016/j.bpj.2014.03.019

Aronsen, D., Webster, J., and Schenk, S. (2014). RU 24969-produced adipsia and hyperlocomotion: differential role of 5HT1A and 5HT1B receptor mechanisms. *Pharmacol. Biochem. Behav.* 124, 1–4. doi: 10.1016/j.pbb.2014.05.008

Bailey, D. M., Catron, M. A., Kovtun, O., Macdonald, R. L., Zhang, Q., and Rosenthal, S. J. (2018). Single quantum dot tracking reveals serotonin transporter diffusion dynamics are correlated with cholesterol-sensitive threonine 276 phosphorylation status in primary midbrain neurons. *ACS Chem. Neurosci.* 9, 2534–2541. doi: 10.1021/acschemneuro.8b00214

Bakthavachalam, V., Baindur, N., Madras, B. K., and Neumeyer, J. L. (1991). Fluorescent probes for dopamine receptors: synthesis and characterization of fluorescein and 7-nitrobenz-2-oxa-1,3-diazol-4-yl conjugates of D-1 and D-2 receptor ligands. *J. Med. Chem.* 34, 3235–3241. doi: 10.1021/jm00115a012

Beikmann, B. S., Tomlinson, I. D., Rosenthal, S. J., and Andrews, A. M. (2013). Serotonin uptake is largely mediated by platelets versus lymphocytes in peripheral blood cells. *ACS Chem. Neurosci.* 4, 161–170.

Bell, E. W., and Zhang, Y. (2019). DockRMSD: an open-source tool for atom mapping and RMSD calculation of symmetric molecules through graph isomorphism. *J. Cheminform.* 11:40. doi: 10.1186/s13321-019-0362-7

Bentzen, E. L., Tomlinson, I. D., Mason, J., Gresch, P., Warnement, M. R., Wright, D., et al. (2005). Surface modification to reduce nonspecific binding of quantum dots in live cell assays. *Bioconjug. Chem.* 16, 1488–1494. doi: 10.1021/bc0502006

Bermingham, D. P., and Blakely, R. D. (2016). Kinase-dependent regulation of monoamine neurotransmitter transporters. *Pharmacol. Rev.* 68:888.

Blakely, R. D., Berson, H. E., Fremeau, R. T., Caron, M. G., Peek, M. M., Prince, H. K., et al. (1991). Cloning and expression of a functional serotonin transporter from rat brain. *Nature* 354, 66–70. doi: 10.1038/354066a0

Blakely, R. D., Mason, J. N., Tomlinson, I. D., and Rosenthal, S. J. (2011). *Fluorescencent Substrates for Neurotransmitter Transporters*, US 7,947,255 B2. Mountain View, CA: Google.

Block, E. R., Nuttle, J., Balcita-Pedicino, J. J., Caltagarone, J., Watkins, S. C., Sesack, S. R., et al. (2015). Brain region-specific trafficking of the dopamine transporter. *J. Neurosci.* 35:12845. doi: 10.1523/jneurosci.1391-15.2015

Botev, Z. I., Grotowski, J. F., and Kroese, D. P. (2010). Kernel density estimation via diffusion. *Ann. Statist.* 38, 2916–2957.

Bouzigues, C., Lévi, S., Triller, A., and Dahan, M. (2007). "Single quantum dot tracking of membrane receptors," in *Quantum Dots: Applications in Biology*, eds M. P. Bruchez and C. Z. Hotz (Totowa, NJ: Humana Press), 81–91. doi: 10.1385/1-59745-369-2:81

Caltagarone, J., Ma, S., and Sorkin, A. (2015). Dopamine transporter is enriched in filopodia and induces filopodia formation. *Mol. Cell. Neurosci.* 68, 120–130. doi: 10.1016/j.mcn.2015.04.005

Cha, J. H., Zou, M.-F., Adkins, E. M., Rasmussen, S. G. F., Loland, C. J., Schoenenberger, B., et al. (2005). Rhodamine-labeled 2β-carbomethoxy-3β-(3,4-dichlorophenyl)tropane analogues as high-affinity fluorescent probes for the dopamine transporter. *J. Med. Chem.* 48, 7513–7516. doi: 10.1021/jm050431y

Chang, J. C., Tomlinson, I. D., Warnement, M. R., Ustione, A., Carneiro, A. M. D., Piston, D. W., et al. (2012b). Single molecule analysis of serotonin transporter regulation using antagonist-conjugated quantum dots reveals restricted, p38 MAPK-dependent mobilization underlying uptake activation. *J. Neurosci.* 32:8919. doi: 10.1523/JNEUROSCI.0048-12.2012

Chang, J. C., Kovtun, O., Blakely, R. D., and Rosenthal, S. J. (2012a). Labeling of neuronal receptors and transporters with quantum dots. *WIREs Nanomed. Nanobiotechnol.* 4, 605–619.

Chang, J. C., and Rosenthal, S. J. (2011). "Real-time quantum dot tracking of single proteins," in *Biomedical Nanotechnology: Methods and Protocols*, ed. S. J. Hurst (Totowa, NJ: Humana Press), 51–62.

Chang, J. C., and Rosenthal, S. J. (2013). "Quantum dot-based single-molecule microscopy for the study of protein dynamics," in *NanoBiotechnology Protocols*, eds S. J. Rosenthal and D. W. Wright (Totowa, NJ: Humana Press), 71–84.

Cheng, M. H., and Bahar, I. (2019). Monoamine transporters: structure, intrinsic dynamics and allosteric regulation. *Nat. Struct. Mol. Biol.* 26, 545–556. doi: 10.1038/s41594-019-0253-7

Coleman, J. A., and Gouaux, E. (2018). Structural basis for recognition of diverse antidepressants by the human serotonin transporter. *Nat. Struct. Mol. Biol.* 25, 170–175. doi: 10.1038/s41594-018-0026-8

Coleman, J. A., Green, E. M., and Gouaux, E. (2016). X-ray structures and mechanism of the human serotonin transporter. *Nature* 532, 334–339.

Coleman, J. A., Navratna, V., Antermite, D., Yang, D., Bull, J. A., and Gouaux, E. (2020). Chemical and structural investigation of the paroxetine-human serotonin transporter complex. *Elife* 9:e56427. doi: 10.7554/eLife.56427

Coleman, J. A., Yang, D., Zhao, Z., Wen, P.-C., Yoshioka, C., Tajkhorshid, E., et al. (2019). Serotonin transporter–ibogaine complexes illuminate mechanisms of inhibition and transport. *Nature* 569, 141–145. doi: 10.1038/s41586-019-1135-1

Cool, D. R., Leibach, F. H., and Ganapathy, V. (1990). High-affinity paroxetine binding to the human placental serotonin transporter. *Am. J. Physiol. Cell Physiol.* 259, C196–C204.

Cooper, A., Woulfe, D., and Kilic, F. (2019). Post-translational modifications of serotonin transporter. *Pharmacol. Res.* 140, 7–13.

Crane, J. M., and Verkman, A. S. (2008). Long-range nonanomalous diffusion of quantum dot-labeled aquaporin-1 water channels in the cell plasma membrane. *Biophys. J.* 94, 702–713. doi: 10.1529/biophysj.107.115121

Dahan, M., Lévi, S., Luccardini, C., Rostaing, P., Riveau, B., and Triller, A. (2003). Diffusion dynamics of glycine receptors revealed by single-quantum dot tracking. *Science* 302:442. doi: 10.1126/science.1088525

Deskus, J. A., Epperson, J. R., Sloan, C. P., Cipollina, J. A., Dextraze, P., Qian-Cutrone, J., et al. (2007). Conformationally restricted homotryptamines 3. Indole tetrahydropyridines and cyclohexenylamines as selective serotonin reuptake inhibitors. *Bioorgan. Med. Chem. Lett.* 17, 3099–3104. doi: 10.1016/j.bmcl.2007.03.040

dos Santos, J. L., Lanaro, C., Lima, L. M., Gambero, S., Franco-Penteado, C. F., Alexandre-Moreira, M. S., et al. (2011). Design, synthesis, and pharmacological evaluation of novel hybrid compounds to treat sickle cell disease symptoms. *J. Med. Chem.* 54, 5811–5819.

Duan, H., Hu, T., Foti, R. S., Pan, Y., Swaan, P. W., and Wang, J. (2015). Potent and selective inhibition of plasma membrane monoamine transporter by HIV protease inhibitors. *Drug Metab. Dispos.* 43:1773. doi: 10.1124/dmd.115.064824

Erb, S. J., Schappi, J. M., and Rasenick, M. M. (2016). Antidepressants accumulate in lipid rafts independent of monoamine transporters to modulate redistribution of the G Protein, Gαs. *J. Biol. Chem.* 291, 19725–19733. doi: 10.1074/jbc.M116.727263

Eriksen, J., Rasmussen, S. G. F., Rasmussen, T. N., Vaegter, C. B., Cha, J. H., Zou, M.-F., et al. (2009). Visualization of dopamine transporter trafficking in live neurons by use of fluorescent cocaine analogs. *J. Neurosci.* 29, 6794–6808. doi: 10.1523/JNEUROSCI.4177-08.2009

Gussin, H. A., Tomlinson, I. D., Little, D. M., Warnement, M. R., Qian, H., Rosenthal, S. J., et al. (2006). Binding of muscimol-conjugated quantum dots to GABAC receptors. *J. Am. Chem. Soc.* 128, 15701–15713. doi: 10.1021/ja064324k

Hahn, M. K., and Blakely, R. D. (2007). The functional impact of SLC6 transporter genetic variation. *Annu. Rev. Pharmacol. Toxicol.* 47, 401–441. doi: 10.1146/annurev.pharmtox.47.120505.105242

Hu, X.-Z., Lipsky, R. H., Zhu, G., Akhtar, L. A., Taubman, J., Greenberg, B. D., et al. (2006). Serotonin transporter promoter gain-of-function genotypes are linked to obsessive-compulsive disorder. *Am. J. Hum. Genet.* 78, 815–826. doi: 10.1086/503850

Jacobson, K. A., Fischer, B., and van Rhee, A. M. (1995). Molecular probes for muscarinic receptors: functionalized congeners of selective muscarinic antagonists. *Life Sci.* 56, 823–830.

Jaqaman, K., Loerke, D., Mettlen, M., Kuwata, H., Grinstein, S., Schmid, S. L., et al. (2008). Robust single-particle tracking in live-cell time-lapse sequences. *Nat. Methods* 5, 695–702. doi: 10.1038/nmeth.1237

Jørgensen, T. N., Christensen, P. M., and Gether, U. (2014). Serotonin-induced down-regulation of cell surface serotonin transporter. *Neurochem. Int.* 73, 107–112. doi: 10.1016/j.neuint.2014.01.005

Kaya, C., Cheng, M. H., Block, E. R., Bartol, T. M., Sejnowski, T. J., Sorkin, A., et al. (2018). Heterogeneities in axonal structure and transporter distribution lower dopamine reuptake efficiency. *eNeuro* 5:ENEURO.0298-17.2017. doi: 10.1523/ENEURO.0298-17.2017

Kittler, K., Lau, T., and Schloss, P. (2010). Antagonists and substrates differentially regulate serotonin transporter cell surface expression in serotonergic neurons. *Eur. J. Pharmacol.* 629, 63–67. doi: 10.1016/j.ejphar.2009.12.010

Kovtun, O., Sakrikar, D., Tomlinson, I. D., Chang, J. C., Arzeta-Ferrer, X., Blakely, R. D., et al. (2015). Single-quantum-dot tracking reveals altered membrane dynamics of an attention-deficit/hyperactivity-disorder-derived dopamine transporter coding variant. *ACS Chem. Neurosci.* 6, 526–534. doi: 10.1021/cn500202c

Kovtun, O., Thal, L. B., Josephs, T., and Rosenthal, S. J. (2020). "Quantitative analysis of single quantum dot trajectories," in *Quantum Dots: Applications in Biology*, eds A. Fontes and B. S. Santos (New York, NY: Springer US), 109–123.

Kovtun, O., Tomlinson, I. D., Bailey, D. M., Thal, L. B., Ross, E. J., Harris, L., et al. (2018). Single quantum dot tracking illuminates neuroscience at the nanoscale. *Chem. Phys. Lett.* 706, 741–752. doi: 10.1016/j.cplett.2018.06.019

Kovtun, O., Tomlinson, I. D., Ferguson, R. S., and Rosenthal, S. J. (2019). Quantum dots reveal heterogeneous membrane diffusivity and dynamic surface density polarization of dopamine transporter. *PLoS One* 14:e0225339. doi: 10.1371/journal.pone.0225339

Kovtun, O., Tomlinson, I. D., Sakrikar, D. S., Chang, J. C., Blakely, R. D., and Rosenthal, S. J. (2011). Visualization of the cocaine-sensitive dopamine transporter with ligand-conjugated quantum dots. *ACS Chem. Neurosci.* 2, 370–378. doi: 10.1021/cn200032r

Kristensen, A. S., Andersen, J., Jørgensen, T. N., Sørensen, L., Eriksen, J., Loland, C. J., et al. (2011). SLC6 neurotransmitter transporters: structure, function, and regulation. *Pharmacol. Rev.* 63:585.

Kusumi, A., Sako, Y., and Yamamoto, M. (1993). Confined lateral diffusion of membrane receptors as studied by single particle tracking (nanovid microscopy). Effects of calcium-induced differentiation in cultured epithelial cells. *Biophys. J.* 65, 2021–2040. doi: 10.1016/S0006-3495(93)81253-0

Kusumi, A., Tsunoyama, T. A., Hirosawa, K. M., Kasai, R. S., and Fujiwara, T. K. (2014). Tracking single molecules at work in living cells. *Nat. Chem. Biol.* 10, 524–532. doi: 10.1038/nchembio.1558

Lam, W. Y., Wang, Y., Mostofian, B., Jorgens, D., Kwon, S., Chin, K., et al. (2019). HER2 cancer protrusion growth signaling regulated by unhindered, localized filopodial dynamics. *bioRxiv* [Preprint] doi: 10.1101/654988

Lavis, L. D. (2017). Teaching old dyes new tricks: biological probes built from fluoresceins and rhodamines. *Annu. Rev. Biochem.* 86, 825–843. doi: 10.1146/annurev-biochem-061516-044839

Lee, S. H., Jin, C., Cai, E., Ge, P., Ishitsuka, Y., Teng, K. W., et al. (2017). Super-resolution imaging of synaptic and Extra-synaptic AMPA receptors with different-sized fluorescent probes. *Elife* 6:e27744.

Lee, Y., Phelps, C., Huang, T., Mostofian, B., Wu, L., Zhang, Y., et al. (2019). High-throughput, single-particle tracking reveals nested membrane domains that dictate KRasG12D diffusion and trafficking. *Elife* 8:e46393. doi: 10.7554/eLife.46393

Lippert, L. G., Hallock, J. T., Dadosh, T., Diroll, B. T., Murray, C. B., and Goldman, Y. E. (2016). NeutrAvidin functionalization of CdSe/CdS quantum nanorods and quantification of biotin binding sites using Biotin-4-fluorescein fluorescence quenching. *Bioconjug. Chem.* 27, 562–568. doi: 10.1021/acs.bioconjchem.5b00577

Ma, S., Cheng, M. H., Guthrie, D. A., Newman, A. H., Bahar, I., and Sorkin, A. (2017). Targeting of dopamine transporter to filopodia requires an outward-facing conformation of the transporter. *Sci. Rep.* 7:5399. doi: 10.1038/s41598-017-05637-x

Madras, B. K., Canfield, D. R., Pfaelzer, C., Vittimberga, F. J., Difiglia, M., Aronin, N., et al. (1990). Fluorescent and biotin probes for dopamine receptors: D1 and D2 receptor affinity and selectivity. *Mol. Pharmacol.* 37, 833–839.

Maynard, S. A., and Triller, A. (2019). Inhibitory receptor diffusion dynamics. *Front. Mol. Neurosci.* 12:313. doi: 10.3389/fnmol.2019.00313

Michalet, X., and Berglund, A. J. (2012). Optimal diffusion coefficient estimation in single-particle tracking. *Phys. Rev. E* 85:061916.

Minelli, A., Brecha, N. C., Karschin, C., DeBiasi, S., and Conti, F. (1995). GAT-1, a high-affinity GABA plasma membrane transporter, is localized to neurons and astroglia in the cerebral cortex. *J. Neurosci.* 15:7734. doi: 10.1523/jneurosci.15-11-07734.1995

Miner, L. H., Schroeter, S., Blakely, R. D., and Sesack, S. R. (2000). Ultrastructural localization of the serotonin transporter in superficial and deep layers of the rat prelimbic prefrontal cortex and its spatial relationship to dopamine terminals. *J. Comp. Neurol.* 427, 220–234. doi: 10.1002/1096-9861(20001113)427:2<220::aid-cne5>3.0.co;2-p

Mittal, R., and Bruchez, M. P. (2011). Biotin-4-fluorescein based fluorescence quenching assay for determination of biotin binding capacity of streptavidin conjugated quantum dots. *Bioconjug. Chem.* 22, 362–368. doi: 10.1021/bc100321c

Montgomery, T. R., Steinkellner, T., Sucic, S., Koban, F., Schüchner, S., Ogris, E., et al. (2014). Axonal targeting of the serotonin transporter in cultured rat dorsal raphe neurons is specified by SEC24C-dependent export from the endoplasmic reticulum. *J. Neurosci.* 34:6344. doi: 10.1523/JNEUROSCI.2991-13.2014

Nirenberg, M. J., Chan, J., Vaughan, R. A., Uhl, G. R., Kuhar, M. J., and Pickel, V. M. (1997). Immunogold localization of the dopamine transporter: an ultrastructural study of the rat ventral tegmental area. *J. Neurosci.* 17:5255.

Nolan, T. L., Lapinsky, D. J., Talbot, J. N., Indarte, M., Liu, Y., Manepalli, S., et al. (2011). Identification of a novel selective serotonin reuptake inhibitor by coupling monoamine transporter-based virtual screening and rational molecular hybridization. *ACS Chem. Neurosci.* 2, 544–552. doi: 10.1021/cn200044x

Quinlan, M. A., Robson, M. J., Ye, R., Rose, K. L., Schey, K. L., and Blakely, R. D. (2020). Ex vivo quantitative proteomic analysis of serotonin transporter interactome: network impact of the SERT Ala56 coding variant. *Front. Mol. Neurosci.* 13:89. doi: 10.3389/fnmol.2020.00089

Radian, R., Ottersen, O. P., Storm-Mathisen, J., Castel, M., and Kanner, B. I. (1990). Immunocytochemical localization of the GABA transporter in rat brain. *J. Neurosci.* 10:1319.

Rahbek-Clemmensen, T., Bay, T., Eriksen, J., Gether, U., and Jørgensen, T. N. (2014). The serotonin transporter undergoes constitutive internalization and is primarily sorted to late endosomes and lysosomal degradation. *J. Biol. Chem.* 289, 23004–23019. doi: 10.1074/jbc.M113.495754

Ramamoorthy, S., Bauman, A. L., Moore, K. R., Han, H., Yang-Feng, T., Chang, A. S., et al. (1993). Antidepressant- and cocaine-sensitive human serotonin transporter: molecular cloning, expression, and chromosomal localization. *Proc. Natl. Acad. Sci. U.S.A.* 90:2542.

Ramamoorthy, S., Giovanetti, E., Qian, Y., and Blakely, R. D. (1998). Phosphorylation and regulation of antidepressant-sensitive serotonin transporters. *J. Biol. Chem.* 273, 2458–2466. doi: 10.1074/jbc.273.4.2458

Rao, A., Richards, T. L., Simmons, D., Zahniser, N. R., and Sorkin, A. (2012). Epitope-tagged dopamine transporter knock-in mice reveal rapid endocytic trafficking and filopodia targeting of the transporter in dopaminergic axons. *FASEB J.* 26, 1921–1933. doi: 10.1096/fj.11-196113

Rayport, S., and Sulzer, D. (1995). Visualization of antipsychotic drug binding to living mesolimbic neurons reveals D2 receptor, acidotropic, and lipophilic components. *J. Neurochem.* 65, 691–703. doi: 10.1046/j.1471-4159.1995.65020691.x

Resch-Genger, U., Grabolle, M., Cavaliere-Jaricot, S., Nitschke, R., and Nann, T. (2008). Quantum dots versus organic dyes as fluorescent labels. *Nat. Methods* 5, 763–775. doi: 10.1038/nmeth.1248

Rosenthal, S. J. (2019). Nanotechnology in neuroscience reveals membrane mobility matters. *ACS Chem. Neurosci.* 10, 30–32. doi: 10.1021/acschemneuro.8b00495

Rosenthal, S. J., Chang, J. C., Kovtun, O., McBride, J. R., and Tomlinson, I. D. (2011). Biocompatible quantum dots for biological applications. *Chem. Biol.* 18, 10–24. doi: 10.1016/j.chembiol.2010.11.013

Rosenthal, S. J., Tomlinson, I., Adkins, E. M., Schroeter, S., Adams, S., Swafford, L., et al. (2002). Targeting cell surface receptors with ligand-conjugated nanocrystals. *J. Am. Chem. Soc.* 124, 4586–4594. doi: 10.1021/ja003486s

She, X., Pegoli, A., Gruber, C. G., Wifling, D., Carpenter, J., Hübner, H., et al. (2020). Red-emitting dibenzodiazepinone derivatives as fluorescent dualsteric probes for the muscarinic acetylcholine M2 receptor. *J. Med. Chem.* 63, 4133–4154. doi: 10.1021/acs.jmedchem.9b02172

Shen, H., Tauzin, L. J., Baiyasi, R., Wang, W., Moringo, N., Shuang, B., et al. (2017). Single particle tracking: from theory to biophysical applications. *Chem. Rev.* 117, 7331–7376. doi: 10.1021/acs.chemrev.6b00815

Singh, Y. S., Altieri, S. C., Gilman, T. L., Michael, H. M., Tomlinson, I. D., Rosenthal, S. J., et al. (2012). Differential serotonin transport is linked to the rh5-HTTLPR in peripheral blood cells. *Transl. Psychiatry* 2:e77. doi: 10.1038/tp.2012.2

Solis, E., Zdravkovic, I., Tomlinson, I. D., Noskov, S. Y., Rosenthal, S. J., and De Felice, L. J. (2012). 4-(4-(Dimethylamino)phenyl)-1-methylpyridinium (APP+) is a fluorescent substrate for the human serotonin transporter. *J. Biol. Chem.* 287, 8852–8863.

Steiner, J. A., Carneiro, A. M. D., and Blakely, R. D. (2008). Going with the flow: trafficking-dependent and -independent regulation of serotonin transport. *Traffic* 9, 1393–1402. doi: 10.1111/j.1600-0854.2008.00757.x

Sucic, S., Dallinger, S., Zdrazil, B., Weissensteiner, R., Jørgensen, T. N., Holy, M., et al. (2010). Terminus of monoamine transporters is a lever required for the action of amphetamines. *J. Biol. Chem.* 285, 10924–10938. doi: 10.1074/jbc.M109.083154

Tao-Cheng, J. H., and Zhou, F. C. (1999). Differential polarization of serotonin transporters in axons versus soma–dendrites: an immunogold electron microscopy study. *Neuroscience* 94, 821–830. doi: 10.1016/s0306-4522(99)00373-5

Thal, L. B., Kovtun, O., and Rosenthal, S. J. (2020). "Labeling neuronal proteins with quantum dots for single-molecule imaging," in *Quantum Dots: Applications in Biology*, eds A. Fontes and B. S. Santos (New York, NY: Springer US), 169–177.

Tinevez, J.-Y., Perry, N., Schindelin, J., Hoopes, G. M., Reynolds, G. D., Laplantine, E., et al. (2017). TrackMate: an open and extensible platform for single-particle tracking. *Methods* 115, 80–90. doi: 10.1016/j.ymeth.2016.09.016

Tomlinson, I. D., Iwamoto, H., Blakely, R. D., and Rosenthal, S. J. (2011). Biotin tethered homotryptamine derivatives: high affinity probes of the human serotonin transporter (hSERT). *Bioorgan. Med. Chem. Lett.* 21, 1678–1682. doi: 10.1016/j.bmcl.2011.01.102

Tomlinson, I. D., Kovtun, O., Crescentini, T. M., and Rosenthal, S. J. (2019). Biotinylated-spiperone ligands for quantum dot labeling of the dopamine D2 receptor in live cell cultures. *Bioorgan. Med. Chem. Lett.* 29, 959–964. doi: 10.1016/j.bmcl.2019.02.024

Tomlinson, I. D., Mason, J. N., Blakely, R. D., and Rosenthal, S. J. (2005). Inhibitors of the serotonin transporter protein (SERT): the design and synthesis of biotinylated derivatives of 3-(1,2,3,6-tetrahydro-pyridin-4-yl)-1H-indoles. High-affinity serotonergic ligands for conjugation with quantum dots. *Bioorgan. Med. Chem. Lett.* 15, 5307–5310. doi: 10.1016/j.bmcl.2005.08.030

Torres, G. E., Gainetdinov, R. R., and Caron, M. G. (2003). Plasma membrane monoamine transporters: structure, regulation and function. *Nat. Rev. Neurosci.* 4, 13–25.

Weimer, M., Jiang, X., Ponta, O., Stanzel, S., Freyberger, A., and Kopp-Schneider, A. (2012). The impact of data transformations on concentration–response modeling. *Toxicol. Lett.* 213, 292–298. doi: 10.1016/j.toxlet.2012.07.012

Zhou, F. C., Tao-Cheng, J.-H., Segu, L., Patel, T., and Wang, Y. (1998). Serotonin transporters are located on the axons beyond the synaptic junctions: anatomical and functional evidence. *Brain Res.* 805, 241–254. doi: 10.1016/s0006-8993(98)00691-x

Conflict of Interest: The authors declare that the research was conducted in the absence of any commercial or financial relationships that could be construed as a potential conflict of interest.

frontiers | Frontiers in Cellular Neuroscience

ORIGINAL RESEARCH
published: 09 May 2022
doi: 10.3389/fncel.2022.832536

Structure-Activity Relationships of Dopamine Transporter Pharmacological Chaperones

*Charles Sutton[1†], Erin Q. Williams[1†], Hoomam Homsi[1†], Pieter Beerepoot[1], Reza Nazari[1], Dong Han[1], Amy J. Ramsey[1], Deborah C. Mash[2], David E. Olson[3,4,5], Bruce Blough[6] and Ali Salahpour[1]**

[1] Department of Pharmacology and Toxicology, Faculty of Medicine, University of Toronto, Toronto, ON, Canada, [2] Departments of Neurology and Molecular and Cellular Pharmacology, University of Miami Miller School of Medicine, Miami, FL, United States, [3] Department of Chemistry, College of Letters and Science, University of California, Davis, Davis, CA, United States, [4] Department of Biochemistry and Molecular Medicine, School of Medicine, University of California, Davis, Davis, CA, United States, [5] Center for Neuroscience, University of California, Davis, Davis, CA, United States, [6] Center for Drug Discovery, RTI International, North Carolina, NC, United States

Mutations in the dopamine transporter gene (SLC6A3) have been implicated in many human diseases. Among these is the infantile parkinsonism-dystonia known as Dopamine Transporter Deficiency Syndrome (DTDS). Afflicted individuals have minimal to no functional dopamine transporter protein. This is primarily due to retention of misfolded disease-causing dopamine transporter variants. This results in a variety of severe motor symptoms in patients and the disease ultimately leads to death in adolescence or young adulthood. Though no treatment is currently available, pharmacological chaperones targeting the dopamine transporter have been shown to rescue select DTDS disease-causing variants. Previous work has identified two DAT pharmacological chaperones with moderate potency and efficacy: bupropion and ibogaine. In this study, we carried out structure-activity relationships (SARs) for bupropion and ibogaine with the goal of identifying the chemical features required for pharmacological chaperone activity. Our results show that the isoquinuclidine substituent of ibogaine and its analogs is an important feature for pharmacological chaperone efficacy. For bupropion, the secondary amine group is essential for pharmacological chaperone activity. Lastly, we describe additional ibogaine and bupropion analogs with varying chemical modifications and variable pharmacological chaperone efficacies at the dopamine transporter. Our results contribute to the design and refinement of future dopamine transporter pharmacological chaperones with improved efficacies and potencies.

Keywords: dopamine transporter (DAT), ibogaine, bupropion, structure activity relationship, SAR, pharmacological chaperones

OPEN ACCESS

Edited by:
Renae Ryan,
The University of Sydney, Australia

Reviewed by:
Sonja Sucic,
Medical University of Vienna, Austria
Angela M. Carter,
University of Alabama at Birmingham, United States

***Correspondence:**
Ali Salahpour
Ali.salahpour@utoronto.ca

[†]These authors share first authorship

Specialty section:
This article was submitted to Cellular Neurophysiology, a section of the journal Frontiers in Cellular Neuroscience

Received: *10 December 2021*
Accepted: *21 March 2022*
Published: *09 May 2022*

Citation:
Sutton C, Williams EQ, Homsi H, Beerepoot P, Nazari R, Han D, Ramsey AJ, Mash DC, Olson DE, Blough B and Salahpour A (2022) Structure-Activity Relationships of Dopamine Transporter Pharmacological Chaperones. Front. Cell. Neurosci. 16:832536. doi: 10.3389/fncel.2022.832536

INTRODUCTION

The dopamine transporter (DAT) is a member of the solute carrier 6 (SLC6) family (Bu et al., 2021). DAT is a neuronal plasma membrane protein responsible for controlling extracellular levels of dopamine in addition to maintaining dopamine stores by transporting dopamine back into neurons after its release (Efimova et al., 2016). This recycling of dopamine is essential for locomotion, motivation, learning, and reward (Wise, 2004).

Dysfunction in the DAT is implicated in disorders including autism (Hamilton et al., 2013), attention deficit/hyperactive disorder (ADHD) (Mazei-Robison et al., 2008), Parkinson's disease (Hansen et al., 2014), and the newly characterized infantile Parkinson's-dystonia known as dopamine transporter deficiency syndrome (DTDS) (Ng et al., 2014). DTDS is a hereditary disease resulting from autosomal recessive loss-of-function mutations in the DAT sequence (Kurian et al., 2009).

The severity of DTDS is related to the level of mature DAT expression at the plasma membrane (Ng et al., 2014). Patients with variants that result in low DAT expression in heterologous cells experience a milder clinical phenotype than patients with variants resulting in no functional DAT expression. For some DTDS variants, the DAT protein does not mature past the endoplasmic reticulum (ER) and is not trafficked to the plasma membrane (Kurian et al., 2011). However, ER-retained DAT does not necessarily indicate a dysfunctional protein (Sanders and Myers, 2004). The stringent ER quality control will mark partially or even fully functional proteins for degradation if they are misfolded (Morello et al., 2000a). Indeed nearly 30% of newly synthesized wild-type (WT) proteins are immediately degraded (Schubert et al., 2000). For some membrane proteins, folding efficacy is less than 50% (Petäjä-Repo et al., 2000). However, small selective molecules known as pharmacological chaperones provide a unique way to address this problem of stringent ER quality control (Lindquist and Kelly, 2011; Beerepoot et al., 2017). Chemical chaperones are not selective and can help the folding of a wide range of proteins. Pharmacological chaperones differ from chemical chaperones in that they selectively target and bind to proteins in order to increase the proportion of the target protein that is properly folded. In fact, pharmacological chaperones have been used as therapeutic tools, for example, to rescue the vasopressin 2 receptor (Morello et al., 2000b) and the cystic fibrosis transmembrane conductance regulator (Hanrahan et al., 2013).

In a previous study, it was shown that noribogaine, a metabolite of ibogaine, acts as a DAT pharmacological chaperone, capable of rescuing DTDS and misfolded DAT variants in both cell culture and *Drosophila melanogaster* models (Kasture et al., 2016; Asjad et al., 2017). A recent structure-activity relationship (SAR) study also identified a tropane-based ibogaine analog that was capable of rescuing several DAT variants (Bhat et al., 2021). This analog also restored DAT function to WT levels for one variant, G386R. In another study, ibogaine and the atypical DAT inhibitor bupropion were able to rescue expression and function of select DTDS-causing variants in cells (Beerepoot et al., 2016). In contrast, typical inhibitors such as cocaine do not act as pharmacological chaperones for DAT. Interestingly the compounds that display pharmacological chaperone activity on DAT function as atypical inhibitors by stabilizing an inward-facing or occluded conformation of the transporter, as opposed to the outward-facing conformation induced by typical inhibitors (Bulling et al., 2012; Beerepoot et al., 2016).

Though the discovery of these DAT pharmacological chaperones is an important step to therapeutic intervention for DTDS, there are limitations with the current compounds that decrease their clinical utility. For instance, ibogaine, an efficacious chaperone, produces cardiotoxic effects at high concentrations (Koenig and Hilber, 2015). Bupropion, an effective antidepressant and smoking cessation intervention, has limited efficacy as a pharmacological chaperone. Both compounds have low potency (Beerepoot et al., 2016). Therefore, additional studies are required to improve the efficacy and potency of bupropion and ibogaine. Here, we describe SAR studies to identify the key molecular features necessary for the pharmacological chaperoning effect of these compounds. Our results demonstrate that the isoquinuclidine group of ibogaine and the secondary amine of bupropion are essential to confer high pharmacological chaperone efficacy. These studies will facilitate further refinement and design of improved DAT pharmacological chaperones.

MATERIALS AND METHODS

Drugs

Bupropion hydrochloride and 6-hydroxybupropion were obtained from Toronto Research Chemicals (Toronto, Canada), ibogaine from Ibogaworld, cocaine from Medisca (Montreal, Canada), β-PEA, pinoline, indole, tryptamine, ephedrine, frovatriptan, alprenolol, isoproterenol, evodiamine, and tyramine from Sigma (Oakville, Canada), fluoxetine and amphetamine were from Tocris Bioscience (Bristol, United Kingdom). PAL analogs, RTI analogs, and bicifadine were synthesized at RTI in the Blough laboratory as described previously (Carroll et al., 2009, 2011; Blough et al., 2011, 2014). Noribogaine (Batch No. 606950002) was from Deborah Mash, Ph.D. (Obach et al., 1998). Ibogamine was obtained from Specs (Zoetermeer, The Netherlands). Sodium phenylbutyrate was purchased from Enzo Life Sciences Inc. (Farmingdale, NY). Ibogaminalog, ibogainealog, noribogainalog, fluorogainalog, and tabernanthalog were synthesized in the lab of David E. Olson (Cameron et al., 2020).

Constructs

The β-lactamase (βlac) sequence was cloned from the ampicillin resistance gene within the pcDNA3.1 plasmid (Lam et al., 2013), using *Spe*I and *Asc*I restriction sites. An HA epitope was added to the N terminus of the βLAC, yielding HA-βLAC (Lam et al., 2013). To insert HA-βLAC into the second extracellular loop of YFP-HA-DAT, Quikchange II site-directed mutagenesis (Agilent, Mississauga, Canada) was used to insert *Spe*I and *Asc*I restriction sites on either side of the HA sequence of YFP-HA-DAT. The HA sequence in YFP-HA-DAT was removed by cuts with the *Spe*I and *Asc*I restriction enzymes prior to ligation of the HA-βLAC sequence. The *Spe*I and *Asc*I sites were then removed using site-directed mutagenesis, yielding YFP-HA-βLAC-DAT (referred to as βLAC-DAT). The human β2-adrenergic receptor (β2AR) cDNA expression vector was a gift from Dr. Michel Bouvier. HA-βLAC construct was subsequently inserted into this vector via *Asc*I and *Not*I restriction sites. Ligation of the HA-βLAC construct and into the β2AR cDNA expression vector yielded HA-βLAC-β2AR. To study the effects of alterations in the DAT, single point mutations were introduced into YFP-HA-DAT

using Quikchange II site-directed mutagenesis. The resulting DAT variant and lysine-590-alanine (K590A), were confirmed by DNA sequencing.

Transfections and Generation of Stable Cell Lines

HEK293 cells were obtained from ATCC (Manassas, VA) and maintained in Dulbecco's Modified Eagle's Medium (DMEM) (Sigma) supplemented with 10% FBS (Sigma), 100 U/mL penicillin and 100 μg/mL streptomycin. Cells were kept in 5% atmospheric CO_2 and 37°C. Cells expressing SS-HA- βLAC- β 2AR were further supplemented with 1 μg/mL puromycin. All cells were treated with plasmocyin (250 μg/mL) for 2 weeks to ensure they were not infected.

On day 1, cells (2×10^6) were seeded on a 10 cm tissue culture plate and incubated for 24 h. On day 2, seeded cells were transfected with 1–2 μg of plasmid DNA and 3 μL of polyethylenimine (1 mg/mL) (Polyscience Inc., Warminster, PA) per μg of DNA. Cells were then incubated in DMEM and transfection agent for 24 h. On day 3, to create stable lines, the media was replaced with media containing the selection agent G418 (500 μg/mL) (Bioshop, Burlington, Canada). In 5–7 days, most cells died and the media was replaced with fresh G418 selection media. The cells remaining were expanded until the 10 cm plate was approximately half-confluent. Cells were seeded onto 96-well plates at a density of 5 cells/mL with the goal of obtaining 1 cell per well. Plates were then incubated for 1–2 weeks. Clonal cell lines were generated by choosing wells with only 1 visible colony. These colonies were expanded and protein expression was confirmed via western blot or the βlac surface expression assay.

Immunoblotting

Cells (1×10^6 cells/well) were seeded onto a 6-well plate and incubated for 24 h. Cells were then treated with drugs and incubated for 16 h. After the incubation period, cells were lysed in RIPA buffer supplemented with protease inhibitors (working concentrations: pepstatin A, 5 μg/mL; leupeptin, 10 μg/mL; aprotinin, 1.5 μg/mL; benzamidine, 0.1 μg/mL; PMSF, 0.1 mM) on ice. At 4°C, cell lysates were gently shaken for 15 min followed by centrifugation at 15,000 rpm for 15 min to pellet debris. The Pierce BCA protein assay kit (Thermo Fisher Scientific, Canada) was used to determine the protein concentration of the supernatant. To reach a concentration of 40 μg of protein per 20 μL, samples were diluted in fresh RIPA buffer with 12.5% Laemmli sample buffer and 2.5% β-Mercaptoethanol prior to being heated to 55°C. The protein was then loaded on a 7.5 or 10% SDS-PAGE gel and run at 100 V for approximately an hour or until the dye front reached the bottom of the gel. Next, protein was transferred to a PVDF membrane at 22 V for 16 h or 100 V for 1 h. Blots were blocked with LI-COR blocking buffer for 1 h and incubated for 1 h at room temperature with rabbit anti-GFP (1:1,000 dilution; Life Technologies, cat#A11122). After washing three times with TBST, blots were incubated with goat anti-rabbit IRDye-680RD secondary antibody (1:15,000; LI-COR, cat#926-68071). As a loading control, blots were incubated with mouse anti-GAPDH (1:5,000, Sigma-Aldrich, Canada, cat#G8795) prior to secondary antibody goat anti-mouse IRDye-800GR (1:5,000 dilution, Rockland, Limerick, PA, cat#610-132-007). All antibodies were diluted in LI-COR blocking buffer. Additionally, REVERT total protein staining (LI-COR, Lincoln, NE) was used as a loading control. Drug treatments did not have an effect on GAPDH levels as determined by comparing GAPDH to total protein staining. Mature, fully glycosylated DAT (mDAT = 110 kDa) and immature, ER-resident DAT (iDAT = 75 kDa) were visualized using the Odyssey Imaging System (LI-COR, Lincoln, NE) and Image Studio Version 5.2 software (**Supplementary Figure 1**).

β-Lactamase Surface Expression Assay

The βlac surface expression assay was performed by following the method outlined in Lam et al. (2013) and Beerepoot et al. (2015, 2016). The assay substrate nitrocefin (BD biosciences) was dissolved in dimethyl sulfoxide (DMSO) at a concentration of 10 mM and frozen at −80°C. Immediately before use, it was thawed and diluted to a final concentration of 100 μM in phosphate buffered saline (PBS). Cells (1×10^5/well) were seeded into a poly-D-lysine-coated 48-well plate and incubated for 24 h, prior to drug treatment. Drugs were added to individual wells at varying concentrations and incubated for 16 h. Subsequently, the media was aspirated, and the cells were washed twice with PBS. After removal of the final PBS wash, 200 μL of the nitrocefin solution was added to each well and the absorbance was immediately read. The EPOCH microplate spectrophotometer (BioTek) was used to measure absorbance (486 nm) for each well every minute for 30 min. The rate of reaction (slope of the curve) was used as the readout for the assay (Beerepoot et al., 2015). To determine suitable concentration ranges for each drug, they were dissolved in PBS or DMSO at the highest concentration possible. From here, the solutions were serial diluted 1/10 to yield 8 different concentrations. βLAC cells were then treated with the varying drug concentrations and cell viability was recorded using light microscopy. For additional measure, nitrocefin was added and the absorbance was read. For certain cases, Trypan Blue was used to quantitatively differentiate increased cell death from reduced cell division. Drug doses that resulted in significant cell death and zero or heavily impaired reaction rates were not used in further experiments. Five or six doses were generally used in subsequent dosing experiments, starting at the highest non-toxic concentration.

Dopamine Uptake

Dopamine uptake inhibition was conducted using the Neurotransmitter Transporter Uptake Assay Kit (Molecular Devices, prod#R8173). Cells (1×10^5/well) were seeded into 96-well plates and incubated for 24 h. The cells were subjected to overnight drug treatment. The following day, wells were washed and incubated for 30 min with a mixture of 1X Hank's Balanced Salt Solution (HBSS) and 0.1% Bovine Serum Albumin (BSA) Buffer. Dopamine uptake inhibitors were added during the incubation period. Following the incubation, the fluorescent dye was added, and the plate was immediately transferred to the bottom-read fluorescence microplate reader (Spectramax M3,

Molecular Devices) for kinetic read-mode. The assay reads the amount of fluorescent activity which increases as fluorescent dye molecules are transported into the cells by the DAT. The read-out for this assay is the slope which equals the fluorescent measurements/time, ultimately denoting the uptake rate.

Data Analysis and Statistics

Data analysis was performed using GraphPad Prism (GraphPad Software, La Jolla, CA). Linear regression analysis was performed on βLAC time points to determine the slope, thus the rate of reaction, for comparison. Furthermore, the slope was also used to determine the degree of dopamine uptake in the dopamine uptake assays. Non-linear regression, fitting to the log(agonist) vs. response and log(inhibitor) vs. response model curve, was used to determine dose-response relationships of surface expression and uptake assays, respectively. One-way ANOVA with Dunnett's *post hoc*-test was used for the β-lactamase assay and one-way ANOVA with Bonferroni correction was used for western blot analysis.

RESULTS

Bupropion Analogs Differ in Their Ability to Increase Dopamine Transporter Surface Expression

The pharmacological chaperone ability of 37 bupropion analogs, three 6-hydroxybupropion analogs, and the phenylamine uptake inhibitor bicifadine were measured using the microplate βlac surface expression assay (shown in **Figure 1** and select compounds listed in **Table 1**). Importantly, this assay has been previously established and validated for measuring surface expression of DAT and was used by Lam et al. (2013) and Beerepoot et al. (2015) to show that bupropion and ibogaine are pharmacological chaperones of DAT. **Figure 1** shows the results of HEK cells expressing YFP-HA-βlac-DAT that were incubated overnight with 100 μM concentrations of test drugs except for ephedrine which had a concentration of 1 mM. Previous experiments showed that bupropion increased WT DAT surface expression by 137% above vehicle treatment (Beerepoot et al., 2016) similar to what we are observing in this study, E_{Max} = 144 ± 7.7%. Many other bupropion analogs were also able to increase WT DAT surface expression. Analogs with minor derivations from the bupropion backbone had similar efficacy. Among these were RTI-1, RTI-2, RTI-5, RTI-6, RTI-11, RTI-20, and PAL-1007. Bupropion's primary metabolite, 6-hydroxybupropion (148 ± 5.4%), and its analog, PAL-594 (166 ± 8.7%), also induced comparable surface expression effects as bupropion. Some compounds with larger derivations from the parent structure, such as ephedrine and bicifadine, were also able to increase WT DAT surface similar to bupropion. The E_{Max} values of all the analyzed drugs are included in **Figure 1**.

Dose-response curves were generated to assess the potency of compounds in **Figure 1**. None of the tested compounds in **Figure 1** displayed an EC_{50} that was significantly better than bupropion (data not shown). Dose response curves for select compounds with varying chemical modifications of the bupropion backbone are shown in **Figure 2**. For most compounds, full dose-response curves were not obtained since higher concentrations of drugs induced cellular toxicity. As such the values reported in this study are assumed effective E_{Max}. Of note, the chaperone potency of bupropion in the βlac assay (39 μM) is nearly 100-fold higher and right-shifted compared to the reported IC_{50} value of bupropion for dopamine uptake inhibition (0.6 μM) (Carroll et al., 2010). Therefore we next determined whether the insertion of HA-βlac into the second extracellular loop of DAT resulted in a reduction of bupropion's uptake inhibition potency compared to YFP-HA-DAT (WT DAT). Our results show that within our experimental conditions, bupropion's IC_{50} for inhibiting uptake activity of YFP-HA-βlac is 1.3 μM, similar to that of the WT construct (0.84 μM) (**Supplementary Figure 2**).

Ibogaine and Tryptamine Analogs Differ in Their Ability to Increase Dopamine Transporter Surface Expression

The pharmacological chaperone ability of the 15 ibogaine and tryptamine analogs, shown in **Figure 3**, were measured using the βlac surface expression assay. HEK cells expressing YFP-HA-βlac-DAT were incubated overnight with these compounds at concentrations varying by log and half-log dilutions, starting at 100 μM final concentration. Here, it was of particular interest to ascertain whether any of the ibogaine analogs could display a greater E_{Max} and/or more potent EC_{50} than what was observed with the bupropion analogs. Furthermore, it was important to determine whether the β-carboline analogs could also elicit a chaperone effect because they are not classified as DAT ligands (Cao et al., 2007). Our results here showed that ibogaine has an E_{Max} of 222 ± 7.9%, close to what we reported previously (187%) (Beerepoot et al., 2016). Analogs ibogamine and noribogaine were also shown to have high efficacy for increasing WT DAT surface expression. Ibogaine analogs lacking the isoquinuclidine substituent had varied efficacy. One compound, ibogainealog (169 ± 13.7%) had less efficacy than ibogaine (222 ± 7.9%). The βcarbolines pinoline (141 ± 4.4%) and tetrahydroharmine (137 ± 6.8%) also had reduced efficacy compared to ibogaine. Removing the nitrogen from the ring reduced efficacy as observed with frovatriptan (103 ± 1.4%). Tryptamine analogs were significantly less efficacious than ibogaine. Evodiamine (54 ± 1.7%) had no chaperone ability and caused a substantial reduction in the surface expression of DAT. Dose-response curves were generated to assess the pharmacological chaperone potencies of select compounds (**Figure 4**). As with the bupropion analogs, there were only modest differences in EC_{50} values of the ibogaine and tryptamine analogs.

Test Compounds Are Selective Pharmacological Chaperones of Dopamine Transporter

To ascertain whether the increase in DAT surface expression shown in **Figures 1**, **3** were the result of selective pharmacological chaperone activity on the dopamine transporter, we tested the

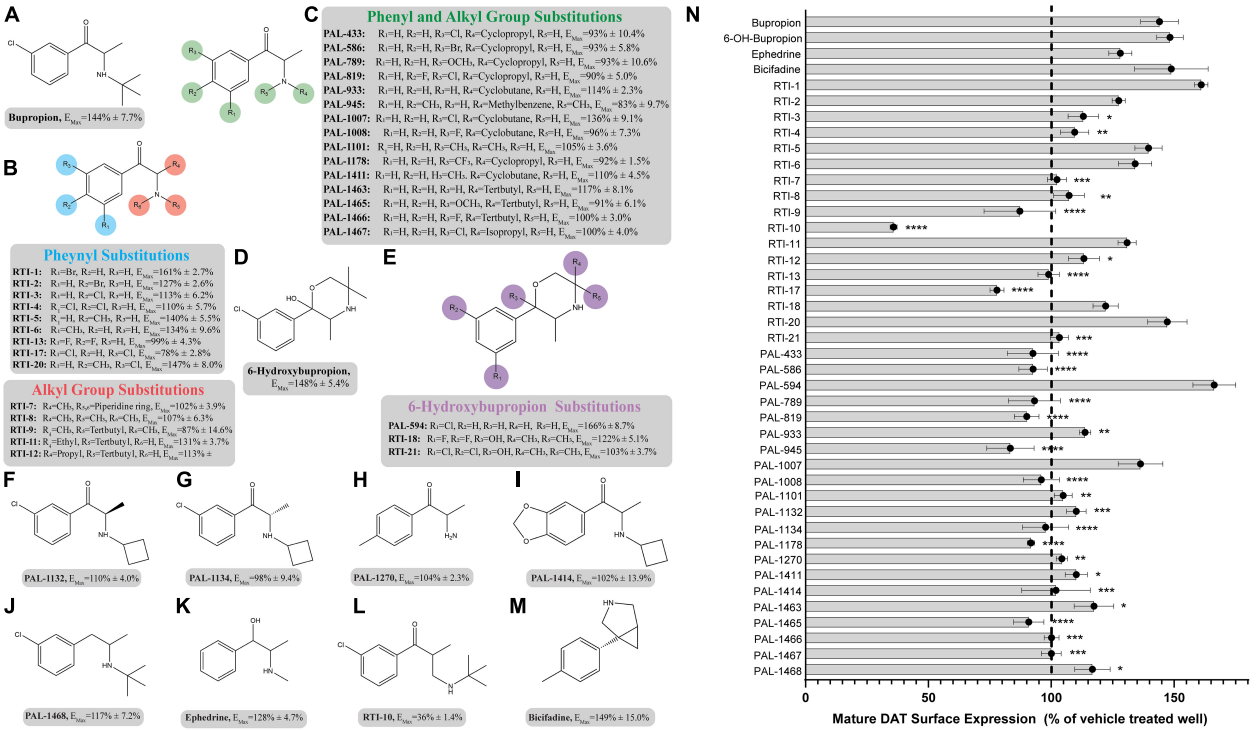

FIGURE 1 | Structures of bupropion analogs and their maximal effects (E_{Max}) on WT DAT surface expression. **(A)** Structure and E_{Max} of bupropion. **(B)** Bupropion analogs with phenyl substitutions (blue) or alkyl group substitutions (red). E_{Max} included for each compound. **(C)** Bupropion analogs with both phenyl and alkyl group substitutions. E_{Max} included for each compound. **(D)** Structure and E_{Max} of bupropion's primary metabolite, 6-Hydroxybupropion. **(E)** 6-Hydroxybupropion analogs. E_{Max} included for each compound. **(F)** Structure and E_{Max} of bupropion analog PAL-1132. **(G)** Structure and E_{Max} of bupropion analog PAL-1134. **(H)** Structure and E_{Max} of bupropion analog PAL-1270. **(I)** Structure and E_{Max} of bupropion analog PAL-1414. **(J)** Structure and E_{Max} of bupropion analog PAL-1468. **(K)** Structure and E_{Max} of bupropion analog ephedrine. **(L)** Structure and E_{Max} of bupropion analog RTI-10. **(M)** Structure and E_{Max} of bupropion analog bicifadine. **(N)** Bar graph of bupropion analogs E_{Max} (****$p < 0.0001$, ***$p < 0.001$, **$p < 0.01$, and *$p < 0.05$, one-way ANOVA compared to bupropion with Dunnett's test). Analogs are grouped in gray boxes based on similarities to the bupropion backbone. Data were normalized to vehicle treatment.

effects of select compounds on the surface expression of β2AR, an unrelated membrane protein. Alprenolol and isoproterenol were used as positive controls for increasing or decreasing β2AR surface expression, respectively (January et al., 1997; Kobayashi et al., 2009; Lam, 2013). The tested bupropion and ibogaine analogs did not significantly increase β2AR surface expression, demonstrating that their effects are selective for DAT (**Supplementary Figures 3A,B**).

Dopamine Transporter Pharmacological Chaperones Increase Total Dopamine Transporter Protein Levels

We next assessed whether drugs that increase DAT surface expression also increase total protein levels of DAT. Cells expressing YFP-HA-DAT were incubated with select test compounds and DAT protein levels were examined by western blot. The effects of the compounds were assessed on WT DAT and K590A DAT. The K590A mutant is a well-characterized ER-retained, trafficking-deficient DAT mutant (Miranda et al., 2004) that can be rescued by pharmacological chaperones (Beerepoot et al., 2016).

We compared the effects of the following five compounds on DAT protein expression: noribogaine (251 ± 17.8%), tetrahydroharmine (137 ± 6.8%), PAL-594 (166 ± 8.7%), bicifadine (149 ± 15.0%), and RTI-20 (147 ± 8.0%). These compounds were chosen because they have varying efficacy in increasing DAT surface expression. As shown in **Figure 5**, all compounds, with the exception of tetrahydroharmine, were able to significantly increase mature WT DAT protein levels, with noribogaine having the largest effect (**Figures 5A,B**). Similarly all compounds except RTI-20 had a statistically significant effect on K590A protein levels (**Figures 5C,D**). Overall, these data suggest that noribogaine and PAL-594 are the most efficacious chaperones for both WT and K590A DAT as assessed by western blot and the βlac surface expression assay.

Dopamine Transporter Inhibition and Dopamine Transporter Chaperoning Are Distinct Processes

When assessing the pharmacological chaperone efficacies of the test compounds, we noted that the reported DAT binding affinity and dopamine uptake inhibition values of the studied analogs did not appear to be predictive of their chaperone ability. These results are summarized in **Supplementary Table 1**, along with DAT binding and dopamine uptake inhibition data from Carroll et al. (2009, 2010, 2014). Five compounds, bupropion

TABLE 1 | Select bupropion analogs.

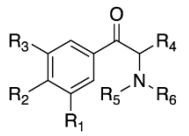

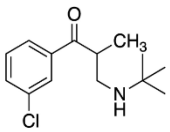

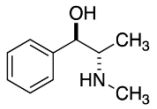

							Ephedrine
Compound	**R1**	**R2**	**R3**	**R4**	**R5**	**R6**	**E_{Max} (%)**
Bupropion	Cl	H	H	CH_3	H	tBu	144 ± 7.7%
Phenyl substitution							
RTI-1	Br	H	H	CH_3	H	tBu	161 ± 2.7%
RTI-2	H	Br	H	CH_3	H	tBu	127 ± 2.6%
RTI-3	H	Cl	H	CH_3	H	tBu	113 ± 6.2%
RTI-4	Cl	Cl	H	CH_3	H	tBu	110 ± 5.7%
RTI-5	H	CH_3	H	CH_3	H	tBu	140 ± 5.5%
RTI-6	CH_3	H	H	CH_3	H	tBu	134 ± 9.6%
RTI-13	F	F	H	CH_3	H	tBu	99 ± 4.3%
RTI-17	Cl	H	Cl	CH_3	H	tBu	78 ± 2.8%
RTI-20	Cl	CH_3	H	CH_3	H	tBu	147 ± 8.0%
Alkyl group substitution							
RTI-7	Cl	H	H	CH_3		Piperidine	102 ± 3.9%
RTI-8	Cl	H	H	CH_3	CH_3	CH_3	107 ± 6.3%
RTI-9	Cl	H	H	CH_3	CH_3	tBu	87 ± 14.6%
PAL-1007	Cl	H	H	CH_3	H	Cyclobutane	136 ± 9.1%
RTI-11	Cl	H	H	CH_2CH_3	H	tBu	131 ± 3.7%
RTI-12	Cl	H	H	$CH_2CH_2CH_3$	H	tBu	113 ± 6.3%
PAL-1270	H	CH_3	H	CH_3	H	H	104 ± 2.3%
Other analogs							
Ephedrine	–	–	–	–	–	–	128 ± 4.7%
RTI-10	–	–	–	–	–	–	36 ± 1.4%
PAL-945	H	CH_3	H	CH_3	CH_3	Benzyl	83 ± 9.7%
PAL-1101	CH_3	H	H	CH_3	H	CH_3	105 ± 3.6%
PAL-1411	CH_3	H	H	CH_3	H	Cyclobutane	110 ± 4.5%

(144 ± 7.7%), RTI-2 (127 ± 2.6%), RTI-5 (140 ± 5.5%), RTI-6 (134 ± 9.6%), and RTI-11 (131 ± 3.7%), highlight the major trends in the table. Specifically, RTI-5 and RTI-11 show similar surface expression chaperoning efficacies of 140 ± 5.5 and 131 ± 3.7%, respectively. However, RTI-5 (140 ± 5.5%) has a K_i of > 10,000 nM and an IC_{50} of 6,840 nM, thus suggesting it has poor inhibition and essentially no binding affinity for DAT (Carroll et al., 2009). Comparatively, RTI-11 (131 ± 3.7%) has a K_i of 459 nM and IC_{50} of 31 nM (Carroll et al., 2014). RTI-4 (110 ± 5.7%) has nearly no chaperone effect on DAT but is reported to bind strongly to DAT and is an effective inhibitor of dopamine uptake (K_i = 472 nM and IC_{50} = 271 nM) (Carroll et al., 2009). These data suggest that there is low correlation between pharmacological chaperone efficacy and classical DAT binding affinity or dopamine uptake inhibition of DAT compounds.

Following this observation, we tested select chaperone compounds to see if they followed the same trend. **Figure 6A** shows dose response curves of uptake inhibition (left *Y*-axis) and surface expression chaperoning efficacy (right *Y*-axis) of select test compounds. This figure also shows that a compound's inhibitory effect on dopamine uptake is not strongly correlated with its chaperoning efficacy. Two curves that clearly show the absence of a strong correlation are noribogaine (251 ± 17.8%) and RTI-12 (113 ± 6.3%). Noribogaine has a maximal dopamine uptake inhibition of 76%, whereas RTI-12 has a maximal inhibition of 96%. Interestingly, the effects are reversed with regards to pharmacological chaperoning. **Figure 6B** shows that indeed there is low correlation relationship between uptake inhibition and chaperone efficacy. Altogether, the results in **Figure 6** indicate that pharmacological chaperone and inhibitory effects of DAT compounds are distinct processes.

DISCUSSION

Structure-Activity Relationship: Bupropion Scaffold

Based on the study of 37 bupropion analogs, certain structural features of bupropion appear to be necessary to increase WT DAT surface expression. Phenyl substitution seemed to be an important factor in chaperone activity. The para-bromo compound RTI-2 (127 ± 2.6%) has an efficacy similar to

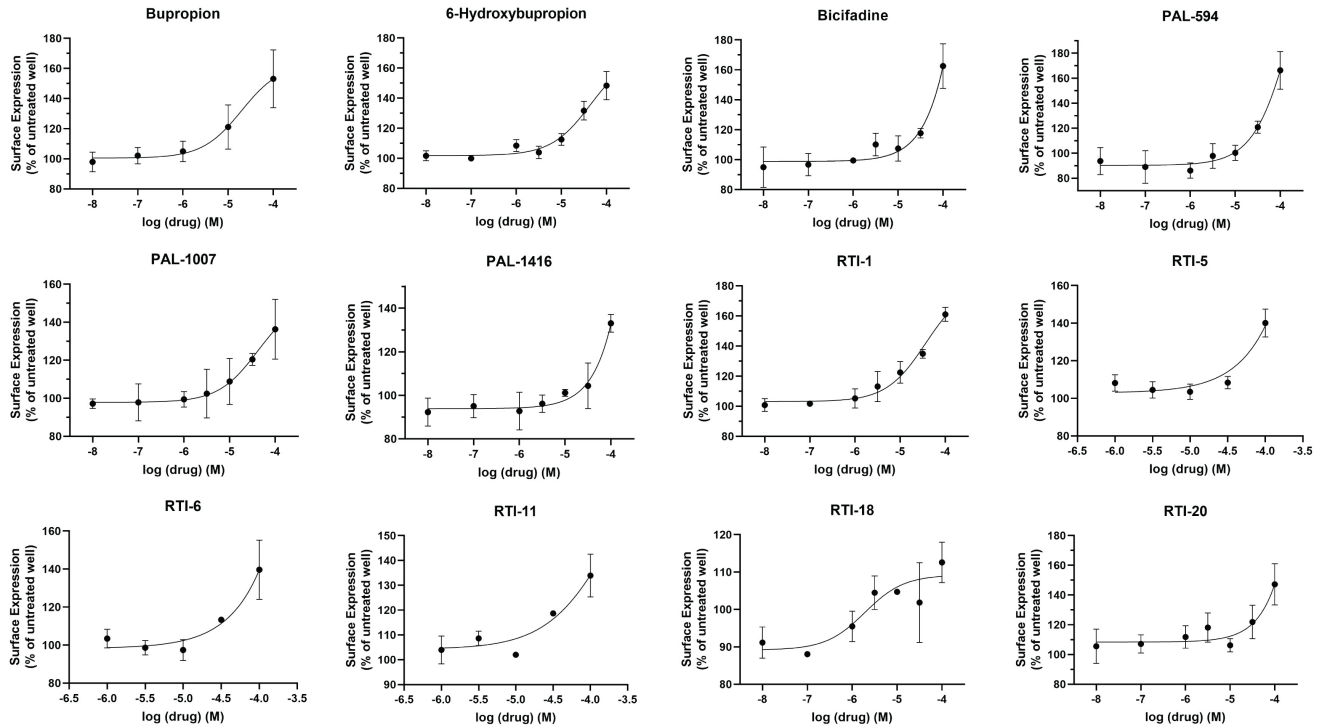

FIGURE 2 | Effect of overnight bupropion analog treatment on YFP-HA-βlac-DAT surface expression. Dose-dependent curves for most hit compounds of the bupropion backbone. Data were normalized to vehicle treatment. Data were fitted to one-site dose-response non-linear regression curves using GraphPad Prism. Data are means ± S.E.M. n = 3–6.

bupropion while the para-chloro compound RTI-3 (113 ± 6.2%) is less efficient than bupropion. Replacing a chlorine with a methyl group also affects chaperone activity, as observed when replacing the chlorine in PAL-1007 (136 ± 9.1%), which has a similar efficacy to bupropion, with a methyl in PAL-1411 (110 ± 4.5%), which is less efficient than bupropion. A similar trend is observed when comparing bupropion (144 ± 7.7%) with RTI-6 (134 ± 9.6%) although not statistically significant (**Supplementary Figure 4B**). Meta-substitution leads to more efficaciousness than para-substitution. This is observed when comparing bupropion (144 ± 7.7%) to RTI-3 (113 ± 6.2%) and comparing RTI-1 (161 ± 2.7%) to RTI-2 (127 ± 2.6%) which shows a similar trend (**Supplementary Figure 4A**). The addition of a second chloride to the ring caused a dramatic reduction in efficacy, essentially eliminating chaperone activity, as seen in RTI-4 (110 ± 5.7%), RTI-17 (78 ± 2.8%), and RTI-21 (103 ± 3.7%) (**Supplementary Figure 4C**). Interestingly, the addition of the second halogen has a favorable effect on DAT binding affinity and dopamine uptake (**Supplementary Table 1**) but is deleterious for chaperone efficacy.

A broader study of 3-phenyl substituents on bupropion showed that no other substitution improved chaperone activity. In fact, most substitutions rendered the compound inactive and less efficacious than bupropion as seen with 3-methoxy compound PAL-1465 (91% ± 6.1) and 3-fluoro compound PAL-1466 (100% ± 3.0%) (**Supplementary Figure 5A**). Similar sets of compounds were studied with an N-cyclopropyl and N-cyclobutyl in place of the N-tertbutyl group and a similar trend was observed. The N-cyclobutyl series mirrored the N-terbutyl series, with the 3-chloro compound PAL-1007 (136 ± 9.1%) being similar to bupropion, while the unsubstituted analog PAL-993 (114 ± 2.3%) and 3-methyl analog PAL-1411 (110 ± 4.5%) were less efficacious than bupropion (**Supplementary Figure 5B**). The 3-fluoro analog PAL-1008 (96 ± 7.3%) was inactive. A series of N-cyclopropyl compounds was also synthesized but surprisingly, none of the compounds were active (**Supplementary Figure 5C**). PAL-433 (93 ± 10.4%), PAL-586 (93 ± 5.8%), PAL-789 (93 ± 10.6%), PAL-819 (90 ± 5.0%), and PAL-1178 (92 ± 1.2%) were all inactive.

The cyclopropyl results suggest that N-alkylation is an important factor in chaperone activity, one that possibly overrides the effects of phenyl substitution. Tertiary amines RTI-7 (102 ± 3.9%), RTI-8 (107 ± 6.3%), RTI-9 (87 ± 14.6%), and PAL-945 (83 ± 9.7%) were less effective than bupropion (**Supplementary Figure 6A**). Smaller alkyl groups such as in the N-methyl compound PAL-1101 (105 ± 3.6%), and the primary amine PAL-1270 (104 ± 2.3%) were also less effective than bupropion (**Supplementary Figure 6B**). Interestingly, the N-cyclobutyl analog PAL-1007 (136 ± 9.1%), had similar activity to bupropion but the N-cyclopropyl analog PAL-433 (93 ± 10.4%) was completely inactive. The N-isopropyl analog PAL-1467 (100 ± 4.0%) was also inactive (**Supplementary Figure 6C**). These data suggest that chaperone activity required a somewhat bulky alkyl group on the amine, but a hydrogen

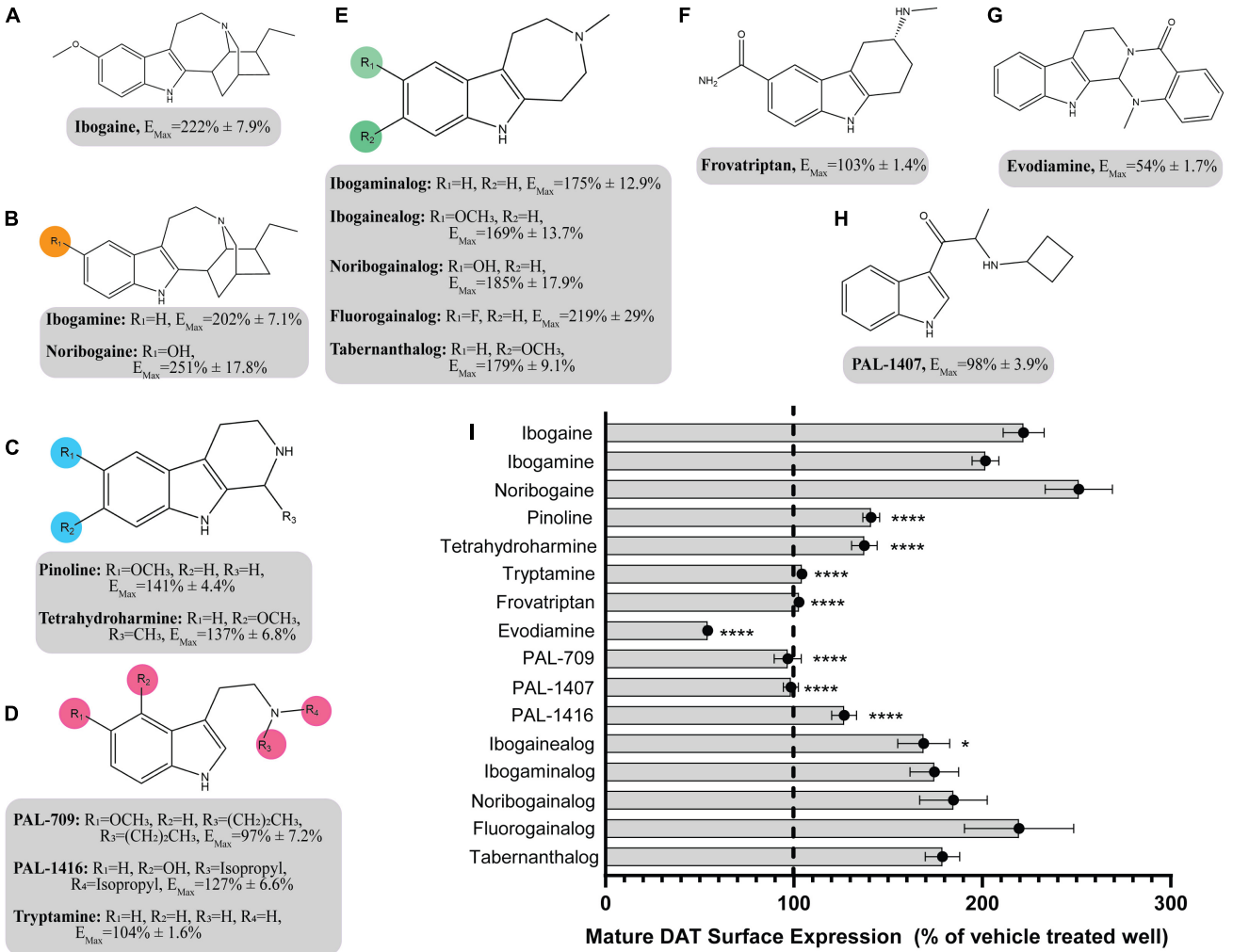

FIGURE 3 | Structures of ibogaine analogs and their effects (E_{Max}) on WT DAT surface expression. **(A)** Structure and E_{Max} of ibogaine. **(B)** Ibogaine analogs. E_{Max} included for each compound. **(C)** The βCarbolines. E_{Max} included for each compound. **(D)** Tryptamine analogs. E_{Max} included for each compound. **(E)** Analogs without the isoquinuclidine substituent. E_{Max} included for each compound. **(F)** Structure and E_{Max} of frovatriptan. **(G)** Structure and E_{Max} of evodiamine. **(H)** Structure and E_{Max} of PAL-1407. **(I)** Bar graph of ibogaine analogs E_{Max} (****$p < 0.0001$ and *$p < 0.05$, one-way ANOVA compared to ibogaine with Dunnett's test). Analogs are grouped in gray boxes based on similarities to the ibogaine backbone. Data were normalized to vehicle treatment.

was also needed. These trends may correlate with basicity or possibly, lipophilicity.

Differences in the alkyl chain as well as lengthening the link between the amine and phenyl ring also affected chaperone efficacy. Lengthening the chain appeared to have a negative effect on chaperone efficacy (**Supplementary Figure 7A**). Bupropion (144 ± 7.7%) and RTI-12 (113 ± 6.3%) have methyl and propyl groups, respectively. The addition of a methylene group in RTI-10 (36 ± 1.4%) also eliminated the chaperone effect, and in fact may have induced DAT internalization (**Supplementary Figure 7B**). We also observed that a ketone is not required for chaperone efficacy, as seen with ephedrine (128 ± 4.7%) (**Supplementary Figure 7C**).

Interestingly, the primary human metabolite of bupropion, 6-hydroxybupropion (148 ± 5.4%), which is obtained by oxidation of one of the t-butyl methyl groups, had similar efficacy as bupropion (144 ± 7.7%). This is a bit surprising given the large structural differences between the two scaffolds. However, phenyl morpholines have been shown to be good DAT ligands (Lukas et al., 2010). As with the bupropion analogs, the di-chloro 6-hydroxybupropion analog RTI-21 (103 ± 3.7%) was less efficacious than bupropion (**Supplementary Figure 8A**). PAL-594 (166 ± 8.7%), in which the hydroxyl and methyl groups have been removed had similar efficacy as bupropion (**Supplementary Figure 8B**). This was an interesting finding because one explanation for the activity of 6-hydroxybupropion could be that the compound binds in its ring-opened form, which is bupropion with a hydroxyl on one of the t-butyl methyl groups (**Supplementary Figure 9**). PAL-594 (166 ± 8.7%) cannot ring open suggesting that its activity is probably due to the ring-closed morpholine structure. This should be explored further to elucidate the mechanism behind this observation.

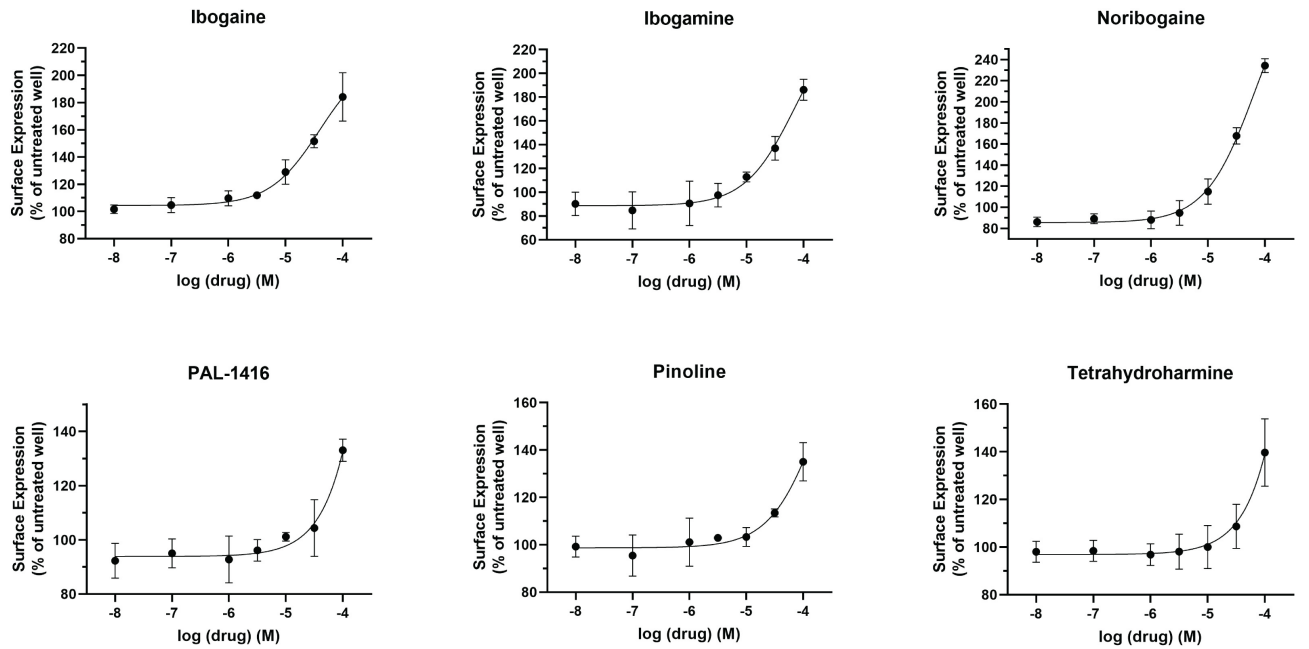

FIGURE 4 | Effect of overnight ibogaine analog treatment on YFP-HA-βlac-DAT surface expression. Dose-dependent curves for ibogaine analogs of interest. Data were normalized to vehicle treatment. Data were fitted to one-site dose-response non-linear regression curves using GraphPad Prism. Data are means ± S.E.M. n = 3–6.

Finally, the small phenylamine triple uptake inhibitor bicifadine (149 ± 15.0%) (Basile et al., 2007) was found to be just as efficacious as bupropion and may represent another scaffold from which to develop pharmacological chaperones (**Supplementary Figure 10A**). It should be noted that the 4-methyl analog of bupropion RTI-5 (140 ± 5.5%) was also similarly efficacious as bupropion (**Supplementary Figure 10B**).

Structure-Activity Relationship: Ibogaine Scaffold

The SAR of the ibogaine backbone was not nearly as extensive as that of bupropion due to the difficulty of synthesizing ibogaine analogs. However, several structural trends were evident. Although not statistically significant, our observations show that replacing the methoxy group of ibogaine (222 ± 7.9%) with a hydroxyl group on noribogaine (251 ± 17.8%) results in a slightly higher chaperone efficacy trend. Interestingly, removal of the methoxy group resulted in trends toward reduction of chaperone efficacy, as seen with ibogamine (202 ± 7.1%) (**Supplementary Figure 11**). Our observatons are in line with reports from other groups showing that noribogaine has a slightly bigger efficacy than ibogaine as a pharmacological chaperone (Kasture et al., 2016).

Deconstruction of the ibogaine ring system was explored in order to determine if the complex ring system is required for chaperone activity. Three of the seven analogs with the isoquinuclidine ring removed were less efficacious than ibogaine (pinoline, tetrahydroharmine, and ibogainealog). The methoxy, hydroxy, and unsubstituted analogs ibogainealog (169 ± 13.7%), ibogaminalog (175 ± 12.9%), noribogainalog (185 ± 17.9%), and tabernanthalog (179 ± 9.1%) lost approximately half their chaperone efficacy compared to ibogaine (222 ± 7.9%) with only ibogainealog achieving statistical significance (**Figure 3** and **Supplementary Figure 12A**). The fluorinated compound, fluorogainalog (219 ± 29.0%), had an efficacy comparable to ibogaine (222 ± 7.9%). Interestingly, a recent paper by Bhat et al. (2021), also reported that a fluorinated tropane analog of ibogaine had enhanced chaperone efficacy on DAT. In fact, in our studies we also observed that the presence of other halogens such as bromine and chlorine were shown to be toxic for cells (data not shown). The tetrahydroharmine pinoline (141 ± 4.4%) which has lower efficacy than ibogaine, lacks the isoquinuclidine ring and contains a smaller ring (6-membered vs. 7-membered), suggesting that ring size matters (**Supplementary Figure 12B**). The natural product evodiamine (54 ± 1.7%), which has a tetrahydroharmine embedded in the structure, was also studied. Surprisingly, evodiamine may also induce DAT internalization, with an E_{Max} of only 54%.

Tryptamines are biogenic amine compounds with activity on transporters but generally, they do not have chaperone efficacy in the βlac assay (**Supplementary Figure 13**). Tryptamine (104 ± 1.6%), PAL-709 (97 ± 7.2%), PAL-1416 (127 ± 6.6%), and PAL-1407 (98 ± 3.9%) vary by ring substitution and N-alkylation and were all inactive or had very little chaperone activity relative to ibogaine (222 ± 7.9%). Tryptamines were studied because they are more deconstructed analogs of ibogaine and it is possible they could adapt a suitable conformation to be chaperones, similar to noribogaine (251 ± 17.8%), due to the highly flexible carbon chain and tertiary amine. However, their E_{Max} values appear

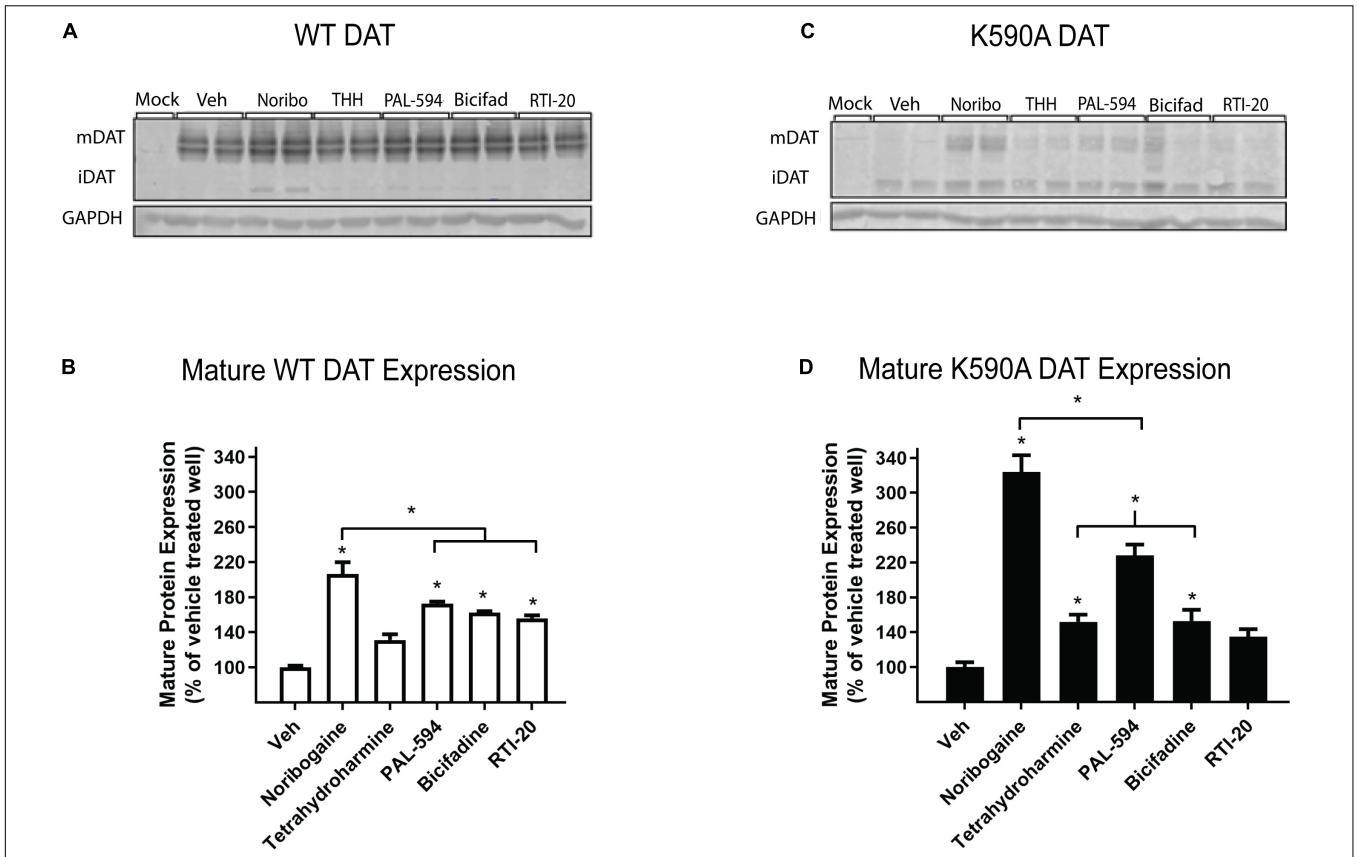

FIGURE 5 | Effect of noribogaine, tetrahydroharmine, PAL-594, bicifadine, and RTI-20 on WT and K590A DAT expression. **(A)** Representative blot of WT DAT cells treated overnight with 100 μM noribogaine, tetrahydroharmine, PAL-594, Bicifadine, and RTI-20. Mature, fully glycosylated DAT (mDAT = 110 kDa) and immature, ER-resident DAT (iDAT = 75 kDa) are shown. **(B)** Quantification of WT mDAT protein levels. Data are means ± S.E.M; * = $P < 0.05$; $n = 3$–4. **(C)** Representative blot of K590A DAT cells. Mature, fully glycosylated DAT (mDAT = 110 kDa) and immature, ER-resident DAT (iDAT = 75 kDa) are shown. **(D)** Quantification of K590A mDAT protein levels. Data are means ± S.E.M; * = $P < 0.05$; $n = 3$–4.

to indicate otherwise and thus, further work on the tryptamine scaffold may be futile.

When combined, these studies show that the complex ring system of ibogaine may be required for chaperone activity. In support of this, a recent study has shown that several ibogaine analogs, with the isoquinuclidine ring replaced by a tropane ring, maintain similar levels of chaperone efficacy as ibogaine (Bhat et al., 2021). In that study one or two analogs also displayed enhanced potency.

Discrepancy Between Dopamine Uptake Inhibition and Chaperoning Effect

Figure 6 shows there is very low correlation between pharmacological chaperone efficacy and dopamine uptake inhibition. Conventionally, this discrepancy could be explained by differing binding affinities between the extracellular transporter and the ER-resident intermediates. Indeed, it is possible that changes in intracellular ion concentrations could alter binding affinity of inhibitors (Amejdki-Chab et al., 1992; Chen et al., 2002). Furthermore, the immature DAT intermediates that are the targets for pharmacological chaperones are likely to have different affinities for inhibitors due to incomplete folding, unprocessed glycosylation, and interactions with chaperone proteins. Generally, pharmacological chaperones have lower potencies than what their reported binding affinities would suggest (Leidenheimer and Ryder, 2014). Though this explanation could provide insight to the observed dosing discrepancy, it does not explain the lack of correlation between the two effects.

One other explanation is that the various ligands stabilize different conformations of DAT. It is reported that classical inhibitors, such as cocaine, stabilize an outward-facing conformation of the transporter while atypical inhibitors, such as bupropion and ibogaine, induce an inward-facing or occluded conformation (Schmitt et al., 2013). Previous studies have suggested that compounds inducing an inward-facing or occluded conformation also exhibit a chaperone effect, as is the case with bupropion and ibogaine (Beerepoot et al., 2016). As such, some of the discrepancies we have noted with the analogs tested in this study could potentially be due to the different conformations stabilized by these compounds. Therefore, greater chaperoning efficacy may indicate that the analogs stabilize inward-facing or occluded DAT conformations.

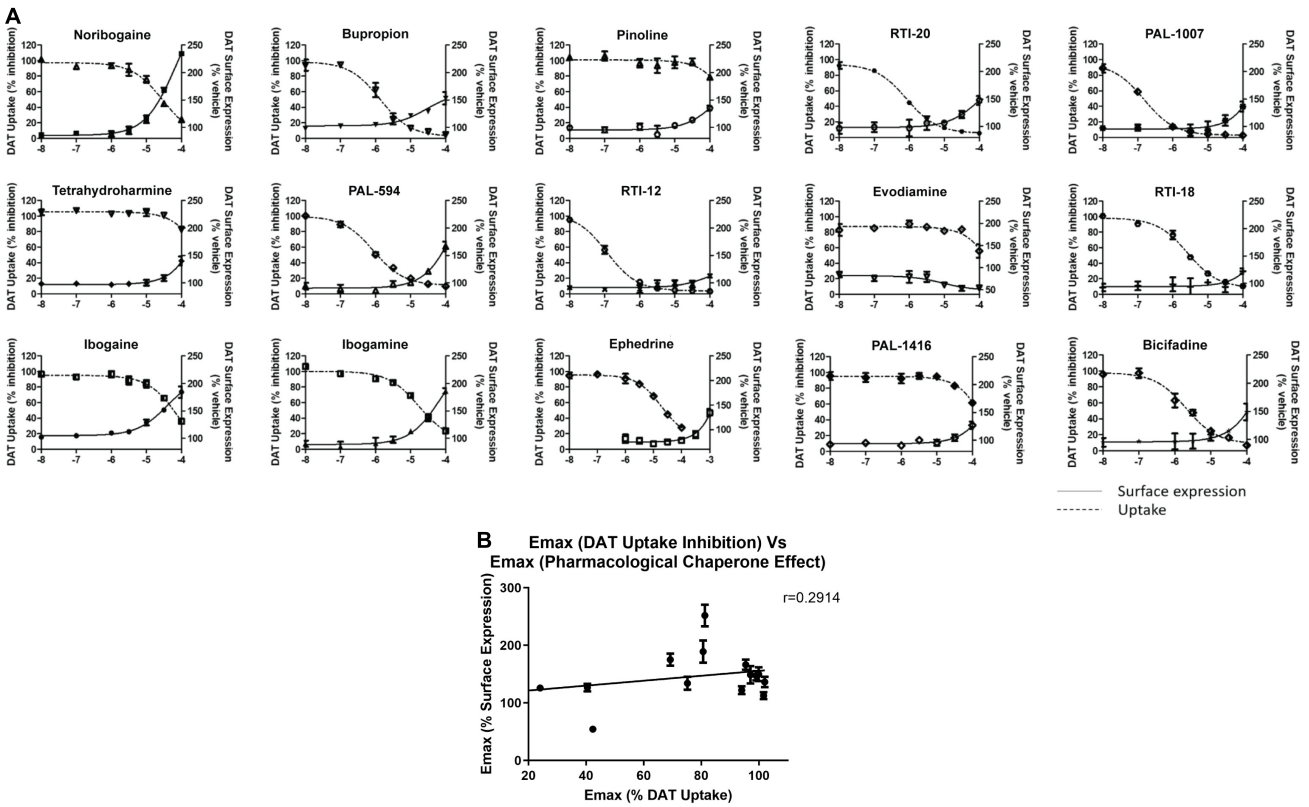

FIGURE 6 | Comparison of dopamine uptake inhibition and DAT surface expression for hit compounds. **(A)** Dose responses of 15 hit compounds are represented with uptake inhibition represented on the left *Y*-axis and surface expression on the right *Y*-axis. Doses used are half-log dilutions between 100 μM and 100 nM, with 2 full log dilutions yielding 10 and 1 nM. Data were normalized to vehicle treatment. Data were fitted to one-site dose-response non-linear regression curves using GraphPad Prism. Data are means ± S.E.M. **(B)** Correlation graph of pharmacological chaperone E_{Max} (*y*-axis) and dopamine uptake inhibition E_{Max} (*x*-axis) of the 15 compounds in **(A)**. There was low correlation between pharmacological chaperone effect and dopamine uptake inhibition as demonstrated by the Pearson correlation coefficient, $r = 0.2914$. Data are means ± S.E.M.

Future molecular dynamics and modeling studies will be needed to better understand what conformations within the transporter underlie the pharmacological chaperone activity of various compounds.

CONCLUSION

In this study we identified some key structural features required for high chaperone efficacy on DAT (**Supplementary Figure 14**). These include the isoquinuclidine group and hydroxyl substituent on the ibogaine backbone. For bupropion we found that the secondary amine and halogen derivation at the meta position are necessary for chaperone activity. While we did identify these important features that affect chaperone efficacy, we were less successful in identifying features that would increase potency. Thus, future work should be focused on identifying compounds with increased chaperone potency. A recent study identified a tropane-based ibogaine analog that displayed high efficacy and restored dopamine uptake of a DTDS disease-causing DAT variant up to 40% of that of WT DAT. This exceeds the restored uptake by noribogaine by approximately fourfold (Bhat et al., 2021). Studies such as these lay the groundwork for discovering more potent DAT pharmacological chaperones. By consolidating SAR data from our study and others, the search for potent and efficacious DAT pharmacological chaperones will be greatly accelerated.

DATA AVAILABILITY STATEMENT

The original contributions presented in the study are included in the article/**Supplementary Material**, further inquiries can be directed to the corresponding author/s.

AUTHOR CONTRIBUTIONS

CS, EQW, HH, PB, RN, and DH carried out the experiments. CS, EQW, HH, PB, RN, DH, AJR, BB, and AS analyzed data. EQW, BB, and AS wrote the manuscript. CS, EQW, HH, PB, RN, DH, AJR, DCM, DEO, BB, and AS edited the manuscript. DCM, DEO, and BB contributed unique reagents. All authors contributed to the article and approved the submitted version.

FUNDING

CS was supported by the CGS-M CIHR Master's Fellowship. PB was supported by the CIHR Doctoral Fellowship. This research was supported by a CIHR operating grant 407961 to AS, an NIH grant R01DA12970 to BB, an NSERC discovery grant RGPIN-201806409 to AJR, and an NIH grant R01GM128997 to DEO.

ACKNOWLEDGMENTS

We thank members of Salahpour and Ramsey labs for helpful discussions.

SUPPLEMENTARY MATERIAL

The Supplementary Material for this article can be found online at: https://www.frontiersin.org/articles/10.3389/fncel.2022.832536/full#supplementary-material

Supplementary Figure 1 | YFP-HA-DAT Immunoblot Bands. First lane: molecular weight ladder. Second lane: YFP-HA-DAT with two bands representing mature DAT (110 kDa) and immature, ER-resident DAT (75 kDa).

Supplementary Figure 2 | Dose response inhibition of dopamine uptake by bupropion on WT and YFP-HA-βlac-DAT. Data were normalized to vehicle treatment. Data are means ± S.E.M.

Supplementary Figure 3 | E_{Max} comparison between βlac-DAT and βlac-β2AR surface expression of hit compounds showing selectivity of chaperones for βlac-DAT. **(A)** Summary of the maximum observed effects of hit compounds on WT DAT surface expression. Data were normalized to vehicle treatment and analyzed with one-way ANOVA (****$p < 0.0001$, ***$p < 0.001$, **$p < 0.01$, and *$p < 0.05$, one-way ANOVA compared to vehicle with Dunnett's test). **(B)** Summary of the maximum observed effects of hit compounds on β2AR. Data were normalized to vehicle treatment and analyzed with one-way ANOVA (****$p < 0.0001$, ***$p < 0.001$, **$p < 0.01$, and *$p < 0.05$, one-way ANOVA compared to vehicle with Dunnett's test). The final concentration of drugs used was 100 μM, except for ephedrine at 1 mM. Data are means ± S.E.M; $n = 3$–6.

Supplementary Figure 4 | Impact of phenyl substitutions on the efficacy of bupropion in the WT DAT blac assay. **(A)** Impact of para substitution compared to meta substitution on chaperone efficacy. **(B)** Impact of phenyl substitution at the meta position on chaperone efficacy. **(C)** Impact of addition of a second Cl on chaperone efficacy.

Supplementary Figure 5 | Broader study of the impact of phenyl substitutions on the efficacy of bupropion in the WT DAT blac assay. **(A)** Impact of 3-phenyl substitutions on chaperone efficacy of compounds with an N-tertbutyl group. **(B)** Impact of 3-phenyl substitutions on chaperone efficacy of compounds with an N-cyclobutyl group. **(C)** Impact of 3-phenyl substitutions on chaperone efficacy of compounds with an N-cyclopropyl group.

Supplementary Figure 6 | Impact of N-alkylation on the efficacy of bupropion in the WT DAT blac assay. **(A)** Impact of tertiary amines on chaperone efficacy. **(B)** Impact of smaller alkyl groups on chaperone efficacy. **(C)** Impact of iso-alkyl groups on chaperone efficacy.

Supplementary Figure 7 | Effect of the alkyl chain length and ketone substituent on the efficacy of bupropion in the WT DAT blac assay. **(A)** Impact of alkyl chain length on chaperone efficacy. **(B)** Impact of the addition of a methylene group on chaperone efficacy. **(C)** Impact of the addition of a ketone on chaperone efficacy.

Supplementary Figure 8 | Efficacy of 6-hydroxybupropion in the WT DAT blac assay. **(A)** Impact of the addition of a second halogen on chaperone efficacy of 6-hydroxybupropion. **(B)** Impact of the removal of hydroxyl and methyl groups from 6-hydroxybupropion on chaperone efficacy.

Supplementary Figure 9 | Demonstration of bupropion converted to its metabolite 6-hydroxybupropion.

Supplementary Figure 10 | Bicifadine and RTI-5 are potential bupropion analogues to be explored further for SAR analysis. **(A)** Bupropion and bicifadine have similar chaperone efficacy. **(B)** Bupropion and RTI-5 have similar chaperone efficacy.

Supplementary Figure 11 | Effect of the hydroxyl substitution on the efficacy of ibogaine in the WT DAT βlac assay.

Supplementary Figure 12 | Effect of the isoquinuclidine substituent and ring size on the efficacy of ibogaine in the WT DAT blac assay. **(A)** Impact of the removal of the isoquinuclidine substituent in addition to various phenyl substitutions on chaperone efficacy. **(B)** Impact of ring size on chaperone efficacy.

Supplementary Figure 13 | Effect of the tryptamines on the efficacy of tryptamine analogs in the WT DAT βlac assay.

Supplementary Figure 14 | Key structural features of bupropion and ibogaine for pharmacological chaperone efficaciousness. **(A)** Bupropion's key structural features for pharmacological chaperone activity include the halogen derivation at the meta position (pink) and the secondary amine (green). **(B)** Ibogaine's key structural features for pharmacological chaperone activity include hydroxyl substitution (blue) and the presence of the isoquinuclidine group (orange).

REFERENCES

Amejdki-Chab, N., Benmansour, S., Costentin, J., and Bonnet, J.-J. (1992). Effects of Several Cations on the Neuronal Uptake of Dopamine and the Specific Binding of [3H]GBR 12783: Attempts to Characterize the Na+ Dependence of the Neuronal Transport of Dopamine. *J. Neurochem.* 59, 1795–1804. doi: 10.1111/j.1471-4159.1992.tb11012.x

Asjad, H. M. M., Kasture, A., El-Kasaby, A., Sackel, M., Hummel, T., Freissmuth, M., et al. (2017). Pharmacochaperoning in a Drosophila model system rescues human dopamine transporter variants associated with infantile/juvenile parkinsonism. *J. Biol. Chem.* 292, 19250–19265. doi: 10.1074/JBC.M117.797092

Basile, A. S., Janowsky, A., Golembiowska, K., Kowalska, M., Tam, E., Benveniste, M., et al. (2007). Characterization of the Antinociceptive Actions of Bicifadine in Models of Acute, Persistent, and Chronic Pain. *J. Pharmacol. Exp. Ther.* 321, 1208–1225. doi: 10.1124/JPET.106.116483

Beerepoot, P., Lam, V. M., and Salahpour, A. (2015). A β-lactamase based assay to measure surface expression of membrane proteins. *Methods Mol. Biol.* 1270, 107–114. doi: 10.1007/978-1-4939-2309-0_8

Beerepoot, P., Lam, V. M., and Salahpour, A. (2016). Pharmacological chaperones of the dopamine transporter rescue dopamine transporter deficiency syndrome mutations in heterologous cells. *J. Biol. Chem.* 291, 22053–22062. doi: 10.1074/jbc.M116.749119

Beerepoot, P., Nazari, R., and Salahpour, A. (2017). Pharmacological chaperone approaches for rescuing GPCR mutants: Current state, challenges, and screening strategies. *Pharmacol. Res.* 117, 242–251. doi: 10.1016/j.phrs.2016.12.036

Bhat, S., Guthrie, D. A., Kasture, A., El-Kasaby, A., Cao, J., Bonifazi, A., et al. (2021). Tropane-Based Ibogaine Analog Rescues Folding-Deficient Serotonin and Dopamine Transporters. *ACS Pharmacol. Transl. Sci.* 4, 503–516. doi: 10.1021/acsptsci.0c00102

Blough, B. E., Landavazo, A., Partilla, J. S., Baumann, M. H., Decker, A. M., Page, K. M., et al. (2014). Hybrid dopamine uptake blocker-serotonin releaser ligands: a new twist on transporter-focused therapeutics. *ACS Med. Chem. Lett.* 5, 623–627. doi: 10.1021/ML500113S

Blough, B. E., Rothman, R., Landavazo, A., Page, K. M., and Decker, A. M. (2011). *Phenylmorpholines and analogues thereof. Patent No.WO 2011/146850 A1*. USA: Research Triangle Institute

Bu, M., Farrer, M. J., and Khoshbouei, H. (2021). Dynamic control of the dopamine transporter in neurotransmission and homeostasis. *Npj Parkinson's Dis.* 7:22. doi: 10.1038/s41531-021-00161-2

Bulling, S., Schicker, K., Zhang, Y. W., Steinkellner, T., Stockner, T., Gruber, C. W., et al. (2012). The mechanistic basis for noncompetitive ibogaine inhibition of serotonin and dopamine transporters. *J. Biol. Chem.* 287, 18524–18534. doi: 10.1074/jbc.M112.343681

Cameron, L. P., Tombari, R. J., Lu, J., Pell, A. J., Hurley, Z. Q., Ehinger, Y., et al. (2020). A non-hallucinogenic psychedelic analogue with therapeutic potential. *Nature* 589, 474–479. doi: 10.1038/s41586-020-3008-z

Cao, R., Peng, W., Wang, Z., and Xu, A. (2007). beta-Carboline Alkaloids: Biochemical and Pharmacological Functions. *Curr. Med. Chem.* 14, 479–500. doi: 10.2174/092986707779940998

Carroll, F. I., Blough, B. E., Abraham, P., Mills, A. C., Holleman, J. A., Wolckenhauer, S. A., et al. (2009). Synthesis and biological evaluation of bupropion analogues as potential pharmacotherapies for cocaine addiction. *J. Med. Chem.* 52, 6768–6781. doi: 10.1021/JM901189Z

Carroll, F. I., Blough, B. E., Mascarella, S. W., Navarro, H. A., Eaton, J. B., Lukas, R. J., et al. (2010). Synthesis and biological evaluation of bupropion analogues as potential pharmacotherapies for smoking cessation. *J. Med. Chem.* 53, 2204–2214. doi: 10.1021/jm9017465

Carroll, F. I., Blough, B. E., Mascarella, S. W., Navarro, H. A., Lukas, R. J., and Damaj, M. I. (2014). Bupropion and bupropion analogs as treatments for CNS disorders. *Adv. Pharmacol.* 69, 177–216. doi: 10.1016/B978-0-12-420118-7.00005-6

Carroll, F. I., Muresan, A. Z., Blough, B. E., Navarro, H. A., Mascarella, S. W., Eaton, J. B., et al. (2011). Synthesis of 2-(substituted phenyl)-3,5,5-trimethylmorpholine analogues and their effects on monoamine uptake, nicotinic acetylcholine receptor function, and behavioral effects of nicotine. *J. Med. Chem.* 54, 1441–1448. doi: 10.1021/JM1014555/SUPPL_FILE/JM1014555_SI_001.PDF

Chen, N.-H., Ding, J.-H., Wang, Y.-L., and Reith, M. E. A. (2002). Modeling of the Interaction of Na+ and K+ with the Binding of the Cocaine Analogue 3β-(4-[125I]Iodophenyl)tropane-2β-Carboxylic Acid Isopropyl Ester to the Dopamine Transporter. *J. Neurochem.* 68, 1968–1981. doi: 10.1046/j.1471-4159.1997.68051968.x

Efimova, E. V., Gainetdinov, R. R., Budygin, E. A., and Sotnikova, T. D. (2016). Dopamine transporter mutant animals: A translational perspective. *J. Neurogen.* 30, 5–15. doi: 10.3109/01677063.2016.1144751

Hamilton, P. J., Campbell, N. G., Sharma, S., Erreger, K., Herborg Hansen, F., Saunders, C., et al. (2013). De novo mutation in the dopamine transporter gene associates dopamine dysfunction with autism spectrum disorder. *Mol. Psychiat.* 18, 1315–1323. doi: 10.1038/mp.2013.102

Hanrahan, J. W., Sampson, H. M., and Thomas, D. Y. (2013). Novel pharmacological strategies to treat cystic fibrosis. *Trends Pharmacol. Sci.* 34, 119–125. doi: 10.1016/j.tips.2012.11.006

Hansen, F. H., Skjørringe, T., Yasmeen, S., Arends, N. V., Sahai, M. A., Erreger, K., et al. (2014). Missense dopamine transporter mutations associate with adult parkinsonism and ADHD. *J. Clin. Investigat.* 124, 3107–3120. doi: 10.1172/JCI73778

January, B., Seibold, A., Whaley, B., Hipkin, R. W., Lin, D., Schonbrunn, A., et al. (1997). β2-Adrenergic receptor desensitization, internalization, and phosphorylation in response to full and partial agonists. *J. Biol. Chem.* 272, 23871–23879. doi: 10.1074/jbc.272.38.23871

Kasture, A., El-Kasaby, A., Szöllosi, D., Mazhar Asjad, H. M., Grimm, A., Stockner, T., et al. (2016). Functional rescue of a misfolded Drosophila melanogaster dopamine transporter mutant associated with a sleepless phenotype by pharmacological chaperones. *J. Biol. Chem.* 291, 20876–20890. doi: 10.1074/jbc.M116.737551

Kobayashi, H., Ogawa, K., Yao, R., Lichtarge, O., and Bouvier, M. (2009). Functional rescue of β1-adrenoceptor dimerization and trafficking by pharmacological chaperones. *Traffic* 10, 1019–1033. doi: 10.1111/j.1600-0854.2009.00932.x

Koenig, X., and Hilber, K. (2015). The anti-addiction drug ibogaine and the heart: A delicate relation. *Molecules* 20, 2208–2228. doi: 10.3390/molecules20022208

Kurian, M. A., Li, Y., Zhen, J., Meyer, E., Hai, N., Christen, H. J., et al. (2011). Clinical and molecular characterisation of hereditary dopamine transporter deficiency syndrome: An observational cohort and experimental study. *Lancet Neurol.* 10, 54–62. doi: 10.1016/S1474-4422(10)70269-6

Kurian, M. A., Zhen, J., Cheng, S. Y., Li, Y., Mordekar, S. R., Jardine, P., et al. (2009). Homozygous loss-of-function mutations in the gene encoding the dopamxsine transporter are associated with infantile parkinsonism-dystonia. *J. Clin. Investigat.* 119, 1595–1603. doi: 10.1172/JCI39060

Lam, V. (2013). *Development and Validation of a Novel Quantitative Assay for Cell Surface Expression of GPCRs using a Receptor β-lactamase Fusion Protein and the Colourometric Substrate Nitrocefin*. Master's thesis. Toronto, ON: University of Toronto.

Lam, V. M., Beerepoot, P., Angers, S., and Salahpour, A. (2013). A Novel assay for measurement of membrane-protein surface expression using a β-lactamase. *Traffic* 14, 778–784. doi: 10.1111/tra.12073

Leidenheimer, N. J., and Ryder, K. G. (2014). Pharmacological chaperoning: A primer on mechanism and pharmacology. *Pharmacol. Res.* 83, 10–19. doi: 10.1016/j.phrs.2014.01.005

Lindquist, S. L., and Kelly, J. W. (2011). Chemical and biological approaches for adapting proteostasis to ameliorate protein misfolding and aggregation diseases-progress and prognosis. *Cold Spring Harbor Perspect. Biol.* 3:a004507. doi: 10.1101/cshperspect.a004507

Lukas, R. J., Muresan, A. Z., Damaj, M. I., Blough, B. E., Huang, X., Navarro, H. A., et al. (2010). Synthesis and characterization of in vitro and in vivo profiles of hydroxybupropion analogues: aids to smoking cessation. *J. Med. Chem.* 53, 4731–4748. doi: 10.1021/JM1003232

Mazei-Robison, M. S., Bowton, E., Holy, M., Schmudermaier, M., Freissmuth, M., Sitte, H. H., et al. (2008). Anomalous dopamine release associated with a human dopamine transporter coding variant. *J. Neurosci.* 28, 7040–7046. doi: 10.1523/JNEUROSCI.0473-08.2008

Miranda, M., Sorkina, T., Grammatopoulos, T. N., Zawada, W. M., and Sorkin, A. (2004). Multiple molecular determinants in the carboxyl terminus regulate dopamine transporter export from endoplasmic reticulum. *J. Biol. Chem.* 279, 30760–30770. doi: 10.1074/jbc.M312774200

Morello, J. P., Bouvier, M., Petäjä-Repo, U. E., and Bichet, D. G. (2000a). Pharmacological chaperones: A new twist on receptor folding. *Trends Pharmacol. Sci.* 21, 466–469. doi: 10.1016/S0165-6147(00)01575-3

Morello, J.-P., Salahpour, A., Laperrière, A., Bernier, V., Arthus, M.-F., Lonergan, M., et al. (2000b). Pharmacological chaperones rescue cell-surface expression and function of misfolded V2 vasopressin receptor mutants. *J. Clin. Invest.* 105, 887–895. doi: 10.1172/JCI8688

Ng, J., Zhen, J., Meyer, E., Erreger, K., Li, Y., Kakar, N., et al. (2014). Dopamine transporter deficiency syndrome: Phenotypic spectrum from infancy to adulthood. *Brain* 137, 1107–1119. doi: 10.1093/brain/awu022

Obach, R. S., Pablo, J. and Mash, D. C. (1998). Cytochrome P4502D6 catalyzes the O-demethylation of the psychoactive alkaloid ibogaine to 12-hydroxyibogamine. *Drug Metab. Dispos.* 25, 1359–69.

Petäjä-Repo, U. E., Hogue, M., Laperrière, A., Walker, P., and Bouvier, M. (2000). Export from the endoplasmic reticulum represents the limiting step in the maturation and cell surface expression of the human δ opioid receptor. *J. Biol. Chem.* 275, 13727–13736. doi: 10.1074/jbc.275.18.13727

Sanders, C. R., and Myers, J. K. (2004). Disease-related misassembly of membrane proteins. *Annu. Rev. Biophys. Biomol. Struct.* 33, 25–51. doi: 10.1146/annurev.biophys.33.110502.140348

Schmitt, K. C., Rothman, R. B., and Reith, M. E. A. (2013). Nonclassical pharmacology of the dopamine transporter: Atypical inhibitors, allosteric modulators, and partial substrates. *J. Pharmacol. Exp. Ther.* 346, 2–10. doi: 10.1124/jpet.111.191056

Schubert, U., Antón, L. C., Gibbs, J., Norbury, C. C., Yewdell, J. W., and Bennink, J. R. (2000). Rapid degradation of a large fraction of newly synthesized proteins by proteasomes. *Nature* 404, 770–774. doi: 10.1038/35008096

Wise, R. A. (2004). Dopamine, learning and motivation. *Nat. Rev. Neurosci.* 5, 483–494. doi: 10.1038/nrn1406

Conflict of Interest: DEO is a co-founder of Delix Therapeutics, Inc., and currently serves as the Chief Innovation Officer and Head of the Scientific Advisory Board. DCM is an inventor on patents pertaining to noribogaine. She is the CEO, founder and a shareholder in DemeRx, Inc.

The remaining authors declare that the research was conducted in the absence of any commercial or financial relationships that could be construed as a potential conflict of interest.

Advantages of publishing in Frontiers

OPEN ACCESS
Articles are free to read for greatest visibility and readership

FAST PUBLICATION
Around 90 days from submission to decision

HIGH QUALITY PEER-REVIEW
Rigorous, collaborative, and constructive peer-review

TRANSPARENT PEER-REVIEW
Editors and reviewers acknowledged by name on published articles

Frontiers
Avenue du Tribunal-Fédéral 34
1005 Lausanne | Switzerland

Visit us: www.frontiersin.org
Contact us: frontiersin.org/about/contact

REPRODUCIBILITY OF RESEARCH
Support open data and methods to enhance research reproducibility

DIGITAL PUBLISHING
Articles designed for optimal readership across devices

FOLLOW US
@frontiersin

IMPACT METRICS
Advanced article metrics track visibility across digital media

EXTENSIVE PROMOTION
Marketing and promotion of impactful research

LOOP RESEARCH NETWORK
Our network increases your article's readership